# QUIET DRONES 2022

## SECOND INTERNATIONAL SYMPOSIUM ON NOISE FROM UASs/UAVs and eVTOLs

## SYMPOSIUM PROCEEDINGS

**Version 4 - 13th June 2022**

JUNE 27-30, 2022

e-Symposium from Paris

INCEEUROPE

CidB
Centre d'information sur le Bruit

# Welcome

**Quiet Drones 2020**, the first International Symposium devoted to all aspects of noise and acoustics from drones and eVTOLs was held online mid-October 2020 and despite the pandemic, turned out to be a huge success in terms of attendance and delegate networking.

Extensive discussions between 170 delegates from 22 countries confirmed that, after safety, security and privacy, noise was becoming a fourth hurdle that could impede the widespread deployment of drones and eVTOLs.

Quiet Drones 2022, the second Symposium, is held as an online meeting on 27, 28 and 29 June.

It presents methods under development for establishing measurement standards on noise from drones and eVTOLs, as well as new metrics to characterize the impact of their noise on people and environment.

It explains about recent advances in the study of noise generation and control at its source as well as propagation in different flying conditions and environments.

It also presents acoustic tools for the detection and identification of drones as well as drone audition methods for search and rescue.

And it discusses public acceptance of the noise of delivery drones as well as of air taxis in European cities and the rest of the world.

This Symposium lasts 3 days and is live for about 8 hours a day with

- 4 invited keynote presentations describing international activities of exchange working groups, collaborative projects, workshops, and symposia dedicated to noise,
- over 35 papers coming from 16 countries presented in 8 structured sessions,
- two panel-discussions organized on hot topics

Jean Tourret / Dick Bowdler

## PROGRAMME AT A GLANCE

*The programme for the symposium will consist of eight technical sessions at which authors will make presentations. At the end of sessions #1 to #8 there will be a discussion centred around the session topic at which authors will be encouraged to take part. Four keynote presentations are also scheduled, as well as two panel discussions and two, more informal, conversations.*

*We are keen that delegates from all time zones will be able to view all sessions. For this reason, sessions will be recorded and published for offline viewing as soon as they are finished.*

*Please note that all times listed below are expressed in Central European Summer Time (CEST).*

### Monday June 27

**09:00** – **Welcome to participants**
**10:00** – Session # 1 – **Propeller and motor noise modelling**
**12:00** – Panel discussion #1 - **Managing Community Noise from Drone Delivery**

**13:45** – **Welcome to new participants**
**14:15** – Keynote #1 – **Advancing Aerial Mobility: A national blueprint**
**14:45** – Keynote #2 - **A Summary of the 2020 e-Workshop: Aerial Mobility - Noise Issues and Technology held at the US National Academy of Engineering**
**15:30** – Session #2 - **Acoustic Detection and Identification of Drones**
**17:15** – Conversation #1 - **Come and meet the other delegates**

### Tuesday June 28

**09:00** – Session #3 – **Drone audition for search and rescue**
**10:30** – Session #4 – **Propeller and motor noise experiments**

**14:00** – Keynote #3 – **Activities of the NASA Urban Air Mobility Noise Working Group (UNWG)**
**15:00** – Session #5 – **Assessing Noise and its Impact on People and Environment**
**16:00** – Conversation #2 – **Come and meet the other delegates**

### Wednesday June 29

**09:00** – Session #6 – **Measurements of noise produced by drones and related standards**
**11:15** – Session #7 – **Noise prediction in different environments and flying conditions**

**14:00** – Keynote #4 – **Public acceptance and noise considerations in urban air mobility research – Intermediate results of DLR’s HorizonUAM project.**
**14:45** – Session #8 – **Public Acceptance of Drones and eVTOLs in the light of noise**
**16:30** – Panel discussion #2 – **Air taxis integration in cities in the light of mobility and noise.**

## MONDAY JUNE 27

**09:00** **Welcome to participants**

Informal conversations between delegates and last information for the organisation

**10:00** **SESSION #1 – Propeller and motor noise modelling**

*Co-chairs:* Christophe Schram (VKI, BELGIUM)
Franck Cléro (ONERA, FRANCE)

| | | |
|---|---|---|
| *Aeroacoustic investigation of co-rotating rotors* | Edoardo Grande<br>Delft University of Technology | THE NETHERLANDS |
| *Computational aeroacoustics of the urban air mobility using APAC method* | Yuhong Li<br>The Hong Kong University of Science and Technology | CHINA |
| *Numerical study of the aeroacoustics of shrouded propellers for Urban AirMobility vehicles* | Sinforiano Cantos<br>The Hong Kong University of Science and Technology | CHINA |
| *Turbulence ingestion noise from multi-rotor UAVs* | Ryan McKay<br>(Dotterel Technologies) | NEW ZEALAND |
| *Application of Acoustic-Vortex Decomposition for Numerical Simulation of Drone Prop. Noise* | Sergei Timushev<br>Moscow Aviation Institute - National Research University | RUSSIA |

**Break**

**12:00** **PANEL DISCUSSION #1: Managing Community Noise from Drone Delivery**

*Organized by:* Marion Burgess (UNSW, AUSTRALIA)
Eddie Duncan (RSG, USA)

*This panel discussion will start with 2 short overview presentations (3-4 minutes) from the organisers: Eddie Duncan somewhat focussing on the US and Marion Burgess on the Asia Pacific. Before opening the general discussion, some panellists from both the operators and from the government agencies will be invited to comment on their experiences with the management of community reactions to the noise from drone deliveries, minimising annoyance and challenges in the regulatory framework. These will include Jesse Suskin from Wing Australia; Zac Kennedy from Swoop Australia; Kevin Houston from Manna Ireland; Ed Weston from CAA UK; Severine Charmant from DGAC-DTA France. The session will then be opened for a general discussion with other operators, government authorities and researchers sharing their experiences and their views on the future for drone deliveries in regard to noise matters.*

**Break**

## MONDAY JUNE 27

**13:45** — **Welcome to new participants**

**14:15** — **Keynote #1 - Advancing Aerial Mobility: A National Blueprint**

Nicholas Lappos (Lockheed Martin, USA)

*Chaired by:* George Maling (Managing director emeritus INCE-USA and NAE, USA)

**Break**

**14:45** — **Keynote #2 - A Summary of the 2020 e-Workshop: Aerial Mobility - Noise Issues and Technology held at the US National Academy of Engineering**

Robert D. Hellweg (Hellweg Acoustics, USA)

*Chaired by:* Jean Tourret (President INCE/Europe, FRANCE)

**Break**

**15:30** — **SESSION #2 - Acoustic Detection and Identification of Drones**

*Co-chairs:* Lucille Pinel- Lamotte (MicrodB, FRANCE)
Martin Blass (Joanneum Research, AUSTRIA)

| | | |
|---|---|---|
| *Towards mobile microphone array-based UAV tracking* | Martin Blass<br>Joanneum Research | AUSTRIA |
| *UAV acoustic localization in a maritime environment: from first results to improvements perspectives* | Mathis Bonotto<br>Gipsa-Lab | FRANCE |
| *Acoustic-based detection of drone noise under practical uncertainty factors* | Han Wu<br>The Hong Kong University of Science and Technology | CHINA |
| *Comparison of different processing for DOA estimation of an Unmanned Aerial Vehicle with few sensors* | Nathan Itare<br>Le Mans University | FRANCE |
| *Deeplomatics: A deep-learning based multimodal approach for aerial drone detection and localization* | Eric Bavu<br>LMSSC, CNAM Paris | FRANCE |

**Break**

**17:15** — **Conversation #1: Come and meet the other delegates**

## TUESDAY JUNE 28

### 09:00 SESSION #3 - Drone audition for search and rescue

*Co-chairs:* Antoine Deleforge (INRIA, FRANCE)
Shaun Edlin (Dotterel Technologies, NEW ZEALAND)
Michael Kingan (Auckland University, NEW ZEALAND)

| | | |
|---|---|---|
| *Improvement of Rotor Noise Reduction for Unmanned Aerial Vehicle Audition by Rotor Noise PSD Informed Beamformer Design* | Yameizhen Li<br>Acoustics Research Center, University of Auckland | NEW ZEALAND |
| *Autonomous Kiteplane System for Drone Audition* | Makoto Kumon<br>Kumamoto University | JAPAN |
| *Sound source localization and enhancement from a flying micro aerial vehicle* | Lin Wang<br>Queen Mary University of London | UK |

Break

### 10:30 SESSION #4 - Propeller and motor noise experiments

*Co-chairs:* Tiziano Pagliaroli (Unicusano, ITALY)
Hélène Parisot-Dupuis (ISAE -SUPAERO, FRANCE)

| | | |
|---|---|---|
| *Experimental analysis on pitch angle effect on a small-scale propeller to quiet drones' flight* | Paolo Candeloro<br>Unicusano | ITALY |
| *Investigation on lightweight double-leaf cylindrical microperforated-panel structures for motor noise reduction of UAVs* | Gianyujie Qian<br>Hohai University | CHINA |
| *Experimental investigation on the noise related to rotors interaction* | Tiziano Pagliaroli<br>Unicusano | ITALY |
| *An Experimental Investigation of Multi-Rotor Drone Based on Acoustic Hemisphere* | Yeong-Ju Go<br>Chungnam National University | KOREA |

Break

## TUESDAY JUNE 28

**14:00 Keynote #3: Activities of the NASA Urban Air Mobility Noise Working Group (UNWG)**

Stephen A. Rizzi (NASA Langley Research Center, USA)

*Chair:* Patricia Davies (I-INCE V-President Technical Activities, USA)

**Break**

**15:00 SESSION #5 - Assessing Noise and its Impact on People and Environment**

*Co-chairs:* Antonio J. Torija (University of Salford, UK)
Roalt Aalmoes (NLR, THE NETHERLANDS)

| | | |
|---|---|---|
| *Estimation of noise exposure due to drone operations* | Carlos Ramos-Romero<br>Acoustics Research Centre, University of Salford | UK |
| *Noise impact on humans – calculation methods and results for some conceivable applications* | Stefan Becker<br>BeSB GmbH Berlin<br>Schalltechnisches Büro | GERMANY |
| *Recent NASA research into the psychoacoustics of Urban Air Mobility (UAM) vehicles* | Andrew Christian<br>NASA | USA |
| *Experimental investigations and psychoacoustic analysis of a DJI Phantom 3 quadcopter* | Erica Gallo<br>Von Karman Institute for Fluid Dynamics | BELGIUM |

**Break**

**17:00 Conversation #2: Come and meet the other delegates**

## WEDNESDAY JUNE 29

### 09:00 SESSION #6
### Measurements of noise produced by drones and related standards

*Co-chairs:* Xin Zhang (The Hong Kong University of Science and Technology, CHINA)
Jean-Claude Guilpin (DGAC-DTA, FRANCE)

| | | |
|---|---|---|
| *Accurate measurement of Drone Noise on the ground* | Per Rasmussen<br>GRAS Sound & Vibration | DENMARK |
| *Measurement of sound emission characteristics of quadcopter drones under cruise condition* | Gert Herold<br>Technische Universität Berlin | GERMANY |
| *Estimating Unmanned Aircraft Takeoff Noise Using Hover Measurement Data* | Christopher Cutler-Wood<br>US DOT Volpe Center | USA |
| *Acoustic evaluation of multi-rotor drones in anechoic and semi-anechoic chamber* | Zhida Ma<br>The Hong Kong University of Science and Technology | CHINA |
| *Development of the standardized noise measurement procedures for unmanned aircraft system* | Siyang Zhong<br>The Hong Kong University of Science and Technology | CHINA |
| *Development of a comprehensive drone performance evaluation platform* | Alex McGinn<br>Trinity College Dublin | IRELAND |
| *Noise measurements procedures for eVTOLs* | Jean-Claude Guilpin<br>DGAC-DTA | FRANCE |

**Break**

### 11:15 SESSION #7
### Noise prediction in different environments and flying conditions

*Co-chairs:* Julien Caillet (Airbus Helicopters, FRANCE)
Ignacio Gonzalez-Martino (Dassault Systèmes, FRANCE)

| | | |
|---|---|---|
| *A virtual flight simulation platform for community drone noise assessment* | Qichen Tan<br>The Hong Kong University of Science and Technology | CHINA |
| *Numerical aerodynamics and aeroacoustics predictions of a drone under real urban environments* | Rémy Atassi<br>Dassault Systèmes | FRANCE |
| *Numerical Investigation of Noise Emissions from a Cargo eVTOL UAV* | Michael Schmähl<br>TU München | GERMANY |

**Break**

## WEDNESDAY JUNE 29

14:00 **Keynote #4:**
**Public acceptance and noise considerations in urban air mobility research – Intermediate results of DLR's HorizonUAM project.**

Bianca I. Schuchardt (DLR-FL, GERMANY)

*Chair:* Fabrice Cuzieux (ONERA, FRANCE)

14:45 **SESSION #8**
**Public Acceptance of Drones and eVTOLs in the light of noise**

*Co-chairs:* Bianca I. Schuchardt (DLR-FL, GERMANY)
Fabrice Cuzieux (ONERA, FRANCE)

| | | |
|---|---|---|
| *Drones disruptions: Exploring the social and cultural implications of drone noise* | Anna Jackman<br>University of Reading | UK |
| *Airport regions authorities dealing with drones* | Sergi Alegre Calero<br>Airport Regions Council | BELGIUM |
| *Making access to the skies seamless* | Zachary Kennedy<br>Swoop Aero | AUSTRALIA |
| *A greenery-based solution for low-noise delivery hub for unmanned aerial transport* | Claudio Pasquali<br>Università degli Studi Roma Tre | ITALY |

**Break**

## WEDNESDAY JUNE 29

**16:30** **Panel Discussion #2:**
**Air taxis integration in cities in the light of mobility and noise**

***Moderators:*** **Sergi Alegre Calero (Airport Regions Council, BELGIUM)**
**Patricia Davies (I-INCE V-President Technical Activities, Purdue Univ. USA)**

***Topics addressed:***

- information on UAM projects in European Cities.
- noise performances of eVTOLs prototypes to be integrated in those projects
- acoustic requirements and solutions for vertiports and other infrastructures
- specific situation of European cities in terms of acceptance.

***Panelists:***

- Vassilis Agourida (Airbus), leader of UAM Initiative Cities Community
- Cristina Barrado (Polytechnic University of Catalonia), involved in the CORUS-XUAM project
- Kathryn Bulanowski (European Federation of Passengers), involved in AURORA project
- Julien Caillet (Airbus Helicopters), Acoustic Expert – ETGV
- Jean-Claude Guilpin (DGAC-DTA), Head of aircraft environmental performance department
- Dominique Lazarski (President of the European Union Against Aircraft Nuisances)

# Papers in Alphabetical Order

QUIET DRONES
Second International e-Symposium
on
UAV/UAS Noise
27th to 30th June 2022

# Numerical aerodynamics and aeroacoustics predictions of a drone under real urban environments


**Authors 1: ATASSI Rémy - DASSAULT SYSTEMES: Remy.ATASSI.intern@3ds.com**
**Authors 2: PAĐEN Ivan – TU Delft: I.Paden@tudelft.nl**
**Authors 3: FUERKAITI Yunusi - TU Delft: Y.Fuerkaiti@tudelft.nl**
**Authors 4: GONZALEZ-MARTINO Ignacio - DASSAULT SYSTEMES: Ignacio.GONZALEZ-MARTINO@3ds.com**
**Authors 5: CASALINO Damiano - DASSAULT SYSTEMES: Damiano.CASALINO@3ds.com**
**Authors 6: GARCIA-SANCHEZ Clara - TU Delft: C.Garcia-Sanchez@tudelft.nl**



**Abstract**

For the purpose of studying noise impact of drones in communities and public acceptance, we aim to conduct several analysis using Very-Large Eddy Simulations (VLES), which is a mathematical model for turbulence used in computational fluid dynamics (CFD). CFD Lattice-Boltzmann unsteady simulations coupled with Ffowcs-Williams Hawkings integration method are used to predict both UAV aerodynamics and radiated acoustics.

The present study starts with a particular interest on urban flows. As a matter of fact, this first part of the study aims to predict and to understand all behavioral patterns of airflows in a specific urban area. Experimental data from wind-tunnel campaigns are used to assess and validate the numerical predictions in terms of airflows.

Then, the second part of this study is dedicated to the analysis of the performance and the aeroacoustics of a generic isolated eVTOL in real flight conditions.

Finally, the third and last part of this study carries on with the demonstration of the flight of this same drone in the urban environments we studied in the first part. With the experimental validation of our numerical model of a specific urban flow, we will have an accurate computational model to study the influence of the flight of a generic drone on the environment it flies in.

The complete study performed will allow to accurately assess the noise generated by the flight of a generic drone in a specific urban area, and the airflow interaction between the evolving field where the drone flies and the drone itself.

## 1. Introduction

Urban Air Mobility (UAM), powered with electric vertical takeoff and landing (eVTOL) vehicles, is a new opportunity for aviation that is anticipated to revolutionize the transportation system by extending it in three-dimension. Rotorcrafts are expected to become an indispensable tool due to its unique capability to take off and land vertically. Along with many others expected benefits, such as faster and safer travel, UAM noise appears to be the main barrier to the community acceptance of eVTOL operations. Indeed, these vehicles are first envisioned to operate for short-range low-altitude missions over densely populated areas not usually exposed to aircraft noise.

In recent years, there has been a growing interest and continuing investment in eVTOL aircrafts for UAM or urban air taxi operations. However, Urban Air Mobility is a challenging use case for transporting cargo and passengers in an urban environment. eVTOL vehicles are expected to fly at relatively low altitudes over populated areas that have not normally been exposed to aircraft noise. In addition, the character of the noise is expected to be different from existing helicopters and general aviation aircraft as most eVTOL designs consist of multirotor. This means that both aerodynamics and acoustics will be drastically different from conventional helicopter designs. Rotor-to-rotor aerodynamic interactions could also lead to disturbing noise, which is one of major concerns of eVTOL designs. For drones, there is the potential that new populations will routinely be exposed to aircraft noise because drones vehicles are anticipated to be flying in much greater numbers than helicopters. Vertiports will likely be located in populated areas where the eVTOLs noise will be the highest due to low altitude flight and landing/takeoff operations. All these new noise exposures and annoyance from these vehicles could limit the success of integrating eVTOLs into the transportation system.

A challenge unique to drones noise assessment is that one aircraft design may have an entirely different acoustic signature from another design in terms of its spectral and temporal characteristics. This is why, with the introduction of eVTOLs vehicles, new tools and technologies will need to be developed to reach a certain level of confidence for predicting and reducing noise.

While many research institutes have performed multidisciplinary analysis of several eVTOL designs, little consideration has been given to performance and acoustic analysis in a real urban environment. Therefore, the main objective of this study is to analyze the numerical aerodynamics and the aeroacoustics predictions of a quadrotor eVTOL design under real urban environments with high-fidelity CFD simulations. It is, therefore, in this specific context that we have defined the objectives of the study we are conducting. The first step of the study is to predict and understand all behavioral patterns of an airflow in a specific urban area and validate these numerical predictions in terms of airflows with field and wind tunnel experimental data. The second part is dedicated to the study of the performance and aeroacoustics of an isolated eVTOL in real flight conditions. Finally, the third and last part of the study is to demonstrate the flight of a generic drone in real urban environment and to obtain an accurate computational model to study the influence of the flight of a generic drone on the environment it flies in.

## 2. Computational method

In order to realize this study, we will use Lattice Boltzmann methods for fluid simulation (CFD). This method is designed for high performance in realistic conditions. With high fidelity, transient Lattice Boltzmann based solution, accurate across most flow regimes (laminar to transonic); we can solve the most complex CFD design problems in Transportation & Mobility and Aerospace & Defense. All cases are prepared, simulated and post-processed using SIMULIA PowerFLOW, a high-fidelity CFD solver based on this Lattice-Boltzmann/Very-Large Eddy Simulation (LB/VLES) method.

The relaxation time and other parameters of the equilibrium distribution function are computed by considering scales related to the turbulent motion and to the strain rate and rotation of the resolved flow field. Such a procedure is based on the paradigm of a kinetic theory applied to a “gas of eddies”. PowerFLOW has been already used in the past for a variety of large aeroacoustics problems in a variety of ground-transportation and aerospace applications and a variety of Reynolds and Mach conditions and at various degree of complexity, from component level to full vehicle. One of the crucial aspects of using this CFD solver for this application is the capability to manage complex geometries and multi-level rotations of parts, as a tilting counter-rotating rotor, in a simple and automated way from the user’s point of view. This is primarily due to the capability of the software to generate automatically the surface and volume CFD meshes starting from faceted CAD geometries imported as separate entities in a specific reference system that can be both translated and rotated.

The aerodynamic noise generated by the rotation of the rotor, as well as the interaction noise between the body and rotor is then predicted using two acoustic analogies based on the Ffowcs-Williams and Hawkings’ (FW-H) equation. Multiple cap-averaged permeable surfaces, shaped like cylinders around the aircraft geometry and wake are fitted to extract pressure, density and velocity as an input to the FW-H solver. This approach is used to determine the overall noise emission. For component analysis, the solid FW-H approach is used, where pressure is saved on the surface of the body. The resulting predictions of far-field radiated noise are used to analyze the flow phenomena responsible for the noise generation and as input to the acoustic footprint calculator to predict full flight envelope noise information according to noise certification requirements.

For the purpose of studying noise impact of drones in communities and public acceptance, we aim to conduct several analysis to predict both UAV aerodynamics and radiated acoustics. The first case study we made is an urban airflow analysis of a district of Shinjuku city in order to validate the numerical model with wind tunnel and field data. With this first case study, we obtain an accurate numerical model of an airflow in a specific urban area. We created a natural turbulence model upstream the city to simulate the turbulence and velocity inlet profile of the city. We also carried a case study on another city: Delft city center, in order to understand the influence of the geometry level of detail (LoD) on the predictions of the airflows in the city. We can mention City4CFD and 3D BAG by 3D geoinformation research group (TU Delft, 3dbag.nl) that allowed us to obtain all these data.

For the second part of our study, we have selected a drone that best fits our case of study. The eVTOL we chose is the NASA’s quadrotor concept vehicle. As a first step, we simulated this drone in an isolated domain to analyze the performance and acoustics of the drone alone. To perform this simulation, we used the Multicopter Aero and Acoustic Simulations (MAAS) workflow which is a fully automated workflow using PowerFLOW and OptyDB. In this continuity, the last step of this study is to incorporate the flight of this drone in a specific urban area with real urban flow to see how the environment where the drone flies in influence the performance and the aeroacoustics of the eVTOL. In our case, we will perform this study above the TU Delft campus.

## 3. Prediction of behavioral patterns of an airflow in a specific urban area

In order to predict all behavioral patterns of an airflow in a specific urban area and validate these numerical predictions in terms of airflows, we chose to take the case of Shinjuku city because we had access to field and wind tunnel experimental data for this city.

### 3.1 Numerical predictions of an urban airflow: Shinjuku case study

A full-scale wind tunnel has been created in PowerCASE to conduct this urban flow analysis. The dimensions of this recreated fluid domain are *6.5 km x 1.35 km x 1 km*. A natural turbulence model has been implemented upstream the city to simulate the velocity and turbulence inlet profile. This natural turbulence model is composed of three main elements: a castellated barrier wall, five Counihan vortex generators and several surface roughness elements (LEGO cube) as we can see in the Figure 1.

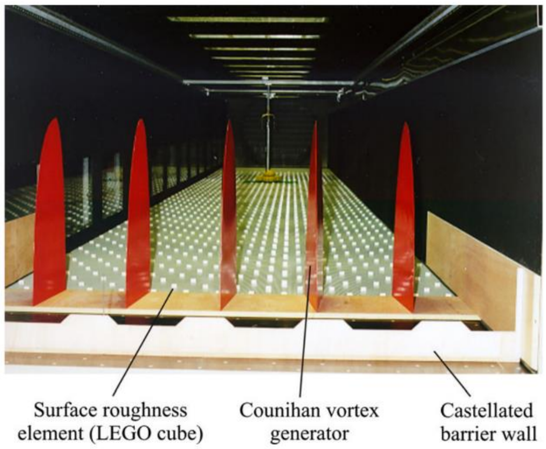


***Figure 1:*** *Elements of the natural turbulence model*

To initiate the velocity and turbulence inlet profile at the entry of the city, we setup the boundary conditions upstream the natural turbulence model with an initial velocity of 25 m/s, which is the reference velocity at 500 m that we have through the experimental data on this case study. The upper surface of the computational domain is frictionless wall with a free slip wall condition. We implemented several measurements probes all around the 3D model of the city, which correspond exactly to the locations of the field and wind tunnel measurements positions where several fluid variables are measured like the pressure, velocity or turbulence info for example. These measurements will allow us to assess the hypothesis of this study we conducted to verify that we obtain an accurate numerical model of an urban flow in a specific city. The locations of these measurements probes can be seen in the Figure 2 below.

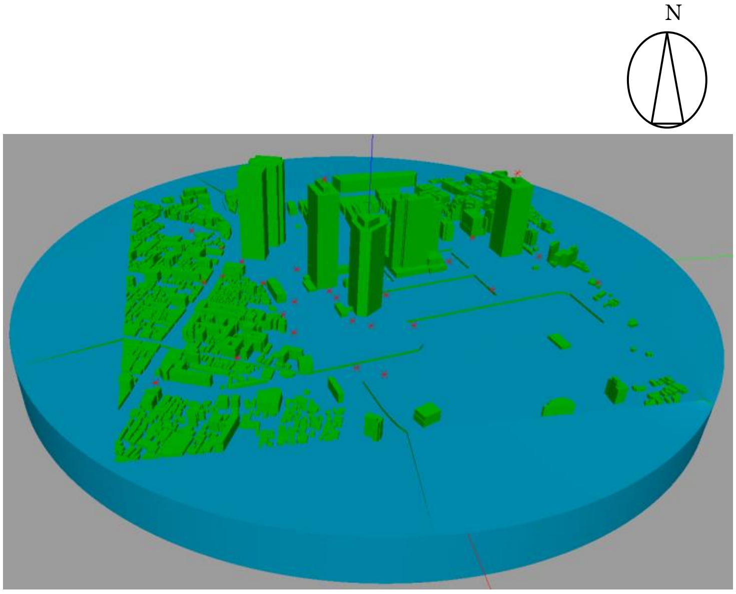


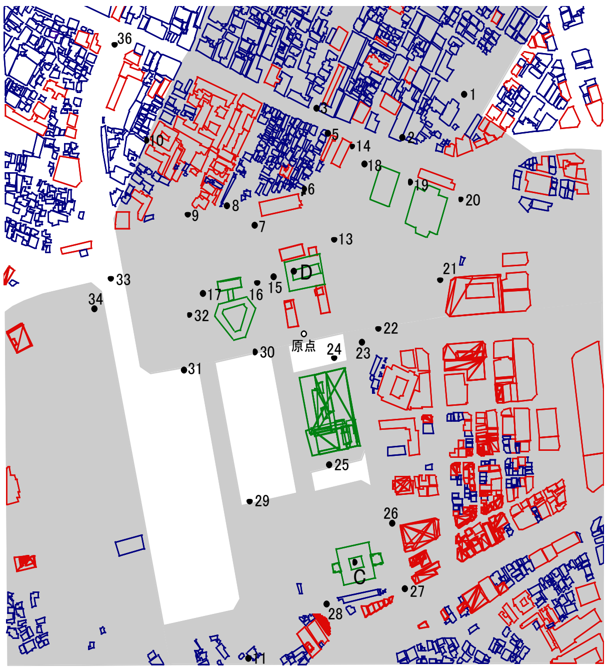

***Figure 2:*** *3D and 2D model of Shinjuku with measurement probes*

We conducted three different case of simulation:

- Without turbulence and with an inlet velocity profile defined in the boundary conditions
- With the natural turbulence model
- With a turbulence and velocity inlet profile defined in the boundary conditions

First, we need to assess the velocity and turbulence inlet profile at approximately 100 m upstream of the city. We normalized the inlet velocity and the inlet turbulence with the reference velocity at 500 m. In figure 3, we show the comparison of average and turbulent velocity profiles for wind tunnel measurements and two CFD simulations: (1) Simulation with natural turbulence model and (2) Simulation with a synthetic turbulence profile imposed. We can see that the natural turbulence model gives us a better assessment than the turbulence profile imposed. In terms of velocity, the velocity profile when we impose it in the boundary conditions is closer to the wind tunnel measurement data.

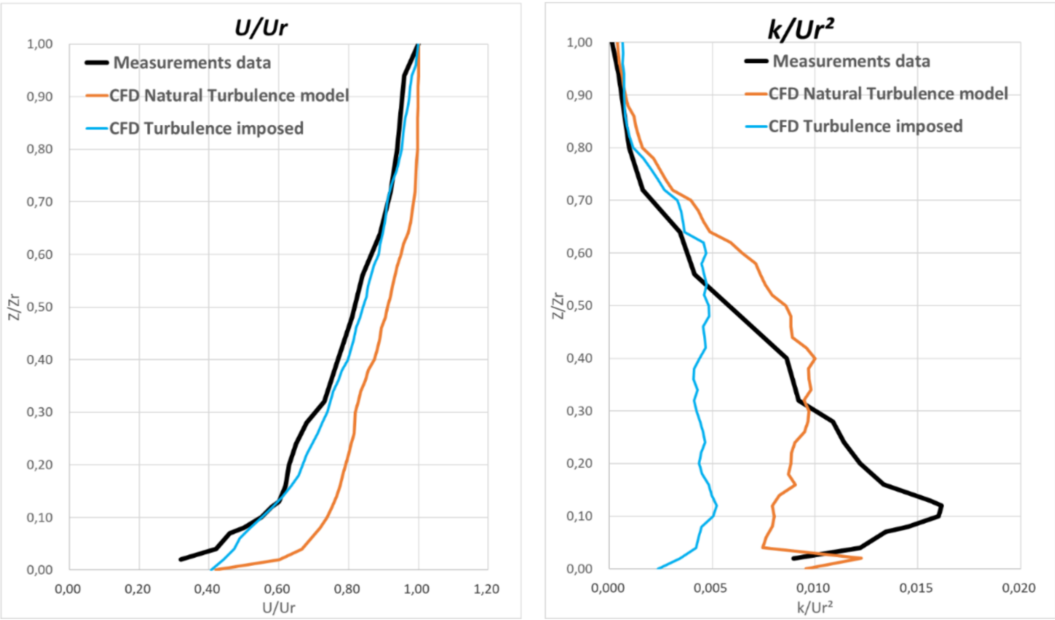


***Figure 3:*** *Velocity and turbulence inlet profile for each case*

Once this setup ready, we carried out different simulations to see in which case we are closer to the experimental data. We can see on the Figure 4 the result of an unsteady view of our numerical model with the natural turbulence model upstream Shinjuku city. Each vortex generator element produces turbulence structure in different directions, intensity and length scales. With this, we reproduce realistic atmospheric turbulent flows.

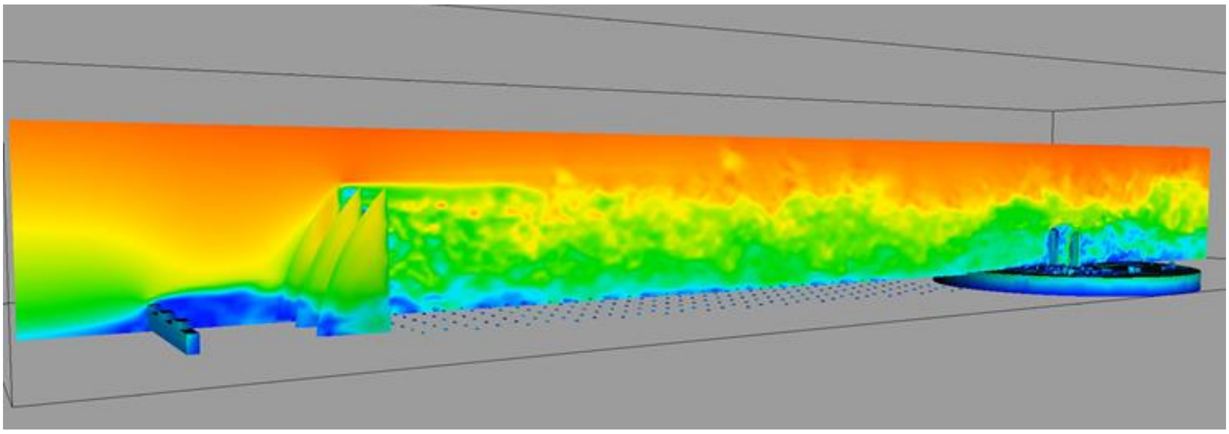

***Figure 4:*** *Unsteady results of the numerical model for Shinjuku city*

In Figure 5, we can see the visualization of the flow over the city for each case of simulation we performed, we see that each setup produces different levels of turbulence above the city.

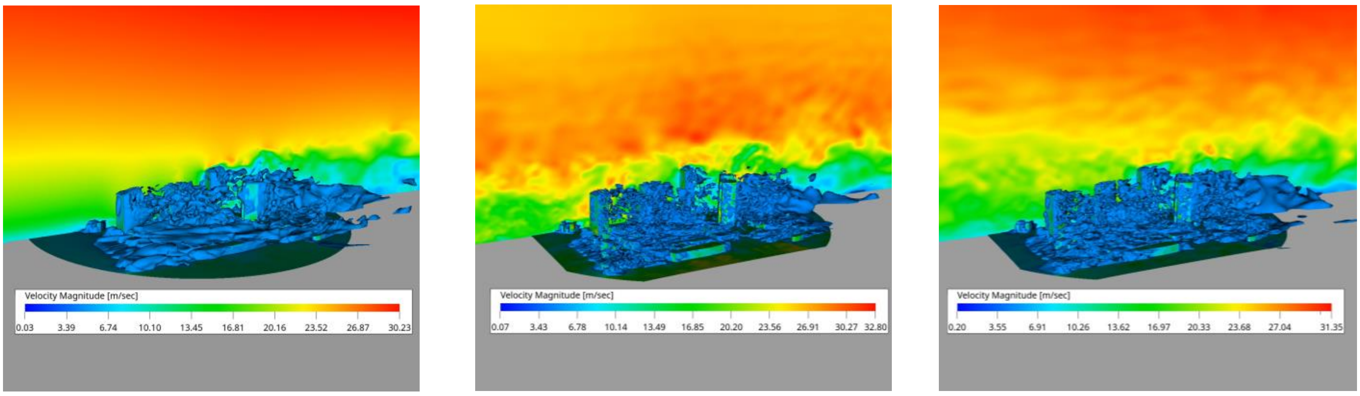


***Figure 5:*** *results with 1) velocity profile, 2) natural turbulence model and 3) velocity and turbulence profile*

This study was performed in order to have a real assessment of the turbulence downstream the buildings. The main objective of these several simulations is to understand in which case we are the closer to reality and to have a real turbulence model in the environment where the drone flies in. To assess these results, we compared each case we simulated with the wind tunnel and field measurements. We recall that to compare these numerical results with the experimental data of this specific case, we look at different fluid variables (velocity, pressure, turbulence info, etc…) at the location of each probe we mentioned above and that we can see Figure 2. To have a real assessment of our numerical model, we normalized the velocity with the reference velocity, which is located at 500 m altitude and is around 25 m/s. The comparison of these normalized velocities for each case we simulated and with the experimental data are given in the Figure 6.

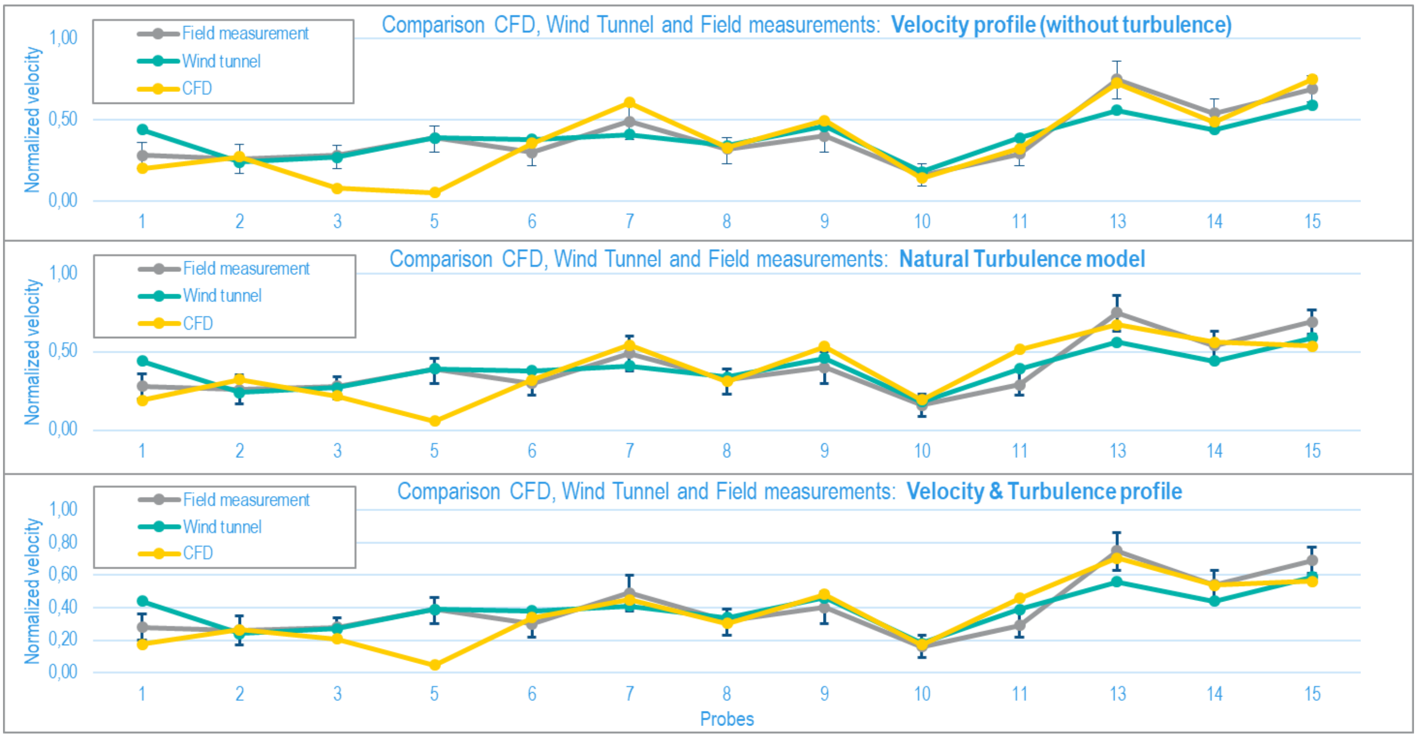


***Figure 6:*** *Comparison between CFD results, wind tunnel and field measurements data*

In order to give a spatial point of view of the incertitude we have between the numerical and experimental results at each probe location, we plot the percentage of error for each of these probes above the 2D view of the city. We give these graphic representations for the case of the natural turbulence model and for the case of the velocity and turbulence inlet profile applied in the boundary conditions in the Figure 7 below.

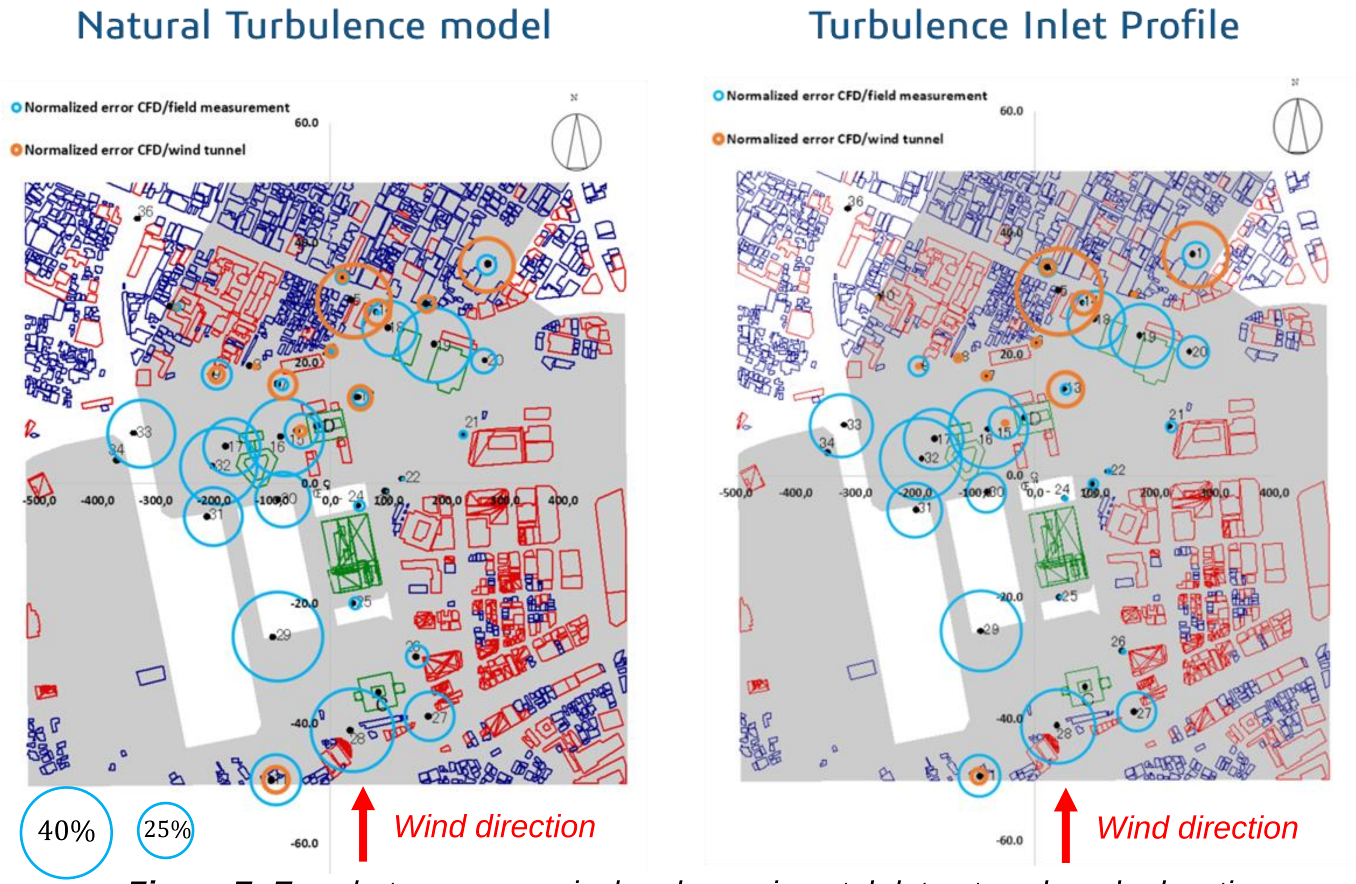


***Figure 7:*** *Error between numerical and experimental data at each probe location*

With these numerical results very close to the experimental data we have for this case of study of the city of Shinjuku, we can presume and consider that we have a real assessment of the turbulence and velocity profile inside the city. This case of study allowed us to prove that our numerical model of the simulation of the urban flow in a specific urban area is correct and close to reality. Now that we validated our numerical model for this city, we can presume that with the exact same way of setting up our case, we can obtain a very close assessment of the real urban flow in any urban area, which is of interest for us. Therefore, an urban area that would be a better fit for our project is the campus of the Delft University of Technology. Indeed, we work in collaboration with TU Delft for this project and thanks to their help; we had access to the 3D geometry and mesh of the city completely ready for the CFD simulation.

### 3.2 Numerical model of the urban airflow in an area of interest: TU Delft case study

The creation of this new numerical model for this case study is straightforward. We directly use again the exact same fluid domain and the same dimensions for the wind tunnel simulated in the case of Shinjuku city (with the natural turbulence model). The setup is the same; the only difference is the geometry of the city, which in this case is the campus of the Delft University. Building geometry is directly available on the 3D BAG [9] website in OBJ format. The terrain is reconstructed from a point cloud (AHN3 Dutch national database [10]) and vegetation and water surfaces (obtained from BGT database [ref]) are imprinted into the terrain. The whole workflow of creating and integrating building and terrain geometries is carried out in City4CFD [11], an open-source tool for automatic reconstruction of 3D city models. We prepare the tessellation and the final mesh of this geometry using the SIMULIA PowerDELTA tool. The obtained final geometry ready for the simulation, with the buildings, terrain, vegetation and water, is shown in the Figure 8.

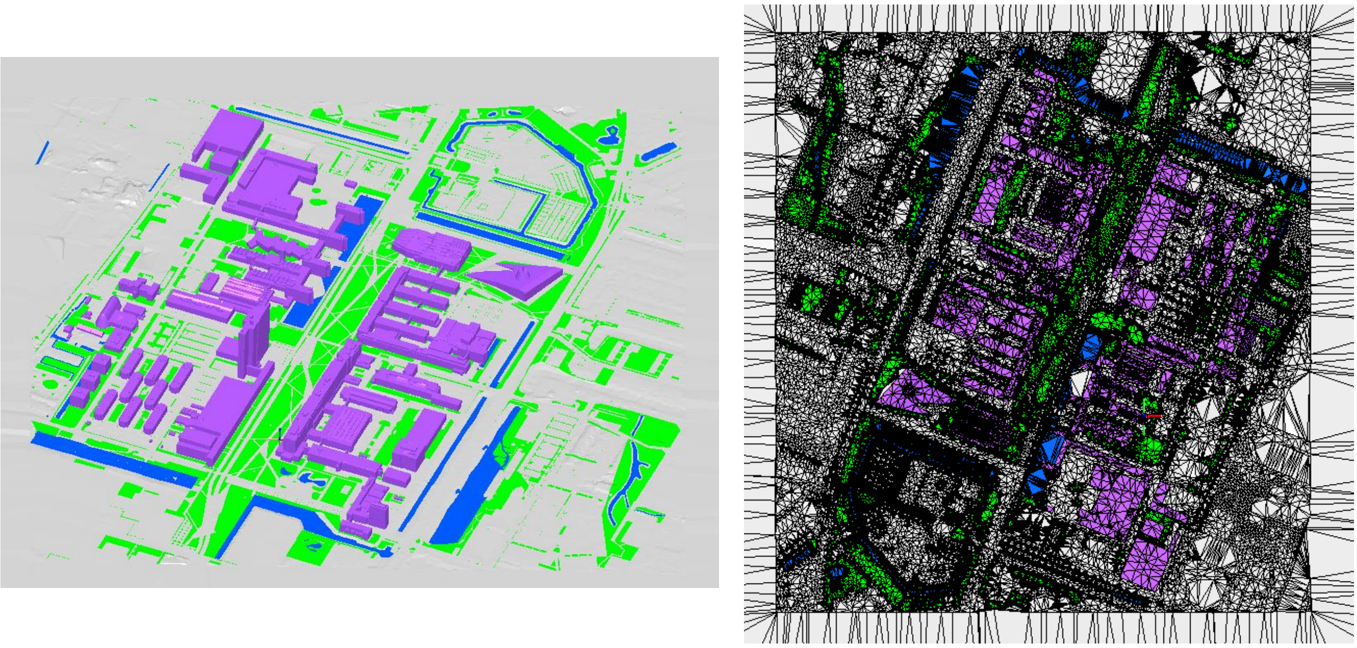

***Figure 8:*** *3D geometry of part of the campus of  Delft University of Technology*

In the following part of this project, the drone that we will be studying will be flying in this campus at a height of 100 meters. The location of this eVTOL will be in the wake turbulence of the tallest building of the campus. With the real urban flow simulated in this numerical model, we will see how the environments of the drone affects its flight characteristics. The plane of wake turbulence behind the building where the drone will be located is shown in the Figure 9.

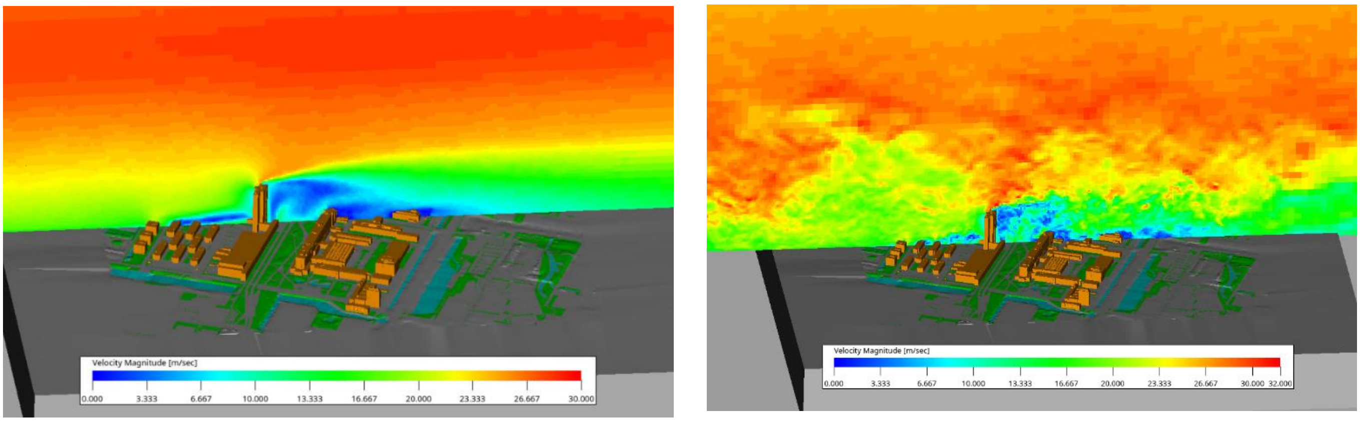

***Figure 9:*** *Average and steady velocity profile behind the building where the drone will fly*

Now that the complete study of the environment where the drone will fly is done, we can start to study the performance and aeroacoustics, as a first step, of an isolated drone and, in a second part, in this Delft Campus numerical model.

## 4. Performance and aeroacoustics of an isolated eVTOL in real flight conditions

To simulate the performance and aeroacoustics of an isolated eVTOL in real flight condition, we chose the case study of the NASA's quadrotor concept vehicle that we can see in the Figure 10.

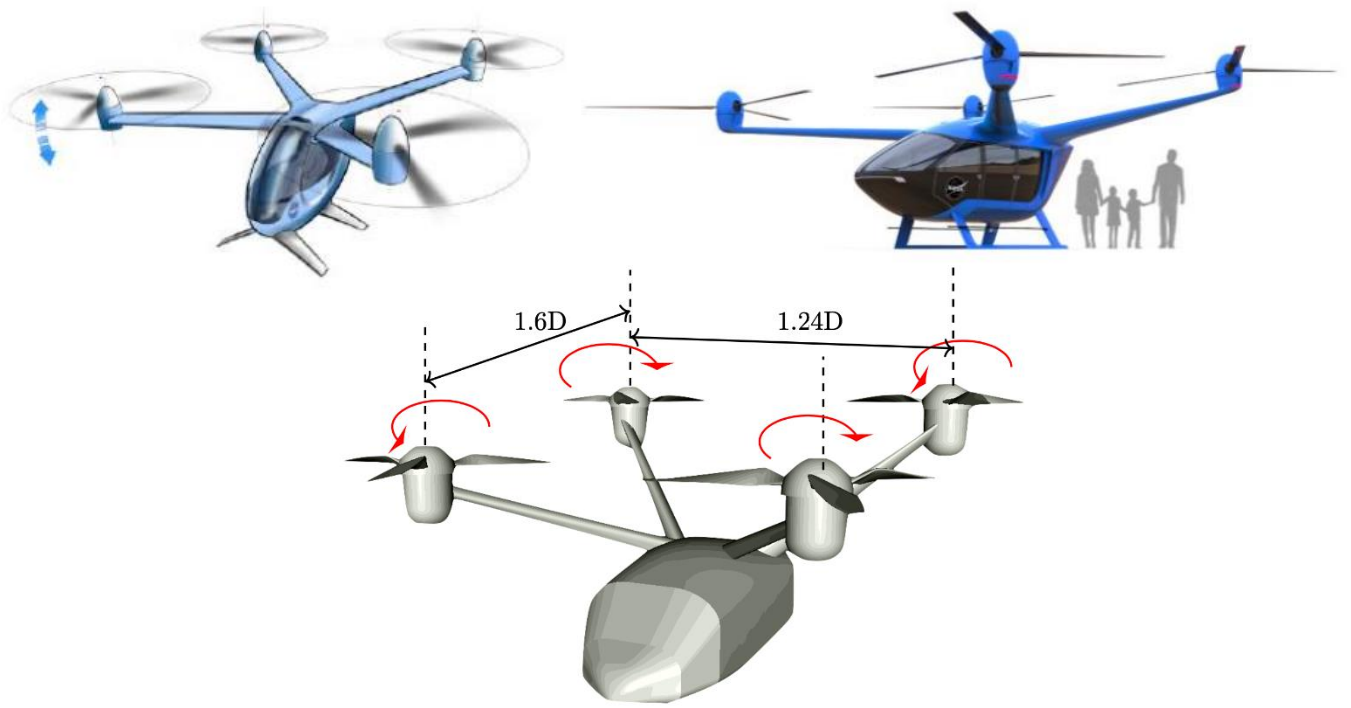


***Figure 10:*** *NASA's quadrotor concept vehicle [12]*

The vehicle's gross weight is assumed to be 629 kg that can carry a max of two people. The eVTOL is powered with four rotors, as shown in Fig. 9. Each rotor has three blades, and the rotor diameter $D$ is 3 m. In the local reference system of the vehicle, the relative distance between the two rotors along the fuselage is set to $1.6\ D$ to avoid aerodynamic interference. At the same time, the distance between the rotors at the two sides of the fuselage is set to $1.24\ D$. The rear rotors are elevated by $0.2\ D$ with respect to the front rotors to decrease the aerodynamic interaction between front, and rear rotors. It is assumed that all four rotors rotate at the same rotational speed. Moreover, the total required thrust is distributed evenly at all rotors. Each rotor generates 1/4 of the target thrust, which is achieved by trimming the rotor blade pitch angle for a given rotor speed of 1400 RPM.

To perform this simulation, we used the Multicopter Aero and Acoustic Simulations (MAAS) workflow which is a fully automated workflow using SIMULIA PowerFLOW and OptyDB [4]. The operation of this MAAS workflow is very simple and straightforward: in an input parameters file, we give to the workflow the location of the geometry and all the parameters of the setup we want to create (characteristic pressure, velocity, RPM, number of blades, etc…). Once this file ready, we can start the script of the workflow, and we will get as an output, a PowerCASE file ready for the simulation.

### 4.1 Performance for the isolated VTOL case

In terms of performance, we will analyze several elements. The objective of this is to have some first results with the case of the isolated drone alone in order to compare these results with the case where the drone flies in a real urban environment. First, we can see in the Figure 11 the Thrust force of the propeller during the simulation and in the Figure 12 the Torque force.

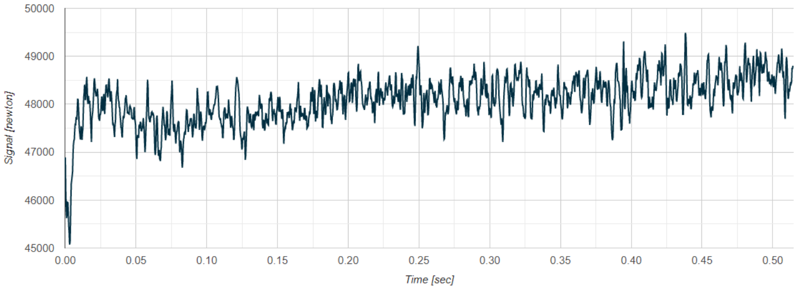


***Figure 11****: Thrust force in function of the simulation time*

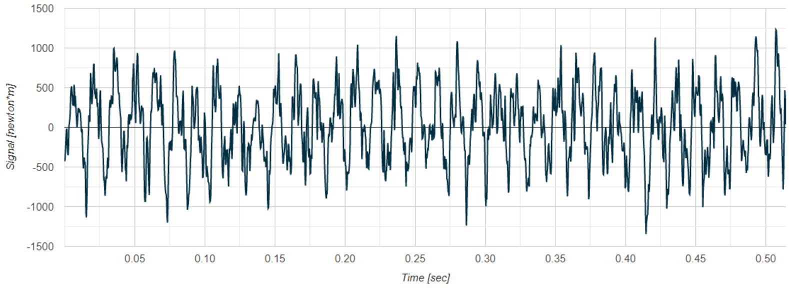


***Figure 12****: Torque force in function of the simulation time*

Then, we will compare the vortices and the static pressure generated by the blades of the propellers to see the vorticity generated by the blade and the pressure sides of those blades. In second part, we will analyze the lift of this VTOL, as well as the thrust and the total torque. We will plot several graphs to show all values we measured during the simulation and then to be able to compare them with the next part of our study to see the influence of the urban airflows on the performances of this quadrotor. To begin with, the vortices generated by one blade are given in the Figure 13 and the pressure sides on the blades are given in the Figure 14.

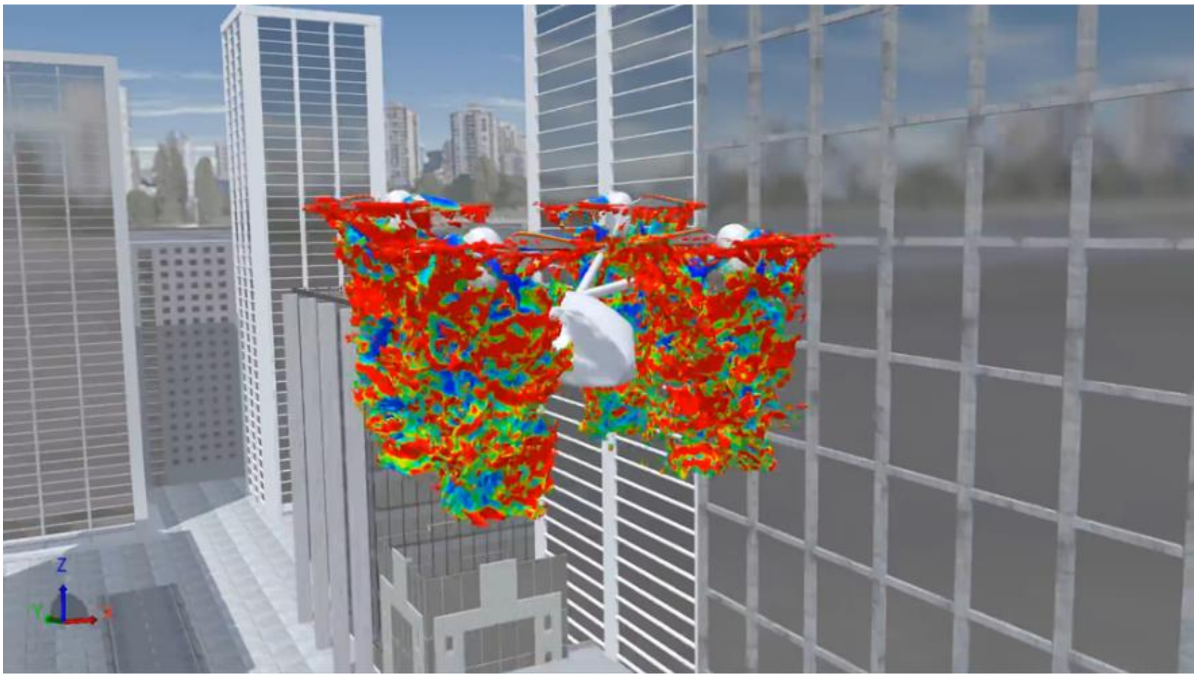

***Figure 13:*** *Vortices generated by the blade of the eVTOL*

The static pressure on the blades shown in the Figure 14 allows us to see clearly the differential of pressure between the suction side and the pressure side of the blades. Indeed, because of the curved shape of the blade, the air is traveling faster on the extrados of the blade and thus creating a zone of lower pressure. Inversely, on the intrados the air is moving slower, thus creating a zone of higher pressure.

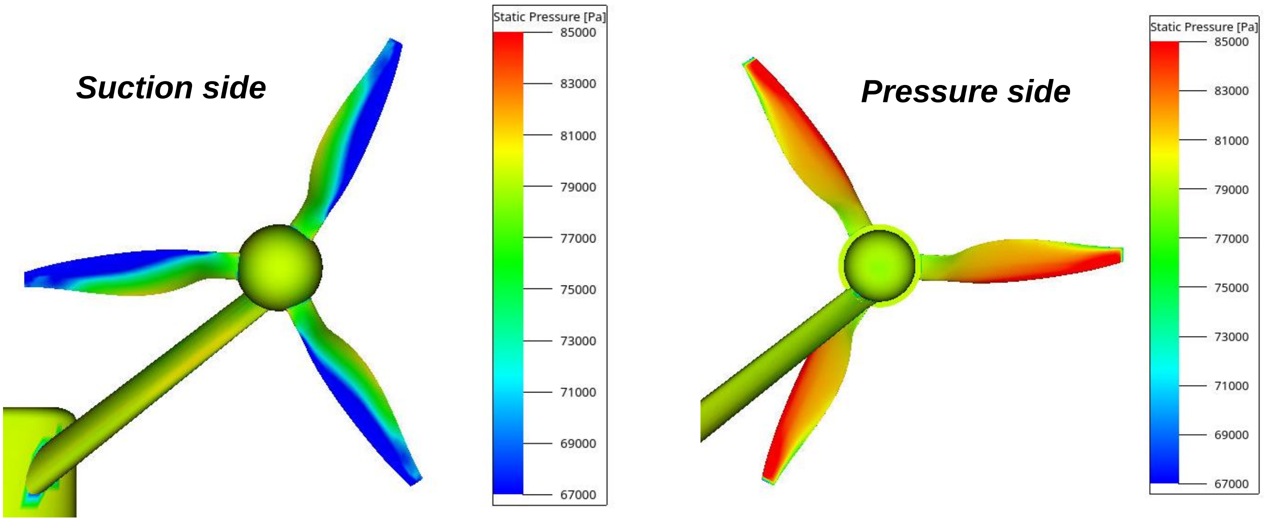


***Figure 14:*** *Pressure sides of the blade of the eVTOL*

We can also see this phenomenon on the graph of the figure 15. Indeed, the upper curves of this graph represents the higher static pressure along the lower part of the blade and the lower curves represents the lower static pressure along the upper part of the blade. On the graph given in the Figure 15, the green curve represents the 2D extruded profile while the red curve represent the real 3D profile of the blade.

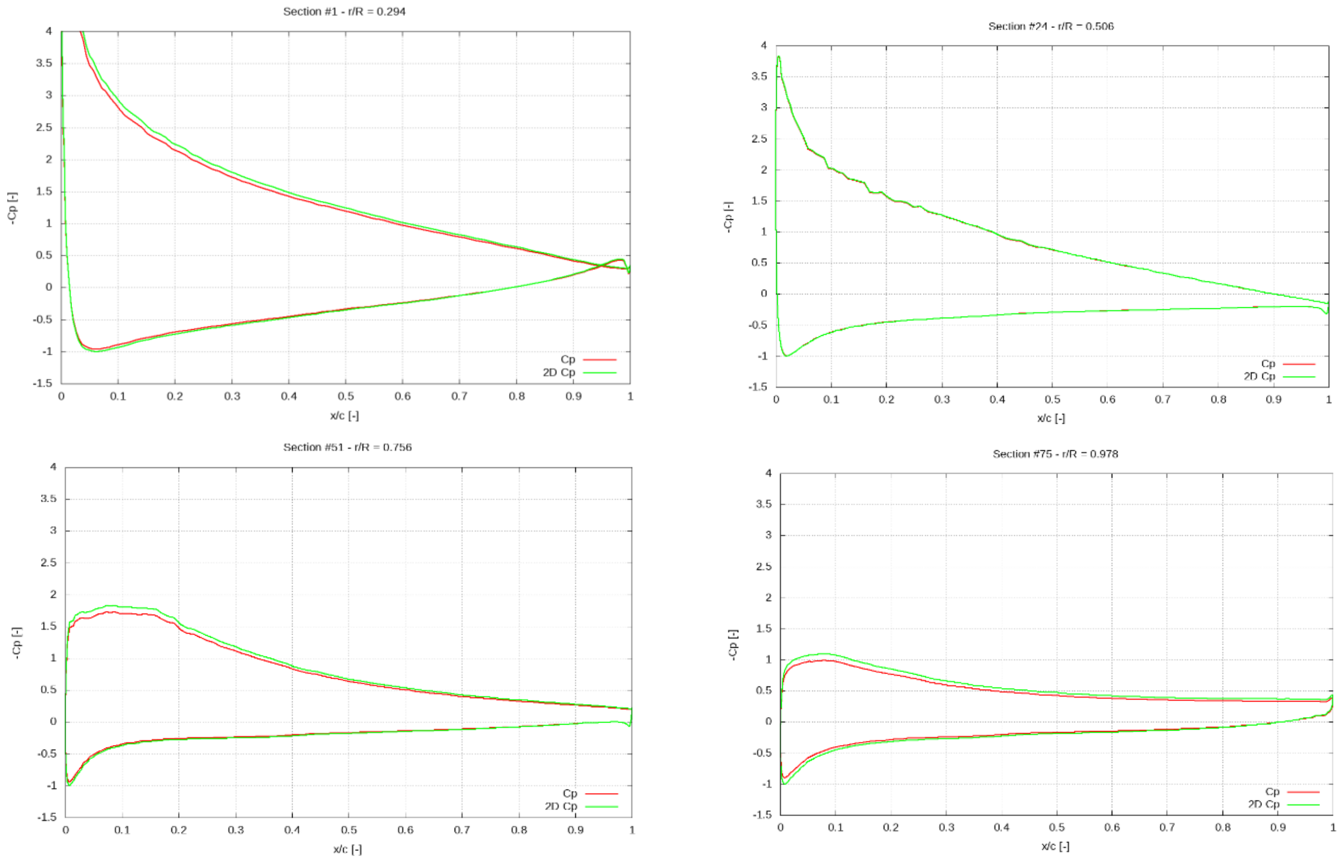


***Figure 15:*** *Static pressure along several position on the blades of the eVTOL*

We can also plot the Thrust Development and Sectional Thrust for each blade as shown in Figure 16.

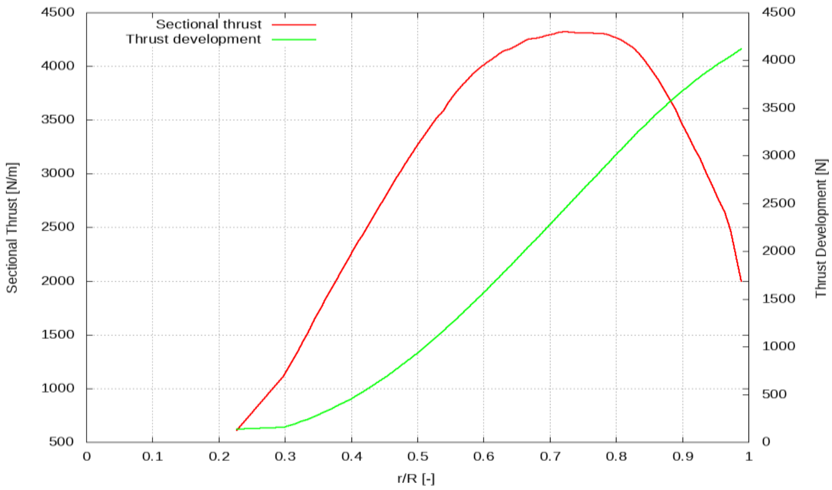


***Figure 16:*** *Thrust Development and Sectional Thrust of the blades*

As we can see typically on this type of Thrust graph of a general blade in the aerospace industry, we see the maximum Thrust force at a location of approximately 75% of the blade and then the decrease of the Thrust due to the drag induced on the tip of the blade.

In the same way that with the Thrust Development and Sectional Thrust, we can also plot the Torque Development and Sectional Torque for each blade as shown in Figure 17.

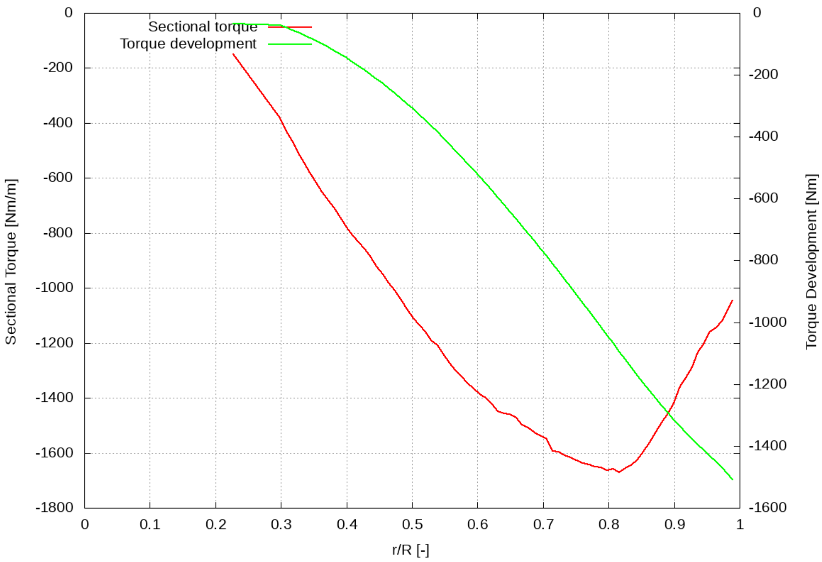


***Figure 17:*** *Torque Development and Sectional Torque of the blades*

Here again, we see that we have the maximum Torque value at a location of approximately 80% of the blade and then again, the decrease of the Torque due to the drag induced on the tip of the blade.

We will use these data in the next part of this study to compare the case of the isolated eVTOL and the case of this same drone flying in a real urban environment in order to have an accurate assessment of the influence of the urban flow on the performance of a drone.

### 4.2 Acoustic for the isolated VTOL case

Now that we have presented the results we obtained relative to the performance for the case of the isolated eVTOL, we can pass on to the analysis of the acoustics results that we obtained with the MAAS workflow.

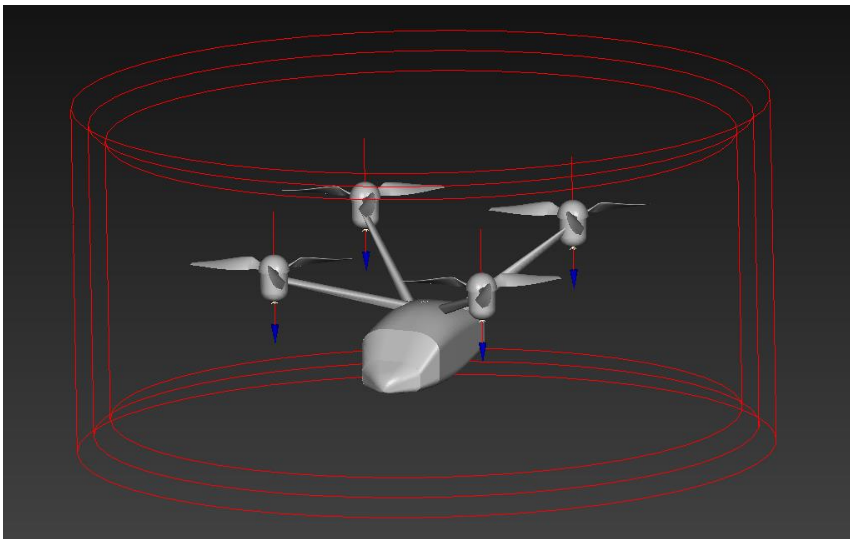

***Figure 18***: *Case output of the MAAS workflow*

In terms of aeroacoustics, the workflow creates a noise sphere all around the eVTOL measuring all the noise generated by the drone. We can see in the Figure 19 several points of this sphere with the noise measurements at each of these points. Notice tonal noise emerge differently over broadband depending on the microphone position. The highest tonal noise harmonics appear for microphone 270, which is close to the propeller planes.

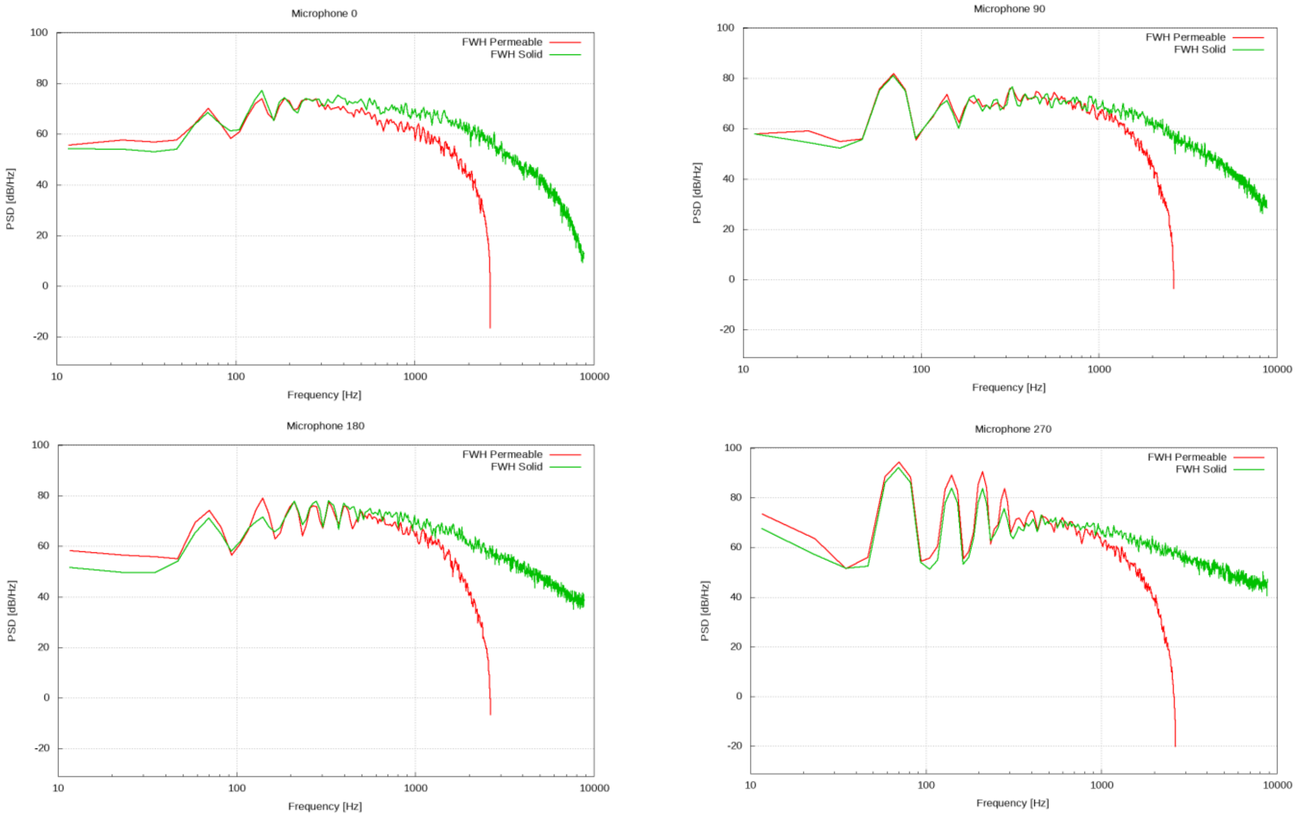


***Figure 19:*** *Noise measurement at several microphone location on the noise sphere*

We can plot the acoustics propagation of the drone in several plane and at different blade passing frequencies (BPF). In the Figure 20, we can see the acoustic at BPF1 and in the Figure 21, we have the BPF2. In both cases, the noise radiation is much more important in the plane of the blades than above or below the drone. This is coherent with the spectra shown in Figure 19.

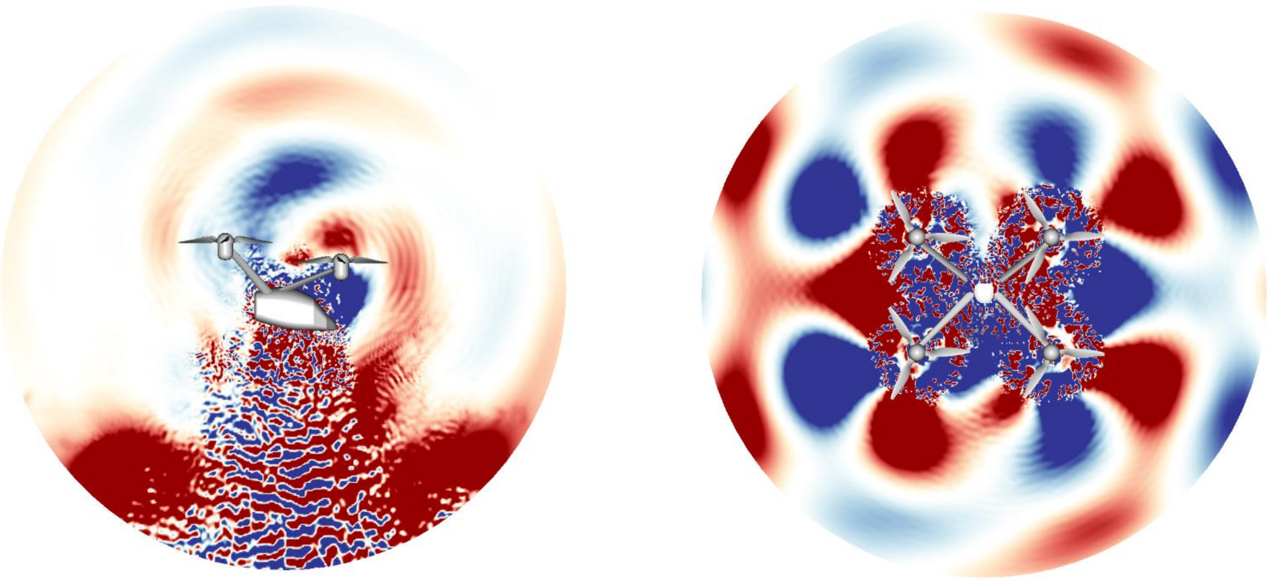

***Figure 20:*** *Noise propagation at BPF1*

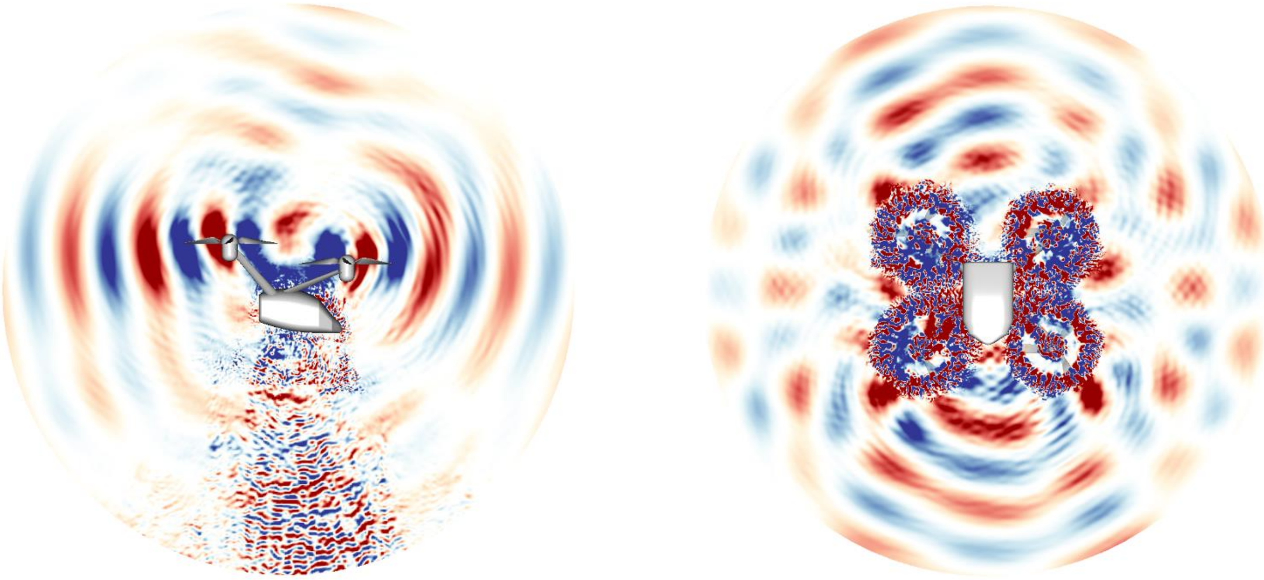

***Figure 21:*** *Noise propagation at BPF2*

### 4.3 Performance and acoustic for the installed VTOL case and comparison with the isolated case

In the last part, we studied the performances and acoustics of our VTOL in an isolated environment. In this part, we will compare this case of the isolated simulation with another case which will consist on an installed simulations of the drone. In order to perform this latter analysis, we have imposed a velocity profile on the drone (identical to the TU Delft campus inlet velocity profile). The simulation is hence seeded with the turbulence profile of the simulation of the TU Delft campus. We can see in the Figure 22 the velocity profile on the drone for each case.

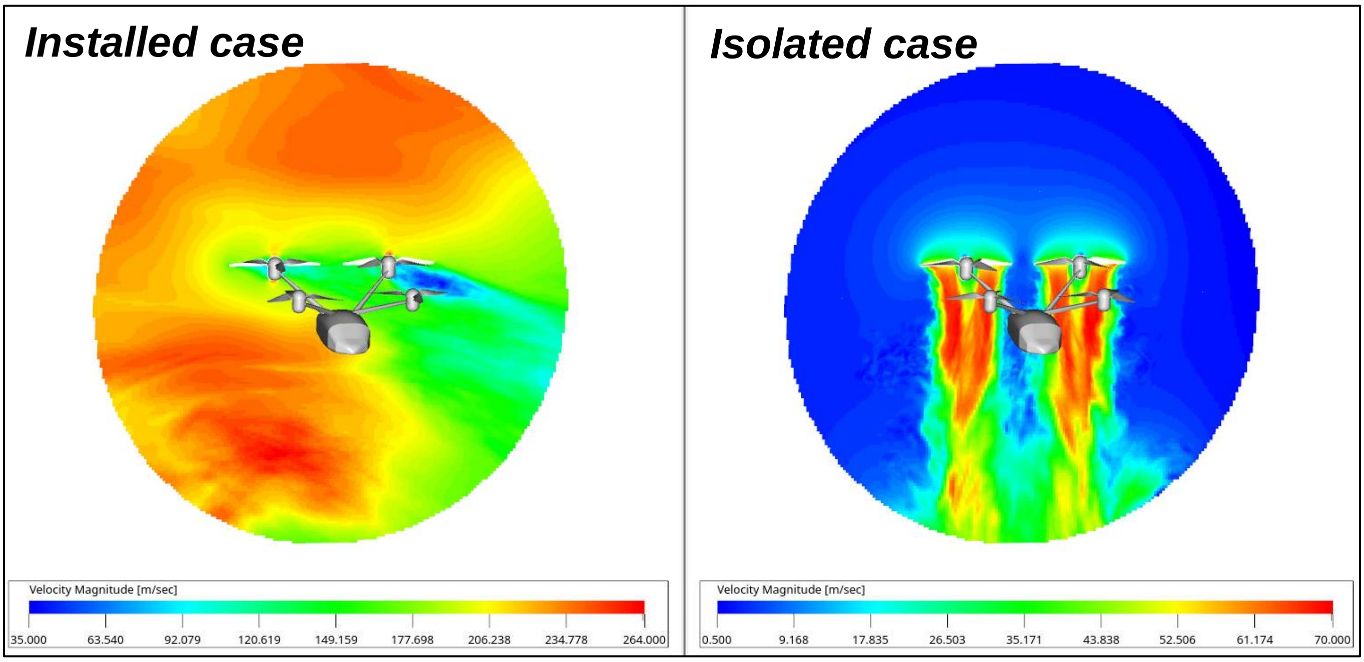


***Figure 22****: velocity profiles for the installed and the isolated cases.*

We can see on the pictures above how the wind affects the wakes of the propellers. For the case of the installed case, the velocity and the turbulences clearly impact the performance of the drone.

Similarly, we can see in Figure 23 the isosurfaces of the average velocity magnitude at 95 m/s for the installed case and 62 m/s for the isolated case. These isosurfaces are colored by the vorticity magnitude of each case.

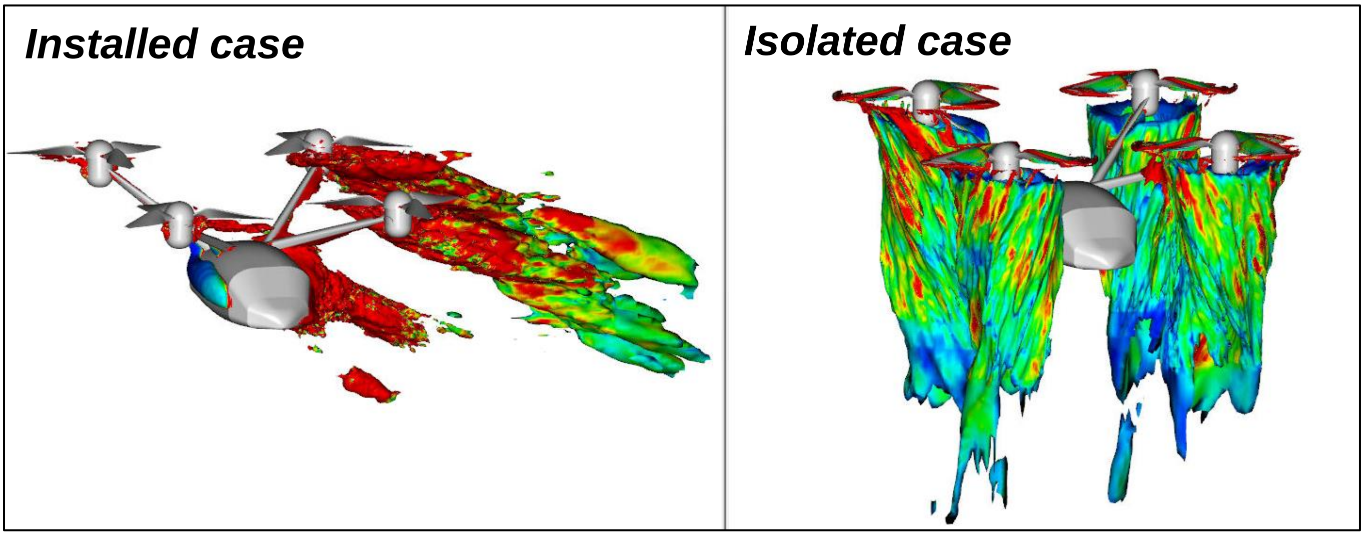


***Figure 23****: location of the drone in the TU Delft campus*

With the isosurfaces given in the Figure 23, we can clearly see the change of direction of the wakes of the propellers. Here again, this phenomenon will generate a difference of performance for the propellers upstream and downstream to the wind. This will also largely impacts the performance of the drone for the installed case.

We can also compare the Thrust and Torque Development and Sectional Thrust and Torque of the blades. These results for the installed case are given in the Figure 24.

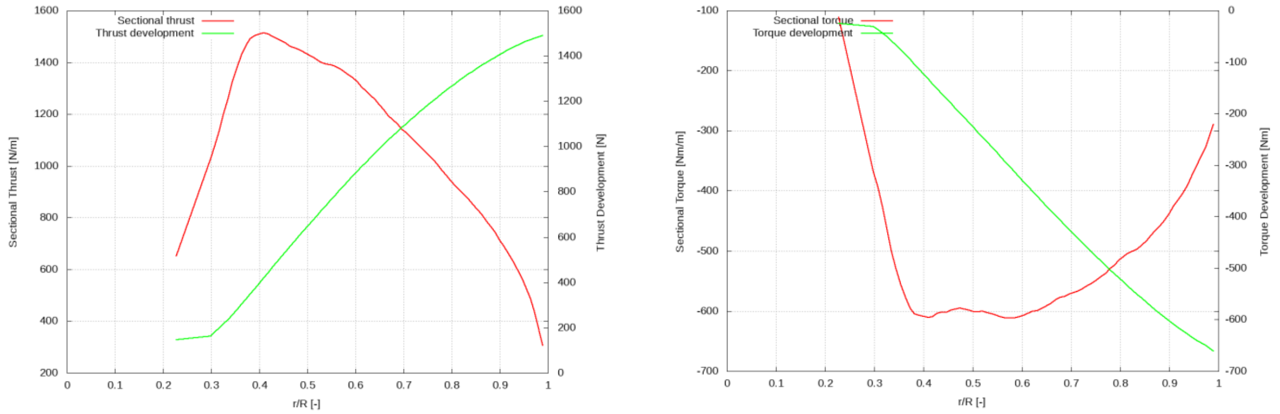


***Figure 24:*** *Thrust and Torque Development and Sectional Thrust and Torque for the installed case*

We can also compare the plots of the acoustics propagation of the drone in several plane for the installed and the isolated cases. We give in the Figure 25 and 26 the pressure derivative for both cases.

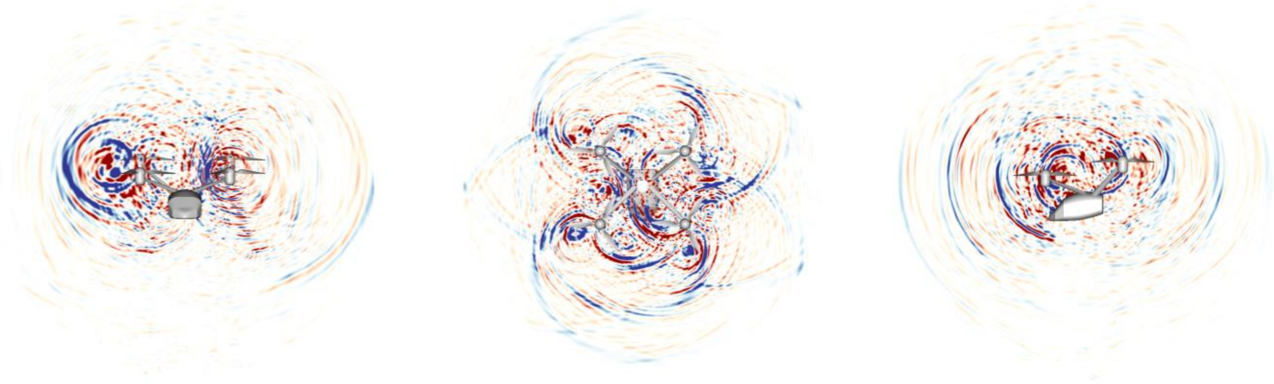

***Figure 25:*** *Noise propagation for the isolated case*

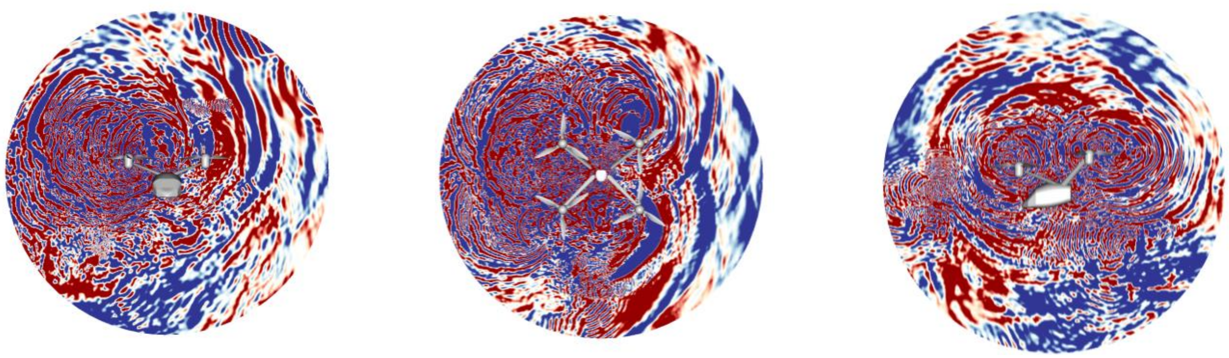

***Figure 26:*** *Noise propagation for the installed case*

Here again, we can see how the velocity and turbulence impact the acoustic of the drone. In the installed case, the noise propagation is much higher and the directions of the noise propagation are also affected by the wind.

## 5. Performance and aeroacoustics of an eVTOL under real urban environment

This part of the study will consist on the analysis of the CFD numerical simulation of the same drone, but this time, under a real urban area environment. We chose to study the flight of a drone downstream the wakes of a building in the TU Delft campus. The precise location of the drone in this city is shown by the cross in the right picture of the Figure 27.

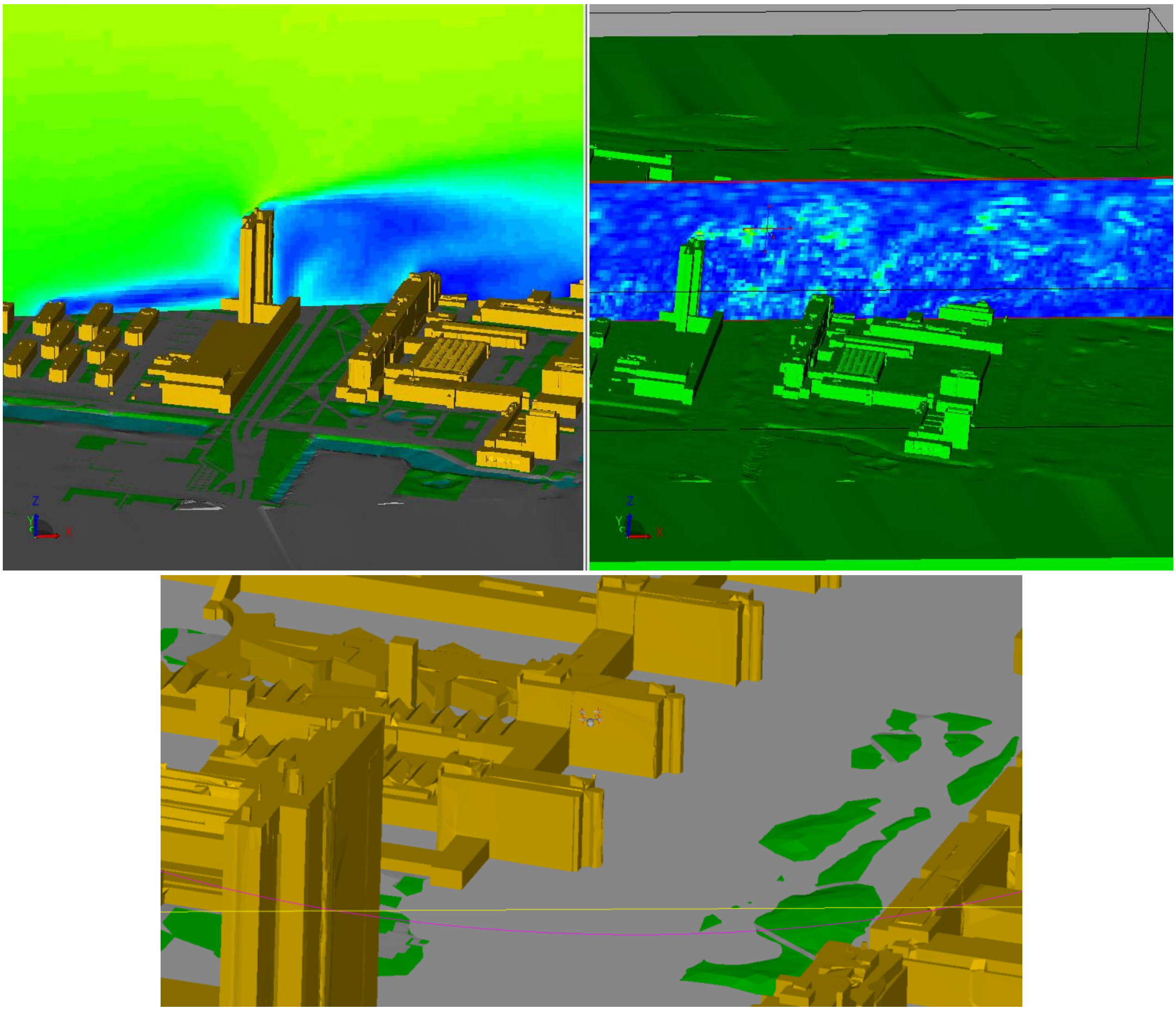

***Figure 27**: Location of the drone in the TU Delft campus*

Simulations of the eVTOL in an urban flow environment are still ongoing and will finish in the following days. With these results, we will be able to have an accurate assessment of the influence of the real urban airflow on the performance and aeroacoustics of an eVTOL.

We will be able to present all our results for the conference.

# 6. Conclusions

The main objective of this project was to study the noise impact of drones in communities and public acceptance. We aimed to conduct several analysis using Very-Large Eddy Simulations (VLES) as exposed in this paper. CFD Lattice-Boltzmann unsteady simulations coupled with Ffowcs-Williams Hawkings integration method were used to predict both UAV aerodynamics and radiated acoustics.

This study started with a particular interest on urban flows. In fact, the first part of the study was dedicated to predict and to understand all behavioral patterns of airflows in a specific urban area. In order to do this, we chose the case study of Shinjuku city because we had experimental data from wind-tunnel and field measurement campaigns. We used these data to assess and validate the numerical predictions in terms of airflows for this specific case. The results we obtained with the several simulations we performed were very close to the experimental data that exist for this case. That allowed us to validate our numerical model of urban flows.

Once we had an accurate numerical model of an urban flow in a specific urban area, we were able to validate this numerical model and to choose another city that made more sense for our study. In this context, we decided to use the case study of the Delft University. We thus performed the same simulation with this second urban area.

Then, the second part of this study was dedicated to the analysis of the performance and the aeroacoustics of a generic isolated eVTOL in real flight conditions. To conduct this work, we chose the NASA’s quadrotor vehicle concept and performed a complete CFD simulation on this eVTOL. The tool used to conduct this CFD numerical model was the MAAS workflow which is a fully automated workflow using PowerFLOW and OptyDB. Thanks to this workflow, we were able to obtain as an output several performance and acoustics data. With the results that we will obtain with the last part of this study, we will be able to compare the data that we obtained in this part to understand the influence of the urban environment on the performance and acoustic of a drone.

Finally, the third and last part of this study carried on with the demonstration of the flight of this same drone in the urban environments of the TU Delft Campus. In fact, the simulations for this last part are still ongoing and will finish in the following days. With these results, we will be able to have an accurate assessment of the influence of the real urban airflow on the performance and aeroacoustics of an eVTOL and will allow to accurately assess the noise generated by the flight of a generic drone in a specific urban area, and the airflow interaction between the evolving field where the drone flies and the drone itself.

**References**


[1] Yunusi Fuerkaitia, Edoardo Grandea, Damiano Casalinoa, Francesco Avallonea, Daniele Ragni (2022) *Efficient low-fidelity aeroacoustic permanence calculation of propellers* Aerodynamics, Wind Energy, Flight Performance and Propulsion Department, Delft University of Technology, Delft 2629HS, The Netherlands.

[2] Y. Fuerkaiti, D. Casalino, F. Avallone, and D. Ragni (2022) *Urban air mobility noise prediction in a 3D environment using Gaussian beam tracing*
Delft University of Technology, Delft 2629HS, The Netherlands.

[3] Zhongqi Jia and Seongkyu Lee (2019) *Acoustic Analysis of a Quadrotor eVTOL Design via High-Fidelity Simulations*
Department of Mechanical and Aerospace Engineering University of California, Davis, California, 95616

[4] W.C.P. van der Velden, G. Romani, D. Casalino (2021) *Validation and insight of a full-scale S-76 helicopter rotor using the Lattice-Boltzmann Method*
Dassault Systemes & B.V., Utopialaan 25, 5232 CD,'s-Herthogenbosch, Netherlands & Deutschland GmbH, Meitnerstraße 8, 70563, Stuttgart, Germany

[5] Gianluca Romani, Damiano Casalino (2019) *Rotorcraft blade-vortex interaction noise prediction using the Lattice-Boltzmann method*
Delft University of Technology, AWEP Department, 2629 HS, Delft, The Netherlands

[6] G. Romani, E. Grande, F. Avallone, D. Ragni and D. Casalino (2021) *Low-Reynolds Number Propeller Noise Prediction Using the Lattice-Boltzmann/Very Large Eddy Simulation Method*
Delft University of Technology, Kluyverweg 1, 2629HS, Delft, The Netherlands

[7] Fujii, K., Asami, Y., Iwasa, Y., Fukao, Y., et al., 1978. *Wind in Shinjuku sub-central area: Comparison between field measurement and wind tunnel experiment*. Proceedings of 5th Symposium on Wind Resistance of Structures, 91-98. (in Japanese)

[8] The Research Committee on Strong Wind Around High-rise Buildings, Development Council of Shinjuku Sub-central Area, 1985. Technical Report on Wind in Shinjuku Sub-central Area - Field Measurement, Experiment, and Observation. (in Japanese)

[9] 3D BAG website: https://3dbag.nl/

[10] PDOK website: *Dataset: Current Altitude File & Topography Netherlands*: BGT - PDOK & AHN3 - PDOK

[11] City4CFD: GitHub - tudelft3d/City4CFD: City4CFD

[12] Christopher Silva, Wayne Johnson, Kevin R. Antcliff and Michael D. Patterson (2018) *VTOL Urban Air Mobility Concept Vehicles for Technology Development*
NASA Ames Research Center. Moffett Field, CA 94035
NASA Langley Research Center, Hampton, VA 23681

QUIET DRONES
Second International e-Symposium
on
UAV/UAS Noise
27th to 30th June 2022

# Deeplomatics: A deep-learning based multimodal approach for aerial drone detection and localization

**Éric Bavu, LMSSC, Cnam Paris, HESAM Université, France**
**Hadrien Pujol, LMSSC, Cnam Paris, HESAM Université, France**
**Alexandre Garcia, LMSSC, Cnam Paris, HESAM Université, France**
**Christophe Langrenne, LMSSC, Cnam Paris, HESAM Université, France**
**Sébastien Hengy, French-German Research Institute of Saint-Louis, France**
**Oussama Rassy, French-German Research Institute of Saint-Louis, France**
**Nicolas Thome, CEDRIC, Cnam Paris, HESAM Université, France**
**Yannis Karmim, CEDRIC, Cnam Paris, HESAM Université, France**
**Stéphane Schertzer, French-German Research Institute of Saint-Louis, France**
**Alexis Matwyschuk, French-German Research Institute of Saint-Louis, France**

## Summary

Protection against illicit drone intrusions is a matter of great concern. The relative stealthy nature of UAVs makes their detection difficult. To address this issue, the Deeplomatics project provides a multimodal and modular approach, which combines the advantages of different systems, while adapting to various topologies of the areas to be secured. The originality lies in the fact that acoustic and optronic devices feed independent AI to simultaneously localize and identify the targets using both spatial audio and visual signatures.

Several microphone arrays are deployed on the area to be protected. Within its coverage area (about 15 hectares), each microphone array simultaneously localizes and identifies flying drones using a deep learning approach based on the BeamLearning network. Each array is attached to a local AI which processes spatial audio measurements in realtime (40 estimations per second), independently to the other units of the surveillance network.

A data fusion system refines the estimates provided by each of the AI-enhanced microphone arrays. This detected position is shared in real-time with an optronic system. Once this system has hooked its target, a Deep Learning tracking algorithm is used to allow an autonomous visual tracking and identification.

The optronic system is composed of various cameras (visible, thermal, and active imaging) mounted on a servo-turret. The active imaging system can capture scenes up to 1 km, and only captures objects within a given distance, which naturally excludes foreground and background from the image, and enhances the capabilities of computer vision.

The Deeplomatics project combines benefits from acoustics and optronics to ensure real-time localization and identification of drones, with a high precision (less than 7° of absolute 3D error, more than 90 % detection accuracy). The modular approach also allows to consider in the long term the addition of new capture systems such as electromagnetic radars.

## 1. Introduction

The illegal or hostile use of aerial drones is an emerging threat, which is only partially addressed by current ground or airborne anti-intrusion systems. The techniques required to identify moving targets with weak acoustic and visual signatures, and locating them for predictive trajectory tracking, represent more than ever a scientific and technical challenge. There are many applications related to defence in the context of securing sites, but also for locating targets thanks to compact and portable modules, which could complete the equipment of the 21st century soldier. They have many applications related to civil security (surveillance and security of critical energy access infrastructures, fight against industrial espionage, or security of demonstrations). These techniques are also of interest for civil applications in monitoring or controlling noise pollution caused by road or air vehicles, and for ecosystem monitoring applications (inventory and monitoring of animal species to protect biodiversity).

The DEEPLOMATICS project is aiming to achieve a scientific and technological leap forward to optimize multimodal detection and UAV threat tracking. We propose to integrate in an original way to the sensors of a surveillance network a set of independent artificial intelligences, specifically trained to respond to the tasks of real-time dynamic localization and target recognition. The majority of the project's tasks are based on a knowledge base acquired by the DEEPLOMATICS project partners in projects related to artificial intelligence for image recognition, acoustic source localization using Deep Learning, sound source recognition, but also in the development of sensors and specialized microphone arrays for the localization and imaging of acoustic sources, as well as in sniper detection projects, or acoustic beacons for helicopter detection. The DEEPLOMATICS project also involves an active imaging optronic system that has been adapted to automatic UAV identification and tracking using a real-time deep detector to perform drone recognition.

## 2. Multimodal sensors, Deep-Learning, and data fusion for UAV tracking and identification

### 2.1 Global system description

This interdisciplinary project uses advanced Deep Learning techniques, using the raw acoustic date measured by compact microphone arrays distributed over the site to be monitored, complemented by an active imaging optronic system, which feeds an independent artificial intelligence for a computer vision task (see Figure 1.)

We believe that this modular surveillance network organization allows to adapt the sensor topology to the diversity of sites to be protected. The objective is to take advantage of the convergence of data-sciences, acoustics and optronic signal processing. When multiple acoustic and optronic systems are deployed in a fixed or reconfigurable manner at a site (urban or not) to locate a weak signature moving target, the first challenge is the real-time tracking of the moving target in a potentially noisy environment, and the orientation of the optronic systems towards the target.

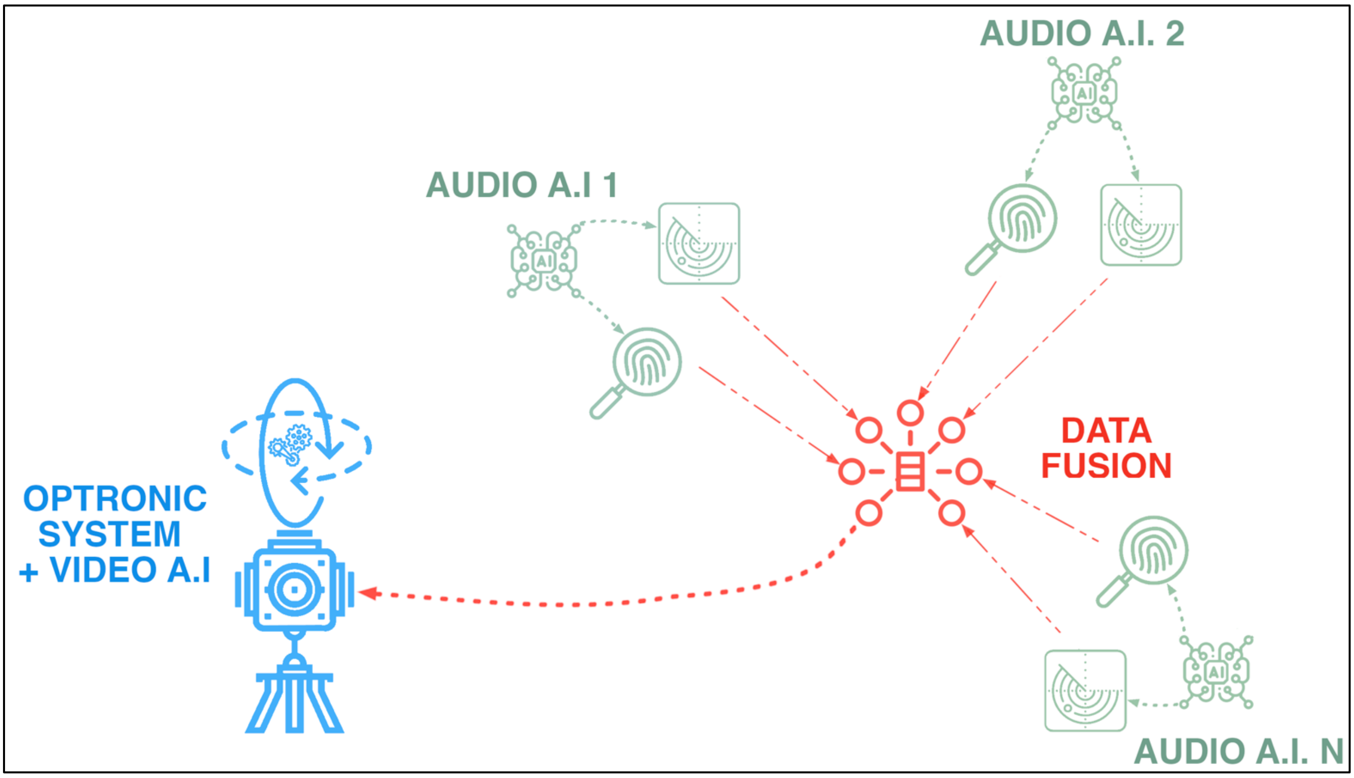


*Figure 1: Multimodal detection and tracking using a set of N (3 depicted) A.I-enhanced microphone arrays, an optronic system feeding a realtime video drone detection A.I. The data fusion system refines the estimates provided by each of the AI-enhanced microphone arrays. This detected position is shared in real-time with an optronic system.*

### 2.2 Acoustic surveillance network using A.I. units

For this purpose, the DEEPLOMATICS surveillance network is partly based on the use of a set of independent transportable broadband compact microphone arrays. The overall surveillance range using the audio modality is therefore only dependent on the number of AI-enhance microphone arrays in the surveillance network. The miniaturization of these microphone arrays is obtained thanks to the use of digital MEMS microphones. Their main advantages are their compactness, their adaptability, and their low cost. These microphone arrays, equipped with independent compact deep learning processors (see Figure 2), provide a solution adapted to the diversity of sites to be protected by recognizing the flying UAV while accurately identifying its position. The acoustic localization and recognition system will be further detailed in section 3 of the present paper.

*Figure 2: AI-enhanced MEMS microphone array used in the project, with a compact, low-power AI processor (bottom right).*

### 2.3 Video tracking

To confirm the presence of a UAV on the area to be protected, it is important to complete the information transmitted by the AI-enhance microphone arrays, which can sometimes generate false alarms, especially when many sound sources are present in the vicinity of the microphone array. Indeed, the trained acoustic deep learning networks allow a substantial screening of the detected and localized sound sources, but can generate false positive detections. For that purpose, an optronic system is also deployed in the area. This optical system is mounted on a motorized steerable turret stand and its orientation can be controlled by the data fusion application. In contrast to the microphone arrays, cameras have a much narrower solid angle of observation, but have the strong advantage of having a maximum range of 1 km, which can allow the video tracking of a non-cooperative UAV (see Figure 3). The optronic system is composed of various cameras (visible, thermal, and active imaging) mounted on a servo-turret.

The active imaging system can capture objects within a given selected distance, which naturally excludes foreground and background from the image [1,2], and can enhance the capabilities of computer vision . For example, when the drone blends into the background with the visible camera, active imaging can isolate the UAV by visually eliminating the background on the image. The parameters of these imaging systems are controlled by the fusion of information provided in real time by the AIs of each microphonic arrays placed on site.

In the Deeplomatics project, the images provided by the optronic systems are processed in real time to detect and track a drone present in the field of view of the optronic system. This task refers to the field of computer vision detection, which will be detailed in section 3, a task dominated today by deep neural network algorithms with convolution filters that perform by extracting visual features from the data. We decided to choose the YOLO [3,4,5] model as the final model. Its very fast inference time are perfectly with the constraint on the detection time per frame was imposed so that the camera has time to adjust and track the drone. It was therefore necessary to have the fastest possible model.

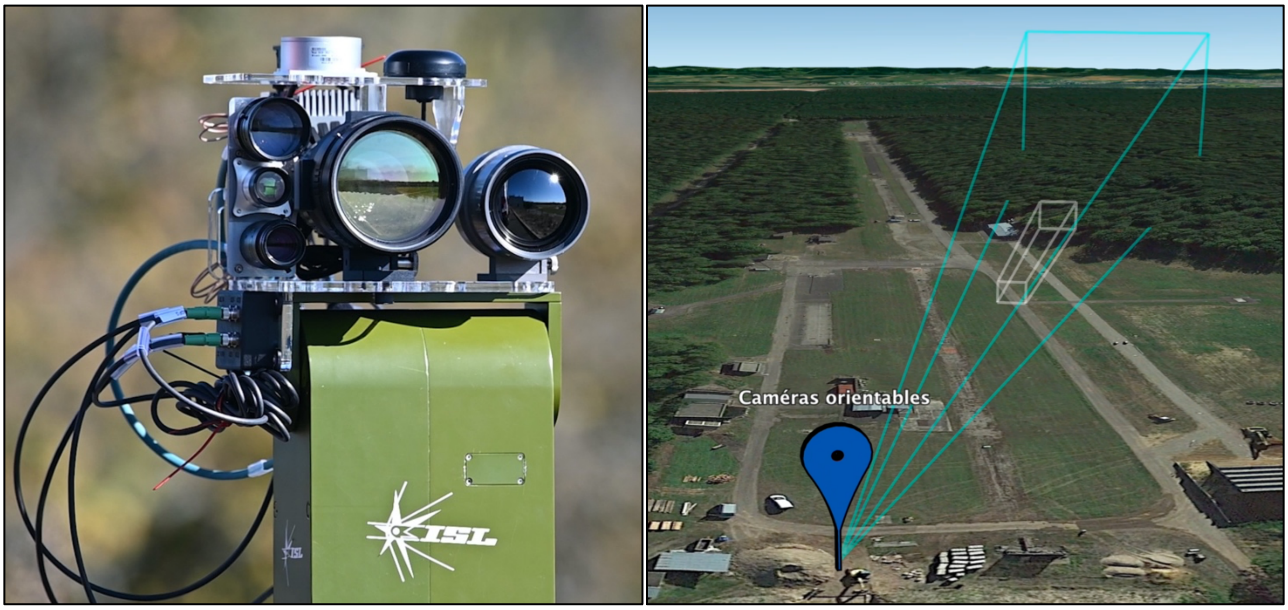


*Figure 3: Left: The optronic system composed of various cameras (visible, thermal, and active imaging) mounted on a servo-turret. Right: On-site field of view of the various cameras used in the optronic system. Cyan: visible field of view. White: active imaging field of view. The active imaging range is selectable and controlled by the fusion unit which processes the inferred UAV positions transmitted in real time by the acoustic monitoring nodes.*

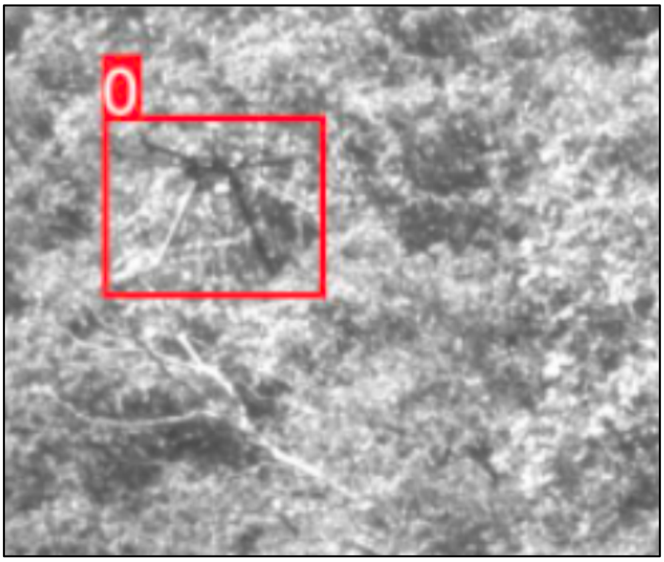


*Figure 4: Exemple of a detection of a flying drone on a textured background using the trained YOLO v5 network using in-house dataset constituted during the project.*

### 2.4 Data fusion

The data fusion application developed in the DEEPLOMATICS project must allow the analysis of data from different types of sensors deployed on the area to be monitored. Various types of sensors must be able to transmit information to the data fusion, including acoustic and optical sensors at this point. In future developments, the fusion should also be able to integrate information from other types of sensors, including for example Radar, Lidar, and electromagnetic sensors.

Additionally, when monitoring a large area, the number of connected sensors can be large, so it is mandatory to establish a simplified information exchange, limiting the bandwidth used for communication. This information must then be processed quickly to locate the source with sufficient accuracy to be visible in the camera's field of view. To meet these constraints, the communication protocol between the sensors and the fusion application was defined based on the National Marine Electronics Association (NMEA) protocol, which was adapted to define "proprietary" messages. Using this data exchange protocol, the data fusion application manages the metadata transmitted by the different sensors present in the area to be monitored. The standard scenario consists in deploying several microphone arrays around the area to be protected in order to detect intrusions in the area. When a threat is detected, the data fusion allows to estimate its geographical position (latitude, longitude, altitude) and transmits this information to a camera which undertakes a second phase of detection/identification of the threat. In case of confirmed intrusion, the camera starts an independent tracking of the target and transmits information about its orientation to the data fusion. This information is then used to display the camera's field of view and its orientation on a map and to verify that the acoustic and optical data are consistent (see Figure 5).

In order to improve the tracking performance of a drone entering a sensitive area, a particle filter process is applied at various stages of the data fusion process. Particle filtering is a Bayesian recursive filtering method using discrete "particles" to approximate the posterior distribution of the system state. This filter has the advantage of being efficient whatever the distribution of the input data, but has a high computational cost because it requires a large number of "particles", i.e. samples, representative of the data distribution [6].

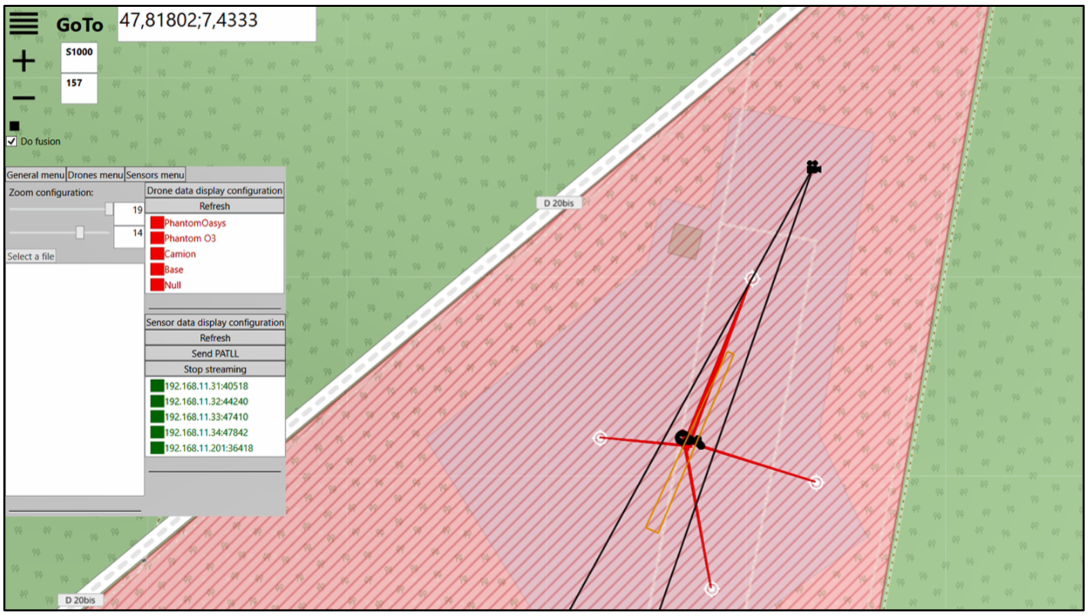


*<u>Figure 5</u>: Human Machine Interface (HMI) of the fusion server integrating the position of four microphone arrays (white dots) and the associated estimated direction of arrival (red line), the position of the camera (black camera icon), its orientation and the associated field of view (black and orange lines). The fusion of the estimated UAV position provided by the 4 acoustic AIs allows to control the orientation of the visible and active imaging system to realize an automated video tracking of the drone.*

# 3. Acoustic localization and detection using Deep Learning

In the DEEPLOMATICS project, each microphone array is attached to a deep neural network, trained for source localization and sound signature identification tasks. The neural network is a variant of the *BeamLearning* architecture [7] that we previously published for sound source localization. This variant of the network, *Beamlearning-ID,* has been specifically designed to simultaneously perform the recognition and localization tasks in real time [8]. The specialized AIs have been trained on a multi-channel dataset of acoustic signals from small UAVs in flight, under realistic conditions. These data acquisitions are augmented by a 3D spatializer. This augmentation will allow the neural network to respond as efficiently as possible to the localization and source identification tasks that will be performed simultaneously by the AI modules at the output of the compact microphone arrays.

## 3.1 Dataset: live measurements and higher order ambisonics 3D synthesis

A multichannel dataset of multichannel audio data was built throughout the Deeplomatics project to train the *Beamlearning-ID* network for drone localization and recognition. The acoustic signals recorded by the microphone arrays intrinsically convey information on the position of the acoustic source and its nature. The objective of the developed *BeamLearning-ID* deep network is to retrieve this information through supervised learning. Supervised learning requires a priori knowledge of this information. The audio data must therefore be annotated with the position and nature of the drone in flight.

The entire acoustic dataset is heavily annotated. To achieve this tedious task, a semi-automated process has been developed during the Deeplomatics project. During the flight of the drones, a GPS-RTK beacon is mounted on the drone and allows to know the position of the drone in real time. In parallel, several ambisonic microphone arrays record the 3D sound scene. The GPS and acoustic data are then synchronized. Moreover, a 3D spatialization step of the sound scene can be implemented if the antenna used to record the sound scene on site is different from the one used for the inference using the *BeamLearning-ID* network. This 3D spatialization process has been developed to produce an automated annotation of the multichannel audio (with labels denoting the drone model, and its 3D position synchronized with audio data) [8].

During the DEEPLOMATICS project, various measurement campaigns have allowed us to accumulate more than 34 hours of usable data of UAV flying data (simultaneous measurements of multichannel audio using high-order ambisonic microphone arrays and georeferenced position using a high precision realtime kinematics (RTK) GPS carried by the flying drones).

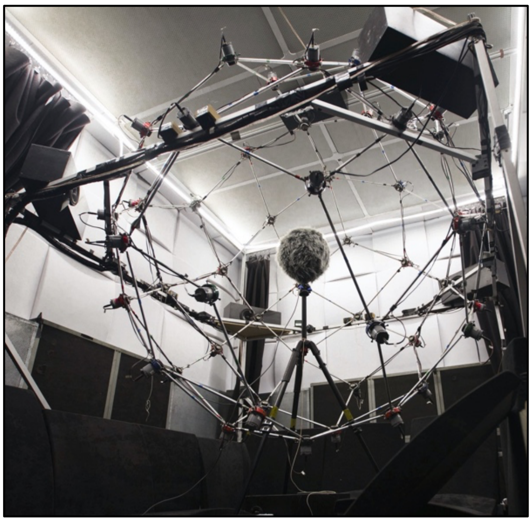

*Figure 6: Higher order ambisonics spatializer used in the training process and dataset augmentation.*

A large and realistic database allows deep neural networks to extract hidden patterns in the observation data. The size of the dataset is obviously not the whole story. For the deep neural network to be effective, it is necessary to build a dataset with a large variability of data. This is the reason why computer giants now have neural networks at their disposal that can exceed human capabilities in the field of image recognition. Image recognition researchers are now looking for ways to generate realistic synthetic images to train neural networks where the data sets are not yet large enough. We have, for localization or acoustic recognition tasks, access to a tool that allows to lift this lock and to generate simulated, augmented, or modified databases, while respecting the realism and the physical validity of the 3D pressure field.

The LMSSC has developed in the last few years a device that will allow to offer to localization and identification techniques by Deep Learning a flexibility and a realism not reached until now. Two tools developed and validated at the LMSSC are at our disposal [9-11]. The first device allows the spatialized capture of the sound environment, used in the measurement campaigns, and the second allows the restitution of the three-dimensional field (see Figures 6 and 7). These two devices allow us to render the 3D pressure fields of drones in flight on compact microphone arrays to train their individual artificial intelligence, even if the specific microphone arrays were not used for the on field experiments. One of the major advantages of this process is that we will also be able to "augment" the data captured during the measurement campaigns, by superimposing the 3D field of a large number of noisy environments, corresponding to potential locations for the installation of smart compact antennas (see Figure 7). These environments are also recorded by HOA ambisonic microphonic arrays.

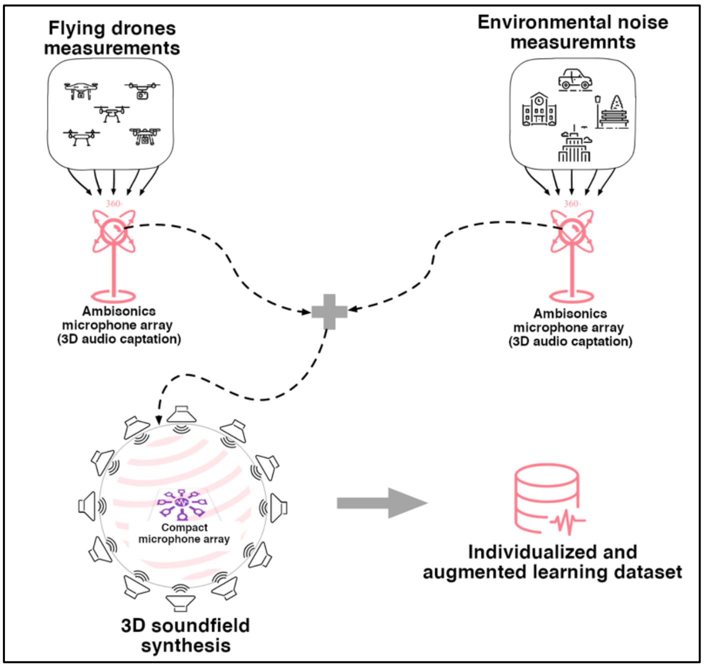


*Figure 7: Schematic of the data augmentation strategy using the 3D spatializer for building an individualized audio learning dataset on a compact microphone: example of spatially noisy environment additions.*

The flexibility of the ambisonic encoding operated by these two devices also allows us to modify the three-dimensional sound scene (e.g., modify the trajectory of the drone by rotation or dilation in the ambisonic domain / vary the signal-to-noise ratio and modify the spatial profiles of the ambient noise / etc ...).

The reproducibility of this physical synthesis of 3D acoustic fields will allow us to specifically train neural networks on different compact microphonic arrays, even other geometries than those used in the project. These AIs are trained to overcome or exploit the specificities of the environment in which the microphone will be installed, while implicitly performing a self-calibration of the several microphones included in the array [12]. This original approach provides Deep Learning for acoustics with the necessary variability to achieve abstraction and generalization capabilities that cannot be achieved by approaches based on array or environment models.

### 3.2 Beamlearning-ID deep neural network

Figure 8 shows the global architecture of *BeamLearning-ID* neural network developped specifically for this project. For more details on the underlying *BeamLearning* architecture, please refer to [7]. The BeamLearning-ID network is divided into blocks. The first block represents the raw input multichannel audio data, corresponding to the microphonic signals measured by the microphone array. The second block corresponds to a succession of several filter banks that allow to project the data into representative subspaces for the localization problem, thanks to residual subnetwork of atrous convolution kernels. The two parallel blocks in the third position are used to compute a pseudo-energy of the output channels of this succession of learnable filter banks, respectively for the localization and for the acoustic signature recognition tasks. Finally, the last two blocks allow to exploit these pseudo-energies, in order to deduce either the 3D angular position of the drone, or the type of drone having emitted the pressure field captured by the microphone array. The regression and classification approaches for source location have been compared by Tang *et al* [20]. In this project, the UAV angular localization problem, a regression approach is used. the source location will be given from a regression approach. Unlike the position of the source, the type of drone cannot be considered as part of a continuum. We therefore use a classification approach for the sound signature task. In our case, 6 classes are considered: one for the absence of drones and five for different drones used in this study (see Figure 9).

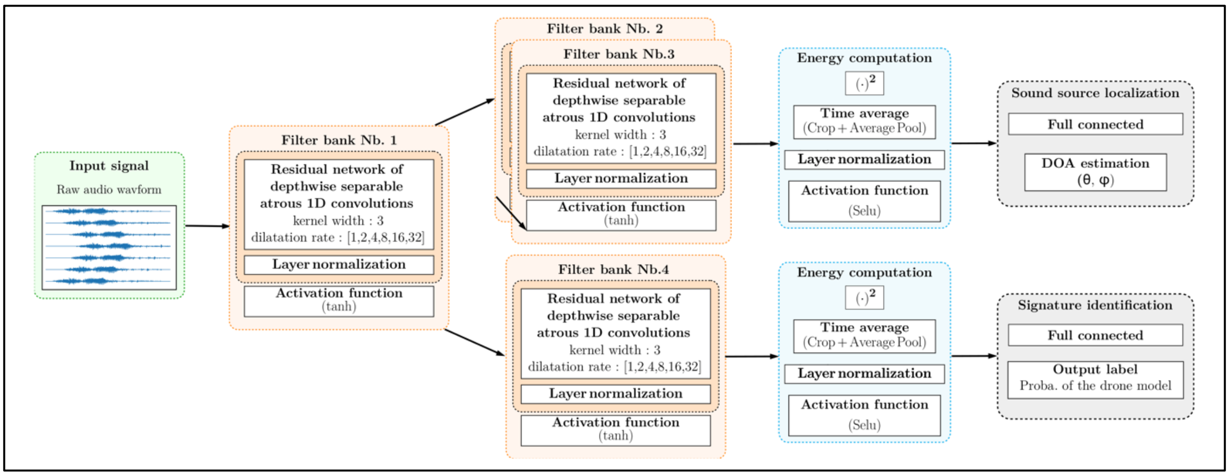


*Figure 8: General architecture of the Beamlearning-ID network developed for the Deeplomatics project, consisting of two branches, one for drone recognition (bottom), one for realtime 3D localization (right)*

Some deep learning architectures in the literature exploit pre-processed signals as input data, for example by using either the covariance of the signals, or their spectral representation, or the information contained in the modulus, or/and the phase [14-20]. We propose, on contrary, to use raw temporal signals. The different convolutions used to process the data are precisely intended to project the temporal data into a representational space that is most appropriate to the problem at hand. Thus, we do not a priori constrain the data by pre-processing them. This approach, commonly called "Joint Feature Learning", represents an increasingly important area of research for Deep Learning applications in acoustics, and is since an a priori priori choice of representation for the input data can potentially omit features that the neural network could extract by itself. Moreover, thanks to this approach without pre-processing, the inference latencies are minimized and it is possible to maintain a real-time data processing approach.

*Figure 9: Drones used for the flying drones dataset. From left to right: S1000, Phantom, Mavic pro 2, Mavic air, Spark.*

### 3.3 Example of the localization and recognition performances for a single microphone array on a test flight

In order to illustrate the performance of the *Beamlearning-ID* trained network, this section presents the results of position and identification estimation obtained from a recording made by an AI-enhance microphone array (see Figure 2) during the June 2021 measurement campaign of the Deeplomatics project (data not used for the training process).

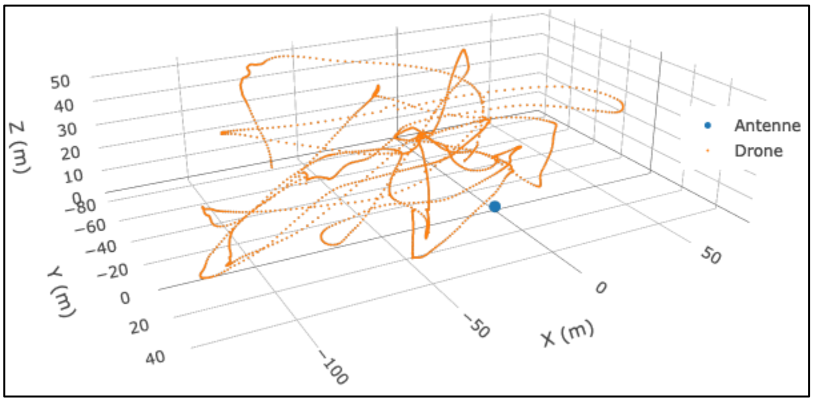


*Figure 9: Relative position of the flying drone during the testing flight. Those positions are obtained using the mounted RTK-GPS beacon. Each point corresponds to a georeferenced position, sampled each 200 ms.*

The drone used for this flight is an S1000 (see Figure 9). The flight lasted 7 min, which corresponds to 19734 consecutive estimates of drone positions and model identification (40 estimations/second). A 3D plot of the actual positions obtained using the RTK-GPS beacon mounted on the flying drone. Those positions are plotted on Figure 10 in a reference system centered on the microphone array, where the x axis points towards the north direction.

The way we designed the *Beamlearning-ID* deep neural network as well as its training process allows us not only to provide an angular position estimate at the output of the network, but also a confidence index noted r, which allows us to refine the estimated positions and to naturally filter the sound sources present in the environment of the microphonic array which are not flying drones. Figure 10 illustrates the statistical analysis for the angular localization performances for this flight, and Figure 11 illustrates the statistical analysis for the drone recognition task that is handled concurrently by the *Beamlearning-ID* network.

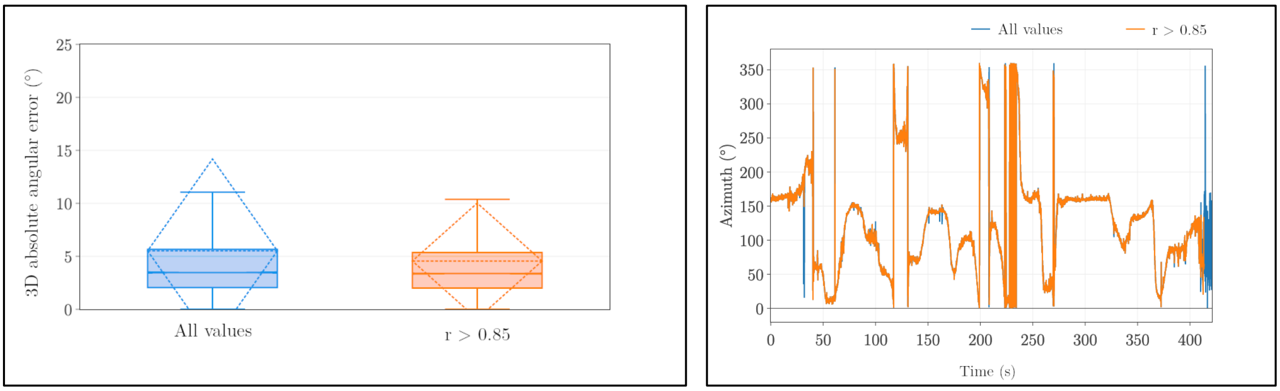


<u>*Figure 10*</u>*: Left : Boxplot analysis of the 3D absolute angular error on the estimated position during the testing flight, without filtering data with the confidence index (blue), or with the use of the confidence index by only keeping the estimations that correspond to r > 0.85 (orange). Right : corresponding azimuthal estimations during the flight.*

The analysis of figure 10 allows us to observe that the obtained 3D absolute angular errors are satisfactory during the whole flight, with a median of less than 4° (with or without the use of the confidence index as a filter). Using the confidence index to reject estimates due to non-UAV noise sources improves the results, with the mean 3D localization error improving by 16%, from 5.5° to 4.6°. On the other hand, the median varies only slightly, from 3.5° to 3.4°, which means that the confidence index has automatically removed outlier angular estimates due to auxiliary noise sources. This interpretation is confirmed by the estimated azimuthal trajectory plot on the right of Figure 10, especially at seconds 40 and 430: the estimates that are rejected are indeed estimates that are outliers with respect to the UAV trajectory.

The drone recognition functionality can also be evaluated. Figure 11 shows a histogram of the 19734 consecutive classifications obtained by the trained *Beamlearning-ID* network during the test flight presented above. The true-class inference rate is 76% for the raw data (in blue). On the other hand, after applying the r confidence criterion (in orange), the true-class inference rate is of 78%. The Deeplomatics project aims at protecting sites from drone overflights. Even if the recognized drone is not the right one, it is important that it is still recognized as a drone. The rate of non-detection of a drone observed in Figure 11 is 3% without using the confidence criterion and improves to 1% of non-detection of a drone on this flight. This observation confirms the effectiveness of the trained recognition system based on *Beamlearning-ID* archicture.

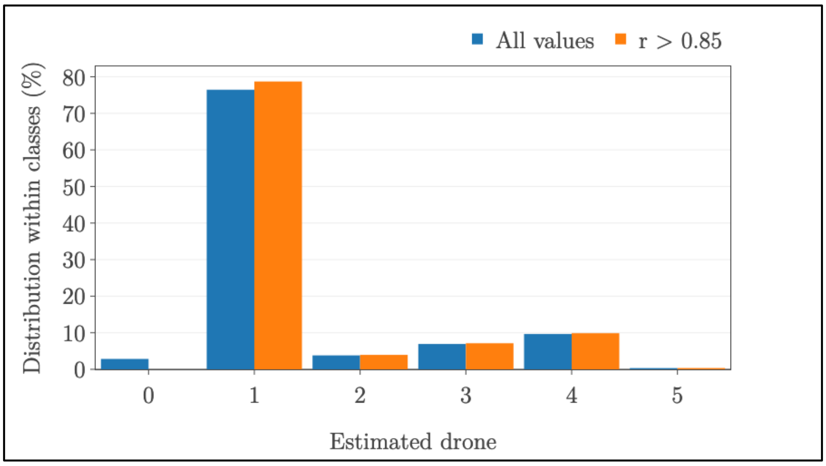


*Figure 11: Drone recognition performances for the testing flight (total of 19734 estimations for 7 seconds of flight). The drone classes are 0 (no drone), 1 (S1000), 2 (Phantom), 3 (Mavic Pro), 4 (Mavic Air), 5 (Spark). The recognition histograms are shown without filtering data with the confidence index (blue), or with the use of the confidence index by only keeping the estimations that correspond to r > 0.85 (orange).*

Thanks to the deep learning approach developed during the DEEPLOMATICS project, it is therefore possible to detect, localize and recognize a drone intrusion using a single AI-enhanced microphone array in its coverage area. The main benefit of the proposed approach is to perform these three tasks simultaneously which allows to spare a significant amount of time during the estimation process. With this approach, it is actually feasible to perform these three tasks in real time on relatively light hardware architectures (see Figure 2).

## 4. Conclusions

All the technological bricks of the Deeplomatics project are now functional and interoperate in realtime. Each microphone array associated to its own Beamlearning-ID network allows to detect and localize a drone intrusion, at a rate of 40 estimations per second. The estimations of each microphone array are sent in realtime to the data fusion unit in order to refine the georeferenced position of the drone in flight and its identification. The analysis of the output data of the fusion unit shows that for all the flights tested, the position error obtained is on average 13 meters when the drone is in the middle of the acoustic antenna cluster, ensuring the presence of the threat in the camera's field of view when the camera is 200 meters away from the microphone array cluster. Further developments concerning the acoustic devices include the industrialization of custom microphonic arrays with custom AI processors, and the potential use of informed spatial filtering in order to improve the detection and localization range.

**Acknowledgements**
This work has been funded by the DGA/AID Grant No. ANR-18-ASTR-0008.

**References**

[1] Christnacher, F., Monnin, D., Laurenzis, M., Lutz, Y., & Matwyschuk, A. (2011). Imagerie active: la maturité des systèmes ouvre de vastes perspectives. *Photoniques*, (55), 44-51.

[2] F. Christnacher, S. Hengy, M. Laurenzis, A. Matwyschuk, P. Naz, S. Schertzer et G. Schmitt, «Optical and acoustical UAV detection,» *Proc. of SPIE Security + Defence 2016,* vol. 9988, 2016.
[3] Redmon, J., Divvala, S., Girshick, R., & Farhadi, A. (2016). You only look once: Unified, real-time object detection. In *Proceedings of the IEEE conference on computer vision and pattern recognition* (pp. 779-788).
[4] Bochkovskiy, A., Wang, C. Y., & Liao, H. Y. M. (2020). Yolov4: Optimal speed and accuracy of object detection. *arXiv preprint arXiv:2004.10934*.
[5] Glenn Jocher et al. ultralytics/yolov5 : v3.1 - Bug Fixes and Performance Improvements. Version v3.1. Oct. 2020. doi : 10.5281/zenodo.4154370. url : https://doi.org/ 10.5281/zenodo.4154370.
[6] Orlande, H., et al., Kalman and Particle filters. METTI V-Thermal Measurements and Inverse Techniques, 2011.
[7] Pujol, H., Bavu, E., & Garcia, A. (2021). BeamLearning: an end-to-end Deep Learning approach for the angular localization of sound sources using raw multichannel acoustic pressure data. *The Journal of the Acoustical Society of America*, *149*(6), 4248-4263.
[8] Pujol, H., Bavu, E., Garcia, A., Langrenne C., Hengy S., Schertzer S., Matwyschuk A. (2022, April). Deeplomatics : Localisation et reconnaissance acoustique de drones . In *16ème Congrès Français d'Acoustique, CFA 2020*.
[9] P. Lecomte, Ambisonie d'ordre élevé en trois dimensions: captation, transformations et décodage adaptatifs de champs sonores, Thèse de doctorat: Paris, CNAM, 2016.
[10] P. Lecomte, P. A. Gauthier, C. Langrenne, A. Garcia et A. Berry, «On the use of a Lebedev grid for ambisonics,» *Audio Engineering Society Convention,* 2015.
[11] P. Lecomte, P. A. Gauthier, C. Langrenne, A. Berry et A. Garcia, «Cancellation of room reflections over an extended area using Ambisonics,» *The Journal of the Acoustical Society of America,* vol. 143(2), pp. 811-828, 2018.
[12] Bavu, E., Pujol, H., & Garcia, A. (2018, April). Antennes non calibrées, suivi métrologique et problemes inverses: une approche par Deep Learning. In *14ème Congrès Français d'Acoustique, CFA 2018*.
[13] Eric L Ferguson, Stefan B Williams, and Craig T Jin. Sound source localization in a multipath environment using convolutional neural networks. In 2018 IEEE International Conference on Acoustics, Speech and Signal Processing (ICASSP), pages pp.2386–2390. IEEE, 2018.
[14] Weipeng He, Petr Motlicek, and Jean-Marc Odobez. Deep neural networks for multiple speaker detection and localization. In 2018 IEEE International Conference on Robotics and Automation (ICRA), pages 74–79. IEEE, 2018.
[15] Ryu Takeda and Kazunori Komatani. Sound source localization based on deep neural networks with directional activate function exploiting phase information. In IEEE International Conference on Acoustics, speech and Signal Processing (ICASSP), pages pp.405–409. IEEE, 2016.
[16] Fabio Vesperini, Paolo Vecchiotti, Emanuele Principi, Stefano Squartini, and Francesco Piazza. A neural network based algorithm for speaker localization in a multi-room en- vironment. In 2016 IEEE 26th International Workshop on Machine Learning for Signal Processing (MLSP), pages 1–6. IEEE, 2016
[17] Sharath Adavanne, Archontis Politis, and Tuomas Virtanen. A Multi-room Reverberant Dataset for Sound Event Localization and Detection. In Submitted to Detection and Classification of Acoustic Scenes and Events 2019 Workshop (DCASE2019), Munich, Germany, 2019.
[18] Soumitro Chakrabarty and Emanuel A.P. Habets. Multi-speaker DOA estimation using deep convolutional networks trained with noise signals. IEEE Journal of Selected Topics in Signal Processing, Vol. 13(No. 1) :pp.8–21, 2019.
[19] Zhenyu Tang, John D Kanu, Kevin Hogan, and Dinesh Manocha. Regression and classification for direction-of-arrival estimation with convolutional recurrent neural networks. arXiv preprint arXiv :1904.08452, 2019.

**QUIET DRONES**
**Second International e-Symposium**
**on**
**UAV/UAS Noise**
**27th to 30th June 2022**

# Noise impact on humans – calculation methods and results for conceivable applications

**Stefan Becker, BeSB GmbH Berlin s.becker@besb.de**


## Summary

As part of a study for the German Environment Agency, it has been investigated among other things, whether it is possible to apply ISO 9613-2 or the German aircraft noise assessment method DIN 45684-1 for to calculate noise immissions resulting from the use of drones.

In principle, plausible results can be obtained with both calculation methods. However, both methods have their own limitations. Neither method is suitable for universal use. The German standard organisation DIN has therefore started a new project for to develop a new standard, which is more adopted to drone flights.

All drone sounds of multicopter design studied so far have a pronounced tonality. This makes the operation of drones easily audible and therefore more annoying than other sounds. If the evaluation is based on the noise limits of the German TA Lärm [7], a surcharge of 6 dB must be taken into account.

The results calculated for 3 conceivable applications can be summarized as follows: Overflights of residential houses at a height of 100 m above ground will only exceed the noise limits of the German TA Lärm [7] if a large number (> 100) of overflights take place. If a certain minimum distance to residential properties is provided, drone operations tend to be rather uncritical. On the other hand, if drone operations take place in a short distance to a residential property, only a short time of operation is needed for to exceed the noise limits.

# 1. Introduction

Unmanned Aerial Vehicles (UAV), commonly referred to as "drones", are becoming more and more powerful, which will lead to an increasing number of applications. With regard to the noise effects of the operation of these devices, there are currently no substantiated findings.

The German Environmental Agency (Umweltbundesamt – UBA) has therefore introduced a study [1] to compile the current state of knowledge on the following topics:

- ► Development of the Drone Market
- ► Noise Measurements
- ► Noise effects of drones
- ► Legal Framework
- ► Impact on humans and environment

The study was led by BeSB and done in cooperation with the Swiss Federal Laboratories of Material Science EMPA and lawyer company Redeker Sellner Dahs.

The vast majority of the investigations documented in the literature refer to the drone type multicopter. Consequently, all discussed aspects discussed below refer to drones of multicopter design.

In many countries (including Germany) there are currently a large number of restrictions on the operation of drones. In particular, a flight outside of the pilot's line of sight is currently not allowed These legal aspects are not considered in the present report. This report deals exclusively with the potential acoustic effects of some of today's conceivable applications.

# 2. Noise calculation methods

To illustrate the impact of a drone operation on humans and environment, calculations according to ISO 9613-2 (edition 12-1996) [4] and DIN 45684-1 (edition 07-2013) [5] were tested.

## 2.1 DIN 45684

Purpose of DIN 45684-1 is the calculation of noise impact (immissions) resulting from flight operations in the vicinity of smaller airports. To carry out the calculations, the aircrafts are assigned to individual aircraft groups and acoustic parameters are given for each aircraft group. DIN 45684-1 specifies acoustic parameters from ultralight aircrafts up to propeller or jet aircrafts with a maximum take-off weight up to 20,000 kg and helicopters with a maximum take-off weight up to 10,000 kg.

The calculation methodology is specially adapted to the application of light aircrafts. Therefore, changings in flight speed and statistical deviations from the target path can easily been taken into account. By now, the software products available on the market have also been able to import flight routes digitally (esp. radar tracks), thereby avoiding time-consuming manual modelling.

The acoustic parameters implemented in DIN 45684-1 have an open design, thus it is possible to adapt them to new circumstances or to define additional aircraft groups. The possibility of adaptation is only limited by the scope of the parameter set provided for the description of an aircraft group.

For the application on drones of a multicopter design, however, it is unfortunate that DIN 45684 only considers a horizontal, but not a vertical directional characteristic. As of today, all drones of the multicopter type have a pronounced vertical directional characteristic. In the horizontal direction, there is no pronounced directional characteristic (see [1] - [3]).

Furthermore, reflections on buildings or any other reflecting surface or shielding effects are not considered in DIN 45684-1. Regarding noise from planes operating at airports, the issue of shielding is usually not a concern because planes usually fly so high that shielding has no relevant influence on the result. Regardless, at least some software products still offer the possibility of taking reflections and shielding into account.

Overall, the optimization and simplification of the calculation method lead to short calculation times, so that calculations for large areas can be carried out in an adequate amount of time.

### 2.2 ISO 9613-2

In Germany, ISO 9613-2 is currently the standard method for calculating the noise impact (immissions) in the neighbourhood especially for all kind of industrial noise sources. It is used in particular within the scope of application of the German TA Lärm [7], which defines noise limits in the neighbourhood especially for industrial noise sources.

With regard to the options for modeling noise sources and situations, ISO 9613-2 is very flexible, so that almost all situations can be modeled. Both shielding and reflection can also be considered. However, the method is designed for static sources of noise or those moving at a constant speed. Changing speeds can therefore only be modeled by dividing the entire route into several sections, each with a constant speed. Therefore, modelling could be time consuming.

The flexibility of the method and the consideration of many factors influencing the sound propagation can lead to very long calculation times, which could be problematic in large calculation areas. This applies in particular when considering higher (3rd or higher) order reflections.

## 3. Modelling

### 3.1 General

Sound propagation calculations were carried out for the following scenarios:

A. Delivery of goods to the front door
B. Geo-exploration of an area by slowly flying over it
C. Light show with several hundred drones

For the calculations a professional software package (CADNA A) was used. In case of the first two scenarios, the digital terrain and building model (LOD1) of the city of Berlin was used to consider a realistic environment (see *Figure 1*). In the third case a flat terrain was assumed.

Figure 1 Szenario A and B, 3-D calculation model

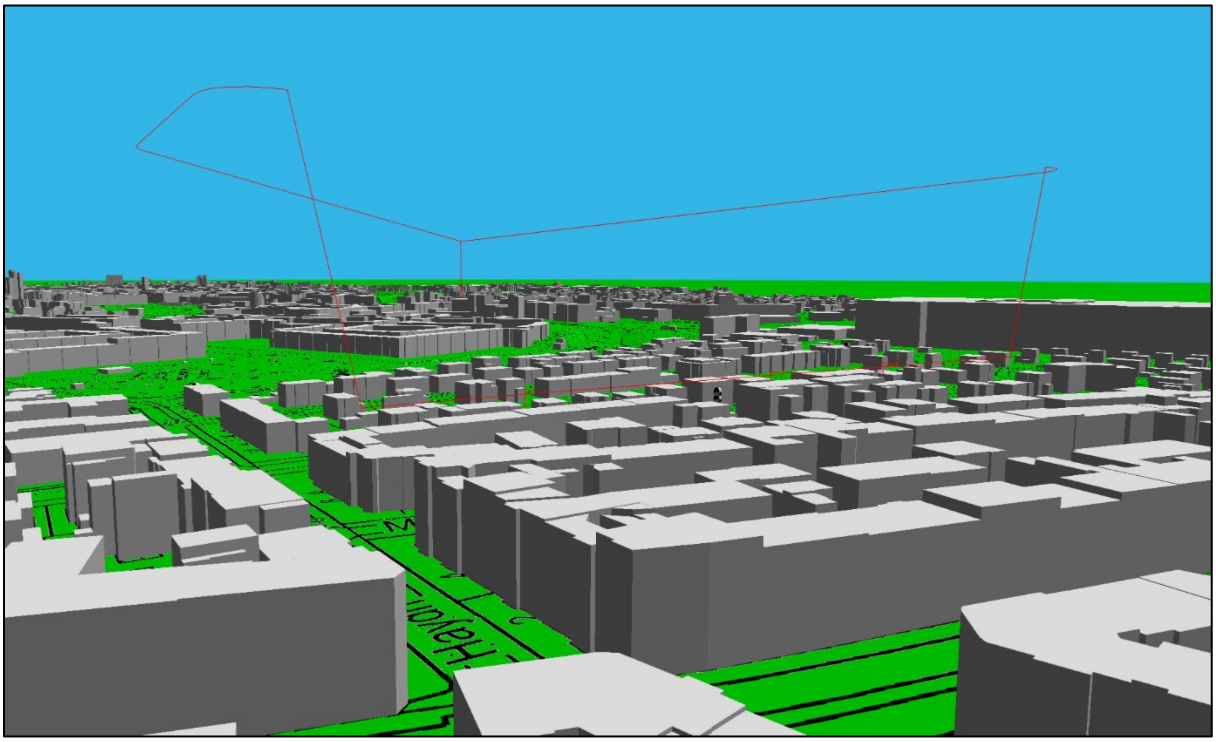

Source: BeSB

### 3.2 Modelling according to DIN 45684-1

For scenario A and B a small airfield was taken into account, from which the drone takes off and to which it returns. Basically, the process corresponds to the execution of a traffic pattern at a "normal" landing site. According to DIN 45684-1, traffic patterns consist of take-off, level flight and landing parts. In case of a drone flight, however, it is difficult to switch between the take-off and landing situation. We decided to model the whole flight as one traffic pattern. (If the flight route is available digitally in the form of radar tracks or similar, these could also be used directly for the calculations.)

As the altitude of a common aircraft usually depends on the flight situation, the traffic pattern used in DIN 45684-1 does not have information about the altitude of the aircraft. The altitude is described in the flight groups, which are specific for each type of aircraft. This system was adopted to drones. The hovering of a drone at a specific location (e.g. at delivery) was modeled by a very slow flight speed. Disadvantage of this method is that the aircraft group has to be created or at least modified individually for each flight route. If this is done manually, it is a time-consuming process. Table 1 shows an example of an aircraft group according to DIN 45684-1 adapted to a drone flight route.

In the flight groups, different noise emissions (e.g. during take-off, landing, en-route flight) can be taken into account by adding a supplement to the sound power level (German: Zusatzpegel). Since we currently have no reliable information about different levels of noise emissions in different flight phases, the same sound power level was always considered for the calculations shown in this report.

As previously mentioned, the special vertical directional characteristics of multicopter-type drones is not implemented in DIN 45684-1. The calculations were therefore carried out with an omni directional characteristic. In the case of flight movements that take place above an observed immission point, this leads to an underestimation of the calculated level.

*Table 1 Example of a flight group input field according to DIN 45684-1 as implemented in CADNA A*

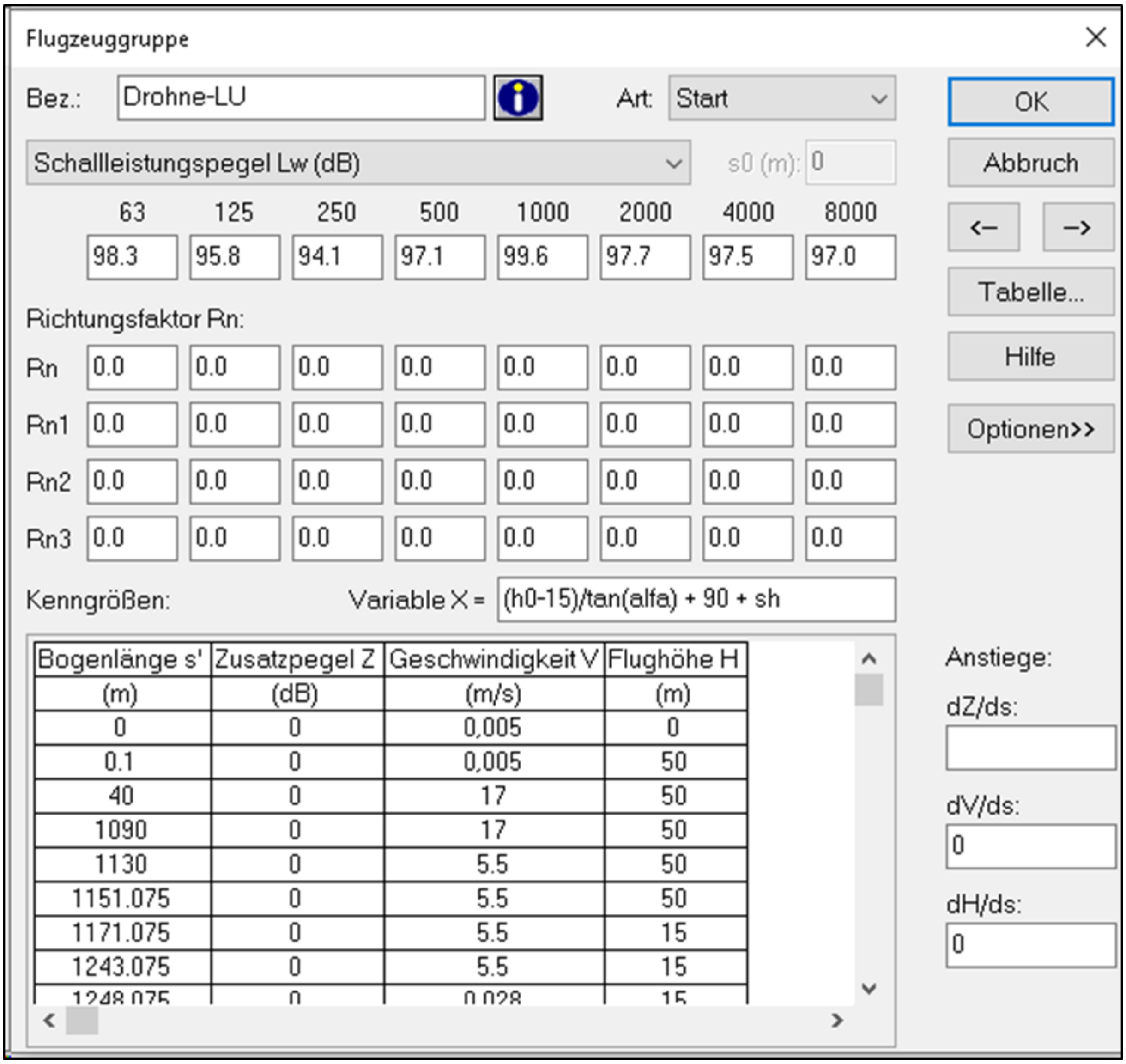

Flugzeuggruppe

Bez.: Drohne-LU

Art: Start

OK

Abbruch

<-  ->

Tabelle...

Hilfe

Optionen>>

Schallleistungspegel Lw (dB)

s0 (m): 0

| | 63 | 125 | 250 | 500 | 1000 | 2000 | 4000 | 8000 |
|---|---|---|---|---|---|---|---|---|
| Lw | 98.3 | 95.8 | 94.1 | 97.1 | 99.6 | 97.7 | 97.5 | 97.0 |

Richtungsfaktor Rn:

| | | | | | | | | |
|---|---|---|---|---|---|---|---|---|
| Rn | 0.0 | 0.0 | 0.0 | 0.0 | 0.0 | 0.0 | 0.0 | 0.0 |
| Rn1 | 0.0 | 0.0 | 0.0 | 0.0 | 0.0 | 0.0 | 0.0 | 0.0 |
| Rn2 | 0.0 | 0.0 | 0.0 | 0.0 | 0.0 | 0.0 | 0.0 | 0.0 |
| Rn3 | 0.0 | 0.0 | 0.0 | 0.0 | 0.0 | 0.0 | 0.0 | 0.0 |

Kenngrößen: Variable X = (h0-15)/tan(alfa) + 90 + sh

| Bogenlänge s' | Zusatzpegel Z | Geschwindigkeit V | Flughöhe H |
|---|---|---|---|
| (m) | (dB) | (m/s) | (m) |
| 0 | 0 | 0,005 | 0 |
| 0.1 | 0 | 0,005 | 50 |
| 40 | 0 | 17 | 50 |
| 1090 | 0 | 17 | 50 |
| 1130 | 0 | 5.5 | 50 |
| 1151.075 | 0 | 5.5 | 50 |
| 1171.075 | 0 | 5.5 | 15 |
| 1243.075 | 0 | 5.5 | 15 |
| 1248.075 | 0 | 0.028 | 15 |

Anstiege:

dZ/ds:

dV/ds: 0

dH/ds: 0

Schallleistungspegel: sound power level; Richtungsfaktor: directivity;
Bogenlänge: Distance along the flight path (projection to the ground); Geschwindigkeit: velocity; Flughöhe: altitude;
Zusatzpegel: supplement to the sound power level

### 3.3 Modeling according to ISO 9613-2

In case of calculations according to ISO 9613-2, reflections up to the 3rd order were considered and a reflection loss of 1 dB was assumed for all surfaces of houses. Wind statistics were not used, i.e. all calculations were based on weather conditions with excellent sound propagation.

The flight path and flight movement were modeled using line and point sources. The line sources represent the en-route flight, while the point sources represent the noise emissions at a fixed point (e.g. hovering during delivery). A specific flight speed is assigned to the line sources, which determines the average time spent on the route of the line source. The allocation takes place automatically in the calculation program CADNA A. The point sources are used to model a drone hovering over a fixed point. The noise impact at a certain point in the neighbourhood due of a certain line or point source was first calculated individually and then energetically added.

In ISO 9613-1, three-dimensional directional characteristics can be taken into account by entering the deviation from the mean value for individual angle segments in a source-specific manner. This was considered from the results given in [1] - [3]

The advantages and disadvantages of the two calculation methods examined are summarized again below.

Table 11 Advantages and disadvantages of the investigated calculation methods when applied to drone noise.

| DIN 45684-1 | ISO 9613-2 |
|---|---|
| - Complex modeling, as the altitude profile of the flight route and the speeds along the flight route have to be entered individually. Subsequent changes to the flight route are very time consuming. A description in digital form (e.g. radar track) is very desirable | + Modeling by line sources and point sources is very fast and flexible. (Subsequent changes can easily be implemented) |
| + Simple consideration of special flight characteristics such as: <br>• continuous changes in speed and altitude and <br>• Flight corridors to consider deviations from the target path | - The consideration of special aeronautical properties such as continuous changes in speed and altitude and flight corridors to account for deviations from the target path is not possible or only possible with great modeling effort |
| - No consideration of the vertical directional characteristics typical of multicopters | + The vertical directional characteristics typical of multicopters can be taken into account |
| + Fast calculation algorithm. This makes it possible to take larger wraparounds into account, (as long as according to DIN 45684-1 reflections and shielding are not considered.) | High computing time (especially when considering shielding and reflections) |
| - Usually reflections are not taken into account (although this is still an option in some software packages) | + Usually reflections and shielding are taken into account in the calculation |

# 4. Calculation results

### 4.1 Scenario A - Delivery of Goods

As an example of a delivery, the delivery of a newspaper by a drone with a take-off mass of approx. 15 kg to three houses in one street was considered (see Figure 21 and Figure 22). For the calculations, it was assumed that the drone takes off in a commercial area and lands again at the same point after the tour.

The sequence of the flight was assumed as follows: After take-off, the drone climbs vertically to a height of 100 m and then accelerates to a flight speed of 60 km/h. The drone then flies in a direct path to the beginning of the street where the delivery is to take place. Before the drone pivots to a flight direction along the road, it slows its flight to a speed of 20 km/h. After the drone swings to the flight direction along the street, it descends to a flight altitude of 15 m (in the present case, about 2 - 3 m above the roofs of houses) and flies along the street. At the three delivery points, the drone swings away from the road in the direction of the property. Above the property, at the defined delivery point, the drone stops its forward flight and descends vertically to the delivery height of 4 m above the ground. At this point, the drone hovers for 12 seconds and disengages the newspaper. With the delivery completed, it climbs back to 15 m above ground, accelerates to 20 km/h, and leaves the site to continue its flight along the road. At the next two delivery points, the described sequence is repeated. After completing all three deliveries, the drone flies to the end of the road, climbs back up to 100 m altitude and then swings onto a course toward the starting point. In doing so, it accelerates again to 60 km/h. Before the take-off/landing point, the drone brakes to a standstill and descends vertically toward the ground until landing.

When modelling according to DIN 45684-1, routes on which acceleration takes place or routes with constant speed can easily be taken into account because of the special tools implemented in DIN 45684-1. This is not possible with modelling according to ISO 9613-2. Here, only constant speeds can be considered. In the sense of an approach to the safe side, the calculations according to ISO 9613-2 took into account an overall longer dwell time for the acceleration and braking sections by assuming a constant, lower speed of 10 km/h. The state of hovering during the acceleration and braking sections can only be taken into account if the speed is constant.

The state of hovering during delivery was modelled in the application case of ISO 9613-2 by a static point source taking into account the corresponding stay time of the drone. When applying DIN 45684-1, a path length of 0.1 m was defined at the delivery point and the predefined stay time of 12 seconds was considered by a correspondingly low flight speed.

Regarding the noise emissions of the drone during the flight, the results of reference [1] given there in chapter 3.3.2 were used. Accordingly, it can be assumed that a drone with a take-off mass of 15 kg has a sound power level of approx. 105 dB(A) during operation.

Figure 2 shows a visualization of the previously described flight path. For this purpose, a vertical grid was calculated along the flight path. The coloured representation serves exclusively for visualization purposes. The take-off and landing area can be seen on the left edge of the figure. Due to the lower flight speed and the use of the same flight path for take-off and landing, relatively long durations of stay and, as a consequence, relatively high noise immissions result here (expressed here by yellow and red colours).

At the right edge of the figure, the noise situation as a result of delivery can be seen. As expected, the highest noise immissions occur where the drone hovers for a while close to the ground and close to the buildings for the purpose of delivery. At these points, the vertical directivity of the drone can also be seen (as explained above, a vertical directional characteristic cannot be taken into account in calculations according to DIN 45684-1).

*Figure 2 Calculated vertical grids according to ISO 9613-2 scenario A – delivery*

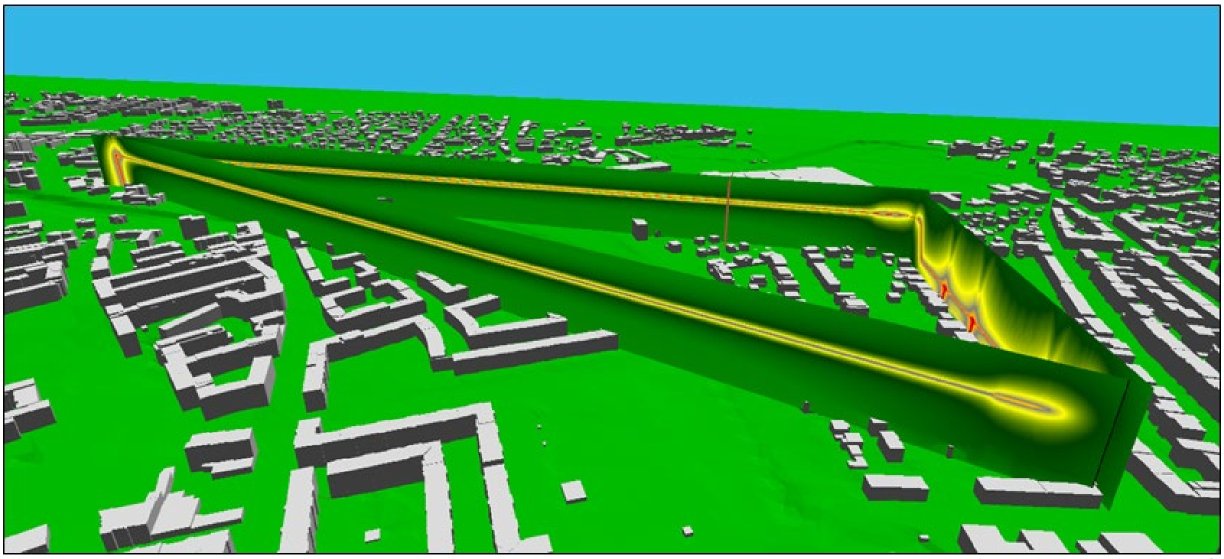

Source BeSB

Results

At present, no guideline exists in Germany for the assessment of noise immissions caused by drones. However, it is becoming apparent that an assessment analogue to that for industrial noise will be used for noise caused by drones.

Industrial noise is assessed in Germany on the basis of TA Lärm [7]. According to this, normally a rating level of 55 dB(A) may not be exceeded during daytime (6 a.m. to 10 p.m) in residential areas. The rating level essentially corresponds to the energy equivalent level averaged over the 16 hours of daytime ($L_{Aeq,day}$) plus surcharges for tonal and/or impulsive noise.

Figure 3 shows the results of the calculation according to ISO 9613-2 as three-dimensional facade levels. The numerical values represent the average energetic level ($L_{Aeq,day}$) over the entire day (16 hours), assuming one event per day. Based on the results in reference [1], the noise from drones is classified as highly tonal. For this reason, a supplement of 6 dB must be added to the values given in Figure 3 to form the rating level as defined in the TA Lärm.

It has to be said that the data concerning the sound power of drones is still very thin. The results shown in Figure 3 are therefore only to be considered as an orientation.

In Figure 3, the higher levels are clearly visible in those areas where the drone descends to a low flight altitude and delivers the newspaper. For the buildings for which the delivery is intended, energy equivalent levels of $L_{Aeq,day}$ = 48 dB(A) were calculated. For neighbouring buildings directly connected to the delivered house, levels 2 dB lower have been determined. If neighbouring houses are not directly connected, 4-6 dB lower levels were calculated, depending on the distance. Houses on the opposite side of the street have up to 7 dB lower levels with up to $L_{Aeq,day}$ = 41 dB(A).

As explained above, an exemplary assessment according to TA Lärm would have to take into account an additional 6 dB for the tonality. If one were to exclude the supplied houses from the assessment and only consider the affected neighbouring houses, an assessment level of 52 dB(A) would result for directly adjacent neighbouring buildings; for a delivery by drone during the day. Adding a second drone would even result in a rating level of 55 dB(A). As explained above, normally a rating level of 55 dB(A) should not exceed in residential areas. Compliance with the requirements of TA Lärm could therefore become easily problematic.

If a house is flown over at a distance of 100 m, much lower average levels result. In the selected example, energy equivalent levels of up to 24 dB(A) result for one drone flying over during the day. Assuming 100 drones flying over a house, this would result in an energetic average level of $L_{Aeq,day}$ = 44 dB(A). Even if a supplement of 6 dB due to tonality is taken into account, the requirements of TA Lärm for residential areas would still be undercut during daytime. Cross-country flights at high altitudes are therefore generally not critical in terms of compliance with the requirements of TA Lärm.

The calculations according to DIN 45684-1 basically lead to similar results. However, due to the non-consideration of reflections at the facades of houses and the non-consideration of the vertical directivity, lower (and thus presumably too low) noise immissions are calculated within the street where the delivery takes place. Along the remaining part of the flight path, however, very similar noise immissions result.

*Figure 3 Calculation results for scenario A – delivery, Energy equivalent sound pressure level $L_{Aeq,day}$ assuming one delivery per day*

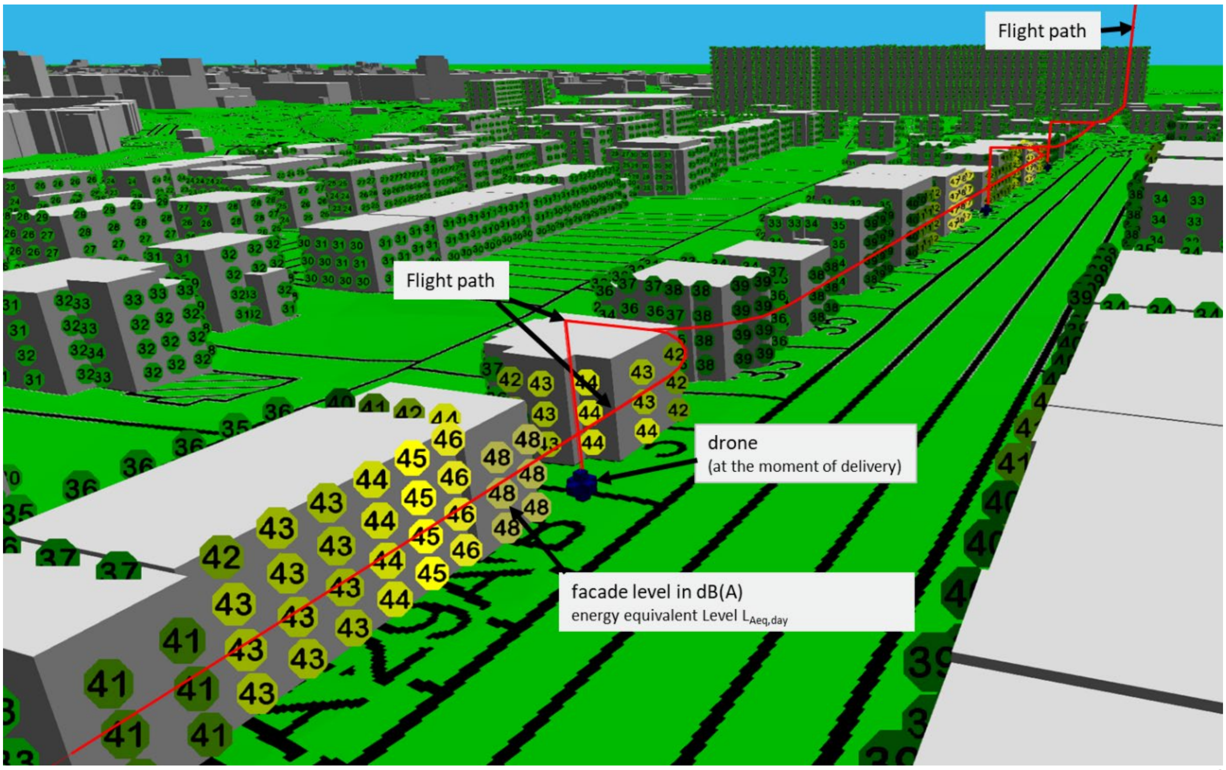


Source BeSB

### 4.2 Scenario B - Geospatial Exploration

For this scenario, the examination of an area of approx. 3.5 ha was considered. It is assumed that the drone is delivered by a vehicle and takes off and lands right next to the area to be examined. For the calculation it was assumed that the drone flies over the area to be examined at a constant height (50 m above ground) in several meandering loops at a constant speed (5 km/h). For the selected example, the above information results in a flight duration of approx. 45 minutes. Since the drone does not have to carry any loads apart from a camera, a 5 kg drone is assumed to be sufficient. According to reference [1] (chap. 3.3.2), a sound power level of 97 dB(A) can be assumed for such a device.

Figure 4 shows a visualization of the previously described flight path in same way as shown in Figure 2 (vertical grid). Higher noise emissions are given next to the take-off and landing area due to the double use of the flight path.

*Figure 4 Calculated vertical grids according to ISO 9613-2 Scenario B - geo-exploration*

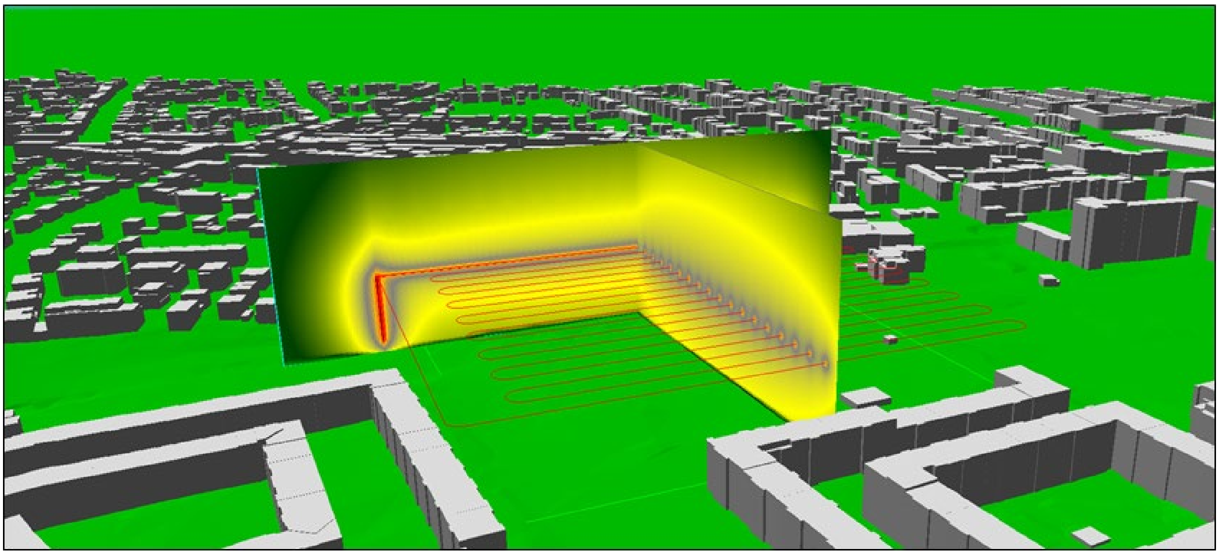

Source BeSB

Figure 5 shows the results of the calculation according to ISO 9613-2 as a three-dimensional facade level. Energy averaging levels $L_{Aeq,da}$ of 35 dB(A) were calculated for buildings that are closest to the flight path of the drone. However, it can be assumed that the reconnaissance flight should be clearly audible in the area of the nearest residents, so that a supplement of 6 dB seems justified to determine the rating level according to TA Lärm. This would result in a rating level of 41 dB(A) for the nearest residents. The requirement of TA Lärm for residential areas (normally 55 dB(A)) would be significantly undercut.

The results according to DIN 45684-1 lead to similar results, since the differences in the calculation methods have no relevant effect in this application.

*Figure 5 Calculation results for Scenario B - geo-exploration of the energetic mean $L_{Aeq,day}$*

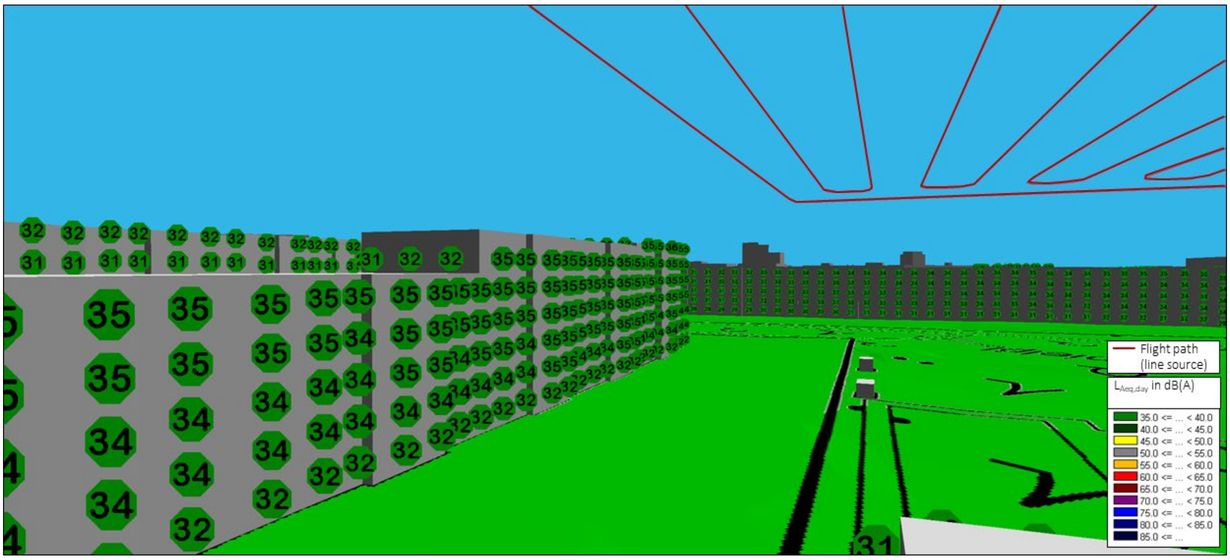


Source BeSB

### 4.3 Scenario C - Drone Light Show

A large number of small drones equipped with controllable lighting elements are used for light shows. Using information provided by an operator, the constellation currently used to carry out light shows with drones is shown in Figure 6. As a result, the drones hover within a fixed area in the sky (so-called animation grid) during the demonstration, which is located in front of the audience. Within the animation grid, the drones are arranged in a grid, with an assumed distance of approx. 3 × 3 m between the individual drones. The centre of the animation grid is about 125 m above the ground at a horizontal distance of about 100 m to the centre of the audience area (see Figure 6).

*Figure 6 Scenario C – drone light show, basic arrangement and 3D representation of the calculation model*

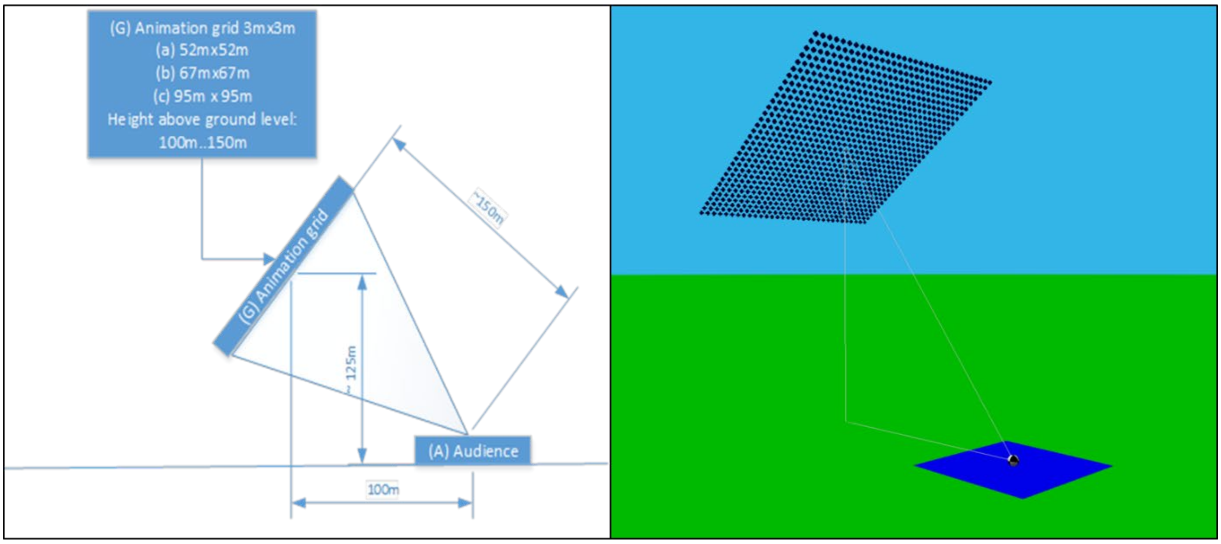


Source BeSB

For the calculations it was assumed that the event takes place in an open field or square and that shielding and reflections can therefore not be taken into account. Since the drones only move in a limited area and do not cover long flight distances, a calculation according to DIN 45684-1 does not make sense. Therefore, only calculations according to ISO 9613-2 were carried out. Each drone was considered by its own point source (see Figure 6). An event with 1024 drones, each with a mass of 0.35 kg, was assumed for the calculations. With regard to the maximum allowed noise emissions according to the COMMISSION DELEGATED REGULATION (EU) 2019/945 [6], a single drone must not exceed a sound power level of 91 dB(A). With the above assumptions, a sound pressure level of approx. 67 dB(A) would result in the spectator area during the performance of the event. Such events are usually accompanied by music. It can be assumed that the sound pressure levels generated by the accompanying music are generally higher than the sound pressure levels generated by the drone light show.

## 5. Conclusion

In summary, it can be stated that it is possible to carry out noise immission forecasts with both ISO 9613-2 and DIN 45684-1 and thus to obtain meaningful results. However, since the two guidelines are not optimized for drones, this currently still involves considerable modelling effort. In this respect, a calculation program adapted to drones would be useful especially in order to be able to perform such calculations more quickly. A corresponding standardization procedure is in preparation in Germany.

More problematic is the currently still very thin data situation with regard to the noise emissions (sound power) of the individual drones. Therefore, calculated noise immission forecast could vary from measurement results. The COMMISSION DELEGATED REGULATION (EU) 2019/945 defines maximum sound power levels, but these apply only to drones of type Multicopter up to a total weight of 5 kg and only for the "hover" operating mode. They are therefore only useful in a few cases.

All drone noises investigated so far have a pronounced tonality in common. Thus, drone noise differs significantly from all other environmental noise. The operation of drones is thus easily audible among other noises and is clearly more annoying than other traffic noises. It can be assumed that the tonal sound reduces the acceptability of drones. If the noise from drones were to be assessed on the basis of the German TA Lärm, a supplement of 6 dB would have to be added in most cases.

If the noise from drones were to be assessed on the basis of a rating level of 55 dB(A), which is, according to the German TA Lärm, usually the limit for residential areas, even one minute of operation per day in the vicinity of residential houses would exceed the limit. In order to let drones operate in the vicinity of residential areas, a significant noise reduction is needed.

If drones are cruising above residential houses at a minimum distance of 100 m, noise limits will not be exceeded even if 100 drones per day were passing by.

**References**


[1] Becker S, Schäffer B, Heutschi K, Eckart C, Gutsche D, *Lärmauswirkungen des Einsatzes von Drohnen auf die Umwelt*, Umweltbundesamt (D), 1-2022 https://www.umweltbundesamt.de/publikationen/laermauswirkungen-des-einsatzes-von-drohnen-auf-die-0

[2] Schäffer B, Pieren R, Heutschi K, Wunderli J, Becker S, *Drone Noise Emission Characteristics and Noise Effects on Humans—A Systematic Review*, Int. J. Environ. Res. Public Health 2021, 18, 5940. https://doi.org/10.3390/ijerph18115940

[3] Treichel J, Körper S, *Investigation of the noise emission of drones*. Lärmbekämpfung, 14, 108-114, 2019.

[4] DIN 45684-1 „*Akustik — Ermittlung von Fluggeräuschimmissionen an Landeplätzen — Teil 1: Berechnungsverfahren*“, Ausgabe 7-2013

[5] ISO 9613-2 „*Acoustics — Attenuation of sound during propagation outdoors — Part 2: General method of calculation”* 12-1996

[6] EU 2019/945, *COMMISSION DELEGATED REGULATION (EU) 2019/945 of 12 March 2019 on unmanned aircraft systems and on third-country operators of unmanned aircraft systems*

[7] TA Lärm 2017, *Sechste Allgemeine Verwaltungsvorschrift zum Bundes-Immissionsschutzgesetz (Technische Anleitung zum Schutz gegen Lärm - TA Lärm)* vom 28. August 1998 (GMBl Nr. 26/1998 S. 503) zuletzt geändert durch Bekanntmachung des BMU vom 1. Juni 2017 (BAnz AT 08.06.2017 B5) in Kraft getreten am 9. Juni 2017

QUIET DRONES
Second International e-Symposium
on
UAV/UAS Noise
27th to 30th June 2022

# Towards mobile microphone array based UAV tracking

**Martin Blass (JOANNEUM RESEARCH): martin.blass@joanneum.at**
**Anna Maly (JOANNEUM RESEARCH): anna.maly@joanneum.at**
**Franz Graf (JOANNEUM RESEARCH): franz.graf@joanneum.at**
**Peter Wellig (armasuisse Science and Technology S+T): peter.wellig@armasuisse.ch**
**Beat Ott (armasuisse Science and Technology S+T): beat.ott@armasuisse.ch**

## Summary

The emergence of new technologies for UAVs and their commercial availability offer great opportunities in supporting humans in a wide variety of tasks. However, when used as a means of attack, single UAVs or swarms may create a potential asymmetric threat situation, which cannot be satisfactorily countered with existing sensor technology. Currently, multimodal approaches are being investigated in which UAVs can be detected, localized, and tracked using a composite of different sensors. In the development of such multi-sensor solutions, the acoustic domain has emerged as an indispensable element. However, existing systems relying on acoustic sensors primarily focus on stationary operation and detection of a single UAV. In this work, we present approaches for the development of a mobile acoustic sensor system that can detect and track multiple drones based on the direction of sound incidence. In contrast to the majority of solutions existing in the literature, where the focus lies on either detection or localization, we propose joint estimation of UAV sound presence and incidence. We evaluate our proposed system on a dataset acquired in the course of a measurement campaign conducted at a military camp near Bure, Switzerland, for a stationary as well as for a mobile scenario, where a microphone array was mounted on the roof of a vehicle.

## 1. Introduction

Within the past century, drones and other unmanned aerial vehicles (UAV) have become a well-established technology in the fields of industrial monitoring, aerial surveying, logistics, public safety and agriculture to name a few [1]–[3]. Besides professional applications there is also growing popularity of UAVs operated by amateur pilots. Since commercial off-the-shelve drones are available at low cost and do not require any explicit expert knowledge, they may also easily be used to deliberately or accidently violate privacy, raise public annoyance due to noise or even pose a threat to society or public facilities when used as a means of attack. An ever-growing list of potentially dangerous UAV-related incidents [4], [5] clearly shows that aerial threats of this kind cannot be adequately countered with existing methods. In order to prevent or quickly stop incidents with unwanted UAVs in the civilian sector or to achieve military sovereignty in the detection and defense of UAVs as a means of war, a growing number of research projects and counter-UAV products have been launched in recent years to develop suitable UAV detection and defense strategies [6]. Existing systems primarily use a multi-sensor approach and address the task of UAV detection and localization using RADAR, computer vision, radio frequency and acoustic technologies [7], [8]. While often neglected due to limited detection ranges, the acoustic domain provides cost-efficient solutions and serves as an indispensable element for the automatic detection of UAV presence in terms of noise signatures in situations where other sensor modalities face their own difficulties.

In the field of acoustic UAV detection, sensor systems based on single or multiple microphones are used to capture audio signals, which may be analyzed in real-time by machine learning models to discriminate between presence and absence of UAV sound. In state-of-the-art literature on acoustic event detection and classification the current trend is towards the use of deep learning models, which use a large database of online available sounds for training neural networks (NN) and try to learn audio features from common time-frequency representations, such as Short-Time Fourier Transform (STFT), Mel-frequency spectrograms or Mel-Frequency Cepstral Coefficients (MFCC) [9]. Typical NN architectures comprise recurrent neural networks (RNN), convolutional neural networks (CNN) or a mixture of both (CRNN) [10]. In Marinopoulou et al. [11] three different 2D CNNs were trained on STFT data of 3 s audio segments taken from a large recorded and manually annotated dataset containing 2500 h of single-channel audio data. With the help of data augmentation strategies, the proposed system reached a macro-average F1 score of 0.95. In the work of Al-Emadi et al. [12] different network architectures (RNN, CNN, CRNN) were trained using recorded as well as online available drone sounds together with synthetically generated UAV audio data using a generative adversarial network (GAN). Casabianca and Zhang [13] also compare RNN, CNN and CRNN with mel-spectrograms computed from online audio sources as input features and propose a late fusion of network ensembles for improved performance. Alaparthy et al. [14] compared detection performance of a CNN and a Support Vector Machine (SVM) classifier with MFCC as features and conducted a survey with 35 participants to measure machine learning versus human classification performance, which indicated that humans clearly outperform machine learning system when it comes to identifying UAV noise. In a publication of Kolamunna et al. [15] the proposed system *DronePrint* was trained on UAV (target) and non-target audio solely obtained from online sources. They also use MFCC as features and utilize feature scaling and data augmentation to increase the robustness of their LSTM model (RNN). Similar works have been carried out by Dumitrescu et al. [16] and Svanström et al. [17].
Besides this kind of approaches there is still a considerable share of other works, in which conventional machine learning models are used together with selected feature extraction methods to perform UAV detection. This process is also known as feature engineering and relies on choosing adequate acoustic low-level features as well as various types of time-frequency transforms [18]. Wang et al. [19] compare different machine learning models such as SVM, Gaussian Naïve Bayes (GNB), K-Nearest Neighbor (KNN) to a simple feed-forward NN trained with common audio features, e.g. Chroma and Mel-STFT, MFCC, spectral contrast [20]. The work of Ohlenbusch et al. [21] shows that an SVM model together with a well-designed feature set may outperform CNN-based systems relying solely on STFT input features. Another contribution by Uddin et al. [22] presents a time-varying drone detection technique to detect single and multiple drones by applying signal unmixing using independent component analysis (ICA) as a pre-processing step to separate drone sounds from background and interference noise.

Unmixed signals are then classified as drone targets or non-targets by an SVM taking linear predictive cepstral coefficients (LPCC) and MFCC as input features. A comprehensive overview of machine learning based acoustic drone detection systems published before the year 2020 is given in [23].

In order to be able to not only detect but also localize the incident direction of drone sounds, multiple microphones need to be operated as microphone arrays, which enable the use of direction-of-arrival (DOAE) and beamforming (BF) methods. In addition, sound source tracking algorithms may be applied to process frame-based DOA estimates and to reconstruct movements of multiple sound sources in space. Itare et al. [24] perform 3D DOAE using a 9-channel microphone array and compare conventional time-domain delay-and-sum beamforming (DSB) to a proposed method, where only the strongest frequency bins of UAV sound based on its harmonic structure are used for DOAE. In the aforementioned work of [25] a planar spiral-shaped array composed of 30 MEMS microphones is used for DOAE by applying the MUSIC algorithm with the aim to improve detection performance.
In the sense of a UAV localization framework DOAE is only half of the story. To arrive at robust acoustic localization in moving sound setups an appropriate source tracking strategy is required. Herold et al. [26] propose Kalman filtering and solving a linear assignment problem for reconstructing flight trajectories of multiple moving UAVs. DOA candidates are estimated using functional beamforming and detecting local power maxima within the 3D spatial sampling grid. Another approach to improve acoustic localization is used in Liu et al. [27] where a wireless sensor network of tetrahedron arrays is employed to estimate the 3D location from the acoustic energy decay measurements of each sensor using multilayer perceptrons (MLP) as a simple NN architecture in real-time. However, this method is only applicable to the presence of a single UAV.

In the literature, there is still a limited amount of publications combining both detection and localization with regard to UAVs. However, the relatively young research field of sound event localization and detection (SELD) has gained popularity over the past years, which aims at solving the association problem of detection and localization estimates [28]–[31]. From a practical perspective, SELD models tend to be large in terms of network size and require huge amounts of data to achieve satisfying performance. Hence, papers addressing this issue in the context of UAV detection and localization have rarely used SELD methods so far, but have come up with their own strategies. Similar to [25], Baron et al. [32] propose DOAE using MUSIC followed by applying DSB to each sound source to extract enhanced versions of noisy signals. Detection is then performed by an SVM that uses a mix of 96 temporal, spectral and cepstral audio features. One limitation of using MUSIC is specifying a fixed number of eigenvalues for finding DOA candidates, which however does not match real-life conditions, where one or multiple sources may be present at different times. Guo et al. [33] performed simulations of adaptive beamforming using a circular microphone array to find and extract sound sources. A Hidden Markov Model (HMM) then uses MFCCs computed from beamformer outputs for classification of drones and other non-target classes. One exemplary work based on a SELD approach is by Toma et al. [34], where a novel radio-frequency assisted detection and localization method of UAVs is proposed. This method uses a four-stage CNN to learn intrinsic features from covariance matrices of STFT audio data and received signal strength RF data to perform detection as well as localization in terms of DOA and distance through regression. Our former contribution, Blass et al. [35], presents one of the first systems for joint detection and localization of UAVs in real-time using a GMM-based sound source tracking algorithm together with a Random Forest classifier trained on 10h of audio data containing real UAV flights and engineered audio features to describe UAV noise.

In this paper, we want to take a step further and investigate approaches for the development of a mobile acoustic sensor system that can detect and track multiple drones based on the direction of sound incidence. Our extensive research revealed that such mobile systems are currently not present in the literature and may be relevant for public security or military applications in the

future. We evaluate our proposed system on a small dataset acquired in the course of a measurement campaign conducted at a military camp near Bure, Switzerland, for a stationary as well as for a mobile scenario, where a microphone array was mounted on the roof of a vehicle. In contrast to our former work [35], we recorded audio data using a small tetrahedron microphone array with 4 channels to provide a proof-of-concept for UAV detection and localization capabilities with smaller and simpler array geometries.
The remainder of this paper is organized as follows: Section 2 describes the methods used for UAV localization and detection both as separate and joint systems, Section 3 presents our experimental results and Section 4 concludes the work and gives a future outlook.

## 2. Methodology

Similar to our previous contribution [35], we propose a modular system comprised of two components: First, an acoustic localization algorithm providing DOA estimates of multiple sound sources in order to capture potential UAV candidates and second, a binary classifier to discriminate between UAV presence or absence using the reference microphone signal (MIC).

### 2.1 UAV Localization

For the task of DOAE we adapted a model-based approach [36]–[38] for the use in 3D space with custom frequency and sampling grid settings. This offers probabilistic modelling and tracking of an unknown number of sound sources, source extraction using masked beamformer outputs. It provides good localization accuracy even for coarse search grids and the computational load allows application in real-time. For details, please refer to [36]–[38].
DOA estimates are obtained within a Cartesian space from a spatial scanning grid serving as support points for each time block $b$ and frequency bin $k$ using a steered response power (SRP) functional $J_{SRP}\,(\theta, k, b)$. Under the assumption of time-frequency (TF) disjointness, each TF point is attributed to a single dominant DOA as

$$\hat{\theta}(k,b) = \underset{\theta}{\operatorname{argmax}} J_{SRP}(\theta, k, b)$$

By clustering estimates of all frequency bins using a GMM in 3D (XYZ) a distribution of $I$ active sound sources is fitted for each time frame. Within the GMM each sound source $q$ is attributed a mean $\theta_q$, a variance $\sigma_q^2$ and weight $P_q$. Since the number of active sources may change from frame to frame, each source is assigned a time-to-live (TTL) once it has appeared. By using an age-token-based temporal smoothing method, the source locations are updated over time [34].
Given the DOA estimates, $\theta_q$ the corresponding DSB outputs are computed for each time frame. Since the DSB does not actively cancel interferers and only provides limited signal enhancement, a mask-based approach using the GMM parameters is formulated to achieve better noise suppression. The softmask for source $q$ is computed as the posterior probability that a particular TF point belongs to $q$, given the GMM model for that frame and the estimates $\hat{\theta}(k,b)$ [35].

### 2.2 UAV Detection

As elaborated in [35], we propose to use a mix of different audio features to properly describe characteristics of UAV sound. For the acoustic description of the UAV rotor sound, the harmonic content within the frequency range between 100 Hz and 2 kHz and its temporal modulation play an important role. Wind turbulences of rotors and electric motors contributing to broadband noise in the range of 1-12 kHz are also distinct sound characteristics, but are less reliable when used as acoustic features due to masking of interference noise and sound dissipation increasing with frequency. Hence, following our feature engineering approach we adapted our audio feature set of [35] and use generic low-level audio descriptors [18], MFCCs with custom frequency ranges, and spectral peak track features together with smoothing and statistical functionals to model temporal characteristics. For binary classification of *UAV* (target) or *NO-UAV* (non-target) classes,

we choose a frame-based Random Forest (RF) classifier due to simple parametrization and fast execution in real-time. As post-processing, we apply temporal smoothing over frames using a first-order IIR filter on the class confidence output of RF.
In addition, we propose a deep learning approach to provide a comparison to the RF as a conventional machine learning model. Similar to various works within the literature, we use a logarithmic Mel-frequency spectrogram as input features for an RNN, which is implemented as a multiple LSTM-layers and one fully connected (dense) output layer. For this model, we omit the post-processing step of RF as the RNN inherently learns temporal relations within audio signals.

### 2.3 UAV Detection and Localization

Using independent systems for UAV localization and detection is only sufficient in the rare case, where a UAV represents the dominant sound source within a sound scene. Hence, following the reasoning in our former work [35], we propose a system that jointly localizes and classifies multiple sound sources by adding extracted BF signals of localized sources as spatially filtered inputs for the MIC detector. An overview of this system is given in Figure 1. The performance of this *track-before-detect* type of approach strongly depends on reliable sound source tracks, which poses a twofold challenge: First, the DOAE must be sufficiently accurate to focus on the sound sources and to provide the tracker with correct measurements. Second, if a track is distracted from a source or intermittently lost, the detector may not be able to recover the temporal signal context and thus miss a potential target. Nonetheless, this approach provides a simple and modular way to robustly detect and track even multiple UAVs given an appropriate DOAE and tracking algorithm. It is modular in a sense that each component of the source extraction pipeline, i.e. DOAE, beamformer and source tracker, may be exchanged and improved. In this work, we put our emphasis on detecting and tracking a single UAV using our proposed approach from [35]:

$$\hat{q} = \underset{q}{\operatorname{argmax}}\, C(q)\,,$$

where $C$ denotes the class confidence outputs for $Q$ BF signals and sound source $\hat{q}$ is regarded as the target UAV candidate. Joint classification is then achieved by taking the maximum of MIC and BF confidences. In Section 3.8 we investigate whether this approach may improve detection performance given the classifier models described in Section 2.2.

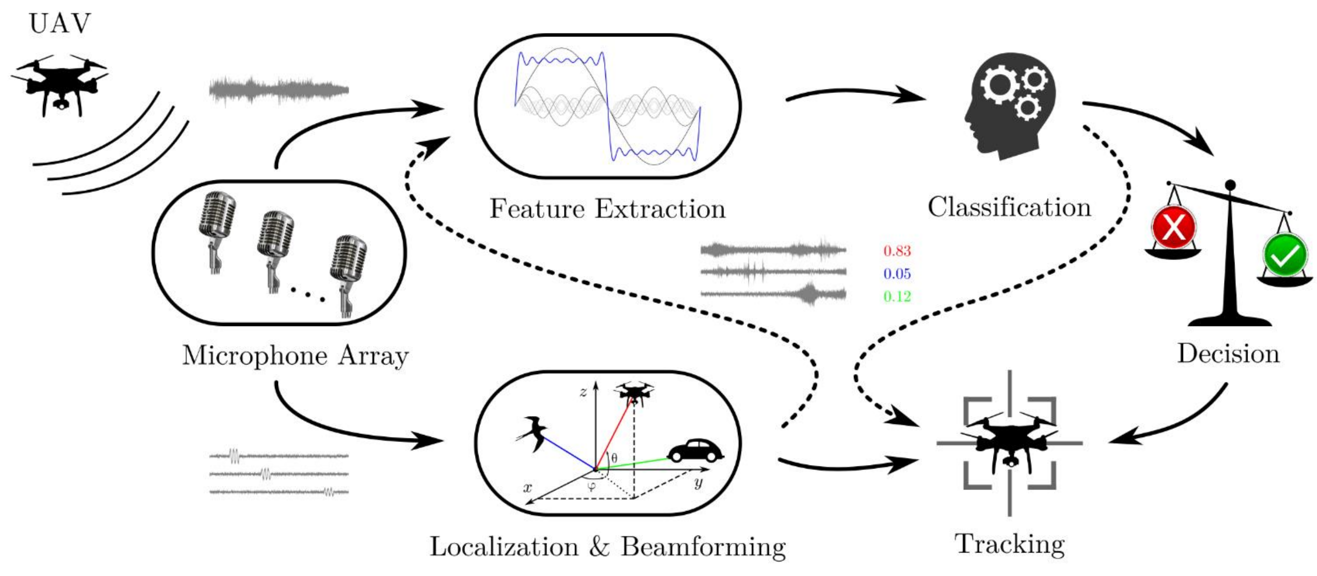


*Figure 1: Overview of the proposed system for joint UAV detection and localization [35]. A microphone array captures audio signals, which are used for DOAE and tracking. BF audio signals of localized sources and a reference microphone signal serve as inputs for audio feature extraction. Binary classification is performed on reference and beamforming signals to discriminate between UAV and non-UAV classes yielding confidence outputs for sound source tracking and decision-making.*

# 3. Experimental Results

## 3.1 Microphone Array

The microphone array used in our experiments comprises four sensors arranged in a tetrahedron shape. The radius in the XY-plane and the height along the Z-axis measure 144 mm (*mic01-mic03*) and 125 mm (*mic04*), respectively. Prior to using this array for acoustic localization tasks we explored its theoretical frequency range, which is determined by half the wavelengths fitting within the minimum and maximum effective inter-sensor distances, as well as other frequency dependent performance metrics, such as half-power beamwidth, sidelobe levels and directivity index. For numerical simulations we considered a DSB with third-octave center frequencies. The resulting list of array parameters and metrics are given in Figure 2 (right). In addition, we simulate the spatial response as point spread functions (PSF) depicted in Figure 3. Compared to a large array comprised of more microphones, as we used in our former experiments [35], this 4-channel array is in fact not well-suited for UAV localization tasks. The choice for using this array geometry is mainly motivated by exploring the physical limits for UAV localization with small microphone arrays, which may be used in both fixed and mobile scenarios.
The hardware implementation of the array was carried out by *IAV Engineering* and features four digital MEMS microphones connected to a printed circuit board with a microcontroller and a GNSS receiver that provides GPS ground truth positions Figure 2 (right). This sensor board serves as an audio capture unit for recording multichannel audio signals together with GPS log files. All signal processing is done offline.


| Parameter | Value |
|---|---|
| Number of microphones | 4 |
| Radius in XY | 144 mm |
| Height in Z | 125 mm |
| Effective minimum frequency | 689 Hz |
| Effective maximum frequency | 2318 Hz |
| Half power beamwidth (BW)* | 53.8° |
| Maximum sidelobe level (MSL)* | -1.9 dB |
| Average sidelobe level (ASL)* | -2.4 dB |
| Directivity index (DI)* | 6.2 dB |

*Figure 2: MEMS microphone array by IAV Engineering with four sensors, microcontroller for audio capturing and GNSS receiver (left), and array parameters and metrics* averaged over third-octave center frequencies within the effective freq. range (right).*

## 3.2 Measurement Setup

The experiments for acoustic UAV detection and localization were conducted in the course of a measurement campaign at a military camp near Bure, Switzerland, in August 2020. The UAV flights were organized as missions and runs with defined sensor placement and flight paths, which were logged using onboard GPS receivers. As UAVs, two types of commercial off-the-shelve (COTS) multicopters (*DJI Phantom 4 Pro*, *DJI Mavic 2 Pro*), four custom-built rotary-wing quadcopters (RW) and four fixed-wing (FW) drones (*E-flite Opterra 1.2 m*) were used. Figure 4 shows pictures of the custom RW and FW drones.
Multiple acoustic sensor arrays were distributed over the camp area with the intent not only to evaluate the DOAE capabilities of a single sensor, but also to investigate the possibility of 3D acoustic localization and tracking by using triangulation of DOA estimates. In this work, however, we only focus on the task of DOAE and tracking using a single sensor array. The sensor placement was split in two different scenarios, as shown in Figure 5: a fixed setup, where the array was placed on the ground and a mobile setup with the array mounted on the roof of a car.

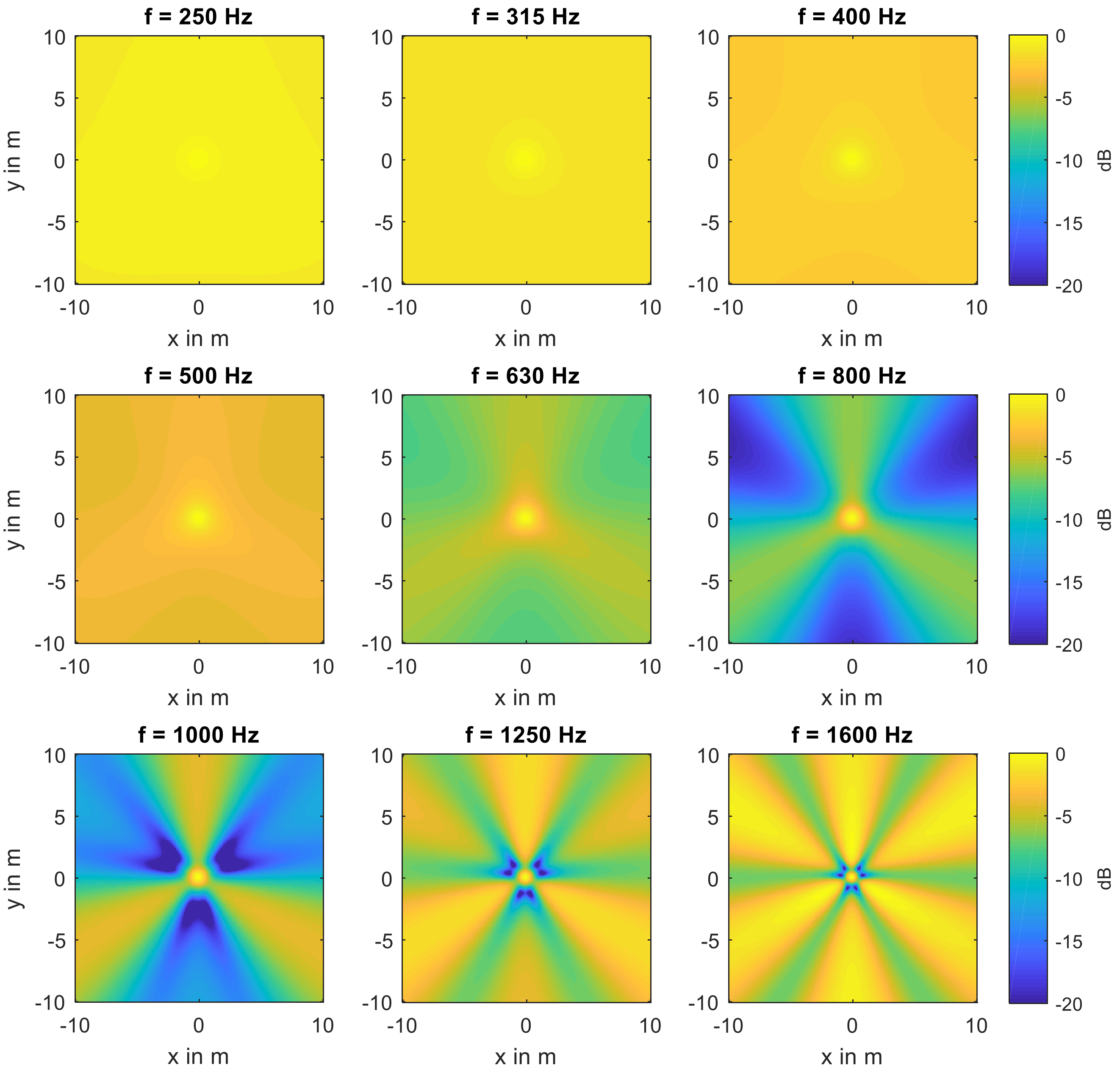


*Figure 3: Point spread functions (PSF) of the used 4-channel tetrahedron microphone array for third-octave center frequencies. The PSF provides the spatial response in dB to a synthetic sound source in the center of the scanning area at a height of 1 m.*

*Figure 4: UAVs deployed in the field: custom-built quadcopter (RW) drones (left) and customized fixed-wing (FW) drones E-flite Opterra 1.2 m with one rotor (right). These custom UAVs use certified DJI and PixHawk hardware components.*

Runs with fixed sensor setup were performed in the manner: take-off between 200-400 m from the sensor, approach, fly-by, depart. The total fight time of all runs was 46 min, of which 11 min were spent at speeds below 1 km/h or hovering. The average speed of all runs was 21.7 km/h. The average and maximum flight heights were measured as 10 m and 115 m, respectively. The average distance between UAV and sensor was 124 m for fixed and 76 m for mobile setups.
Audio signals were recorded as multichannel wav-files with four channels at a sampling rate of 48 kHz with 32 bit resolution. GPS times and positions were logged at a rate of approximately 10 Hz, 25 Hz and 1 Hz for COTS, custom drones and sensors, respectively. In a data pre-processing step all GPS logs were aligned to the respective audio signal of each run and resampled to match the chosen audio processing frame rate.

*Figure 5: Different scenarios of sensor placement: fixed setup with the microphone array placed on the ground (left), and mobile setup with the array mounted on the roof of a car (right). A faux fur cover protects the array from excessive wind noise.*

### 3.3 Audio Dataset

Our test dataset of the Bure 2020 measurement campaign consists of 28 runs out of which 16 runs were captured with the fixed sensor and 12 runs were recorded in the mobile setup specifying a predefined driving route with a car driving at a minimum and maximum speed of 25 and 50 km/h, respectively. The audio recordings of the fixed and mobile setup have a duration of 36 min and 10 min respectively, resulting in 46 min in total out of which approx. 70% are positives (*UAV*). The audio dataset was manually annotated by human ear to provide ground truth classes. Table 1 provides a list of associated UAVs and setups for all runs within the test dataset.

*Table 1: List of associated UAVs and sensor setups for all runs in the test dataset for detection and localization experiments.*

| UAV | Runs (fixed) | Runs (mobile) | Runs (total) |
|---|---|---|---|
| DJI Phantom 4 Pro | 8 | 0 | 8 |
| DJI Mavic 2 Pro | 0 | 1 | 1 |
| RW custom | 6 | 4 | 10 |
| FW custom | 2 | 7 | 9 |

The training dataset for fitting the classifier models RF and RNN comprise 13 h of independent audio recordings from nine different multicopter UAV types and various background sounds. The portion of positives frames is 40%. This dataset is an extended version of the training set of [35].

### 3.4 System Parameters

In this Section, we outline the settings used for the UAV localizer composed of DOAE and sound source tracking as well as the classifier models RF and RNN described in Sections 2.1 and 2.2.

For both localization and detection tasks we perform block processing on audio signals with Hann windowed frames of 50% overlap. For DOAE and BF, we choose a sampling frequency of 8 kHz together with a frame size of 128 ms and a 1024-point FFT. The localization algorithm requires a predefined search grid, which we specify as 300 quasi-uniformly distributed points on the surface of a hemisphere [39]. A plot illustrating the DOAE and BF setup is shown in Figure 6 (left). As practical frequency range for DOAE, we use a modified version of the array's theoretical frequency range, where we use frequencies from 300 to 1300 Hz. As can be seen in the PSF plots of Figure 3, there is only limited directivity gain around the frequency band of 300 Hz, however it still contains characteristic UAV rotor sound components. Due to strong sidelobes above 1200 Hz we set the upper frequency limit to 1300 Hz. A list of other parameters used for the localizer is given in Figure 6 (right).

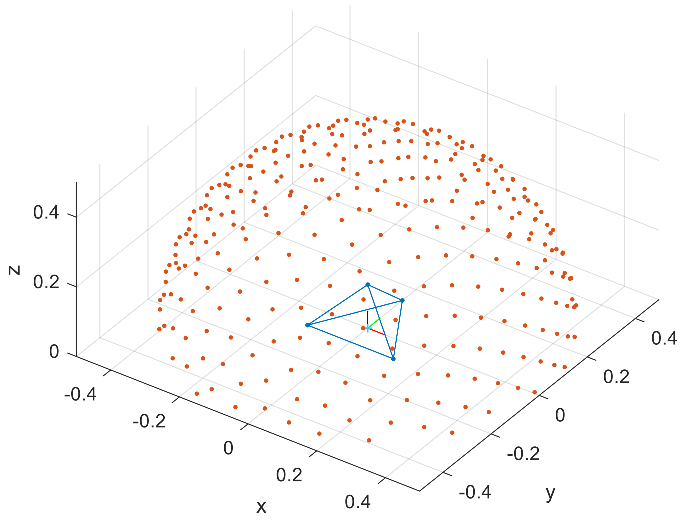


| Parameter | Value |
|---|---|
| Number of DOAE search points | 300 |
| Number of DOAE frequencies | 128 |
| Minimum DOAE frequency | 300 Hz |
| Maximum DOAE frequency | 1300 Hz |
| Number of DOAE sources + BF | 3 |
| Number of tracked sources | 16 |
| Minimum source confidence | 0.1 |
| Minimum source separation | 30° |
| Minimum/maximum source TTL | 1 s |
| Exp. smoothing of source tracks | 0.7 |

*Figure 6: Settings for the UAV localization algorithm: DOAE and beamforming setup with tetrahedron microphone array (blue) and 300 predefined search locations (red) for frequency selective DOAE and GMM fitting (left), and table of specified parameters for DOAE and sound source tracking (right).*

For the classifier models RF and RNN we set the sampling rate to 24 kHz and use a frame size of 85 ms with an FFT size of 2048. The RF is trained using the *perClass Toolbox*[1] and specifies 30 trees each with a maximum number of 10000 leaf nodes and 20% of randomly selected features for each split during training. The RNN is implemented using the *Keras* API of *TensorFlow 1.15*[2] and comprises three LSTM-layers with 50 units each and default parameter settings. We use the Adam optimizer [40] to minimize the binary cross-entropy loss function.

### 3.5 Selected Flights

In this Section, we show plots of three selected flights of the RW drones:

- *Run-A*: one drone with fixed sensor setup (Figure 7),
- *Run-B*: two drones with fixed sensor setup (Figure 8),
- *Run-C*: one drone with mobile sensor setup (Figure 9).

In each figure, the top subplot shows the spectrogram as power spectral density of the reference microphone signal. The second subplot draws the distance computed from the GPS logs as ground truth (GT) between the UAV and the sensor over time. Subplots 3 and 4 visualize the DOAE of three tracked sound sources (SRC1-3) in azimuth and elevation angles against GT and plot the absolute DOA error for each source. The bottom plot shows detector outputs, confidence (CONF), decision (DEC), and classification metrics of the RNN with the reference signal as input.

[1] https://www.perclass.com/perclass-toolbox/product
[2] https://devdocs.io/tensorflow~1.15/keras/layers/lstm

### ***Run-A*: One drone with fixed sensor setup**

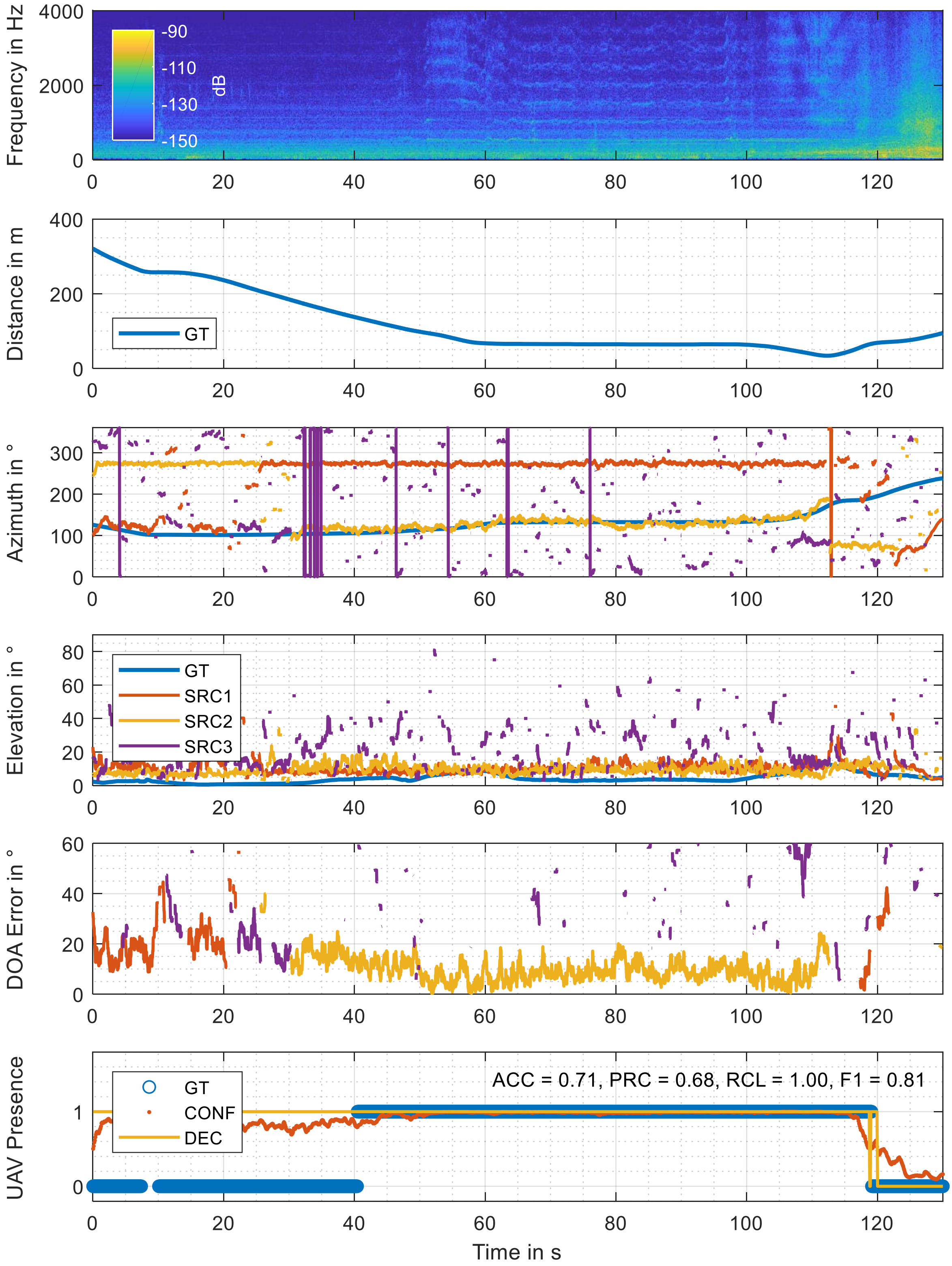


*Figure 7: Run-A: One custom RW drone approaches the fixed sensor array from a distance of 300 m. The drone is successfully tracked starting at approx. 200 m (at 30 s) by SRC2 of the DOAE. The resulting DOA error is below 20° until second 115, where a car passes by and the track is lost. The detector (RNN) classifies the signal as UAV, before it was actually annotated (GT) as present (false positive). The classification of this run achieved an accuracy of 71%, a precision of 68%, a recall (hit rate) of 100% and an F1-score of 81%.*

### ***Run-B*: Two drones with fixed sensor setup**

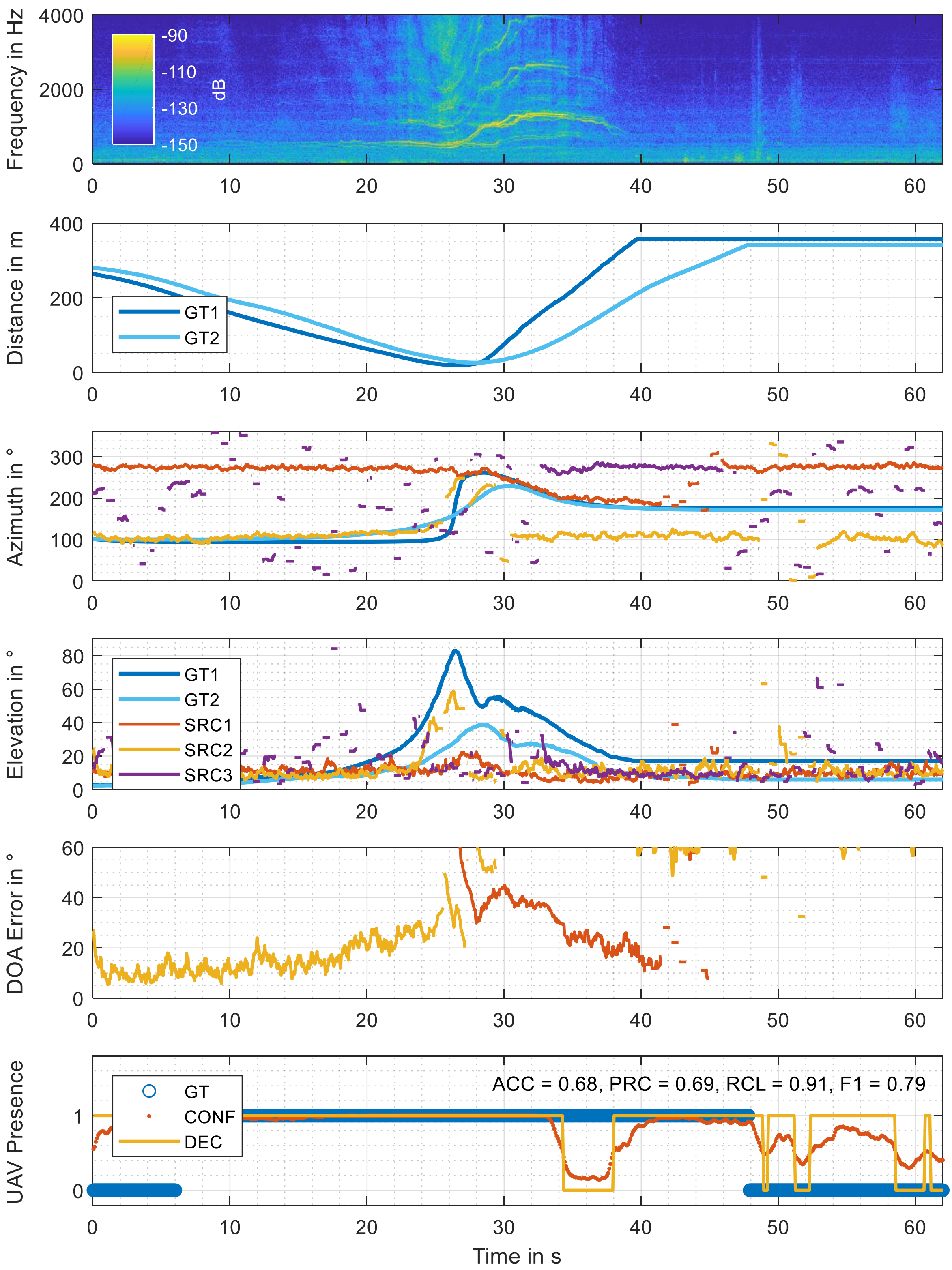


*Figure 8: Run-B: Two custom RW drones approach and fly past the fixed sensor array from a distance of 300 m. From the beginning, the DOAE captures both drones as one sound source (SRC2) since they are too close to be separated. At second 25, where the drones are about to fly past the array, the DOAE tries to track both UAVs as separated sources (SRC1-2). The respective elevation estimations show large angle error, which may also be attributed to altitude inaccuracies of the GNSS receiver. The track of both UAVs is lost after 42 s (250 m). In this plot, the DOA error is computed w.r.t. GT1. The detector (RNN) misclassifies the signal after the fly-over (miss) and after the UAVs landed (false alarm) after 48 s. The classification of this run achieved an accuracy of 68%, a precision of 69%, a recall (hit rate) of 91% and an F1-score of 79%.*

### ***Run-C*: One drone with mobile sensor setup**

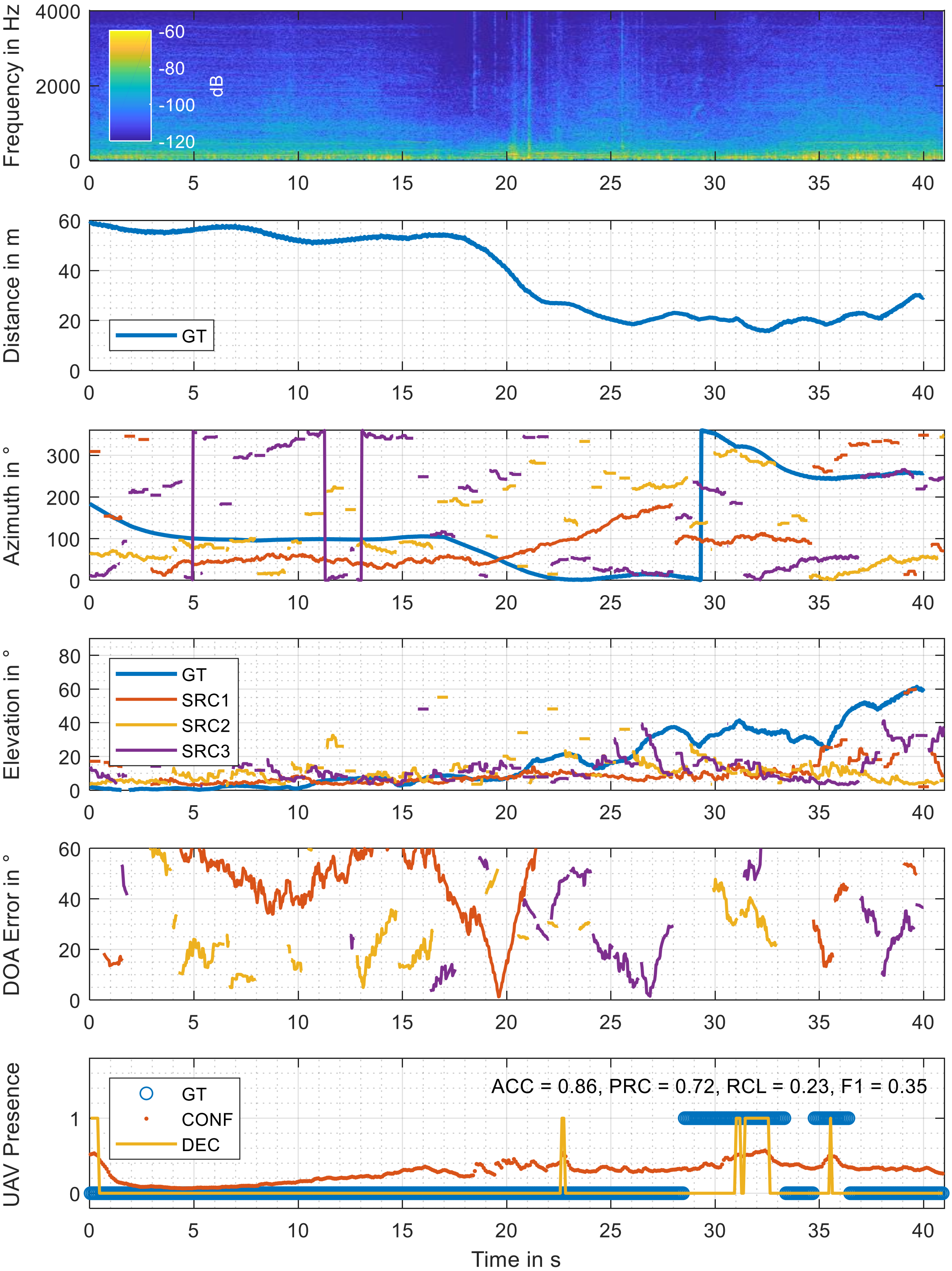


*Figure 9: Run-C: One custom RW drone flies in the vicinity of the mobile sensor array, which is mounted on the car. In this run the DOAE is not capable of tracking the UAV, which is mainly attributed to excessive motor and tyre rolling noise masking the target UAV sound. This was also verified when annotating the reference signal as the UAV was inaudible even when it was only 20 m away from the sensor. Hence, only few frames show a reasonable localization result in azimuth, e.g. at seconds 24-27 (SRC3) and seconds 37-40. The detector (RNN) correctly rejects the UAV class until second 28 (true negatives), and provides correct classification at seconds 31-33 and 35-36. The classification of this run achieved an accuracy of 86%, a precision of 72%, a recall (hit rate) of 23% and an F1-score of 35%.*

### 3.6 Localization Performance

As already seen in the plots of selected flights of Section 3.5, the sound source tracker outputs three source hypotheses. In case a new sound source appears or an old source falls silent, a new track with a potentially different source index is created. As a consequence, a target source is not always assigned to a specific hypothesis placeholder (e.g. SRC1), but yields varying source indices over time. Moreover, the target is not always the dominant sound source, which in turn prevents the possibility of ranking sound sources based on their track confidence. To consider this phenomenon for the evaluation of localization performance, we propose to extract the *oracle* sound source, i.e. the ensemble source track out of all tracks that is closest to the GT in the sense of the minimum DOA error. We assess the DOAE performance in terms of absolute DOA error for discrete distance ranges to provide a statistical observation in dependence of the UAV distance from the sensor. To this end, we use boxplots to provide an informative summary of DOAE accuracy and precision by studying the median and the interquartile ranges. In addition, we split the evaluation into the fixed, mobile and total datasets, to explore the influence of using fixed or mobile sensor arrays for DOAE. The results of this evaluation are shown in Figure 10.

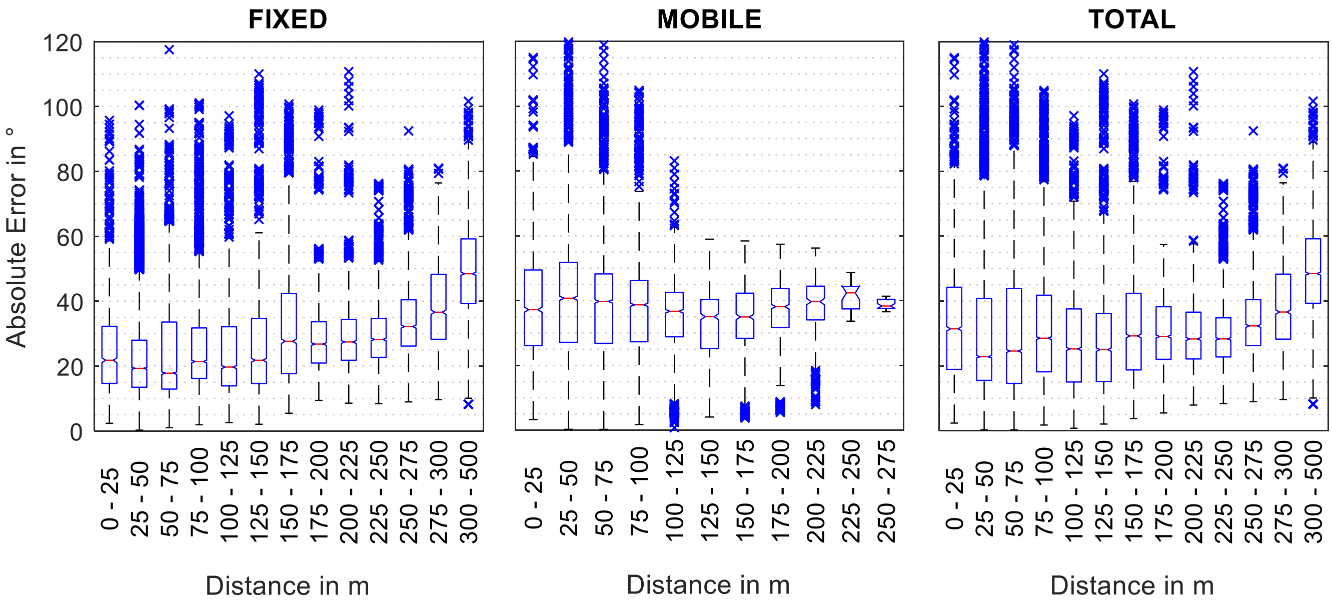


*Figure 10: Evaluation of DOAE performance of oracle sound source tracks in terms of absolute DOA error over different distance ranges for fixed (left), mobile (center) sensor scenarios and for the total dataset (right). For the fixed setup, the error is below 30° up to a distance of 250 m, whereas in the mobile setup, errors are constantly larger around 40°. Each boxplot shows the median as red line, the interquartile range as blue box, whiskers as black dashed lines and outliers as blue crosses.*

In Section 3.8 we will see, that the DOAE performance is not only imported for UAV localization itself, but also for detection as the quality of beamforming signals directly impacts on the possible performance gain of a joint detection and localization system.

### 3.7 Detection Performance

In this Section, we separately evaluate the RF and RNN classifiers taking the single-channel reference microphone signal (MIC) as input. For the classifier performance analysis we choose the metrics accuracy (ACC), precision (PRC), recall (RCL) and F1-score (F1) as well as confusion matrices and the area under the curve (AUC) of precision-recall curves. We select the F1-score w.r.t. UAV (target) class as key metric. To find the optimal decision threshold of a classifier model, it is common practice to study its receiver operating characteristic (ROC) curve. However, in case of test datasets with a skewed class distribution, it is recommended to choose precision-recall curves over ROC curves [41], [42]. Since in our case the portion of positives in our test set is approx. 70%, we create precision-recall curves from confidence outputs each model and choose the threshold that minimizes the distance to the optimum working point (PRC = 1, RCL = 1). The single-channel detection results for both RF and RNN are presented in Figure 11 and Figure 12.

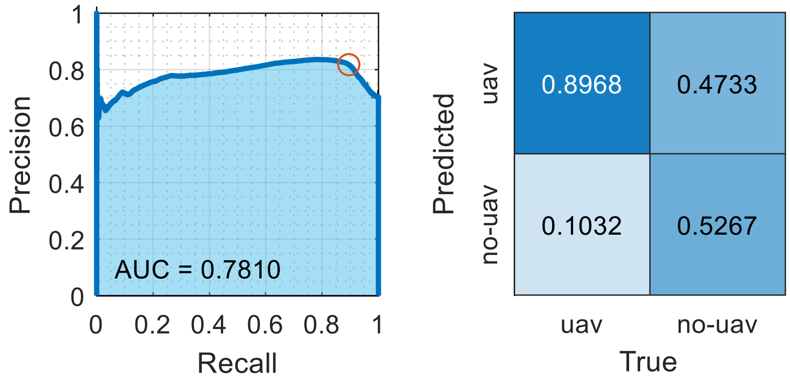


| | PRC | RCL | F1 |
|---|---|---|---|
| **uav** | 0.8162 | 0.8968 | 0.8546 |
| **no-uav** | 0.6853 | 0.5267 | 0.5956 |
| **ACC** | | | 0.7861 |
| **m-avg.** | 0.7508 | 0.7117 | 0.7251 |
| **w-avg.** | 0.7771 | 0.7861 | 0.7772 |

*Figure 11: Detection performance of the **single-channel (MIC) RF model**: Precision-recall curve (left) with optimum threshold (red), confusion matrix (center) showing predictions relative to the number of true samples, and binary classification metrics accuracy (ACC), precision (PRC), recall (RCL) and F1-score (F1) for both UAV and NO-UAV classes with macro-averaged and weighted-average scores (right). The model achieves an **F1-score of 0.8546**.*

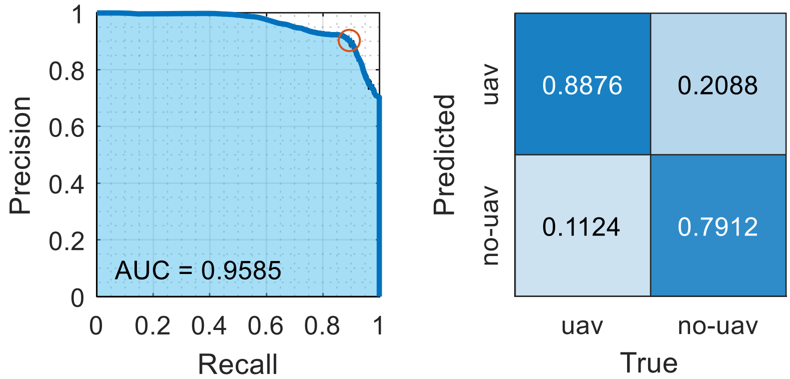


| | PRC | RCL | F1 |
|---|---|---|---|
| **uav** | 0.9090 | 0.8876 | 0.8982 |
| **no-uav** | 0.7496 | 0.7912 | 0.7699 |
| **ACC** | | | 0.8588 |
| **m-avg.** | 0.8293 | 0.8394 | 0.8340 |
| **w-avg.** | 0.8615 | 0.8588 | 0.8599 |

*Figure 12: Detection performance of the **single-channel (MIC) RNN model**: Precision-recall curve (left) with optimum threshold (red), confusion matrix (center) showing predictions relative to the number of true samples, and binary classification metrics accuracy (ACC), precision (PRC), recall (RCL) and F1-score (F1) for both UAV and NO-UAV classes with macro-averaged and weighted-average scores (right). The model achieves an **F1-score of 0.8982**.*

### 3.8 Joint Detection and Localization Performance

Following our proposed approach in Section 2.3, we now investigate whether the usage of BF signals as additional classifier inputs result in an overall performance gain. For this purpose, we compute confidence outputs from the BF inputs using the same classifier models as in the single-channel case and apply the maximum to both confidence hypotheses, MIC and BF. From the resulting joint confidence hypothesis, we obtain predictions by applying the same threshold as for the MIC classifier. Figure 13 and Figure 14 show the results for the RF and RNN model, resp. It becomes apparent that the RNN model (Figure 14) did not profit from additional BF signal inputs. What is worse, the false positive rate increased by 2%. In a more detailed analysis, we discovered that the RNN merely produced confidences above 0.5 for the BF signals. One reason for this could be overfitting to the training dataset, which means that the model is not capable of generalizing unseen feature frames originating from BF data. Another possible reason may be that the DOA errors had a too strong impact on the quality of the BF signals such that the UAV target sound was attenuated and thus relevant noise characteristics were suppressed.
In contrast, the joint RF classifier (Figure 13) was able to improve its performance in F1 by 1% compared to its single-channel counterpart. This is mostly attributed to the gain in RCL, which confirms that the BF signals could improve the model without affecting PRC. It seems that the manually engineered audio features better preserved relevant audio information within the BF signals than the Mel-spectra used as the RNN input.
From an objective point of view, the RNN model yields better scores in AUC, F1 and PRC compared to RF. However, these results should be handled with care, since the evaluation was performed on a small and quite specific test dataset.

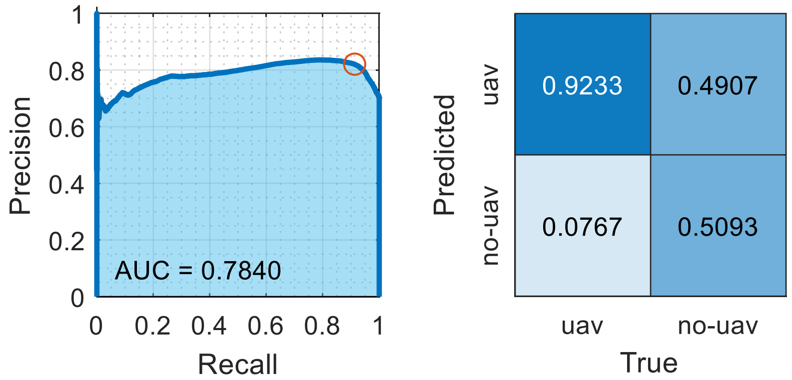


| | PRC | RCL | F1 |
|---|---|---|---|
| **uav** | 0.8152 | 0.9233 | 0.8659 |
| **no-uav** | 0.7392 | 0.5093 | 0.6031 |
| **ACC** | | | 0.7995 |
| **m-avg.** | 0.7772 | 0.7163 | 0.7345 |
| **w-avg.** | 0.7924 | 0.7995 | 0.7873 |

*Figure 13: Detection performance of the **joint (MIC+BF) RF model**: Precision-recall curve (left) with optimum threshold (red), confusion matrix (center) showing predictions relative to the number of true samples, and binary classification metrics accuracy (ACC), precision (PRC), recall (RCL) and F1-score (F1) for both UAV and NO-UAV classes with macro-averaged and weighted-average scores (right). The model achieves an **F1-score of 0.8659**.*

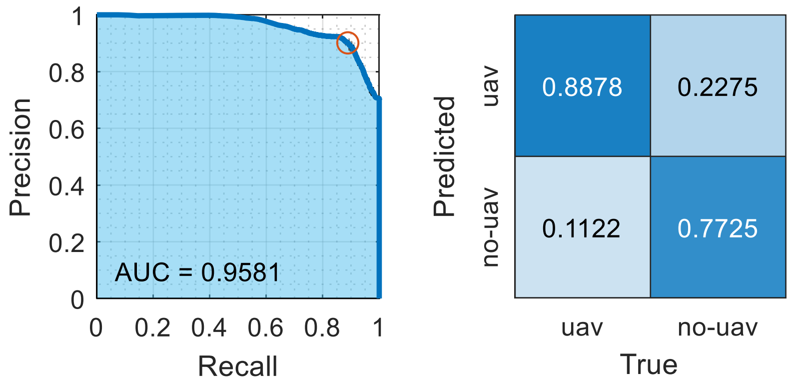


| | PRC | RCL | F1 |
|---|---|---|---|
| **uav** | 0.9017 | 0.8878 | 0.8947 |
| **no-uav** | 0.7455 | 0.7725 | 0.7588 |
| **ACC** | | | 0.8534 |
| **m-avg.** | 0.8236 | 0.8302 | 0.8267 |
| **w-avg.** | 0.8551 | 0.8534 | 0.8541 |

*Figure 14: Detection performance of the **joint (MIC+BF) RNN model**: Precision-recall curve (left) with optimum threshold (red), confusion matrix (center) showing predictions relative to the number of true samples, and binary classification metrics accuracy (ACC), precision (PRC), recall (RCL) and F1-score (F1) for both UAV and NO-UAV classes with macro-averaged and weighted-average scores (right). The model achieves an **F1-score of 0.8947**.*

## 4. Conclusions

In this work, we presented an approach for both separate and joint detection and localization of UAVs in a fixed as well as in a mobile sensor scenario. In the course of field experiments conducted at a military camp near Bure, Switzerland, a test dataset of UAV flights was recorded with a small 4-channel MEMS microphone array with an onboard GNSS receiver for collecting ground truth sensor positions. The dataset contains 46 min of UAV audio and GPS data and is used for evaluating an acoustic localization and detection algorithms.

The localizer uses a GMM-based approach for DOA estimation and tracking of multiple sound sources. In our experiments, we investigated the DOA error over UAV distance from the sensor in both fixed and mobile setups. We found that even though the median absolute DOA error was around 20° in the fixed setup, the algorithm was able to track the target UAV in most cases. In contrast, the localizer of the mobile sensor yielded DOA errors above 35° for almost all distance ranges and thus was not capable to provide satisfying DOA tracks due to excessive car noise, mechanical vibrations and a minimalistic sensor array design. We argue that a larger and more sophisticated microphone array design comprised of more sensors and mechanical suspension, e.g. shock absorbers, may be able to alleviate the difficulties of this challenging task.

For acoustic detection of drone sound presence, we compared two different binary classifier models: a Random Forest (RF) classifier with engineered audio features as an example for a conventional machine learning pipeline and a recurrent neural network (RNN) based on LSTM-layers representing a deep learning approach. We trained both models on independent datasets consisting of 13 h audio data with 40% UAV sound. Our results show that both RF and RNN models are capable of discriminating UAV from non-UAV sound by achieving F1-scores above

0.85 on the test dataset. Following our proposed joint detection and localization approach, in which we additionally provide extracted beamforming (BF) signals of tracked sound sources as classifier inputs, only improved the RF model.

This paper marks a first step in the direction of mobile acoustic UAV tracking for public security or military applications. Through our experiments and results, we gained deeper insights in the challenges associated with the acoustic detection and localization of UAVs and we are confident to improve our system in the near future. Potential follow-up topics are the manifold: Data augmentation strategies offer opportunities to extend the amount of training data and have the potential to overcome the overfitting problem in deep learning models, such as large CNN and RNN architectures. State-of-the-art tracking and data association algorithms, such as Extended Kalman filters and Joint Probabilistic Data Association filters, may improve acoustic localization in order to provide more robust sound source tracks, which are crucial in the context of a track-before-detect approach as it is the case for joint localization and detection of UAVs.

## Acknowledgements

The authors would like to thank the representatives of the company *IAV Engineering Sàrl* for providing multiple units of the acoustic sensor array system for the measurement campaign conducted near Bure in August 2020. Furthermore, we express our gratitude to all involved in the planning and in the implementation of the experiments. The main author particularly thanks the co-authors of *armasuisse Science and Technology S+T* for the fruitful collaboration.

**References**

[1] B. Alzahrani, O. S. Oubbati, A. Barnawi, M. Atiquzzaman, and D. Alghazzawi, "UAV assistance paradigm: State-of-the-art in applications and challenges," *Journal of Network and Computer Applications*, vol. 166, p. 102706, 2020.
[2] H. Shakhatreh *et al.*, "Unmanned aerial vehicles (UAVs): A survey on civil applications and key research challenges," *Ieee Access*, vol. 7, pp. 48572–48634, 2019.
[3] Wikipedia, "List of unmanned aerial vehicle applications." Apr. 2022. [Online]. Available: https://en.wikipedia.org/wiki/List_of_unmanned_aerial_vehicle_applications
[4] Dedrone, "Worldwide Drone Incidents." Apr. 2022. [Online]. Available: https://www.dedrone.com/resources/incidents/all
[5] Wikipedia, "List of UAV-related incidents." Apr. 2022. [Online]. Available: https://en.wikipedia.org/wiki/List_of_UAV-related_incidents
[6] D. Mototolea, "A Study on the Methods and Technologies Used for Detection, Localization, and Tracking of LSS UASs," *Journal of Military Technology*, vol. 1, no. 2, pp. 11–16, Dec. 2018, doi: 10.32754/jmt.2018.2.02.
[7] S. Samaras *et al.*, "Deep learning on multi sensor data for counter UAV applications—A systematic review," *Sensors*, vol. 19, no. 22, p. 4837, 2019.
[8] G. Lykou, D. Moustakas, and D. Gritzalis, "Defending airports from UAS: A survey on cyber-attacks and counter-drone sensing technologies," *Sensors*, vol. 20, no. 12, p. 3537, 2020.
[9] H. Wang, Y. Zou, and D. Chong, "Acoustic Scene Classification with Spectrogram Processing Strategies," *arXiv preprint arXiv:2007.03781*, 2020.
[10] J. Abeßer, "A review of deep learning based methods for acoustic scene classification," *Applied Sciences*, vol. 10, no. 6, 2020.
[11] T. Marinopoulou *et al.*, "Two Dimensional Convolutional Neural Network Frameworks Using Acoustic Nodes for UAV Security Applications," 2020.
[12] S. Al-Emadi, A. Al-Ali, and A. Al-Ali, "Audio-Based Drone Detection and Identification Using Deep Learning Techniques with Dataset Enhancement through Generative Adversarial Networks," *Sensors*, vol. 21, no. 15, p. 4953, 2021.

[13] P. Casabianca and Y. Zhang, “Acoustic-Based UAV Detection Using Late Fusion of Deep Neural Networks,” *Drones*, vol. 5, no. 3, p. 54, 2021.
[14] V. Alaparthy, S. Mandal, and M. Cummings, “A comparison of machine learning and human performance in the real-time acoustic detection of drones,” 2021.
[15] H. Kolamunna *et al.*, “Droneprint: Acoustic signatures for open-set drone detection and identification with online data,” *Proceedings of the ACM on Interactive, Mobile, Wearable and Ubiquitous Technologies*, vol. 5, no. 1, pp. 1–31, 2021.
[16] C. Dumitrescu, M. Minea, I. M. Costea, I. Cosmin Chiva, and A. Semenescu, “Development of an acoustic system for UAV detection,” *Sensors*, vol. 20, no. 17, p. 4870, 2020.
[17] F. Svanström, C. Englund, and F. Alonso-Fernandez, “Real-time drone detection and tracking with visible, thermal and acoustic sensors,” in *2020 25th International Conference on Pattern Recognition (ICPR)*, 2021, pp. 7265–7272.
[18] F. Eyben, *Real-time speech and music classification by large audio feature space extraction*. Springer, 2015.
[19] Y. Wang, F. E. Fagiani, K. E. Ho, and E. T. Matson, “A Feature Engineering Focused System for Acoustic UAV Payload Detection,” *Proceedings of the 14th International Conference on Agents and Artificial Intelligence (ICAART 2022)*, vol. 3, pp. 470–475, 2022.
[20] B. McFee *et al.*, *librosa/librosa: 0.9.1*. Zenodo, 2022. doi: 10.5281/zenodo.6097378.
[21] M. Ohlenbusch, A. Ahrens, C. Rollwage, and J. Bitzer, “Robust drone detection for acoustic monitoring applications,” in *2020 28th European Signal Processing Conference (EUSIPCO)*, 2021, pp. 6–10.
[22] Z. Uddin, A. Qamar, A. G. Alharbi, F. A. Orakzai, and A. Ahmad, “Detection of Multiple Drones in a Time-Varying Scenario Using Acoustic Signals,” *Sustainability*, vol. 14, no. 7, p. 4041, 2022.
[23] B. Taha and A. Shoufan, “Machine Learning-Based Drone Detection and Classification: State-of-the-Art in Research,” *IEEE Access*, vol. 7, pp. 138669–138682, 2019, doi: 10.1109/access.2019.2942944.
[24] N. Itare, T. Blanchard, J.-H. Thomas, and K. Raoof, “Tracking of an Unmanned Aerial Vehicle with few sensors using time-frequency representation,” in *Forum Acusticum*, 2020, pp. 3143–3147.
[25] C. Dumitrescu, M. Minea, I. M. Costea, I. Cosmin Chiva, and A. Semenescu, “Development of an acoustic system for UAV detection,” *Sensors*, vol. 20, no. 17, p. 4870, 2020.
[26] G. Herold, A. Kujawski, C. S. Svenja Huschbeck, M. U. de Haag, and E. Sarradj, “Detection And Separate Tracking Of Swarm Quadcopter Drones Using Microphone Array Measurements,” 2020.
[27] H. Liu, K. Fan, B. He, and W. Wang, “Unmanned Aerial Vehicle Acoustic Localization Using Multilayer Perceptron,” *Applied Artificial Intelligence*, vol. 35, no. 7, pp. 537–548, 2021.
[28] S. Adavanne, A. Politis, J. Nikunen, and T. Virtanen, “Sound event localization and detection of overlapping sources using convolutional recurrent neural networks,” *IEEE Journal of Selected Topics in Signal Processing*, vol. 13, no. 1, pp. 34–48, 2018.
[29] A. Politis, A. Mesaros, S. Adavanne, T. Heittola, and T. Virtanen, “Overview and Evaluation of Sound Event Localization and Detection in DCASE 2019,” *arXiv preprint arXiv:2009.02792*, 2020.
[30] A. Politis, S. Adavanne, D. Krause, A. Deleforge, P. Srivastava, and T. Virtanen, “A dataset of dynamic reverberant sound scenes with directional interferers for sound event localization and detection,” *arXiv preprint arXiv:2106.06999*, 2021, doi: .org/10.5281/zenodo.4844825.

[31] K. Shimada, Y. Koyama, N. Takahashi, S. Takahashi, and Y. Mitsufuji, “ACCDOA: Activity-Coupled Cartesian Direction of Arrival Representation for Sound Event Localization and Detection,” 2021.
[32] V. Baron, S. Bouley, M. Muschinowski, J. Mars, and B. Nicolas, “Acoustic localization and identification of drones with a disturbance source,” in *Forum Acusticum 2020*, 2020, pp. 3149–3154.
[33] J. Guo, I. Ahmad, and K. Chang, “Classification, positioning, and tracking of drones by HMM using acoustic circular microphone array beamforming,” *EURASIP Journal on Wireless Communications and Networking*, vol. 2020, no. 1, Jan. 2020, doi: 10.1186/s13638-019-1632-9.
[34] A. Toma, N. Cecchinato, C. Drioli, G. L. Foresti, and G. Ferrin, “Towards Drone Recognition and Localization from Flying UAVs through Processing of Multi-Channel Acoustic and Radio Frequency Signals: a Deep Learning Approach,” NATO, University of Udine - Dept. of Mathematics, Computer Science and Physics, 2021.
[35] M. Blass and F. Graf, “A Real-Time System for Joint Acoustic Detection and Localization of UAVs,” 2020.
[36] N. Madhu and R. Martin, “A Scalable Framework For Multiple Speaker Localization And Tracking,” *Proceedings of the International Workshop for Acoustic Echo Cancellation and Noise Control (IWAENC)*, 2008.
[37] N. Madhu, C. Breithaupt, and R. Martin, “Temporal smoothing of spectral masks in the cepstral domain for speech separation,” *2008 IEEE International Conference on Acoustics, Speech and Signal Processing*, pp. 45–48, 2008.
[38] N. Madhu and R. Martin, “A versatile framework for speaker separation using a model-based speaker localization approach,” *IEEE Transactions on Audio, Speech and Language Processing*, vol. 19, no. 7, pp. 1900–1912, 2011, doi: 10.1109/TASL.2010.2102754.
[39] L. Wimmer, “Gleichmaessige Verteilung von Punkten auf der Einheitskugel,” PhD Thesis, Universitaet Salzburg, 1992.
[40] D. Kingma and J. Ba, “Adam: A Method for Stochastic Optimization,” *International Conference on Learning Representations*, Dec. 2014.
[41] T. Fawcett, “An introduction to ROC analysis,” *Pattern recognition letters*, vol. 27, no. 8, pp. 861–874, 2006.
[42] D. M. Powers, “Evaluation: from precision, recall and F-measure to ROC, informedness, markedness and correlation,” *arXiv preprint arXiv:2010.16061*, 2020.

INCE EUROPE

CidB
Centre d'information sur le Bruit

**QUIET DRONES**
**Second International e-Symposium**
**on**
**UAV/UAS Noise**
**27th to 30th June 2022**

# UAV acoustic localization in a maritime environment: from first results to improvements perspectives

**Mathis BONOTTO, Gipsa-Lab: mathis.bonotto@gipsa-lab.grenoble-inp.fr**
**Valentin BARON, MicrodB: Valentin.Baron@microdb.fr**
**Lucille LAMOTTE, MicrodB : lucille.lamotte@microdb.fr**
**Jonathan DUMON, Gipsa-Lab: jonathan.dumon@gipsa-lab.grenoble-inp.fr**

## Summary

Thanks to their high maneuverability and low cost, UAVs are increasingly used on military operation fields to threaten valuable assets. To assess this threat, numerous counter UAV systems have been developed, based on different physical modalities like radar, optics, or radio-frequency. However, in this fast evolving domain, recent studies tend to show that each modality taken separately is not self-sufficient to work in all the possible scenarios.

As the targeted UAVs are mostly quadcopters that emit significant noise due to their propellers, the acoustic modality has been naturally studied. It has the advantage to work at night or in foggy weather, to deal with autonomous targets, and also to identify them through their acoustic signature. Nevertheless, acoustic localization directly depends on the power of the ambient noise in which the sensor is buried, from very low into rural areas to very high into dense urban ones. If the rural and urban areas have already been studied, data and studies are lacking in a major military field: the maritime environment.

This paper aims at filling this gap thanks to recordings that have been made on a coastal area, in windy conditions, with a strong backwash. Acoustic signals are first thoroughly analyzed to understand the contribution of UAV and ambient noise. Then, a validated localization method based on MUSIC method is tested against this complex scenario to evaluate its performances. The pipeline limitations are explained, and improvement perspectives are proposed to increase the initial results.

## 1. Introduction

The need to counter UAVs by localizing and neutralizing them becomes more and more a priority as they are increasingly used on military and civil fields to threaten valuable asset (Johnson, 2022), (Woody, 2020).
Numerous counter UAV technologies are existing using different physical modalities such as optics, radar and radio-frequency. The number of technologies is evolving along the years with 10 existing in 2015 (Birch, 2015) to 537 in 2019 (Michel, Counter-Drone systems, 2018), (Michel, 2019). As UAVs, especially quadcopters, have specific acoustic signatures due to their propellers the development of a counter technology relying on the acoustic modality is justified. Within 323 existing counter UAV technologies able to detect UAVs, only 34 are using acoustic. To increase their detection rate and cover more possible scenarios, different physical modalities must be used together (Christnacher, 2016), (Lykou, 2020). The benefit of using acoustic localization is its efficiency to detect a UAV threat in a foggy environment, at night and in the near field. It can assess autonomous UAVs, and it can identify them via their acoustic signature. However, it is sensible to background noise which can limit its use, especially in noisy environments.
The need of deploying counter UAV technology in a maritime environment is strong as it is a theater for many malicious operations using UAVs. Nevertheless, all the past researches about UAV localization are oriented toward rural (quiet) and urban (noisy) environments (Albert D. D., 2017), (Heutschi, 2021), (Cabell, 2016) and the maritime field remain uncovered by the literature. To extend the research to the maritime environment, an acoustic localization experiment have been specifically conducted on a coastline using an array processing method. Three different models of micro-UAVs (< 2 kg) were evaluated during this experiment: the DJI Phantom 4 Pro, the Parrot Anafi and a handmade one named “BM42”. Using an 81 microphone array, the goal is first to characterize the spectral content of the coastline background noise, and find the UAV frequency band of interest in which the signal-to-noise ratio (SNR) between its emitted signal and the ambient noise is favorable. Then, the goal is to measure the detection range $Dr$ of the UAVs with acoustic localization in this specific environment, using a high resolution method.

The purpose of this study is to estimate the performance of a localization method- which was successful in a controlled environment - in a maritime environment. It draws new perspectives to improve the method for better detection performances in difficult conditions.

The paper is organized as follows. First in section 2, the high resolution Multiple Signal Classification (MUSIC) method used to localize UAVs through their direction of arrival (DOA) is described. Then in section 3, the spectral contribution of the background environment as well as the studied UAVs are determined thanks to an analysis based on the literature and measurements made on a coastline environment. The section 4 focuses on the results of the UAVs DOA. Finally section 5 details the obtained performances to propose perspectives to improve its efficiency.

## 2. Localization method

In this section, we briefly review the method used to estimate the DOA through array processing. This method is based on the processing pipeline developed in (Baron, 2020) which has been validated in a controlled environment.

A microphone array of M microphone channels is recording acoustic pressure signals $p^i(t)$, with $i \in [1, M]$. UAVs are considered as non-stationary sources over a whole flight of duration T, nevertheless during a shorter time of duration $\Delta T_{frame}$ they can be considered as stationary (Strauss, 2018). The signals are then cut into N time frames of duration $\Delta T_{frame}$ as described in Figure 1, which provides the acoustics pressure signals $p_n^i(t)$ with $n \in N$.

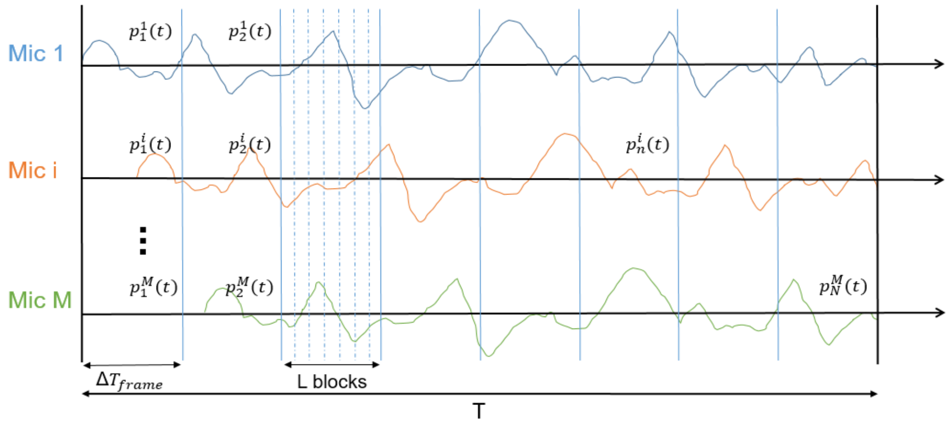


**Figure 1 : Cutting procedure of the acoustical signals along the time.**

For each time frame a cross-spectral matrix $\Gamma_n$ is estimated for L successive blocks to compute a Welch's periodogram (Welch, 1967):

$$\hat{\Gamma}_n(f) = \frac{1}{L}\sum_{l=1}^{L} q_n^l(f) q_n^{l*}(f)\,,(1)$$

with $q_n^l$ the Fourier transform of the $l^{th}$ block of the input time frame signals. For the following the frequency dependency is omitted for sake of clarity.

The MUSIC method (Bienvenu, 1983), (Schmidt, 1986) is used to localize the sources. This method uses the estimated cross-spectral matrix as input to compute an eigenvalue decomposition. The signal subspace and noise subspace are obtained, orthogonal one to the other. The signal subspace is composed of the K first eigenvalues when the noise subspace is composed of the M-K others:

$$\Gamma_n(f) = \sum_{k=1}^{K} \lambda_k u_k u_k^* + \sum_{k=K+1}^{M} \lambda_k u_k u_k^* \;,(2)$$

with $\lambda_k$ the eigenvalues, and $u_k$ the eigenvectors.

In this study the choice of K is manually set to the number of present acoustic sources equal to the number of UAVs but it exists some criteria to automatically estimate the number of eigenvalues to attribute to the signal subspace (Akaike, 1998) (Bienvenu, 1983) (Ferreol, 2006), (Quinlan, 2006) (Wax, 1985). The MUSIC estimator is computed for a given direction $\theta$ by the inverse of the projection of the steering vector $g(\theta)$ on the noise subspace:

$$V_{MUSIC}(\theta) = \frac{1}{g^*(\theta)\sum_{k=K+1}^{M} u_k u_k^*\, g(\theta)}.(3)$$

The acoustic source DOA $\theta_{max}$ is then estimated from the MUSIC map by taking its maximum.

This localization process is applied for each frequency line. It is interested to focus on the ones with the best signal to noise ratio, leading to the following spectral analysis.

## 3. Spectral Analysis

The first aim of this paper is to analyze the spectral characteristic of the maritime background noise in one hand and of UAVs in another hand. This analysis relies first on the information found in the state-of-art, and then on the experimental data gathered during the experiment realized for this paper. The purpose is to compare the spectral contribution of the background noise with the different UAVs' ones to identify the frequency bands where the SNR $\Delta_L$ is favorable – i.e. the frequencies for which the UAVs emit significantly while the ambient noise contribution is fading - both theoretically through the literature and practically with the use of the experimental data.

### 3.1 Specification

A bibliographic study has been made in order to specify the spectral characteristic of the environment and the UAVs. The results presented here are coming from different data gathered across the literature about the subject. The difficulty of this task is to find coherent data across the state-of-art. To tackle the possible inhomogeneity between the data, they all have been expressed as weightless third octave band pressure levels in dB brought back to $1\ m$.

Bounds have been built from the gathered data for both different environments (Albert D. D., 2017), (Heutschi, 2021), (Cabell, 2016) and UAVs (Schäffer, 2021) to be representative of the sound pressure level scale along the spectrum. The DGA provided additional measurement data on different coastline with various wind and backwash conditions to be representative of the maritime environment.
An example in Figure 2 is presenting the third band octave for different UAVs weighting between $1\ kg$ and $10\ kg$ from which the bounds are determined.

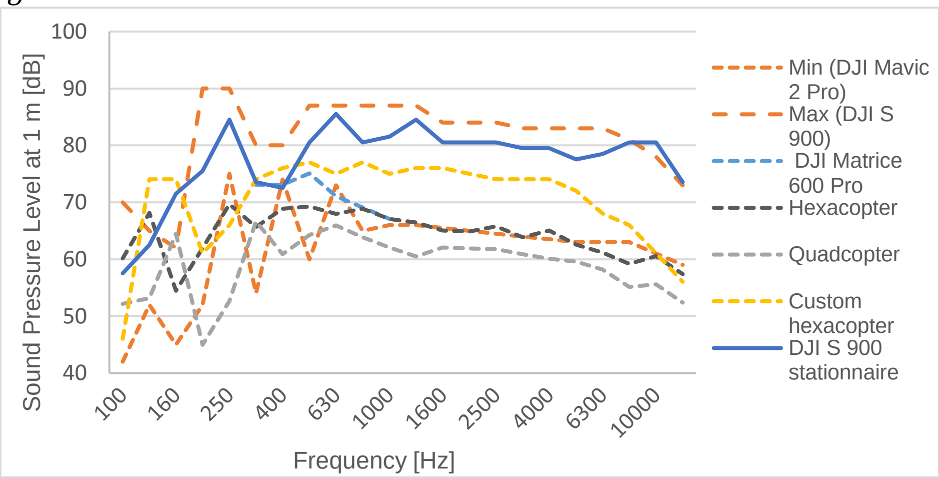


**Figure 2 : Third band octave of the sound pressure level at 1 m for different UAVs between 1 and 10 kg.**

The UAV corresponding to the maximum bound is a hexacopter weighting around $4\ kg$ while the one corresponding to the minimum bound is a quadcopter (without any information concerning the weight).
For the environment noises, the maximum bound is corresponding to the loudest maritime environment recorded (equivalent to a loud urban environment) and the minimum one to a rural environment.

The comparison between the ambient noise and the UAV bounds provides the theoretical frequency bands of interest for UAV localization from which the SNRs are estimated. Then the detection ranges are deducted from these SNRs. Different parameters can impact the SNR such as the attenuation of the sound pressure level with the distance, mask effect, atmospheric absorption, wind effect and reflective/absorbent surface. In this paper, only the influence of the distance from the source is taken into account, using a spherical propagation model to determine the UAV level for a given distance, so reducing this level of 6 dB each time the distance doubles. The detection range is then defined by the distance for which the theoretically propagated UAV level is equal to the ambient noise level, which corresponds to a null SNR.

Frequency band, SNR and detection range are estimated for four distances: $100\ m$, $200\ m$, $500\ m$, and $1\ km$. The corresponding third octave band results for $100\ m$ and $1\ km$ are presented in Figure 3.

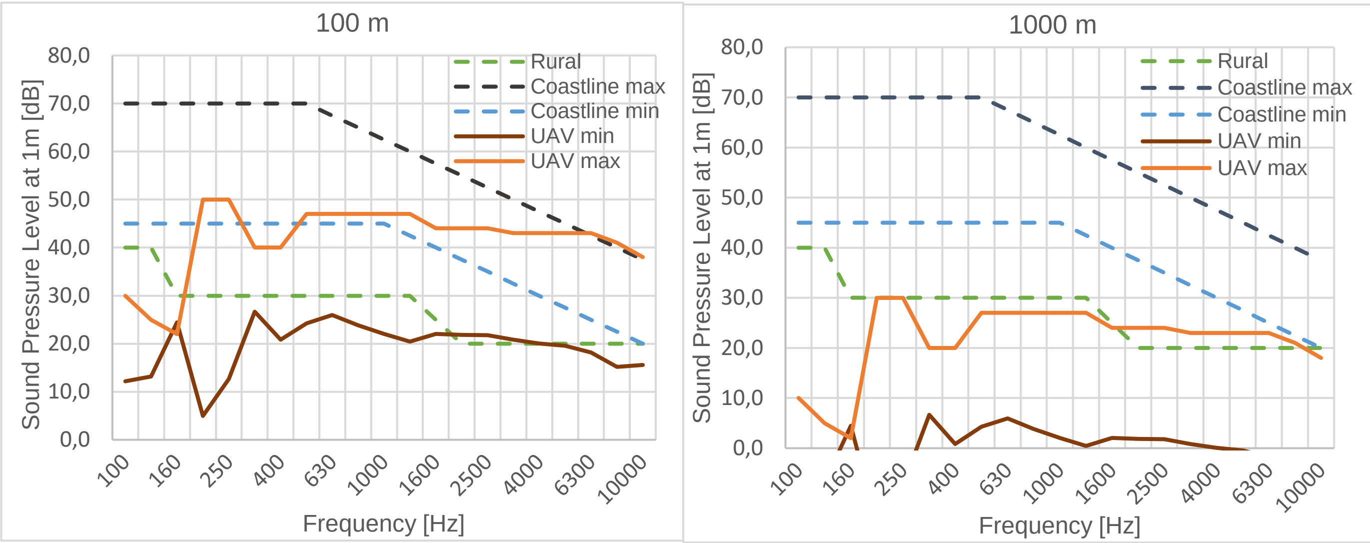


**Figure 3 : Bounds comparison between ambient and UAVs noise for four different distance from the UAV (100 m and 1000 m).**

The bounds superposition outlines a frequency band of interest localized between $2\ kHz$ and $6\ kHz$. This frequency band is particularly interesting to use for the localization process as the UAVs continue to emit while the background noise is suffering a strong decay. For the following SNR analysis the chosen frequency is $5\ kHz$, for example purposes.

The SNRs at this frequency are summarized in Table 1. In this table, three colors are indicating the UAV detection complexity according to the measured SNR at 5 kHz: green, given for SNR $\in [-10\ dB, +\infty]$ represents an easy detection as it has already been shown that UAVs can be detected in the presence of disturbance source that emit louder (Baron, 2020), orange for SNR $\in [-20\ dB;\ -10\ dB]$ with a medium detection complexity, and red for SNR below $-20\ dB$ for which it's supposed to be very complex to detect the UAV.

| UAV / array distance (meter) | SNR UAV quietest / ambient noise (dB) | SNR UAV noisiest / ambient noise (dB) |
|---|---|---|
| 1000 | Coastline max : - 45<br>Coastline min : -30<br>Rural : -20 | Coastline max : - 20<br>Coastline min : -2<br>Rural : 0 |
| 500 | Coastline max : - 40<br>Coastline min : - 20<br>Rural : - 10 | Coastline max : - 15<br>Coastline min : 0<br>Rural : 10 |
| 200 | Coastline max : - 30<br>Quiet : - 15<br>Rural : - 5 | Coastline max : - 5<br>Coastline min : 10<br>Rural : 20 |
| 100 | Coastline max : - 20<br>Coastline min : - 5<br>Rural : 0 | Coastline max : 0<br>Coastline min : 20<br>Rural : 25 |

**Table 1 : Summary of the third band octave SNR in function of the different type of background noises and UAVs.**

This analysis led to the following results:

- UAVs can be detected beyond $1\ km$ in a rural environment
- At $500\ m$ and $200\ m$ the UAVs should emit quite significantly to be detected in every environment
- At $100\ m$ the UAVs can be detected in any environments.

### 3.2 Spectral analysis of coastline measurements

Among all the previous UAV signals, anyone has been recorded from a maritime environment. To fill this gap but also validate the noise produced by UAVs in a realistic ambient noise, measurements have been performed on a coastline. Three models of micro-UAVs ($< 2\ kg$) of different size have been tested. The first two DJI Phantom 4 Pro (Quadcopter - $1.4\ kg$) and Parrot Anafi (Quadcopter – $320\ g$) are UAVs from the market and the other one is handcrafted (Quadcopter – $1.2\ kg$) made by the robotic and automatic team of ROBOTEX and it will be called BM42 for the rest of the paper. The measurements have been conducted with the Simcenter Sound Camera Digital Acoustic Array (Siemens), a $60\ cm$ diameter planar microphone array composed of 81 MEMS microphones. The analyzed frequency band is between $[100\ Hz, 20\ kHz]$.

The background noise correspond to a coastline environment constituted of rock submitted to windy conditions with a strong backwash. It has been analyzed with a sound pressure level third octave band and compared to the literature bounds. This analysis is presented in Figure 4. The background noise sound pressure level is included in the bounds built from the literature and follow the same variations as it presents a strong decreasing ($20\ dB\ /\ decade$) after $1\ kHz$. It is rather a loud ambient noise.

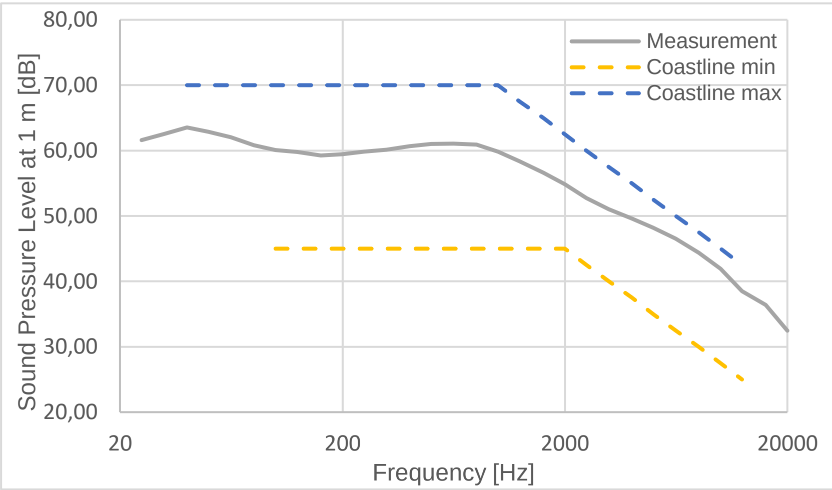


**Figure 4** : **Sound pressure level third band octave analysis of the measured coastline compared to the literature bounds.**

The UAVs spectral characteristic are analyzed by two means: with a Power Spectrum Density (PSD) to identify their frequency bands of interest, and with a sound pressure level third octave band analysis brought back to 1 meter to compare their sound pressure level with the literature bounds. During the measurements the UAVs are performing stationary flight at a distance between $10\ m$ and $20\ m$.
The PSD of the UAV signals compared to the corresponding ambient noise taken just after the flight are presented in Figure 5. It provides the frequency bands of interest.

The broadband ambient noise contribution is decreasing by $6\ dB/decade$ with the increase of frequency which turns to be an advantage to detect the UAVs as their spectral contributions are perceivable at high frequencies ($> 1\ kHz$).

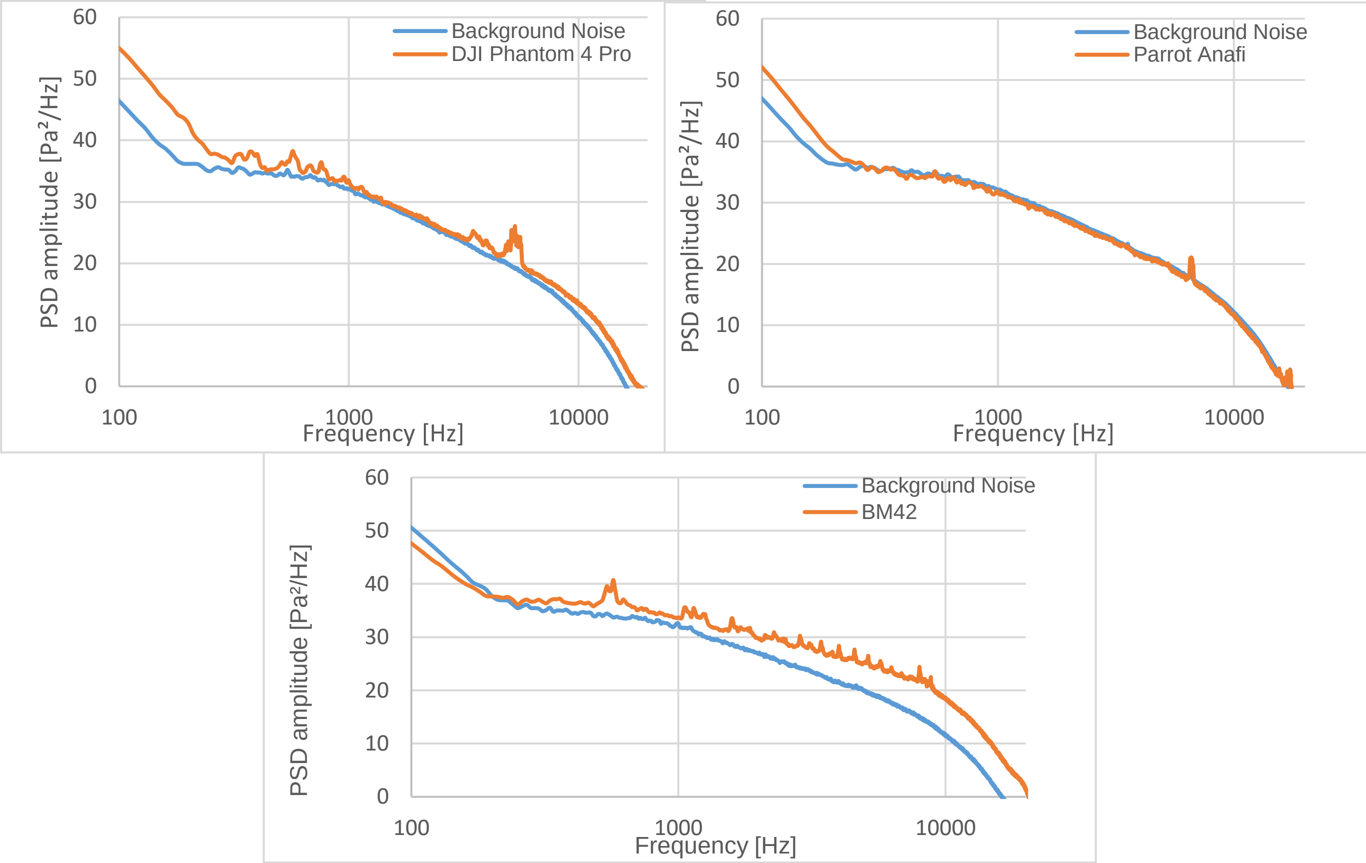


**Figure 5 : Power Spectrum Density analysis of the three studied UAVs compared to the contextual background noise.**

The sound of the BM42 UAV is very rich: nine harmonics of fundamental frequency $575\ Hz$ are present. The UAV sound level is greater than the ambient noise from $200\ Hz$. This gap is increasing from $1\ kHz$ where the ambient noise curve slope decay is increasing. It leads to a UAV that is easily localizable and it offers a large frequency band scale for the localization process.

For the DJI Phantom 4 Pro the contribution in the low end frequencies are due to the wind blowing on the microphones. The only frequency bands belonging to the contribution of the UAV are around $3600\ Hz$ and $5000\ Hz$. Thus, these are the bands of interest to perform the localization process.

For the Parrot Anafi, only one frequency at $6600\ Hz$ emerges from the background noise. It is particularly quiet UAV as it's a little model. This frequency is the only one found to use for the localization process.

The frequency bands of interest for each model of UAV are summarized in the Table 2.

| | BM42 | DJI Phantom 4 Pro | Parrot Anafi |
|---|---|---|---|
| Frequency band of interest | 200 Hz – 20 kHz | 3300 Hz – 5800 Hz | 6400 Hz – 7000 Hz |

**Table 2 : Frequency band of interest to perform the locasization process for each UAV.**

In order to compute the sound pressure level third octave band analysis brought back to $1\ m$ for each UAV, only the third octave bands corresponding to the frequency band of interest are chosen. The result compared to the literature bounds is presented in Figure 6.

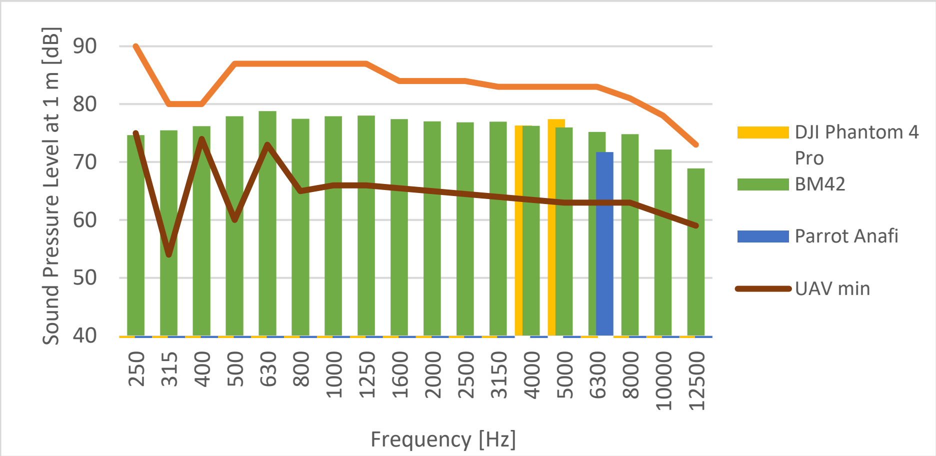


**Figure 6 : Sound pressure level third band octave analysis of the UAVs at 1 m for their frequency bands of interest compared to the literature bounds.**

The UAVs sound pressure levels are included in the literature bounds. In the corresponding bands the loudest UAV analyzed is the DJI Phantom 4 Pro, then the BM42 and finally the Parrot Anafi. These results are in coherence with the size and weight of the UAV as the DJI Phantom 4 Pro is the largest and heaviest one and the Parrot Anafi the smallest and quietest of the selection.

This analysis demonstrates that in a maritime environment, UAV localization must be done around high frequencies ($3\ kHz\ to\ 7\ kHz$) to benefit from a favorable SNR.

## 4. UAV acoustic localization

### 4.1 Description of the measurement

The aim of this measurement is to determine the detection range of the three UAVs analyzed in the previous section in a maritime environment with the method detailed in section 2. In order to validate the acoustic DOA estimation, the position of the UAVs and the array are tracked by GPS with a precision in the range of the meter. The DOA angles $(\theta, \varphi)$ and the distance between the array and the UAVs are then calculated from these positions and serve as reference for each time frame. The duration of each time frame is $\Delta T_{seq} = 200\ ms$ in order to follow the UAV trajectory with enough spatial samples. The sampling frequency is $51200\ Hz$.

The array position and orientation is represented in Figure 7, and described as follows: the plane of the array is orthogonal to the coastline floor and it faces the open sea, the azimuth angle $\varphi$ turns in the plane of the array from $0°$ to $360°$ and the elevation angle $\theta$ from $0°$ to $90°$ which is elevated from the plan of the array to the perpendicular direction of it (z axis).

The typical flight for this measurement is described in Figure 7. It consists of a $100\ m$ round trip of the UAV above the sea in front of the array. The UAV starts from a point at the right of the array which correspond to an angle of approximately $\varphi = 190°$ and $\theta = 0°$. Then the UAV comes right in front of the array in the middle of it, i.e. along the z axis orthogonal to the center of the array plan. This implies the decreasing of the azimuth around $\varphi = 100°$ for the BM42. The θ angle quickly increases up to $\theta = 80°$ when the UAV is coming in front of the array, and then slightly tends to 90° when it is moving away from the array. When it arrived at 100 m from the array the UAV flight its trip back which is represented by the opposite described trajectory.

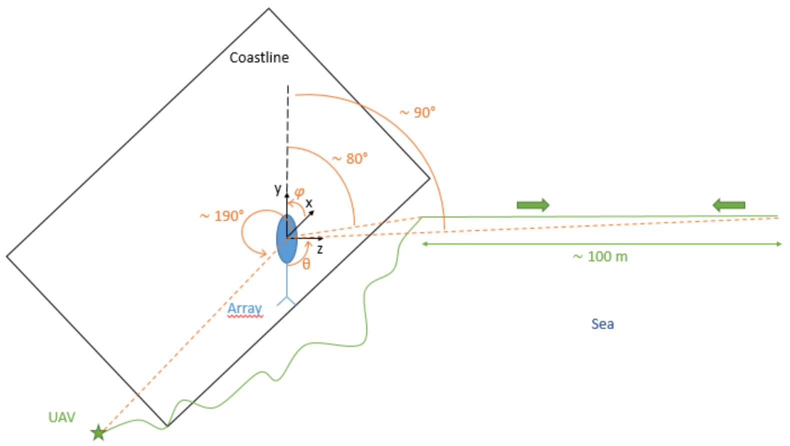


**Figure 7 : Plan of the measured UAV trajectory.**

### 4.2 Results from real measurements

The output of the localization method is the maximum angles $(\theta_{max}, \varphi_{\max})$ found from the MUSIC map. Those angles can be represented as in Figure 8 corresponding to the BM42 flight with a analysis frequency set to $5000\ Hz$. The blue dots are representing the localization estimation for one time frame and the colored line is representing the validated trajectory captioned by GPS. The color of the later is function of distance.

To determine the detection range the criterion chosen is to identify when wrong estimations of the DOA are encountered, i.e. when the continuity of valid estimation of DOA is broken. When the discontinuity is reached, the detection range is the distance between the UAV and the center of the array for the given time. The graphics in Figure 8 are providing a visualization to identify the discontinuity of the estimation from the validated trajectory.

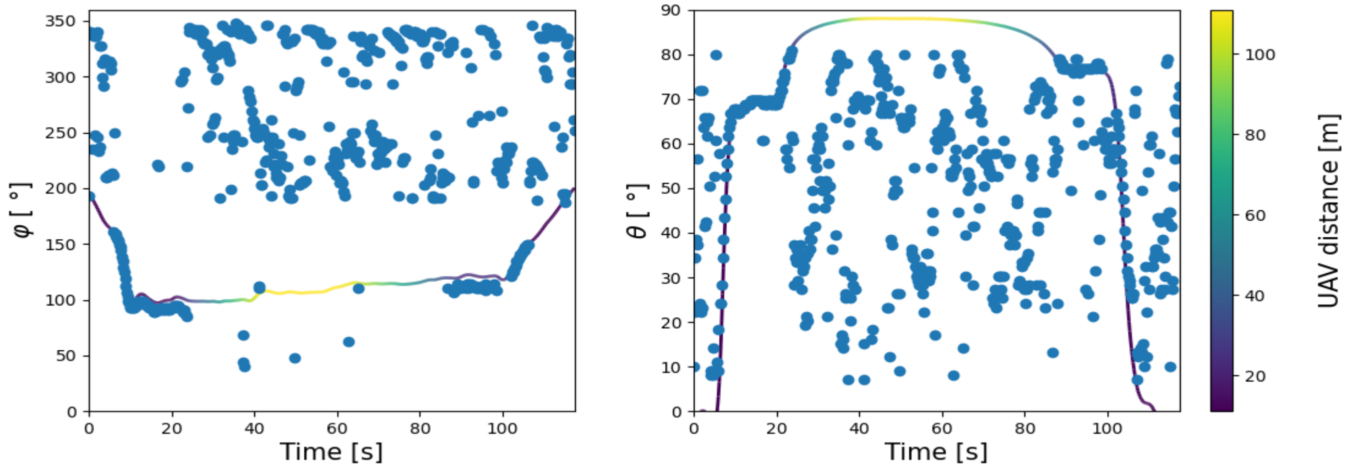


**Figure 8 : Maximum angles $(\theta_{max}, \varphi_{\max})$ deducted from MUSIC for each time frame compared to the reference DOA.**

To perform the DOA estimation, the chosen analysis frequency is $5000\ Hz$ for the DJI Phantom 4 Pro and the BM42, and $6600\ Hz$ for the Parrot Anafi. The results and the associated SNRs for each model of UAVs are given in

Table 3. The given SNR values are calculated at the third octave band corresponding to the frequency used for the localization process.

| | Outward flight | | Return flight | |
|---|---|---|---|---|
| | Detection Range [m] | SNR [dB] | Detection Range [m] | SNR [dB] |
| BM42 | 24 | -2.20 | 29 | -3.84 |
| DJI Phantom 4 | 51.2 | -7.16 | 54.9 | -7.77 |
| Parrot Anafi | 28 | -7.07 | 19 | -3.70 |

**Table 3** : **Detection range estimation and associated SNR for each UAV from the maritime measurement.**

The detection performance of the localization method in a maritime environment is $Dr = 19\,m$ for the quietest UAV (Parrot Anafi) to $Dr = 55\,m$ for the loudest one (DJI Phantom 4 Pro). The SNRs corresponding to these results are comprised between $\Delta_L = -2.2\ \mathrm{dB}$ and $\Delta_L = -7.77\ dB$. Those values are similar to the one of a previous indoor experiment in which the disturbing source was a loudspeaker and not the ambient noise (Baron, 2020). They also confirm the Table 1 synthesis, with difficulties to be able to localize quiet UAVs at 100 m distance while it could be possible for loudest ones.
These are promising results as the environment is very noisy, strongly disturbed by the wind and the backwash. Furthermore, the method is for now at its most basic level. It is just set with parameters that have been proven efficient in a controlled environment, far quieter than the maritime one. Some improvements can be made on several parts of the method in order to push further these detection ranges in the maritime environment, and achieve detection for SNR that could be as low as -20 dB. The next section will focus on these research axes.

## 5. Improvement perspectives

Some perspectives are considered to improve the given localization method and their implementation is the continuation of the work presented in this paper. In the current procedure, the localization estimation is made at a single frequency, the number of values to represent the signal subspace is manually set to one per source and it is using the raw recorded acoustic signals.
Three major improvement avenues are considered:

- Denoise the temporal acoustic signals recorded by the array.
- Combine frequencies to perform a wideband MUSIC.
- Find automatically the number of sources, and automatize the number of the singular values chosen to represent the signal subspace for the MUSIC method.

### 5.1 Pre-process – Temporal signal denoising

One major perspective is about denoising the temporal acoustic signals recorded by the array. Because the ambient noise is considerably present in a maritime environment, the localization method performance would remain limited without a pre-process on the acquired signals. The aim is to remove the ambient noise as much as possible from the recorded signals even before using the localization method in order to enhance the SNR. This development would improve the localization detection range compared to the current signals and provide more reliable results, as the current method performed correctly in quiet environment (Baron, 2020).

### 5.2 Multi-frequency localization process

In section 3 it has been seen that UAV noise emerges at multiple frequencies. But the DOA estimation uses only one of them. The aim of this perspective is to exploit the whole spectral content in order to combine the results at different frequencies and obtain more reliable and robust final MUSIC map.
The method considered for this improvement for now are based on either the post-processing of the MUSIC map (e.g. combining MUSIC maps through the use of a 2D-histogram) (Delikaris-Manias, 2016) or on the use of wideband MUSIC estimator (Zeng, 2010).

### 5.3 Automatic detection of source number

In the experiment only one source was present, but in reality many sources can be present in the acoustic scene. It is essential to be able to estimate the number of present sources automatically. Once this is obtained, by default in the current method only one singular value per source is kept to represent the signal subspace during the eigenvalue decomposition process. However, this can introduce artefacts in the MUSIC map as the number of sources can be underestimated (unexpected acoustic sources can be present in the scene). To overcome this issue, the signal subspace selection can be automatized in order to detect the right number of eigenvalues to keep in, and end up with a more understandable DOA map (Akaike, 1998) (Bienvenu, 1983) (Ferreol, 2006) (Quinlan, 2006) (Wax, 1985).

## 6. Conclusion

In this study a specific experiment has been conducted in a challenging context: the measurement of the detection range of three different UAV models in a maritime environment through array processing. We firstly proposed a spectral analysis of the background noise submitted to wind and backwash in comparison with the state-of-art, and defined frequency bands of interest where the UAV are perceivable, i.e. where SNR is favorable. This analysis helped to define some specific characteristics that can help to achieve UAV detection. The background noise is broadband and strongly present in a maritime environment which confirms that localization in such an environment is a challenge. The SNR is favorable in high frequency ($3\ kHz\ to\ 7\ kHz$) as the ambient noise decreases in this frequency range, which is an important feature for the localization process. The frequency bands located in high frequency in which the UAVs are dominant are variable as they depends on the propellers spectral characteristics and the loudness of the UAV.

Then the detection range of the three studied UAVs were analyzed in the noisy coastline environment. With the current localization method, the UAVs can be correctly localized from $20\ m$ to $50\ m$ from the array depending on the type of UAV, which corresponds to a SNR from $-\ 2.2\ dB\ to -\ 7.7\ dB$ at the studied frequency. These results are promising with a method that have not been optimized.

Finally, this study identifies the improvement avenues to follow for the current localization method. Three major improvements have been selected to improve the method’s performance, robustness, and reliability: denoising the temporal signal before applying the localization method in order to have a better SNR for the source of interest, combining frequencies in order to go from a narrowband MUSIC to a broadband estimator, and automating the detection of the number of sources and the singular values selection to form the noise subspace, to obtain more understandable MUSIC maps.

**Acknowledgments**
This work is part of the RAPID project ALARM supported by French organizations AID and DGA.
This work was supported by the Equipex ROBOTEX (ANR-10-EQPX-44-01).
The authors would like to thank CerbAir for their assistance during the experiment.

**References**

Akaike, H. (1998). Information theory and an extension of the maximum likelihood principle. *Springer Series in Statistics*. doi:10.1007/978-1-4612-1694-0_15

Albert, D. D. (2017, April). Acoustic and seismic ambient noise measurements in urban and rural areas. *119*, 135-143. Applied Acoustics.

Baron, V. B. (2020, December). Acoustic localization and identification of drones with a disturbance source. *Forum Acusticum.* Lyon. doi:10.48465/fa.2020.0402

Bienvenu, G. K. (1983). Optimality of high resolution array processing using the eigensystem approach. *IEEE Transactions on Acoustics, Speech, and*, 1235-1248.

Birch, G. G. (2015). UAS detection classiffication, and neutralization: market survey. SANDIA REPORT SAND2015-6365.

Cabell, R. M. (2016). Measured Noise from Small Unmanned Aerial Vehicles. In N. G. NASA (Ed.), *NOISE-CON.* Hampton.

Christnacher, F. H. (2016). Optical and acoustical UAV detection. *9988*, 83-95. (SPIE, Ed.) Edinburgh: SPIE Security + Defence. doi:10.117/12.2240752

Delikaris-Manias, S. P. (2016). 3D localization of multiple audio sources utilizing 2D DOA histograms. *24th European Signal Processing Conference (EUSIPCO)* (pp. 1475-1476). Budapest: IEEE. doi:10.1109/EUSIPCO.2016.7760493

Ferreol, A. L. (2006). On the asymptotic performance analysis of subspace DOA estimationin the presence of modeling errors: case of MUSIC. *IEEE Transactions on Signal Processing*, 907-920.

Heutschi, K. O. (2021, April). Virtual microphone signls of flying drones. Wakefield, MA, USA: In Proceedings of the NATO STO MSG-SET-183.

Johnson, B. (2022, Fevrier 21). ISIS shows seizure, study od U.S. - made drone in SInai. *Homeland Security Today*.

Lykou, G. M. (2020). Defending Airports from UAS: A Survey on CyberAttacks and Counter-Drone Sensing Technologies. *Sensors*. doi:10.3390/s20123537

Michel, A. (2018, February). Counter-Drone systems. Technical Report.

Michel, A. (2019). Counter-Drone Systems. CSD-CUAS-Technical Report 2nd Edition.

Quinlan, A. B. (2006). Automatic determination of the number of targets present when using the time reversal operator. *The Journal of the Acoustical Society of America*. doi:10.1121/1.2180207

Schäffer, B. P. (2021). Drone Noise Emission Characteristics and Noise Effects on Humans - A systmatic Review. *MDPI*. doi:10.3390/ijerph18115940

Schmidt, R. (1986). Multiple Emitter Location and Signal Parameter. *IEEE Transactions on Acoustics, Speech, and Signal Processing*, 276-280. doi:10.1109/TASSP.1983.1164185

Siemens. (n.d.). Simcenter Sound Camera. Retrieved from https://www.plm.automation.siemens.com/media/global/en/Siemens-PLM-Simcenter-Sound-Camera-eb-63902-A13_tcm27-56488.pdf

Strauss, M. M. (2018). DREGON: Dataset and Methods for UAV-Embedded Sound Source Localization. *IEEE/RSJ International Conference on Intelligent Robots and Systems (IROS),*, (pp. 1-8). Madrid. doi:10.1109/IROS.2018.8593581

Wax, M. a. (1985). Detection of signals by information theoretic criteria,". *IEEE Transactions on Acoustics, Speech, and Signal Processing*.

Welch, P. (1967). The use of fast Fourier transform for the estimation of power spectra: A method based on time averaging over short, modified periodograms. *IEEE Transactions on Audio and Electroacoustics*, 70-73. doi:10.1109/TAU.1967.1161901.

Woody, C. (2020, March 11). *Drones are dropping bombs on US troops in Syria, and it's not clear who's doing it.* Retrieved from https://www.businessinsider.in.

Zeng, W.-J. a.-L. (2010, June). High-Resolution Multiple Wideband and. (IEEE, Ed.) *IEEE Transaction on Signal Processing*(58), 3125-3136. doi:10.1109/TSP.2010.2046041

QUIET DRONES
Second International e-Symposium
on
UAV/UAS Noise
27th to 30th June 2022

# An Aeroacoustic Experimental Analysis on Pitch Angle Effect on a small-scale Propeller to Quiet Drones Flight

**Paolo Candeloro, Department of Engineering, Niccolò Cusano University, Via Don Carlo Gnocchi 3, Rome, 00166, Italy: paolo.candeloro@unicusano.it**

**Edoardo Martellini, Department of Engineering, Niccolò Cusano University, Via Don Carlo Gnocchi 3, Rome, 00166, Italy: edoardo.martellini@unicusano.it**

**Tiziano Pagliaroli, Department of Engineering, Niccolò Cusano University, Via Don Carlo Gnocchi 3, Rome, 00166, Italy: tiziano.pagliaroli@unicusano.it**

## Summary

The aim of the present study is to investigate the pitch angle effect on the rotor noise generated by small scale rotor for mini drone propulsion. The experimental tests were performed on a two bladed propeller within an anechoic chamber. The rotor was instrumented with an embedded load cell in order to measure thrust and torque. The study consists also in near-field pressure measurements executed by means of a single microphone mounted on a rotating automatic support. Main goal of the present study is to investigate the noise signature of a propeller in hover at different rotational velocities and different pitch angles.

Drone noise is addressed as a central issue for the scientific community due to the very fast growth of the UAV market for both civil and military applications in the last few years. A lowering of their acoustic impact is essential for the market of these vehicles in the future. Since, the interest on this topic involve both academic and industrial point-of-view. Noise of

such vehicles is a very challenging task for scientific community. This aspect justifies the presented work, in fact a simple approach aimed at reducing the number of variables in the optimization process is reported.

For the experimental tests the chord-based Reynolds number ranged from 20.000 to 50.000 and the tip Mach number was about 0.025. Such conditions gave rise to complex phenomena as a laminar separation bubble and the transition from laminar to turbulent boundary layer, that is proved to be the counter part of a complex noise signature.

The results in the Fourier domain reveals that the main noise component is the broadband one despite the tonal noise is still relevant and can't be neglected. To investigate both the noise component singularly a POD-based decomposition strategy has been performed with very promising results.

# 1. Introduction

Drones, also known as Unmanned Aerial Vehicles (*UAV*), are commonly employed as tactical surveillance tools, or for reconnaissance purpose. Mini Aerial Vehicles (*MAVs*) are also employed in civilian roles and are flown in close proximity to populated areas. Despite different applications, achieving the acoustic stealth is an essential feature which may lead to mission success. This led to a great interest of the scientific community on reducing the noise impact of those surveys.

Furthermore, the main companies are working to move the urban mobility into airspace, this is the concept of Urban Air Mobility (*UAM*). It is estimated that by 2030 almost the 60% of the world's population will be urban. This significant population growth is expected to create a real need for innovative mobility options as ground infrastructure becomes increasingly congested. Providing people with a safe, sustainable and convenient solution that leverages the airspace above cities could be a solution. EASA in the Drones Amsterdam Declaration of 2018 recognized the social need for smarter mobility to improve quality of life. Such declaration encourages the European community to develop the public and infrastructural conditions for smart mobility solutions and stated that drones are an integral part in this scenario. Such consideration justify the present work that can represent a useful starting point for the design of future UAVs.

At the actual state-of-the-art, most of MAVs are equipped with electric motors, that contribute to simplify operations and significantly reduce their noise signature, mostly regarding brushless engine (Candeloro et al., 2020; Gur & Rosen, 2009b; Sinibaldi & Marino, 2013). Moreover, a lowering of drone noise can also guarantee the safety of this technology in the future and can be seen as a key aspect in the wide-spread deployment of these vehicles, in fact the MAVs' acoustic signature has a relevant effect on their detection and on public acceptance for city flight.

It is well-known that the main acoustic source of electric motor-equipped MAVs is the propeller. For this reason, there is a renewed interest in the literature in reducing the noise produced by small-scale propeller at low Reynolds number (Candeloro et al., 2020; Gur & Rosen, 2009b; JANAKIRAM & SCRUGGS, 1981; Leslie et al., 2008; Pagliaroli et al., 2018; Sinibaldi & Marino, 2013). The reduction of the propeller's noise requires special attention in the design process so as not to affect the performance and the efficiency of the propulsion system. As a matter of fact, the rotor efficiency maximization and its acoustic signature minimization are contradictory goals. As a result, most of this investigation is focused on identifying the best compromise between these objectives.

In the literature several authors provided a study regarding rotors. For example, as cost function for an optimization process Gur and Rosen (Gur & Rosen, 2009b) proposed the Sound Pressure Level of the propeller or the power extracted from the battery, separately, indeed the cost function herein proposed takes into account both the efficiency of the rotor and its acoustic performance. Moreover, Succi and Farassat (Farassat & Succi, 1980) or Miller and Sullivan (Miller & Sullivan, 1985) work for reducing the acoustic signature maintaining propeller efficiency constant. Furthermore, Leslie (Leslie et al., 2008, 2010) has introduced a method to reduce the propeller broadband noise component by employing a boundary layer tripping system in order to anticipate its transition from laminar to turbulent, which is known as one of the most important rotor noise source. Sinibaldi and Marino have provided some experimental tests on a traditional and acoustic optimized propeller, keeping the thrust constant and measuring the SPL generated by the models (*Leishman - 2008*; Lv et al., 2018; Marino, 2010; Shkarayev et al., 2008; Sinibaldi & Marino, 2013).

In 2008, Shkarayev and Moschetta introduced the efforts on the aerodynamic design of a MAV named *miniVertigo*, that presents a tilt-body configuration (Shkarayev et al., 2008). Within the community of MAVs, tilt-body configurations have been developed in order to offer a wide range of services as they offer great versatility in the field of urban reconnaissance through the quick switching between horizontal and vertical flights. Tilt-body drones can both hover and fly forward. In hover, the inflow velocity is small and the propellers must provide the necessary thrust to support the aircraft weight. On the contrary, in forward flight, the inflow velocity is relatively large and the low thrust required is just to overcome the drag (Lv et al., 2018). Despite the difference in the inflow and thrust requirement between the two flight configuration suggests different blade pitch angles in order to optimize overall flight performance. Drones are usually equipped with fixed pitch propellers of small diameters (Gur & Rosen, 2009b, 2009a). In compliance with this remark, the research activity hereafter described examines the behaviour of a small-scale propeller equipped with variable collective pitch from an aeroacoustic point of view.

The effect of the pitch angle on aeroacoustic signature for small rotor has not been documented in literature at the actual state-of-the-art, in fact, commonly little attention is payed to the noise of a small propeller running at low values of the advance ratio, which correspond to poor efficiency values. In particular, at fixed point, where a sizable part of the disk is stalled, the effect of the recirculation bubble on aerodynamic and acoustic field become significant as in the present study cases. The present work is aimed at providing experimental data on a low Reynolds number rotor in hover mode and at giving the instruments to quantificate the aeroacoustic properties of small-scale propellers.

In this manuscript is demonstrated that drone noise signature is dominated by broad band noise, despite the narrow band component is not negligible. Such effect suggests that the analysis tools commonly employed, focused on the tonal noise, must be extend to the more relevant broad band component for the case of small-scale propellers in hovering.

As a matter of fact, the acoustic contribution of the tonal noise is buried by the broadband contribution and it is indistinguishable within a single microphone measurement. Such characteristic makes the problem really challenging and lead us to implement an innovative and effective technique in order to separate the noise component which will be described in the following.

The broad band noise is generated by several sources. Mainly, leading edge noise is dominant in presence of inflow turbulence. Instead, in absence of the inflow turbulence this mechanism, e.g. for fixed-point flight, as the case of the present investigation, when the inflow velocity is very low, the more important broad band noise sources are: generation of vortices at the blade tip (Rozenberg et al., 2010), vortex- shedding due to blunt trailing edge (TE) (Rozenberg et al., 2010), scattering of the boundary layer turbulence as sound at the trailing edge (Rozenberg et al., 2010), laminar boundary layer vortex shedding at leading edge (LE) (Leslie et al., 2008, 2010), separated flow. In addition, turbulent boundary layer (TBL) at trailing edge is generally considered to be the most important source of noise. The unsteady pressure waves in TBL are amplified and radiated by the sharp trailing edge. This mechanism can excite the laminar boundary layer, localized near the LE, that emits a sound radiation, as illustrated in Figure 1. Such a phenomenon is well-known as trailing edge back scattering. As the angle of attack increases, the thickness of the TBL increases and large-scale unsteady structures can dominate noise production from the trailing edge. For fully separated chord flow the noise can be radiated from entire chord (Migliore & Oerlemans, 2004).

The present manuscript is organized as follows: Sec. 2 reports some theoretical information considered fundamental for the following of the study; then, the experiment is qualified through extensive dynamic measurements which are presented in Sec. 3. The instrumentation devices and the acquisition parameters are also described in Sec. 3. The results are presented in Sec. 4 while final discussions and conclusions are given in Sec. 5.

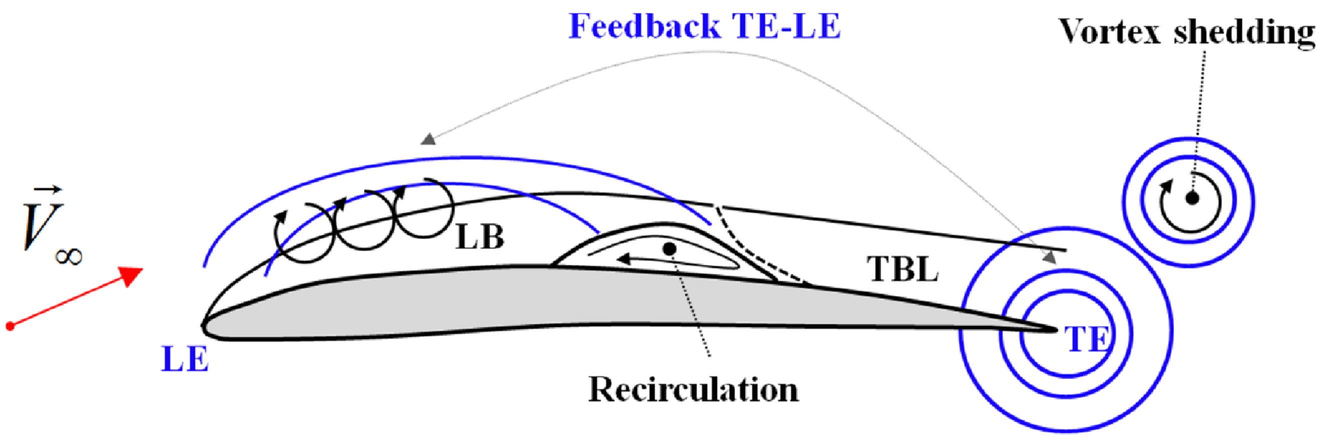


*Figure 1: Sketch of the flow field and aeroacoustic sources around a blade section.*

# 2. Theoretical Background

## 2.1. Propeller Noise

Small-scale UAVs provide a great challenge to the task of noise characterization and prediction. Indeed, the main noise sources remain consistent with those associated with helicopters, but there are numerous unknowns to be investigated, as the effect of reduced size or the balance between tonal noise and broadband noise.

An important difference between small size UAVs and conventional rotor-craft is the flow speed regime in which they fly, commonly measured by the chord-based Reynolds number at 75% span

$$Re_{75\%} = \frac{0.75 R \rho_\infty \Omega c}{\mu_\infty}$$

(2. 1)

where R is the rotor tip radius, $\rho_\infty$is the air density, $\Omega$ is the rotational regime, c is the rotor blade chord and $\mu_\infty$ is the air dynamic viscosity.

For a full-scale helicopter, a representative $Re_{75\%}$ is in the order of $10^6$, while for a UAV it may range from $10^4$to $10^5$In terms of conventional flat plate aerodynamics, the former Reynolds number explicates in a turbulent flow regime while the latter in a laminar-transitional flow regime (Zawodny & Boyd Jr, 2017). This difference calls into question the applicability of the model already employed for helicopter applications and the necessity of the development of a more specific noise prediction tool.

As already mentioned, the pressure fluctuation field $\mathrm{p}'(\mathbf{x},\mathrm{t})$ radiating from a propeller can be divided into two main components in the Fourier domain: narrow (or tonal) and broad-band contributions (Candeloro et al., 2020; FARASSAT, 1986; Intravartolo et al., 2017; Sinibaldi & Marino, 2013). This led to the separation reported hereinafter:

$$p'(\boldsymbol{x},t) = p_{NB}'(\boldsymbol{x},t) + p_{BB}'(\boldsymbol{x},t)$$

(2. 2)

where $p_{NB}{}'(\boldsymbol{x},t)$ is the narrow-band component, whereas $p_{BB}{}'(\boldsymbol{x},t)$ is the broad-band counterpart.

Narrow (or tonal) components are directly related to the periodic motion of the blade in the surrounding fluid. Therefore, the radiated noise presents a frequency and magnitude connected to the rotational velocity of the propeller. The thickness term takes into account the fluid displacement due to the body, whereas the loading counterpart takes count of the unsteady force distribution over the body surface.

The theoretical prediction of the periodic noise generated by propellers is based on the solution of the Ffowcs, Williams and Hawkings non-homogeneous wave equation, known as the Ffowcs-Williams/Hawkings equation (Ffowcs Williams, J. E., and Hawkings, 1969; Gur & Rosen, 2009a)

$$\frac{1}{a^2} \cdot \frac{\partial^2 (p')}{\partial t^2} - \frac{\partial^2 (p')}{\partial x_i^2} = \frac{\partial^2 T_{ij}}{\partial x_i \cdot \partial x_j} + \left\{\rho_a \cdot v_i \cdot \delta(f) \cdot \frac{\partial f}{\partial x_i}\right\} - \nabla \cdot \{\Delta p_{ij} \cdot \delta(f) \cdot \frac{\partial f}{\partial x_i}\}$$

(2. 3)

where $a$ is the speed of sound,$p'$ is the perturbation on the static pressure, $t$ is the observer time, $x_i$ are the components of the position vector, $T_{ij}$ are the components of the Lighthill stress tensor, $\rho_a$ is the air density, $\delta$ is the Kronecker's delta function, $v_i$ the components of the source velocity vector, $f$ is a function that defines the surface of the body producing the pressure wave, $p_{ij}$ are the components of the generalized stress tensor.

In this equation, there are 3 forcing terms on the right-hand side which are related to vortex (quadrupole), thickness and loading. For thin blades and low Mach numbers ($M<1$), as in the present study, the vortex term is negligible and the narrow-band contribution is given by the sum of a sound source related to blade thickness $p_T^{'}$ and one related to aerodynamic loading $p_L^{'}$, as distributed force over the blade:

$$p'_{NB}(\boldsymbol{x},t) = p'_T(\boldsymbol{x},t) + p'_L(\boldsymbol{x},t)$$

(2. 4)

A numerical evaluation of these two quantities can be achieved by discretizing the blade in $N$ finite elements along the span. The resulting overall radiation field is approximated as the sum of $N$ point-wise sources.

$$p'_T(\boldsymbol{x},t) = \sum_{k=1}^{N} p_{T,k}(\boldsymbol{x},t)$$

(2. 5)

$$p'_L(\boldsymbol{x},t) = \sum_{k=1}^{N} p_{L,k}(\boldsymbol{x},t)$$

(2. 6)

The two components can be calculated using Eqs. (Farassat & Succi, 1980; Sinibaldi & Marino, 2013; Succi, 1979).

$$p_{L,k}(\boldsymbol{x},t) = \frac{1}{4\pi}\left\{\frac{\dot{\boldsymbol{F}}_k \cdot \hat{\boldsymbol{r}}_k + \boldsymbol{F}_k \cdot \hat{\boldsymbol{r}}_k \left[\frac{\dot{\boldsymbol{M}}_k \cdot \hat{\boldsymbol{r}}_k}{1 - M_{r_k}}\right]}{a r_k (1 - M_r)^2} + \frac{\boldsymbol{F}_k \cdot \hat{\boldsymbol{r}}_k \left[\frac{1 - \boldsymbol{M_k} \cdot \boldsymbol{M_k}}{1 - M_r}\right] - \boldsymbol{F}_k \cdot \boldsymbol{M_k}}{{r_k}^2 (1 - M_r)^2}\right\}$$

(2. 7)

$$p_{T,k}(\boldsymbol{x},t) = \frac{\rho}{4\pi}\frac{\partial}{\partial^2 \tau^2}\left\{\frac{\Phi_k}{r_k(1 - M_r)}\right\}^2$$

(2. 8)

where $\boldsymbol{F}_k$ is the aerodynamic force on the k-point blade element of volume $\Phi_k$, $\hat{\boldsymbol{r}}_k$ is the position vector of an observer relative to the k-point noise source $\left|\hat{\boldsymbol{r}}\right| = 1$, $M_{r_k}$is a scalar magnitude that represents the component of the Mach vector $\boldsymbol{M_k} = \frac{\boldsymbol{v_k}}{\boldsymbol{a}}$ on $r_k$. If $\boldsymbol{t}$ is time as measured in the observer's reference frame, retarded time $\tau$ indicates the time when the pressure wave left the noise source. Observer time $t$ and retarded time $\tau$ are connected by:

$$\tau = t - \frac{r(\tau)}{a}$$

(2. 9)

In Eq.(2. 7) the first term represents the far field, while the second is representative of near field contribution. These two terms differ by the power of $r_k$ in the denominator. The far-field term is proportional to $r_k^{-1}$while the near field term is proportional to $r_k^{-2}$, thus the last term becomes relatively small at large distances from the noise source (Gur & Rosen, 2009a).

On the other hand, broad-band noise counter-part is radiated by the interaction of turbulent flow structures with the blade edge. Therefore, it is either generated at the blade leading/trailing edge or at the blade tip.

Moreover, the propeller broad-band noise component is related to the interaction of turbulent flow structures with the blade edge. Thus, it is either generated at the blade leading/trailing edge or at the blade tip, and it is generally related to three main sources: *i*)} noise related to the turbulence of the incoming flow (*LE noise* $p'_{LE}$); *ii*) noise produced by the interaction of the turbulent boundary layer over the blade surface with the trailing edge (*TE noise* $p'_{TE}$) and *iii*) noise generated by the possible separation of the flow (*Separation noise* $p'_S$) (Candeloro et al., 2020; Sinibaldi & Marino, 2013) Therefore, the broad-band contribution con be divided as:

$$p'_{BB}(\boldsymbol{x},t) = p'_{TE}(\boldsymbol{x},t) + p'_{LE}(\boldsymbol{x},t) + p'_S(\boldsymbol{x},t) \tag{2. 10}$$

where $p'_{TE}(\boldsymbol{x},t)$ is the trailing edge component, $p'_{LE}(\boldsymbol{x},t)$ is the leading edge component and $p'_S(\boldsymbol{x},t)$ is the laminar separation bubble term.

### 2.2.Proper Orthogonal Decomposition

The Proper Orthogonal Decomposition (POD) is a mathematical procedure for extracting a basis for modal decomposition from an ensemble of signals. The method has been widely used in turbulent flows since it provides a low-dimensional representation of a characteristic large-scale structure by decomposing it into a set of uncorrelated, data-dependent components. The components are the eigenfunctions of a two-point correlation tensor. For a comprehensive review about the mathematical formulation of proper orthogonal decomposition and its application to turbulent flows the reader may refer to the large body of literature (e.g. (Berkooz et al., 1993; Kirby et al., 1990; Sirovich, 1987).

In this paper a novel application of the POD is reported, the modal decomposition is applied to a pressure time series $p(t)$in the near field in order to split the signal into its main components: tonal and broadband (see Sec. 2.1}). The starting point for the innovative formulation presented here is the so-called *snapshot*-POD (Meyer et al., 2007; Sirovich, 1987). The idea is to apply a windowing to the pressure time series $p(t)$and, subsequently, to re-arrange the obtained vector in a matrix $\boldsymbol{P}$.

$$\tilde{\boldsymbol{C}} = \boldsymbol{P}^T \boldsymbol{P} \tag{2. 11}$$

Then, the procedure is to resolve the corresponding eigenvalue problem:

$$\tilde{C} A^i = \lambda^i A^i \tag{2. 12}$$

and to re-order the obtained solutions by the size of the obtained eigenvalues:

$$\lambda_1 > \lambda_2 > .. > \lambda_N \tag{2. 13}$$

The eigenvectors of the Eq.(2. 6) compose the basis of the POD modes $\phi^i$, defined as:

$$\phi^i = \frac{\sum_{n=1}^{N} A_n^i \, \boldsymbol{p}_n}{\left\| \sum_{n=1}^{N} A_n^i \, \boldsymbol{p}_n \right\|}, i = 1, \dots, N$$

(2. 14)

where $A_n^i$ is the *n*-th component of the eigenvectors corresponding to $\lambda^i$ of the Eq.(2. 5) and the || || represent the discrete 2-norm defined as $\|\boldsymbol{l}\| = \sqrt{l_1^2 + l_2^2 + \cdots + l_N^2}$ (where $\boldsymbol{l}$ is generic vector of N components).

The time signal can be reconstructed as:

$$p(t) = \sum_{\{n=1\}}^{N} a_n \; \phi_n$$

(2. 15)

where the $a_n$ are called POD coefficients defines as the projection of the pressure signal onto the POD modes:

$$a^N = \sum_{n=1}^{N} a_i^n \, \phi_i = \boldsymbol{\Psi}^T \boldsymbol{a}^n$$

(2. 16)

the matrix $\Psi$ is composed of the POD modes as

$$\boldsymbol{\Psi} = [\phi^1, \phi^2, \dots, \phi^N]$$

Having imposed the Eq.(2. 6) it is ensured that the most energetic mode is the first one. Generally, this means that the first mode is associated with first harmonics namely the dominant tonal peak is reflected in the first POD mode. Therefore, the tonal noise component can be reconstructed correctly by looking at the more energetic modes. Finally, it is possible to reconstruct the broadband noise by subtracting the tonal component thus obtained from the starting pressure time history.

Figure 2 reports the application of this innovative separation technique to two synthetic signals: a simple sin wave and a sin wave with the addition of white noise. These figures shows a very good agreement in both time, see figures (b) and (f), and frequency domain, figures (c)-(d)-(g)-(h), for the obtained decomposed signal. The first column reports the synthetic signals employed for the validation; the second column reports the obtained signals compared with the original one in the time domain. Finally, third and fourth columns reports the Fourier transform of the tonal(figures (c)-(g)) and broad band components (figures (d)-(h)). The main evidence is that, as expected, the sin wave is perfectly reconstructed by its tonal component, see in particular Figure 2(b)-(c), while the broad band component is equal to zero. On the other hand, by adding a white noise to a sin wave a broad band counterpart born and the mathematical model fit properly even this component (Figure 2(f)). Such results can be interpreted as a validation for the presented strategy so it can represent a powerful tool to study a time series for the application where a periodic effect is embedded in a broadband phenomenon, like the one investigated in this manuscript.

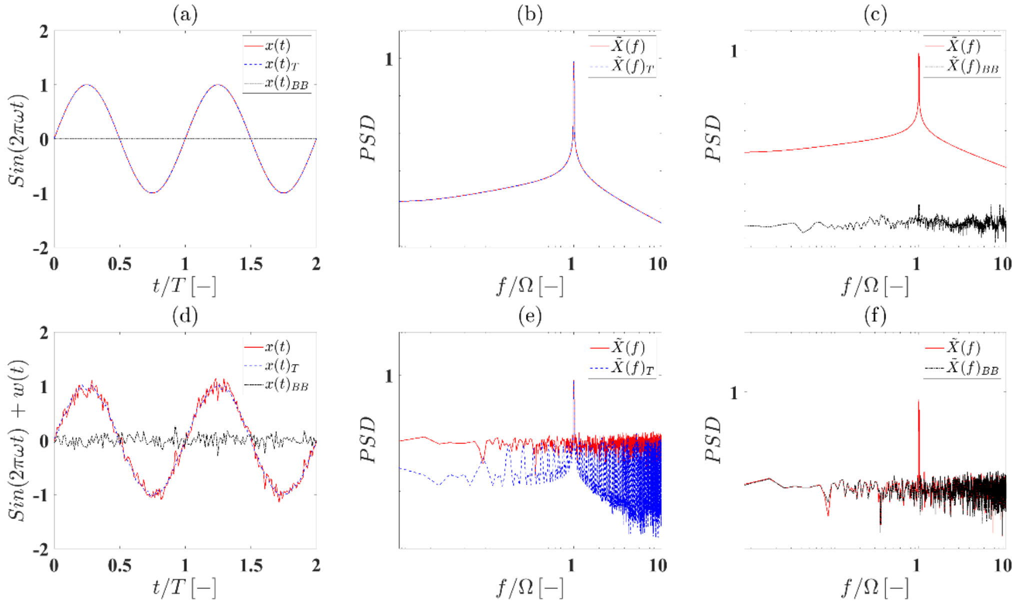


*Figure 2: Application of the POD-based decomposition strategy to synthetic signals: a sin wave and a noisy sin wave.*

## 3. Experimental Setup

For the experimental tests blades 12.4 mm in radius were employed, with maximum thickness of 2 mm and twist angle equal to zero. The blade profile was constant in spanwise direction and demonstrating satisfactory matching with NACA001234. Two blades were mounted on a collective pitch that allows to vary the pitch angle.

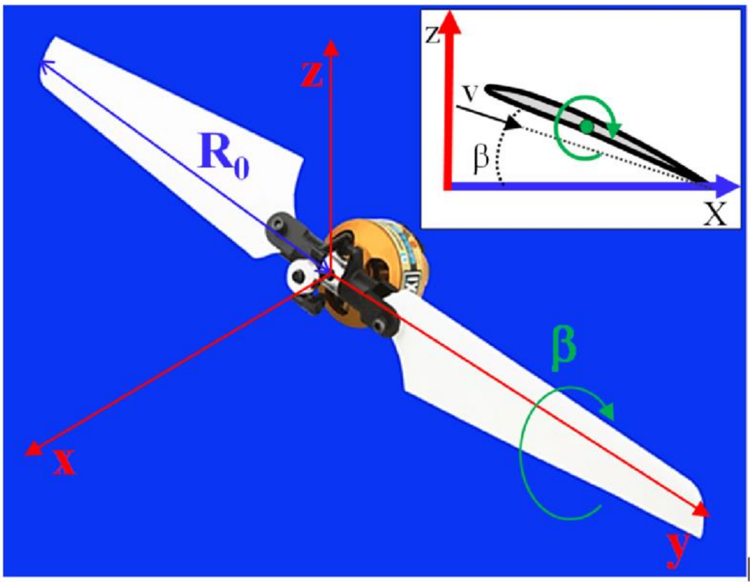


*Figure 3: Sketch showing engine, rotor, collective pitch. The reference system is also illustrated.*

For the presents study the pitch angle ranges from 0 to 21 deg. A sketch of this system is reported in Fig.1. Furthermore, the rotational regime of the investigated propeller ranges from 2800 to 7000 RPM. All tests were realized in *ONERA* within an anechoic chamber $4.0 \times 4.5\times 8.0 \rm{m}$ in size and a low frequency cut off of 90 Hz. Fig.2 reports a picture of the the experimental setup. The acoustic measurement equipment consisted in a Bruel and Kjaer (B & K) ¼ inch microphone mounted on an aluminum rotating support (as shown in Fig.2). The microphone rotor distance was tunable and the supporting arm could be rotated using a Newport ESP 301 controller in order to obtain the directivity pattern automatically. For the sake of brevity only the measurements of the noise generated in close proximity of the rotor tip are herein considered (y/R_0=1, x/R_0=0.2, see Fig.2}). The microphone was connected to a B & K Nexus 2690 signal conditioner allowing the amplification and anti-aliasing filtering of the signals at 10 kHz. The 80 KHz sampling frequency of acoustic instruments is selected on the NI 9234 acquisition board employed. In the measurements a frequency resolution equal to 1 Hz has been adopted, which guarantees a quite sharp definition of the acoustic discrete tones radiated by the propeller.

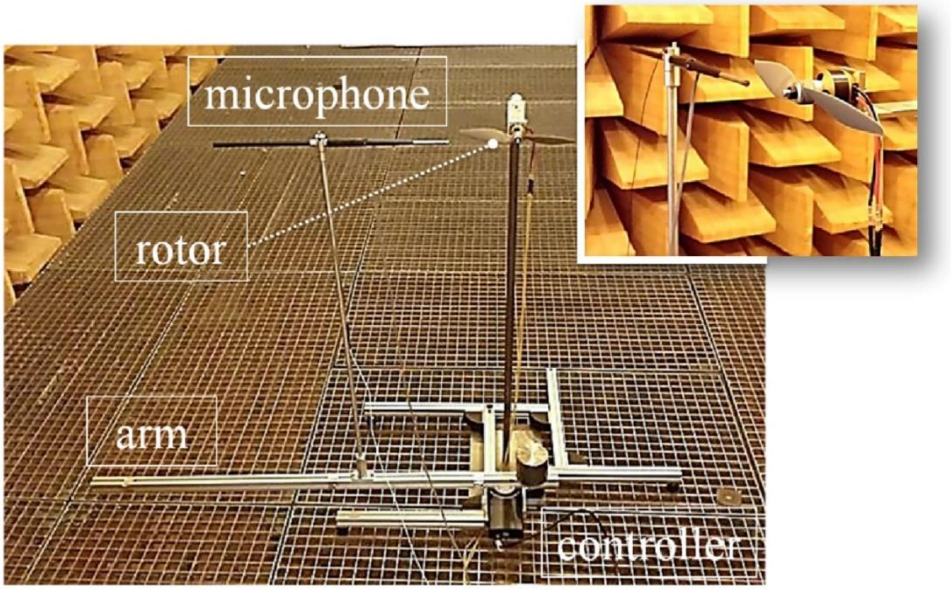


Figure 4: *Picture of the experimental set-up located within ONERA anechoic chamber; microphone, rotor, controller, arm position is indicated using a label. Enlargement of the motor, rotor and microphone, picture taken to different prospective.*

The rotor was driven by an electric brushless motor model AXI 2808/24. The rotational velocity of the motor has been determined measuring the frequency response of an optical photodiode. The thrust and torque were measured by means of an aerodynamic balance.

## 4. Results

Thrust, torque and pressure fluctuations generated at the blade tip by varying pitch and the rotational regime has been measured for a propeller with tunable pitch angle. The test matrix is composed by over 50 measurement conditions obtained keeping the rotational regime constant and varying the pitch angle. In Table 1 are listed the 5 rotational speed investigated and the ranges of the values assumed by the pitch angle.

| Ω, RPM | Θ, deg |
|---|---|
| 6540 | 0÷21 |
| 6060 | 0÷21 |
| 5640 | 0÷21 |
| 5100 | 0÷21 |
| 4740 | 0÷21 |

*Table 1: Experimental values assumed by rotational regime ($\Omega$)and pitch angle ($\Theta$).*

Furthermore, the values of rotational regime, pitch angle and thrust corresponding to hovering condition are gathered in Table 2. Despite in the following the investigation is focused to 5 fixed flight conditions, or rather constant thrust, it is noticeable that the thrust values, reported in Table 2, are weakly different. This aspect is ascribable to the accuracy of the digital speed controller of the rotational regime.

| Conf. | Ω, RPM | Θ, deg | T, cN | $C_T$ |
|---|---|---|---|---|
| 1 | 4740 | 20 | 149 | 0.009 |
| 2 | 5100 | 17 | 147 | 0.008 |
| 3 | 5640 | 15 | 154 | 0.007 |
| 4 | 6060 | 13 | 154 | 0.006 |
| 5 | 6540 | 11 | 152 | 0.005 |

*Table 2: Configuration number, rotational regime, pitch angle, thrust and thrust coefficient for the 5 different rotational regimes corresponding to fixed point flight conditions.*

The first step of the present study consists in an aerodynamic characterization of the propeller. Commonly, propeller propulsive efficiency is represented in terms of figure of merit $FM$, that is equivalent to the static thrust efficiency and defined as the ratio between the ideal power required to hover and the actual one (*Leishman - 2008)*. Such coefficient is commonly expressed in terms of thrust and power coefficient as:

$$\boldsymbol{FM} = \frac{\boldsymbol{c_T^{3/2}}}{\sqrt{2}\boldsymbol{c_P}}$$

*(4. 1)*

where $c_T$is the thrust coefficient and $c_P$ the power coefficient.

For the investigated propeller the maximum value achieved by $FM$ is relatively low, as can be observed in Figure 5. Such aspect is due to the symmetric profile and the not-twisted blade. As a consequence of the zero advance ratio and the blade geometry, a sizable part of the disk can be considered in stall (Sinibaldi & Marino, 2013). The most efficient configuration corresponds to thrust coefficient equal to 0.005, achieved for pitch angle of 11 deg, which corresponds to configuration 5 (see Table 2).

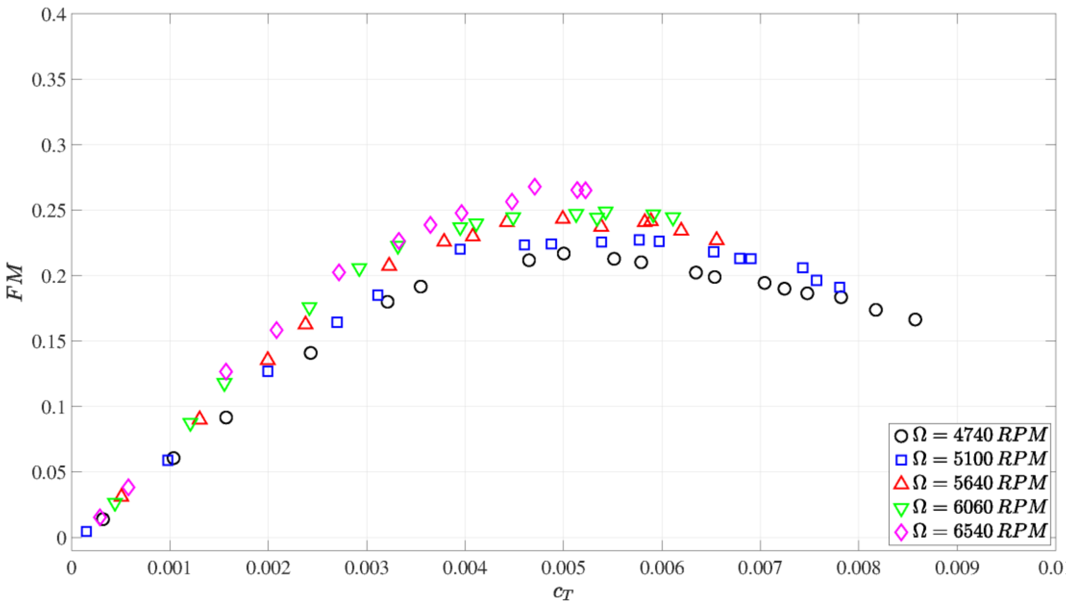


*Figure 5: Figure of merit realized for the 5 rotational regimes investigated provided by varying the rotational regime of the rotor (b).*

In order to identify the condition that corresponds to lower noise emission some considerations are reported below.

Usually, the acoustic impact of the rotor is evaluated in term of sound pressure level. As well-known, the SPL depends on the blade radius and thickness, the number of blades and the rotational regime. In order to reduce the number of variables to pitch angle value, in analogy with figure of merit, some preliminary consideration must be given. Generally, two components on the rotor noise are generally distinguished, i.e. tonal and broad band noise (as seen in Sec 2.1). According to Marino (Marino, 2010) the pressure fluctuations related to tonal noise can be normalized defining a reference pressure as:

$$p_{ref} = \rho(\omega R)^2$$

*(4. 2)*

such definition for the reference pressure leads to a satisfactory collapse the tonal noise signature (Marino, 2010).

This assumption has been also confirmed by several simulations based on blade element momentum theory (BEMT) and Ffowcs-Williams and Hawkings (FW-H) solver that have been carried out by the authors and not detailed here for the sake of brevity. An example of this results is given in Figure 6.

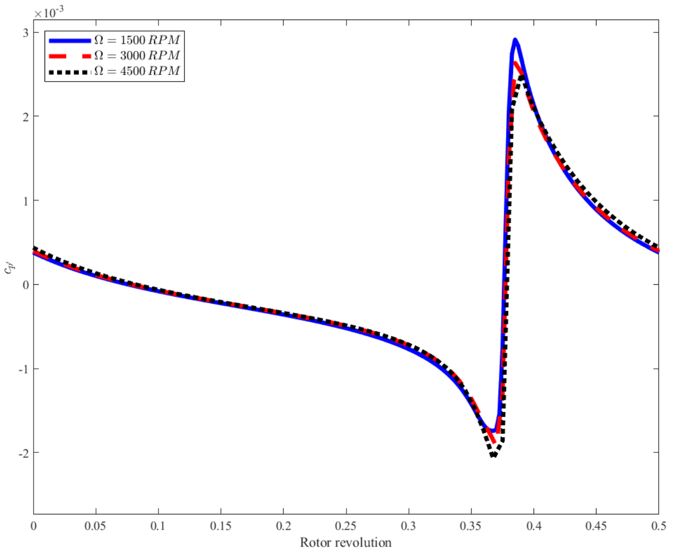


*Figure 6: Simulation of the acoustic signature generated by the blade passage and calculated for an half rotor revolution.*

As a consequence of this argumentation a novel non-dimensional coefficient has been defined as follows:

$$c_{P\prime} = \frac{\sigma_P}{p_{ref}}$$

*(4. 3)*

where $\sigma_p$ represents the standard deviation of the pressure time history. Such coefficient called *Pressure Fluctuations coefficient* is written as the ratio between an overall amplitude pressure coefficient normalized by the defined reference pressure.

Such coefficient gives a measure the noise impact regardless of the propeller rotational regime. On the other hand, it depends only on propeller geometry. Therefore, the pressure fluctuation coefficient can represent a very useful parameter in order to characterize a rotor.

Moreover, a further non-dimensional coefficient was defined to relate the aerodynamic and aeroacoustic properties of the propeller, and in this sense can be seen as the equivalent of the figure of merit:

$$AP = \frac{{c_T}^2}{c_{P'}}$$

*(4. 4)*

This coefficient called Aeroacoustic Performance $AP$ is written as the ratio between the squared thrust coefficient and pressure fluctuation coefficient. Figure 7 reports the AP coefficient, calculated for different rotational speed and pitch angles, so fixed thrust coefficient. As expected, the coefficient distribution is invariant with rotational speed, whereas it is markedly dependent by pitch angle, in analogy with the $FM$. As a consequence, $AP$ can be considered as the counterpart of $FM$ to characterize the acoustic efficiency of a propeller. The comparison between $FM$ and the $AP$ highlights that the maximum thrust efficiency and the lowest acoustic emission are achieved for the thrust coefficient equal to 0.005 and 0.007 respectively. Such a result confirms, in accordance with literature, that thrust generation and noise reduction are contradictory goals and a compromise solution must be found in the design process.

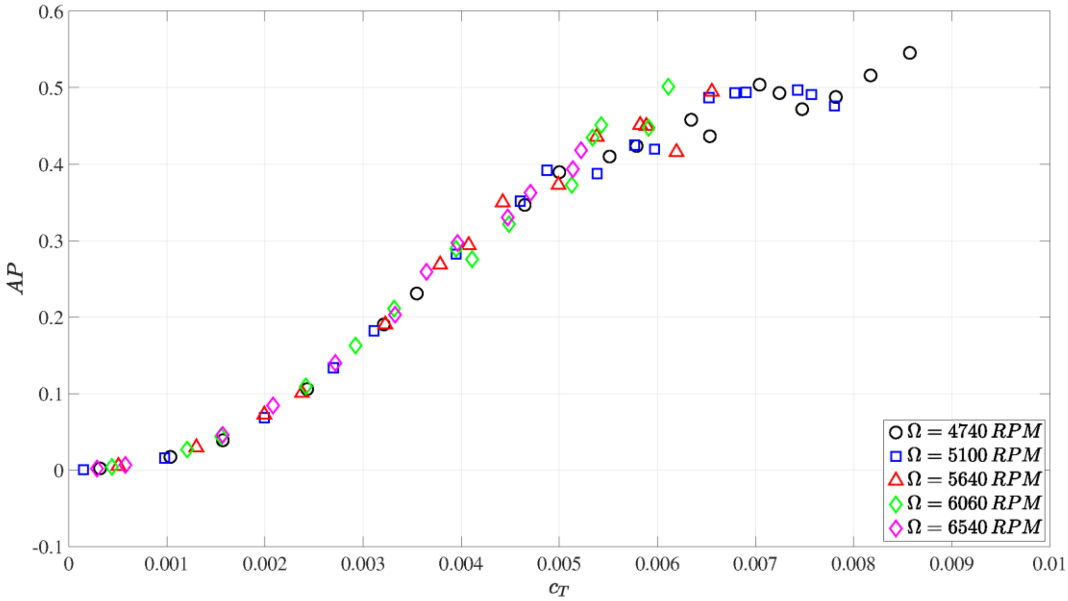


*Figure 7: Aeroacoustic performance coefficient distribution provided by varying the rotational regime of the rotor.*

Finally, Figure 8 reports the FM distribution for different values of the AP coefficient. The main result of this figure is that the figure of merit reaches a maximum after which it remains mostly constant by varying pitch angle and rotational speed. Such result implies that it is possible to define an optimal pitch angle leading to a good compromise between aerodynamic and aeroacoustic efficiency. Such result suggests that the calculation of $c_P$, and $AP$ should be an interesting approach for designing and, subsequently, testing of propeller.

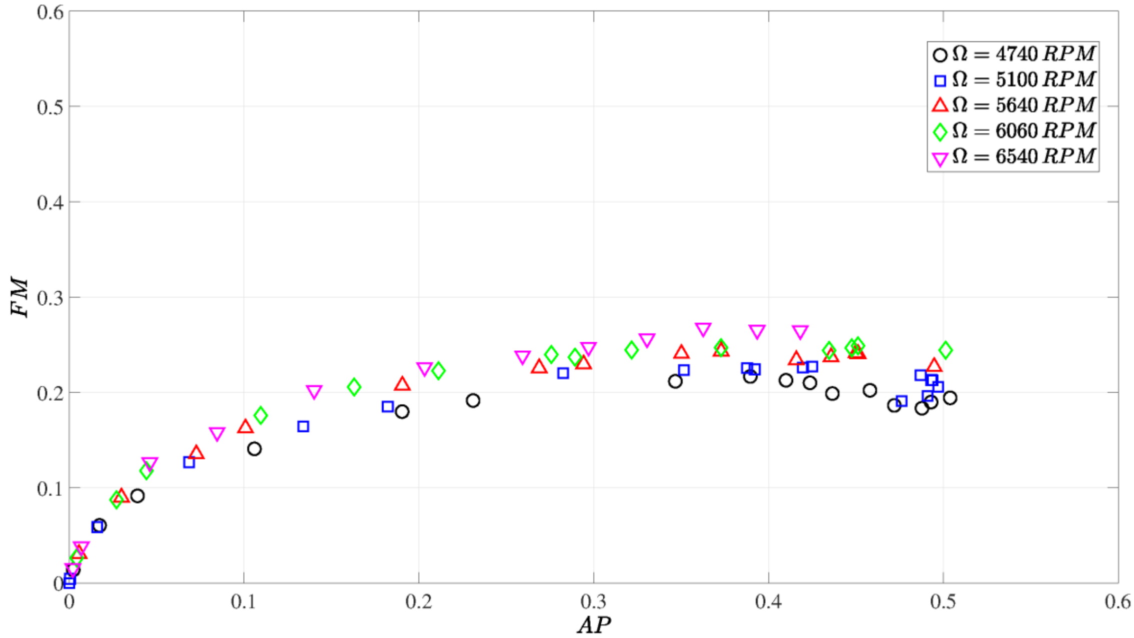


*Figure 8: Figure of merit at different values of the aeroacoustic performance.*

With reference to condition reported in Table 2, in this section the attention is focused on the measurement at constant thrust equal to weight. Figure 9 reports the SPL calculated for the 5 test cases. It can be observed that the minimum sound pressure level is achieved for configuration 3, which corresponds to 15 deg of pitch angle and 0.007 of thrust coefficient. Such results are in agreement with the thrust coefficient value that maximizes the AP. As showing in Figure 9 the noise reduction achieved changing the pitch angle from 20 to 15 deg is of the order of 2 dB.

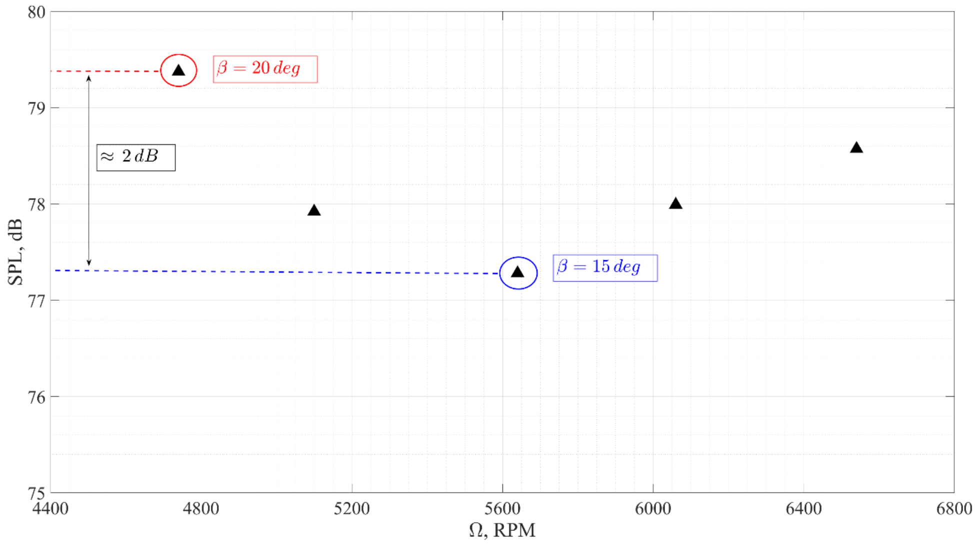


*Figure 9: Sound pressure level produced by the 5 different rotational regimes studied*

To further investigate the noise reduction a spectral analysis is provided. The spectra referred to these two configurations are represented in nondimensional frequency, specifically in terms of harmonics of the blade passing frequency defined as:

$$HBPF = \frac{2\pi f}{B\Omega}$$

*(4. 4)*

Where f is the frequency of the sound emission, B is the number of the blade and $\Omega$ the rotational speed of the rotor.

In Figure 10 it can be observed that tonal component generated by configuration 1 is lower than configuration 3, hence the highest value of the SPL observed in Figure 9 is not ascribed to tonal component, but it is justified by an important broad band noise increasing at low frequency range.

It is seen that in separated boundary layers the energy content in the low frequency range increases as one approaches larger scale dynamics (Camussi et al., 2008). Further it could be concluded that for configuration 1 a sizeable part of the disk is stalled and the separation region generates intense low frequency pressure fluctuation. Physically, it can be interpreted that the occurring recirculation bubble has became a significant broadband noise source (Glegg et al., 1987; Leslie et al., 2008; R.H., 1983).

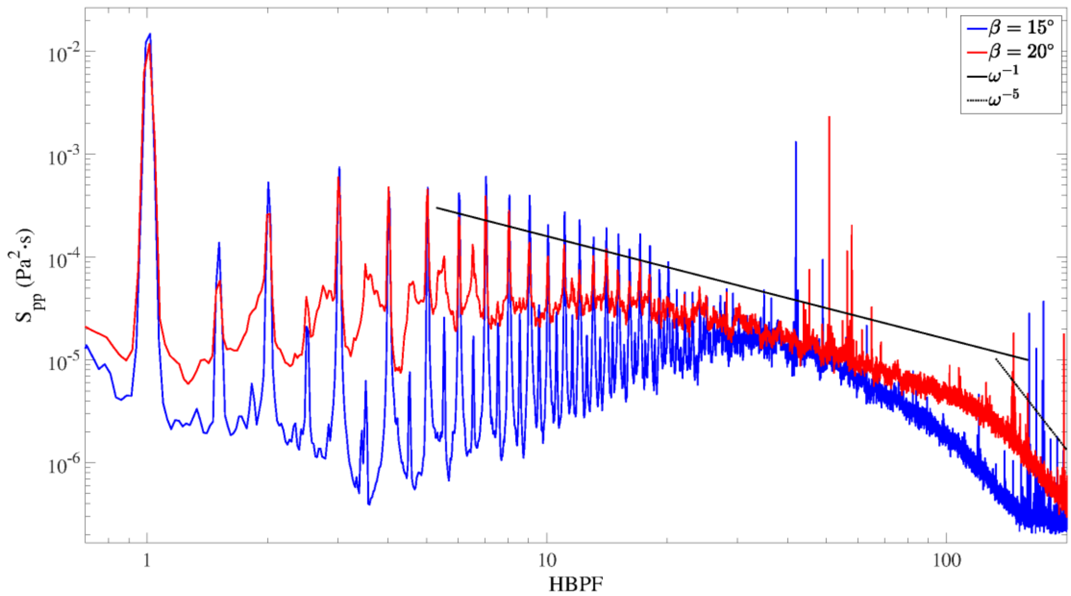


*Figure 10: Power spectrum computed for two pitch angle ( β=15 and 20 deg) an rotational speed (Ω = 4740 and 6540, rpm ) at iso-thrust.*

This aspect is further clarified by the analysis of the Probability Density Functions (PDFs) of these signals reported in Figure 11. The random variable is represented in reduced form in order to have zero mean and unitary standard deviation. PDFs are positive skewned toward positive values and, despite in every case a departure from the reference Gaussian curve is visible the highest Skewness is achieved for configuration 1. The origin of such a behavior can be ascribed to the effect of pressure surges, which are statistically relevant. In this regard, Kiya and Sasaki (Kiya, M. and Sasaki, n.d.) observed a positive skewness of the wall pressure fluctuations in the reattaching zone of a separated region and interpreted this behaviour as induced by inrush of irrotational flow toward the wall. More recently, a positive skewness in the pressure fluctuation statistics has been observed in front of forward facing step located along the fuselage of an instrumented aircraft (Steinwolf & Rizzi, 2006). Moreover, Pagliaroli observes a similar behavior in the pressure fluctuation generated in close proximity of a recirculation bubble located into the neck of enclosure (T.Pagliaroli, 2013).

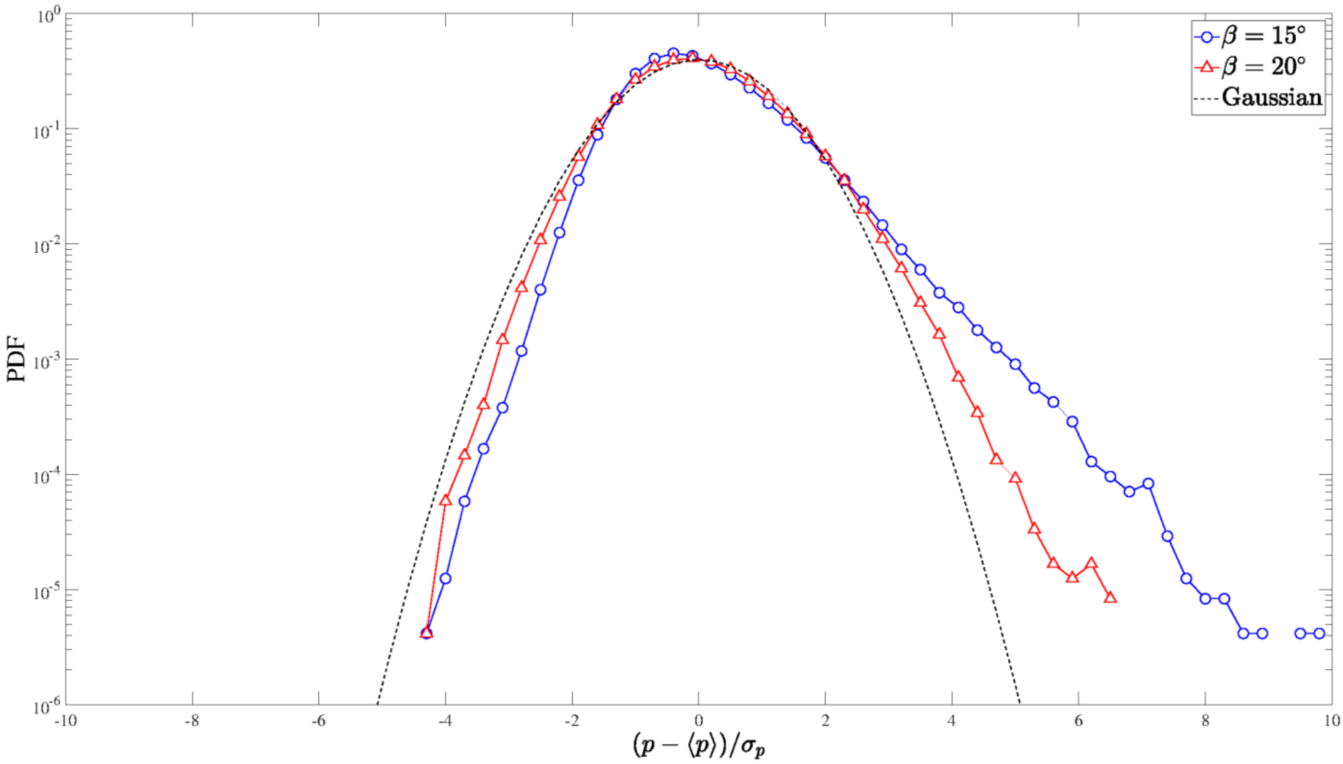


*Figure 11: Semi-log plot of probability density functions of the pressure fluctuation normalized with respect to the standard deviation, dashed line represents a reference Gaussian curve having zero mean and unitary standard deviation.*

Furthermore, in order to quantify the energy associated individually to the tonal and broadband noise components the time pressure signal has been decomposed by means of the proposed POD-based decomposition strategy, see Sec. 2.2. To further validate the employed algorithm Figure 1Figure 12 reports the noise spectra of the raw signals and the obtained subparts. These figures show a perfect agreement between the tonal component and the raw signal regarding the harmonic peaks. Moreover, the broadband component is also described with high precision.

Such results are independent from the pitch angle considered confirming the validity of the decomposition strategy.

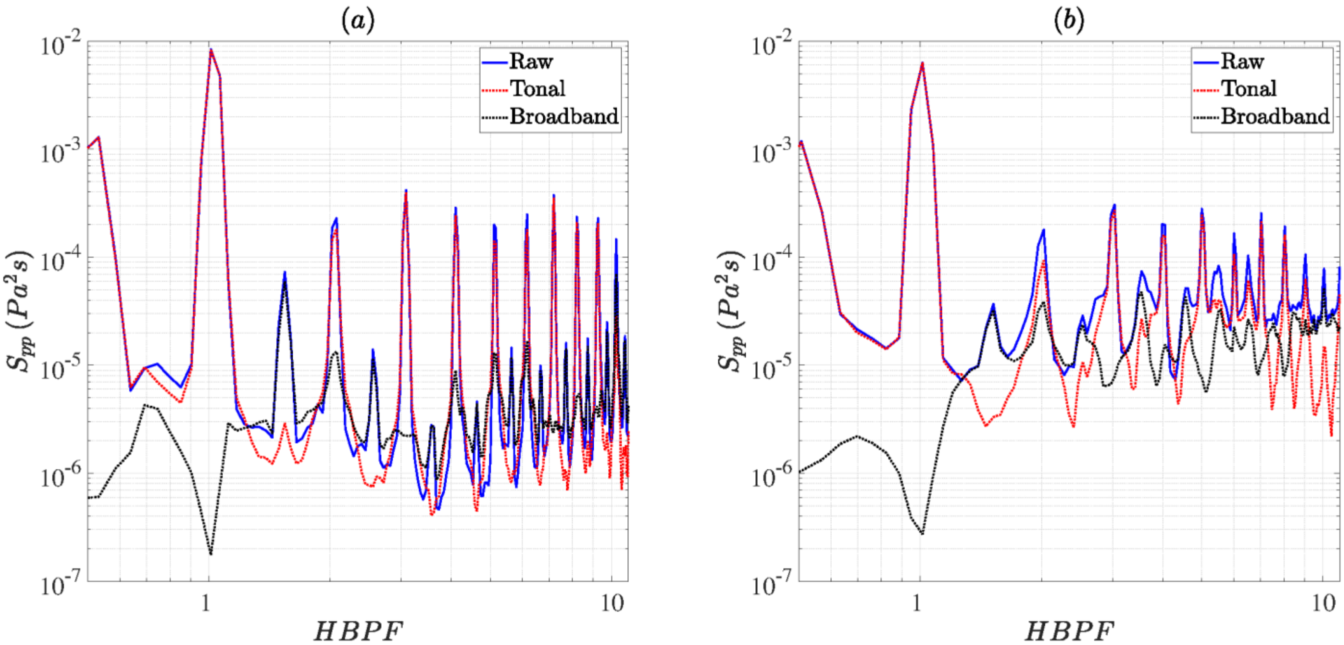


*Figure 12: Noise decomposition computed for two pitch angles ( $\Theta = 15$ (a) and and 20 deg (b)) an rotational speed $\Omega = 4740$ and 6540) at iso-thrust. The blue line represents the raw signal, the red dotted line the tonal component and the black dotted line the broadband component.*

The effect of pitch angle on the two noise component is shows in Figure 13.The main results, in agreement with those obtained previously (see Figure 10), is that by increasing the pitch angle the broadband noise grows accordingly; in fact looking at the Figure 12(b) the blue line, representative of $\Theta = 20$ deg , is always positioned above the red line relative to $\Theta = 15$ deg. Such effect is associated with a reduction of the tonal components, see figure (a). Since, by varying the pitch angle the energy moves from the tonal to the broadband noise component. These features should be of great interest to designers because in fact it seems possible to obtain the same thrust with different values of and to define, depending on the application, which noise component to favour. Moreover, as already mentioned the tonal noise is related to the loading distribution over the blade surface since it is possible to assume that configuration 3 configuration 3 has a smaller recirculation region than configuration 1 because stall has not yet occurred.

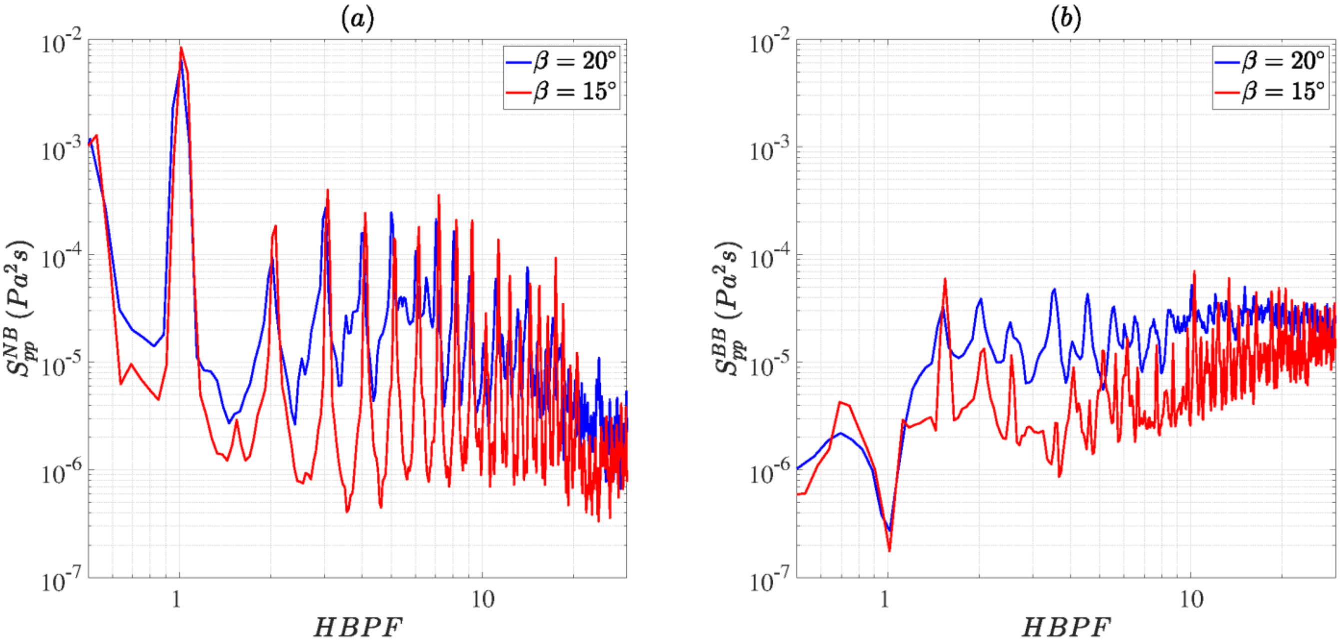


*Figure 13: Noise spectra computed for the narrow band (a) and broadband (b) component for the two pitch angles ( $\Theta = 15$ and 20 deg) and rotational speed $\Omega = 4740$ and 6540 at iso-thrust.*

## 5. Conclusions

The aeroacoustic behavior of a rotor by varying the pitch angle has been investigated through an experimental analysis carried out using microphones and balance measurements. The optimization strategy herein proposed appears interesting in order to reduce the number of variables in a multi-disciplinary problem as rotor optimization; in particular the independency of the acoustic performance coefficient to rotational regime seems useful for this kind of optimization. The classical analysis of the rotor noise computing the SPL leads to the same conclusion of the optimization approach proposed, confirming the validity of the strategy.

To achieve a further quantification of the propeller aerodynamic and aeroacoustic properties two novel non dimensional parameter have been defined which gives us the acoustic and aeroacoustic efficiency excluding rotational speed dependency. This makes it possible to characterize the acoustics of a propeller on the basis of its geometry and not on the basis of its operating conditions.

The wall pressure measurements show that the pressure signature is dominated by the broad band component probably generated by separation bubble, showing that the more commonly study of the tonal rotor noise, in the case of small rotor in hovering must be extend to the more relevant broad band. Furthermore, the noise spectrum exhibits two slopes, typical of the wall pressure fluctuation in turbulent boundary layer. This last information suggest a passive noise control strategy based on the boundary layer transition forcing.

In addition, the noise spectra show that increasing the pitch angle the energy moves from the tonal to the broad band noise component suggesting a particular attention in the design process. Since, it seems possible to favour one noise component over another.

Finally, a collective pitch it is demonstrate as an interesting mechanic component for rotor noise reducing.

## 6. References


Berkooz, G., Holmes, P., & Lumley, J. L. (1993). *The proper orthogonal, decomposition in the analysis of turbulent flows*. *1971*. https://doi.org/10.1146/annurev.fluid.25.1.539

Candeloro, P., Nargi, R. E., Patanè, F., & Pagliaroli, T. (2020). Experimental Analysis of Small-Scale Rotors with Serrated Trailing Edge for Quiet Drone Propulsion Experimental Analysis of Small-Scale Rotors with Serrated Trailing Edge for Quiet Drone Propulsion. *J. Phys.* https://doi.org/10.1088/1742-6596/1589/1/012007

Farassat, F. (1986). Prediction of advanced propeller noise in the time domain. In *AIAA Journal* (Vol. 24, Issue 4, pp. 578–584). https://doi.org/10.2514/3.9310

Farassat, F., & Succi, G. P. (1980). A review of propeller discrete frequency noise prediction technology with emphasis on two current methods for time domain calculations. *Topics in Catalysis*. https://doi.org/10.1016/0022-460X(80)90422-8

Ffowcs Williams, J. E., and Hawkings, D. L. (1969). SOUND GENERATION BY TURBULENCE AND SURFACES IN ARBITRARY MOTION BY J . E . FFOWCS WILLIAMS AND D . L . HAWKINGSt. *Philosophical Transactions of the Royal Society of London. Serie A, Mathematical and Physical Sciences*, *264*(1151), 321–342. https://doi.org/10.1098/rsta.1969.0031

Gur, O., & Rosen, A. (2009a). *Design of a Quiet Propeller for an Electric Mini* (Vol. 25, Issue 3, pp. 717–728). https://doi.org/10.2514/1.38814

Gur, O., & Rosen, A. (2009b). Optimizing Electric Propulsion Systems for Unmanned Aerial Vehicles. *Journal of Aircraft*, *46*(4), 1340–1353. https://doi.org/10.2514/1.41027

Intravartolo, N., Sorrells, T., Ashkharian, N., & Kim, R. (2017). Attenuation of Vortex Noise Generated by UAV Propellers at Low Reynolds Numbers. *55th AIAA Aerospace Sciences Meeting*. https://doi.org/10.2514/6.2017-2019

Janakiram, D., & Scruggs, B. (1981). Investigation of performance, noise and detectability characteristics of small-scale remotely piloted vehicle /RPV/ propellers. *7th Aeroacoustics Conference*, *19*(12), 1052–1060. https://doi.org/doi:10.2514/6.1981-2005

Kirby, M., Boris, J. P., & Sirovich, L. (1990). A proper orthogonal decomposition of a simulated supersonic shear layer. *International Journal for Numerical Methods in Fluids*, *10*(4), 411–428. https://doi.org/10.1002/fld.1650100405

*Leishman - 2008 - principles of helicopter aerodynamics.pdf*. (n.d.). https://doi.org/10.1016/S0743-0167(03)00045-7

Leslie, A., Wong, C., & Auld, D. (2010). *Experimental analysis of the radiated noise from a small propeller*.

Leslie, A., Wong, K. C., & Auld, D. (2008). Broadband Noise Reduction on a mini-UAV Propeller. *14th AIAA/CEAS Aeroacoustics Conference (29th AIAA Aeroacoustics Conference)*. https://doi.org/10.2514/6.2008-3069

Lv, P., Prothin, S., Zawawi, F. M., Bénard, E., Lv, P., Prothin, S., Zawawi, F. M., Bénard, E., & Morlier, J. (2018). *Study of A Flexible Blade for Optimized Proprotor To cite this version : HAL Id : hal-01851611*.

Marino, L. (2010). *Experimental analysis of UAV-propellers noise*. *D*, 1–14.

Meyer, K. E., Pedersen, J. M., & ̈Ozcan, O. (2007). A turbulent jet in crossflow analysed with proper orthogonal decomposition. *Journal of Fluid Mechanics*, *583*(2007), 199–227. https://doi.org/10.1017/S0022112007006143

Migliore, P., & Oerlemans, S. (2004). *Aiaa 2004-1186*. *January*, 1–15.

Miller, C. J., & Sullivan, J. P. (1985). *Noise constraints Effectinf Optimal Propeller Design*.

Pagliaroli, T., Camussi, R., Candeloro, P., Giannini, O., Bella, G., & Panciroli, R. (2018). Aeroacoustic Study of small scale Rotors for mini Drone Propulsion: Serrated Trailing Edge Effect. *2018 AIAA/CEAS Aeroacoustics Conference*. https://doi.org/10.2514/6.2018-3449

Paolo, C., Tiziano, P., & Ragni, D. (n.d.). *Aeroacoustics of small scale rotors for drone propulsion : a review of noise sources and control strategies*.

Rozenberg, Y., Roger, M., & Moreau, S. (2010). Rotating Blade Trailing-Edge Noise: Experimental Validation of Analytical Model. *AIAA Journal*. https://doi.org/10.2514/1.43840

Shkarayev, S., Moschetta, J. M., & Bataille, B. (2008). Aerodynamic design of micro air vehicles for vertical flight. *Journal of Aircraft*, *45*(5), 1715–1724. https://doi.org/10.2514/1.35573

Sinibaldi, G., & Marino, L. (2013). Experimental analysis on the noise of propellers for small UAV. *Applied Acoustics*. https://doi.org/10.1016/j.apacoust.2012.06.011

Sirovich, L. (1987). Turbulence and the dynamics of coherent structures. III. Dynamics and scaling. *Quarterly of Applied Mathematics*, *45*(3), 583–590. https://doi.org/10.1090/qam/910464

Succi, G. P. (1979). *Succi_1979.pdf* (p. 14). https://doi.org/10.4271/790584

Zawodny, N. S., & Boyd Jr, D. D. (2017). Investigation of rotor-airframe interaction noise associated with small-scale rotary-wing unmanned aircraft systems. *AHS Paper 20180001470*.

INCEEUROPE

CidB
Centre d'information
sur le Bruit

QUIET DRONES
Second International e-Symposium
on
UAV/UAS Noise
27th to 30th June 2022

# A numerical study of the aeroacoustics of shrouded propellers for urban air mobility vehicles

**Sinforiano Cantos[1], Hanbo Jiang[1,*], Siyang Zhong[1,$], Xin Zhang[1,2]**
**[1] Department of Mechanical and Aerospace Engineering, The Hong Kong University of Science and Technology, Clear Water Bay, Kowloon, Hong Kong SAR, China.**
**[2] HKUST-Shenzhen Research Institute, Hi-Tech Park, Nanshan, Shenzhen, 518057, China.**

## Summary

The aerodynamic performance and noise generation of ducted propellers were studied with numerical simulations for different incoming flow conditions. Steady simulations were performed to efficiently evaluate the aerodynamic performance of the ducted propeller over wide operating conditions. For noise performance, delayed detached eddy simulations were performed for the near-field turbulent flow fields. The far-field directivities were calculated from integral solutions of the Ffowcs-Williams and Hawkings equation. The present results reveal that, in addition to the propeller, the duct can also generate thrust. When the axial flow speed increases, the thrust generated by the duct decreases rapidly. The spectra and directivity of the aerodynamic noise are compared, showing that the contribution from the shroud is mainly for broadband noise, which is reduced with the flow speed.

## 1. Introduction

The interest in urban air mobility (UAM) has increased rapidly over the last few years. Potential applications of UAM vehicles include inspection operations for agriculture and farming, transport of parcels and passengers. Air taxis such as electrical vertical take-off and landing aircraft show great potential as future fast and convenient means of transportation. As UAM vehicles typically operate in an urban environment, their noise emissions should be controlled to reduce their impact on residents. Therefore, studying the noise radiated from the propulsive propellers is essential as they are the main source of noise [1].

* Hanbo Jiang: jianghanbo@ust.hk
$ Siyang Zhong: zhongsy@ust.hk

Adding a short duct (or shroud) to a propeller can potentially increase the aerodynamic performance of the propeller, providing more thrust for a given power due to the suction on the inlet lip of the duct and increased static pressure in the diffuser outlet [2]. Increasing the duct's expansion ratio may further improve the aerodynamic performance if the flow does not separate in the inner wall of the shroud [3]. Furthermore, using a duct also increases the safety of operation of UAM vehicles in case of blade detachment.

The acoustic characteristics of the propeller are also expected to change when adding a duct [4]. Malgoezar *et al*. [5] experimentally studied the noise generated by a ducted propeller, identifying new noise sources at the leading edge of the duct. They attributed the increment of noise to the interaction of the rotor tip vortices with the duct walls as well as resonance. Ventura Diaz *et al*. [6] performed numerical simulations to study the influence of adding the duct to the propeller. The authors mainly focused on aerodynamics, showing improved performance when a shroud with small tip clearance was used. They also qualitatively observed the alteration of the noise emission for ducted coaxial rotors. Zhang and Barakos [7] also studied the aerodynamic and aeroacoustic performance of a ducted propeller numerically, optimizing the shape of the propeller. They concluded that adding the duct can reduce the noise radiated to the far-field due to duct shielding. Moreover, the acoustic performance of ducted propellers can be further improved using noise attenuating treatments applied on the duct surface. Guo *et al*. [8] used a simple duct to explore the applicability of sound absorbers to a ducted propeller with experimental means, showing that significant noise reduction can be achieved using a lined duct instead of a rigid one.

While previous studies mainly focused on hover flight, drones and UAM vehicles may fly in other phases, such as climb and descent. Yilmaz *et al*. [9] studied the aerodynamics of a ducted propeller with axial flow experimentally, showing reduced thrust for increasing flow velocity. However, the aeroacoustic performance of a ducted propeller in the presence of incoming flow has not been considered.

This present study aims at studying the effect of an incoming flow on a ducted propeller in climbing conditions using computational fluid dynamics (CFD) and computational aeroacoustics (CAA) methods. The CAA approach allows a detailed investigation of the propeller's flow features and acoustic properties. The variations of aerodynamic performance are investigated by solving Reynolds-averaged Navier-Stokes (RANS) equations using CFD. Delayed detached eddy simulations (DDES) are also conducted to resolve the transient flow field. The far-field acoustic pressure predictions for different flow speeds were obtained by solving the Ffowcs-Williams and Hawkings (FW-H) equation [10].

## 2. Problem statement

The propeller used in this work has a radius of 0.115 m with two truncated blades. The blade is designed with a larger chord at the tip, allowing the use of a duct with a higher expansion ratio as it can reduce flow separation inside the duct due to the injection of more momentum in the boundary layer [3]. Figure 1(a) shows the observer angle definition $\theta$ and the propeller coordinates, $r$ in the radial direction and $z$ in the streamwise direction, with the origin in the center of rotation. The chord and pitch angle distribution of the blade can be seen in Figure 1(b). Figure 1(a) also shows the geometric parameters defining the duct, including diffuser radius ($R_D$), diffuser length ($L_D$), diffuser angle ($\theta_D$), tip clearance ($TC$), rotor placement ($P_R$) and diffuser distance ($D_D$). The geometry of the lip used in this work, controlled using B-Splines [11], is chosen to ensure the quality of the flow incoming to the propeller. The duct has an expansion ratio of 1.15 and a tip clearance of 0.5% of the rotor radius. A detailed sketch of the propeller and duct profile is depicted in Figure 1(a).

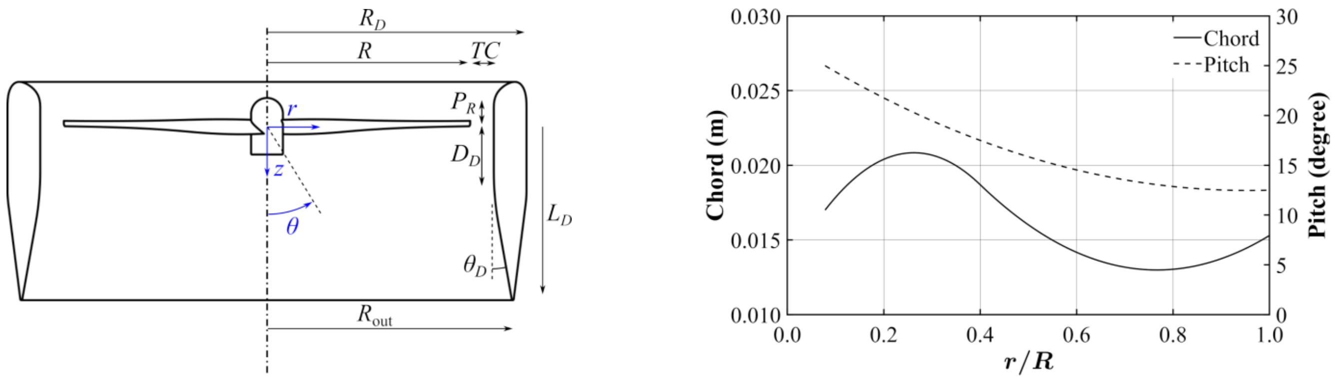


(a) (b)

Figure 1. (a) Coordinates and geometric parameters of the ducted propeller, including the blade and duct used in this study. (b) Chord and pitch angle distribution of the blade.

This study focuses on the influence of different incoming flow speeds on the propeller, accounting for the climb stage of UAM vehicles. The rotational speed of the propeller is $N = 90$ revolutions per second. The incoming flow speed is nondimensionalized considering the propeller advance ratio $J = U_\infty/(N\ D)$, where $U_\infty$ is the axial flow speed, and $D$ is the rotor diameter. The maximum considered flow speed is 12 m/s ($J = 0.58$).

## 3. Numerical method

The computational domain of the simulations is a cylindrical volume aligned with the propeller's rotation axis. The domain has a radius of $70R$, extending upstream and downstream of the rotor plane by a distance of $70R$. The domain is divided into two different regions to model the propeller's rotating motion. Figure 2(a) shows a rotating zone containing the ducted propeller and a stationary region for the rest of the domain. Both zones are connected using arbitrary mesh interfaces [12].

The numerical grid used in this study is shown in Figure 2(b). It contains hexahedral cells and is generated using an unstructured approach to capture the complex geometry of the propeller. The mesh is gradually refined towards the surface of the rotor and the duct, with additional grid refinement in the wake of the propeller for a better resolution in the region. The mesh for all the simulations has 28.7 million cells.

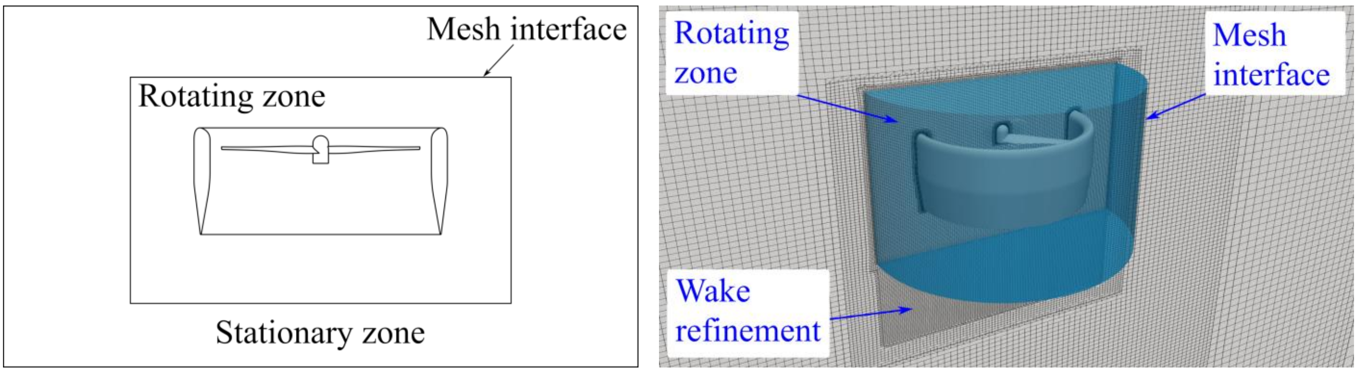


(a) (b)

Figure 2. (a) Computational domain for shrouded propeller simulations. (b) Slice of the numerical grid at a cross section.

The aerodynamic performance of the shrouded propeller is studied using steady RANS calculations, which solve the incompressible Navier-Stokes equations. The turbulence is modeled with the Spalart-Allmaras turbulence model [13]. The rotor's motion is considered using the multiple reference frames approach. This method introduces additional sources in the momentum equation to account for Coriolis and centrifugal forces [14]. Each case is calculated for 4000 iterations until convergence. The thrust evolution of the propeller and duct in hover conditions is shown in Figure 3.

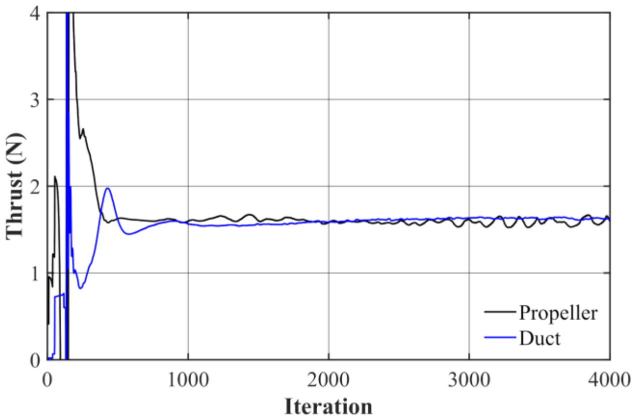


Figure 3. Propeller and duct thrust evolution for the steady simulation of the ducted propeller in hover conditions.

A hybrid CAA method is employed to predict the noise radiated from the propeller. DDES simulations [15,16] are performed to obtain the near-body turbulent flow. A transient solver using an acoustic-wave preserved artificial compressibility (APAC) method is employed, which was previously used for propeller noise computation [17]. This method can efficiently capture acoustic waves in low-Mach-number turbulent flows. In this case, the rotating motion is considered using a dynamic mesh. The noise radiated to the far field is predicted using the integral solution of the FW-H equation on the surface of the ducted propeller. The power spectral density in the frequency space is calculated using Welch's method [18], allowing the computation of the far-field sound pressure level (SPL) at observer angles $\theta \in [0°, 180°]$, with a distance of 1.5 m from the center of rotation. Each case is calculated for a total of 36 rotor revolutions.

## 4. Results and discussion

For an isolated propeller, when the flow speed is increased, the thrust decreases due to the lower angle of attack of the blades, as the pitch of the blades is not varied. The shrouded propeller can provide a higher thrust in hover conditions ($J = 0$). However, the thrust decreases at a higher rate than for the isolated propeller when the flow speed increases, as shown in Figure 4. It is observed that the thrust generated by the propeller decreases at a similar rate for both the isolated and the ducted propellers. However, the thrust provided by the duct decreases at a higher rate.

The reduction in thrust for the ducted propeller is due to the decreased suction on the duct lip, which leads to over-pressure for even larger incoming flow speeds. The pressure changes along the streamwise coordinate of the duct can be seen in Figure 5, where $l$ is the total length of the duct, $p$ denotes the static pressure, and $\rho$ is the density.

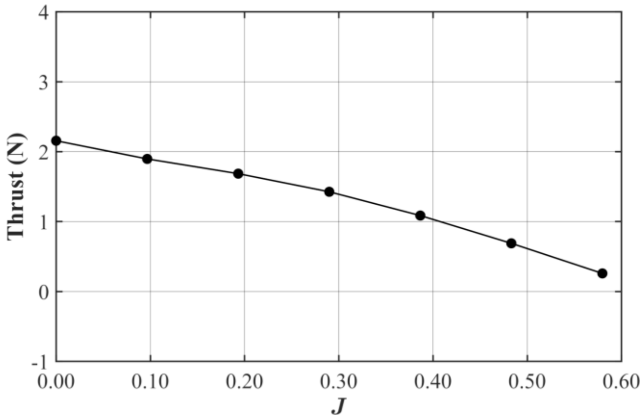

(a)

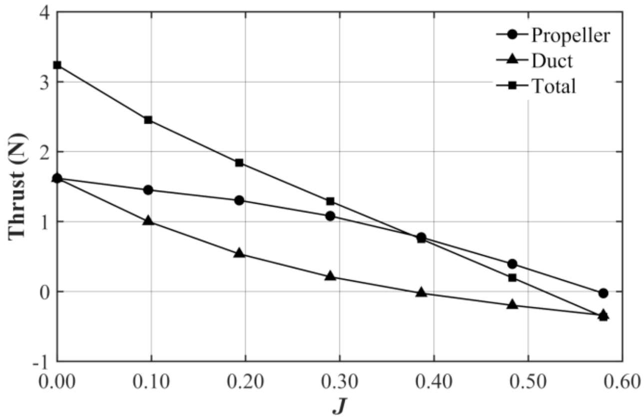

(b)

Figure 4. Influence of the incoming flow speed on the thrust of (a) the isolated propeller and (b) the ducted propeller.

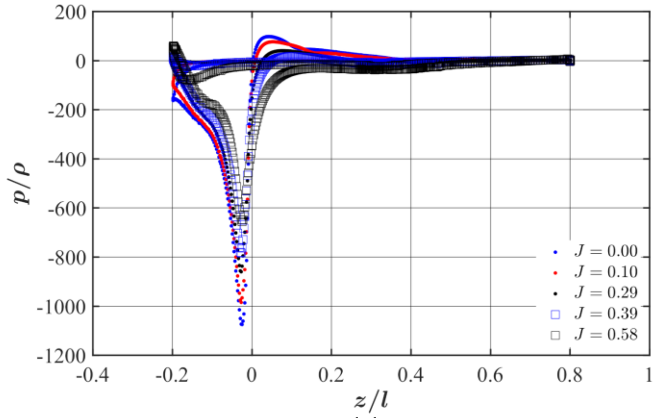

(a)

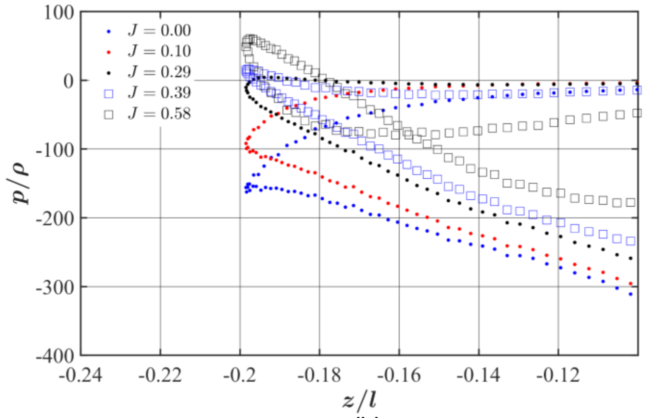

(b)

Figure 5. (a) Pressure distribution on the shroud for different flow speeds. (b) Detail of the pressure distribution on the lip of the duct.

The phase-averaged streamwise velocity distribution is obtained using DDES simulations and shown in Figure 6(a) for the hovering case. There are small regions where the flow separates downstream of the rotor on the inner wall of the duct, with a larger separated region in the diffuser region. The vorticity field is shown in Figure 6(b), with the most prominent vorticity generation in the blade tip, the lip of the duct and the hub of the rotor. Figure 7(a) shows the phase-averaged streamwise velocity distribution for a case with incoming flow ($J = 0.29$), where it can be observed the presence of vortex shedding flow structures from the duct when the incoming flow speed is high. This phenomenon is also seen in the vorticity distribution in Figure 7(b).

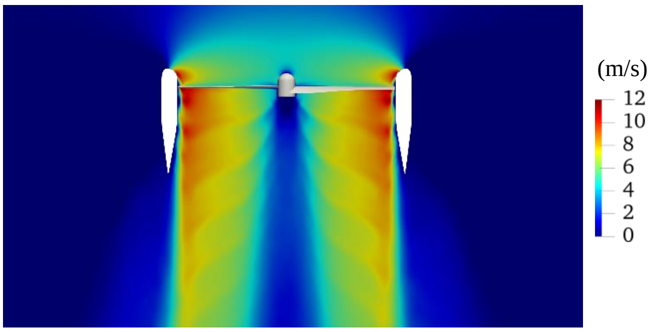

(a)

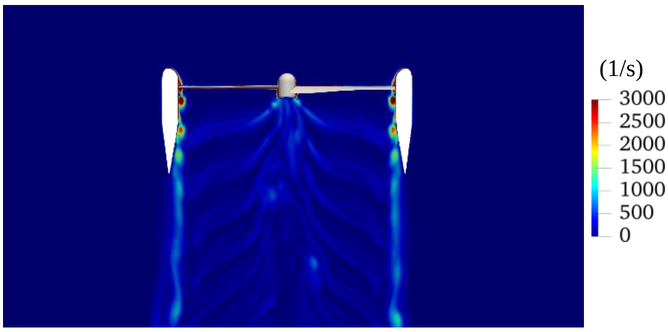

(b)

Figure 6. (a) Phase-averaged streamwise velocity and (b) vorticity magnitude in hover condition.

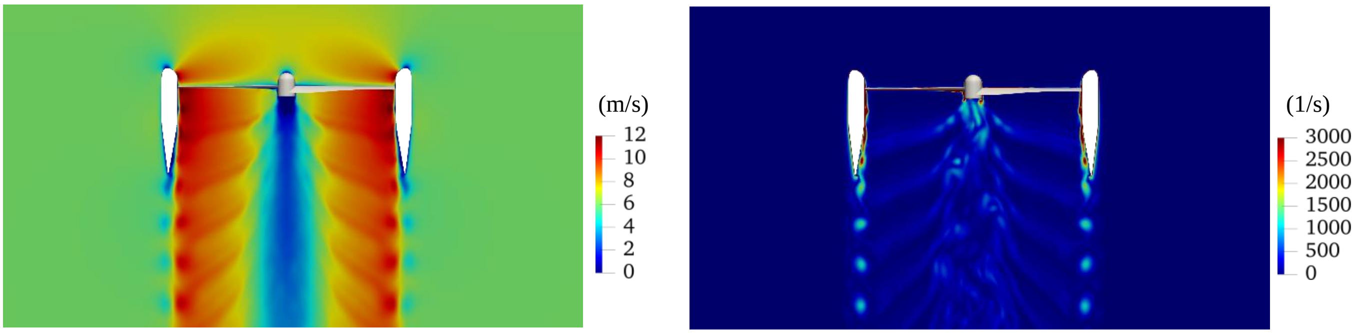


(a) (b)

Figure 7. (a) Phase-averaged streamwise velocity and (b) vorticity magnitude for $J = 0.29$.

The far-field sound pressure level of the ducted propeller is predicted using a sampling frequency of 10 kHz, considering frequencies under 5 kHz. The blade-passing frequency (BPF) of the propeller is 180 Hz. The noise spectrum at different observer angles is presented in Figure 8, showing that the tonal noise at the BPF is slightly reduced as the flow speed is higher, while the shroud contributes to broadband noise, which is also reduced for increasing velocity. The directivity results at the BPF are shown in Figure 9(a), with a reducing noise level for higher speeds and the maximum noise generation close to the rotor plane. The overall sound pressure level (OASPL) considering frequencies larger than 50 Hz is shown in Figure 9(b), with noise reduction for most observer angles as the flow speed increases. The dependence of the OASPL and the total thrust when the flow speed is changed is shown in Figure 10 for different observer angles.

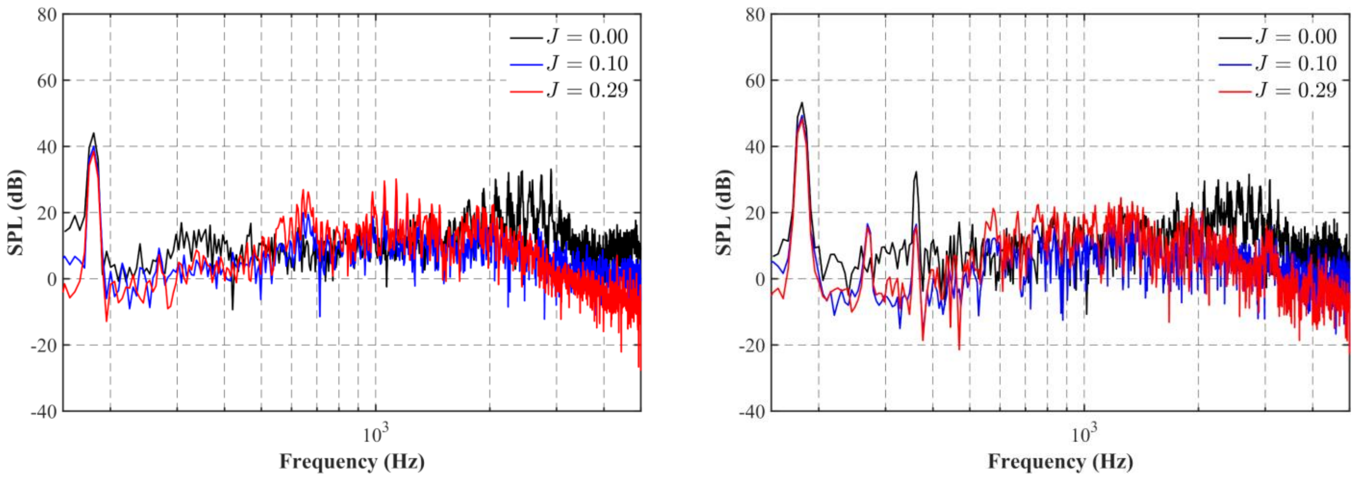


(a) (b)

Figure 8. Far-field SPL spectrum comparison for different incoming flow speeds at observer angles: (a) $\theta = 30°$ and (b) $\theta = 90°$.

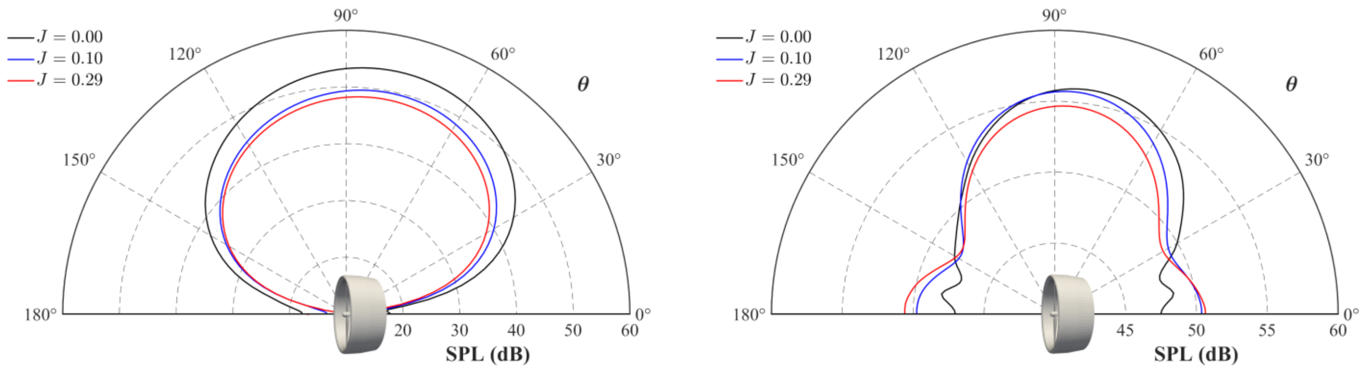


(a) (b)

Figure 9. Directivity results for a ducted propeller with different incoming flow speeds. (a) BPF. (b) OASPL.

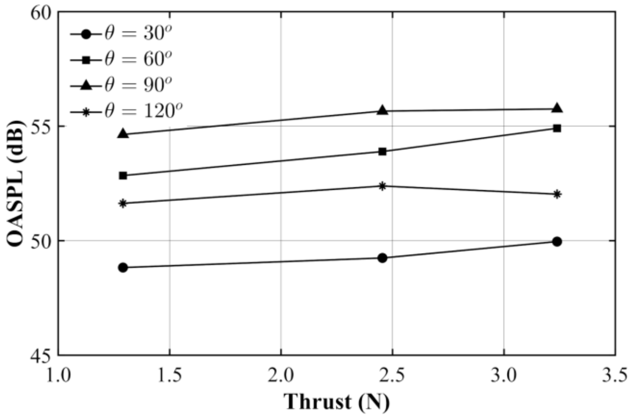


Figure 10. Dependence of OASPL and total thrust for different observer angles when the flow speed is changed.

## 5. Conclusions

The propeller is the main noise contributor for small drones, as well as for larger UAM vehicles. Adding a duct to the propeller modifies its aerodynamic and aeroacoustic characteristics while enhancing operational safety. In this work, we studied the effect of different incoming flow speeds during the climb stage of the vehicle. For higher flow speeds, the thrust provided by the ducted propeller decreases, and it happens at a higher rate than an isolated propeller due to the reduced suction on the lip of the duct, which agrees with the literature [9]. It is found that the noise radiated from the ducted propeller decreases as the flow speed is higher. The current results also suggest that ducted propellers are promising to reduce noise further, while the design of the propeller could be modified for better performance under different flow conditions.

## 6. Acknowledgements

Sinforiano Cantos is supported by the Hong Kong PhD Fellowship Scheme (No. PF19-35038). This work has been partially supported by the National Science Foundation of China (11972029). This study was performed at the Aerodynamics Acoustics & Noise control Technology Centre (aantc.ust.hk).

### References

[1] Rizzi, S., Huff, D., Jr, D., Bent, P., Henderson, B., Pascioni, K., Sargent, D., Josephson, D., Marsan, M., He, H., and Snider, R, “Urban Air Mobility noise: current practice, gaps, and recommendations,” NASA Technical Paper TP-20205007433, 2020.
[2] Pereira, J. L., “Hover and wind-tunnel testing of shrouded rotors for improved micro air vehicle design,” PhD thesis, The University of Maryland, 2008.
[3] Qing, J., Hu, Y., Wang, Y., Liu, Z., Fu, X., and Liu, W, “Kriging assisted integrated rotor-duct optimization for ducted fan in hover,” AIAA Paper 2019-0007, 2019.
[4] Zhang, T., and Barakos, G. N., “Review on ducted fans for compound rotorcraft,” The Aeronautical Journal, Vol. 124, No. 1277, pp. 941-974, 2020.
[5] Malgoezar, A. M., Vieira, A., Snellen, M., Simons, D. G., and Veldhuis, L. L., “Experimental characterization of noise radiation from a ducted propeller of an unmanned aerial vehicle,” International Journal of Aeroacoustics, Vol. 18, Nos. 4-5, pp. 372-391, 2019.
[6] Ventura Diaz, P., Caracuel Rubio, R., and Yoon, S, “Simulations of ducted and coaxial rotors for air taxi operations,” AIAA Paper 2019-2825, 2019.
[7] Zhang, T., and Barakos, G. N., “High-fidelity numerical analysis and optimisation of ducted propeller aerodynamics and acoustics,” Aerospace Science and Technology, Vol. 113, 106708, 2021.

[8] Guo, J., Zhou, T., Fang, Y., and Zhang, X., “Experimental study on a compact lined circular duct for small-scale propeller noise reduction,” Applied Acoustics, Vol. 179, 108062, 2021.
[9] Yilmaz, S., Erdem, D., and Kavsaoglu, M. S., “Performance of a ducted propeller designed for UAV applications at zero angle of attack flight: An experimental study,” Aerospace Science and Technology, Vol. 45, pp. 376-386, 2015.
[10] Ffowcs Williams, J. E., and Hawkings, D. L., “Sound generation by turbulence and surfaces in arbitrary motion,” Philosophical Transactions of the Royal Society of London. Series A, Mathematical and Physical Sciences, Vol. 264, No. 1151, pp. 321-342, 1969.
[11] Schaller, D. F., “A technique for shape optimization of ducted fans,” Master of Science thesis, Iowa State University, 2007.
[12] Chandar, D. D., and Gopalan, H., “Comparative analysis of the arbitrary mesh interface (AMI) and overset methods for dynamic body motions in OpenFOAM,” AIAA Paper 2016-3324, 2016.
[13] Spalart, P.R., and Allmaras, S.R., “One-equation turbulence model for aerodynamic flows,” AIAA Paper 1992-439, 1992.
[14] Bento, H. F., de Vries, R., and Veldhuis, L. L., “Aerodynamic performance and interaction effects of circular and square ducted propellers,” AIAA Paper 2020-1029, 2020.
[15] Spalart, P.R., Jou, W.H., Strelets, M., and Allmaras, S.R., “Comments on the feasibility of LES for wings, and on a hybrid RANS/LES approach,” First AFOSR international conference on DNS/LES, 1997.
[16] Spalart, P.R., Deck, S., Shur, M. L., Squires, K. D., Strelets, M. Kh., and Travin, A., “A new version of detached-eddy simulation, resistant to ambiguous grid densities,” Theoretical and Computational Fluid Dynamics, Vol. 20, 181, 2006.
[17] Jiang, H., and Zhang, X., “An acoustic-wave preserved artificial compressibility method for low-Mach-number aeroacoustic simulations,” Journal of Sound and Vibration, Vol. 516, 116505, 2022.
[18] Welch, P., “The use of fast Fourier transform for the estimation of power spectra: A method based on time averaging over short, modified periodograms,” IEEE Transactions on Audio and Electroacoustics, Vol. 15, No. 2, pp. 70-73, 1967.

QUIET DRONES
Second International e-Symposium
on
UAV/UAS Noise
27th to 30th June 2022

# Estimating Unmanned Aircraft Takeoff Noise Using Hover Measurement Data

**Chris Cutler-Wood, US DOT Volpe Center: Chris.Cutler-Wood@dot.gov**
**Michael Barzach, US DOT Volpe Center: Michael.Barzach@dot.gov**
**Dr. Robert Downs, US DOT Volpe Center: Robert.Downs@dot.gov**
**Chris Hobbs, US FAA: Christopher.M.Hobbs@faa.gov**
**Susumu Shirayama, US FAA: Susumu.Shirayama@faa.gov**

## Summary

The Volpe Center, in support of FAA, has collected acoustic data from multiple unmanned aircraft over the last few years in a series of measurement campaigns. With this expanding dataset, it is now possible to estimate the noise produced by various types of flight operations and test the validity of those methods. Of particular interest in the context of environmental analyses is the noise produced during takeoff operations. This paper describes the process of using hover noise measurement data including directivity patterns to estimate the noise generated during takeoff procedures for an unmanned aircraft and presents a comparative analysis of the results and actual measurements.

## 1. UA Noise Measurement Campaigns

The FAA Office of Environment and Energy (AEE-100) sponsored two full-scale noise measurement campaigns with the Volpe Center's Environmental Measurement & Modelling Division (V-324) in 2021 to capture time-synchronized acoustics, tracking, and weather data to characterize noise emissions for various unmanned aircraft (UA). The first of the two campaigns took place in July 2021 at Causey Aviation Services (Causey), a small municipal airport near Liberty, NC. This location was chosen both for its relative remoteness (and the associated low ambient noise levels), and because it already served as a testing location for one of the UA operators whose platform was to be measured. The second measurement campaign was held at the Aviation Weather Research Facility (AWRF) on Joint Base Cape Cod (JBCC) in September 2021. This facility is a parcel of land operated by the Volpe Center and contains a large, grassy, runway-like area normally used for testing and validation of meteorological sensing and measurement equipment. Both campaigns used the same basic microphone array configuration pictured in Figure 1.

The microphone array comprised three distinct arrays: a linear array normal to the flight tracks of level overflights of the aircraft; a 50 ft. radius circular array whose center is below the aircraft hover position; and an elevated array consisting of 5 microphones up to 100 ft. above the ground to capture noise emitted from the plane of the rotors during both types of operations.

Microphones on the ground were inverted above ground boards. Microphones suspended from the crane were oriented vertically. All microphones used were pressure-field type and covered with windscreens. It should be noted that while the array configurations used at Causey and JBCC were the same, the orientation of East and West was flipped (the elevated and hover array mics were on the West side). For this paper, the Causey microphone positions will be referred to with the JBCC nomenclature; thus, the furthest mic position from the hovering UA was F45E at Causey, but it will be referred to as the F45W position in relation to Figure 1.

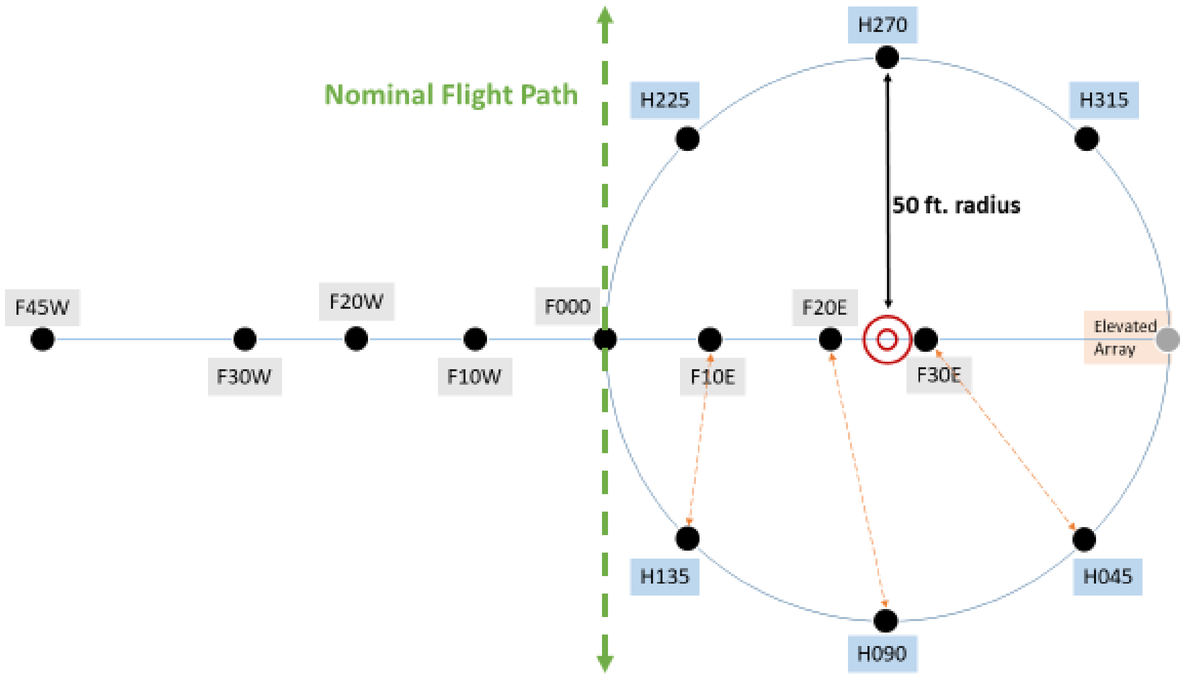

*Figure 1. Microphone array configuration*

## 1.1 Aircraft

This paper presents acoustic results for a pair of similar, six-rotor “hexcopters” measured during the two campaigns. The DJI M600 is a six rotor UA flown at JBCC and is similar to the Flytrex FTX-M600P flown at Causey. The following figures show these UA during their respective measurement campaigns and note their maximum takeoff weight. Aircraft were outfitted with a Volpe-designed differential GPS tracking device (“START” system) synchronized to the acoustic recording data. Flight log data were collected for each UA, including vehicle state, engine parameters, and orientation.

Figure 2. DJI M600 UA pictured at JBCC has a maximum takeoff weight of 33.3 pounds.


Figure 3. The Flytrex FTX-M600P flown at Causey has a maximum takeoff weight of 33.4 pounds.

## 1.2 Flight Test Points

During both measurement campaigns, the UA noise emissions were recorded when they were hovering at 50 ft. above the center of the circular array. The UA also performed vertical takeoffs starting near the center of the hover array. Local meteorological data were recorded from nearby weather stations to verify that the wind speed did not exceed 10 knots during measurement events. For the Causey measurement campaign, data were collected for all microphones during the test points. For the JBCC measurement campaign, all hover-, elevated-, and lateral-ground array microphones collected data, except for F10E, F20E, and F30E which were moved to positions on the circular array for the hover test points. Data for the DJI M600 and Flytrex M600P were collected at maximum takeoff weight performing these maneuvers, including a total of 6 events for each test point. All test points were not used in the analysis due to aircraft condition instability and/or position anomalies during the measured events. Table 1 shows a summary of the test points used for this analysis. The takeoff test points at Causey are not used here due to a pause during climb made by the Flytrex M600P as part of its programming. The takeoffs at JBCC were at constant speed for the length of the climb, though data from two takeoffs to an altitude of 100 ft. above the ground were trimmed to be the same height as the others to increase the number of test points used in the 50 ft. climb comparison. Recordings were made of the ambient noise levels throughout the days of testing. Ambient recordings were used to define the signal to noise ratio of the spectral time histories for each microphone recording. There was little to no evidence of noise levels above the ambient emitted from the UA below the 100 Hz one-third octave band. Accordingly, the spectra analysed in this paper comprise the 100 Hz through 10 kHz one-third octave bands. The 10 kHz one-third octave band is the upper frequency limit in the Advanced Acoustic Model (AAM), which is described in Section 2.

*Table 1. Test Points used for Analysis*

| Test Point | Measurement Location | Aircraft & Configuration | Used For: |
|---|---|---|---|
| **Hover** | Causey | Flytrex M600P, Max Weight | FTRX Directional & Omnidirectional Spheres |
| **Ambient** | Causey | NA | Ambient for Causey |
| **Takeoff** | JBCC | DJI M600, Max Weight | Measured takeoff compared to Directional and Omnidirectional Spheres |
| **Hover** | JBCC | DJI M600, Max Weight | M600M Omnidirectional Sphere |
| **Ambient** | JBCC | NA | Ambient for JBCC |

## 2. Noise Hemisphere Creation

The AAM is used here to estimate sound levels from vehicles performing typical operations whose noise emissions have been characterized in the form of noise sphere files (Page, 2012). Noise sphere files represent the noise emissions from a vehicle in a particular orientation and for a operating state. Spherical coordinates are used to define the vehicle orientation. One-third octave band spectral noise levels were used for this analysis. The noise sphere spectra represent the free field emissions in each direction, starting at a fixed radius of 100 ft with no atmospheric absorption. This allows the noise sphere files to be used to model different meteorological conditions.

### 2.1 Omnidirectional Sphere Creation

Hover test point data were nominally collected for 30 seconds during which the UA was in a stable flight condition. Data were analysed to create one-third octave band time histories. Spectral time history and synchronized tracking data were reviewed to confirm the stability of the aircraft position and identify any potential intrusive or contaminating noise.

The $L_{eq}$ for each one-third octave band was calculated from the spectral time history for each microphone. The actual distance between the UA and microphone was used to normalize the distance of each $L_{eq}$ spectrum to the same distance using spherical spreading. An average spectrum was calculated from the normalized spectra for each UA event hovering at 50 ft to produce an average one-third octave band spectrum from each of the 6 recordings of the UA.

Any average spectrum identified as an outlier was removed from further processing. The remaining spectral averages were averaged together using simple arithmetic mean to produce a spectrum representing the UA hovering at 50 ft.

The average spectrum was used to create an omnidirectional noise sphere for use in the AAM. To make the noise sphere from the average spectrum of the UA hovering at 50 ft., the atmospheric absorption had to be removed using the normalized distance and average meteorological data. The levels were then corrected for the difference between the normalized distances of the spectra to the radius of the sphere (100 ft.) using spherical spreading. Finally, 6 dB was subtracted dB from each one-third octave band level in the average spectrum to account for ground effect.

## 2.2 Directional Hover Sphere Creation

In order to estimate any directionality of the noise emissions from the hovering UA, another approach to sphere making was undertaken. By considering the noise emissions from hovering UA to be axisymmetric, the spectrum recorded at each ground mic can be used to represent the noise emissions from any point about the vehicle at the same angle from the vehicle's vertical axis. In terms of noise spheres, this is equivalent to replicating the same spectrum at all longitudes for the same latitude on a sphere whose axis is vertical. Because the noise spheres used by AAM have their axis horizontally oriented, a coordinate transformation had to be performed before creating the sphere. While noise levels at frequencies corresponding to the blade passage frequencies are not necessarily constant due to destructive and constructive interference of the frequencies emitted from each of the motors, one-third octave band spectra and analysis that relies on the average sound level should reduce the influence of those interference effects.

Because the spectra from each microphone have been corrected for the effects of propagation to a distance of the sphere radius and the atmospheric absorption was added back into the recorded levels, they can be considered as depropagated noise levels. Furthermore, the noise sphere format for AAM requires noise levels on a fixed grid of points at even intervals in (Phi, Theta) coordinates, as shown in Figure 4. In order to create a regular grid of noise levels from the data from the ground microphone positions, the grid data were estimated using a Laplacian interpolation in the Acoustic Repropagation Technique (ART) program (Page, 2004). The interpolation procedure uses nearest-neighbor data points on the sphere's surface to estimate the levels for each grid point. This results in estimated levels at grid points on the sphere representative of higher elevation angles than the furthest away microphones.

Consider the contours of the 1 kHz one-third octave band levels on the directional sphere created from ground microphone recordings during the Flytrex M600P hovering at 50 ft. in Figure 4. The noise received at each microphone will have been emitted from a direction represented by a point on the sphere. Assuming symmetry about the vertical axis of the UA for noise emissions, the depropagated noise received at a microphone can be assigned to a ring of coordinates with the same angle relative to the UA's vertical axis. Depropagated spectra from all ground microphone recordings will be used in the ART program to find the spectra on a regular grid. Note the black lines in the Figure 4 show the rings on the sphere (one for each microphone position). The abundance of rings crossing 0 degree phi and 45 and 135 degree theta angles represent the hover mics all being near the same position relative to the vehicle during the hover recordings. The directionality of the 1 kHz one-third octave band noise emissions is evident in the decrease in level from underneath the UA (0° Phi, 90° Theta) towards the plane of the rotor (90° Phi). It is understood that broadband noise from rotors should follow this pattern (George, 1984).

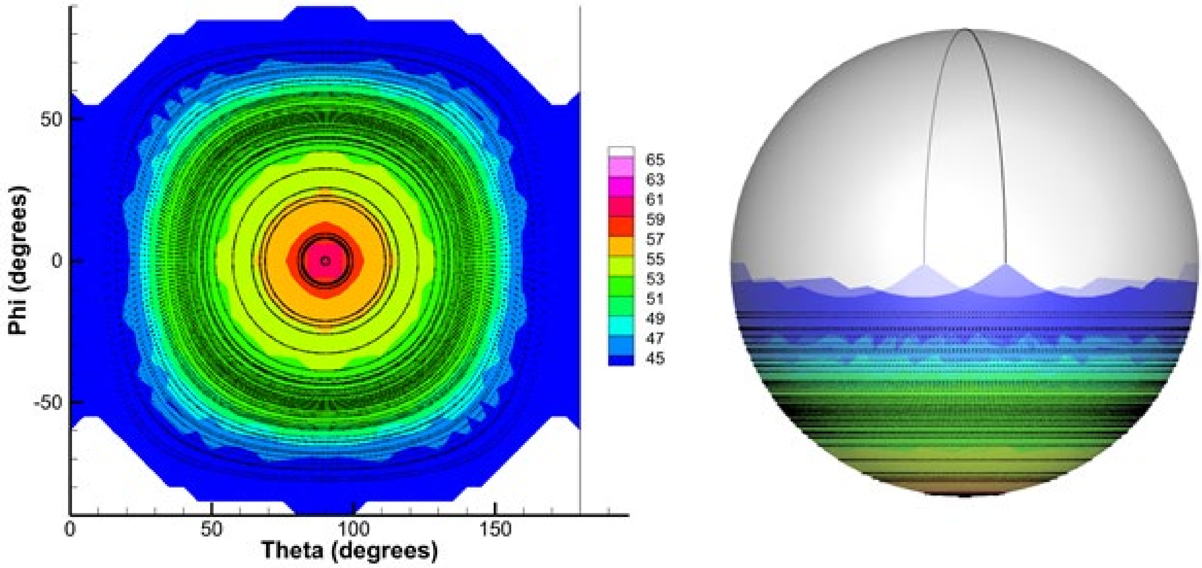


*Figure 4. Contours of 1 kHz one-third octave band levels on two views of the directional noise sphere with decibel levels noted in legend and microphone data input represented by dashed black lines assuming axisymmetric noise emissions.*

The result of this reduction and processing was noise spheres containing the average one-third octave band spectra of each UA hovering at 50 ft. The aircraft are listed in Table 2, along with their configurations and the name of the noise sphere ".NC" file.

*Table 2. Omnidirectional Noise Spheres Created from JBCC and Causey Measurements*

| UA Model | Test Point | Configuration | Sphere Name (*.NC) | Directionality |
|---|---|---|---|---|
| **DJI M600** | 50 ft. Hover | Max. Weight (33.3 lbs) | M600M | **Omni** |
| **Flytrex M600P** | 50 ft. Hover | Max. Weight (33.4 lbs) | FTRXM | **Omni** |
| **Flytrex M600P** | 50 ft. Hover | Max. Weight (33.4 lbs) | FTRXD | **Directional** |

A comparison of the two spectra used to make the omnidirectional hover spheres is shown in Figure 5. The behaviour of the broad band portion of the spectra is similar in amplitude and shape. The bands at the blade passage frequencies do show a difference. The DJI M600's blade passage frequency noise is shared between the 100 and 125 Hz one-third octave bands. It is important to understand that the spectra shown in Figure 5 have no atmospheric absorption and represent the levels spherical spread to 100 ft. The two spectra represent the average levels measured only on the hover ring microphones while the vehicles were hovering at 50 ft. above the center of the ring, as detailed above.

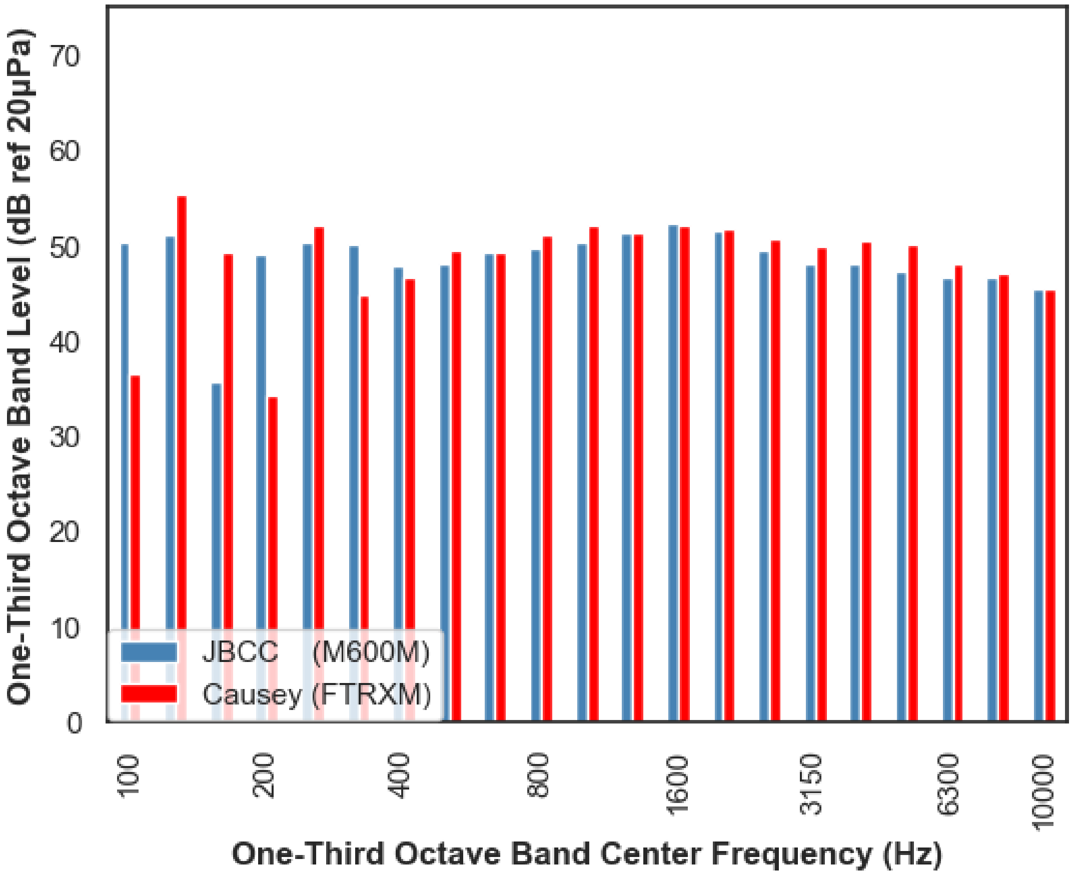


*Figure 5. Comparison of average spectra of DJI M600 and Flytrex M600P from 50 ft. hover condition.*

# 3. Analysis

The analysis consisted of comparisons between the noise sphere and measured acoustic data using AAM to model the noise for the as-flown test points. The run-specific weather conditions and associated atmospheric absorption effects were used with each noise sphere to predict noise levels at microphone locations.

## 3.1 Estimating Hover Noise Levels Using Omnidirectional Hover Noise Hemisphere

The first analysis used the omnidirectional hover noise sphere in conjunction with the tracking data from the 50 ft. hover events to estimate noise levels at the hover ring microphone locations originally used to create the noise spheres. Although the noise spheres are an average of noise from similar hover events, this comparison was expected to produce noise levels similar to the actual measured data for each of the hover events included in the noise hemisphere. A sample comparison is shown in Figure 6 for one run at the 50 ft. hover test point at JBCC.

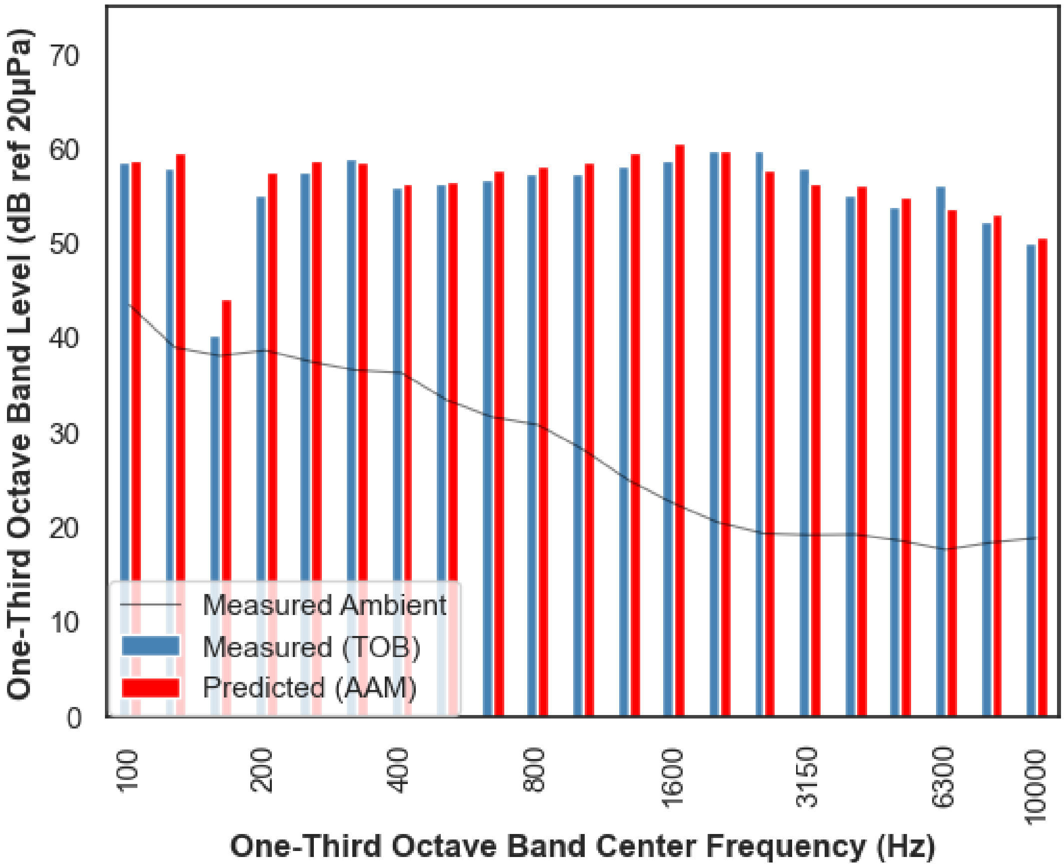


*Figure 6. Measured and estimated levels of M600M at hover ring microphone H270.*

Overall, the results follow the expected outcome. Generally, the estimated one-third octave band levels are in agreement with the actual measured levels for the 50 ft. hover events for all aircraft, especially in the broadband spectra (around 1 kHz). There was some discrepancy in the lower frequencies close to the blade passage frequency of each aircraft (generally the 100 Hz or 125 Hz one-third octave bands), which could potentially be attributed to band-sharing or slight variations in blade passage frequency that push the acoustic energy into neighbouring one-third octave bands.

### 3.2 Estimating Lateral Noise Levels Using Omnidirectional Hover Noise Hemisphere

The second comparison used the omnidirectional hover noise sphere to predict the noise levels at the lateral ground microphone locations on the linear microphone array extending outside the hover array. Note these microphone data were not used to create the omnidirectional noise sphere. It was expected that the broadband noise levels at these lateral microphone positions would be over-predicted (that is, the estimated noise levels would be higher than the actual measured noise levels) due to the observed directional nature of the broadband noise shown in Figure 4. A comparison of the difference in broadband noise at a lateral microphone located 150 ft. to the side of the hover point is shown in Figure 7. The difference in the levels 400 to 3150 Hz one-third octave bands is evident.

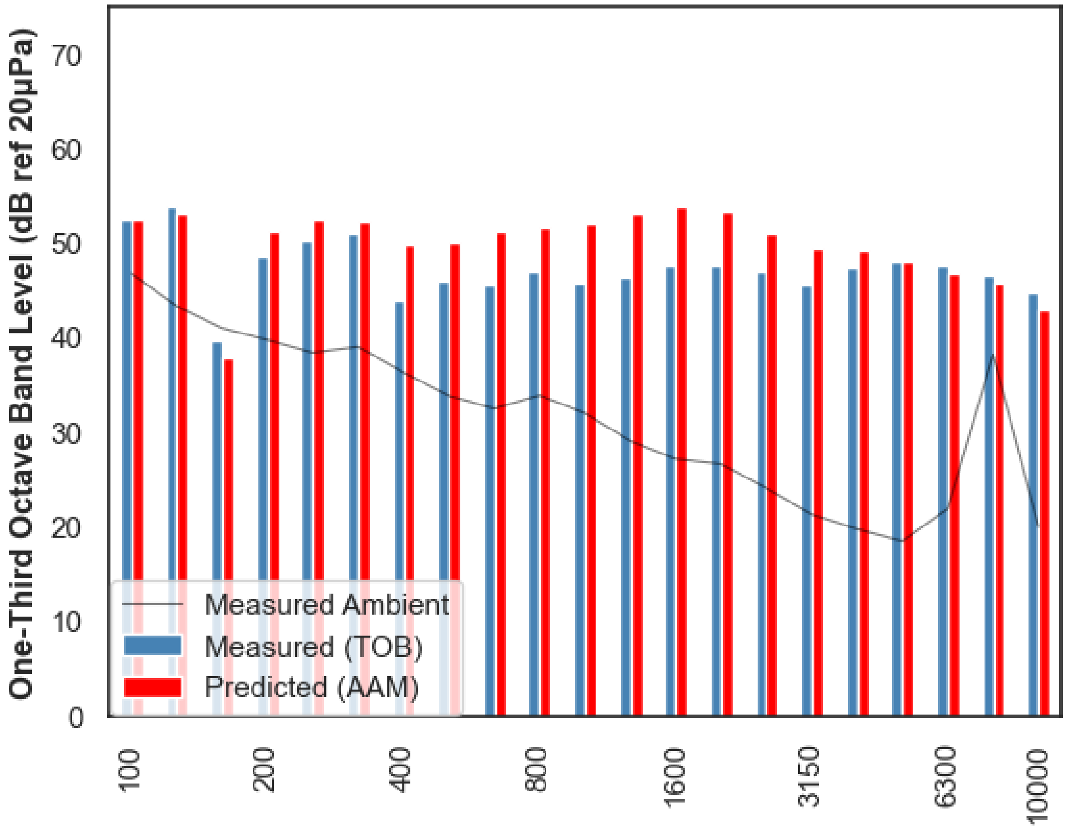


*Figure 7. Measured and estimated levels of M600M at lateral microphone F45W.*

### 3.3 Estimating Lateral Noise Levels Using Directional Hover Noise Hemisphere

To investigate the relative accuracy of hover noise predictions using the directional hover noise sphere, the initial comparison was replicated using the directional hover noise sphere. The results show that the directional noise sphere more accurately predicts noise levels at the lateral microphone positions, when compared to the noise levels predicted by the omnidirectional noise sphere. Figure 8 shows the predicted versus measured noise levels at the Causey F45W lateral microphone position for the FTRXD noise sphere during a 50 ft. hover event. Compared to Figure 7, the prediction of one-third octave band noise levels, especially broadband noise around 1 kHz, is much more in line with the actual measured noise levels for the hover event.

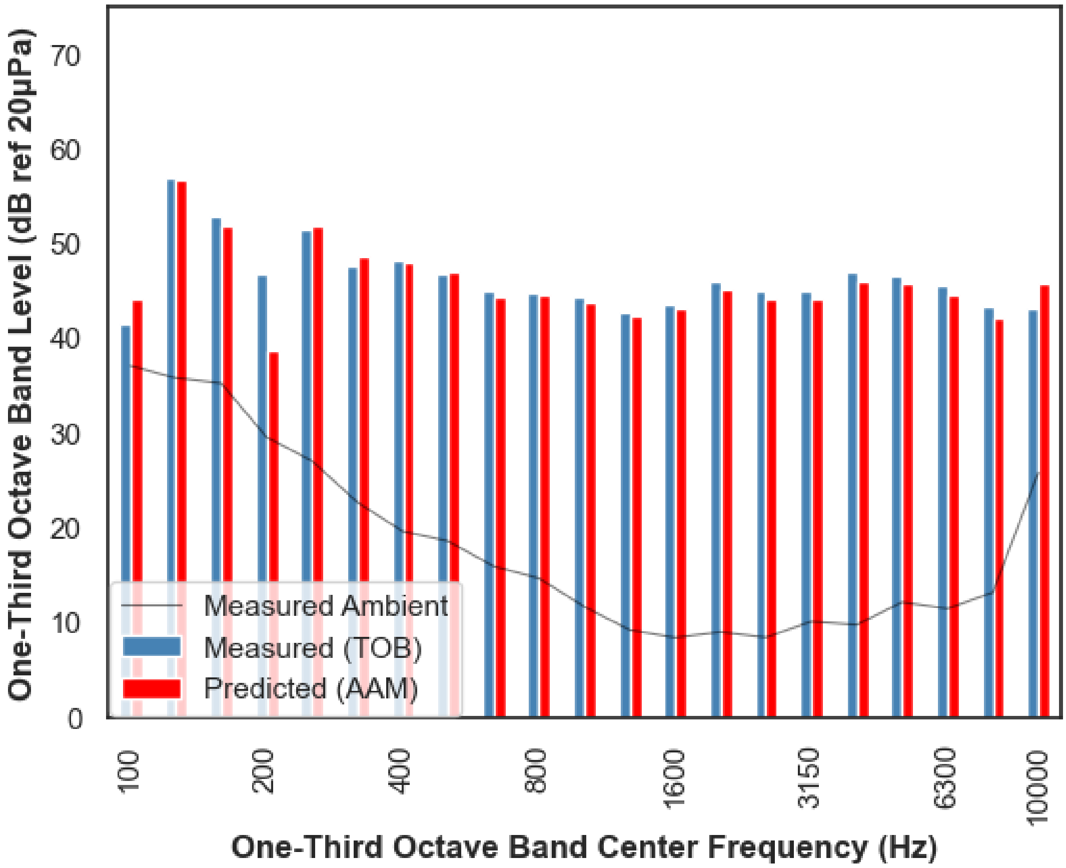


*Figure 8. Measured and estimated levels of FTRXD at lateral microphone F45W during Causey measurements.*

### 3.4 Estimating Takeoff Noise Levels Using Hover Noise Sphere

The final comparison used the spheres created above with takeoff event trajectory data. Five takeoff events recorded at JBCC were used for this comparison. Four events were takeoffs to approximately 50 ft. before transitioning to horizontal flight, while one event was a takeoff to 100 ft. before transitioning to horizontal flight. All five events behaved similarly near the ground, with the initial ascent being a slow climb to about 6 ft. above the ground followed by a constant speed ascent to the transition altitude. Figure 9 shows a plot of the takeoff event to 100 ft. before transitioning to horizontal flight by the DJI M600 at JBCC. The elevated microphone array mentioned in Figure 1 is shown to scale. The altitude profile is shown in the following figure with the initial change in climb rate around 6 ft. above ground level.

In order to isolate just the climb portion of the takeoff events, the trajectories of all five events were trimmed to start when the aircraft reached 6 ft. in altitude and end at 47 ft. The 47 ft. upper altitude was used because it was the lowest common top altitude of the 5 events. The average position was used for the horizontal position during the climb events. This was done to smooth out the tracking data and more accurately represent how the noise spheres were created, relative to the horizon. All three noise spheres were used to model a takeoff event in AAM. The estimated arrival time of the sound at each of the microphone locations was used to calculate the sound exposure level ($L_{AE}$) of the A-weighted time history for each microphone. This is not the same as the total event $L_{AE}$ which would include the transition noise between hover and vertical ascent, and initial motor start up. The objective of this exercise was to have a consistent set of trajectories and recordings to compare the effects of directivity in levels recorded as a function of distance along the ground from a takeoff event.

Recall that the recordings at JBCC were of the DJI M600 UA taking off at maximum weight. The comparisons with the Flytrex noise spheres are being done because the directional noise sphere could only be made with the data captured during the Causey measurement campaign due to the microphone array configuration during the hover events. The takeoff events of the Flytrex M600P could not be used for the comparison because of a significant pause at around 30 ft. above ground level in the takeoff ascent.

Because the Flytrex M600P and DJI M600 platforms are similar in configuration and weight, along with the spectral comparison shown above, it is reasonable to expect the DJI M600 to have a similar broadband directivity pattern as the Flytrex M600P. Therefore, it is justifiable to use the modelling substitute for the takeoff recordings at JBCC below.

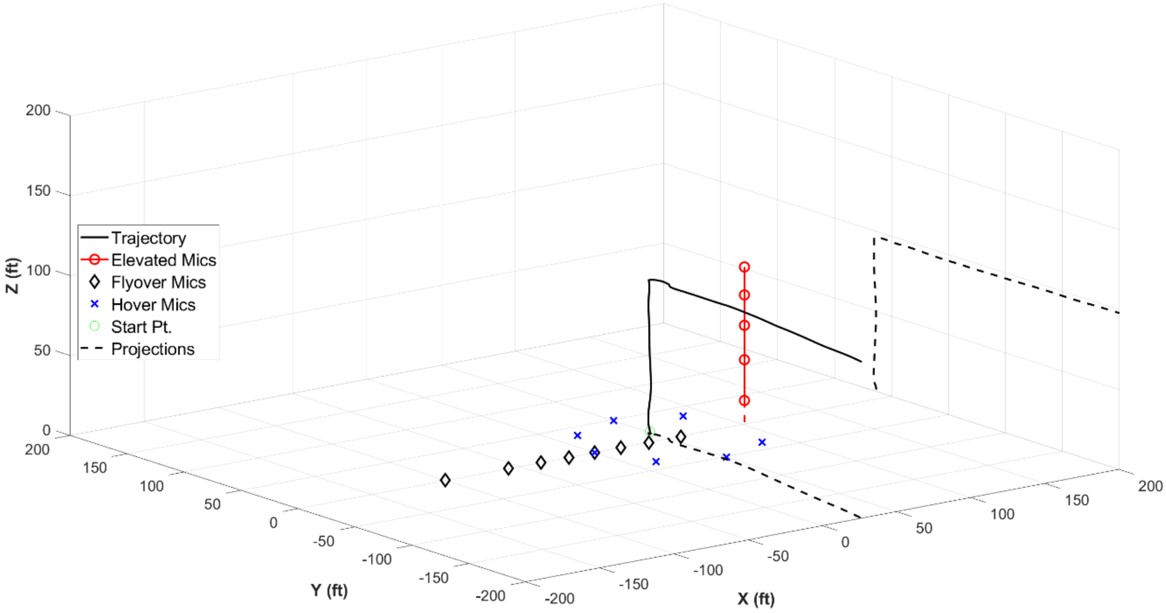


*Figure 9. Takeoff event of DJI M600 at JBCC with transition to horizontal flight at 100 ft. above ground level.*

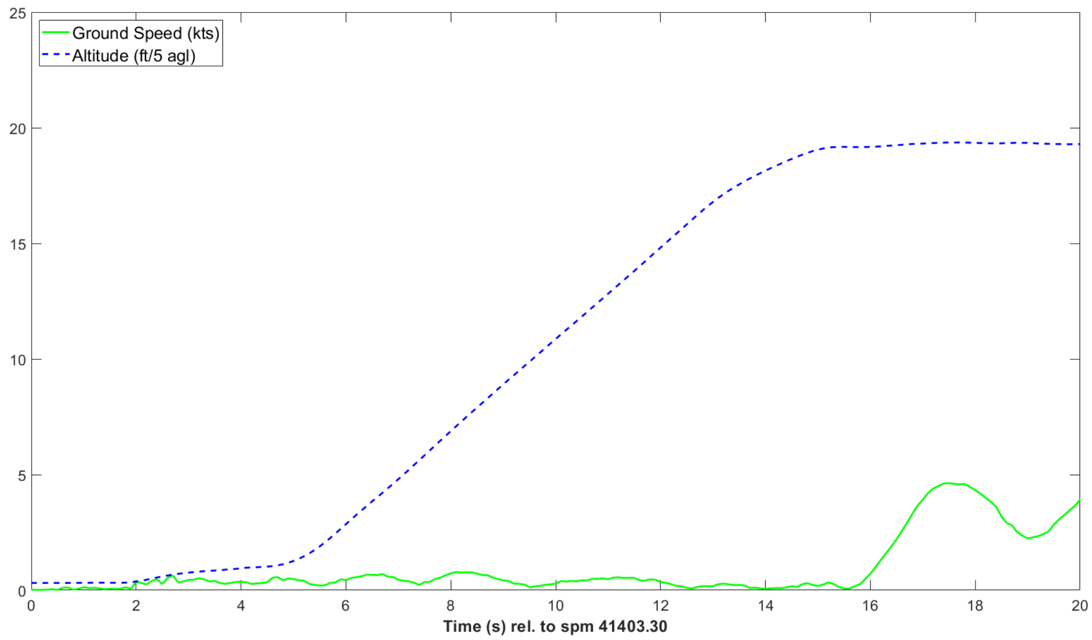


*Figure 10. Altitude profile of takeoff event to 100 ft. transition shown with ground speed.*

The results of modelling the trimmed trajectories of the five event and calculating the received noise at each microphone are listed in Table 3.

*Table 3. Measured and Modelled $L_{AE}$ for Trimmed Takeoffs at JBCC*

| Source | Lateral Distance (ft.) | 7 | 14 | 33 | 50 | 67 | 86 | 108 | 150 |
|---|---|---|---|---|---|---|---|---|---|
| | Event\Mic | F30E | F20E | F10E | F000 | F10W | F20W | F30W | F45W |
| Measured | RUN0064 | 87.8 | 88.3 | 83.4 | 79.8 | 76.0 | 72.2 | 69.1 | 63.3 |
| | RUN0072 | 90.0 | 92.1 | 84.6 | 80.4 | 76.9 | 73.2 | 70.0 | 64.3 |
| | RUN0074 | 90.6 | 90.0 | 83.6 | 80.0 | 76.7 | 73.1 | 69.6 | 64.5 |
| | RUN0081 | 88.3 | 86.6 | 81.0 | 77.6 | 74.5 | 71.5 | 69.1 | 64.0 |
| | RUN0089 | 91.6 | 89.9 | 83.1 | 79.3 | 75.9 | 72.0 | 69.2 | 64.2 |
| | RUN0100 | 87.8 | 88.3 | 83.4 | 79.8 | 76.0 | 72.2 | 69.1 | 63.3 |
| Modelled | RUN0064_FTRXD | 85.9 | 85.4 | 80.1 | 76.7 | 73.3 | 70.2 | 68.0 | 63.8 |
| | RUN0064_FTRXM | 85.2 | 84.8 | 81.6 | 79.0 | 76.8 | 74.9 | 73.0 | 70.1 |
| | RUN0064_M600M | 84.4 | 83.9 | 80.7 | 78.1 | 76.0 | 74.0 | 72.2 | 69.3 |
| | RUN0072_FTRXD | 86.7 | 88.2 | 83.1 | 78.3 | 75.7 | 72.9 | 69.5 | 64.9 |
| | RUN0072_FTRXM | 85.9 | 86.9 | 83.3 | 80.5 | 78.2 | 76.1 | 74.2 | 71.2 |
| | RUN0072_M600M | 85.0 | 86.0 | 82.5 | 79.6 | 77.3 | 75.3 | 73.4 | 70.4 |
| | RUN0074_FTRXD | 87.0 | 86.6 | 81.1 | 77.1 | 74.3 | 71.5 | 68.5 | 64.1 |
| | RUN0074_FTRXM | 85.9 | 85.8 | 82.2 | 79.5 | 77.3 | 75.3 | 73.4 | 70.5 |
| | RUN0074_M600M | 85.1 | 84.9 | 81.4 | 78.7 | 76.4 | 74.5 | 72.6 | 69.7 |
| | RUN0081_FTRXD | 86.5 | 85.9 | 80.8 | 77.5 | 74.5 | 71.4 | 69.0 | 64.8 |
| | RUN0081_FTRXM | 85.8 | 85.2 | 82.1 | 79.6 | 77.5 | 75.6 | 73.8 | 70.9 |
| | RUN0081_M600M | 85.0 | 84.4 | 81.3 | 78.8 | 76.7 | 74.8 | 72.9 | 70.1 |

By calculating the difference levels between each of the estimates from modelling the noise spheres in AAM and deriving the average of the difference levels, the improvement in estimating lateral noise during the ascent portion of a takeoff operation using the noise sphere with directivity is apparent, as shown in Table 4.

*Table 4. Difference Levels of Modelled and Measured $L_{AE}$ for Takeoffs Events at JBCC*

| Lateral Distance (ft.) | 7 | 14 | 33 | 50 | 67 | 86 | 108 | 150 |
|---|---|---|---|---|---|---|---|---|
| **RUN_Sphere\Mic** | **F30E** | **F20E** | **F10E** | **F000** | **F10W** | **F20W** | **F30W** | **F45W** |
| RUN0064_FTRXD | -2 | -3 | -3 | -3 | -3 | -2 | -1 | 1 |
| RUN0072_FTRXD | -3 | -4 | -2 | -2 | -1 | 0 | -1 | 1 |
| RUN0074_FTRXD | -4 | -3 | -3 | -3 | -2 | -2 | -1 | 0 |
| RUN0081_FTRXD | -2 | -1 | 0 | 0 | 0 | 0 | 0 | 1 |
| RUN0089_FTRXD | -4 | -3 | -2 | -3 | -2 | -1 | -1 | -1 |
| **FTRXD-Ave-Diff** | **-3** | **-3** | **-2** | **-2** | **-2** | **-1** | **-1** | **0** |
| RUN0064_FTRXM | -3 | -4 | -2 | -1 | 1 | 3 | 4 | 7 |
| RUN0072_FTRXM | -4 | -5 | -1 | 0 | 1 | 3 | 4 | 7 |
| RUN0074_FTRXM | -6 | -5 | -2 | -1 | 0 | 1 | 3 | 5 |
| RUN0081_FTRXM | -3 | -1 | 1 | 2 | 3 | 4 | 5 | 7 |
| RUN0089_FTRXM | -5 | -4 | -1 | 0 | 1 | 3 | 4 | 6 |
| **FTRXM-Ave-Diff** | **-4** | **-4** | **-1** | **0** | **1** | **3** | **4** | **6** |
| RUN0064_M600M | -3 | -4 | -3 | -2 | 0 | 2 | 3 | 6 |
| RUN0072_M600M | -5 | -6 | -2 | -1 | 0 | 2 | 3 | 6 |
| RUN0074_M600M | -6 | -5 | -2 | -1 | 0 | 1 | 3 | 5 |
| RUN0081_M600M | -3 | -2 | 0 | 1 | 2 | 3 | 4 | 6 |
| RUN0089_M600M | -6 | -5 | -2 | -1 | 0 | 2 | 3 | 5 |
| **M600M-Ave-Diff** | **-5** | **-5** | **-2** | **-1** | **1** | **2** | **3** | **6** |

As expected, and similar to the hover event comparisons, the omnidirectional hover spheres overestimated takeoff noise at the far lateral microphone positions when used to predict takeoff noise levels. There was generally good agreement between the $L_{AE}$ values determined using the Causey and JBCC omnidirectional spheres, despite being from different measurement campaigns. Both the omnidirectional and directional noise spheres underestimated the noise levels underneath the vehicle during takeoff. The predictions using the omnidirectional noise sphere generally over predicted the noise levels at the furthest lateral mic by 6 dB.

## 4. Conclusion

Despite their small size, the UA studied here show directivity in their broadband noise emissions. Because of this directivity, using the noise levels from 45 degrees below the UA as an estimate for noise emissions in all directions may result in an overestimate of takeoff noise at further lateral positions. Estimation of takeoff sound exposure levels is more accurate using noise spheres which include the directionality of the UA noise, even if the directionality is taken from a different flight condition, such as a hover.

It is worth noting that the $L_{AE}$ values predicted using directional noise spheres more closely match actual measured values at both hover and lateral microphone positions. The predicted noise levels using the directional hover sphere accurately estimate the takeoff noise levels ($L_{AE}$) at the lateral microphone positions within at least 1 dB. That being said, the predicted noise levels using the directional noise sphere still underestimate the noise generated underneath the aircraft (though, to a smaller degree than the omnidirectional noise sphere predictions).

### References

Page, J.A., Wilmer, C., Schultz, T., Plotkin, K.J., Czech, J., (2010) *Advanced Acoustic Model Technical Reference and User Manual*, SERDP Project WR-1304, Wyle Laboratories Research Report No. WR 08-12, Wyle Laboratories, Inc., Arlington, VA., Sept. Available from: http:// www.serdp.org/Program-Areas/Weapons-Systems-and-Platforms/Noise-and-Emissions/Noise/WP-1304

Page, J.A. and K.J. Plotkin, (2004) *Acoustic Repropagation Technique, Version 3 (ART3)*, Wyle Research Report, WR 03-25, Wyle Laboratories, Inc., Arlington, VA. April.

George A.R. and S-T Chou, (1984) *Comparison of Broadband Noise Mechanisms, Analyses, and Experiments on Rotors*, Vol. 21, No. 8, Jrnl Aircraft, August.

QUIET DRONES
Second International e-Symposium
on
UAV/UAS Noise
27th to 30th June 2022

# Experimental investigation and psychoacoustic analysis of a DJI Phantom 3 quadcopter

**Guillaume Beaulieu,**
**von Karman Institute for Fluid Dynamics: guillaume.beaulieu@sonaca.be**
**Erica Gallo,**
**von Karman Institute for Fluid Dynamics: erica.gallo@vki.ac.be**
**Christophe Schram,**
**von Karman Institute for Fluid Dynamics: christophe.schram@vki.ac.be**

## Summary

Drones, and in particular multicopters, are already present in our environment, i.e. for parcel delivery, medical support or industrial inspections, and are seeing their application range increasing fast. Yet, their social acceptance is pending upon their noise emissions and resulting annoyance. In this work we have measured the noise emitted by a DJI Phantom 3 quadcopter in hovering, flyover and transition flight conditions, in a view to rank those three manoeuvres in terms of annoyance. The data have then been processed to examine their time-frequency content and sound quality metrics, used to finally obtain a psychoacoustic annoyance factor. The ranking reveals that the most annoying manoeuvres are not necessarily those with the largest Sound Pressure Level spectra, but that loudness and sharpness correlate well with annoyance.

## 1. Introduction

Unmanned Aerial Vehicles (UAV), also called drones, have become part of our daily life. Package delivery performed by UAVs is becoming very common, offering a potential solution to reduce traffic congestion and the resulting pollutant emissions in urbanized areas. They also start being exploited in the medical sector for safe and fast organ procurement [1], shipping blood, vaccines, medicines and other life-saving medical supplies and equipment [2]. In the industrial field, UAVs can perform monitoring missions, such as Structural Health Monitoring (SHM) of off-shore wind turbines [3][4].

Despite the usefulness of those services, the development of drone technologies can be hindered by an insufficient community acceptance. Overall, the general concerns are related to safety issues and disturbance of the living environment, of which the perceived noise represents the prominent factor of aversion. Recent psychoacoustic studies have demonstrated that for equivalent standard metric levels (dB-A, dB-C, Effective Perceived Noise Levels), people are more disturbed by drones than by typical ground vehicles [6]. And unfortunately, the places where drones will cause the most acoustic nuisance are also the places where they are likely to have the highest added value [5].

The acoustic signature produced by UAVs depends mostly on their size, design and the importance of unsteady aerodynamic installation effects; to a lesser extent on the payload and flight conditions [7]. More specifically, multicopter noise is strongly tonal and mostly associated with the steady and unsteady forces exerted by the propellers blades when traversing the distorted field that is induced by neighbouring propellers and by the nearby fuselage [8]. The rich tonal content is causing the characteristic “buzzing” noise of drones.

So far, most of the drone noise studies have been focused on two phases of the flight: hovering and forward translation [7]. If the mechanisms of noise generation in these phases are being better understood and modelled, one must note that they do not contribute the most to the annoyance, the latter being rather associated with transient manoeuvres [10], which are the focus of this paper.

The work described below follows closely the approach proposed by Torija *et al.* [11], who investigated the noise emitted by a quadcopter (the same model as in this work, as a matter of fact), considering Sound Quality Metrics (SQM) accounting for human perception aspects: loudness, tonality and sharpness. These SQMs can be combined to form different psychoacoustic annoyance indicators, which they compared for drone, aircraft, car and motorbike noise. The conclusion was that at equivalent SPL, the drone was found more annoying than the other sources. The present work extends the analysis for a manoeuvring quadcopter drone, comparing three types of drone operation: hovering, flyover and transition. In the last case, the manoeuvre includes both the forward translation-hovering and hovering-forward translation transitions.

The paper is organized as follows: Section 2 describes the measurement protocols as well as the signal processing that was implemented for the data analysis in time and Fourier domains and psychoacoustic characterization. Section 3 provides the main results, SQMs and psychoacoustic annoyance. Section 4 wraps up the main conclusions, discusses their range of validity and suggests ways of improvement and future perspectives.

## 2. Anechoic laboratory and outdoor measurements of the noise emitted by a quadcopter and psychoacoustic annoyance

In this section we describe the drone model that was used for the tests, the measurement protocols, and the data processing techniques that have been applied to quantify the noise emissions and annoyance.

### 2.1 Drone model

The DJI Phantom 3 SE (Figure 1) was used for this study. It has a maximal forward translation speed of 16 m/s and maximal ascend and descend speeds of 5 and 3 m/s, respectively. The drone has four two-bladed propellers and a weight of 1.236 kg. The propellers model for the DJI Phantom 3 SE is 9450.

*Figure 1: DJI Phantom 3 SE.*

### 2.2 Acoustic measurements

Drone noise measurements can be performed within an anechoic room or outdoors. The first option offers a better controlled acoustic environment with lower background noise and minimal reflections from the walls, ceiling and floor, while outdoor measurements usually suffer from unwanted and hardly controllable background noise, atmospheric turbulence and ground reflections. But conversely, in an anechoic room extraneous noise can be produced by the re-ingestion of the propellers slipstream recirculating in the room. Moreover, piloting a drone within an anechoic room is far from trivial. For this reason, fly-over and manoeuvring noise is usually measured outdoors.

Nevertheless, it remains relevant to compare the noise measurements obtained in both conditions. Our experimental campaign has thus been carried out in the von Karman Institute (VKI) aeroacoustic laboratory JAFAAR (Jet Aeroacoustic Facility for Aeronautical and Aerospace Research) in a first step, then outdoors on the VKI basketball field, with a scattering environment approaching semi-anechoic conditions (Figure 2). JAFAAR has 4 x 3 x 4 $m^3$ dimensions, and is anechoic down to 150 Hz.

Hovering flight was measured in both cases, in order to assess the importance of background noise and uncontrolled flow effects. The main difference between our measurement protocol and that of Torija *et al.* [11] is that they fixed the drone on a test stand for the hovering in their anechoic room. We preferred to pilot the drone and let the built-in systems of the drone stabilize it both in JAFAAR and outdoor, to have a better comparison highlighting the effects of the scattering environments and of the atmospheric turbulence.

*Figure 2: acoustic measurements performed in the VKI anechoic room (left) and over the basketball field (right).*

For both JAFAAR and outdoor measurements, four microphones G.R.A.S. 40PL were used to measure the noise induced by the drone. The microphones are positioned at the corners of a square of 2.1 m side and at a height of 1.23 m, as it can be seen in Figure 3. Each microphone has been calibrated using a pistonphone calibrator delivering a sound pressure level of 94 dB at a frequency of 1 kHz. Each microphone is protected from aerodynamic disturbances using a wind shield.

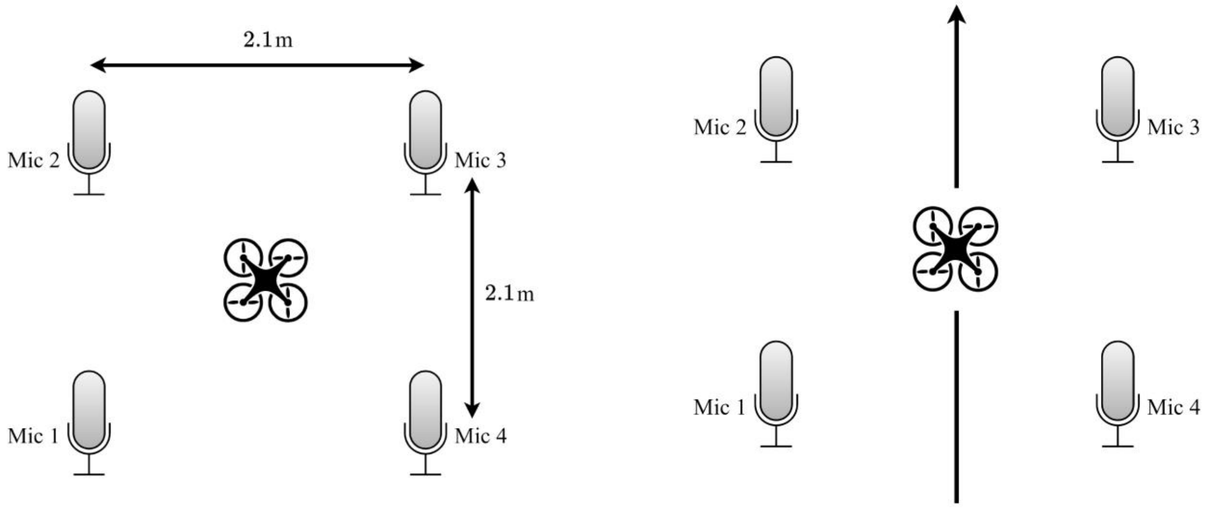


*Figure 3: microphones arrangement (each microphone is at a height of 1.23 m from the ground). Left: hovering conditions, right: forward translation and transition (in the last case, the drone marks a stop at the centre of the array before restarting forward).*

Three operations of the drone have been measured: steady hovering, flyover at constant speed and transition. For the last two, the drone enters the measurement square from the side formed by the microphones 1 and 4, and leaves through the side of microphones 2 and 3. The flyover is performed at a forward translation speed which varied between 1.5 and 3 m/s. The transition manoeuvre consists in entering the square in forward translation, do a quick stop in the centre of the array (or as close to that point as possible, anyway), and restarting in forward translation again. A constant altitude of approximately 1.8 m was maintained for all three manoeuvres.

### 2.3 Data acquisition and processing

The signals delivered by the microphones has been sampled by a National Instrument CompactDAQ cDAQ-9171 system with a NI 9234 acquisition card, which also provides the power supply to the microphones and includes an anti-aliasing filter. A sampling frequency of 51.2 kHz has been used for all measurements. The acquisition duration depends on the considered manoeuvre: for hovering an acquisition time of 30 s was used, while for the transient manoeuvres the duration was typically about 5 s, i.e. the duration of the manoeuvre.

The analysis of the acoustic signals has been performed in the time domain, in the frequency domain and in the time-frequency domain, depending on which is the most appropriate for statistically stationary signals (hovering) or transient ones (flyover and transition). In the frequency domain, the Power Spectral Density has been calculated using time segments of $2^{14}$ points and 50% overlap. In the time domain, the signals have been processed to obtain a moving standard deviation over segments with a duration of 0.15 s. This is meant to verify the statistical stationarity of the hovering microphone signals, and to study transient features of the flyover and transition manoeuvres. Finally, the time-frequency analysis was performed calculating the spectrograms (using the Python matplotlib function ‘specgram’), the purpose being to look at the stationarity of the frequency content of the signals, and to evaluate the modulation of the BPFH tones during the transient manoeuvres. The levels obtained from the PSD and spectrograms have been calculated with the usual definition of the Sound Pressure Level:

$$SPL = 20 \ log_{10}\left(p'_{rms}/p'_{ref}\right) \qquad (1)$$

where $p'_{ref} = 20$ µPa.

In addition to the standard engineering units defined above, sound quality metrics have been computed, using the MoSQITo python package [12]. The loudness, expressed in sone, is calculated following the ISO 532-1 norm [13], which implements the Zwicker algorithm [14] developed for both stationary and time-varying sounds. In the latter case, a specific loudness is obtained through a signal processing model that reproduces the physiological and psychological characteristics of the human hearing system. The second metric is the sharpness $S$, a measure of the proportion of high frequencies contained in the noise signal, with unit acum [15]. A narrowband noise with centre frequency of 1000 Hz and amplitude of 60 dB has a sharpness of 1 acum. In MoSQITo, the sharpness is calculated following the DIN 45692 norm [16]. The third metric is the roughness $R$, characterizing fast amplitude modulations of the sound, having the asper as a unit. Modulation frequencies between 15 Hz and 300 Hz contribute to the roughness of a sound, 1 asper being the roughness produced by a 1000 Hz tone of 60 dB mean amplitude, with 100% modulation at 70 Hz [14]. In contrast with the loudness and sharpness, there is no standard for the calculation of the roughness. The algorithm used in MoSQITo is described by Daniel and Weber [17].

Based on those three sound quality metrics, an empirical Psychoacoustic Annoyance (PA) has been proposed by Fastl and Zwicker [14] :

$$P_A \approx N_5\left(1 + \sqrt{w_S^2 + w_R^2}\right) \qquad (2)$$

where $N_5$ is the percentile loudness exceeded 5% of the time, expressed in sone, $w_S$ depends on the sharpness through

$$w_S = (S - 1.75) \ log_{10}(N_5 + 10) \text{ for } S > 1.75 \qquad (3)$$

and $w_R$ depends on the roughness as

$$w_R = \frac{1.31}{N_5^{0.4}} R \, . \qquad (4)$$

The annoyance due to sharpness is thus enhanced when the loudness increases. It should be noted that despite the important amplitude modulation caused by the varying distance between the drone and the microphones during flyover and transition, we have decided to not use the fluctuation strength defined in Ref. [14], in Eq. (2). This is because the amplitude modulation can hardly be described as harmonic; and also because the fluctuation strength is maximum for a modulation of 4 Hz, while the timescale of the modulation is of the order of several seconds in our measurements.

## 3. Results

The results detailed below are meant to verify if the outdoor measurements reliable, and to provide the time-frequency characteristics of the three manoeuvres (hovering, flyover and transition) as well as their psychoacoustic ranking.

### 3.1 Hovering flight noise: anechoic room vs. outdoor measurements

Figure 4 shows the SPL measured by the microphone 1 in hovering conditions, in the anechoic room and outdoors. The levels are compared with the background noise in each case. As expected, the background noise outdoors exceeds the one of the anechoic room, especially below 2 kHz. It even exceeds the hovering drone noise in narrow frequency bands below 300 Hz, illustrating its variation over time. Nevertheless, both measurements appear to be valid as the drone noise exceeds the background over most of its spectrum.

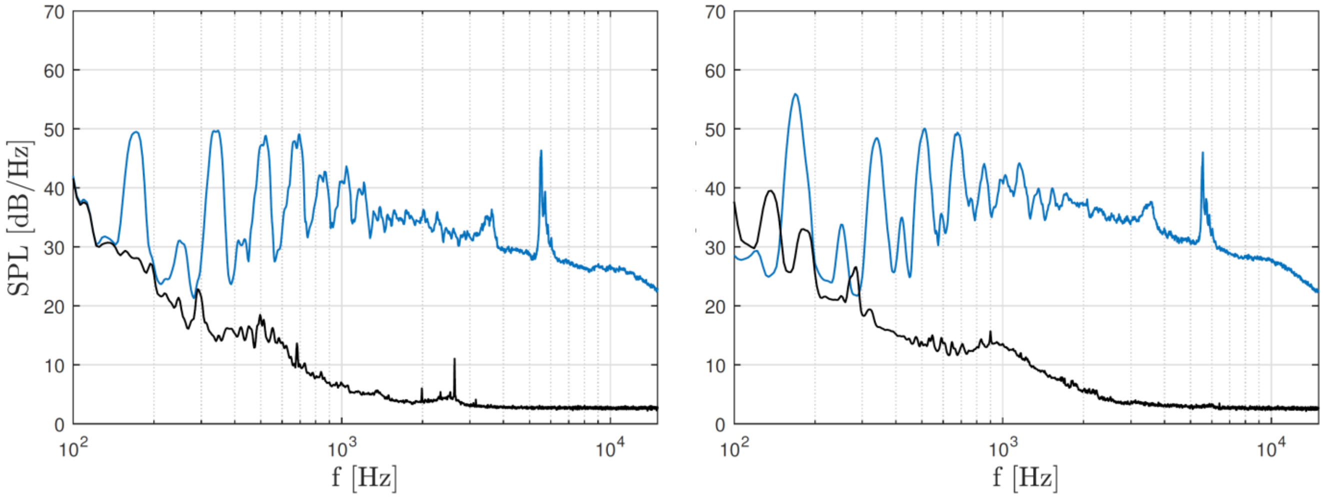


*Figure 4: Sound Pressure Level of the hovering drone, recorded by microphone 1, in the anechoic room of the VKI JAFAAR laboratory (left) and outdoors over the VKI basketball field (right). Blue: drone noise, black: background noise.*

A closer examination the hovering noise recorded in both environments (Figure 5) reveals that the spectra are fairly similar below 1 kHz, with a series of peaks that correspond to the Blade Passing Frequency Harmonics (BPFHs) of the four propellers. The fact that each BPFH spans over a certain bandwidth is probably the result of some jitter in the RPMs of the four propellers, which are continuously adjusted as the Phantom 3 stabilization system tries to maintain its position. The first peak BPFH below 200 Hz exhibits a larger amplitude for the case of the outdoor measurements, possibly caused by atmospheric turbulence ingestion. Both spectra above 1 kHz are fairly broadband, with a narrowband peak between 5 and 6 kHz associated with the electric motors. The broadband levels of the outdoor measurements exceed those of the anechoic room by about 3 dB, which is consistent with a full reflection of incoherent source by the concrete ground of the basketball field.

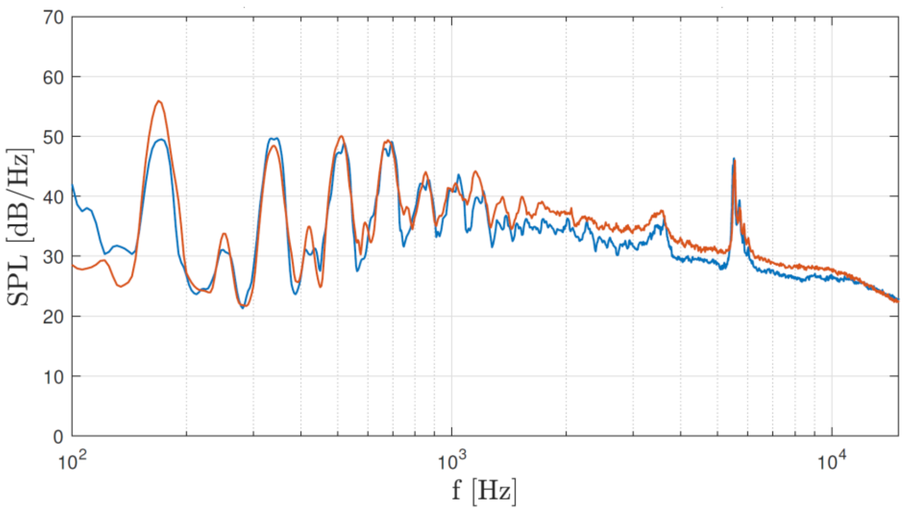


*Figure 5: hovering drone SPL measured by microphone 1 in JAFAAR (blue) and outdoors (red).*

The moving RMS of the signals recorded by the four microphones (Figure 6) remains overall constant for the microphones 1 and 4, with levels below those recorded by the other two microphones, which also show more fluctuations over time. It seems that the drone was closer to the microphones 2 and 3 during hovering.

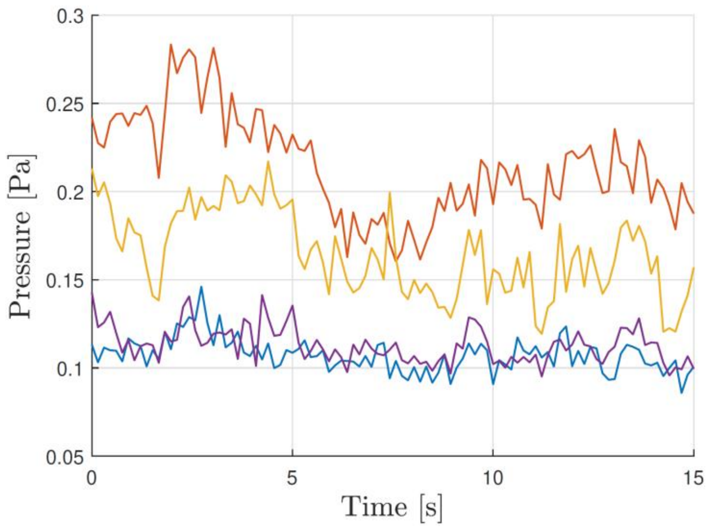


*Figure 6: moving RMS of the hovering noise measured by the 4 microphones (blue: mic1, red: mic2, yellow: mic3, purple: mic4).*

### 3.2 Flyover noise

The flyover noise tests were performed along the path described in Figure 3. The moving RMS of the acoustic pressure recorded by the four microphones is shown in Figure 7, with levels peaking when the drone crosses the line between the microphones 1 and 4 at first, then microphones 2 and 3 about 1.5 s later. This corresponds to a forward flight speed of about 1.4 m/s. The reason why the signals recorded by the microphones 2 and 3 have again a larger amplitude is uncertain, but should be related to the scattering environment of the basketball field, as all four microphones were calibrated prior to the tests.

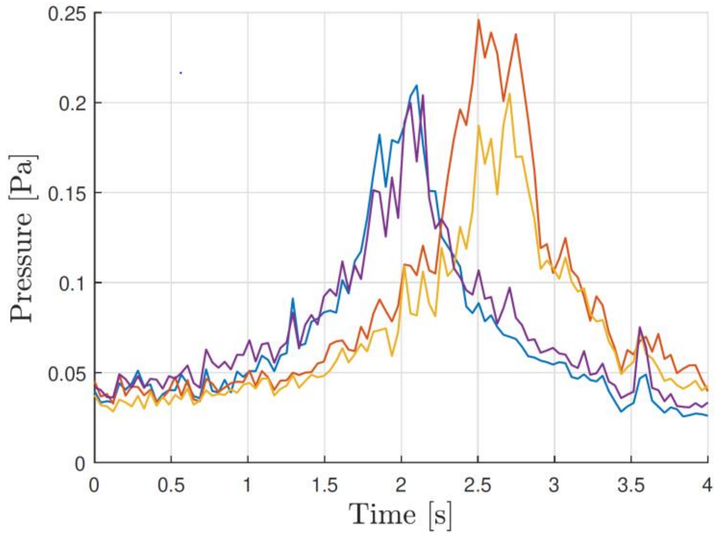


*Figure 7: moving RMS of the flyover noise measured by the 4 microphones (blue: mic1, red: mic2, yellow: mic3, purple: mic4).*

Considering the SPL spectrum (Figure 8), the tones appear this time broader, each hump containing several peaks, which can be tentatively explained by the fact that the different propellers wouldn't have the same RPM in order to maintain a steady forward translation. A nosedown pitching moment should indeed be needed to maintain the negative angle of incidence, given the centre of gravity is well below the propeller plane and thus stabilizing.

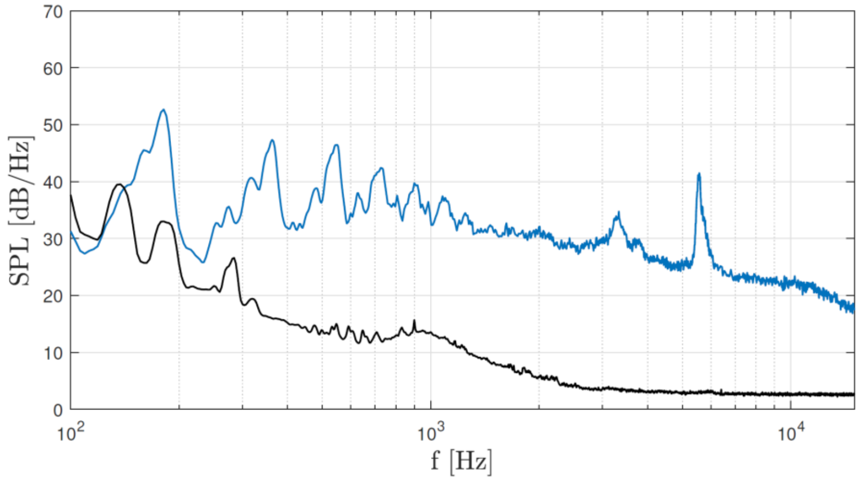


*Figure 8: flyover Sound Pressure Level at microphone 1 (blue: drone noise, black: background noise).*

The spectrogram of microphone 1 (Figure 9) shows a burst of sound emission around 2 s of acquisition time, consistent with the moving RMS plot of Figure 7. Besides, the spectrogram provides additional details about the evolution of the sub-tones that constitute the BPFH humps in Figure 8. It appears that the first BPFH is fairly concentrated around 180 Hz as it approaches the microphone 1, and then splits into multiple sub-tones as it leaves. A qualitatively similar behaviour is observed for the second BPFH, though the map is probably too noisy to draw any further conclusion. More flight tests, synchronized with the exact position of the drone would be necessary in order to position-average the spectrograms and obtain a finer analysis of the transient features of the tonal spectral content.

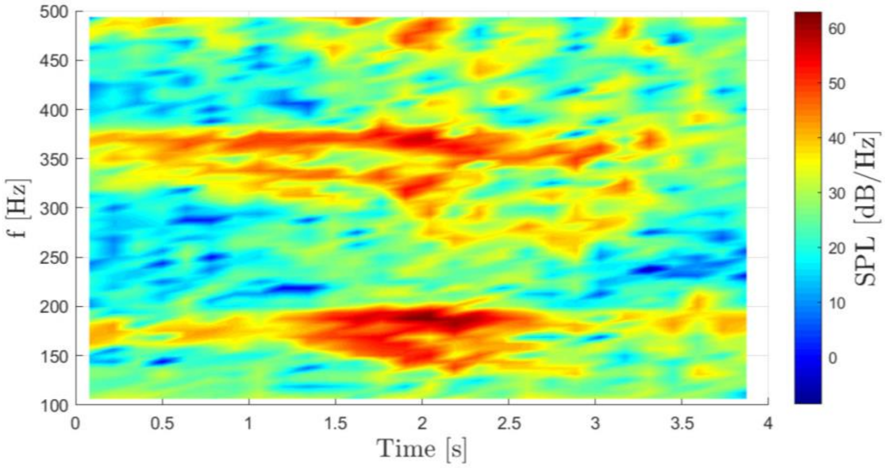


*Figure 9: flyover spectrogram.*

### 3.3 Transition noise

The same analysis can be performed for the transition noise. The different phases of the manoeuvre can be first identified in the moving RMS time series (Figure 10): the drone is approaching the microphone array in a similar way as for the flyover until 0.6-0.7 s. Then, the sudden deceleration is achieved around 1 s to immobilize the drone approximately in the centre of the array, and the drone is then re-accelerated in forward transition to leave the array after 3 s.

Remarkably, the sudden deceleration appears to be much noisier and more impulsive than the sudden forward re-acceleration. We may conjecture that the flight physics of both manoeuvres is indeed quite different. For the deceleration, the drone increases its angle of incidence to generate the necessary longitudinal force opposed to its motion, and is thus moving towards its own wake. In contrast, for the hovering-to-forward transition, the drone adopts a negative angle of incidence and is moving away from its wake. It may be reasonable to assume that the propeller-wake interaction is generating more noise, in a way analogous to the intense blade-vortex interaction noise that can be emitted by a descending helicopter.

Again, we would also need to consider the actual negative and positive accelerations of the drone during both phases of this manoeuvre to perform a finer analysis. But assuming that the RPM variations that are imposed to the front and back rotors are sensibly the same with the stick full-forward or full-backward, it may be assumed that the differences of noise emissions are caused by the drone transient aerodynamics, and not strong RPM variations. This will be somehow supported by the results of the spectrogram below.

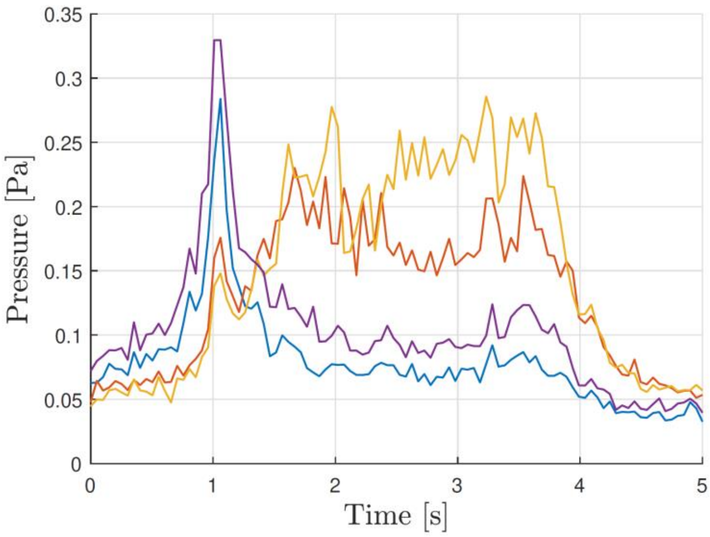


*Figure 10: moving RMS of the transition noise measured by the 4 microphones (blue: mic1, red: mic2, yellow: mic3, purple: mic4).*

The SPL, integrated over the complete manoeuvre (Figure 11), displays a much more broadband content than the two previous cases. But rather than a truly broadband noise emission, this illustrates mainly the limitation of a conventional Fourier analysis for such transient manoeuvre, as all the phases of the flight are integrated together to yield a smeared out spectrum.

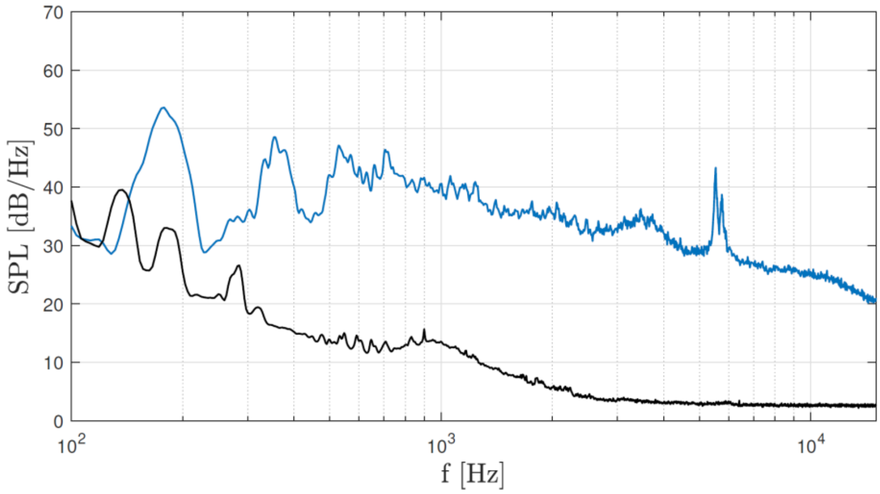


*Figure 11: transition Sound Pressure Level at microphone 1 (blue: drone noise, black: background noise).*

A more pertinent analysis is enabled by the spectrogram (Figure 12). Again, the peak of emission is found at 1 s of acquisition time, with a noticeable modulation of the frequencies of the different propellers that can be inferred from the contour levels for the first and second BPFHs. But this time also, the maps would benefit from a drone position-averaging, in order to yield less noisy maps.

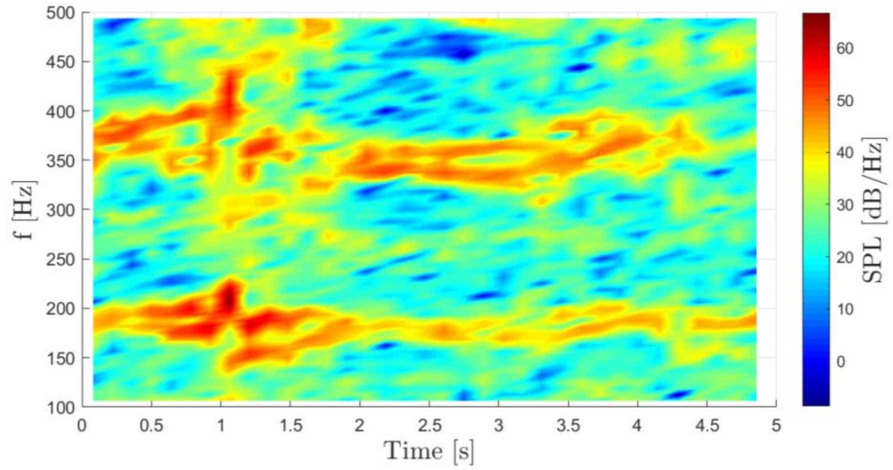


*Figure 12: transition spectrogram at microphone 1.*

### 3.4 Sound quality and psycho-acoustic indicators

The conventional, time-integrated SPL of Figure 5, Figure 8 and Figure 11 have been gathered in Figure 13 for direct comparison. It should be noted that the overall levels are not directly comparable, as the spectra of the flyover and transition manoeuvres depend on the speed at which each phase of the manoeuvre (especially transition) is executed. An arbitrary but sensible way to take this into account may be to offset the flyover and transition spectra to match the high-frequency part of the hovering spectrum. If we do this, it appears that beyond the different tonal characteristics that have been discussed above, the transition manoeuvre spectrum is on top of the two others. But not much more can be told at this stage in terms of annoyance.

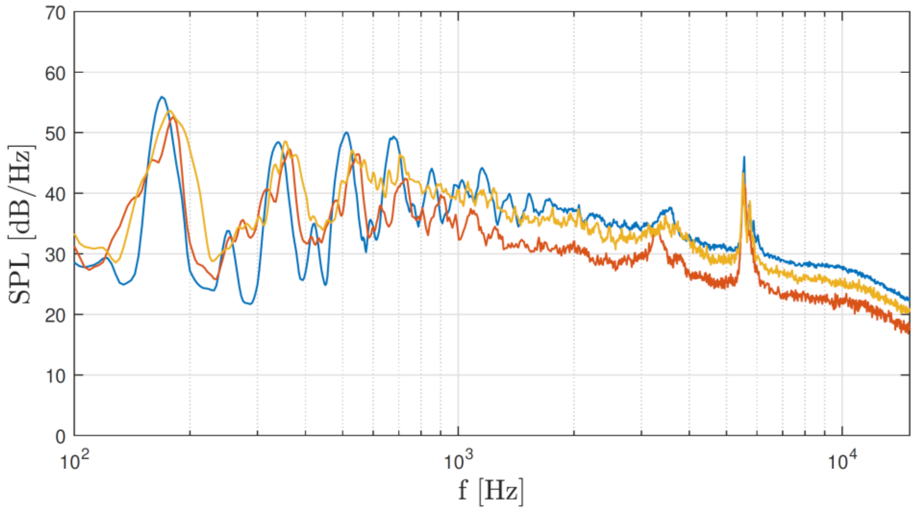


*Figure 13: Sound Pressure Level at microphone 1 of the hover (blue), flyover (red) and transition (yellow) manoeuvres.*

The first sound quality indicator, loudness, has been calculated over sliding intervals for each manoeuvre as shown in Figure 14. As expected, it features the same transient features as discussed above for the moving RMS, but provides now a perception-related assessment thanks to the dB-A weighting of the spectra. Both flyover and transition manoeuvres yield loudness levels much higher than hovering, the flyover producing peaks of loudness that are a couple of sones higher than the transition.

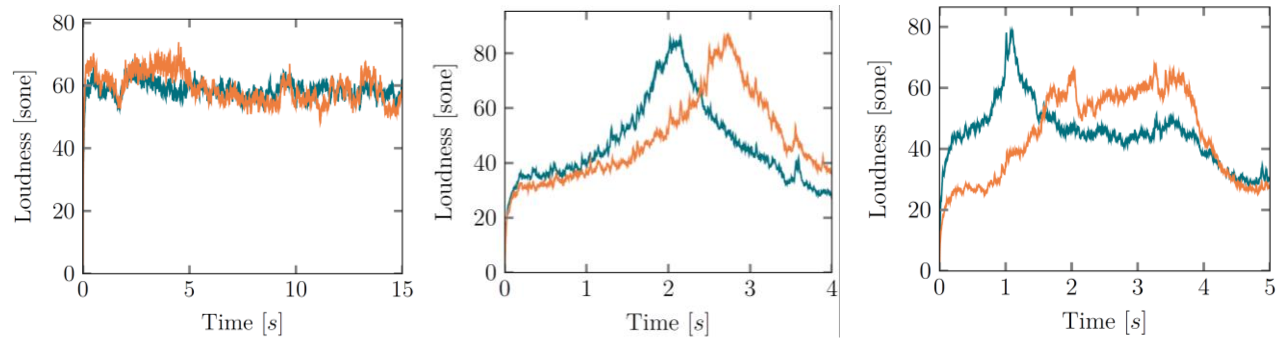


*Figure 14: loudness of the hovering noise (left), flyover noise (centre) and transition noise (right). Blue: microphone 1, orange: microphone 2.*

The sharpness of the three manoeuvres (Figure 15) shows also higher and more frequent peaks for the flyover than the two other cases. Interestingly, the transition yields an average sharpness level that is below that of the hovering.

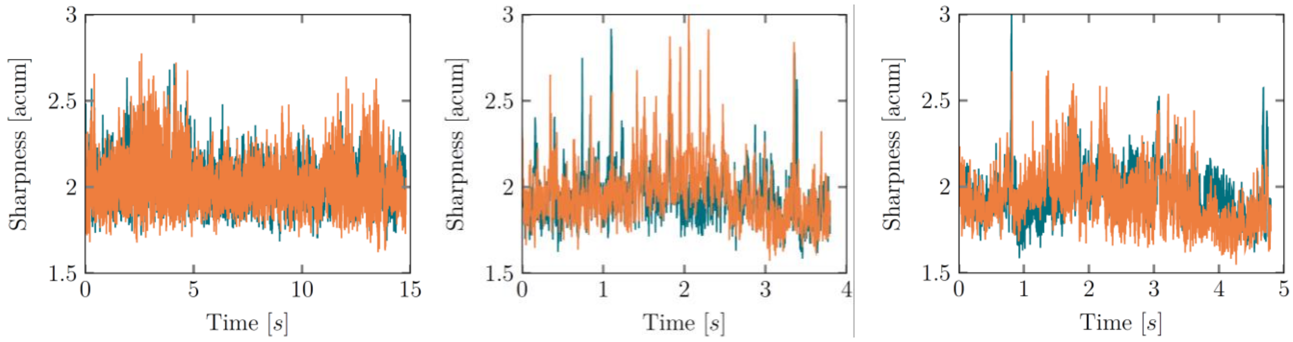


*Figure 15: sharpness of the hovering noise (left), flyover noise (centre) and transition noise (right). Blue: microphone 1, orange: microphone 2.*

The last sound quality indicator analysed in this study, roughness, is somehow more difficult to interpret as is shows some transient behaviour for the hovering, which is not a priori expected. It might be caused by the ingestion of atmospheric turbulence, but this is largely conjectural at this stage. But overall, the transition seems to be associated with larger roughness.

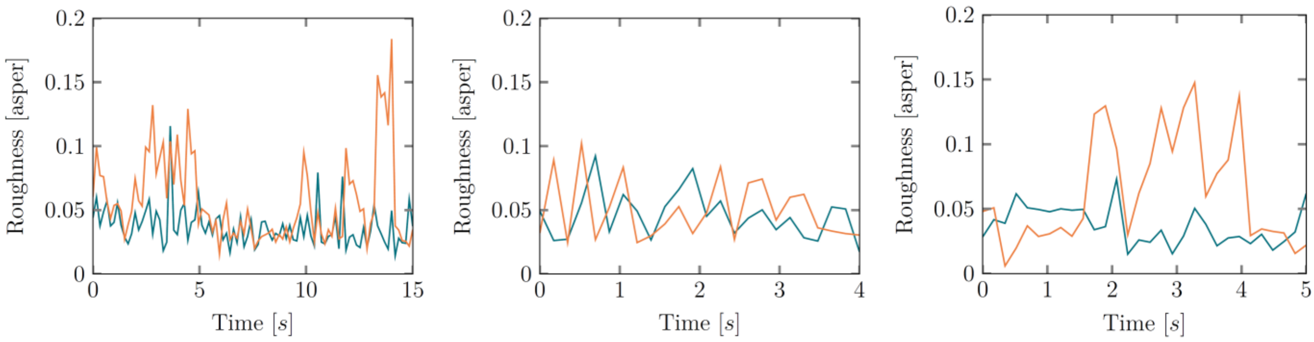


*Figure 16: roughness of the hovering noise (left), flyover noise (centre) and transition noise (right). Blue: microphone 1, orange: microphone 2.*

The final comparison concerns the psychoacoustic annoyance indicator defined in Eq. (2), which gives the following result:

- Hovering: $PA = 88$ ,
- Flyover: $PA = 158$ ,
- Transition: $PA = 144$ .

This shows that flyover and transition are ‘twice’ as annoying as hovering, and relatively equivalent to each other. Noteworthy, the transition would be slightly less annoying than the flyover, which contrasts with the conclusions drawn from the integrated SPLs or from the roughness. In this instance, the loudness and sharpness would correlate best with the annoyance.

## 4. Discussion

The main objective of this work was to establish a measurement protocol permitting to quantify the noise and psychoacoustic annoyance caused by drones, extending previous works to the comparison of different manoeuvres deemed representative of multicopter operation.

We have demonstrated that despite minor differences that can be attributed to atmospheric turbulence and ground reflections, the outdoor noise measurements were sufficiently close to those obtained in a controlled anechoic laboratory environment to be considered as reliable. One point of improvement for future campaigns would be the measurement of the position of the drone, either by a system of cameras or an embarked GPS-like sensor, as it would permit averaging together the time-dependent results (moving RMS and periodograms) and enable a finer analysis. The periodograms, in particular, proved difficult to read when trying to identify the RPM variations of the different propellers.

Despite this limitation, the outdoor measurements have nevertheless produced results that are consistent between the four microphones of the array, and with the control strategy of small multicopter drones for which the attitude is controlled by varying the RPM of the different propellers. Naturally, the results are also affected by an inevitable feature of ground-based microphones: the measured acoustic pressure depends on the distance between the drone and the listener, and probably also on the directivity of the drone (not addressed in this work). While the resulting amplitude modulation at the immission – in contrast with emission – point is also inherent to its perception by ground communities, it complicates the attempts to correlate the noise emissions to the drone operational parameters, mainly the RPM in this case. It would be of interest to devise a measurement protocol where the noise would be measured by the drone itself, in order to decouple the source effects from the source-listener propagation effects.

About the psychoacoustic annoyance indicator used in this work, two key issues should be mentioned. Firstly, it has been derived from psychoacoustic tests, using synthetic or recorded sounds that may not be representative of drone noise. Dedicated psychoacoustic tests may have to be conducted to verify if the annoyance ranking of drones conforms with other types of noise sources (aircraft, cars, domestic appliances, …). Secondly, transient noise tends to be more noticeable than constant noise, and the manoeuvres of drones have timescales quite different from those associated with the passage of an aircraft, which has the time to blend in the background. In the case of quadcopters, manoeuvres require a rapid variation of the rotational speed of some rotors. This modulates the Blade Passing Frequency, which fundamental and higher harmonics are known to dominate the emitted sound spectrum. One refers to a strongly annoying “buzzing” noise. It isn’t obvious how existing sound quality indicators account for the rapid, non-harmonic modulation of the tonal spectra of multiple propellers.

As a final remark beyond the scope of this particular study, the societal acceptance of drones will likely depend on their use, in addition to their noise impact. Civil aviation has a well identified and simple role, being for passenger or freight transport. But the perception of drone noise is likely to be quite different whether they deliver pizzas or medical support, inspect dangerous installations or seek survivors of an accident, to only mention a few of the many potential applications of this technology.

## References


[1] Phillips, J., "Medical unmanned aerial system for organ transplant delivery," California University of Pennsylvania, 2019.

[2] Poljak, M., and Šterbenc, A., "Use of drones in clinical microbiology and infectious diseases: current status, challenges and barriers," Clinical Microbiology and Infection, Vol. 26, No. 4, 2020, pp. 425–430.

[3] Poozesh, P., Aizawa, K., Niezrecki, C., Baqersad, J., Inalpolat, M., and Heilmann, G., "Structural health monitoring of wind turbine blades using acoustic microphone array," Structural Health Monitoring, Vol. 16, No. 4, 2017, pp. 471–485.

[4] Reagan, D., Sabato, A., and Niezrecki, C., "Unmanned aerial vehicle acquisition of three-dimensional digital image correlation measurements for structural health monitoring of bridges," Nondestructive Characterization and Monitoring of Advanced Materials, Aerospace, and Civil Infrastructure 2017, Vol. 10169, International Society for Optics and Photonics, 2017.

[5] Aurambout, J.-P., Gkoumas, K., and Ciuffo, B., "Last mile delivery by drones: an estimation of viable market potential and access to citizens across European cities," European Transport Research Review, Vol. 11, No. 1, 2019, pp. 1–21.

[6] Cabell, R., Grosveld, F., and McSwain, R., "Measured noise from small unmanned aerial vehicles," INTER-NOISE and NOISE-CON Congress and Conference Proceedings, Vol. 252, Institute of Noise Control Engineering, 2016, pp. 345–354.

[7] Raya Islam, D., Stimpson, A., and Cummings, M., "Small UAV Noise Analysis," Tech. rep., Tech. rep., Humans and Autonomy Laboratory, Durham, NC, USA, 2017.

[8] Zarri, A., Dell'Erba, E., and Schram, C., "Fuselage scattering effects in a hovering quadcopter drone," 28th AIAA/CEAS Aeroacoustics Conference, Southampton, 14-17 June, 2022.

[9] Alexander, W. N., and Whelchel, J., "Flyover noise of multi-rotor sUAS," INTER-NOISE and NOISE-CON Congress and Conference Proceedings, Vol. 259, Institute of Noise Control Engineering, 2019, pp. 2548–2558.

[10] Schäffer, B., Pieren, R., Heutschi, K., Wunderli, J. M., and Becker, S., "Drone Noise Emission Characteristics and Noise Effects on Humans—A Systematic Review," International Journal of Environmental Research and Public Health, Vol. 18, No. 11, 2021, p. 5940.

[11] Torija, A. J., Self, R. H., and Lawrence, J. L., "Psychoacoustic characterisation of a small fixed-pitch quadcopter," INTER-NOISE and NOISE-CON Congress and Conference Proceedings, Vol. 259, Institute of Noise Control Engineering, 2019, pp. 1884–1894.

[12] Green Forge Coop, "MOSQITO," Nov. 2021, https://doi.org/10.5281/zenodo.5639403.

[13] International Organisation for Standardization, "ISO 532-1:2017," https://www.iso.org/cms/render/live/en/sites/isoorg/contents/data/standard/06/30/63077.html.

[14] Fastl, H., and Zwicker, E., Psychoacoustics: Facts and Models, 3rd ed., Springer, Berlin ; New York, 2006.

[15] Fastl, H., and Zwicker, E., "Sharpness and sensory pleasantness," Psychoacoustics, Springer, 2007, pp. 239–246.

[16] Measurement Technique for the Simulation of the Auditory Sensation of Sharpness, german institute for standardization (deutsches institut für normung) ed., DIN: Berlin, Germany, 2009.

[17] Daniel, P., and Weber, R., "Psychoacoustical roughness: Implementation of an optimized model," Acta Acustica united with Acustica, Vol. 83, No. 1, 1997, pp. 113–123.

[18] Besnea, I., "Acoustic imaging and spectral analysis for assessing UAV noise," Master's thesis, Delft University of Technology, 2020, http://resolver.tudelft.nl/uuid:d4e37451-78d6-4b7d-bb34-721d04c176dc.

**QUIET DRONES**
**Second International e-Symposium**
**on**
**UAV/UAS Noise**
**27th to 30th June 2022**

# Aeroacoustic investigation of co-rotating rotors

**Edoardo Grande, Delft University of Technology, Delft, The Netherlands: e.grande@tudelft.nl Shubham, Nottingham Trent University, Nottingham, United Kingdom: Shubham.shubham@ntu.ac.uk**
**Francesco Avallone, Delft University of Technology, Delft, The Netherlands: f.avallone@tudelft.nl**
**Daniele Ragni, Delft University of Technology, Delft, The Netherlands: d.ragni@tudelft.nl**
**Damiano Casalino, Delft University of Technology, Delft, The Netherlands: d.casalino@tudelft.nl**

## Summary
Aerodynamic performance and acoustic far-field of a small-scale, co-axial co-rotating rotor in hover are investigated by means of Lattice-Boltzmann Very-Large-Eddy simulations. The study focuses on the effect of the phase angle between the two co-rotating propellers. Co-rotating rotors are further compared with two single isolated rotors. The study demonstrates that increasing the azimuthal separation between the two co-rotating rotors, is beneficial for thrust production and noise reduction in the propeller plane because of destructive interference.

## 1. Introduction
In the past few years, Urban Air Mobility (UAM) has seen a rapid development. It involves developing fully electric Personal Air Vehicles (PAV) for rapid mobility of people. Since these air vehicles operate in an urban environment, public acceptance plays a key role; therefore, amongst other factors, it is essential to lower their noise signature, for given aerodynamic performances. The dominant aerodynamic noise source in these air vehicles is the propulsion system that is based on isolated or distributed propellers.

In order to meet the noise and aerodynamic requirements, keeping into account installation constraints, unconventional configurations must be explored such as co-axial co-rotating rotors [1]. They are characterized by two rotors, connected to the same shaft, rotating in the same direction. The distance between the two rotors can vary as well as the azimuthal angle between the propeller blades (named also phase angle). This configuration has gained scientific interest in the last years due to its potential as a low-noise design for hover and forward flight conditions.

The idea of a stacked co-rotating rotor was used for the first time in the automotive industry in 1909 by Mackaness, who utilized non uniform rotor blade spacing to enhance cooling fan performance. The first aerospace applications were seen in tail rotors of Apache AH-64D helicopters in the 1970s which comprised of non-orthogonal scissor-shaped stacked rotors. These configurations reduce the noise tonal component at the first Blade Passing Frequency (BPF) as shown by Gardner[2] and Melline et al.[3]. This was further proven by Dobrzynski[4] who showed that, due to destructive interference between the pressure signals of azimuthally shifted stacked rotor blades, there is 4 dB(A) drop in sound intensity in the rotor plane.

In 1974, Landgrebe et al.[5] performed experiments with a small scale 2x3-bladed co-rotating rotor in hover and showed that, with azimuthal separations of $30°$ and $45°$, improvements in performance when compared to a co-planar configuration can be obtained. Aerodynamic performances further increase with increasing axial separations between the two rotors. Rorke[6] using a similar full scale rotor, by testing 4 different azimuthal separation ranging from $25.2°$ to $62.1°$, measured 4 dB noise reduction at the first BPF for $43.6°$configuration and 6.1\% thrust increase for $34.4°$configuration. The latter was achieved by setting a differential collective pitch between the two rotors, with the upper rotor pitch angle being $1°$higher than the lower one. Tinney and Valdez[1] performed experiments on a 2x3-bladed co-rotating rotor and showed a 4.5 dB decrease in overall noise value when the upper rotor led the lower rotor by $102°$, compared to the case when this azimuthal separation was $12°$, which shows a higher destructive interference in the former.

Co-rotating rotors also show benefits when compared to contra-rotating ones. A comparison between 2x3-bladed co-rotating and contra-rotating rotor systems by Bhagwat[7] showed that the former achieve a 4\% gain in figure of Merit (FOM) values when the upper rotor led the lower rotor by $15°$. A similar comparison by Uheara et al.[8] showed a 4\% decrease in induced power coefficient with the value of the azimuthal separation being $10°$.

From a fundamental perspective, Tinney ae al.[1] proposed that noise reduction is caused by destructive interference between acoustic waves. In order to prove this statement and further explore the complex aerodynamic interaction between the two rotors, high-fidelity numerical simulations are carried out on the same geometry used in Tinney's experiments. Lattice-Boltzmann Very-Large-Eddy Simulations (LB-VLES) are carried out with the commercial software 3DS Simulia PowerFLOW.

## 2. Computational method

The CFD/CAA solver Simulia PowerFLOW 6-2021 is used in this study to compute the flow around the propellers and extract the resulting noise signature. The software is based on the Lattice-Boltzmann Method (LBM) with a wall-modeled Very Large Eddy Simulation (VLES) approach used for turbulence modelling. PowerFLOW solves the discrete Boltzmann equation for a finite number of directions. For a detailed description of the method, the reader can refer to Succi[9] and Shan[10] while to Chen and Doolen[11] for a review. The LBM determines the macroscopic flow variables starting from the mesoscopic kinetic equation, i.e. the Boltzmann equation. The discretization used for this particular application consists of 19 discrete velocities in three dimensions (D3Q19), involving a third-order truncation of the Chapman-Enskog expansion[12].The distribution of particles is solved by means of the Boltzmann equation on a Cartesian mesh, known as a lattice. An explicit time integration and a collision model are used. For the collision term, the formulation based on a unique Galilean invariant[13] is used. The equilibrium distribution of Maxwell-Boltzmann is adopted[12].

A Very Large Eddy Simulation (VLES) model is implemented to take into account the effect of the sub-grid unresolved scales of turbulence. Following Yakhot and Orszag[14] a two-equations $k-\epsilon$ Renormalization Group is used to compute a turbulent relaxation time that is added to the viscous relaxation time. To reduce the computational cost, a pressure-gradient-extended wall-model is used to approximate the no-slip boundary condition on solid walls[15,16]. The model is based on the extension of the generalized law-of-the-wall model[17] to take into account the effect of pressure gradient. These equations are iteratively solved from the first cell close to the wall in order to specify the boundary conditions of the turbulence model. For this purpose, a slip algorithm[11], obtained as generalization of a bounce-back and specular reflection process, is used.

The LB scheme is inherently unsteady and compressible with the low dissipation and dispersion properties, which allows it to resolve the sound pressure field directly up to a cutoff frequency corresponding to approximately 15 voxels per acoustic wavelength. Due to this requirement, however, it is often more feasible to employ an acoustics analogy for obtaining far-field noise. In this study, far-field noise is computed using the Ffowcs-Williams and Hawkings (FW-H) analogy[18]. In particular, the formulation 1A of Farassat and Succi[19] extended to a convective wave equation is used in this study[20]. The formulation has been implemented in the time domain using a source-time dominant algorithm[21]. Pressure fluctuations are recorded on three permeable surfaces. This approach considers a distribution of acoustic dipoles on the aerofoil surface[22], while other nonlinear contributions (e.g., turbulent aerofoil wake) are neglected.

## 3. Computational setup

A fixed-pitch 2x2-bladed co-rotating co-axial APC 18x5.5 MR propeller with a diameter D = is used. For this study, two configurations with two different azimuthal separations $\Delta\phi$ and fixed axial separation $\Delta z$ are investigated. They were selected from the large database reported by Tinney and Valdez[1]. Both configurations operate in hover conditions with a rotational velocity of 3000 rpm. The blade-tip Mach number and chord-based Reynolds number based on the chord length at 75% of the blade span ($c_{75}$ = 3.02 cm) are $M_t$ = 0.21 and Re = 1.1x10$^5$, respectively. In addition, a single 2-bladed APC 18x5.5 MR and a single 4-bladed 18x5.5 MR propeller are simulated at the same conditions as reference cases.

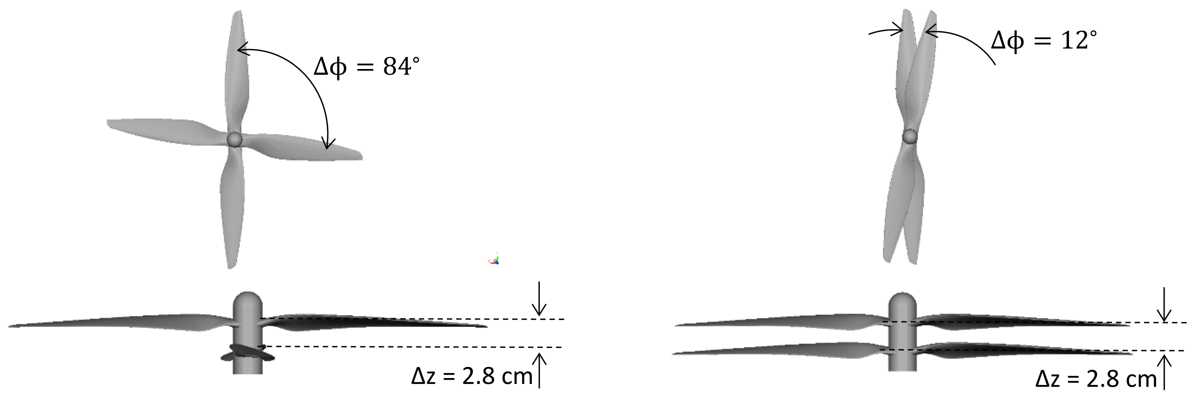


*Figure 1. Co-rotating rotors configurations*

The computational fluid domain is a spherical volume of 185D with the rotor at the center. Free-stream static pressure and velocity and a turbulence intensity of 0.1% of the free-stream velocity are prescribed on its outer boundary. The free-stream static pressure and temperature are set to 101.325 kPa and 288.1 K, respectively.
A total of 16 Variable Resolution (VR) regions are used to discretize the whole fluid domain, with the finest resolution regions placed around the blade leading edge and trailing edge.

Additional mesh refinement is done around the blade leading edge, trailing edge and tips, due to their significance in capturing accurate flow physics in a rotor flow field. The smallest voxel size is 0.054 mm, resulting in y+ = 13 on the blade surface. The resulting number of fine equivalent voxels for the current study is 55 million.

The simulations time is 0.24 sec, which corresponds to a total of 12 rotor rotations. After 2 transient rotations, results are sampled for 10 rotations. The far-field aeroacoustic analysis is performed by using the permeable formulation of the Ffowcs Williams and Hawkings acoustic analogy. A total of 3 spherical surfaces surrounding the rotor flow field are used as permeable FWH surfaces. In order to remove spurious noise caused by the hydrodynamic fluctuations in the wake of the propeller, data are sampled on the 3 permeable surfaces and far-field noise results are averaged. Acoustic data are sampled at 85 kHz and pressure spectra are then calculated using a Hanning window of 50\% overlap and a frequency resolution of 10 Hz.

## 4. Results

### 4.1 Aerodynamic performances

In order to assess the global aerodynamic performances of the two co-rotating configurations, the global thrust T and torque Q are evaluated and reported in the bar graph of Figure 2. The results are compared to the single 2-bladed and 4-bladed rotors. As $\Delta\phi$ decreases, the total thrust decreases from 11.62 N to 11.45N and torque stays almost constant. It is interesting to note that, when $\Delta\phi$ goes from $84°$ to $12°$, the thrust/torque of the upper rotor increases and the thrust/torque of the lower rotor decreases. Furthermore, the thrust of both the co-rotating configurations is higher than the single 4-bladed rotor (11.28 N) and lower of the double of the single 2-bladed rotor (2 x 7.7 N = 15.4 N).

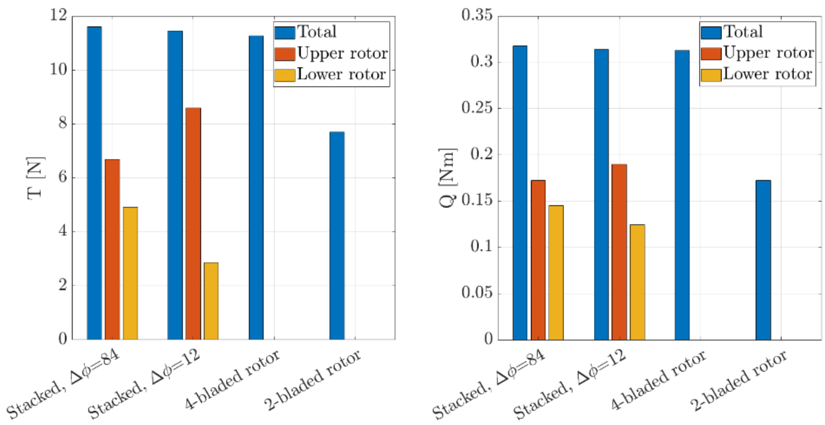


*Figure 2. Comparison of the total thrust T and torque Q between the two co-rotating configurations and the single 2-bladed and 4-bladed rotors.*

The thrust and torque for the two configurations provide integral information on the performances of the co-axial co-rotating configurations. In order to dig into the physics of interaction between the two rotors and the differences between the two configurations, a more detailed analysis is carried out. The radial distribution of thrust is shown in Figure 3, where the two co-rotating configurations are compared with the isolated ones. The figure shows that coupling two rotors has a strong effect on both the amplitude and radial distribution of T. For both $84°$ and $12°$ configurations, the thrust of lower rotor decreases because it operates in the streamtube of the upper rotors. For $\Delta\phi = 12°$, the lower rotor acts as a flap for the upper rotor, increasing the thrust of the latter. As a consequence, the increased upper rotor thrust induces more axial velocity, thus decreasing the angle of attack and the lower rotor thrust to a lower value with respect $\Delta\phi = 84°$. The lower rotor of both the co-rotating configurations is affected by blade vortex interaction (BVI), i.e. the rotor interacts with the tip vortices which affect the flow around the blades. The BVI is responsible of the local maximum at about r/R = 0.9. Finally, the thrust of the single 4-bladed rotor is less with respect to the upper rotor of both co-rotating configuration and this is expected to be caused by a stronger BVI effect. On the other hand, the thrust of the single 2-bladed rotor is higher of the upper rotor for the $84°$ configuration and lower of the upper rotor for the $12°$ configuration.

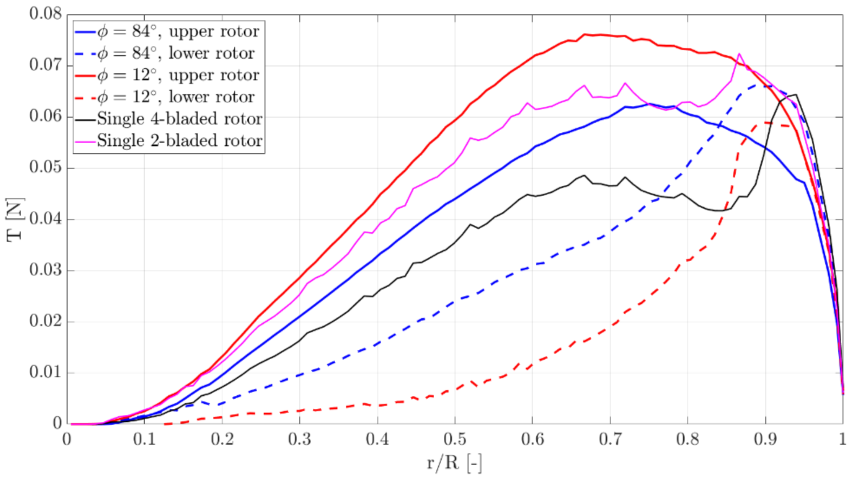

*Figure 3. Radial distribution of thrust for all the configurations.*

Based on the previous observations, it is possible to conclude that the potential flow effect and BVI effect are the two major flow phenomena that characterize the interaction between the two rotors. As potential interaction it is meant the effect on the streamtube (mentioned above) formed around each of the rotor disk because of the presence of two rotors. A co-rotating rotor setup can be seen as a superposition of two streamtubes of the upper and lower rotor. The BVI effect is investigated by showing the instantaneous vorticity in Figure 4 in a plane perpendicular to the rotors. The first row of the figure shows the vorticity in a plane aligned with the upper rotor, while the second row in a row aligned with the lower rotor. For both the configurations, the upper rotor tip vortex travel faster downstream with respect to the lower rotor tip vortex, due to the higher induced velocity from the upper rotor. As a consequence, the BVI is avoided for the upper rotor. The lower rotor instead interacts with the tip vortex (see second row of Figure 4) both for $\Delta\phi = 84°$ and $\Delta\phi = 12°$. For $\Delta\phi = 84°$, the lower rotor sees a vortex (from the upper rotor) above the rotor plane and a vortex (from lower rotor) below the rotor plane. For $\Delta\phi = 12°$, both the tip vortices (from upper and lower rotor) are below the lower rotor plane and the interaction is stronger, due to a reduced distance of the lower rotor tip vortex from the rotor plane.

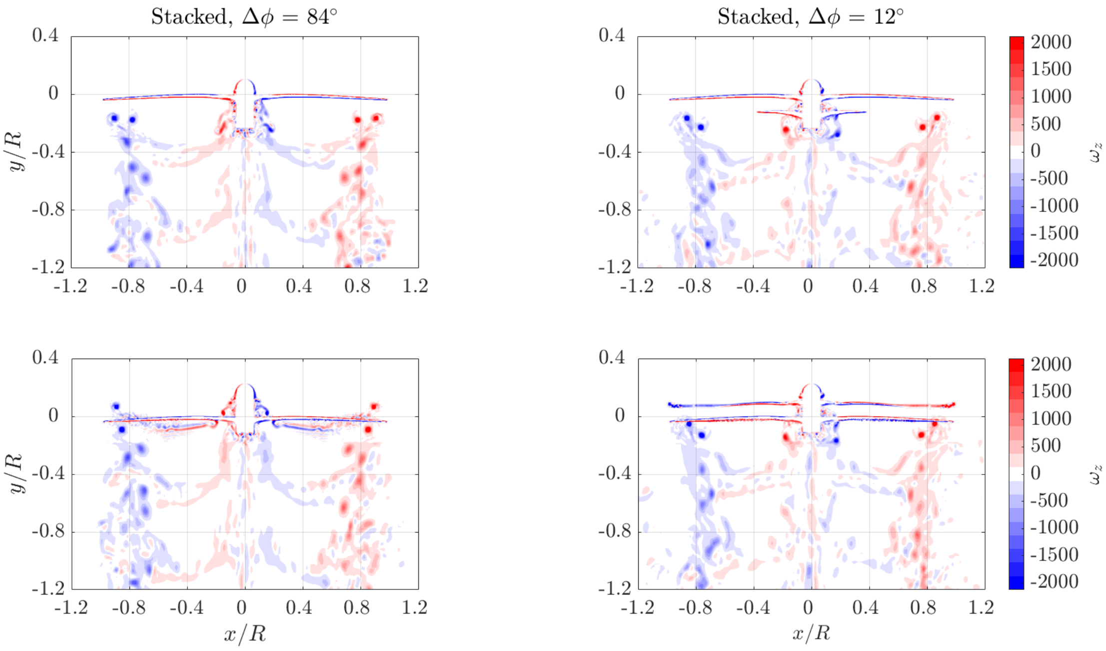


*Figure 4. Instantaneous vorticity contour plot in a plane perpendicular to the rotors and aligned with the upper rotor (first row) and the lower rotor (second row).*

### 4.2 Aeroacoustics

The noise emission is studied using a circular array of 36 microphones, located in a plane perpendicular to the rotor plane. Noise spectra at the rotor plane (Mic 1) and upstream the rotor plane (Mic 28), at a distance of 3D from the center of the rotors, are plotted in Figure 5. As for the aerodynamic loads, the co-rotating configurations are compared with the single 2-bladed and 4-bladed rotors. At both microphones location, the tone at 100 Hz represents the first blade passing frequency (BPF) for the two co-rotating configurations and the single 2-bladed rotor. On the other hand, the single 4-bladed rotor has the first BPF at 200 Hz.

At Mic 1 (in-plane), the low-frequency range is dominated by the tonal noise component and the high-frequency range by the broadband one. The configuration $\Delta\phi = 12°$ exhibits a first BPF tone 17 dB higher with respect to $\Delta\phi = 84°$. This is due to destructive interference between the acoustic wave radiated by the upper and lower rotors. This is clearly shown in Figure 6 where the acoustic pressure signals from the upper and lower rotor at Mic 1 are plotted separately, for four propeller rotations. It is evident that for $\Delta\phi = 84°$, the acoustic waves are more out of phase compared to $\Delta\phi = 12°$, thus justifying the different tonal noise components. For both $84°$ and $12°$, the amplitude of the fluctuations is higher for the upper rotor due to the higher thrust. When comparing the co-rotating setups with the single rotor cases, it appears that the single 4-bladed configuration is characterized by the lowest BPF 1, because of the lower thrust per blade.

At Mic 28 (out-of-plane), the level of first BPF for all the configurations reduces due to the dipolar behaviour of the tonal noise with a maximum at the rotor plane. The effect of the destructive interference is visible also at this location, with the $\Delta\phi = 84°$ setup showing a lower first BPF with respect to $\Delta\phi = 12°$. On the other hand, at high-frequency the overall level of the broadband noise is higher compared to the spectra at Mic 1.

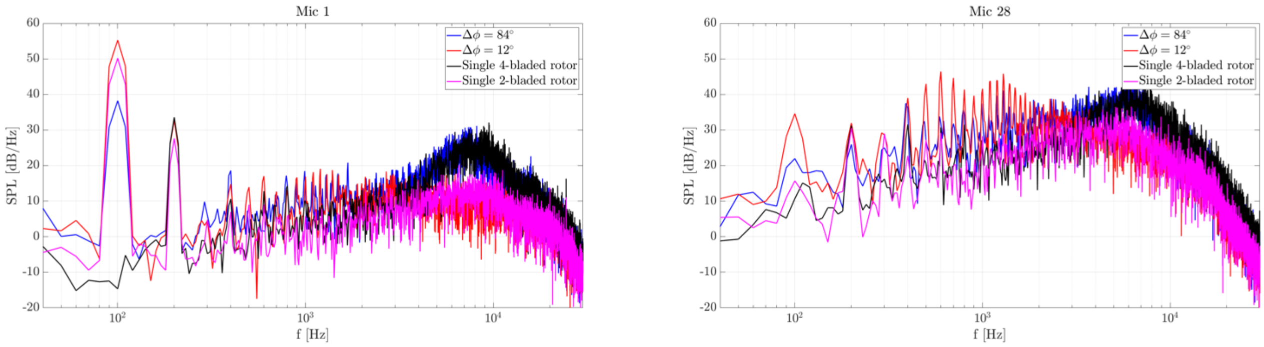


*Figure 5. Noise spectra comparison at the rotor plane (Mic 1) and upstream the rotor plane (Mic 28).*

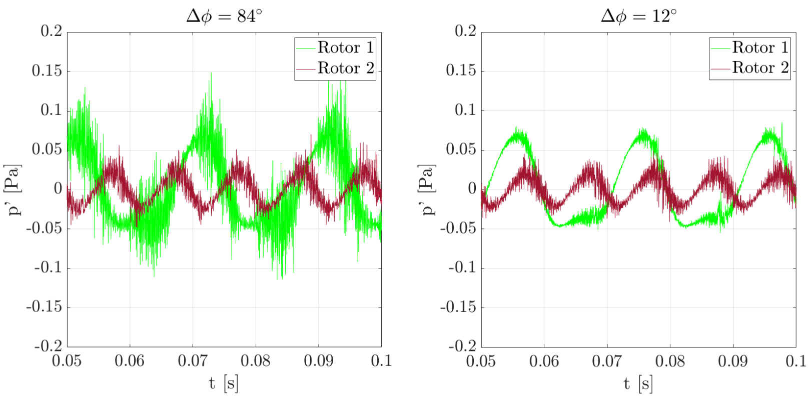


*Figure 6. Time variation of the acoustic pressure signals for the upper and lower rotor.*

Figure 7 shows the OASPL, in the frequency range 80-240 Hz, evaluated for all the microphones of the circular array. For each configuration, the OASPL is scaled with the total thrust. Overall, the single 4-bladed rotor is the configuration that exhibit the lowest tonal noise emission. Both the co-rotating setups are acoustically more efficient than the single two-bladed rotor. In particular, at the rotor plane:

- the $\Delta\phi = 84°$ configuration produces 4.7 dB per unit thrust
- the $\Delta\phi = 12°$ configuration produces 6.2 dB per unit thrust
- the single 2-bladed rotor produces 7 dB per unit thrust.

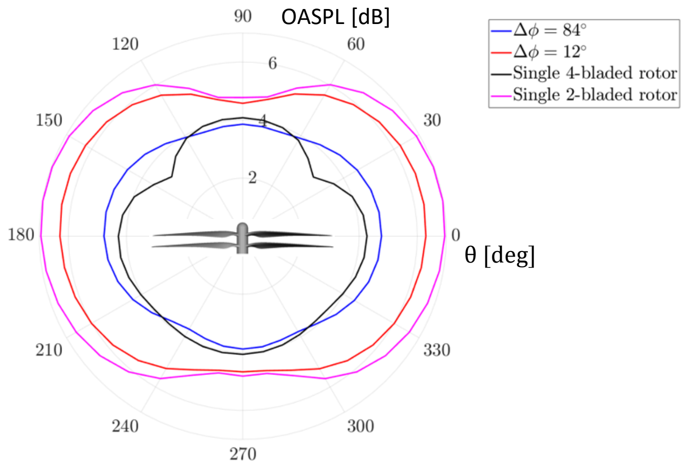


*Figure 7. OASPL (frequency range 80-240 Hz) scaled with the total thrust for each configuration, in a plane perpendicular to the rotor plane.*

It is interesting to note that, the co-rotating configuration $\Delta\phi = 84°$ radiates less tonal noise (per unit thrust) with respect to $\Delta\phi = 12°$ and more noise with respect to a single 4-bladed rotor, which is the most similar single rotor configuration. Conversely, the configuration $\Delta\phi = 12°$ radiates more tonal noise (per unit thrust) with respect to $\Delta\phi = 84°$, but less noise with respect to a single 2-bladed rotor, which is the closest single rotor configuration. Therefore, the $12°$ configuration can be adopted, for instance, in vehicles with retractable propellers, in place of a single 2-bladed rotor, having higher thrust and lower tonal noise per unit thrust.

## 5. Conclusions

An aerodynamic and aeroacoustic investigation was conducted on a 2x2-bladed co-rotating rotor formed by two identical 2-bladed APC 18x5.5 MR propeller stacked on top of each other. By varying the azimuthal separation between the upper and lower rotor blades while keeping all other variables the same, two separate configurations were simulated and compared. To understand the behaviour of upper and lower rotor separately, each of them was compared to the results of a 2-bladed and 4-bladed isolated rotors operating at the same flow conditions.

The rotor with higher azimuthal separation showed an increased thrust value than compared to the rotor with lower azimuthal separation. The aerodynamic behaviour of the co-rotating system is affected by: a potential non-viscous effect because of the mutual interaction of streamtubes of the two rotors; and rotor-wake/rotor-tip vortex interaction. It is further noticed that for the configuration with lower azimuthal separation the lower blade acts as a flap for the upper rotor.

Noise was calculated by performing a far-field analysis using Ffowcs-Williams and Hawkings (FWH) methodology. Overall, the single 4-bladed rotor exhibits the lowest tonal noise emission. When comparing the configuration $\Delta\phi = 84°$ with respect to $\Delta\phi = 12°$, the first one is characterized by a lower tonal noise emission because of the destructive interference between the acoustic waves.

The study provides various points where further investigations can be performed. As mentioned by Tinney and Valdez for a small-scale rotor, tip loss and Reynolds number effects need to be taken into account. It is hypothesized that best aerodynamic and aeroacoustic performances can be obtained using upper and lower rotors with different pitch angles. These studies can be complemented with studies on increased rotational speed of the co-rotating rotor and the corresponding change in noise values.

**References**


1. Tinney CE, Valdez J. Thrust and Acoustic Performance of Small-Scale, Coaxial, Corotating Rotors in Hover. *AIAA J*. Published online 2019:1-11.
2. Gardner AD. Fan. Published online 1932.
3. Mellin RC, Sovran G. Controlling the tonal characteristics of the aerodynamic noise generated by fan rotors. Published online 1970.
4. Dobrzynski W. Propeller noise reduction by means of unsymmetrical blade-spacing. *J Sound Vib*. 1993;163(1):123-126.
5. Landgrebe AJ, Bellinger ED. Experimental investigation of model variable-geometry and ogee tip rotors.[aerodynamic characteristics of variable geometry rotary wings]. Published online 1974.
6. Rorke JB. Hover performance tests of full scale variable geometry rotors. Published online 1976.
7. Bhagwat M. Co-rotating and Counter-rotating Coaxial Rotor Performance. *AHS Aeromechanics Des Transform Vert Flight*. Published online 2018.
8. Uehara D, Sirohi J. Quantification of Swirl Recovery in a Coaxial Rotor System. In:

*Proceedings of the 73rd Annual Forum*. ; 2017.
9. Succi S. *The Lattice Boltzmann Equation: For Fluid Dynamics and Beyond*. Oxford university press; 2001.
10. Shan X, Yuan XF, Chen H. Kinetic theory representation of hydrodynamics: a way beyond the Navier–Stokes equation. *J Fluid Mech*. 2006;550:413-441. doi:10.1017/S0022112005008153
11. Chen S, Doolen GD. Lattice Boltzmann method for fluid flows. *Annu Rev Fluid Mech*. 1998;30(1):329-364.
12. Chen H, Chen S, Matthaeus WH. Recovery of the Navier-Stokes equations using a lattice-gas Boltzmann method. *Phys Rev A*. 1992;45(8):5339-5342. doi:10.1103/PhysRevA.45.R5339
13. Chen H, Zhang R, Gopalakrishnan P. Lattice Boltzmann Collision Operators Enforcing Isotropy and Galilean Invariance. Published online 2015. https://patents.google.com/patent/US20150356217A1/en
14. Yakhot V, Orszag SA. Renormalization group analysis of turbulence. I. Basic theory. *J Sci Comput*. 1986;1(1):3-51. doi:10.1007/BF01061452
15. Teixeira CM. Incorporating Turbulence Models into the Lattice-Boltzmann Method. *Int J Mod Phys C*. 1998;09(08):1159-1175. doi:10.1142/S0129183198001060
16. Wilcox DC. *Turbulence Modelling for CFD (Third Edition)*. DCW Industries, Incorporated; 2006.
17. Launder BE, Spalding DB. The numerical computation of turbulent flows. *Comput Methods Appl Mech Eng*. 1974;3(2):269-289. doi:10.1016/0045-7825(74)90029-2
18. Ffowcs Williams JE, Hawkings DL. Sound generation by turbulence and surfaces in arbitrary motion. *Philos Trans R Soc London Ser A, Math Phys Sci*. 1969;264(1151):321-342.
19. Farassat F, Succi GP. A review of propeller discrete frequency noise prediction technology with emphasis on two current methods for time domain calculations. *J Sound Vib*. 1980;71:399-419.
20. Brès G, Pérot F, Freed D. Properties of the lattice Boltzmann method for acoustics. In: *15th AIAA/CEAS Aeroacoustics Conference (30th AIAA Aeroacoustics Conference)*. ; 2009:3395.
21. Casalino D. An advanced time approach for acoustic analogy predictions. *J Sound Vib*. 2003;261(4):583-612.
22. Curle N. The influence of solid boundaries upon aerodynamic sound. *Proc R Soc London Ser A Math Phys Sci*. 1955;231(1187):505-514.

QUIET DRONES
International e-Symposium
on
Second UAV/UAS Noise
27th to 30th June 2022

# A Summary of the 2020 e-Workshop: Aerial Mobility - Noise Issues and Technology.

**Robert D. Hellweg, Jr., Hellweg Acoustics: Hellweg@HellwegAcoustics.com**
**Adnan Akay, Bilkent University: akay@cmu.edu**
**Gregg Fleming, United States Department of Transportation – Volpe National Transportation Systems Center: Gregg.Fleming@dot.gov**
**George C. Maling, Jr., Managing Director Emeritus INCE-USA: georgemaling.nae@gmail.com**
**Eric W. Wood, Acentech Inc.: ewood@acentech.com**

## Summary

The U.S. National Academy of Engineering (NAE) hosted an e-workshop "Aerial Mobility: Noise Issues and Technology" on December 2-3, 2020 attended by 71 individuals. The purpose of the December 2020 workshop was to examine several facets of the increasing interest in air or aerial mobility vehicles, which are often referred as "urban air mobility" (UAM). The workshop was organized by the INCE Foundation in cooperation with the U.S. National Aeronautics and Space Administration (NASA) and the U.S. Federal Aviation Administration (FAA). The workshop had 22 presentations from representatives of world-wide air mobility vehicle manufacturers and users, U.S. government agencies, universities, consultants and professional societies. There were presentations on a wide-range of topics, including a summary of the 2020 Quiet Drones eSymposium, regulatory issues and standards, community acceptance, modelling, the design of air mobility vehicles, psychoacoustics, noise reduction strategies, measurement techniques, and legal issues. The 2020 workshop report includes a summary of each presentation and images of selected slides, and the report is available on the INCE/USA web page at https://www.inceusa.org/publications/technical-reports/.

# 1. Introduction

The purpose of the December 2020 workshop was to examine several facets of the increasing interest in air or aerial mobility vehicles. "Air mobility" or "aerial mobility" is the preferred term for what was previously referred to as "urban air mobility"; the reason being that there are many vehicles used outside of urban areas and the term aerial mobility vehicle is much broader. The 2020 workshop was a follow-on to the 2018 NAE hosted workshop *UAS and UAV (Drone) Noise Emissions and Noise Control Engineering Technology*. Available at: https://www.inceusa.org/publications/technology-for-a-quieter-america

Opening remarks were provided by workshop steering committee member George Maling (NAE member, and INCE-USA Managing Director Emeritus). He said that this workshop is the eleventh in a series of noise-related workshops hosted by the NAE.

Maling said there were three significant events in the second half of 2020. The first was a National Academies of Science, Engineering, and Medicine consensus study report *Advancing Aerial Mobility: A New Blueprint*, the second was the NASA white paper on *Urban Air Mobility Noise: Current Practice, Gaps, and Recommendations*, and the third was the Quiet Drones 2020 eSymposium organized by INCE Europe. All three of these events were covered in more detail during three presentations as described in 2.1, 2.2, and 2.3 below.

NAE President John Anderson welcomed the delegates to the workshop on the first day and pointed out that the topic of noise played a major role in the development of the National Academies' rigorous review process used to protect the integrity of the Academies' reports and workshop proceedings. There was an NAE consensus report prepared on the noise from supersonic aircraft in the 1960s, and after release it became apparent that the conclusions were not properly reviewed. As a result, the NAE review process was greatly strengthened.

Anderson also pointed out that technology-related issues that affect the public must be presented to the government and citizens alike in a nonpartisan way. This series of NAE hosted noise workshops (including this one as a prime example), which are a follow-on to the 2010 NAE consensus study report *Technology for a Quieter America*, helps fulfil that mission. The 2010 NAE report: https://www.nae.edu/27531/Technology-for-a-Quieter-America

Alton Romig, the NAE executive officer, welcomed the participants on the second day of the workshop. Before his appointment at the NAE, he served as general manager of Lockheed Martin's Skunk Works. With regard to the design of NASA's X-59 supersonic aircraft, Romig said that building the aircraft and flying it is step one. Step two is to send in the psychologists and sociologists to measure the population's reaction. He said that a similar approach to vehicle design and acceptance of the associated noise could be used for aerial mobility vehicles.

The following sections contain brief summaries of each presentation organized by general categories: Keynote addresses and overview presentations; design of aerial mobility vehicles; regulations and standards; community acceptance and modelling; psychoacoustics; and legal issues. Note that many of the presentations covered aspects of more than one category but are included in only one category in this paper.

# 2. Keynote Addresses and Overview Presentations

## 2.1 Advancing Aerial Mobility: A National Blueprint

The first keynote address was by Nicholas Lappos (Lockheed Martin) who served as chair of the committee that developed a National Academies of Sciences, Engineering, and Medicine (NASEM) report on *Advancing Aerial Mobility: A National Blueprint*.

He said that environmental responsibility is central to the vision for advanced aerial mobility, and is important for noise as well as other environmental factors. He pointed out that in early

2020, 205 different aerial mobility vehicles were in development and suggested that perhaps only 20 or 50 would survive. He said that it may take 15 years to see the report's vision through with all its benefits to users, our economy, and our citizens.

The National Academies report made the following recommendation:

*Research should be performed to quantify and mitigate public annoyance due to noise, including psychoacoustic and health aspects, from different types of advanced aerial mobility operations. NASA should facilitate a collaboration between relevant government agencies--including FAA, Department of Defense, National Institutes of Health, academia, state and local governments, industry, original equipment manufacturers, operators, and nonprofit organizations--to prioritize and conduct the research with responsibility allocated per a coordinated plan and accountability for delivery incorporated. The research should be completed in two years.*

### 2.2 A Brief Summary of the Quiet Drones 2020 e-Symposium

The second keynote speaker was Jean Tourret, INCE/Europe President, who spoke about the 2020 Quiet Drones e-Symposium, which was organized by INCE/Europe on October 19-20, 2020. Tourret co-chaired the e-Symposium with Dick Bowdler (Director INCE/Europe).The symposium attracted 80 abstracts and was attended by 170 delegates from 22 countries. A proceedings book with forty-six papers and more than 500 pages was published.

There were nine technical sessions, and Tourret highlighted two technical sessions. He first discussed the session on “Specific noise concerns with packages and deliveries.” Presentations showed successful operation of a drone package delivery system in Australia after addressing noise reduction at the source and community relations. Another presentation discussed the operation of a package delivery system in rural France “with no complaints received about noise.”

He also highlighted a session on “Regulations and Standardization”. One topic covered was the situation with regard to regulation in Europe. David Read and Christopher Roof (U.S. Department of Transportation (DOT), Volpe Center) pointed out that existing aircraft noise certification methods may not fully address needs as these new aerial mobility vehicles enter the airspace. Nicolas Eertmans from the European Commission's Directorate-General for Mobility and Transport discussed the EU's regulatory framework for unmanned aircraft. Michael Wieland with the UAV-DACH Unmanned Aviation Association discussed regulations for unmanned aircraft under European Regulation 2019/945.

Jean Tourret said that the Quiet Drones e-symposium confirmed that noise from drones is a broad, "hard and fast-developing" topic. He also discussed the low pace of noise-related regulation and used as an example wind turbine noise regulations that have been discussed for some two decades, but regulations have not been finalized in Europe or internationally.

### 2.3 Summary of the UAM Noise Working Group White Paper

Stephen Rizzi (NASA) described the NASA Urban Air Mobility Working Group study which was initiated in 2018 to produce a "white paper" on urban air mobility noise. The working group had several subgroups including: 1) tools and technology, 2) ground and flight testing, 3) human response and metrics, and 4) regulation and policy. The result of the working group was the NASA white paper published in October 2020 *Urban Air Mobility Noise: Current Practice, Gaps, and Recommendations*.

Some of the recommendations from the NASA white paper were:

- Further development of system noise projection tools.
- Validation of prediction models for the highest amplitude noise sources.
- Continued development of auralization tools.

- Development of new measurement approaches in collaboration with various stakeholders.
- Development of standardized procedures for measuring and cataloging ambient noise.
- Perform laboratory studies to help inform how different the annoyance to short-term exposure to UAM is from existing aircraft.
- Develop models for audibility, noticeability, and annoyance to UAM aircraft noise. Study above differences in perception of UAM vehicle noise between communities.
- Collaboration with FAA and other agencies on standards for UAM noise.

### 2.4 The Future of the Air Cargo Industry

Stephen Alterman (Cargo Airline Association) said that transformative changes are underway, and more are in store, for the huge and growing air cargo industry. Drones are already handling the so-called "last mile" of product delivery, and urban mobility vehicles—either autonomous or piloted—are expected to play an ever-increasing role in this cargo market. Among other challenges, the industry is eyeing improved environmental friendliness—including decreased noise—for its aircraft, through efficient routes, and eventually even electric aircraft.

## 3. Design of Aerial Mobility Vehicles

### 3.1 From Helicopters to Quiet eVTOLs - a Manufacturer's Perspective

Julien Caillet (Airbus Helicopters) said that the noise of helicopters is well regulated by the International Civil Aviation Organization (ICAO) Annex 16. He discussed design considerations for helicopters and identified rotor design as a key noise level driver. The company's lessons learned about helicopter noise and its impact on communities can contribute importantly to the understanding of noise issues in advanced aerial mobility vehicles. Caillet also said that the community impact from noise is a primary consideration for aerial mobility vehicle manufacturers and operators. He said that Airbus currently uses conventional noise metrics but that other metrics are being considered, and the research community is in a better position than manufacturers to develop such metrics.

### 3.2 Brief History of Unmanned Flying

Brian Yutko (Boeing NeXT) talked about the first principles of design for a new class of air vehicle enabled by alternative propulsion systems. This emerging class of novel air vehicles includes:

- Multicopter design with no wings that flies entirely on hover lift;
- Separate lift-and-cruise-winged electric vertical takeoff and lift (eVTOL) aircraft;
- "Tilt-something" eVTOLs that combine lift propulsors and cruise propulsors into a complex, generally tilted arrangement;
- Electric super-short takeoff and landing (eSSTOL) vehicles; and
- Hybrid eVTOL concepts.

He said that noise is much more than decibels. The physics of noise is one aspect to be considered, but annoyance is complicated and subjective. His own perception of noise was illustrated in a helicopter flyover which he characterized as very annoying and intrusive while the electric VTOL aircraft noise was "much more random and much less annoying."

### 3.3 NATO Work on Progress for Reducing Propeller and Rotor Noise from Unmanned Aircraft

Philip Morris (Pennsylvania State University) described the work of a NATO Science and Technology Organization Research Task Group (RTG) AVT-314. The NATO RTG objectives are to provide an assessment of the state-of-the-art in unmanned aerial systems (UAS) noise prediction and reduction, and a technical assessment of the noise from UAS operations. The focus is on propeller and rotor noise, along with improved operational effectiveness in both the civilian and military contexts.

The research task group has international participation from several NATO countries including Sweden, which is a not a NATO member. The group has met several times to discuss various aspects of UAS noise reduction. The focus of the research is on reducing propeller and rotor noise from UAS. A technical paper on the research is expected to be prepared by the end of 2021 [since updated to mid-2022].

## 4. Regulations and Standards

### 4.1 FAA Perspective on Aerial Mobility

James Hileman (FAA) spoke about regulatory issues. Although the regulations for subsonic aircraft noise are well-defined, the question of helicopter noise is a somewhat different issue because anecdotal evidence suggests that people are troubled by helicopter noise at cumulative noise levels "far below" the cumulative noise levels of fixed-wing aircraft. Helicopter noise is a low frequency phenomenon that travels long distances. The sound sources are complex. However, helicopter noise and its measurement may serve as a guide for the regulation of aerial mobility vehicles. There is work going on both at the USDOT Volpe Center and at universities to define metrics for quantifying community noise from aerial mobility vehicles.

This work will complement the Aviation Environmental Design Tool (AEDT) described by Rizzi in 5.2 below. The FAA is working very closely with NASA and the Volpe Center and welcomes opportunities to collaborate with others in government, industry and academia.

### 4.2 Overview of Future Noise Certification Needs for Aerial Mobility Aircraft

Donald Scata (FAA) continued with the discussion of regulation of aerial mobility vehicles. The FAA considers factors such as the day-to-day operation, flight altitudes, flight speeds, appropriate metrics, and methods of noise measurement in researching the best solution for certification. The FAA is considering revisions to the regulations for fixed-wing aircraft in the U.S. Code of Federal Regulations (CFR) 14 CFR Part 36.

Whether aerial mobility vehicles can fit within some of the categories already specified in the regulation remains to be seen and is an open question. While the current categories may cover some aerial mobility aircraft, new noise considerations are needed for a range of aerial mobility vehicles because of their unique noise characteristics and flight controls. There are many benefits to the FAA from other organizational partnerships and the agency is interested in fostering partnerships to collect environmental information, including noise data to improve the understanding of the acoustics of these aerial mobility aircraft and implications for their incorporation into the national airspace.

### 4.3 Research Considerations for Aerial Mobility and the Role of Noise Certification

David Read (U.S. DOT Volpe Center) said that the idea that public acceptance of aerial mobility aircraft will depend in a large part on effective management of noise. Aircraft noise certification is an important part of the process of determining community acceptance. Certification requires a noise metric, and he pointed out that noise metrics are different for different sources, for example, small propeller-driven fixed wing aircraft, small helicopters, and jets together with large propeller-driven airplanes, as well as large helicopters. He presented data on several typical sources.

He next presented Volpe's recommendations to support noise certification of aerial mobility vehicles. He said that noise from these aircraft may exhibit annoyance effects substantially different from what the public has previously experienced with other aircraft. He said that there is a lack of representative noise datasets, and when these datasets are available, the next step will be evaluation to determine whether any updates are needed to the existing noise certification paradigm.

### 4.4 What Is a Sufficient Noise Metric?

Andrew Christian (NASA) discussed noise metrics as related to UAS and aerial mobility vehicles. A trade-off exists between a metric's simplicity and its power, and a sufficient metric balances the power to resolve features of a noise germane to annoyance with the resources required to evaluate it.

He discussed the tone-corrected perceived noise level (PNLT), which is considerably more complex than metrics based on A-frequency weighting. The PNLT has its roots in the difference between perception of noise from propeller aircraft and noise from early jet engines which have tones. The PNLT approach more faithfully captured the human reaction to noise. Modern instrumentation makes this quantity easy to measure.

Christian concluded that even more complex metrics may be required in the future for the use with aerial mobility vehicles.

### 4.5 Recent Work of ANSI S12/WG58 on Small UAV Sound Measurement

Kevin Herreman (Owens Corning) described the work of one non-governmental organization dealing with standards for the measurements of the sound power emission from small unmanned aerial systems (UAS) - the Acoustical Society of America Accredited Standards Committee S12 (Noise) Working Group 58. Led by Kevin Herreman, this working group has about 30 members and was created in 2016 to develop and maintain a new standard for the determination of sound power level from small unmanned aerial systems measured in an anechoic chamber. Herreman's presentation described considerable testing performed by Owens Corning, NASA and others. A draft American standard for small fixed-wing unmanned aerial vehicles (UAV) was expected by the end of 2021. [This has not yet been drafted--Ed.]

## 5. Community Acceptance and modelling

### 5.1 Advanced Air Mobility: Facilitating Community Acceptance

Mary Ellen Eagan (Harris Miller Miller & Hanson) discussed the importance of effective communications strategies tailored for a range of stakeholders. Essential to the success of community acceptance is effective communication within each group, for example, manufacturers, operators, FAA officials, local governments, and the general public. She also spoke of noise metrics and pointed out that the current metric used for certification of aircraft, effective perceived noise level, and the metric used for assessment of annoyance around airports, the day-night average sound level, may not be sufficient for identifying problems with advanced air mobility vehicles. Conducting and funding research on annoyance from these vehicles is imperative.

### 5.2 UAM Fleet Noise Assessments Using the FAA Aviation Environmental Design Tool

Stephen Rizzi (NASA) made a second presentation on the FAA Aviation Environmental Design Tool (AEDT) for conducting UAM fleet noise assessments. He said that at present AEDT is not fully equipped to handle UAM community noise studies, since the tool's lack of an aircraft noise and performance (ANP) model for UAM vehicles. He discussed many of the factors that must be added to make the AEDT useful for UAM studies including operational state determination, calculation of noise-power-distance (NPD) data, modeling approach, and other aspects. The results of these studies will be input to the AEDT database.

### 5.3 Community Response to UAS Noise in the Virginia IPP

Mark Blanks (Virginia Polytechnic Institute and State University Mid-Atlantic Aviation Partnership) also addressed the general theme of community acceptance. He spoke of a project to measure community acceptance of UAS deliveries of packages to actual residences. Community reaction to the drone delivery service was overwhelmingly positive, breaking down as 86% positive, 13% neutral, and 1% negative.

In addition, Blanks explained the noise mitigation used by the company based on its experience in Australia. The company took three major actions to manage noise from its operations: 1) locating its "nest," which is its operations hub for take-offs and landings, away from residential areas, 2) randomizing flight paths, with the aim of approaching from a different angle for repeated deliveries to the same place, and 3) designing aircraft with noise reduction in mind. Blanks summarized by saying that gaining the needed acceptance for these vehicles relies on maximizing the value to communities while ensuring there concerns are addressed.

### 5.4 Advanced Air Mobility: Facilitating Community Acceptance

Javier Caina (DJI) raised the issue of community acceptance and regulations by saying "is there really even a problem with the drone noise?". Caina recognized, however, that concerns had been raised of late based on the repetitive flights, larger aircraft, and other characteristics of some drone package delivery operations.

He said that there are many challenges with regards to drones, particularly in the European Union. Caina presented some concluding thoughts about EU regulation of small UAS noise, stating that the current European regulation requires a pace of noise reduction that is unrealistic from the industry perspective. Without complaints relating to the type of aircraft DJI is developing, the development of regulatory approaches "seems indeed to be a solution in search of a problem."

### 5.5 Reducing Community Noise from Delivery Drones Through Route Optimization

Eddie Duncan (RSG) and Kenneth Kaliski (RSG) discussed a community noise case study that focused on community acceptance through the design of optimized routes for delivery services. The premise of this work was that noise can be annoying, which requires it to be "at least audible and, more likely, noticeable." Annoyance can be lessened by reducing audibility through sound masking using existing noise or by minimizing population impact.

The community noise map, coupled with historical sound level measurements in the area, provided a baseline for the study. For sound emission data, they used data reported in a conference proceedings for a commercial-grade hexacopter. (Duncan noted that sound emission data for commercial grade drones is sparse.)

Their analysis determined noise exposure of a population considering four flight routes: direct, over roadways, waterways, and railways. Noise mapping, coupled with an analysis of routing options, was shown to represent a powerful tool for quantifying and reducing noise impacts from drone delivery services. However, to take advantage of the potential for routes over certain areas to provide a level of masking and reduce noise impacts, more and better information is needed on drone sound emissions.

### 5.6 Framework for Translating Noise Considerations Into Acceptable Zones for Vehicle Operations and Routing

John-Paul Clarke (University of Texas) covered operations and routing for air mobility vehicles. He said that trajectory optimization can play a key role within a toolkit for addressing community noise concerns associated with air mobility. Trajectory optimization can also play an important role in terms of efficiency, privacy, and safety. He said that rotorcraft noise can be reduced by optimizing arrival (descent) and departure (ascent) trajectories. Such trajectories can also be designed to increase the distance from a receiver and to keep trailing blades away from the wake of preceding blades, etc.

Clarke suggested that noise thresholds can be converted into 3D constraints. And these constraints can be converted to the equivalent of an acoustic terrain to determine optimization for a trajectory. In this way, noise within an acoustic terrain can be treated the same way as a physical terrain. He also suggested that geofences may be created to define areas where aircraft may not enter.

## 6. Psychoacoustics

There were three presentations on psychoacoustic considerations for advanced aerial mobility.

### 6.1 Why Is Predicting Audibility So Hard?

Andrew Christian (NASA) shared his views on the difficulties associated with predicting the audibility of signals in noise. Aarriving at an audibility prediction provides a needed foundation for assessing annoyance from, and understanding community response to, urban air mobility noise. Much of the aerial mobility-related work at NASA in the couple of years preceding the 2020 workshop was focused on creating models of audibility to aid in the prediction of annoyance.

Christian introduced two rules of thumb from the literature regarding the link between annoyance and audibility:

- When sources of noise are sufficiently prominent over the ambient noise level, there is no strong effect of the ambient level on annoyance; and
- When sources of noise get close to the ambient noise, a masking effect occurs that affects annoyance in ways unexplained by the sound reduction of the source itself.

When the background noise is very high, there is little problem detecting when a sound is audible. On the other hand, as the sound is lowered and becomes partially masked by the background noise, audibility is hard to predict, and this was the area studied by Christian.

Christian concluded his presentation with the following points:

- Predicting audibility is difficult, but likely necessary for the assessment of noise-induced annoyance from UAM.
- Many complicating effects may contribute to the audibility of aerial mobility vehicles operating in already-noisy environments.
- UAM audibility models have not yet been fielded, due to a dearth of data and the inability to perform psychoacoustic tests.

### 6.2 Sound Quality and Its Potential Influence on the Acceptability of Noise from Aerial Mobility Vehicles

Patricia Davies (Purdue University) presented information on sound quality. Sound quality greatly influences a person's reaction to sounds and therefore its acceptability. Quantities such as spectral balance, tonalness, signal variations, impulsiveness, and harmoniousness are important characteristics of a signal that influence sound quality.

Davies stated that the following sound characteristics beyond sound level may play an important role in people's judgment of UAM vehicle sound: presence and variation of tonal components, effects from combination of sources, and impulsiveness.

There has been progress in the standardization of sound quality measures, but there are still many outstanding challenges. We already have many measures or metrics for noise emissions, such as day-night average sound level (DNL). Davies said a challenge will be to incorporate some of the sound quality metrics into a metric such as DNL.

Davies concluded with a recommendation: It is important to listen to what people are saying about vehicle sounds; how people describe sounds should be considered alongside quantitative sound metrics. Hearing virtual vehicle designs has an important role in vehicle sound optimization.

### 6.3 Air Mobility Operational Noise: Perception and Other Community Considerations

Judy Rochat (Cross-Spectrum Acoustics) spoke about community impact, including perception, and particularly the spectral content of noise emissions. Rochat said that spectrograms provide a visualization of prominent tones and gave several examples. Noise from aerial mobility vehicles is highly tonal and that affects community response. Rochat pointed out that the existence of three or more harmonics can make a sound more alarming or urgent and contributes to the sound's harshness.

Rochat also discussed the question of flight corridors, and gave several ideas on how to minimize noise issues. For example, selection of a route that helps to shield noise from observers. Another example: Alternating aerial mobility vehicle routes—for neighborhood package delivery, can minimize noise annoyance resulting from the same people being continually exposed to noise.

## 7. Legal Issues

### 7.1 Legal Preemption and Aerial Mobility Noise Concerns

Robert Kirk (Wilkinson Barker Knauer) suggested the "FRISCO" approach provides a useful framework for analyzing noise issues. (FRISCO = Federal Regulation, Industrial Safeguards/Standards, and Community Outreach). He expanded on the FRISCO approach and highlighted the importance of public acceptance for the aerial mobility vehicle industry's success.

There must be coordination with state and local governments in the determination of community impacts, otherwise such governments may attempt to enact airspace regulations even though they are precluded by federal preemption from directly regulating aerial mobility laws.

## 8. Conclusions

There were presentations on a wide-range of topics, including a summary of the 2020 Quiet Drones eSymposium, regulatory issues and standards, community acceptance, modelling, the design of air mobility vehicles, psychoacoustics, noise reduction strategies, measurement techniques, and legal issues.  It was agreed that these additional efforts and research were required for the successful implementation of advanced aerial mobility vehicles.

At the end of the meeting Jean Tourret opined that there was a form of complementarity and even some informal synergy between the current event and the INCE/Europe 2020 Quiet Drones eSymposium. He indicated that both events have contributed to increased communication between individuals and countries, and that it will pave the way for noise regulations in the not too distant future, that will lead to the best acceptability and use of drones.

The 2020 workshop report *Aerial Mobility: Noise Issues and Technology* provides summaries and selected slides from each of the 22 technical presentations. A PDF copy is available from the INCE/USA web page linked in the references.

**References**

Engineering a Quieter America, 2021, *Aerial Mobility: Noise Issues and Technology*, December 2 – 3, 2020, INCE/USA https://www.inceusa.org/publications/technical-reports/

Technology for a Quieter America, 2020. *UAS and UAV (Drone) Noise Emissions and Noise Control Engineering Technology*, Workshop Final Report, December 13 – 14, 2018, INCE/USA https://www.inceusa.org/publications/technology-for-a-quieter-america

National Academy of Engineering, 2010. *Technology for a Quieter America*. Washington, DC, National Academies Press.
https://www.nae.edu/27531/Technology-for-a-Quieter-America

National Academies of Sciences, Engineering, and Medicine. 2020. *Advancing Aerial Mobility: A National Blueprint*. Washington, DC: The National Academies Press.
https://www.nap.edu/catalog/25646/advancing-aerial-mobility-a-national-blueprint

NASA, *Urban Air Mobility Noise: Current Practice, Gaps, and Recommendations*, NASA 2020. https://ntrs.nasa.gov/search?q=20205007433

INCEEUROPE

CidB
Centre d'information sur le Bruit

**QUIET DRONES**
**Second International e-Symposium**
**on**
**UAV/UAS Noise**
**27th to 30th June 2022**

# Measurement of sound emission characteristics of quadcopter drones under cruise condition

**Gert Herold*, Paul Testa, Jan Foerster, Maarten Uijt de Haag, Ennes Sarradj**

**Technische Universität Berlin**

## Summary

Quadcopter drones have distinctive sound emission characteristics, which also depend on their mode of operation. While determining these characteristics is of interest in different contexts, this proves particularly challenging when the mode of operation involves movement of the drone.

In this contribution, a method for characterizing the in-flight sound radiation in terms of sound power and directivity is applied to three different drone configurations flying at different speeds. Based on microphone array measurements, the trajectory of the drone during its flight through the array is reconstructed. The estimated flight path is then used to de-dopplerize the measured signals and determine the directivity based on the time-dependent relative angle of radiation from the drone to the microphones.

The exemplary evaluations include the calculation of sound power spectra and directivity factors. Current limitations of the method are highlighted and ways to overcome them are discussed.

*Corresponding author: gert.herold@tu-berlin.de

# 1. Introduction

Multicopter drones are more and more becoming part of our everyday life. As the number of applications for such devices increases, so does the interest in researching their noise emissions and the effects on humans [1], as well as in taking regulatory measures to ensure the well-being of the general public [2].

While for the individual, it is the sound *immission* that counts, i. e. the noise to which they are exposed, a description of the sound *emission* is more useful, for example, when simulating the noise exposure based on different scenarios or when setting permit limits.

For stationary sources, methods for determining sound emission characteristics by placing microphones around the object are widely used [3]. While many drones can remain stationary in hover mode, cruise flight also constitutes a typical mode of operation that can be associated with unique sound generation, e.g. with specific tonal components exhibiting a strong directivity.

In the following, a novel method for characterizing sound emissions by taking into account a relative movement between the object and the sensors is applied to multiple drone fly-bys. The basis of the multi-step processing are microphone array measurements, which are evaluated to both reconstruct the flight path and determine the directed sound emissions.

# 2. Materials and methods

## 2.1 Measured drones

Figure 1: Drone configurations D1 (left) and D3 (right). Configuration D2 is identical to D3 with a different set of propellers.

Measurements were done with two different consumer quadcopter drones (depicted in Fig. 1). Configuration "D1" has a width of about 38 cm and a height of about 9 cm when viewed from the front. Configurations "D2" and "D3" are the same drone with a different set of propellers, with a width of about 47 cm and a height of 8 cm. Table 1 summarizes several drone-specific parameters.

All drones were steered manually, with the maneuvers consisting of acceleration after hovering, then straight flight and deceleration. For D2 and D3, measurements with two different speeds are evaluated, with an appended "s" denoting a lower flight speed and "f" a higher speed.

Table 1: Drone dimensions and parameters.

| | D1 | D2 | D3 |
|---|---|---|---|
| weight | 500 g | 750 g | |
| diagonal rotor axes distance | 289 mm | 335 mm | |
| dimensions ($l \times w \times h$) | 33 cm × 38 cm × 9 cm | 43 cm × 47 cm × 8 cm | |
| blades per rotor | 3 | 2 | |
| propeller diameter | 154 mm | 210 mm | 216 mm |

### 2.2 Measurement setup

The measurements were done in a fully anechoic room at TU Berlin. Figure 2 shows the general setup. Sound pressures were recorded synchronously with 96 channels distributed over two arrays. The plate array on the side features 32 flush-mounted microphones in a spiral arrangement with a diameter of about 1.5 m. 64 microphones are evenly distributed in a ring with a diameter of 2.1 m.

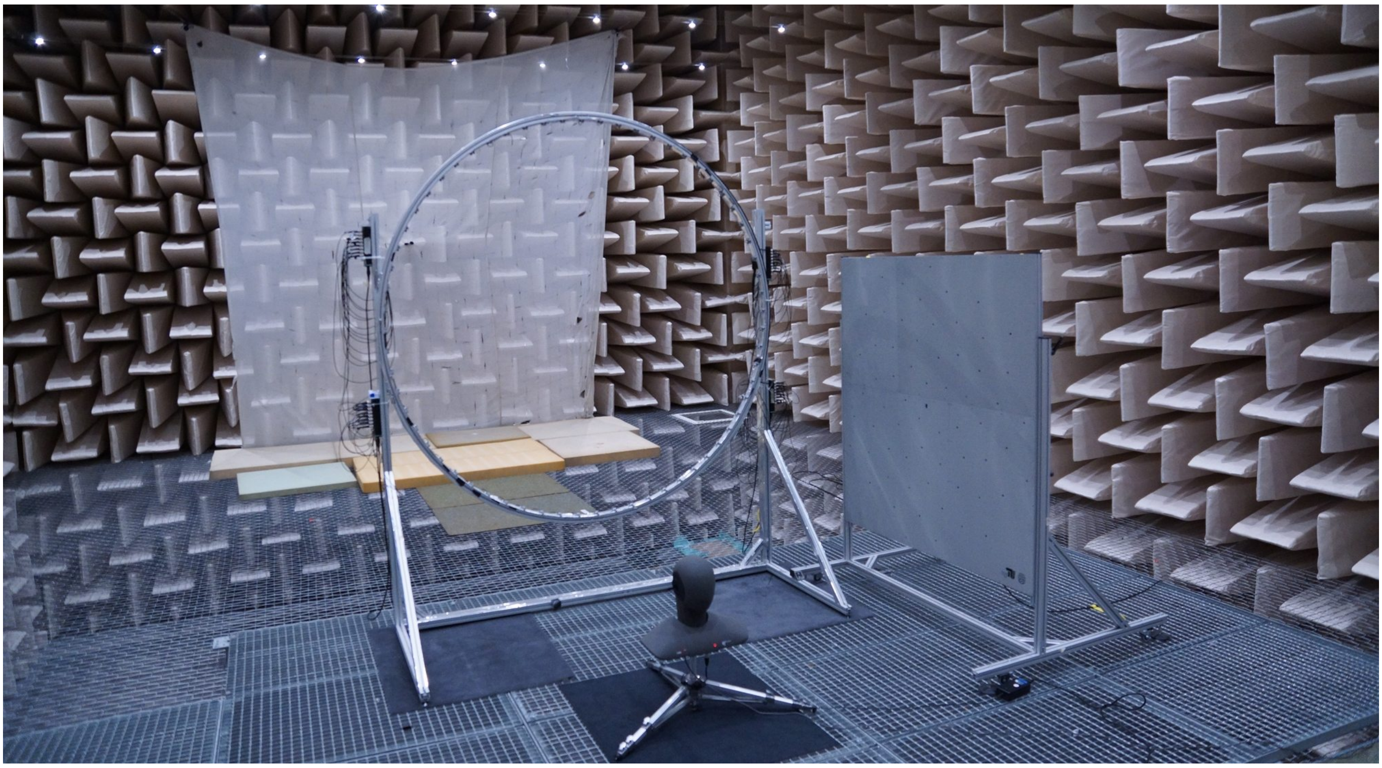

Figure 2: Measurement setup with the two arrays (artificial head not used here). View in flight direction (along the $z$ axis).

The drones' flight paths start approximately 4 m before the ring, on the side of the room where the plate array and the artificial head are positioned. The drones are steered to fly through the ring center and stop approximately 4 m after passing the ring. Due to the spatial constraints in the anechoic room, the drones are not operated at a constant speed during the full 8 m flight path, which includes portions of acceleration and deceleration. In addition, dealing with the wire mesh floor proved to be a challenge for the drone's internal position stabilization, which made it difficult to keep the drone stable in a given hover position.

The microphones of the plate array were used exclusively for the flight path reconstruction. The ring array was used for the emission characterization. This is described in the following section.

## 2.3 Signal processing

The objective of the measurements is to achieve a characterization of the directed sound emission of the moving drones. An advantage of measuring moving drones is that the signals recorded with stationary sensors describe the sound immission from varying incident angles. If the source position is known, emission characteristics can be derived by compensating for the sound propagation through the medium. The necessary steps for this follow the data processing described earlier [4] and shall be summarized here:

1. Reconstruct the flight path of the drone.
2. Compensate for relative distance and motion.
3. Compile a frequency- and direction-dependent description of the emission.

For reconstructing the drone's flight path, signals synchronously recorded with the 32-channel plate array are used. A three-dimensional region where the drone is expected to fly (i. e. a flight corridor) is defined, and Functional Beamforming [5, 6] is used on short-time signal segments to determine the drone's average position by locating the origin of the maximum sound pressure during each time segment. From these coordinates, a coherent trajectory is constructed using a Kalman filter [7]. This part of the processing is described in more in detail in [8]. Important parameters for the trajectory reconstruction are summarized in Table 2.

Table 2: Important parameters for the trajectory detection.

| | |
|---|---|
| number of microphones | 32 |
| sampling rate | 51 200 Hz |
| focus grid ($l_x \times l_y \times l_z$) | $2\,\mathrm{m} \times 2\,\mathrm{m} \times 9\,\mathrm{m}$ |
| focus grid resolution | 0.05 m |
| FFT | 512 samples |
| | von Hann window |
| | 50 % overlap |
| averaging time | 0.1 s |
| beamforming | Functional Bf., $\nu = 8$ |
| | w/o CSM main diagonal |
| | $2.9\,\mathrm{kHz} \pm 150\,\mathrm{Hz}$ |

With the known trajectory, the influence the drone's motion has on the received signal (i. e. the Doppler effect) as well as the dependence of the sound pressure on the distance $r$ between drone and microphone can be compensated via

$$p_{\mathrm{mic,corr,1\,m}}(t) = \frac{r(t)}{(1 - v_{\mathrm{drone,rel}}(t)/c)^2} \cdot p_{\mathrm{mic,meas}}\left(t + \frac{r(t)}{c}\right) . \tag{1}$$

The resulting time signal $p_{\mathrm{mic,corr,1\,m}}$ for a specific microphone of the 64-channel ring array is normalized to a distance of 1 m from the drone. The speed of the drone relative to the microphone $v_{\mathrm{drone,rel}}$ can be derived from the trajectory as well. The speed of sound is represented by $c$ in Eq. (1).

Finally, the corrected time signals again are cut into short segments, fourier-transformed, and then collected and averaged according to the current relative azimuth $\varphi$ and elevation $\theta$ between drone and a microphone. For summarizing several emission angles, the radiation direction space is discretized. The drone-centered coordinate system as well as two angle discretizations are shown in Fig. 3.

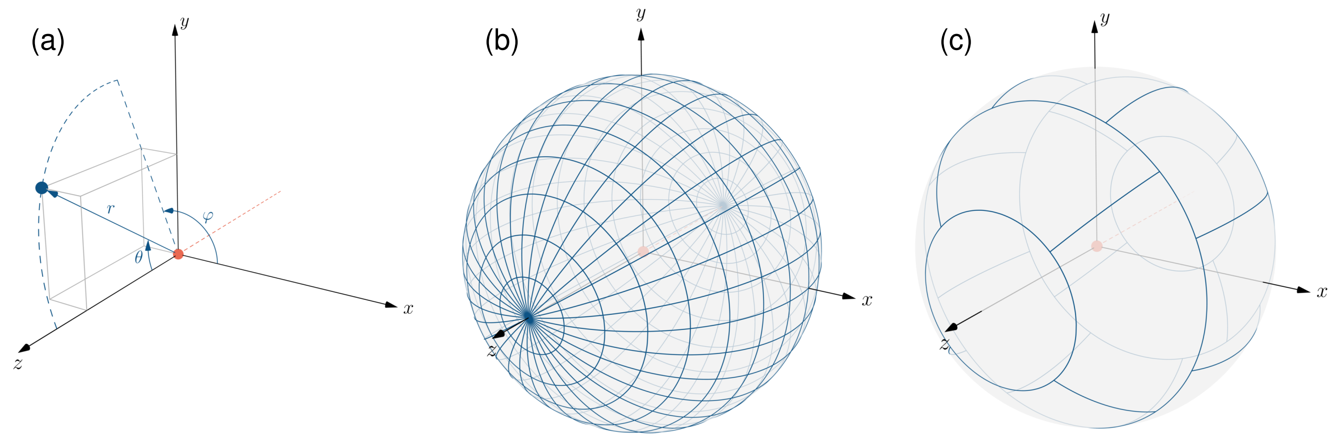


Figure 3: (a) Cartesian and spherical coordinates with the drone (as red dot) at the origin. The dashed red line represents past trajectory. (b) Discretization of sphere into 32×16 sections with equal angle distribution. (c) Discretization of sphere into 18 sections with equal surface area.

The high-resolution angle discretization (Fig. 3b) is used for mapping the 3D radiation characteristics. The equal surface radiation angle discretization (Fig. 3c) is used for calculating the frequency dependent sound power [4]

$$W = \frac{2\,\mathrm{m}^2\,\pi}{9} \sum_{i=1}^{18} \frac{{p_{\mathrm{rms},i}}^2}{\rho_0 c} \tag{2}$$

and directivity factor

$$Q = \frac{18 \cdot {p_{y^-}}^2}{\sum_{i=1}^{18} {p_{\mathrm{rms},i}}^2}\,, \tag{3}$$

where $p_{\mathrm{rms},i}$ is the RMS sound pressure at the $i$-th segment, $p_{y^-}$ the RMS sound pressure at the segment facing towards negative $y$, and $\rho_0$ the air density. Several parameters for the compilation of the directional radiation are summarized in Table 3.

Table 3: Parameters for the directed sample collection.

| | |
|---|---|
| microphones | 64, 2.1 m ring |
| sampling rate | 51 200 Hz |
| FFT | 4096 samples |
| | von Hann window |
| | 97 % overlap |

## 3. Results

### 3.1 Flight paths

Figure 4 shows the reconstructed trajectories of the five separately measured cases. As the drones were steered manually, each path is individual and different from the others. As described in Section 2.3, arbitrary paths are accounted for in the signal processing.

However, the path detection assumes that the position of the dominant sound source is representative for the drone's location. In the case of the drones, major sources can be expected to be close

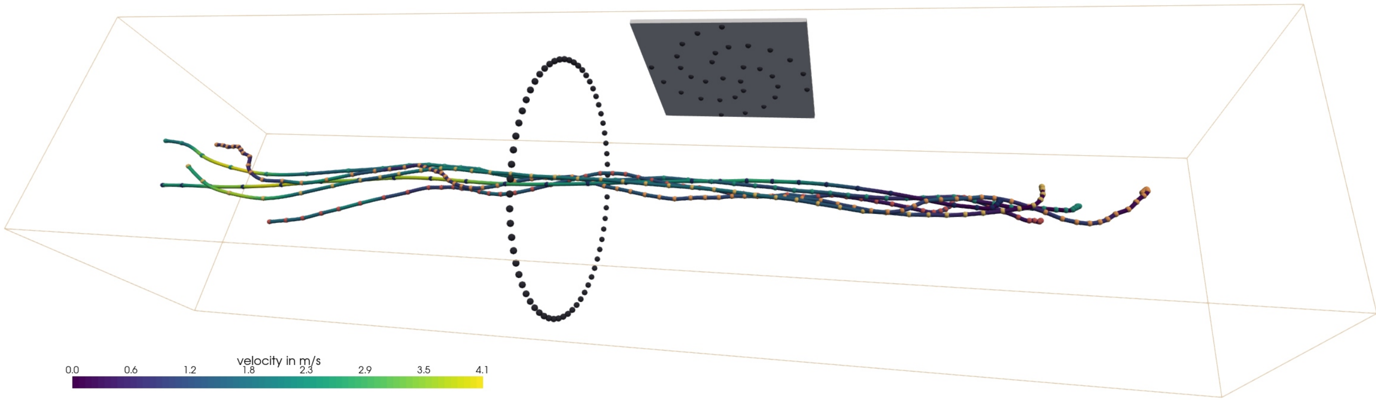


Figure 4: Reconstructed trajectories of the drone flights with velocities. Flight direction from right to left. Colored dots show the respective drone's position every 0.1 s (D1, D2s, D2f, D3s, D3f). Dark gray dots represent microphone positions. The yellow frame indicates the monitored 3D flight corridor.

to the propellers, with the single dominant source possibly switching from one propeller to another throughout the flight. With the propellers of the drones being up to 30 cm apart, this can lead to deviations of the reconstructed from the true path, and to an apparent curved trajectory when the actual cruise flight follows a straight line.

For the calculations done here, the deviation of the position is assumed to be negligible. Furthermore, the orientation of the drone – and with it the direction of the $z$ axis in the coordinate system (Fig. 3a) – is assumed to be constant for the whole flight, with the $z$ axis being oriented from start to the end point of the trajectory.

Table 4: Reconstructed flight paths.

| case | max. speed | distance start-end | time start-end |
|---|---|---|---|
| D1 | 3.9 m/s | 7.4 m | 3.0 s |
| D2s | 2.3 m/s | 7.9 m | 8.1 s |
| D2f | 4.0 m/s | 8.0 m | 4.9 s |
| D3s | 2.1 m/s | 6.3 m | 5.9 s |
| D3f | 3.5 m/s | 7.3 m | 4.5 s |

In Table 4, the distances between start and end point of the trajectories as well as the elapsed time and the maximum speed in each trajectory are listed. As can be seen in Fig. 4, higher speeds are usually only reached during the second half of the trajectory.

### 3.2 Directional sound radiation

Figures 5 to 9 show the sound radiation characteristics for octave bands from 500 Hz to 16 kHz for the evaluated cases. Throughout all drone flights and frequency bands, it can be observed that the drones exhibit a distinct directivity, where more sound is emitted towards the ground and upwards than in other directions. This is in line with what is observed from other multicopter drones as well [1].

For configuration D1 (Fig. 5), however, there appears to be a local minimum at $\theta = \pi/2$ in the 500 Hz octave band. This may be a result of only few samples being available for averaging at this angle due to the array geometry and the comparably high flight speed. Furthermore, the 500 Hz octave contains fewer discrete frequencies than the other bands, where the calculated radiation patterns have a smoother characteristic.

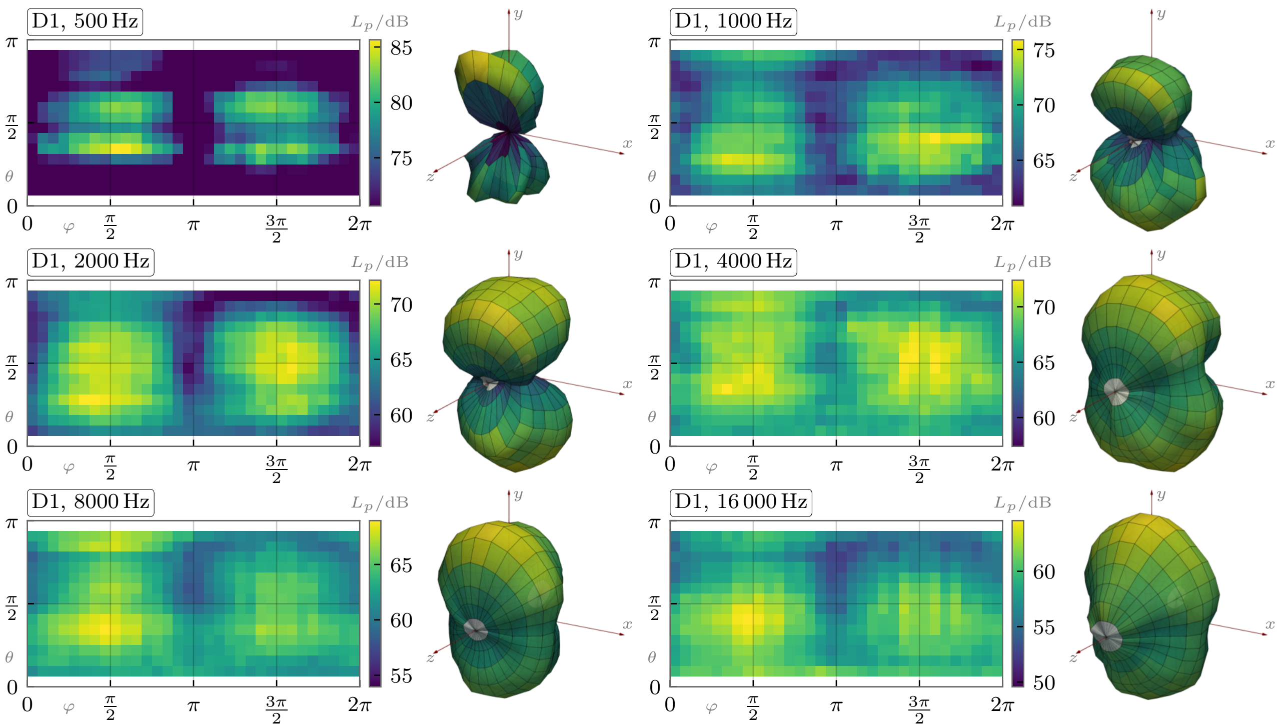


Figure 5: **D1**: Directivity maps for different octave bands. Displayed dynamic up to 15 dB below maximum.

All calculated directivity maps with configurations D2 or D3 exhibit strong levels directed towards the ground and slightly backwards ($\varphi \approx 3\pi/2, \theta \gtrsim \pi/2$). These are not caused by actual acoustic phenomena but by pressure fluctuations on the microphones as a result of the downwash created by the drone's propellers. This effect could be mitigated either by adapting the experimental setup (e. g. by adding windscreens to the microphones) or the data processing (e. g. by evaluating a subset of the microphone signals together for filtering out uncorrelated signal portions).

For the octave bands from 2 kHz to 16 kHz, the flow effects are not present. At 4 kHz and above, the D2 and D3 cases exhibit a slightly forward-oriented directivity in addition to the upwards/downwards characteristic. Furthermore, the downward facing lobe is broader than the upward lobe for the octave bands 8 kHz and 16 kHz.

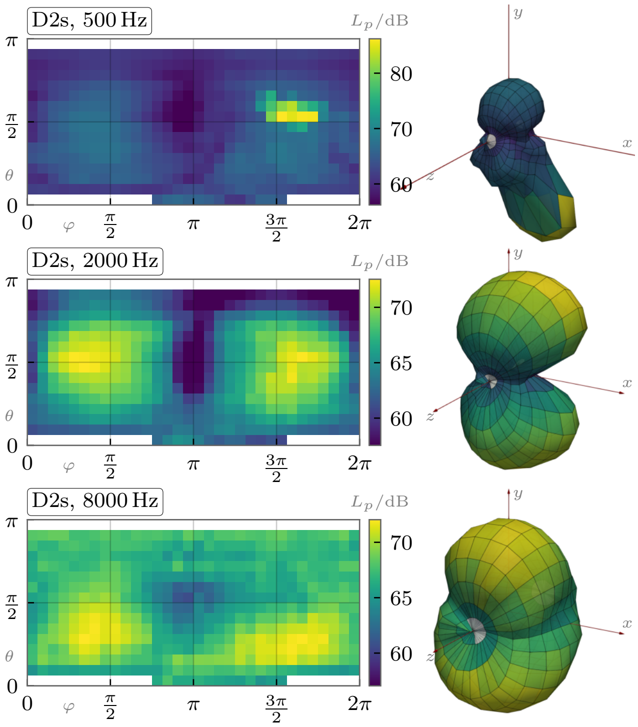

Figure 6: D2s: Directivity maps for different octave bands. Displayed dynamic up to 15 dB below maximum (except 500 Hz: 30 dB).

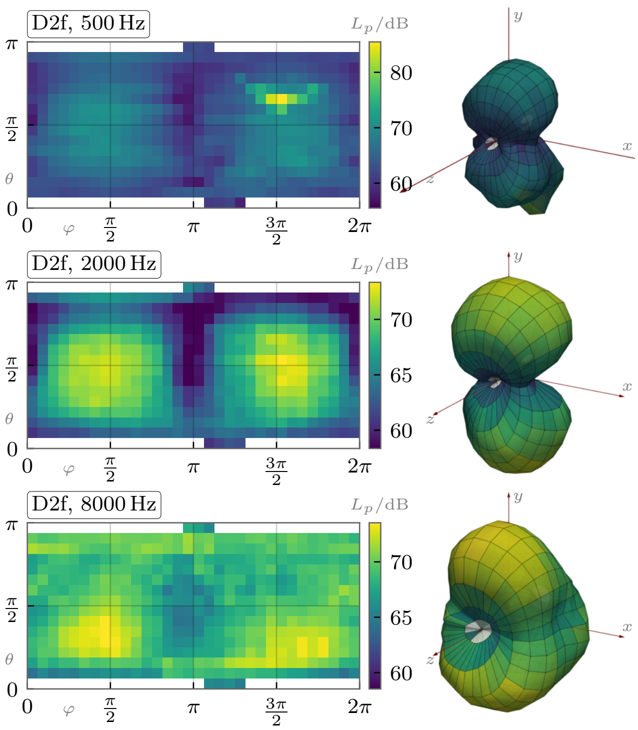

Figure 7: D2f: Directivity maps for different octave bands. Displayed dynamic up to 15 dB below maximum (except 500 Hz: 30 dB).

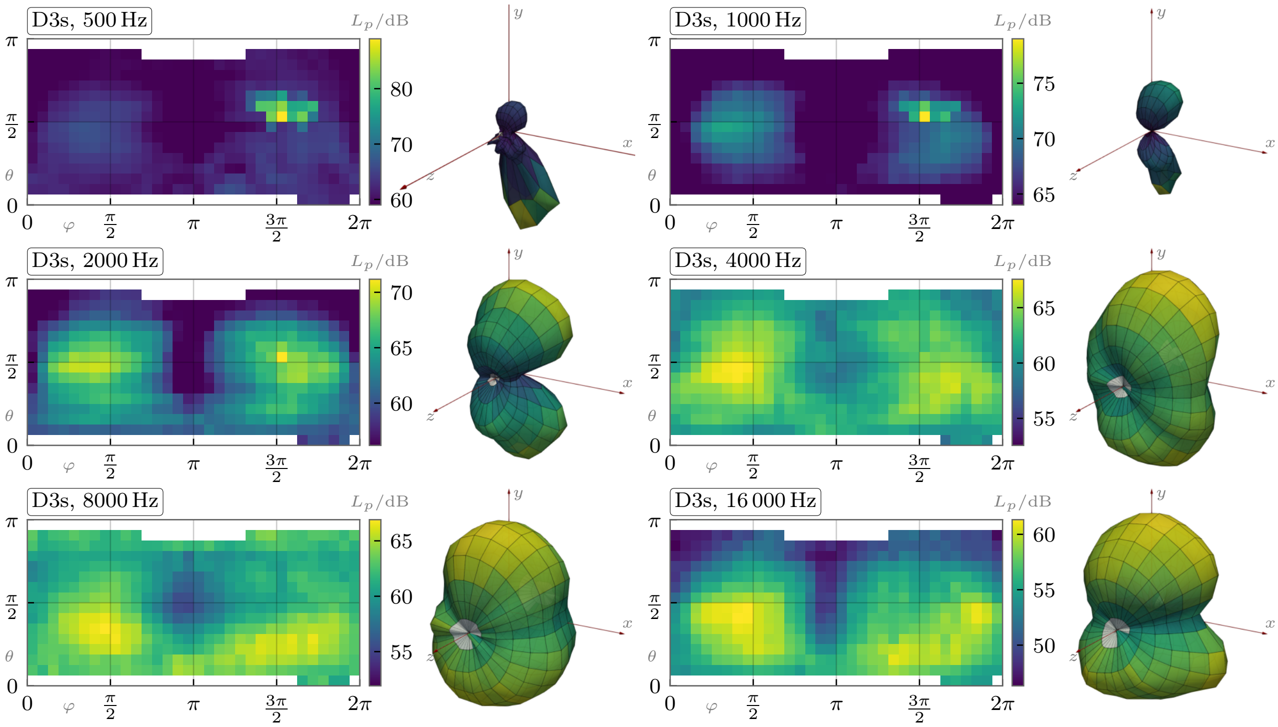


Figure 8: D3s: Directivity maps for different octave bands. Displayed dynamic up to 15 dB below maximum (except 500 Hz: 30 dB).

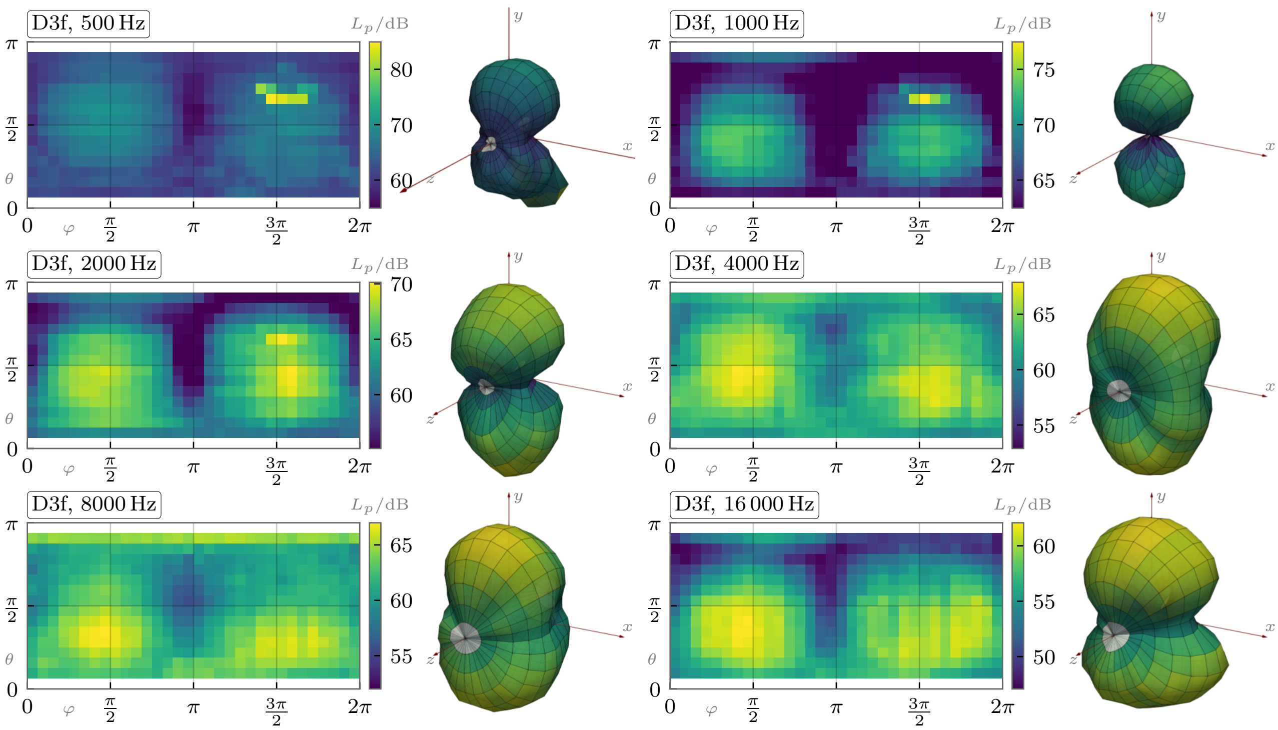


Figure 9: D3f: Directivity maps for different octave bands. Displayed dynamic up to 15 dB below maximum (except 500 Hz: 30 dB).

### 3.3 Sound power and directivity factor

Figure 10 shows the narrow-band sound power spectra, with the sound powers calculated according to Eq. (2). In the legend of the figures, the summed sound power levels (unweighted and A-weighted) are also documented. All spectra feature tonal and broadband components, with higher harmonics of the blade passing frequencies visible up to about 3 kHz and increased levels around 4 kHz.

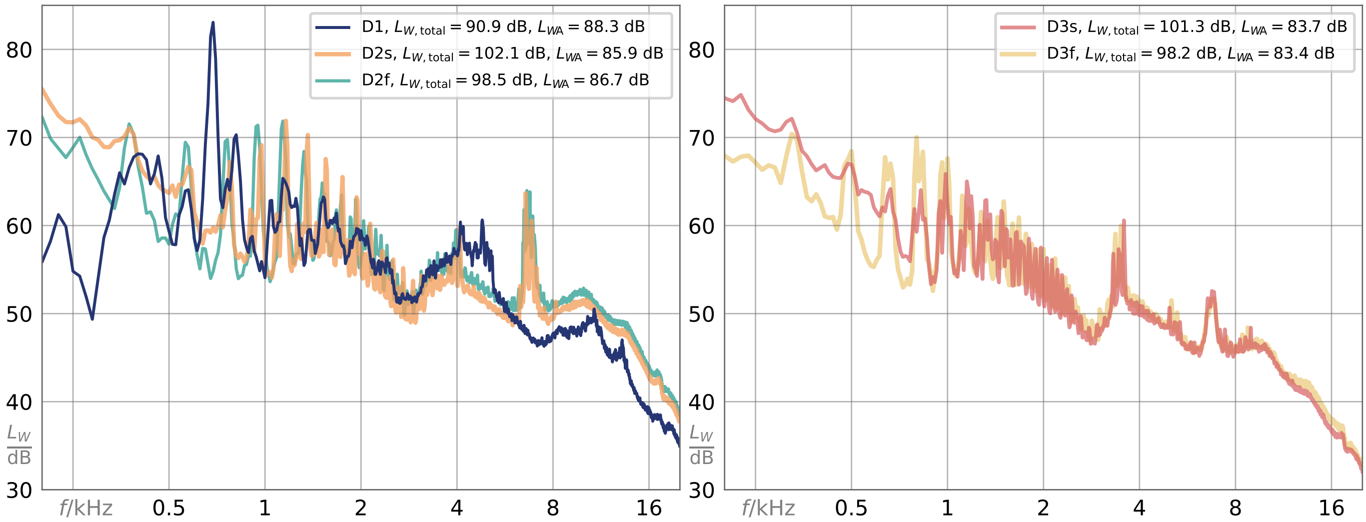


Figure 10: Narrow-band sound power spectra ($\Delta f = 12.5$ Hz) of the drone flights.

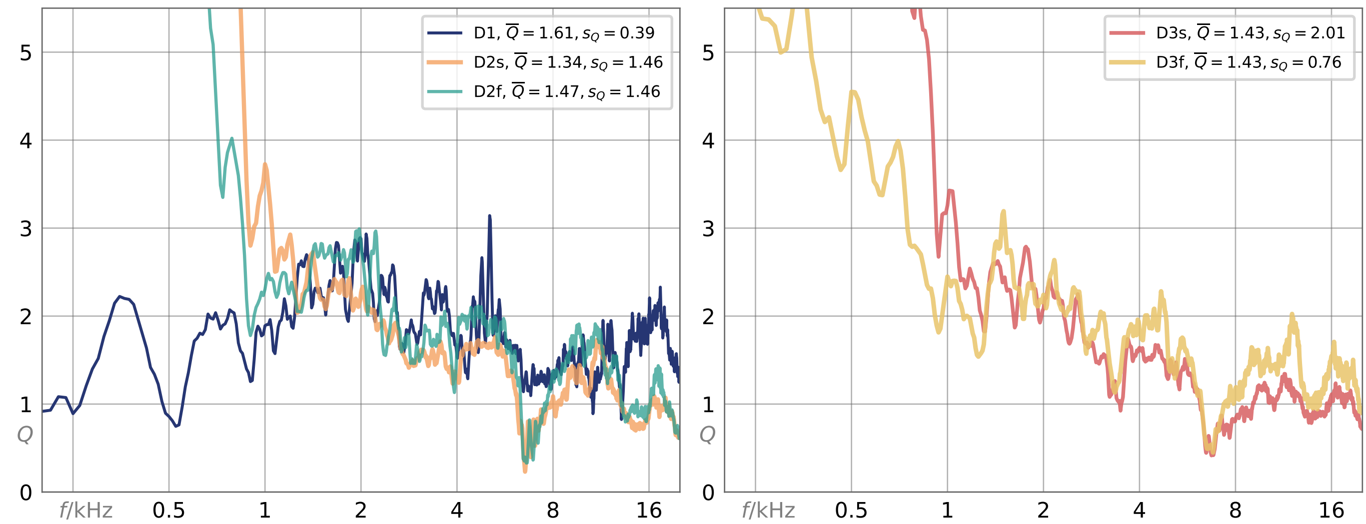


Figure 11: Frequency-dependent directivity factors of the drones (moving average over 10 adjacent frequencies, $\Delta f = 12.5$ Hz).

The most prominent feature in the D1 spectrum is a tonal peak between 500 Hz and 1 kHz, which lies more the 10 dB above other parts of the spectrum. The D2 and D3 spectra have distinct tonal components as well, however, the energy is distributed more evenly over several of the blade passing frequency harmonics. In the D3 cases (with larger propeller diameters), the individual peaks are not as pronounced as in the D2 cases, and the overall level is also lower.

Comparing the spectra at higher frequencies shows that the faster moving cases (D2f/D3f) have slightly higher levels compared to the slow-moving drones. Between 1 kHz and 2 kHz, the tonal components of D2s are increased compared to D2f, whereas D3s and D3f exhibit a similar characteristic in that frequency range. For frequencies below 500 Hz, the broadband components appear to be significantly higher for the slow versus the fast drone flights. This is certainly due to the flow effects mentioned above, which can also be seen to have more impact in the directivity maps.

At 6.5 kHz, the D2/D3 cases feature a strong tonal component which is not present in the D1 spectrum. Looking at the directivity spectrum (Fig. 11) at the same frequency, a minimum with $Q < 1$ can be seen. This means that in contrast to most of the spectrum, at this frequency more energy is radiated in other directions than downwards, which also hints at the underlying sound generating mechanism being a different one here.

The directivity factors of $Q \geq 3$ determined for 1 kHz and below for the D2 and D3 cases are not trustworthy, as the calculations, again, are biased by the pressure fluctuations due to flow over the sensors below the drone. A perfect monpole is characterized by a directivity factor of $Q_{\text{monopole}} = 1$, for a dipole oriented along the $y$ axis $Q_{\text{dipole}} = 3$ [9]. As can be seen in Fig. 11, the results calculated for the drones between 1 kHz and 4 kHz hint at a radiation characteristic that lies between monopole and dipole for these frequencies.

## 4. Conclusion

A novel technique for reconstructing sound emission characteristics of drones in cruise flight mode has been successfully applied to several quadcopter drone fly-by measurements with a microphone array. For each measurement, the drone's directivity pattern was mapped. Moreover, the sound power spectrum and the frequency-dependent directivity factor were calculated.

While the general concept of the signal processing chain proved to be robust, the practical application to different configurations and scenarios uncovered several challenges to be overcome for future investigations:

1. For drones whose dimensions are non-negligible compared to the array, measures should be taken to ensure a sufficiently accurate tracking of the drone's center as reference position.
2. Techniques should be used to mitigate the effect of flow over microphones that may be in the wake of a propeller.
3. For mapping the directivity, the array geometry should be designed so as to uniformly sample all angles of interest over time.
4. The measuring environment should allow for the drones to be operated reproducibly in a representative flight mode.

Bearing these limitations in mind, the presented method has the potential to be a valuable tool for the in-flight characterization of the sound emission of drones.

## References

[1] B. Schäffer, R. Pieren, K. Heutschi, J. M. Wunderli, and S. Becker, “Drone noise emission characteristics and noise effects on humans—a systematic review,” *International Journal of Environmental Research and Public Health*, vol. 18, no. 11, 2021. DOI: 10.3390/ijerph18115940.

[2] The European Commission, “Commission Delegated Regulation (EU) 2019/945 of 12 March 2019 on unmanned aircraft systems and on third-country operators of unmanned aircraft systems,” Official Journal of the European Union L152, vol. 62, p. 1, 11 June 2019 2019.

[3] ISO, *ISO 3744:2010 – Acoustics – Determination of sound power levels and sound energy levels of noise sources using sound pressure – Engineering methods for an essentially free field over a reflecting plane*, 2010.

[4] G. Herold, “In-flight directivity and sound power measurement of small-scale unmanned aerial systems,” preprint, 2022. DOI: 10.36227/techrxiv.19469825.

[5] R. P. Dougherty, “Functional beamforming,” in *Proceedings of the 5th Berlin Beamforming Conference*, Berlin, 2014, pp. 1–25.

[6] E. Sarradj and G. Herold, “A Python framework for microphone array data processing,” *Applied Acoustics*, vol. 116, pp. 50–58, 2017. DOI: 10.1016/j.apacoust.2016.09.015.

[7] B. D. O. Anderson and J. B. Moore, *Optimal filtering*. Englewood Cliffs, N.J.: Prentice-Hall, 1979, 357 pp.

[8] G. Herold, A. Kujawski, C. Strümpfel, S. Huschbeck, M. Uijt de Haag, and E. Sarradj, “Flight path tracking and acoustic signature separation of swarm quadcopter drones using microphone array measurements,” in *Quiet Drones 2020 - International e-Symposium on UAV / UAS Noise*, Paris, France, 2020, pp. 1–19. DOI: 10.5281/zenodo.4548251.

[9] L. L. Beranek and T. J. Mellow, *Acoustics: Sound fields and transducers*. Elsevier, 2012. DOI: 10.1016/B978-0-12-391421-7.00001-4.

**QUIET DRONES**
**Second International e-Symposium**
**on**
**UAV/UAS Noise**
**27th to 30th June 2022**

# Comparison of different processing for DOA estimation of an Unmanned Aerial Vehicle with few sensors

**N. Itare: nathan.itare@univ-lemans.fr**
**Jean-Hugh Thomas: jean-hugh.thomas@univ-lemans.fr**
**Kosai Raoof: kosai.raoof@univ-lemans.fr**
**Laboratoire d'Acoustique de l'Université du Mans (LAUM), UMR 6613, Institut d'Acoustique-Graduate School (IA-GS), CNRS, Le Mans Université, 72085, France**

### Summary

During the last years, many methods have been developed and studied in the field of source localization. A particular area of interest is the tracking of UAVs (Unmanned Aerial Vehicles) because of the numerous threats that can appear near sensitive sites. Delay and Sum Beamforming (DSB) is one of the methods that can be very useful to face this challenge. Indeed, this technique has a good robustness to noise which makes it an interesting tool. Recently, some processes have been studied to enhance the performance of DSB by taking into account the signature of UAVs. Signals obtained from a microphone antenna can be filtered according to the signature of an UAV before beamforming. Beamforming can also be performed from the measured signals, then the harmonic signature can be considered using the time-frequency representation of the focused signal. A pitch tracking algorithm can provide the fundamental frequency of the signals for consideration of the UAV's signature. Another interesting approach is the Steered Response Power (SRP) which can perform well in noisy environment. The use of generalized cross correlation with different spectral weightings provides a wide range of options. This study aims at comparing the performance of beamforming with time-frequency representation and SRP-PHAT on an experimental measurement with a UAV in flight.

## 1. Introduction

Airspace traffic has to be regulated because of the increase of users, particularly unmanned aerial vehicle (UAV) flyers. The amount of recreational flyers is nowadays more important and UAVs can be extremely useful in other activities like deliveries or aerial imagery. These flies can be dangerous near airplane traffic or airports. Privacy is also an issue near sensitive sites or more generally when flyers use UAV for surveillance. Several surveys have been conducted about the threats and the different methods that can be used to counter them [1], [2]. Among these methods, the use of acoustical methods enables to estimate the direction of arrival (DOA) of an UAV thanks to the sound emitted during the flight. Beamforming is often used because of its robustness to noise and its real time implementation. Considering the UAV's acoustic signature enables to enhance the performance of beamforming. This can be made using the time-frequency representation of the temporal beamformer's output [3]. Thus, energy is calculated with time-frequency bins associated with the harmonic signature of the drone. Other algorithms based on the time difference of arrival (TDOA) can estimate the DOA of the drone [4]–[7]. These algorithms exploit the generalized cross correlation (GCC) between pairs of microphone with specific weightings (SCOT [8], PHAT-β [9], …) . GCC with a phase transform also called GCC-PHAT is known to be robust to reverberation. The Steered Response Power with Phase Transformation (SRP-PHAT) makes use of GCC-PHAT to estimate the source DOA estimation. The aim of this study is to evaluate the performance of beamforming with time-frequency representation and SRP-PHAT on an experimental measure.

The work is presented as follows: Part 2 describes the two DOA estimation approaches used, Part 3 tackles the comparison between the two algorithms on the experimental case, and Part 4 concludes and gives some perspectives.

# 2. DOA estimation algorithms

## 2.1 Steered Response Power – Phase Transformation

Given a microphone antenna with N microphones, the signal $p_n(t)$ received by the n^th^ microphone can be described with Equation (1). In this equation, $s(t)$ is the signal emitted by the source, $\Omega_s$ is the direction of the source, $h_n(\Omega_s, t)$ is the impulse response between the source and the n^th^ microphone, and $b_n(t)$ is the noise due to the environment or the microphone system.

$$p_n(t) = s(t) * h_n(\Omega_s, t) + b_n(t). \tag{1}$$

The generalized cross correlation between microphones $n$ and $m$ is given by:

$$R_{nm}(\tau) = \int_{-\infty}^{+\infty} \Phi_{nm}(\mathrm{f})\, G_{nm}(f) e^{2\pi j f \tau} df, \tag{2}$$

with $\Phi_{nm}(\mathrm{f})$ a weighting of the cross-spectrum $G_{nm}(f)$ between microphones $n$ and $m$. The weighting corresponding to the phase transformation is given by: $\Phi_{nm}(\mathrm{f}) = \frac{1}{|G_{nm}(f)|}$. SRP-PHAT is the extension of GCC-PHAT with multiple microphones, it is computed with:

$$P(\Omega) = \sum_{n=1}^{N} \sum_{m=1}^{N} R_{nm}(\tau_{nm}(\Omega)), \tag{3}$$

where $\tau_{nm}(\Omega)$ is the TDOA between microphones $n$ and $m$. The TDOA can be calculated using a plane or spherical wave model given the direction $\Omega$. The direction $\Omega$ which maximizes $P(\Omega)$ gives the estimation of the source DOA.

## 2.2 Two beamforming-based processing

### 2.2.1 Temporal Delay and Sum Beamforming

Delay and Sum Beamforming (DSB) enables to focus a signal in a direction $\Omega$ by calculating the TDOA between the antenna's microphones and a reference microphone. The delays can also be calculated with a plane or spherical wave model. Each signal is delayed with its own TDOA and then all the delayed signals are summed. The DOA estimate is given by the direction $\Omega$ which maximizes the energy of the focused signal.

### 2.2.2 Beamforming adapted to the acoustic signature

The time-frequency representation (TFR) of the focused signal in the direction $\Omega$ enables to consider the acoustic signature of the source. This TFR can be obtained with the Short Time Fourier Transform (STFT). An interesting property of UAVs' signatures is their harmonic characteristics. By using a fundamental frequency detection algorithm, it is possible to automatically select time-frequency bins from the TFR corresponding to chosen harmonics linked to the spectral properties of the signals produced by the UAV. The DOA estimation is therefore given by the direction $\Omega$ that maximizes the energy of these selected bins instead of considering all the spectral content. The algorithm used here for the fundamental frequency detection is the Spectral Harmonic Correlation (SHC) [10]. The choice of this frequency is very important to obtain a good estimate of the DOA. A procedure has been implemented for selecting the fundamental frequency among those given by SHC, which is detailed in part 3.2.

# 3. Comparison on an experimental trajectory

## 3.1 Array geometry and measurement set-up

The measurements were realized with an array of 10 BSWA Technology MPA 416 1/4 in. microphones (20 Hz-20 kHz) in the arrangement shown in Figure 1. Three different inter-microphonic spacings were used to give the [220,5 3430] Hz array bandwidth:

$$\begin{aligned} \|x_1\| = \|x_4\| = \|x_7\| &= 0.05\ m, \\ \|x_2\| = \|x_5\| = \|x_8\| &= 0.2\quad m, \\ \|x_3\| = \|x_6\| = \|x_9\| &= 1.1\quad m. \end{aligned} \tag{1}$$

A PXI-1036 chassis from National instruments is used with a laptop for the recording of the acoustic signals with a sampling frequency of 20 kHz. A source is located from its direction $\Omega = (\varphi, \theta)$, which is respectively the azimuth and the elevation, and with its distance $r$ to the reference microphone (placed at the origin). During the recording, the drone starts with a circular trajectory followed by a smaller one with both a height to the ground around 14 m. The drone used is a Phantom IV from DJI.

## 3.2 TFR parameters

According to the study of the acoustic signature of the drone used [11], [12], two types of harmonics are present. Weak harmonics are produced by the rotation of the rotors and strong harmonics are produced by the aerodynamic phenomenon. The rotor frequency $f_0$ is related to the blade passing frequency $f_{bp}$ with the number of blades $N_b$, $f_{bp} = N_b \times f_0$. Since there are two blades, weak harmonics (of $f_0$) are odd and strong harmonics are even. The spectrogram of the reference microphone is presented in Figure 2. Because of the noise present during the recording, weak harmonics are not visible in the spectrogram and $f_{bp}$ is detected by SHC instead of $f_0$ ($f_{bp}$ detections are visible with red points in Figure 2). In order to select the time-frequency bins

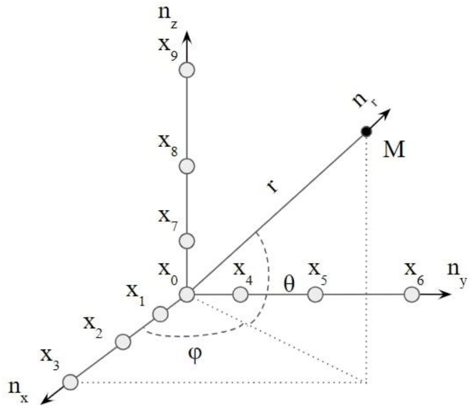


*Figure 1:* Microphone antenna used for the experimental measurements.

corresponding to the drone's signature in the TFR, the bandwidth is defined as dependent of its centre frequency as for bandpass filters. All the bins selected are in bands centred on $f_{bp} * i$ with bandwidth $\Delta f = \frac{f_{bp} \times i}{Q}$, where $i = 1, \dots, N_h$, $N_h$ is the number of harmonics chosen, and $Q$, the quality factor. The signal is cut into portions and for each portion, $f_{bp}$ is detected by taking the maximum of the SHC calculated in a given frequency range. To verify that this $f_{bp}$ gives a good DOA estimation, a validation procedure is added to the TFR. If the DOA estimate is higher or lower of 10° than the previous one in azimuth or in elevation, then another $f_{bp}$ is chosen and another DOA is estimated. This condition enables to select the appropriate frequency content by favouring the continuity of the drone trajectory. The frequency range for the SHC calculation is extended and other DOAs are estimated if no previous DOA estimate meets the conditions.

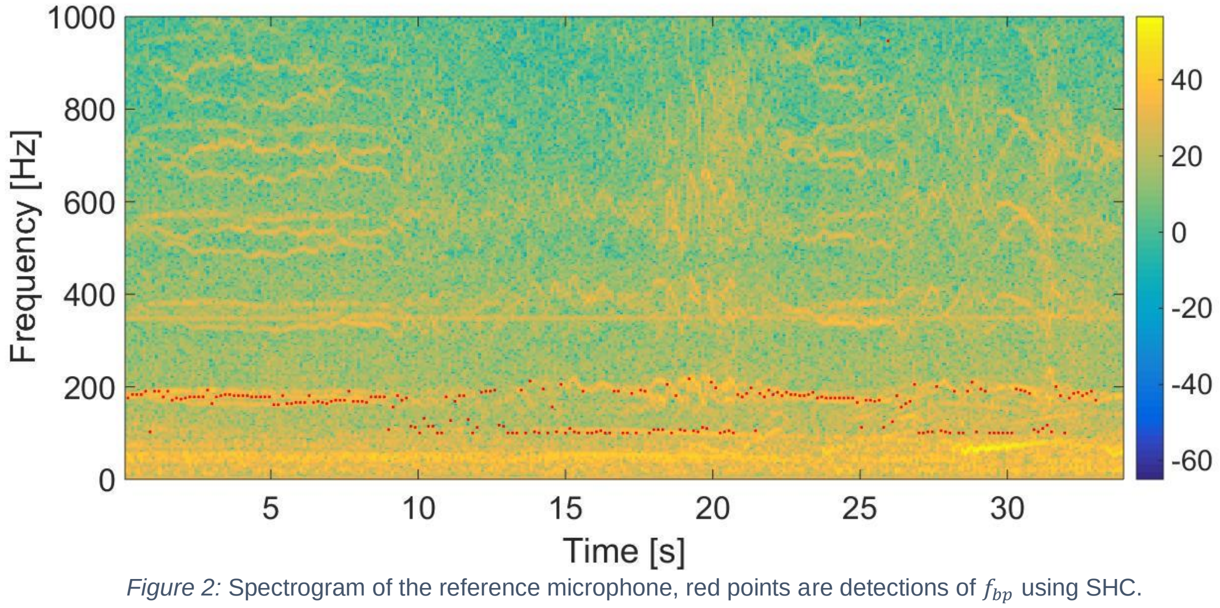


*Figure 2:* Spectrogram of the reference microphone, red points are detections of $f_{bp}$ using SHC.

### 3.3 Results

The DOA estimation is computed with classical DSB, DSB with TFR and SRP-PHAT on signal portions of 3000 points. DSB is performed with 2048 points both for classical and TFR, using a plane wave model with a resolution of 4° in azimuth and 2° in elevation for the spherical search grid with a radius of 1 m. SHC is computed with 8192 points and 5 harmonics. For the energy calculation with the TFR, 5 harmonics are chosen and Q=8. SRP-PHAT is performed with 2048 points for the cross-spectrum calculation with the same search grid as for DSB. Figure 3 shows the evolution of azimuth and elevation during time in comparison with data provided by a GPS embedded in the drone. The drone has an incertitude around 3 meters which can explain the constant bias between the GPS data and the results. It is visible that selecting frequencies from the TFR enables to enhance the performance of beamforming both in azimuth and elevation. SRP-PHAT gives also better results than classical DSB but some fluctuations are still present. Table 1 presents the mean errors and standard deviations for the three approaches. Beamforming with TFR and SRP-PHAT give results very close in azimuth but the TFR approach performs better in elevation.

*Table 1:* Comparison of mean errors and standard deviations for classical DSB, DSB with TFR, and SRP-PHAT

| | Azimuth (°) | | Elevation (°) | |
|---|---|---|---|---|
| | $\mu$ | $\sigma$ | $\mu$ | $\sigma$ |
| Classical DSB | 63,7 | 42.7 | 29,1 | 21,4 |
| DSB with TFR | 53,3 | 14,5 | 8,9 | 4,9 |
| SRP-PHAT | 53 | 20,3 | 14,9 | 9,6 |

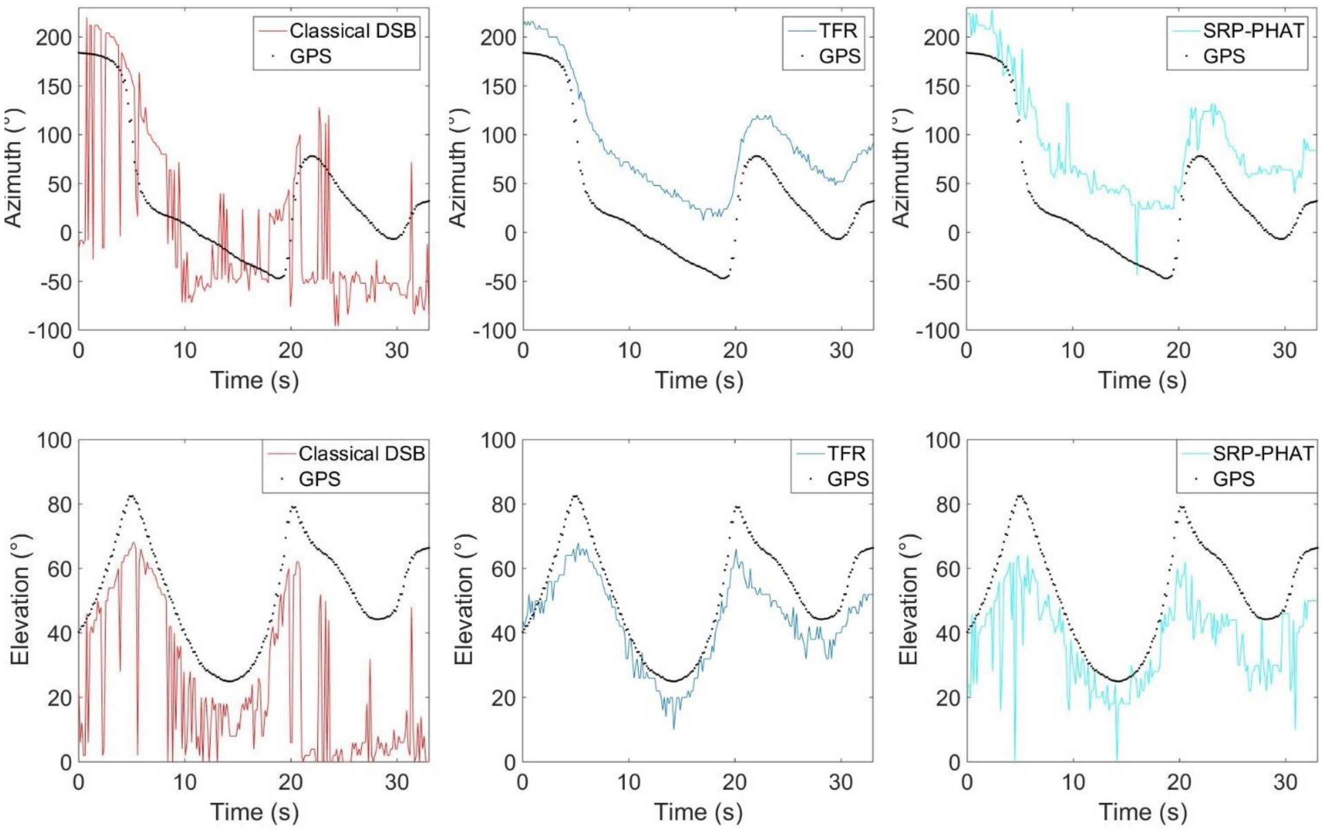


*Figure 3:* Evolution of azimuth and elevation in time for classical DSB, DSB with TFR, and SRP-PHAT. The GPS trajectory is shown in black dotted lines.

Figure 4 shows an example of an energy map in the azimuth/elevation plane of a portion of signals where classical DSB is very noisy and gives a poor estimate of the DOA in comparison with the TFR approach and SRP-PHAT. Because all the frequency content is selected with classical DSB, the signal to noise ratio (SNR) is very low. The TFR enables to enhance the SNR and therefore clarifies the energy map to find the DOA associated to the source. SRP-PHAT gives also a close estimation thanks to the GCC and weighting.

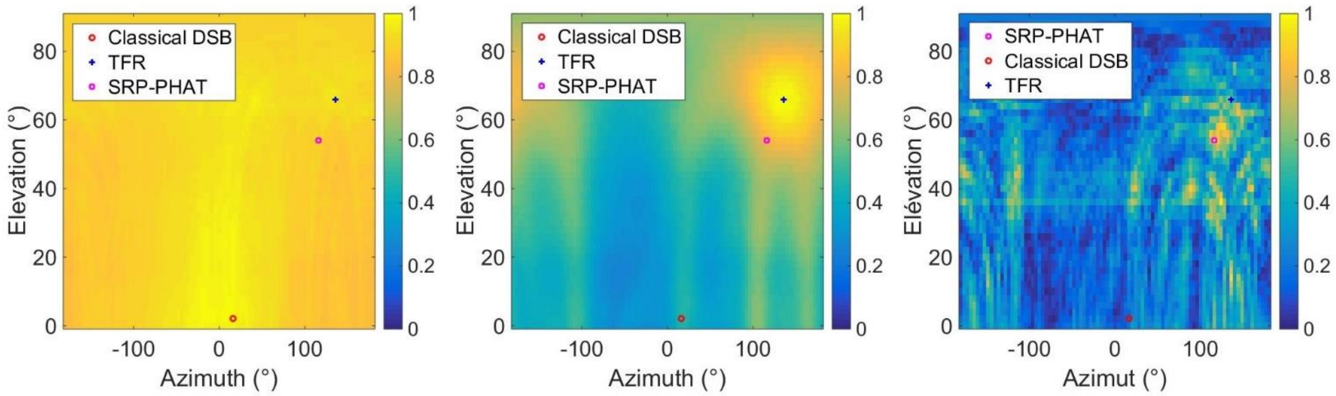


*Figure 4: Energy maps in the azimuth/elevation plane for the same signal portion with classical DSB, DSB with TFR, SRP-PHAT (from left to right). The maximum of each cartography gives the DOA estimate for the considered method. For comparison the three DOA estimates are shown on each map*

Two successive portions of signals have been chosen to demonstrate the importance of choosing the right $f_{bp}$. Figure 5 presents the energy maps associated to both portions for classical DSB and SRP-PHAT. The first portion shows accurate DOA estimates for the three methods. Indeed, despite a map with a lot of energy everywhere, classical DSB gives a good estimate of the DOA (a). SRP-PHAT gives a localized energy maximum near the true DOA for both portions [(c) (d)].

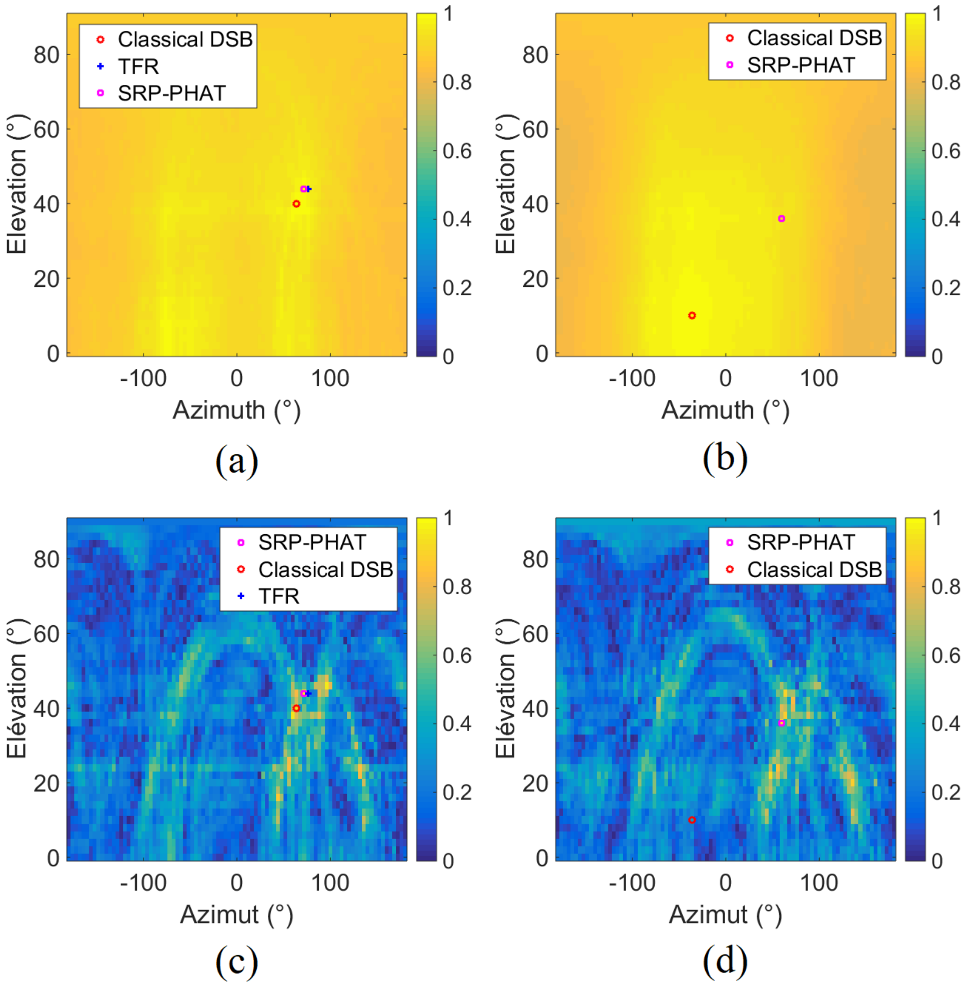


*Figure 5: Energy maps in the azimuth/elevation plane for: the first chosen signal portion with classical DSB (a) and SRP-PHAT (c); the next signal portion with classical DSB (b) and SRP-PHAT (d).*

The second portion gives a good DOA estimate for SRP-PHAT (d) but not for classical DSB (b). Figure 6 shows energy maps in the azimuth/elevation plane as well as SHC calculated between 100 Hz and 250 Hz for both signal portions using the TFR approach. This makes it possible to see which blade passing frequency is chosen for the computation of the energy contributed by its harmonics. The first portion [Fig. 6 (a)] gives a clearer map than classical DSB [fig. 5 (a)] with a good estimate of the DOA (a) using the max of SHC for $f_{bp}$ (d). The second portion gives a poor estimate of the DOA (b) using the max of SHC for $f_{bp}$ (e). Taking another $f_{bp}$ in the SHC (f) enables to change the content selected for the energy calculation and thus gives a good estimate of the DOA (c). In this case, the third maximum (156 Hz) provided by SHC (e) is selected given the cartography (c). The TFR is very interesting in its ability to choose different DOA estimates depending on the blade passing frequency chosen. A good example is between 28 s and 32 s in the trajectory where a low frequency content is present associated to a car acceleration (see Figure 2). During this time, classical DSB is unable to provide a good localization (Figure 3) while the TFR approach performs well choosing the appropriate frequency content in the energy calculation. SRP-PHAT is also more effective than classical DSB but with more fluctuations than the TFR approach.

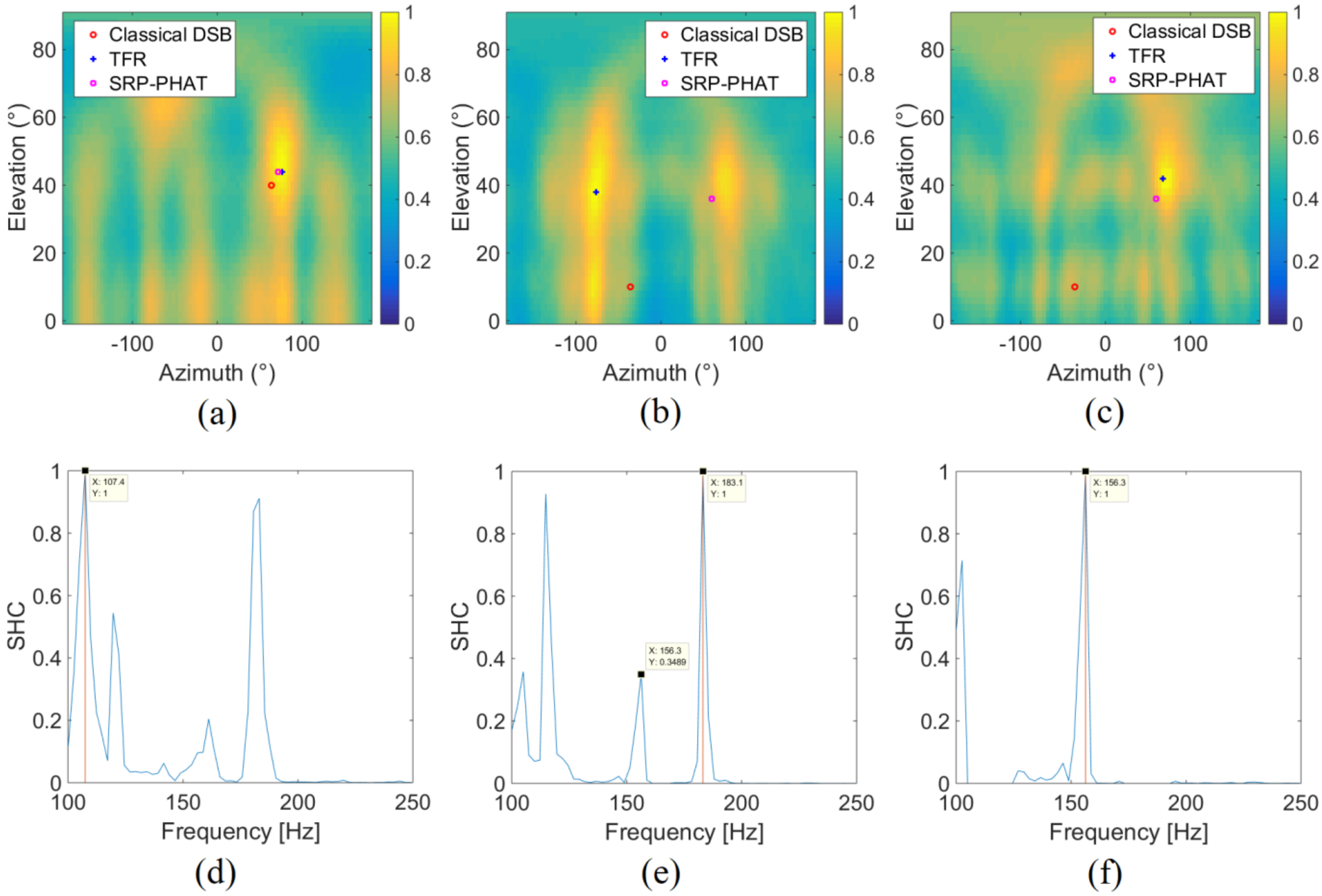


*Figure 6: First signal portion chosen: energy map in the azimuth/elevation plane for the TFR approach (a) and SHC associated (d). Second signal portion: energy map in the azimuth/elevation plane for the TFR approach and for the first $f_{bp}$ estimate (b) with the SHC associated (e), for another (right) $f_{bp}$ estimate (c) with the SHC associated (f).*

## 4. Conclusions

This study compares three approaches for estimating the DOA of an UAV. The first uses beamforming, the second, beamforming with a time-frequency representation and the last concerns the steered response power with a phase transformation. The performance of these approaches is evaluated on an experimental trajectory where the drone is flying in circles. Results show that estimations with the TFR and SRP-PHAT are better than classical DSB. However, TFR approach gives better estimations thanks to frequency content selection. The detection of the blade passing frequency thanks to the SHC is an important step in the process and a bad choice can result in a poor estimate of the DOA. A procedure to avoid this case is presented and enables to better follow the trajectory of the drone. In the presence of strong noise or perturbing sources, classical DSB is not able to estimate the DOAs but SRP-PHAT and the TFR approach still give correct DOAs. To enhance the performance of SRP-PHAT, it could be interesting to compute different weightings as SCOT, PHAT-β, or others.

## References


[1] T. Humphreys, « Statement on the security threat posed by unmanned aerial systems and possible countermeasures », *Overs. Manag. Effic. Subcomm. Homel. Secur. Comm. Wash. DC US House*, vol. 1, p. 9, 2015.

[2] R. Altawy et A. M. Youssef, « Security, Privacy, and Safety Aspects of Civilian Drones: A Survey », *ACM Trans. Cyber-Phys. Syst.*, vol. 1, nº 2, p. 1-25, févr. 2017, doi: 10.1145/3001836.

[3] N. Itare, T. Blanchard, J.-H. Thomas, et K. Raoof, « Tracking of an Unmanned Aerial Vehicle with few sensors using time-frequency representation », in *Forum Acusticum*, Lyon, France, déc. 2020, p. 3143-3147. doi: 10.48465/fa.2020.0965.

[4] A. Brutti, M. Omologo, et P. Svaizer, « Comparison Between Different Sound Source Localization Techniques Based on a Real Data Collection », in *2008 Hands-Free Speech Communication and Microphone Arrays*, Trento, Italy, mai 2008, p. 69-72. doi: 10.1109/HSCMA.2008.4538690.

[5] J. Wang, X. Qian, Z. Pan, M. Zhang, et H. Li, *GCC-PHAT with Speech-oriented Attention for Robotic Sound Source Localization*. 2021. doi: 10.1109/ICRA48506.2021.9561885.

[6] A. Johansson, G. Cook, et S. Nordholm, « Acoustic Direction of Arrival Estimation, a Comparison Between Root-MUSIC and SRP-PHAT », *2004 IEEE Reg. 10 Conf. TENCON 2004*, p. 629--632, 2004.

[7] J. H. DiBiase, H. F. Silverman, et M. Brandstein, *Robust Localization in Reverberant rooms*, from Microphone arrays: signal processing, Techniques and Applications. Berlin: Springer, 2001.

[8] G. C. Carter, A. H. Nuttal, et P. G. Cable, « The smoothed coherence transform », in *Proceedings of the IEEE*, oct. 1973, vol. 61, p. 1497--1498. doi: 10.1109/PROC.1973.9300.

[9] K. Donohue, A. Agrinsoni, et J. Hannemann, *Audio signal delay estimation using partial whitening*. 2007, p. 471. doi: 10.1109/SECON.2007.342946.

[10] S. A. Zahorian et H. Hu, « A spectral/temporal method for robust fundamental frequency tracking », *J. Acoust. Soc. Am.*, vol. 123, nº 6, p. 4559-4571, juin 2008, doi: 10.1121/1.2916590.

[11] T. Blanchard, « Caractérisation de drones en vue de leur localisation et de leur suivi à partir d’une antenne de microphones (Characterization of drones for their localization and their tracking from a microphone array) », PhD thesis, Le Mans Université, 2019.

[12] T. Blanchard, « Acoustic localization and tracking of a multi-rotor unmanned aerial vehicle using an array with few microphones », *J Acoust Soc Am*, p. 12, 2020, doi: https://doi-org.doc-elec.univ-lemans.fr/10.1121/10.0001930.

QUIET DRONES
Second International e-Symposium
on
UAV/UAS Noise
27th to 30th June 2022

# Drone disruptions: Exploring the social and political implications of growing drone noise in UK skies

**Dr Anna Jackman, University of Reading, a.h.jackman@reading.ac.uk**


## Summary

We are in the midst of a global turn to the drone. While domestic drones are the subject of increasing scrutiny – most often along lines of surveillance and privacy, security, and safety, the issue of drone noise and its impacts remains comparatively under-studied. Exploring the drone as it enters and is poised to punctuate UK airspace, this report reflects on the diversity of actors (human and nonhuman), spaces (urban and rural), and understandings (commercial, regulatory, public) of the issue and impacts of drone noise. In so doing, it centrally argues that drone noise is multiple; it is at once contextual (i.e. dependent on both the geographical location, type of land use, and type of drone operation), subjective (i.e. varying by person as well as community), and shifting (i.e. not a static issue). In developing this discussion, it at once demonstrates the value of engaging with interdisciplinary drone scholarship, and aims to raise questions of the political, social, and cultural dimensions of drone noise more widely.


## 1. Introduction: Disruptive drones

Like many countries around the globe, the United Kingdom (UK) is both interested and investing in the growth of civil, commercial, and recreational drone use (House of Commons 2021). Therein, drones are deployed and trialled in an ‘ever-growing number of applications’ (Torija et al. 2020, 1), from emergency services, inspection and monitoring, to the delivery of commercial goods and medical matter. As drones ‘capture the imaginations’ (Christian and Cabell 2017, 1) of a growing number of industries and communities alike, the platforms are associated with both economic opportunity through the ‘opening of new markets’ (Department for Transport 2021; see also PricewaterhouseCoopers 2018; UK Government 2020), and the development of applications and ‘use cases’ enabling ‘social and environmental benefits’ (The International Transport Forum 2021, 8). The UK Government thus continues to take steps, through both the allocation of resource and the adaption of regulation, in order to integrate domestic drones into UK airspace (UK Parliament 2021).

Yet, while drones are often referred to as ‘disruptive’ technologies (Watkins et al. 2020, 1; Eißfeldt 2020), namely those that ‘alter the ways that consumers, industries, or businesses operate’ (Investopedia 2020, n.p), so too can drones act to *otherwise disrupt* people, animals, and environments. In this vein, Government departments and departmental select committees alike have described drones as bound to both ‘substantial opportunities and risks’ (Science and Technology Committee 2019, 3; see also Department for Transport 2017). As such, researchers have examined drone risk along a range of contours, largely centring upon: accidental and deliberate misuse, unsafe flights inclusive of near misses with manned aircraft, drones flown in proximity to sensitive infrastructure, and drones deployed in criminal and/or harmful activities (Abbott et al. 2016; Chávez and Swed 2021; Defence Committee 2019; Jackman 2019; Watkins et al. 2020). Further, in recognition that drone use both raises and requires the ‘addressing of’ a range of ‘psychological, social, economic, political, environmental and legal issues’ (Watkins et al. 2020, 2), so too has the growing popularity of drones raised concerns around ‘noise disturbance’ in UK airspace (IOA 2021, n.p).

Engaging interdisciplinary drone scholarship, this report seeks to highlight the value of considering a greater diversity of experiences (human and nonhuman), spaces (urban and rural), and understandings (regulatory, commercial, public) of the issues and impacts of drone noise. In recognition of the diversity of stakeholders that deploy and experience drone use, it thus aims to consider and contribute to wider efforts to examine the ‘complex ways in which life is lived with, through, and against the drone’ (Bradley and Cerella 2019, n.p) by raising wider questions of the political, social and cultural dimensions of drone noise.

## 2. Disruptive drone noise

### 2.1 Contextualising drone noise

The impacts of noise can be profound. Understood as a ‘significant environmental cause of ill health’, noise from transport systems and technologies can ‘lead to annoyance, stress, sleep disturbance, poor mental health and well-being, impaired cognitive function in children, and negative effects on the cardiovascular and metabolic system’ (The International Transport Forum 2021, 49). Drones are recognised as a ‘growing new source of environmental noise pollution’ (Schäffer et al. 2021, 1). While the drone ‘noise problem’ may not yet have ‘loomed large’ (Regulatory Horizons Council 2021, 30), as the popularity of drones grows, drone noise is likely to become more significant in the future (Schäffer et al. 2021). In reflecting on the potential implications of drone-related ‘rises in noise pollution’ (DEFRA 2020), scholars have noted that the characteristics and impacts of drone noise ‘depend on a variety of factors, including a drone’s design and size’ (The International Transport Forum 2021, 49). With that in mind, they have highlighted the drone’s ‘special acoustic characteristics’ (Schäffer et al. 2021, 1), identifying ‘unconventional noise signatures’, high tonality and ‘irritating frequency and amplitude modulations’ (Torija Martinez 2020, 1), and drone noise as ‘unique’ sound that ‘does not resemble that produced by other common community-noise sources’ (Hui et al. 2021, 1). Thus, while scholars call for drones to be considered in relation to ‘fixity and mobility, enclosure and openness’ (Klauser and Pedrozo 2015, 289), so too we must too acknowledge the drone’s buzzes and hums as silencing, piercing, or disabling (Jablonowski and Jackman 2021: n.p).

### 2.2 Regulating drone noise

While there is a ‘strong relation between aircraft noise and annoyance’ (Torija Martinez 2020, 3), it remains that ‘a range of policies, standards and operational procedures have been developed’ with the aim that their impacts ‘are addressed’ (The International Transport Forum 2021, 13). The same can arguably not yet be said of the impacts of drone noise.

After all, while both the desire and development of drone activity in UK airspace continues apace, the regulation of drone noise remains unfolding. For example, while current regulation from the UK airspace authority, the Civil Aviation Authority (CAA), highlights the importance of ‘protecting citizens’ and ‘limiting noise emissions to the greatest possible extent’ (CAP 1789B 2021), it acknowledges that there are ‘currently no noise specific requirements’ for drones in the UK, adding that the ‘intent is that the UK follows European Commission (EC) regulation’ (CAP 1766 2019). The EC has asserted the importance of ‘limiting noise emissions’ in order to ‘provide citizens with high levels of environmental protection’ (Torija Martinez 2020, 5). As such, the EC (as well as the European Union Aviation Safety Agency) are developing regulations whereby drone operations are ‘separated into different risk-based categories’, with drones sold ‘for use within the open category’ to be subject to a series of proposed, albeit ‘uncertain’, ‘maximum sound levels’ (CAP 1766 2019). There are presently no maximum noise limits proposed for larger drones (CAP 1766 2019). In this vein, scholars have argued both that the ‘sound power level is unable to account for all the typical acoustic features of UAVs’, and that ‘the proposed maximum value does not seem related to public reaction’ (Torija Martinez 2020, 5) (see section 3.1). As such, it is argued that further research is needed to appreciate the drone’s ‘acoustical characteristics’ across varying operational contexts in order to ‘establish drone noise standards and legislations’ (Schäffer et al. 2021, 1).

In this vein, commentators have raised a number of issues and suggestions for areas for regulators to consider and/or enact. These include measures focusing on platform design, including design efforts around aircraft/component weight, ‘larger and slower propellers’, and the use of ‘passive noise reduction’ techniques (CAP 1766). Such suggestions are accompanied by measures focused on both operations, such as the setting of a ‘curfew on hours of operation’ (Paine 2019, n.p) and the development of ‘local drone traffic rules’ (Nesta 2018, 97), and clarification on the placement of responsibility to act in relation to operations. Here, the IOA (2021a, n.p) assert the need for a ‘clarification on the tools available so that significant adverse noise impacts are avoided’, including information on the place of considering drone noise in the granting of both of CAA permissions and ‘planning permission for new operating facilities’, and clarity regarding whether or not drone noise could fall under statutory nuisance or whether it will receive the same ‘special exemption’ as other ‘noise from civil aircraft’ (Regulatory Horizons Council 2021, 30). As the Regulatory Horizons Council (2021, 14) continue, this lack of clarity represents a ‘gap concerning noise regulation’.

While it may appear that the emergence and cementing of the drone has outpaced the development and application of noise testing and compliance given that there is presently ‘no noise standard for UAVs within the UK’ (Depuru Monan and Jude 2022, n.p; Regulatory Horizons Council 2021), the UK Government are taking steps to remedy this situation. For example, in developing a ‘new Aviation Strategy’ to enable a ‘safe, secure and sustainable aviation sector’, the Department for Transport has requested that the Civil Aviation Authority undertake a ‘noise analysis’ (CAP 1766 2019). In this vein, the Department for Transport in 2021 launched the ‘Future of Flight Review’, a process seeking ‘views on areas of flight regulation that are outdated, a barrier to innovation, or not designed with new technologies in mind’ (Department for Transport 2021). While in the process of examining submissions, the consultation featured questions on approaches to the regulation of ‘new and novel aircraft noise’, while stressing the importance of such aircraft to ‘produce a level of noise acceptable to the general public and local authorities’ (Department for Transport 2021).

In summary, while efforts are underway to more carefully and thoroughly regulate drone noise, challenges remain around both the variety of drone 'sizes, physical characteristics, and environments in which they operate' (The International Transport Forum 2021, 13), and 'accounting' for these variations while providing and enforcing 'information about acceptable levels' of drone noise (Torija Martinez 2020, 1; see also Depuru Monan and Jude 2022).

## 3. Actors: Diverse experiences of drone noise

### 3.1 Human experiences of drone noise

> *"Drones are taking to the air without a lot of thought for the ears of people on the ground" (Paine 2019, n.p)*

Alongside prompting concerns around privacy (Finn and Wright 2016; Winkler et al. 2018), questions have been raised of the impact of drones upon our experiences of (air)space, and the impact of drone noise upon wider health and wellbeing. This has involved consideration of 'non-auditory health effects' (Schäffer et al 2021, 4) from annoyance and anxiety to potential 'cognitive distraction' levels (Hui et al. 2021, 5). Here, attention can also be turned to the drone's (potential) contribution to noise pollution, with the United Nations asserting that 'noise pollution is far from being a mere nuisance', rather it is 'understood to have long-term effects on human health' (Andersen 2022, n.p). Here, scholars have urged attention to the reception, experience, and 'public acceptance' of (growing) drone activity and the noise accompanying it, arguing that noise remains 'one of the largest limiting factors for public acceptance and adoption of drone technology' (Torija Martinez 2020, 1).

As such, scholars have undertaken 'human–subject psychoacoustic tests' to explore the 'annoyance generated' by drones, with Christian and Cabell (2017, 1) finding that drone noise may be understood as 'substantially more annoying than road traffic or aircraft noise' (Schäffer et al. 2021, 1). Similarly, in examination of human perceptions of drone noise in different urban settings and 'soundscapes',Torija et al. (2020, 1) found that participants located in 'soundscapes with reduced road traffic noise' reported 'a significantly higher perceived loudness and annoyance' in comparison to those in other areas. In this vein, scholars have also found operational context as potentially 'strongly moderating' perceptions of drone noise, with public acceptance higher for rescue operations over 'private flights' (Schäffer et al. 2021, 4). This is echoed in data from a survey undertaken by PricewaterhouseCoopers (2019, 1) exploring 'public and business attitudes towards drones' in the UK. Here, it was found that the 'most popular uses of drones among the public were: Search and rescue (87%), Identifying and tracking criminals (80%), Observing fires, spills and other emergencies (84%)', while the most opposed use of drones' were: 'Flying taxis (41%), Delivering packages (26%), Air ambulances transferring patients (19%)' (PricewaterhouseCoopers 2019, 4).

In addition, scholars have observed that levels of both acceptance and annoyance associated with drones may be impacted by not just the sound of the drone, but also influenced by the extent to which the drone is visible (Schäffer et al. 2021, 4). Further, in examination of the multiple variables at play in experiencing drone noise, scholars have sought to explore how individual subjectivities and particular identity characteristics may influence perceptions. For example, writing of 'attitudes towards civil drones' and the 'influence of gender on drone acceptance', as explored in a 'telephone survey in Germany', End et al. (2021, 1) found 'males to be less concerned about civil drones than females, regarding noise' (see also Eißfeldt 2020). While further research is required, such studies collectively demonstrate that perceptions and experiences of drone noise are at once 'driven by the characteristics of the local soundscape' (Torija Martinez 2020, 5), operation and altitude dependent (Hui et al. 2021), and remain multiple and subjective.

In this vein, commentators have noted that as drones fly considerably lower than manned aircraft, they can 'give the impression of causing a nuisance' (Regulatory Horizons Council 2021, 30; see also Hui et al. 2021), and further, 'certain noises – such as the buzzing sound of some drones – may be considered more annoying or disturbing than others' (Depuru Monan and Jude 2022, n.p; see also Watkins et al 2020). The advent of drones may also introduce and expose new communities 'not currently affected by aircraft noise' to such issues (Torija Martinez 2020, 1). Such concerns are echoed through the halting of Google's (Wing) delivery drone trials in Australia in 2019 'due to noise complaints' (Regulatory Horizons Council 2021, 30; McCarthy 2019). As The International Transport Forum (2021, 50) note, further work is thus needed to interrogate the perception of drone noise along and across multiple parameters, including the person listening to the noise, and the conditions they are in (for example, weather, environment etc). As they state:

> *'Parameters like the type of noise (consistent vs. fluctuating), frequency of noise (high vs. low), sources of noise (nature vs. human activities), time of noise (day vs. night; weekday vs. weekend), or surroundings of the noise source (residential area vs. industrial zone)…will influence the perception of noise' (The International Transport Forum 2021, 50).*

While pertinent to note that the 'presence of an impending drone' may be associated with excitement for an individual receiving a 'much-awaited delivery', concerns remain around community as well as individual experiences of drones flying 'low and in great numbers' (Watkins et al. 2020), leading the UK's airspace regulator to thus assert that the impacts of drone 'noise exposure' thus 'require further research' (CAP 1766 2019).

### 3.2 Nonhuman experiences of drone noise

Alongside considering the impact of drone noise upon humans, we also need to reflect on the drone's potential 'undesirable impacts on wildlife' (Hodgson and Koh 2016, 404). As the United Nations asserts, noise pollution marks a 'threat to animals, altering communications and the behaviour of various species' (Andersen 2022, n.p). While cognisant that drones can be 'less intrusive to wildlife than occupied aircraft' (Mo and Bonatakis 2022, 111), it remains that the impact of drone noise upon animals is an area requiring further attention, as it both marks a 'new type of anthropogenic disturbance' (Mulero-Pázmány et al. 2017, 1) and enacts distinct 'stressors to wildlife' (Ditmer et al. 2015, 2278).

As Hodgson and Koh (2016, 404) note, wildlife respond in different ways to drones 'in proximity', depending on 'species, environmental context, and the type and method of drone operation'. Here, both 'the characteristics of the animals themselves (animal type, life-history stage, and level of aggregation)' and the 'vehicle's attributes' (such as engine type and drone size) will influence the impact of drone noise upon the animal (Mulero-Pázmány et al. 2017, 1; The International Transport Forum 2021, 57). As such, in systematically reviewing the impact of drone noise upon animals, Mulero-Pázmány et al. (2017, 3) classified the 'reaction caused' by drones into several categories: 'none', 'alert reaction' (i.e. showing 'increased attention or alert' towards the drone), and 'active reaction' (i.e. 'responding actively' towards drone by 'fleeing or attacking'). Here, Mulero-Pázmány et al. (2017, 6) found that flight patterns were particularly significant, with 'target-orientated flights' wherein drones are flown with animals as their focus (e.g. for 'photography, nest inspections and animal control') acting to 'produce more reactions' and disturbance. Further, as Mo and Bonatakis (2022, 112) detail, additional factors from drone shape, size, colour and patterning, take-off distances from animals, and airspeed are also important factors when considering the (potential) impact of drones and drone noise.

In further interrogating the ways in which drones may 'interfere with the natural environment' by 'disturbing wildlife' (The International Transport Forum 2021, 57), scholars have found that ‘terrestrial mammals are overall less reactive’ to drones than birds, and drones have little effect upon ‘aquatic animals’ (Mulero-Pázmány et al. 2017, 7; see also Bevan et al. 2018). As such, existing work has predominantly focused on the responses of birds to drones and the noise associated with them. It is asserted that ‘birds, especially in larger groups, are the most sensitive to drones’ (The International Transport Forum 2021, 57; Mulero-Pázmány et al. 2017, 5). For example, in examination of the impact of ‘drone colour, speed and flight angle on the behavioural responses of mallards’, Vas et al. (2015, 1) argue that ‘approach speed, drone colour and repeated flights had no measurable impact on bird behaviour’, though found that the birds ‘reacted more to drones approaching vertically’. Conversely, in examination of if and how ‘birds perceive common drone platforms as threatening’, scholars have examined ‘behavioural and physiological responses’ of birds to different drones (fixed-wing, multirotor) and different flight modes and forms of approach (head on, overhead) (Egan et al. 2020, 1) with different results. In the case of Red-winged Blackbirds, researchers explored alertness, alarm calls, and vigilance, finding that fixed wing drones were ‘perceived as riskier than multirotor’, and that ‘birds perceived drones with predatory characteristics as riskier than common drone models’ (Egan et al. 2020, 1). In this vein, scholars have also warned of the impact of drone noise upon bird communications. Writing that ‘bird calls are key to species’ survival, ‘letting them warn each other of danger – and find mates’, Paine (2019, n.p) argues that drone noise may impact birds ‘hearing each other’ in a number of ways. However, researchers have also cautioned for the need to consider other forms of 'environment noise' in the area of the drone flight, as this may 'obscure' the noise from the drone itself (Mesquita et al. 2021, 157).

Thus, while attention to the impacts of drones and the their noise upon nonhumans is growing (Mo and Bonatakis 2022), it remains that further attention is needed to both the ‘physiological and long-term consequences’ of drone disturbances, and their ‘observable impacts’ as well as ‘non-visible effects’ more widely (Mulero-Pázmány et al. 2017, 8; Mo and Bonatakis 2022, 112). For example, in examining the impact of drone flights on the ‘movements and heart rate responses of free-roaming American black bears’, Ditmer et al. (2015, 2278) found that there were ‘consistently strong physiological responses’. While the researchers observed ‘infrequent behaviour changes’, they noted that the bears responded to drones with ‘elevated heart rates, rising as much as 123 beats per minute above the pre-flight baseline’ (Ditmer et al. 2015, 2278), thus highlighting the importance of considering non-visible forms of ‘stress on wildlife’. It should be noted that upon undertaking further research into whether the bears ‘habituate to repeated’ drone exposure, the team found that ‘spikes in heart rate, a measure of stress, diminished’ over time (Ditmer et al. 2018, 1). However, while mammals may ‘become and remain habituated to a novel anthropogenic stimulus’ such as drone flights, it remains that ‘such habituation to mechanical noise’ may have other ‘chronic physiological effects’, thus requiring further attention (Ditmer et al. 2018, 1). Further, in developing a deeper understanding of such issues, a greater distinction is required to understand how drone disturbance to animals may be attributed to ‘visual or auditory cues’ (Mesquita et al. 2021, 157), and the balances between these factors, depending on the animal, context, and form of drone (operation).

Lastly, in linking back to section 3.1, when considering drone noise through the lens of the public acceptance of drone applications, it has been found that public opinion on (in this case delivery) drones can be influenced by concerns around ‘animal welfare’ (Eißfeldt 2020, 1). Thus, in addition to recognising the ‘intrusiveness’ of the drone on humans below (Thomasen 2020, 3), so too must we remember that ‘drones are not the only occupants of airspace’ (Jackman 2022, 6). Animals ‘(re-)make’ (air)space in important ways (Oliver et al. 2021, 3), and as such, we must consider both the impact and range of 'disturbances' that 'potentially alarming' drones may prompt to both human and non-human life (Duffy et al. 2018, 16).

## 4. Spaces: Spatial differences and drone noise

In addition to considering the different experiences and impacts of drone noise upon humans and nonhumans, it is also pertinent to consider the role of spatial context. As Torija Martinez (2020, 1) notes, the advent of drones and their noise is likely to usher in alterations to both 'urban and rural soundscapes'. After all, while drones are touted as poised to reshape economies and sectors – with estimates of a UK drone economy creating 628,000 jobs and featuring 76,000 drones in the sky by 2030 (Pricewaterhouse Coopers 2018), it remains that drones are likely to impact urban and rural spaces in distinct and 'different' ways (Klauser 2018, 370), with community experience varying 'depending on context' (Torija Martinez 2020, 2). In this vein, in undertaking surveys on the public perception of drones, scholars have found that spatial context impacts the drone's popularity, with a survey in Germany suggesting 'more support for drone delivery in remote areas (small villages in the mountains, or small islands in the sea) and rural areas, and the lowest levels of support in large cities' (Eißfeldt 2020, 2).

### 4.1 Urban drone noise

Within both commercial and wider drone imaginaries, drones are often anticipated to be deployed in 'highly populated areas' (Hui et al. 2021, 1). Writing of the anticipation and advent of drones in urban environments, scholars have noted that the drone will at once 'require the built environment to change dramatically' (Cureton 2014) and remain bound to a range of 'techno-cultural contestations – from challenges around airspace integration, to concerns around privacy, safety and pollution' (Jackman and Jablonowski 2021, 39; see also Klauser and Pedrozo 2015; Watkins et al. 2020). However, as greater resources and emphasis are placed on the rollout of Unmanned Traffic Management (UTM), it is increasingly anticipated that both greater volumes of drone applications and 'greater operational freedoms for drone use in urban environments' will be enabled (Watkins et al. 2020, 4). As such, drone noise in urban environments is a key consideration. Therein, concerns have been raised around both 'noise volume' and the 'frequency of sound from flights' in urban locales (Depuru Monan and Jude 2022, n.p). It has however also been asserted that in the case of urban areas, existing 'ambient noise' may make 'drone noise less apparent', though, conversely, the proximity of drones to 'residential areas' may make 'drones more noticeable' to residents therein (The International Transport Forum 2021, 13; see also Christian and Cabell 2017; Schäffer et al. 2021).

Consider, for example, the (potential) advent of delivery drones, an innovation which an estimated 26 nations are reportedly 'trialling, planning to test, or have established' (Unmanned Airspace 2019, n.p), and which remain a popular trope and application within the wider context of the 'good drone' (Jumbert and Sandvik 2017). While the 'potential market and economic viability of such services' arguably remain undetermined (Aurambout et al 2019, 1), as scholars have unpacked, popular drone delivery projects such as Amazon's 'Prime Air' reimagine the situation of warehouses (known as fulfilment centres) from urban outskirts to high-rise drone hubs located in densely-populated urban centres (Jackman and Jablonowski 2021). While designed and re-imagined both to enable the rapid servicing of urban populations through deliveries within 30 minutes, and to 'reduce greenhouse gas and other environmental impacts compared to conventional delivery trucks' (Torija et al. 2020, 2), such proposed innovations prompt us to 'imagine round-the-clock hives of aerial activity' (Paine 2019, n.p), and necessitate questions around potential inequalities of drone noise in urban centres.

For example, while 'acknowledging periods of decline and urban renewal', the potential placement of drone delivery hubs in such locations raises critical questions around the experiences of urban residents, and their exposure to different forms of visual and noise pollution (Jackman and Jablonowski 2021, 46). Here, scholars assert that drone 'sounds have been found more annoying than sounds of delivery road vehicles' (Torija et al. 2020, 2). In this vein, while it may be acknowledged that drones may be 'difficult to hear against background noise' in 'urban settings', it remains that 'there have been cases where drones have been unpopular in residential settings because of noise' (Regulatory Horizons Council 2021, 14). Here, it is added that such public resistance to drone noise may be 'especially likely' in the case of 'consumer deliveries which have yet to be trialled at scale in urban areas' (Regulatory Horizons Council 2021, 14). In addition, while there has remained a long association between 'height and power' (Garrett and Fish 2016, n.p) with 'the rich' having 'access to good air while the poor are relegated to the dregs' (Choy in Graham and Hewitt 2012, 84), the advent of urban drones at scale arguably complicates such relations. For example, as cities grapple with congestion, the modelling of potential delivery drone emissions suggests that while 'drones are likely to provide a CO2 benefit' when compared to delivery trucks, this depends and relies upon both the volume of drones and their 'service zones being close to the depot, and/or there being few delivery stops' (Goodchild and Toy 2018, 58; Jackman 2022, 8; Torija et al 2020). Such analysis does not, however, account for both the delivery drone's vertical and volumetric redistribution of congestion, and the ways in which this may influence experiences of airspace, as political and social 'struggle takes on an increasingly three-dimensional character' (Graham 2016).

Further, think tank for transport policy The International Transport Forum (2021, 27) raise questions of the potential impact of the noise associated with drones (and their supporting infrastructure) upon 'land use and property values'. They highlight that 'property values close to droneports or drone activity may decrease' (The International Transport Forum 2021, 27). As such, there remains important public and policy dimensions to consider around the integration of noise-producing drone operations. Lastly, as Watkins et al. (2020, 9) assert, it also remains important to be attentive to the ways in which the 'urban environment varies widely throughout the globe', from high-rise buildings to 'relatively isolated single dwellings', thus adding further complexity to examinations of the experiences and management of drone noise in diverse urban contexts.

### 4.1 Suburban and rural drone noise

While drones may be popularly associated with urban innovations, scholars have noted that 'contrary to many expectations, drone spaces are not primarily urban but rural' (Pauschinger and Klauser 2020, 454). For example, in discussion of a 'large-scale survey of professional drone usage in Switzerland', Pauschinger and Klauser (2020, 443, 445) note that further attention is needed to explore the 'complex and diverse ways' that drones are being used that exceed the 'urban surveillance thesis'. They continue that in the case of 'professional drone usage', as a 'rural phenomena' drones are used in different ways – 'far more sporadic, fragile' and diversely deployed. This assertion is echoed in the pair's work examining the deployment of drones for agriculture, in which Klauser and Pauschinger (2021, 55) argue that while drones continue to 'proliferate in many professional fields', they remain particularly suited to (rural) agricultural deployment 'if the legal constraints imposed on drone usage above more densely populated urban spaces are taken into account'.

In this vein, in attending to the differences and nuances present when considering drone noise specifically in rural environments, scholars have considered the impact of 'different blade configurations' therein, finding that while particular kinds of blade may be less perceptible, so too may they be 'subjectively…more annoying to the receptor, due to the presence of tonality' (Nixon and Dance 2021, 1, 8). Such findings prompt the authors to urge further research in this area, and specifically a greater consideration of the 'ways to quieten drones in rural areas, as there are generally lower background noise levels to mask drone noise' meaning that drones can be 'heard from a large distance' (Nixon and Dance 2021, 8). Just as in urban areas, consideration could thus be given to the design and designation of 'routes and restricted areas or red-zones', as enabled by Unmanned Traffic Management (Connected Places Catapult 2020, n.p; The International Transport Forum 2021).

Further, it is again also worth considering potential inequalities of drone noise in suburban and rural areas. As acoustic ecologist Garth Paine (2019a, n.p) writes, ‘wealthier suburbs’ are at once often ‘farther from big noise sources’ and more fiscally able to put noise reduction measures in place (e.g. tree planting). While not to eschew the challenges besetting ‘suburban delivery’, from ‘animals in garden, to theft’ (Watkins et al. 2020, 9), it remains that while wealthier suburban and rural residents may be in a position of affordance to be served by commercial drones, so too may those drones introduce a range of complex social and political issues, inclusive of noise concerns. This is highlighted in and through the issue of potential ‘NIMBYism’ (Not In My Backyard). As Eißfeldt (2020, 1) found in a survey exploring the public perception of drones in Germany, ‘even residents who envision using drones for the delivery of their own parcels frequently report that they would not agree to flights over their own homes’.

As the UK's ‘innovation accelerator for cities, transport, and places’ Connected Places Catapult (2020, n.p) states, drones are poised to increase ‘noise levels leading to greater exposure’ in both urban and rural settings, which may result in the ‘creation of nuisance’ and/or ‘the potential of wide-spread community rejection’. As we saw in section 3.1, further and careful consideration of drone noise and its spatial specificities, is thus pertinent.

## 5. Understandings: Different perspectives on drone noise

Thus far, this report has sought to demonstrate the value of considering a greater diversity of experiences (both human and nonhuman) and spaces (urban and rural) in discussion of drone noise. In the report’s final section, it highlights that both the issue and (potential) impacts of drone noise may be understood in different ways by different actors and communities, from regulators and commerce, to general publics. After all, drone industries remain eager to deploy, integrate and scale drone business, aviation regulators at once to ‘realise the full potential of drones whilst maintaining aviation safety and addressing’ relevant concerns (Department for Transport 2017, 4), and general publics to enjoy and benefit in different ways from airspace. In this vein, the drone noise issue is complicated by the nature of the drone, and the market that underpins it, as this ‘growing market– variously and differently anticipates drone futures – not as singular or monopolistic platforms and operations, but rather as multiple’ (Jackman and Jablonwski 2021, 49). Therein we see competing perspectives, goals and understandings. This is echoed by the Regulatory Horizons Council (2021, 14) who state that ‘there is a range of opinions among stakeholders with respect to the degree of nuisance that drone noise represents now and in the future’.

This concern is evident, for example, through the issue of *volume*. Here we can think both with the desired volume (loudness or quietness) of drone noise, and the desired volume (number of drone aircraft) in the sky. For example, acoustic ecologist Paine (2019, n.p) notes that commercial drones are often both louder than their recreational counterparts, and emit a ‘higher pitched’ sound than other aerial craft encountered in urban areas, such as helicopters. Further discussion of the drone’s unique noise and the ways in which this may be perceived can be found in sections 2.1 and 3.1. In addition, we can also consider volume in relation to the number of drones that both do and may come to operate in UK skies. For example, forecasts suggest that there may be upwards of 76,000 drones in the UK by 2030 (CAP 1766). In seeking to safely integrate growing drone traffic, plans for ‘Unmanned Traffic Management’ (UTM), namely the at-scale integration of drones into domestic airspace through airspace segmentation and communication between aerial craft, are underway (Kuhn 2017; see also Connected Places Catapult 2020). This is echoed by the passing of the 'Air Traffic Management and Unmanned Aircraft Act 2021', examining the 'licensing regime for air traffic services' (UK Parliament 2021a, n.p) while both 'capitalising on the exciting opportunities drones offer' and 'clamping down on misuse and disruption' (Transport Secretary in Gov.UK 2021, n.p). While cognisant of the complexities of UTM, as an operational approach it is underpinned ‘by the premise and promise of shared and multiply-occupied airspace’ (Jackman 2022, 8). Therefore, discussion of drone noise should exceed analysis at the scale of the single drone and instead should remain cognisant of drone operations at scale, and attentive to the different agendas and understandings of diverse drone deployers and experiences therein.

Further, discussions of drone noise should also recognise that (UK) airspace is not static. As such, it should consider ongoing shifts in the environments and contexts underpinning such discussions. For example, as The International Transport Forum (2021, 50) note, it is envisaged that in the future there will be an ‘uptake of electric, automated and shared vehicles’, which is anticipated to influence levels and volumes of ‘conventional traffic’, making it ‘more efficient and silent’. As such, given that the ‘urban land- and soundscape in the city of the future may therefore be very different to today’s’ (The International Transport Forum 2021, 50), an analysis of drone noise should also aim to consider the implications of ‘emergent, evolving, and unfolding’ future drone-punctuated airspace (Jackman 2019, 373).

In any case, it remains that ‘while desires and developments to enable the integration of drones into airspace continue apace, comparably little consideration of the acoustic effects of drone operations at scale has occurred’ (Jackman and Jablonowski 2021, 49). While not to eschew the 'diversity of the drone industry'  (Finn and Wright 2016, 577), this assertion is arguably echoed through statements by The Entrepreneurs Network (2021, 6), a ‘a think tank for the ambitious owners of Britain's fastest growing businesses and aspirational entrepreneurs’, who assert that the ‘most prominent challenge for the UK is how to safely integrate drones’ into busy airspace, while noting that ‘concerns about noise may need addressing, but these are likely to be secondary’. This can be considered against surveys undertaken with members of the general public. For example, the Institution of Mechanical Engineers (2019, 6) undertook a survey on ‘public attitudes to unmanned aerial vehicles’, collecting 2010 responses from across Great Britain. They found that alongside concerns around ‘drones causing travel disruption at airports, compromising national security, and accidents in the sky with other aircraft and drones’, 8% of respondents expressed concern around ‘noise made by drones’ (Institution of Mechanical Engineers 2019, 7). In this vein, in undertaking a study exploring ‘public and business attitudes towards drones’ in the UK, professional services network PricewaterhouseCoopers (2019, 2) found the top areas of ‘concern about commercial drones among the public’ to be: ‘risk of improper use (41%), risk of use by criminals (27%), risk of accident (26%). While acknowledging the industry-enabling focus of this survey, it is argued that in the case of the 21% of respondents that ‘feel negatively towards drones’, efforts should be taken to ‘build consumer trust and address concerns, from privacy to noise pollution’ (PricewaterhouseCoopers 2019, 2), i.e. drone noise comprises an area of concern.

In recognition of the multiplicity of views and perspectives on the issue of drone noise, the UK Government’s Department for Environment, Food & Rural Affairs (DEFRA) have called for the conducting of ‘a review of stakeholders’ thoughts on noise mapping’ in development of a ‘new noise model’ as part of the Environmental Noise Directive (Defra 2020, n.p). Such an approach would support the idea that there remains a need for care and attention to the different ways in which drones, and the noise associated with them, are understood by diverse communities.

## 6. Conclusions

Drones are increasingly popular, with global markets forecast to ‘climb to almost $43 billion by 2025’ (Heliguy 2020, n.p). Yet, while drones are increasingly entering and poised to enter (UK) airspace, attention to the impacts of drone noise remains comparatively under-considered.

In recognition that drones do not simply inhabit airspace, but rather 'transform it' (Jackman and Jablonowski 2021, 39), this report has explored the issue of drone noise in the context of the UK, reflecting on both the diversity of actors (human and nonhuman), spaces (urban and rural), and understandings (commercial, regulatory, public) on this issue, with the aim of raising questions regarding its political, social and cultural dimensions. Most centrally, the report has suggested that drone noise is multiple; it is at once contextual (i.e. dependent on both the geographical location, type of land use, and type of drone operation), subjective (i.e. varying by person as well as community), and shifting (i.e. not a static issue).

While cognisant that the UK Government and airspace regulator alike are increasingly concerned with the issue and (potential) impacts of drone noise, as the Department for Transport (2021) asserts, in the face of 'an increased number of new and novel aircraft', actions are required from the development of a 'robust approach to measuring noise', to the setting of relevant standards. Both the advent and integration of drones into UK airspace, as well as the management and mitigation of drone noise therein, thus remain a live and unfolding issue, at once warranting further attention and inviting consideration of its political, social and cultural dimensions.

**References**

Abbott C, Clarke M, Hathorn S, and Hickie S (2016) *Hostile drones: The hostile use of drones by non-state actors against British targets*. Open briefing https://www.files.ethz.ch/isn/195685/Hostile%20use%20of%20drones%20report_open%20briefing_0.pdf

Andersen I (2022) *The world's cities must take on the cacophony of noise pollution*. Financial Times https://www.ft.com/content/ffacda24-da6e-4a95-9ce5-a3343e23bc06 March 28 2022

Aurambout JP, Gkoumas K, and Ciuffo B (2019) *Last mile delivery by drones: an estimation of viable market potential and access to citizens across European cities*. European Transport Research Review 11(30), 1-21

Bevan E, Whiting S, Tucker T, Guinea M, Raith A, and Douglas R (2018) *Measuring behavioral responses of sea turtles, saltwater crocodiles, and crested terns to drone disturbance to define ethical operating thresholds*. PLOS one, 1-17 https://doi.org/10.1371/journal.pone.0194460

CAP 1766 (2019) *Emerging Aircraft Technologies and their potential noise impacts.* Civil Aviation Authority https://publicapps.caa.co.uk/modalapplication.aspx?catid=1&pagetype=65&appid=11&mode=detail&id=9012

CAP 1789B (2021) *The UAS Delegated Regulation: UK consolidated text*. Civil Aviation Authority https://publicapps.caa.co.uk/modalapplication.aspx?appid=11&mode=detail&id=9655

Chávez, K, and Swed O (2021) *The proliferation of drones to violent nonstate actors.* Defence Studies 21(1), 1-24

Christian AW, and Cabell R (2017) *Initial Investigation into the Psychoacoustic Properties of Small Unmanned Aerial System Noise*. In Proceedings of the 23rd AIAA/CEAS Aeroacoustics Conference; American Institute of Aeronautics and Astronautics, Denver, CO, USA, 5–9 June 2017

Connected Places Catapult (2020) *Enabling UTM in the UK* https://1hir952z6ozmkc7ej3xlcfsc-wpengine.netdna-ssl.com/wp-content/uploads/2020/12/01296_Open-Access-UTM-Report-V4.pdf

Cureton P (2014) *How drones and aerial vehicles could change cities*. The Conversation https://theconversation.com/how-drones-and-aerial-vehicles-could-change-cities-140907

Defence Committee (2019) *Committee take evidence on domestic threat of drones*. UK Parliament https://old.parliament.uk/business/committees/committees-a-z/commons-select/defence-committee/news-parliament-2017/domestic-threat-of-drones-evidence-19-20/

DEFRA (2020) *Noise Mapping (Round 4). Stakeholder Review.* Report No. 20-0004-0 R01 http://sciencesearch.defra.gov.uk/Default.aspx?Menu=Menu&Module=More&Location=None&Completed=0&ProjectID=20532

Department for Transport (2021) *Future of transport regulatory review: future of flight*. Gov.UK https://www.gov.uk/government/consultations/future-of-transport-regulatory-review-future-of-flight

Department for Transport (2017) *Unlocking the UK's High Tech Economy: Consultation on the Safe Use of Drones in the UK*. Government Response https://assets.publishing.service.gov.uk/government/uploads/system/uploads/attachment_data/file/631638/unlocking-the-uks-high-tech-economy-consultation-on-the-safe-use-of-drones-in-the-uk-government-response.pdf

Depuru Monan K, and Jude S (2022) *Drone noise: trials help build data on sound impact*. Cranfield University https://www.cranfield.ac.uk/press/news-2022/drone-noise-trials-help-build-data-on-sound-impact

Ditmer MA, Vincent JB, Werden LK, Tanner JC, Laske TG, Iaizzzo PA, Garshelis DL, and Fieberg JR (2015) *Bears Show a Physiological but Limited Behavioral Response to Unmanned Aerial Vehicles.* Current Biology, 2278 - 2283 DOI:https://doi.org/10.1016/j.cub.2015.07.024

Ditmer MA, Weden LK, Tanner JC, Vincent JB, Callahan P, Iaizzo PA, Laske TG, and Garshelis DL (2018) *Bears habituate to the repeated exposure of a novel stimulus, unmanned aircraft systems.* Conservation Physiology 6, 1-7 DOI: 10.1093/conphys/coy067

Duffy JP, Cunliffe AM. DeBell L, Sandbrook C, Wich SA., Shutler JD, Myers-Smith IH, Varela MR, and Anderson K (2018) *Location, location, location: Considerations when using lightweight drones in challenging environments*. Remote Sensing in Ecology and Conservation 4, 7–19

Egan CC, Blackwell BF, Fernández-Juricic E, and Klug PE (2020) *Testing a key assumption of using drones as frightening devices: Do birds perceive drones as risky?* The Condor 122, 1-15 DOI: 10.1093/condor/duaa014

Eißfeldt H (2020) *Acceptance of drone delivery is limited (not only) by noise concerns*. First International Conference on Quiet Drones. Institute of Noise Control Engineering. 19. - 21 Oct 2020, Paris, France https://elib.dlr.de/136906/

End A, Vogelpohl V, and Eißfeldt H (2021) *Gender differences in noise concerns about civil drones*. ICBEN Congress on Noise as a Public Health Problem, 14-17 June 2021, Stockholm https://elib.dlr.de/143035/1/End_et_al_ICBEN_2021.pdf

Finn RL, and Wright D (2016) *Privacy, data protection and ethics for civil drone practice: A survey of industry, regulators and civil society organisations*. Computer Law & Security Review, 32(4), 577-586

Goodchild A., and Toy J (2018). *Delivery by drone: An Evaluation of unmanned aerial vehicle technology in reducing CO2 emissions in the delivery service industry*. Transportation Research Part D: Transport and Environment 61(A), 58–67

Gov.UK (2021) *Bill to modernise airspace and tackle illegal use of unmanned aircraft receives Royal Assent* https://www.gov.uk/government/news/bill-to-modernise-airspace-and-tackle-illegal-use-of-unmanned-aircraft-receives-royal-assent

Graham S (2016) *Vertical: The city from satellites to bunkers*. London: Verso

Graham S, and Hewitt L (2012). *Getting off the ground: On the politics of urban verticality*. Progress in Human Geography 37(1), 72–92

Heliguy (2020) *Global drone market will grow to $42 Billion by 2025* https://www.heliguy.com/blogs/posts/global-drone-market-will-grow-to-42-billion-by-2025

Hodgson J, and Koh L (2016) *Best Practice for minimising unmanned aerial vehicle disturbance to wildlife in biological field research*. Current Biology 26(10), 404-405

House of Commons (2021) *Commercial and recreational drone use in the UK*. Twenty-Second Report of Session 2017–19. Science and Technology Committee https://publications.parliament.uk/pa/cm201719/cmselect/cmsctech/2021/2021.pdf

Hui CTJ, Kingan MJ, Hioka Y, Schmid G, Dodd G, Dirks KN, Edlin S, Mascarenhas S, and Shim YM (2021) *Quantification of the Psychoacoustic Effect of Noise from Small Unmanned Aerial Vehicles.* International Journal of Environmental Research and Public Health 18(8893), 1-27

Institution of Mechanical Engineers (2019) *Public perceptions: Drones.* Survey results 2019 https://www.imeche.org/docs/default-source/1-oscar/reports-policy-statements-and-documents/imeche-drones-report-final.pdf?sfvrsn=7b58412_2

IOA (2021) *Industry Working Group on Drone noise recommended by IOA* https://www.ioa.org.uk/news/industry-working-group-drone-noise-recommended-ioa

IOA (2021a) *The Future of Transport Regulatory Review: Future of Flight DfT Open Consultation*. 28 September 2021 Response from the Institute of Acoustics https://www.ioa.org.uk/sites/default/files/ioaresponsetofutureofflightconsultation22nov2021-2-1_0.pdf

Investopedia (2020) *Disruptive Technology* https://www.investopedia.com/terms/d/disruptive-technology.asp

Jablonowski M, Jackman A (2021) *Domestic drone futures: Investments and Imaginations* https://globaldiscourseblog.co.uk/2021/03/01/domestic-drone-futures-investments-and-imaginations/?fbclid=IwAR3wV9TstTyib63Lu0xFQf-Cho1_AQitDh1d6uAEhVB5-BNpWmd8IgxALHg#more-423

Jackman A (2022) *Domestic drone futures*. Political Geography 97 (102653), 1-12 https://doi.org/10.1016/j.polgeo.2022.102653

Jackman A (2019) *Consumer drone evolutions: trends, spaces, temporalities, threats*. Defense & Security Analysis 35(4), 362-383

Jackman A, and Jablonowski M (2021) *Investments in the imaginary: commercial drone speculations and relations.* Global discourse: An interdisciplinary journal of current affairs 11(1-2), 39-62

Jumbert MG, and Sandvik KB (2017) *Introduction: What does it take to be good?* In Sandvik KB, and Jumbert MG (eds) The Good Drone, London: Routledge, 1–25.

Klauser F (2018) *Surveillance Farm: Towards a Research Agenda on Big Data Agriculture*. Surveillance & Society 16(3), 370-378

Klauser F, and Pauschinger D (2021) *Entrepreneurs of the air: Sprayer drones as mediators of volumetric agriculture*. Journal of rural studies 84, 55-62

Klauser F, Pedrozo S (2015) *Power and space in the drone age: a literature review and politico-geographical research agenda*. Geographica Helvetica 70, 285-293

Kuhn (2017) *Small unmanned aerial system certification and traffic management systems*. RAND Corporation https://www.rand.org/pubs/perspectives/PE269.html

McCarthy K (2019) *Strewth! Apoplectic Aussies threaten to blast noisy Google delivery drones out of the sky.* The Register https://www.theregister.com/2019/03/11/australia_google_drones/

Mesquita GP, Rodriguez-Teijeiro JD, Wich SA, and Mulero-Pazmany M (2021) *Measuring disturbance at swift breeding colonies due to the visual aspects of a drone: a quasi-experiment study*. Current Zoology 67(2), 157-163

Mo M, and Bonatakis K (2022) *An examination of trends in the growing scientific literature on approaching wildlife with drones*. Drone Systems and Applications 10, 11-139

Mulero-Pázmány M, Jenni-Eiermann S, Strebel S, Sattler T, Negro JJ, and Tablado Z (2017) *Unmanned aircraft systems as a new source of disturbance for wildlife: A systematic review*. PLoS ONE 12(6), 1–14

Nesta (2018) *Flying High: Shaping the future of drones in UK cities* https://media.nesta.org.uk/documents/Flying-High-full-report-and-appendices.pdf

Nixon J, and Dance S (2021) *'Attack of the drones': Exploration of the sound power levels emitted and the impact drones could have upon rural areas*. Inter-noise 2021, 1-5 August, Washington DC https://openresearch.lsbu.ac.uk/download/38c51c5b5f5315ed53b7202d1932249ad5b94bb514a71b957fbd2fc0a1073ae2/692185/Attack%20of%20the%20Drones%20JN%20%26%20SD%202021%20v4.pdf

Oliver C, Ragavan S, Turnbull S, Chowdhury A, Borden A, Fry T, Gutgutia S, and Srivastava S (2021) *Introduction to the urban ecologies open collection*. Geo: Geography and Environment, 1–7

Paine G (2019) *Drones to deliver incessant buzzing noise, and packages*. The Conversation https://theconversation.com/drones-to-deliver-incessant-buzzing-noise-and-packages-116257

Paine G (2019a) *Have You Heard the Buzz About Delivery Drones' Noise?* Slate https://slate.com/technology/2019/05/delivery-drones-amazon-google-noise-buzzing.html

Pauschinger D, and Klauser F (2020) *Aerial Politics of Visibility: Actors, Spaces, and Drivers of Professional Drone Usage in Switzerland.* Surveillance and Society 18 (4), 443-466

PricewaterhouseCoopers (2019) *Building trust in drones* https://www.pwc.co.uk/intelligent-digital/drones/building-trust-in-drones-final.pdf

PricewaterhouseCoopers (2018) *Skies without limits: Drones - taking the UK's economy to new heights* https://www.pwc.co.uk/intelligent-digital/drones/Drones-impact-on-the-UK-economy-FINAL.pdf

Regulatory Horizons Council (2021) *The regulation of drones: An exploratory study* https://assets.publishing.service.gov.uk/government/uploads/system/uploads/attachment_data/file/1029834/rhc-drones-report.pdf

Schäffer B, Pieren R, Heutschi K, Wunderli JM, and Becker S (2021) *Drone Noise Emission Characteristics and Noise Effects on Humans—A Systematic Review*. International Journal of Environmental Research and Public Health 18, 5940

Science and Technology Committee (2019) *Commercial and recreational drone use in the UK*. Twenty-Second Report of Session 2017–19 https://publications.parliament.uk/pa/cm201719/cmselect/cmsctech/2021/2021.pdf

The Entrepreneurs Network (2021) *Briefing paper: Digitise the skies* https://static1.squarespace.com/static/58ed40453a04116f46e8d99b/t/6166afe260bb950c5d2d174e/1634119652881/Digitise+the+Skies.pdf

The International Transport Forum (2021) Ready for Take-Off? Integrating Drones into the Transport System https://www.itf-oecd.org/sites/default/files/docs/take-off-integrating-drones-transport-system.pdf

Thomasen K (2020) *Robots, regulation, and the changing of public spaces* https://papers.ssrn.com/sol3/papers.cfm?abstract_id=3535658

Torija AJ, Li Z, and Self RH (2020) *Effects of a hovering unmanned aerial vehicle on urban soundscapes perception.* Transportation Research Part D 78, 102195

Torija Martinez AJ (2020) *Drone noise, a new public health challenge?* Quiet Drones International e-Symposium on UAV/UAS Noise 2020 http://usir.salford.ac.uk/id/eprint/59203/1/Torija%20-%20Draft_13072020.pdf

UK Government (2020) *Policy Paper: Aerospace Sector Deal* https://www.gov.uk/government/publications/aerospace-sector-deal/aerospace-sector-deal

UK Parliament (2021) *Air Traffic Management and Unmanned Aircraft Bill* [HL] https://publications.parliament.uk/pa/bills/cbill/58-01/0249/en/20249en.pdf#:~:text=1%20The%20Air%20Traffic%20Management%20and%20Unmanned%20Aircraft,2000%20%28%E2%80%9Cthe%202000%20Act%E2%80%9D%29%2C%20and%20airport%20slot%20allocation.

UK Parliament (2021a) *Air Traffic Management and Unmanned Aircraft Act 2021* https://bills.parliament.uk/bills/2533

Unmanned Airspace (2019) *Drone Delivery Operations Underway in 27 Countries* www.unmannedairspace.info/latest-news-and-information/drone-delivery-operations-underway-in-26-countries/

Vas E, Lescroe IA, Duriez O, Boguszewski G, and Gremillet D (2015) *Approaching birds with drones: first experiments and ethical guidelines*. Biology Letters 11(20140754), DOI: http://dx.doi.org/10.1098/rsbl.2014.0754

Watkins S, Burry K, Mohamed A, Marino M, Prudden S, Fisher A, Kloet N, Jakobi T, and Clothier R (2020) *Ten questions concerning the use of drones in urban environments*. Building and environment 167, 106458

Winkler S, Zeadally S, and Evans K (2018) *Privacy and Civilian Drone Use: The Need for Further Regulation*. IEEE 16(5), 72-80

**QUIET DRONES**
**Second International e-Symposium**
**on**
**UAV/UAS Noise**
**27$^{\mathrm{th}}$ to 30$^{\mathrm{th}}$ June 2022**

# Autonomous Kiteplane System for Drone Audition

**Makoto Kumon, Kumamoto University, Japan :** ***kumon@gpo.kumamoto-u.ac.jp***
**Hiroshi G. Okuno, Waseda University, Japan :** ***okuno@nue.org***

## Summary

This paper presents an autonomous auditory drone system for a kiteplane. Since it has a large delta-shaped main wing, it is capable of flying stably and slowly. This capability is effective for observation tasks such as monitoring and surveillance. The developed system integrates the autonomous flight control and the robot audition functions so that the system can improve the performance of sound source localization from the sky by exploiting the silent glide mode. Alternating Drive-and-Glide Flight Navigation (AltDGFNavi) proposed by the authors controls a kiteplane by driving or gliding alternately. The glide mode reduces ego-noise such as rotor and airflow noise drastically. The kiteplane has a newly designed microphone array consisting of three microphone arrays by taking the nonholonomic flight characteristics of the kiteplane into account. On this auditory kiteplane as a platform, AltDGFNavi is designed in detail and evaluated by test flights. This paper reports the design and implementation of AltDGFNavi and its evaluation in terms of sound source localization. The results of flight tests with AltDGFNavi demonstrate the effectiveness of the developed system.

## 1. Introduction

Listening to acoustic signals on the ground from the sky has a significant potential to enhance our perception for practical tasks, for example, surveillance, area monitoring, search-and-rescue, and natural environment observation. Owing to the progress of drone technology, drones have been expected to have the hearing capabilities to realize such important functions.

Auditory functions for robots have been extensively studied for these two decades as *Robot Audition* (Nakadai 2000, Okuno 2015), and the technologies of robot audition have been extended to work with drones as *Drone Audition* (Basiri 2012, Nakadai 2017, Basiri 2018, Wakabayashi 2020, Martinez-Carranza 2020) recently. Basiri proposed an onboard microphone array to recognize and localize a pre-known sound source on the ground by using a particle filter (Basiri 2012, Basiri 2018). By relaxing this requirement, multirotor helicopters with drone audition localized and estimated unknown sound sources on the ground for search-and-rescue missions (Hoshiba 2018, Nakadai 2017, Wakabayashi 2020). A series of field demonstrations were successfully conducted in the Japanese ImPACT Tough Robotics Challenge project (Tadokoro 2019, Nonami 2019). Through those studies, it has been shown that the difficulty with drone audition arises from ego-noise generated by rotors and airflow. Because the ego-noise of drone audition is much larger than that of robot audition, conventional noise-reduction methods (Wang 2020) are not robust to such ego-noise. *Quiet drone* which is expected to reduce ego-noise is critical in enhancing the hearing capability of drones.

Most drone audition systems utilize the platform of multirotor helicopters owing to their hovering capability because hovering allows the localization and recognition of sources in a *static* scenario. By static, the drone is hovering and the sound sources are not moving or at least both objects are moving slowly enough to avoid the influence of movements on auditory signal processing. For deploying drone audition to practical applications, it should cover wider areas and be able to localize and recognize sound sources, either moving or not, efficiently while the drone is flying. To cope with this issue, the authors proposed to incorporate a fixed-wing airplane that is named a kiteplane after its large delta-shaped main wing, equipped with a microphone array (Kumon 2021). The large main wing results in a slow and stable flight, which is suitable for monitoring the events on the ground. Because a kiteplane can glide for a while without running its rotor, the authors proposed to integrate the glide flight mode to ”listen” and the normal flight with driving the rotor to control its flight, as *alternating drive-and-glide flight navigation* (AltDGFNavi) (Kumon 2021). As numerical simulations showed the effectiveness of AltDGFNavi, the auditory kiteplane is expected as a potential auditory drone platform.

AltDGFNavi requires the integration of flight control and drone audition functions. This integration of perception and control, or *perception-action cycle* (Haykin 2012, Kumon 2020), needs an adequate design under the drone-specific constraints such as weight, size, power consumption, and communication. Especially, auditory signal processing under a low Signal-to-Noise Ratio (SNR) may require a significant amount of computation, which arises a technical challenge for drone audition. By focusing on the kiteplane as the target platform, this paper proposes a specially designed autonomous auditory drone system that is suitable for realizing AltDGFNavi.

Besides the computation device, a microphone array for a kiteplane is also considered in this work. A kiteplane has a nonholonomic flight constraint, and it flies mostly forward. Therefore, the sound source on the ground seen in the front of the drone moves backward during the flight. Taking this property into account, the paper also proposes a newly designed special structure of the microphone array consisting of a pair of linear microphone arrays for the auditory kiteplane.

The remaining of this paper is organized as follows. In Section 2, the kiteplane and the AltDGFNavi approach are briefly introduced. Section 3 proposes the developed onboard system and the microphone array for the kiteplane. Its effectiveness is validated in Section 4 by flight tests. Then, conclusions follow in Section 5.

## 2. Auditory Kiteplane

### 2.1. Kiteplane

A kiteplane is an unmanned aerial vehicle that has a delta-shaped main wing, and it has been used for various applications such as environmental monitoring and aerial shooting (Hirasawa 2019, Kumon 2021). The main wing made of cloth is light and flexible and thus the kiteplane is capable of carrying a large payload. The flexibility of the wing ensures safety and robustness against crashes to the ground. The center of mass is located under the main wing, which forms stable attitude dynamics.

Figure 1: Photo of a Kiteplane (left) and its flight kit (right)

The kiteplane used in this research has two active control surfaces: the elevator, and the rudder. The rotor that generates the thrust to fly is driven by a brushless motor and its rotational speed is controlled by an electric speed controller. The flight control unit of the kiteplane is equipped with multiple sensors: a GPS for the measurement of the delta wing's position; and proprioceptors consisting of a 3D accelerometer, a 3D rate gyro, and a 3D magnetometer for the attitude estimation of the kiteplane.

The dynamics of a kiteplane are restricted by a nonholonomic constraint like a wheeled mobile platform so that it flies almost straightforwardly with the yaw rate bounded (Kumon 2006). The thrust by the rotor controls the flight speed, and the flight speed governs the lift force induced by the main wing. Hence, the altitude can be controlled by the rotation speed of the rotor.

## 2.2. Alternating Drive-and-Glide Flight Navigation

The primary challenge in Drone Audition is caused by significant rotor noise, or is named *ego-noise*, as the microphones are installed closer to the noise source than to the target sound sources on the ground. Audition by the kiteplane also suffers from ego-noise as the rotor thrust is necessary to maintain the flight speed. Therefore, signals captured by the microphones installed on the kiteplane are contaminated by ego-noise. However, the kiteplane can glide once it reaches stable flight, and the gliding kiteplane can listen to the target signal without ego-noise as the rotor is stalled. Of course, the glide flight cannot sustain for a long period because the kiteplane slows down to descend without the rotor thrust. The authors proposed the Alternating Drive-and-Glide Flight Navigation (AltDGFNavi) (Kumon 2021) to make the best use of this silent glide flight for drone audition by cycling the normal flight with rotor running and the glide mode. Numerical simulations proved that AltDGFNavi for the kiteplane is effective to localize a sound source on the ground efficiently.

# 3. Drone Audition System for Kiteplane

To realize AltDGFNavi, the autonomous system is required to integrate flight control and auditory functions with path planning and guidance for sound source localization. This section proposes this onboard auditory drone system for the kiteplane.

## 3.1. Onboard Computer System

Figure 2 depicts a schematic diagram of the system components and software elements. The system components consist of the ground control station and onboard drone audition system with the

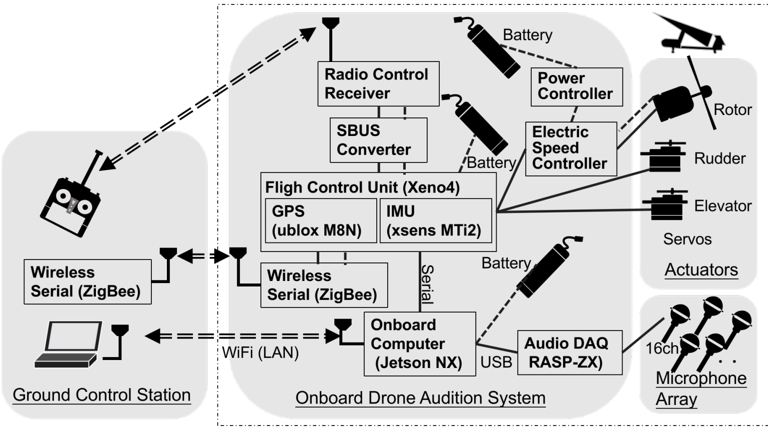


(a) System components

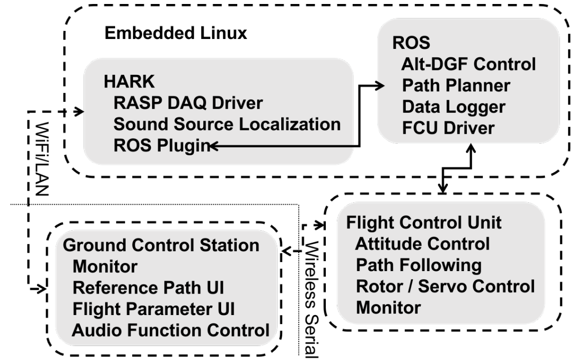


(b) Software elements

Figure 2: Drone Audition System for Kiteplane

(a) Auditory Kiteplane and Laptop PC as Ground-station

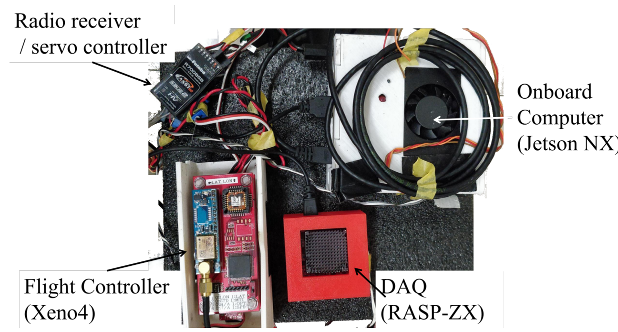


(b) Onboard components

Figure 3: Drone Audition System

actuators and the microphone array. The software elements consist of software at the ground control station and onboard software such as embedded Linux and flight control unit (FCU). FCU uses Xeno4 by Xenocross Inc.[1] which was customized to work with the onboard computer, Jetson Xavier NX[2] (referred to as NX), via serial communication. FCU controls the flight to achieve the way-point guidance and the ground control station monitors the flight via ZigBee wireless serial communication. RASP-ZX by System InFrontier[3] records the acoustic signals from 16 channel microphone array and feeds the information to the main computer NX. NX runs Robot Operating System (ROS) (Stanford AI Lab 2018) and open-sourced Robot Audition software HARK (Nakadai 2017) as the basis of the drone audition, and both FCU signals and auditory signals are managed as ROS topics. The ground control station is realized on a laptop PC that has a wireless serial module to communicate with FCU, and it also can communicate with NX via WiFi or wired LAN to manipulate ROS modules.

A photo of the auditory kiteplane and ground control station is shown in Figure 3(a), and the onboard components taken out from the payload box are displayed in Figure 3(b).

[1] https://xenocross.com/products/xeno4/ in Japanese)

[2] https://www.nvidia.com/en-us/autonomous-machines/embedded-systems/jetson-xavier-nx/

[3] https://www.sifi.co.jp/product/rasp/(in Japanese)

## 3.2. Microphone Array

A microphone array is a device with multiple microphones to measure acoustic signals for auditory scene analysis such as direction of arrival (DOA) estimation, sound separation, and noise reduction owing to its geometric structure. In this study, sound source localization is considered the main task for the drone, and the Multiple Signal Classification (MUSIC) (Schmidt 1986) method is used for DOA estimation. In this subsection, the MUSIC method and its variation are briefly introduced, and then, the structure of the microphone array for the auditory kiteplane is proposed.

### 3.2.1. MUSIC based SSL

The MUSIC method (Schmidt 1986) has been widely used for sound source localization by a microphone array. The method is one of the subspace based signal separation techniques for the linear mixture of the target signal and white noise. It computes the MUSIC spectrum that indicates the source direction.

Denote the channel correlation matrix of the frequency $\mu$ as $\boldsymbol{X}_\mu$ that is defined by $\boldsymbol{X}_\mu = \langle \boldsymbol{x}_\mu \boldsymbol{x}_\mu^H \rangle$ where $\boldsymbol{x}_\mu$ represents the measured multichannel signal represented in the frequency domain, and $^H$ shows the Hermitian operator. The MUSIC spectrum $P(\theta, \mu)$ corresponding to the direction $\theta$ is defined by

$$P(\theta, \mu) = \frac{\boldsymbol{a}^H(\theta, \mu)\boldsymbol{a}(\theta, \mu)}{\sum_{i=N_s+1}^{N_m} \boldsymbol{a}^H(\theta, \mu)\boldsymbol{e}_i}, \tag{1}$$

where $\boldsymbol{a}(\theta, \mu)$, $\boldsymbol{e}_i$, $N_s$ and $N_m$ represent the steering vector to the source at $\theta$, the eigenvector of $\boldsymbol{X}_\mu$, the number of sound sources, and that of microphones, respectively. The eigenvector is indexed as the corresponding eigenvalues that are listed in descending order. As (1) is for the frequency $\mu$, $P(\theta, \mu)$ is integrated over the frequency range to obtain the geometric information, *e.g.* $P(\theta) = \sum_\mu P(\theta, \mu)$. Once $P(\theta)$ is obtained, the estimated DOA that is denoted by $\hat{\theta}$ is estimated as $\hat{\theta} = \underset{\theta}{\operatorname{argmax}} P(\theta)$.

Several extensions of the MUSIC method have been proposed to improve the robustness against noise. In addition to the original MUSIC method, HARK provides various real-time MUSIC-based sound source localization: generalized eigenvalue decomposition of correlation matrices for noise robustness (GEVD-MUSIC) (Nakamura 2009), generalized singular value decomposition (GSVD-MUSIC) (Nakamura 2013), incremental estimation of the noise correlation matrix, iGEVD-MUSIC (Okutani 2012), and iGSVD-MUSIC (Ohata 2014). Even with such sophisticated methods, however, the low SNR of drone audition makes it significantly challenging to localize the distant targets. This is more likely to the case for fixed-wing platforms. Therefore, the original MUSIC method, that is, SEVD-MUSIC of HARK, is used for sound source localization, and its effectiveness is validated.

### 3.2.2. Structure of Microphone Array for Kiteplane

The geometrical structure of the microphone array is critical in the performance of auditory processing because it determines the transfer function, or the steering vector $\boldsymbol{a}(\theta, \mu)$ of Equation (1), which encodes DOA cues. For example, Ishiki (Ishiki 2017) investigated the optimal size of the microphone array which allocates microphones circularly around a multirotor helicopter; Hoshiba (Hoshiba 2017) proposed a compact spherical array suitable for sound source localization. The design of those arrays assumes that a multirotor helicopter localizes a *stationary* sound source while either *hovering* or *nearly stationary*. This assumption, however, does not hold for the kiteplane.

The kiteplane considered in this paper is a fixed-wing platform continuously moving during the flight. According to the flight dynamics, the apparent motion of the target source becomes from the front of the drone to the back. To localize such moving targets along with the flight, accurate sound source localization is expected to attain along the body. From this consideration, this paper proposes

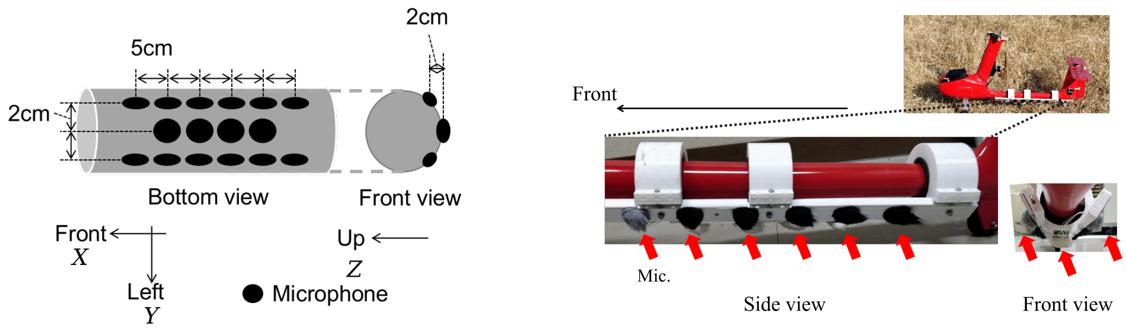


Figure 4: Microphone Array: Structure (left) and Appearance (right)

a combination of three linear microphone arrays as shown in Figure 4; it has 16 microphones in total where two linear arrays of 6 microphones on both sides of the body, and 1 linear array of 4 microphones pointing downward in between two side arrays. This structure is expected to attain an accurate resolution in azimuth for sound sources located on either the left or right side of the body. It is also worth noting that the array can be easily equipped to the kiteplane in a compact form along the main body and that it has little interference with the airflow. These characteristics are desirable from the viewpoint of flight control.

As shown in Section 3.2.1, the MUSIC method relies on the steering vector $\boldsymbol{a}(\theta, \mu)$. Therefore, the uniqueness of $\boldsymbol{a}(\theta, \mu)$ for the source direction $\theta$ is important. To evaluate this property, the similarity between the steering vector from the reference direction $\theta$ and that from the rest direction $\theta'$ is denoted as $s(\theta, \theta') \in [0, 1]$ and the cosine similarity is introduced as the metric. Because the MUSIC integrates the narrow-band spectrum (1) over the frequency range of interest (denote the range as $M$), the mean cosine similarity over $M$ is computed as the average for the frequency $\forall \mu \in M$. The metric $s(\theta, \theta')$ is defined as follows.

$$s(\theta, \theta') = \frac{1}{|M|} \sum_{\mu \in M} \frac{\boldsymbol{a}(\theta, \mu)^H \boldsymbol{a}(\theta', \mu)}{\|\boldsymbol{a}(\theta, \mu)\| \|\boldsymbol{a}(\theta', \mu)\|} \tag{2}$$

Given $\theta$, the distribution of $s(\theta, \theta')$ for $\forall \theta'$ represents the sensitivity to localize $\theta$; the array is expected to perform accurate localization if the distribution forms a steep unique peak.

Figure 5 shows the distribution of $s(\theta, \theta')$ of (2) for given some reference directions $\theta$. Each figure shows a top view of a 30m×30m field around the drone. The drone is located at the center of the square, and a red dot shows the reference direction $\theta$ to test. The top of each square corresponds to the forward direction of the flight or the head of the drone. The color shows the similarity; yellow indicates that the corresponding steering vectors are similar, $s(\theta, \theta') \approx 1$, while blue shows that the steering vectors are different, $s(\theta, \theta') \approx 0$. Because of the symmetric structure of the array, the reference directions of the bottom to the right to the body are only shown in the figure.

Similarity distributions for the targets around the median line of the body are illustrated in the left two columns of Figure 5. The results for the sources deviated to the side are shown in the right three columns of Figure 5. Although the high similarity area displayed by yellow regions spread widely in those figures, that for the sources on the side show steep yellow bands. This implies that the array can attain accurate localization for the sources located at the side of the body as expected. This observation is suitable especially for the auditory kiteplane with AltDGFNavi because the auditory drone localizes the target accurately while it circles the source according to the authors' previous work (Kumon 2021). Note that the high similarity area indicated by the yellow band spreads from the center of the area to the far end because the estimation in elevation contains uncertainty.

The similarity check confirms that the uniqueness of $\boldsymbol{a}(\theta, \mu)$ for the source direction $\theta$ holds with some uncertainty. Since this check is performed at one time-frame, such uncertainty should be

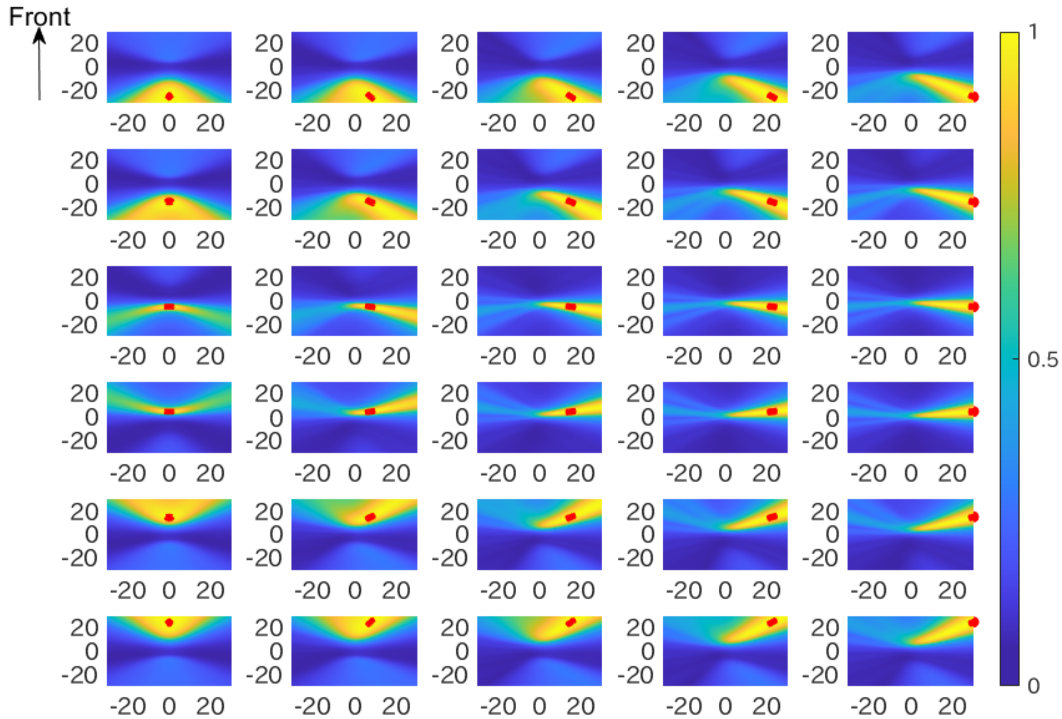


Figure 5: Sound Source Localization Sensitivity of the Proposed Microphone Array

Those figures show the 30m×30m distribution of the similarity (2) for $6 \times 5$ reference points (red dots). Reference points are selected from the median line to the right of the body. The top of each square corresponds to the front of the drone. High similarity regions are represented by yellow.

dissolved by sound source tracking and data association with multi-modal information such as sound source information and vision (Wakabayashi 2020).

## 4. Validation

Two types of flight tests, autonomous guidance flight and auditory flight, were conducted to evaluate the effectiveness of the developed system.

### 4.1. Autonomous Flight

The first test is to confirm the autonomous flight function of the kiteplane with the microphone array because the equipped device may interfere with the flight control. The objective of the flight was commanded to follow the triangle whose vertices were given as the reference way-points. Take-off and landing were operated by manual control.

Figure 6 shows the flight path of the experiment, and the time responses of the altitude and attitude (roll, pitch, and yaw) of the kiteplane. Blue curves show the result of manually operated flight, while red curves show that of autonomous flight. Dotted lines in Figure 6(a) and (b) represent the reference path and altitude respectively. The system succeeded to guide the kiteplane to follow

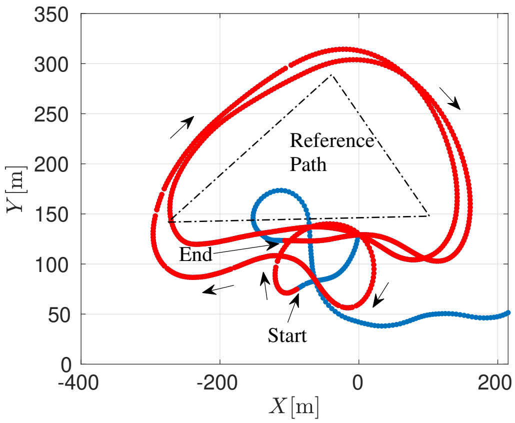


(a) Horizontal Path

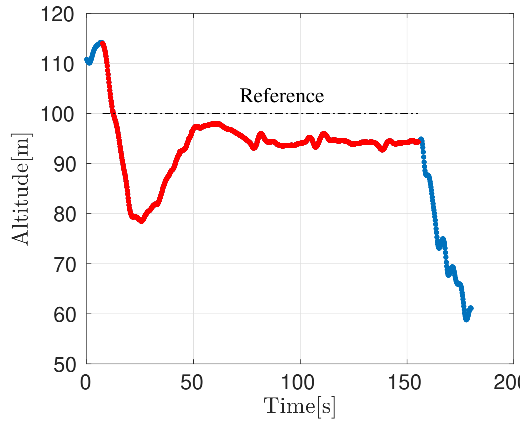


(b) Vertical Response

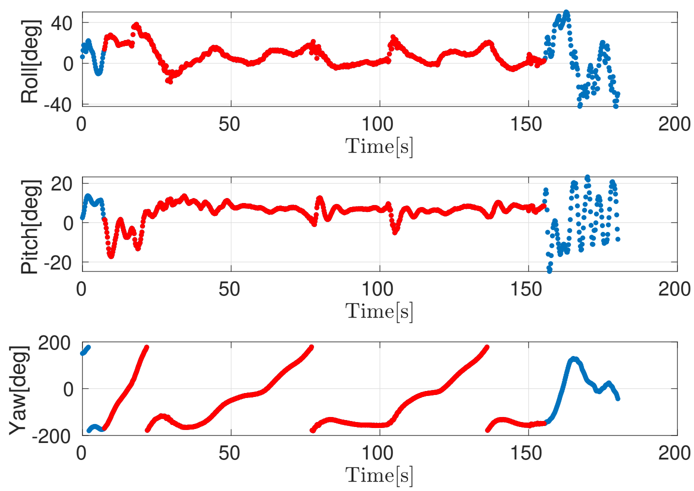


(c) Attitude

Figure 6: Autonomous Flight Result

the reference triangle and maintain a constant altitude. The drone made longer turns to follow the reference path. This was because of a conservative choice of the controller parameters so as to avoid steep turns that might cause oscillation. The offset in the altitude control was acceptable because the rotor control will be overwritten by AltDGFNavi.

## 4.2. Auditory Test

Next, the auditory perception was tested whether the developed system was able to recognize the signal from the sound source on the ground. In this experiment, the drone was manually operated to guide to the appropriate listening area. A whistle call was made on the ground to emit the target signal during the glide flight by manually commanding to stall the rotor.

Figure 7 shows the flight path and the altitude of the kiteplane. Blue and red dots of the figure represent the flight with rotor running and the glide flight, respectively. The whistle call was made at the location indicated by the label ”Sound” in Figure 7(a), and the glide flight was initiated at the altitude of about 95m and about 55m. The drone saw the source on the right side during the glide flight, and the distance between the source and the drone was more than 130m.

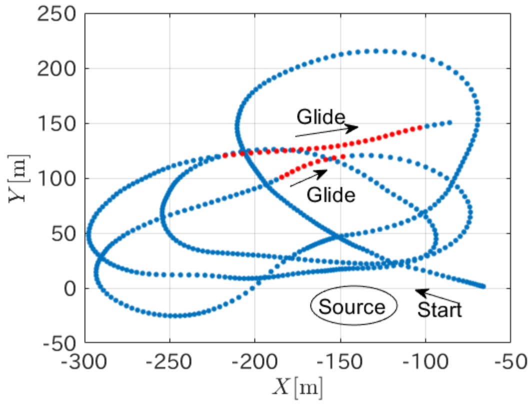


(a) Horizontal Path

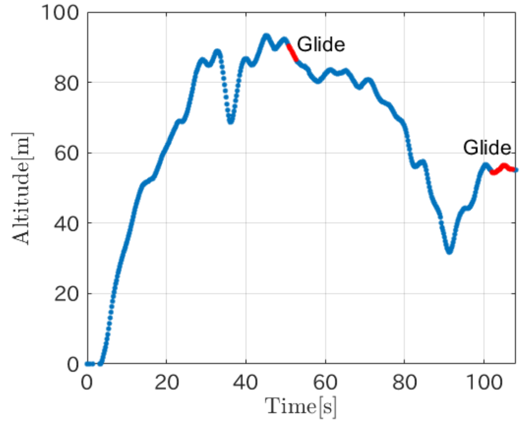


(b) Vertical Response

Figure 7: AltDGFNavi Flight Result

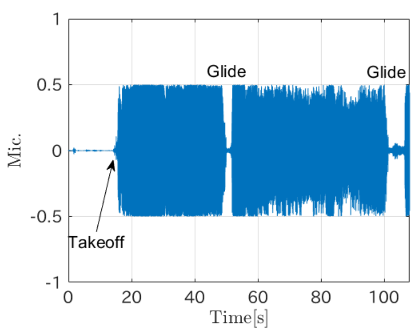


(a) Recorded signal (Ch.3)

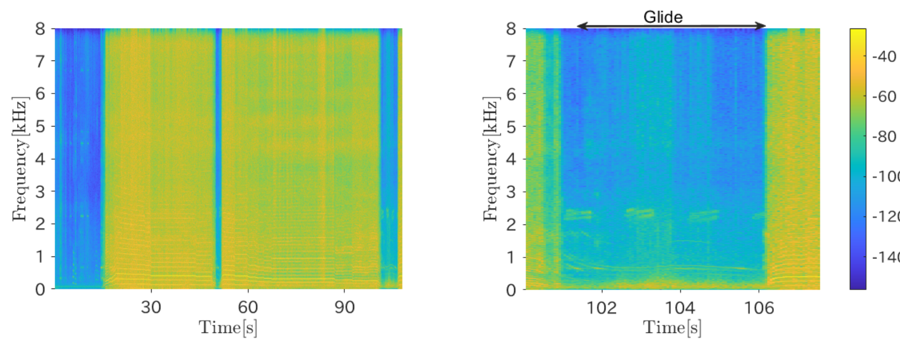


(b) Spectrogram of (a) and its magnified view during glide

Figure 8: Recorded Audio Signal

An example of the recorded acoustic signal is illustrated in Figure 8. Time-domain signal shown in Figure 8(a) has a large amplitude signal that corresponds to the rotor noise, and there are two sections with small amplitude at the section from 55 sec. and at that from 100 sec. corresponding to the glide flight. Figure 8(b) shows a spectrogram of Figure 8(a), and it shows that the rotor noise spread over a wide frequency range with a harmonic structure that depends on the rotor's rotation speed. Figure 8(c), a magnified view of the spectrogram during the second glide flight, depicts three bars around 2.5kHz by whistle calls, which clarifies the effectiveness of the AltDGFNavi approach to recognizing the sound signal.

Furthermore, the multichannel signal obtained by the developed array was analyzed for DOA estimation. Acoustic signal processing was realized by HARK and one of its MUSIC algorithm modules, LocalizeMUSIC (SEVD-MUSIC), was used for this analysis. The estimated results are shown in Figure 9, where each circle shows the MUSIC spectrum distribution at 101.8 sec., 103.6 sec. and 105 sec. corresponding to three whistle calls in Figure 8(c). The color of the circles shows the magnitude of the spectrum where the circular and radial directions correspond to the azimuth and elevation angle, respectively. The top of the circles is aligned to the front direction of the body. As the high MUSIC spectrum shown by the yellow regions appears on the right side of the circles, the DOA estimation shows that a signal was from the right to the body. And the MUSIC spectrum peak at 105s locates back-right direction, which shows that the apparent DOA moved backward as time passed. We can conclude that the proposed system was able to localize the sound source even from more than 100m away during the flight.

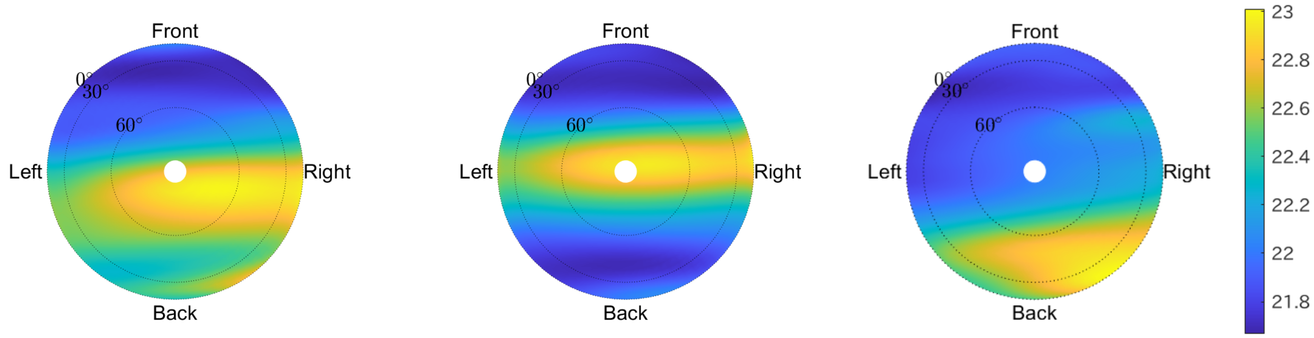


MUSIC spectrum at 101.8s (left), 103.6s (center), and 105s (right).

Figure 9: Sound Source Localization during the glide

## 5. Conclusion

This paper proposes the drone audition system for the kiteplane to incorporate its stable glide flight. The system is capable of realizing autonomous flights such as AltDGFNavi for active drone audition. The microphone array for the developed system was also designed for the auditory kiteplane. Flight experiments demonstrated that the developed kiteplane could fly with way-point navigation, and it could localize the sound source on the ground more than 100m away during the glide flight.

The authors are working to implement the autonomous glide flight to realize full AltDGFNavi, and experimental validation will be conducted in future work.

## Acknowledgment

This work was supported by the Japan Society for the Promotion of Science, KAKENHI Grant Number 19H00750. The authors would like to thank Mr. Kazuo Okabe for his help with the flight experiments.

## References

Basiri M., Schill F., P.U. Lima, and Floreano D. (2012) *Robust acoustic source localization of emergency signals from micro air vehicles* in Proc IEEE/RSJ IROS 4737–4742. doi: `10.1109/IROS.2012.6385608`

Basiri M., Schill F., P.U. Lima, and Floreano D. (2018) *Localization of emergency acoustic sources by micro aerial vehicles* Jnl Field Robot 35(2), 187–201. doi: `10.1002/rob.21733`

Haykins, S. (2012) *Cognitive Dynamic Systems: Perception-Action Cycle, Radar and Radio* Cambridge UK: Cambridge University Press.

Hirasawa N., Hayashi M., Higashino S., Okabe K., Oishi H., Saito .K, Alimasi N., and Funaki M. (2019) *UAV observation in Japanese Antarctic Research Expedition (JARE) (in Japanese)* in Proc JSSI & JSSE Joint Conf – 2019 in Yamagata S2-6 doi: `10.14851/jcsir.2019.0_13`

Hoshiba K., Washisaka K., Wakabayashi M., Ishiki T., Kumon M., Bando Y., Gabriel D., Nakadai N., and Okuno H.G. (2017) *Design of UAV-embedded microphone array system for sound source localization in outdoor environments* Sensors 17(11), 2935. doi: `10.3390/s17112535`

Hoshiba K., Nakadai K., Kumon M., and Okuno H.G. (2018) *Assessment of MUSIC-based noise-robust sound source localization with active frequency range filtering* Jnl Robot & Mechatronics 30(3), 426–435. doi: 10.20965/jrm.2018.p0426

Ishiki T., Washizaki K., and Kumon M. (2017) *Evaluation of microphone array for multirotor helicopters* Jnl Robot & Mechatronics 29(1), 168-176. doi: 10.20965/jrm.2018.p0168

Kumon M., Udo Y., Michihira H., Nagata M., Mizumoto I., and Iwai Z. (2006) *Autopilot System for Kiteplane* IEEE/ASME Trans Mechatronics 11(5), 615-624 doi: 10.1109/TMECH.2006.882994

Kumon M., Okuno H.G., Nakadai K., Hoshiba K., and Noda R. (2020) *Proposal of Cognitive Drone Audition based on Cognitive Dynamic Systems* in Proc Quiet Drones A22, 15p.

Kumon M., Okuno H.G. and Tajima S. (2021) *Alternating drive-and-glide flight navigation of a kiteplane for Sound Source Position Estimation* in Proc IEEE/RSJ IROS 2114–2120. doi: 10.1109/IROS51168.2021.9636136

Martinez-Carranza J. and Rascon C. (2020) *A Review on auditory perception for unmanned aerial vehicles* Sensors 20(24), 7276 (24p). doi: 10.3390/s20247276

Nakadai K., Lourens, Okuno H.G., and Kitano H. (2000) *Active audition for humanoid* in Proc. AAAI 832–839. available at http://www.aaai.org/Papers/AAAI/2000/AAAI00-128.pdf

Nakadai K., Kumon M., Okuno H.G. et al. (2017) *Development of microphone-array-embedded UAV for search and rescue task* in Proc IEEE/RSJ IROS 5985–5990. doi: 10.1109/IROS.2017.8206494

Nakadai K, Okuno H.G., and Mizumoto T. (2017) *Development, deployment and applications of robot audition open source software HARK* Jnl Robot. & Mechatronics 29(1), 16-25. doi: 10.20965/jrm.2018.p0016

Nakamura N., Nakadai K., Asano F., Hasegawa Y., Tsujino H. (2009) *Intelligent sound source localization for dynamic environments* in Proc IEEE/RSJ IROS 664–669. doi: 10.1109/IROS.2009.5354419

Nakamura N., Nakadai K., and Okuno H.G. (2013) *A real-time super-resolution robot audition system that improves the robustness of simultaneous speech recognition* Adv Robotics 27(12), 933–945. doi: 10.1080/01691864.2013.797139

Nonami K., Hoshiba K., Nakadai K., Kumon M., Okuno H.G. et al. (2019) *Recent R&D technologies & future prospective of flying robot in tough robotics challenges* Disaster Robotics (S. Tadokoro, Ed.) Ch. 3, 88–142. doi: 10.1007/978-3-030-05321-5_3

Ohata T., Nakamura K., Mizumoto T., Tezuka T., and Nakadai K. (2014) *Improvement in Outdoor Sound Source Detection using a Quadrotor Embedded Microphone Array* in Proc IEEE/RSJ IROS 5985–5990. doi: 10.1109/IROS.2014.6942813

Okuno H.G. and Nakadai K. (2015) *Robot audition: its rise and perspective* in Proc IEEE ICASSP 5610–5614. doi: 10.1109/ICASSP.2015.7179045

Okutani K., Yoshida T., Nakamura K., and Nakadai K. (2012) *Outdoor Auditory Scene Analysis using a Moving Microphone Array Embedded in a Quadrocopter* in Proc IEEE/RSJ IROS 3288–3293. doi: 10.1109/IROS.2012.6385994

Schmidt, R.O. (1986) *Multiple emitter location and signal parameter estimation* IEEE Trans Antennas and Propagat AP-34(3), 276-280. doi: 10.1109/TAP.1986.1143830

Stanford Artificial Intelligence Laboratory et al. (2018) *Robotic Operating System* available at: https://www.ros.org.

Tadokoro S. (Ed.) (2019) *Disaster robotics - Results from the ImPACT Tough Robotics Challenge* Springer, STAR 128. doi: 10.1007/978-3-030-05321-5

Wakabayashi M., Okuno H.G., and Kumon M. (2020b) *Drone audition listening from the sky estimates multiple sound source positions by integrating sound source localization and data association* Adv Robot 34(11), 744–755. doi: 10.1080/01691864.2020.1757506

Wakabayashi M., Okuno H.G., and Kumon M. (2020a) *Multiple Sound Sounce Position Estimation by Drone Audition Based on Data Association between Sound Source Localization and Identification* IEEE Rob & Autom Letters (RA-L) 5(2), 792–789. doi: 10.1109/LRA.2020.2965417

Wang L. and Cavallaro A. (2020) *A blind source separation framework for ego-noise reduction on multi-rotor drones*, IEEE Trans Audio, Speech, and Lang Process 8, 2523–2537. doi: 10.1109/TASLP.2020.3015027

QUIET DRONES
Second International e-Symposium
on
UAV/UAS Noise
27th to 30th June 2022

# Improvement of Rotor Noise Reduction for Unmanned Aerial Vehicle Audition by Rotor Noise PSD Informed Beamformer Design

**Yameizhen Li, Acoustics Research Centre, University of Auckland, yli432@aucklanduni.ac.nz**
**Benjamin Yen, Acoustics Research Centre, University of Auckland, benjamin.yen@ieee.org**
**Yusuke Hioka, Acoustics Research Centre, University of Auckland, yusuke.hioka@ieee.org**

**Summary**
Unmanned aerial vehicles (UAV) are popular in many areas including search and rescue and filming industries. UAVs are widely used for the convenience in collecting visual information, while using them for the audio recording remains a challenge due to the high levels of rotor noises (a.k.a. ego noise). Previous studies demonstrated an existing speech enhancement algorithm using beamforming and Wiener filter to be effective for reducing rotor noise for UAV audition. The algorithm was later improved by incorporating the rotor noise's power spectral density (PSD) estimated by non-acoustic information. To further improve the rotor noise reduction performance, this paper proposes an alternative design of the MVDR beamformer using a PSD informed spatial noise co-variance matrix estimation. The method separately estimates the magnitude and phase components of the matrix. The magnitude component is calculated from the rotor noise PSD estimated by the previous study, whereas the phase component is calculated by the time delay of arrival due to the relative positions between the microphone array and the rotors. The proposed method was evaluated under low (3000 - 3500 rpm) and high rotor speed (3500 - 4000 rpm) conditions. The proposed method achieved an average improvement in signal to rotor noise ratio (SRNR) of around 23 dB under the low rotor speed condition and approximately 26 dB under the high rotor speed condition. These are significant improvements compared to the existing method performing the average SRNR improvement of around 15 dB and 20 dB under the low and high rotor speed conditions, respectively.

## 1. Introduction and background

Unmanned aerial vehicles (UAVs) have been widely applied in many areas such as military missions [1], agriculture[2], filming [3], and search and rescue [4]. A comprehensive overview of UAVs can be found in [5]. UAVs often use sensors such as optical and infrared cameras to provide visual information about the surrounding environment. However, audio information is often overlooked, although it can complement visual information. For example, unfavourable weather conditions and extensive vegetation coverage in a mountainous region can cause inadequate lighting and blocking view, thus degrading the quality of visual information. This will make cameras less effective in the mission. Thermal sensors have been used to solve this problem, but they may fail to capture the human body temperature if the UAVs are over the land by a large distance. Audio information may address the limitations of visual and other sensory information as described above. In addition, in the filming industry, UAVs are usually used to record video while the audio signals have to be collected from microphones on set. A clean audio recording system on UAVs would bring much convenience. This raises the need for audio applications on UAVs.

A study [6] of audio applications on UAVs summarises audio perception for UAVs into three parts (i.e. detection, classification, and localisation) to recognise a target source, identify what generates the sound and where it is coming from. Other studies [7]–[9] explored the topic of sound source localisation specifically. However, sound enhancement or extraction [10], [11] has not been studied comprehensively, although it is a crucial topic in applying audio information on UAVs.

Developing an algorithm to record audio with little background noise as possible from UAVs is challenged by the high level of rotor noise. A series of recent studies [12], [13] combined machine learning techniques with beamforming, where the machine learning techniques were used to estimate the characteristics of rotor noise by using rotor state information such as rotor speed. Incorporated with MVDR beamforming and Wiener post-filter techniques, the algorithm can effectively reduce a significant amount of rotor noise in the audio recordings on UAVs.

MVDR requires a noise covariance matrix (NCM) across each microphone [14]. Studies from [11], [13] used the measured impulse response in an anechoic chamber to represent the acoustic transfer function from the source in each direction to each microphone. These impulse responses were then used to estimate the NCM for a source in a given direction. This is an archaic method, and better NCM estimation can be applied to improve the performance.

When the target sound is speech, one way of estimating the NCM from noisy speech recording is the use of voice activity detector (VAD). The idea of utilising VAD takes the advantage that the speech always has pauses. This distinguishes the time frames which contain mixed noisy signals and pure noise signals so that the NCM can be updated only when noise-dominating frames are detected. A study [15] has shown that using a perfect VAD to estimate the rotor noise's NCM in the algorithm in [11] tends to give a more significant SRNR improvement compared to using impulse response to estimate the rotor noise's NCM. However, a perfect VAD is not likely to occur in reality, and more effort might be required to improve the VAD techniques. The study [15] also showed that better estimation of NCM would improve the performance of MVDR. Hence, this research will be centred around the rotor noise's NCM estimation in the context of UAV and explore a way to use the PSD of rotor noise in the estimation of NCM. In Section 2. we describe the proposed method of NCM estimation, followed by Section 3. that introduce the experimental conditions. Results and discussion are given in Section 4., and finally the paper is concluded in Section 5..

## 2. Noise co-variance matrix estimation

### 2.1 Model of the problem

The microphone received signals mainly contain the target signals, rotor noise, interfering noises, and residual noises due to the electric noise of the microphones. Assuming these signals are mutually independent, the microphone received signals can be modelled by an additive model in the time-frequency domain (i.e. acquired by applying the short-time Fourier transformation (STFT)). Since this research is only interested in the rotor noise's NCM estimation, interfering noises and the residual noises will not be considered. The simplified model is given by

$$X_m(i,t) = H_{\theta_0,m}(i,t)S(i,t) + \sum_{q=1}^{Q} H_{\theta_q,m}(i,t)V_q(i,t), \tag{1}$$

where $m \in \{1, 2, ..., M\}$ denotes the microphone number. $S(i, t)$ denotes the target source, and $\{V_q : q \in \{1, ..., Q\}\}$ denotes rotor noises. For a source located in known direction, $H_{\theta,m}$ denotes the transfer function between the $m^{th}$ microphone and the sound source. $\theta_*$ represents the direction of source $*$, and $\theta_0$ is the target source direction. $i$ and $t$ denote the frequency bin index and time frame index of the STFT, respectively. For simplicity, we omit $(i, t)$ unless specified. Then, $\mathbf{X}$ denotes an $M \times 1$ vector which is a stack of the mixture signals received by each microphone (i.e. $X = [X_1, ..., X_M]^T$), at a frequency bin and a time frame.

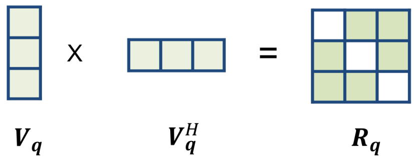

Figure 1: Example visualisation of NCM, $\mathbf{R_q}$

## 2.2 Rotor NCM

First, the case of one rotor ($Q = 1$) is considered. We define an $M \times 1$ vector $\mathbf{V_q}$ to be $V_q \cdot [H_{\theta_q,1}, H_{\theta_q,2}, ..., H_{\theta_q,M}]^T$, and by expansion
$\mathbf{V_q} = [V_q H_{\theta_q,1}, V_q H_{\theta_q,2}, ..., V_q H_{\theta_q,M}]^T$. So

$$\mathbf{V_q} = \left[\ |V_q| \cdot |H_{\theta_q,1}| \cdot e^{j(\angle V_q + \angle H_{\theta_q,1})}, ..., |V_q| \cdot |H_{\theta_q,M}| \cdot e^{j(\angle V_q + \angle H_{\theta_q,M})}\ \right]^T, \tag{2}$$

where $|\cdot|$ and $\angle\cdot$ are the modulus and argument of a complex number.

Let $\mathbf{R_q}$ denote the NCM of rotor $q$, then $\mathbf{R_q} = \mathbf{V_q}\mathbf{V_q}^H$, where $\{\cdot\}^H$ is the Hermitian transpose. An example visualisation of the NCM when $M = 3$ is shown in Figure 1.

When considering all the rotors, the overall rotor noises' NCM can be expressed by

$$\mathbf{R} = \sum_{q=1}^{Q} \mathbf{R_q}. \tag{3}$$

Hence, to estimate rotor noise's NCM, it suffices to develop an approach to estimate $\mathbf{V_q}$. As shown in (2), it is worth considering magnitude and phase separately.

### 2.2.1 Magnitude approximation

Let $E\cdot$ denote the expectation operator. By equation (2), $|\mathbf{V_q}| = [\ |V_q| \cdot |H_{\theta_q,1}|, ..., |V_q| \cdot |H_{\theta_q,M}|\ ]^T$, but the PSD of rotor noise ($\phi_{q,m}$) received by each microphone is $(EV_q H_{\theta_q,m})(EV_q H_{\theta_q,m})^H$ for $m \in \{1, ..., M\}$, which is equal to $|V_q H_{\theta_q,m}|^2 = (|V_q| \cdot |H_{\theta_q,m}|)^2$. Assuming that a highly accurate estimation of $\phi_{q,m}$ is available, we have

$$\left|\widetilde{\mathbf{V_q}}\right| = \left[\ \sqrt{\widetilde{\phi_{q,1}}}, ..., \sqrt{\widetilde{\phi_{q,M}}}\ \right]^T, \tag{4}$$

where $\widetilde{(\cdot)}$ denotes the estimation of a quantity.

### 2.2.2 Phase approximation

By equation (2), $\angle\mathbf{V_q} = [\ (\angle V_q + \angle H_{\theta_q,1}), ..., (\angle V_q + \angle H_{\theta_q,M})\ ]^T$. The main factor that differentiates the phase across different microphones is the propagation path between microphones and sources. So to represent the main feature in the resulting estimation of rotor noise's NCM, it is sufficient to approximate the phase of $\mathbf{V_q}$ by $\angle\mathbf{V_q} \approx [\ \angle H_{\theta_q,1}, ..., \angle H_{\theta_q,M}\ ]^T$.

In theory, the phase shift is related to the time delay of arrival (TDOA), denoted as $\tau$. TDOA can be derived by taking the following assumptions. 1. The position of the rotor with respect to the microphone array is known. 2. The speed of sound is known. 3. The source is far-field, so the interference pattern of the sound wave would not be considered.

With these assumptions, the time delay of the sound wave travelling to a microphone with respect to a reference microphone can be expressed by

$$\tau_{a_1/a_0} = \frac{\mathbf{a_1} \cdot \mathbf{u} - \mathbf{a_0} \cdot \mathbf{u}}{c}, \tag{5}$$

where $\tau_{a_1/a_0}$ denotes the time delay of microphone at position $\mathbf{a_1}$ relative to the reference microphone located at $\mathbf{a_0}$, and $\mathbf{u}$ is the unit vector indicating the direction of the coming wave, and $c$ denotes the speed of sound.

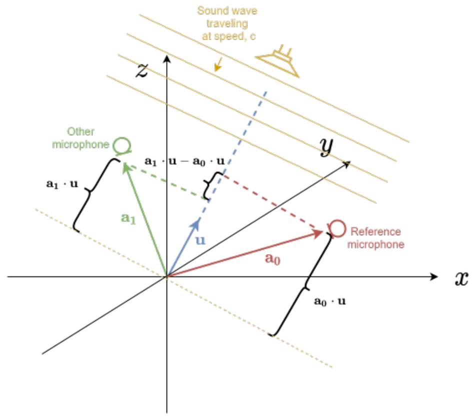


Figure 2: Visualisation of TDOA

With $M$ microphones and assuming microphone 1 is the reference, for a given frequency of wave ($f$) the phase of the frequency response ($H_{\theta_q,m}$) can be approximated by $\widetilde{\angle H_{\theta_q,m}} = 2\pi f \tau_{m/1}$. Hence, the approximation of the phase component of $\mathbf{V_q}$ is $\widetilde{\angle \mathbf{V_q}} = \left[ \widetilde{\angle H_{\theta_q,1}}, ..., \widetilde{\angle H_{\theta_q,M}} \right]^T$. Overall, the approximation of $\mathbf{V_q}$ is given by

$$\widetilde{\mathbf{V_q}} = \left[ |\widetilde{\mathbf{V_{q,1}}}| e^{j\widetilde{\angle H_{\theta_q,1}}}, ..., |\widetilde{\mathbf{V_{q,M}}}| e^{j\widetilde{\angle H_{\theta_q,M}}} \right]^T. \tag{6}$$

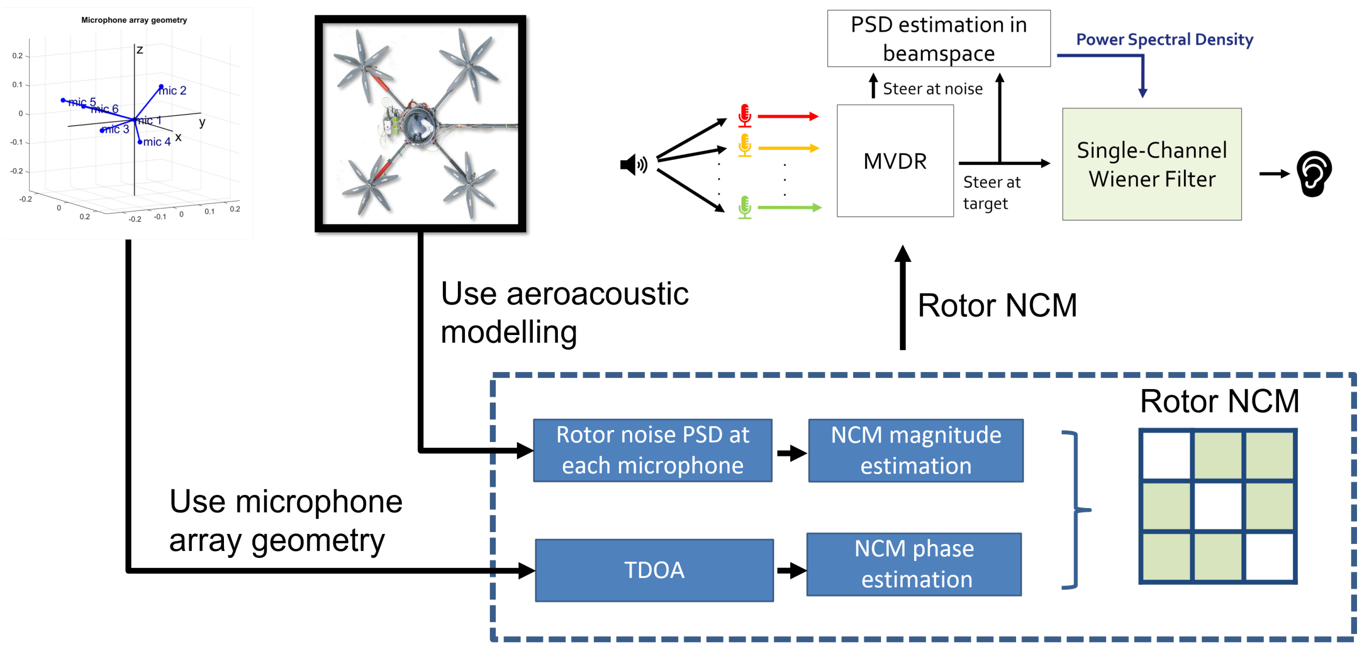


Figure 3: Application of rotor NCM estimation in algorithm in [11]

### 2.3 Application of the noise covariance matrix estimation

The application of the NCM estimation in the existing algorithm [11] is shown in Figure 3. The existing algorithm is an MVDR breamformer cascaded with a single-channel Wiener filter.

#### 2.3.1 MVDR beamformer design

The estimation of NCM is highlighted by the blue-dashed box in Figure 3, and will be used in the calculation of the filter coefficients of MVDR beamformer. NCM is given as a *priori* for MVDR.

Based on the derivation of filter weight of MVDR beamformer [14], the filter weights of MVDR beamformer ($\mathbf{W_{MVDR,0}}$, an $M \times 1$ vector containing the filter weight for each microphone) steering its mainlobe at the target source is calculated by

$$\mathbf{W_{MVDR,0}} = \frac{\mathbf{R}^{-1}\ \mathbf{h}_{\theta_0}}{\mathbf{h}_{\theta_0}{}^H\ \mathbf{R}^{-1}\ \mathbf{h}_{\theta_0}}, \tag{7}$$

where $\mathbf{h}_{\theta_0}$ is an $M \times 1$ vector containing the frequency responses from the target source to each microphone (i.e. $h_{\theta_0} = [H_{\theta_0,1}, ..., H_{\theta_0,M}]^T$).
Meanwhile, the filter weights of the MVDR beamformer steered at rotor noise $q$ is calculated by $\mathbf{W_{MVDR,q}} = \frac{\mathbf{N_q}^{-1}\ \widetilde{\mathbf{V_q}}}{\widetilde{\mathbf{V_q}}^H\ \mathbf{N_q}^{-1}\ \widetilde{\mathbf{V_q}}}$, where $\mathbf{N_q}$ is defined by $\mathbf{N_q} = \mathbf{R} - \mathbf{R_q} + \mathbf{h}_{\theta_0}\mathbf{h}_{\theta_0}{}^H$. For $Q$ rotors there will be $Q$ beamformers which will be used later to estimate the PSD of sources by the PSD estimation in beamspace method [16].

The recovered target signal directly from the MVDR beamformer ($\widetilde{S_{MVDR}}$) can then be calculated by $\widetilde{S_{MVDR}} = \mathbf{W^H_{MVDR,0}}\mathbf{X}$. Also the rotor noise $q$ after applying the MVDR beamformer is given by

$$\widetilde{V_{MVDR,q}} = \mathbf{W^H_{MVDR,q}}\mathbf{X}. \tag{8}$$

### 2.3.2 Wiener filter design

The recovered target signal by MVDR beamformer is then passed into the single-channel Wiener filter [11], and the final output of the proposed algorithm ($\widetilde{S}$ at a frequency bin and a time frame) is calculated by $\widetilde{S} = W_{WF} \cdot \widetilde{S_{MVDR}}$, where $W_{WF} \in \mathbb{R}$ is the coefficient of the Wiener filter. This whole process applies to every frequency bin and time frame.
To design the Wiener filter, the PSDs of all sources (i.e. target source and rotor noises) are required a *priori*. By the method of PSD's estimation in beamspace [16], directivity gain ($D_{l,\theta_d} \in \mathbb{C}$, for $d \in \{0, ..., Q\}$) of the beamformer $l$ ($l \in \{0, ..., Q\}$) to the direction $d$ is needed and calculated by

$$D_{l,\theta_d} = \mathbf{W^T_{MVDR,l}}\mathbf{h}_{\theta_\mathbf{d}}, \tag{9}$$

where $\mathbf{h}_{\theta_\mathbf{d}} = [H_{\theta_d,1}, ..., H_{\theta_d,M}]^T$.
Assuming the sources are uncorrelated [16], the PSDs of all sources (i.e. $[\varphi_0, \varphi_1, ..., \varphi_Q]^T$) can then be estimated by

$$\begin{bmatrix} \varphi_0 \\ \varphi_1 \\ \vdots \\ \varphi_Q \end{bmatrix} = \begin{bmatrix} |D_{0,\theta_0}|^2 & |D_{0,\theta_1}|^2 & \dots & |D_{0,\theta_Q}|^2 \\ |D_{1,\theta_0}|^2 & |D_{1,\theta_1}|^2 & \dots & |D_{1,\theta_Q}|^2 \\ \vdots & \vdots & \ddots & \vdots \\ |D_{Q,\theta_0}|^2 & |D_{Q,\theta_1}|^2 & \dots & |D_{Q,\theta_Q}|^2 \end{bmatrix}^{-1} \begin{bmatrix} \phi_{0,MVDR} \\ \phi_{1,MVDR} \\ \vdots \\ \phi_{Q,MVDR} \end{bmatrix}, \tag{10}$$

where $[\phi_{0,MVDR}, \phi_{1,MVDR} ..., \phi_{Q,MVDR}]^T = [|\widetilde{S_{MVDR}}|^2, |\widetilde{V_{MVDR,1}}|^2, ..., |\widetilde{V_{MVDR,Q}}|^2]^T$ (i.e. the power spectral density of signals after MVDR filtering).
With the estimation of PSDs, the coefficient of Wiener filter can be calculated by

$$W_{WF} = \frac{\varphi_0}{\sum_{q=1}^{Q} \varphi_q}. \tag{11}$$

It should be noted that the PSD estimation by machine learning can also be used in the design of the Wiener filter [12], [13]. However, this is out of the scope, and this project mainly focused on improving the MVDR filter by estimating the noise co-variance matrix. Further combinations of improvements in MVDR and Wiener filters remain as a future study.
In addition, it should be noted that due to the nature of the estimation of Wiener filter coefficients by (9), (10) and (11), the MVDR beamformer's weights and the signals after the MVDR beamforming are primarily involved in the estimation of Wiener filter's coefficients. Hence, the estimation of NCM and the performance of the MVDR beamformer are highly likely to impact the Wiener filter's performance as a sub-component in the whole algorithm.

## 3. Experiment

### 3.1 Experimental conditions

#### 3.1.1 Algorithms to be compared

To test the effectiveness of the rotor noise's NCM estimation method in Section 2.2 and gain further understanding of the effects of different rotor noise's NCM estimation methods, the method in [11] was used as a baseline method. We compared it with three other methods, all of which modify only the NCM's estimation process while the overall structure of the algorithm remains the same.

Table 1: Methods of NCM estimation for comparison

| Methods | Rotor NCM estimation |
|---|---|
| 1. FULL adj | Given rotor noise PSD + TDOA estimation based impulse response |
| 2. PSD adj | Given rotor noise PSD + Measured impulse response of microphones |
| 3. IR adj | TDOA estimation based impulse response |
| 4. Original | Measured impulse response of microphones |

The methods for comparison are summarised in Table 1. Method 1 used the NCM estimation method described in Section 2.2, which uses the given PSD of rotor noise to approximate the magnitude of the NCM whereas the TDOA is used to approximate the phase of the NCM. Method 2 uses the magnitude estimation stated in Section 2.2.1 but the phase approximation is based on the measured impulse response of each microphone in an anechoic chamber. Method 3 uses only the phase approximation described in Section 2.2.2 to estimate the NCM and assuming that the magnitude of the NCM is identical across frequency ($\phi_{q,m} = 1,\ \forall i, t$). Method 4 is the baseline method [11], which uses only the measured impulse responses (i.e. both the magnitude and phase of the impulse response) to estimate the NCM.

#### 3.1.2 Geometry of microphone array

Recordings collected from a real UAV system with microphone array attached was used in the experiment. The microphone array attached to the UAV is shown in Figure 4a with each microphone's number is labelled by a yellow circle. To obtain the TDOA between microphones, the geometry of the microphone array was re-constructed in a 3D coordinate system as shown in Figure 4b by using the measured dimensions of the microphone array assuming the position of microphone one coincided with the origin of the coordinates. The coordinate of each microphone

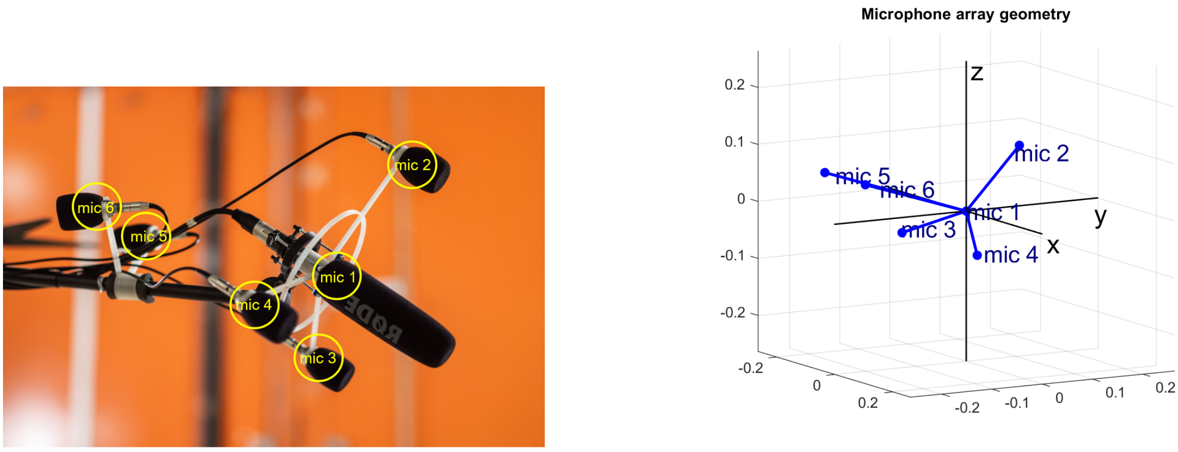


(a) Microphone array in reality (b) Microphone array in 3D coordinate system

Figure 4: Microphone array geometry re-construction

is summarised in Table 2.

Table 2: Coordinates of microphones

| Axis [m] | Mic 1 | Mic 2 | Mic 3 | Mic 4 | Mic 5 | Mic 6 |
|---|---|---|---|---|---|---|
| x | 0 | 0 | -0.1299 | 0.1299 | -0.07 | 0.07 |
| y | 0 | 0.1061 | -0.0530 | -0.0530 | -0.2416 | -0.2416 |
| z | 0 | 0.1061 | -0.0530 | -0.0530 | 0.0783 | 0.0783 |

### 3.1.3 Audio source generation

The impulse response of each microphone was measured in an anechoic chamber at the University of Auckland using a swept sine signal. The target source generation is achieved by convolving a source from a corpus speech with the measured impulse response of the six microphones in the array. The rotor noise was recorded by each microphone in an anechoic chamber, so the rotor noise at each microphone can be regarded as the convolution of the true rotor noise with the impulse response between the rotor's position to the microphones.

### 3.1.4 Placement of audio sources

To simplify the problem, we set the condition of placement of one target source and one rotor noise (i.e. $Q = 1$). The configuration of one rotor and one target source is shown in Figure 5. As highlighted in the blue box, the target source is placed at 90° and the rotor is located at 255°. In addition, the speed of sound was assumed to be 340 m/s for the implementation of phase estimation of NCM mentioned in Section 2.2.2. Also, to implement the magnitude of NCM stated in Section 2.2.1, the oracle PSD of the unprocessed rotor noise at each microphone was used.

### 3.1.5 Other experimental specifications

The sampling frequency of all audio signals was 48 kHz, and the STFT was implemented with a time-frame length of 2048 samples and 50%-overlapping. Two MVDR beamformers by the method in [11] were used for the estimation of rotor noise's PSD. The beamformer steering at the target used the microphone 1, 2, 3 and 4, while the one steering at the rotor used the microphones 1, 5 and 6 as per [11]. In addition, two ranges of rotor speed were used (i.e. 3000-3500 rpm for low speed and 3500-4000 rpm for high speed). Ten types of the target sources were used to test the methods, including five male and five female voices. Also, low input SRNR ranging from -30 dB to -10 dB was used to test the algorithm as the SRNR tends to be below -10 dB for audio recordings on UAVs. The information is summarised in Table 3. Furthermore, the algorithms were implemented via Matlab software.

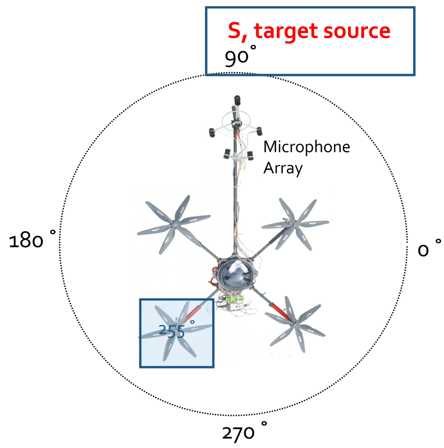


Figure 5: Experiment configuration

## 3.2 Parameter tuning process

There are two regulation parameters (namely $\epsilon_1$ and $\epsilon_2$) to prevent the singularity due to inverse matrix calculation. The value of these parameters has a significant

Table 3: Experiment specifications

| | |
|---|---|
| Sampling rate (kHz) | 48 |
| STFT frame length (overlap shift) | 2048 (1024) |
| # of MVDR beamformers [11] | 2 (steer at the target and the rotor noise respectively) |
| UAV speed range (rpm) | 3000-3500; 3500-4000 |
| # of target source patterns | 10 (5 male, 5 female) |
| Input SRNR (dB) | -30, -25, -20, -15, -10 |

impact on the performance of the algorithm.

The first parameter ($\epsilon_1$) was related to the MVDR beamformer, and the second parameter ($\epsilon_2$) was related to the Wiener filter. To ensure the overall algorithm was tuned optimally, $\epsilon_1$ was tuned first, with $\epsilon_2$ fixed to make the performance of the overall algorithm best. Then, $\epsilon_2$ was tuned to reach the optimal performance of the overall algorithm with $\epsilon_1$ fixed. The parameters were tuned heuristically.

### 3.3 Performance evaluation metric

Signal to rotor noise ratio (SRNR) measures the average power of a target signal against the average power of rotor noises, and the ratio is converted to decibel (dB). It is calculated by $SRNR = 10\log_{10}\left(\frac{E[(s(t)-E[s(t)])^2]}{E[(v(t)-E[v(t)])^2]}\right)$, where $s(t)$ and $v(t)$ are the target signal and rotor noise in time domain, respectively, and $E[\cdot]$ denotes the expectation operator. Positive SRNR value means the power of target signals on average dominates over the power of the rotor noise signals, and vice versa.

The metric used for the performance of the algorithm was SRNR improvement ($\Delta SRNR$). It is an objective metric calculated by $\Delta SRNR = SRNR_{out} - SRNR_{in}$, where $SRNR_{in}$ and $SRNR_{out}$ are the SRNRs before and after the signal processing algorithm is applied. This metric compares how the relative power on average between the target and rotor noise changes after an algorithm is applied. A positive value means that the applied algorithm helps to increase the relative ratio of power between the target speech and the rotor noise.

## 4. Results and discussion

### 4.1 SRNR improvement

Figure 6 shows the SRNR, SINR and STOI improvement for each method under low rotor speed and high rotor speed conditions, respectively. From the first column of plots in Figure 6, it was shown that the overall performance of method 1 (i.e 'FULL adj' ) had the most remarkable SRNR improvement compared to the other three methods under both low and high rotor speed conditions. The algorithm [11] equipped with method 1 of NCM estimation kept a consistent average SRNR improvement at around 23 dB across input SRNR ranging from -30 to -10 dB under low rotor speed condition. Method 1 also kept the average SRNR improvement at around 26 dB under high rotor speed condition. In contrast, method 4 had the highest average SRNR improvement of around 15 dB at the input SRNR of -10 dB under low rotor speed condition and the highest average SRNR improvement of around 21 dB under high rotor speed condition.

In addition, although methods 2 and 3 (i.e. 'PSD adj' and 'IR adj' ) seemed to outperform method 4 (i.e. 'baseline') the differences in the SRNR improvement were minor. For example, under both low rotor speed and high rotor speed conditions, the maximum difference in the average SRNR improvement among methods 2, 3 and 4 was around 3 dB at input SRNR of -30 dB. Compared with 3dB which is the minimum dB difference that can be distinguished by average human hearing, the differences among methods 2, 3, and 4 may not be significant to human perception.

For further investigation, each individual sub-component algorithm (i.e MVDR beamformer and Wiener filter) with the same NCM and PSD used in the overall algorithm was tested under the same experimental conditions, and the results were shown in the second and third columns in Figure 6. It was shown that the performance of the MVDR beamformer and Wiener filter with method 1 outperformed the MVDR and Wiener filter with other methods, while the performance of each sub-component with method 4 performed the worst. This directly explains the best overall algorithm performance with NCM estimated by method 1 and the worst overall performance by method 4.

It was shown that generally there was an increasing trend of SRNR improvement in the performance of the Wiener filter, and the cause of this trend is unclear. Since the Wiener filter's performance is highly dependent on the estimation of rotor noise's PSD, this suggests that the quality of rotor noise's PSD estimation varies across different input SRNRs. However, this is not the focus of this study, and further investigation remains for future studies. In contrast, the SRNR improvement in MVDR beamformer's performance kept stable across different input SRNRs. This trend is in line with the results previously reported in [13] and [15].

For MVDR beamformer, the average SRNR improvement was around 15 dB and 16.5 dB with method 1 under low and high rotor speed conditions, respectively. In contrast, the average SRNR improvement was around 7.5 dB and 11 dB with method 4 under low and high rotor speed con-

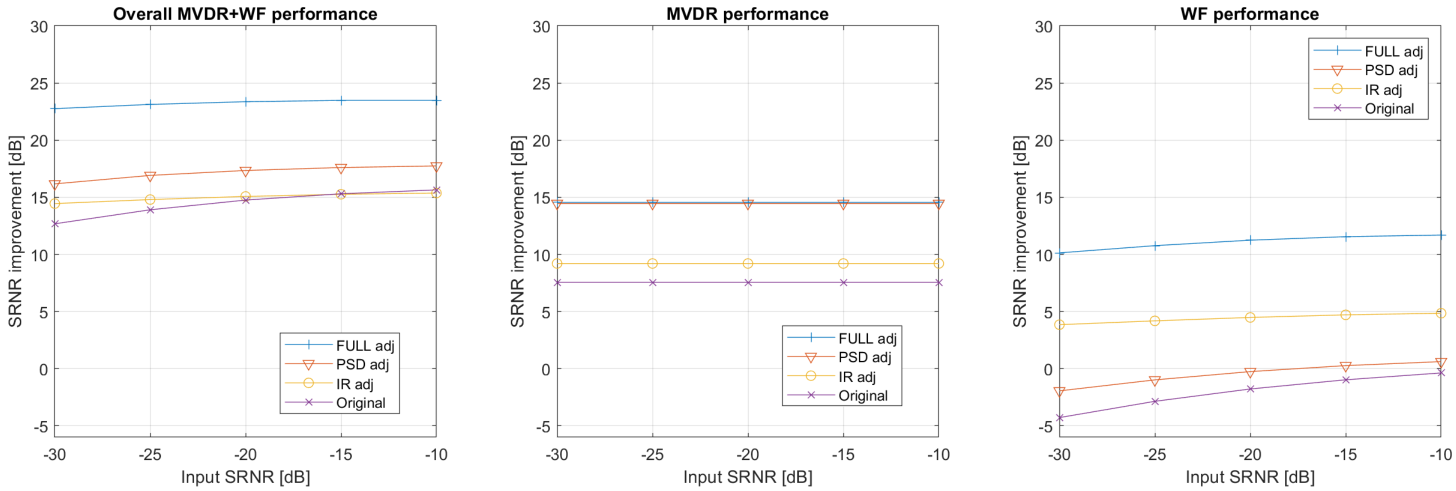


(a) SRNR improvement for low rotor speed range

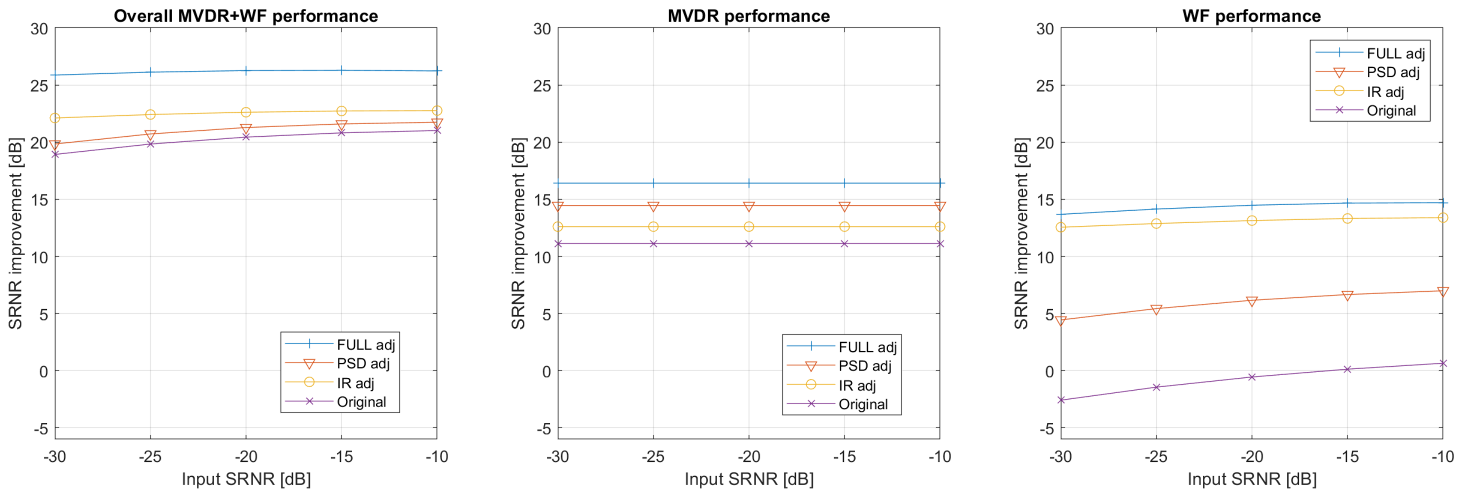


(b) SRNR improvement for high rotor speed range

Figure 6: SRNR improvement across different input SRNR

ditions, respectively. This suggests that method 1 of NCM estimation tends to affect the performance of MVDR positively. Compared with the result in [15] where the MVDR beamformer's performance can be improved to around 20 dB SRNR improvement with an almost ideal NCM, there is still space for method 1 to improve.

For the Wiener filter, the average SRNR improvement with method 1 was around 11 dB and 15 dB under low and high rotor speed conditions, respectively. In contrast, the average SRNR improvement with method 4 was between -5 and 0 dB under low rotor speed condition and between -2.5 and 0.5 dB under high rotor speed condition. The negative SRNR improvement values might be explained by the fact that the tuning parameter of the optimal overall performance of the algorithm may not match the parameter of the optimal Wiener filter. It was also interesting that the trend in the performance of the overall algorithm (shown in column 1, Figure 6) seemed to follow the trend in the Wiener filter's performance. This may be because the performance of MVDR beamformer tends to be stable across the various input SRNRs so that the overall trend would inherit the trend of the Wiener filter.

## 4.2 NCM investigation

To further understand how the estimation of NCM affected the result, the comparison between the true NCM and the estimated NCM (both are the average across time frames) was investigated. The magnitude and phase were compared separately. To quantify the comparison, the root mean square (RMS) error of each entry between the normalised true noise co-variance matrix and the estimated one was calculated for each frequency bin. Generally, it was found that the RMS error of phase had a more random distribution across all the frequencies compared to the RMS error of magnitude. In addition, it is interesting to see that the largest deviation of the RMS error of magnitude from the mean value tended to occur at normalised frequencies below $0.1\pi$ rad/sample and between around $0.3\pi$ and $0.5\pi$ rad/sample. This means the accuracy of magnitude estimation is likely to be related to the frequency. The reason for this remains unknown, hence future studies on this may be required.

Table 4: Mean RMS error between true and estimated NCM across all frequencies

| RMS error | Rotor speed | 1. FULL adj | 2. PSD adj | 3. IR adj | 4. Original |
|---|---|---|---|---|---|
| Magnitude | Low | 0.53262 | **0.42878** | 0.97699 | 0.57064 |
| Phase | Low | **0.75521** | 0.76654 | **0.75521** | 0.77969 |
| Magnitude | High | 0.38536 | **0.27463** | 1.1196 | 0.44396 |
| Phase | High | 0.77243 | **0.76442** | 0.77243 | 0.78763 |

The mean RMS error across all frequencies was summarised in Table 4. It is observed that method 3 had the highest mean RMS error of magnitude of around 0.98 and 1.12 under low and high speed conditions, respectively. This is expected since method 3 nearly has no endeavour in estimating the magnitude of the NCM. In addition, method 1 and 2 has the average RMS error of magnitude less than method 4. This is also expected as the first two methods used the magnitude estimation method by given rotor PSD which is supposed to improve the magnitude estimation. This suggests that the magnitude estimation of NCM in Section 2.2.1 is effective. However, more experiments with different rotor speeds are required to confirm this.

Furthermore, method 1 and 3 has a lower average RMS error of phase than method 4 under low and high speed conditions. It seems that the method of phase estimation in Section 2.2.2 is effective. For now, it is not sure until more data for different rotor speeds is available. However, if it were true, then it would indicate that the direction of the impulse response's measurement and the designed direction of sources might be slightly misaligned so that the theoretical impulse response estimation by TDOA can outperform.

By linking the result in Table 4 and the SRNR improvement of MVDR beamformer's performance in the second column of Figure 6, it is found that method 1 outperformed method 4, and it also has a lower RMS error of magnitude and phase than the NCM estimated by method 4. Similarly, method 2 with a lower error of magnitude and phase outperforms method 4 in MVDR beamformer's performance. However, it is surprising that the NCM estimated by method 2 had the lowest magnitude and phase error under the high rotor speed condition, but the MVDR performance with the method is not the best. In theory, by (7), the MVDR beamformer's weights should only depend on the NCM's estimation holding other variables the same. It is expected that the MVDR beamformer with the best approximation of the rotor noise's NCM has the best performance in SRNR improvement. However, the results do not fully agree with this. Also, studies in NCM estimation in speech enhancement such as [17] tend to use the performance of algorithms to show the effectiveness of the NCM's estimation, and few studies compare the estimated NCM directly although it is important. So it is difficult to validate the result by comparing it with other literature. Further experiments with various profiles of rotor noises were recommended to verify and exclude the likelihood of random errors.

Meanwhile, it is surprising that the NCM by method 3 has a significantly higher RMS error of magnitude than method 4, but MVDR beamformer associated with method 3 performs better than with method 4 under both low and high rotor speed conditions. In contrast, method 3 has a much higher error of magnitude than method 2 but the MVDR beamformer with method 2 outperforms that with method 3. This suggests that the magnitude and phase estimation may have different extents of effect on the performance of the MVDR beamformer. It is worth investigating the quantitative relation between the two types of error and the SRNR improvement in the MVDR beamformer with more data.

### 4.3 Directivity pattern by MVDR

The directivity of MVDR beamformer 1 (steering at the target) is shown in Figure 7. The direction number $[1, 2, 3, 4, 5, 6, 7, 8, 9]$ corresponds to the incoming directions from $[0, 30, 60, 90, 120, 150, 180, 255, 285]$ degrees as shown in Figure 5. It was shown that under conditions of low and high rotor speed, direction 4 (the target position) was emphasised (highlighted by yellow), and direction 8 (rotor position) was reduced (i.e. the column of position 8 was covered mainly by green). The beamformer seemed to be good for NCM estimated by all methods, and this supported the graphs in the second column in Figure 6 that for all methods of the estimation of NCM there was a positive SRNR improvement.

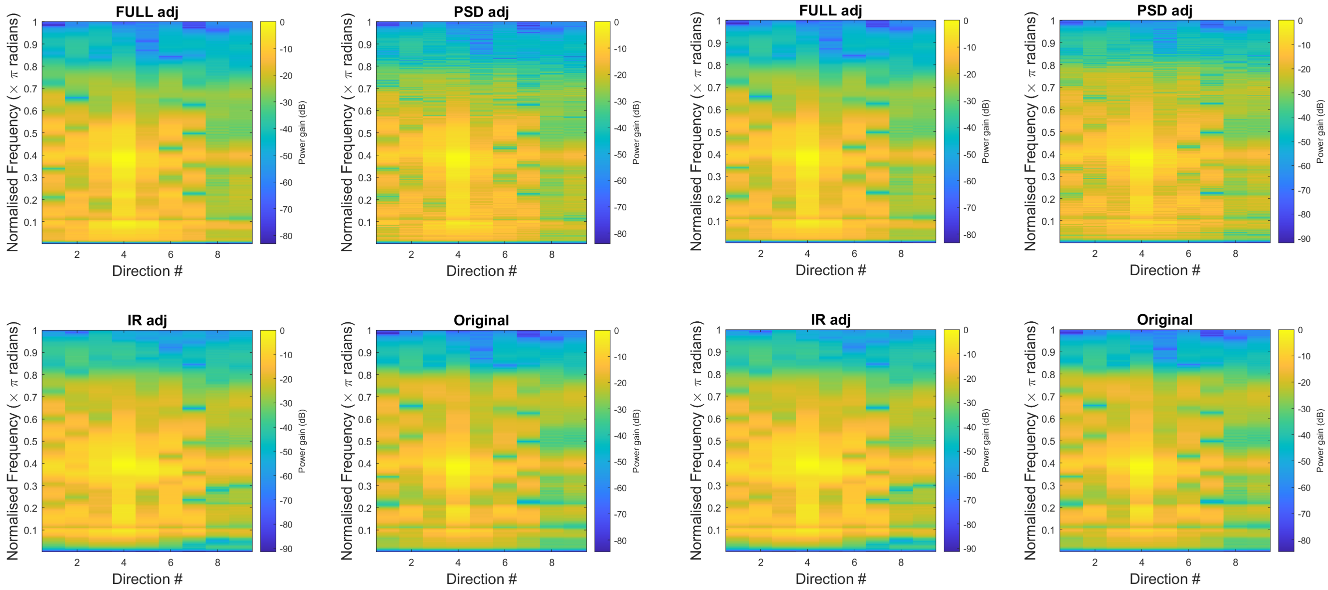


(a) Directivity pattern, low rotor speed

(b) Directivity pattern, high rotor speed

Figure 7: Directivity pattern

### 4.4 Rotor noise PSD in the Wiener filter

The true rotor noise's PSDs of low and high rotor speed are shown in Figure 8. The harmonics of rotor noise are shown in yellow strips. The most noticeable harmonics of low speed rotor noise was at around $0.33\pi$ rad/sample, and that of high speed rotor noise was at around $0.32\pi$ and $0.4\pi$ rad/sample.

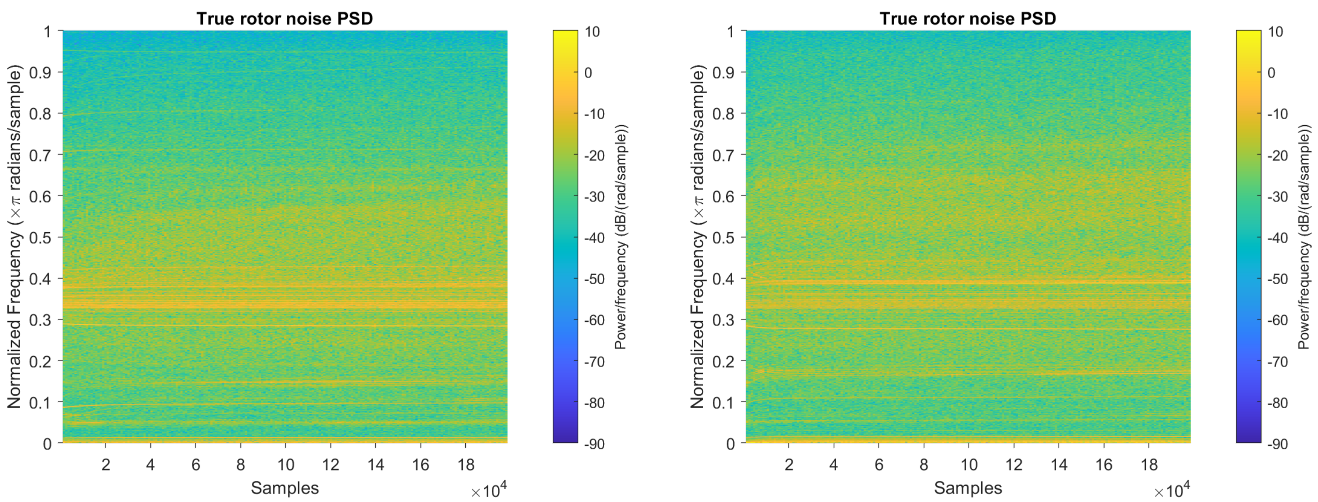


(a) True rotor noise PSD, low speed

(b) True rotor noise PSD, high speed

Figure 8: True rotor noise PSD

The estimation of rotor noise's PSD used in the Wiener filter is shown in Figure 9. It was observed that the PSD associated with method 1 (i.e. 'FULL adj') fitted the true rotor noise PSDs best among all the methods under both low speed and high speed conditions. The PSD associated

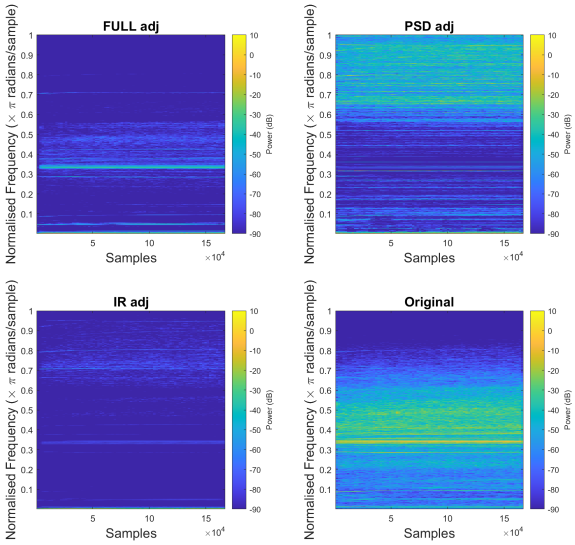


(a) Rotor noise PSD estimation, low speed

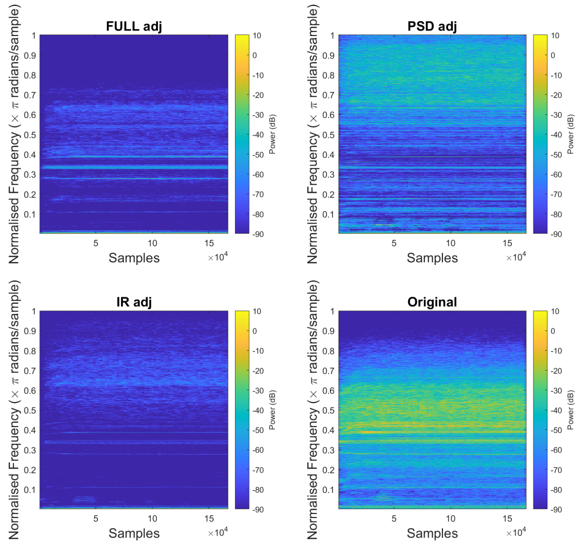


(b) Rotor noise PSD estimation, high speed

Figure 9: Rotor noise PSD estimation

with method 1 was always able to predict the most noticeable harmonics (shown by light blue stripes). It can also match harmonics in frequency ranges below $0.2\pi$ rad/sample and between 0.3 - $0.8\pi$ rad/sample. This may explain why the Wiener filter with method 1 outperformed among other methods (shown in the third column in Figure 6).

It was observed that the PSDs associated with method 2 (i.e. 'PSD adj') and 3 (i.e. 'IR adj') tended to introduce extra noises at high frequencies (i.e. between 0.6 and $0.8\pi$ rad/samples). This degraded the performance of the Wiener filter using these PSDs, although they were able to fit some harmonics of the true rotor noise PSDs. Also, the extra noises at high frequencies were more significant in PSD with method 2 than with method 3 under low and high rotor speed conditions. This implies that the Wiener filter's performance with method 2 would be worse than that of method 3. This agrees with the result in the third column in Figure 6. Similarly, the PSDs associated with method 4 ('original') introduced a significant amount of extra noises between around 0.3 and $0.6\pi$ rad/sample under low and high speed conditions, respectively. In addition, the power difference across all frequencies was significant (ranging from dark blue -90 dB to around yellow 0 dB). This might further distort the PSDs and reduce the effectiveness of this PSD in a Wiener filter more than PSDs with method 2 and 3. This may explain why the performance of the Wiener filter with method 4 had the worst performance.

As indicated by Section 2.3.2, the estimation of rotor noise's PSD is highly related to the performance of the MVDR filter since the PSD's estimation is based on the signals filtered by the MVDR beamformer (by (10)). By comparing the performance of the MVDR filter (shown in the second column in Figure 6) and the estimation of rotor noise's PSD in Figure 9, it is surprising to see that the performance of MVDR beamformer with method 2 outperformed that with method 3 but the estimation of the PSD showed the opposite. This is related to the estimation of rotor noise's NCM and the estimation of directivity by the method discussed in Section 2.3.2. However, the exact reason is unknown. Hence, to incorporate the study in how the NCM affects the performance of the MVDR filter as suggested in Section 4.2, a further quantitative study in the relationship between the estimation of rotor noise's NCM, directivity, and the Wiener filter's performance would be highly valuable.

## 5. Conclusion

In this research, one potential solution to the estimation of NCM for UAV recording was proposed. It was tested by implementing the method in an existing algorithm (an MVDR beamformer cascaded with Wiener filter [11]). The results showed that the algorithm associated with the proposed method outperformed the algorithm with other three approximating methods, including the original method. The algorithm with the proposed method had an average signal to rotor noise ratio (SRNR) improvement of around 23 dB under low rotor speed condition (i.e. 3000 - 3500 rpm) and around 26 dB under high rotor speed condition (i.e. 3500 - 4000 rpm), compared to the average SRNR improvement with the original method of around 15 dB and 20 dB under low and high rotor speed conditions, respectively. In particular, with the proposed method of NCM's estimation, each of the sub-components (i.e. MVDR beamformer and Wiener filter respectively) also outperformed the sub-components associated with the other three methods of NCM's estimation.

In addition, it seems that better magnitude and phase estimations of NCM tend to result in better MVDR beamformer's performance, but this is not always true. How the estimation of NCM affects the MVDR beamformer remains unclear. Moreover, it also seems that better estimation of rotor noise's PSD tends to result in better performance of Wiener filter. The power difference across frequencies in an estimated noise's PSD seems to be related to the performance of the Wiener filter. Also, the effect of the estimation of NCM on the estimation of PSD by [16] remains under-explored. These all require further investigation with more experimental data.

**References**


[1] *Military aircraft - Unmanned aerial vehicles (UAVs) | Britannica*.

[2] *Agriculture Drones: Drone Use in Agriculture and Current Job Prospects*, Apr. 2019.

[3] *Drones In Filmmaking: View From The Top*, Section: Production Features, Mar. 2020.

[4] S. Grogan, R. Pellerin, and M. Gamache, "The use of unmanned aerial vehicles and drones in search and rescue operations – a survey," Sep. 2018.

[5] S. G. Gupta, M. Ghonge, and P. M. Jawandhiya, *Review of Unmanned Aircraft System (UAS)*, 2013.

[6] J. Martinez-Carranza and C. Rascon, *A Review on Auditory Perception for Unmanned Aerial Vehicles*, vol. 20, no. 24, p. 7276, Dec. 2020.

[7] K. Furukawa, K. Okutani, K. Nagira, *et al.*, "Noise correlation matrix estimation for improving sound source localization by multirotor UAV," in *2013 IEEE/RSJ International Conference on Intelligent Robots and Systems*, ISSN: 2153-0866, Nov. 2013, pp. 3943–3948.

[8] K. Hoshiba, K. Washizaki, M. Wakabayashi, *et al.*, *Design of UAV-Embedded Microphone Array System for Sound Source Localization in Outdoor Environments*, vol. 17, no. 11, p. 2535, Nov. 2017.

[9] F. G. Serrenho, J. A. Apolinário, A. L. L. Ramos, and R. P. Fernandes, *Gunshot Airborne Surveillance with Rotary Wing UAV-Embedded Microphone Array*, vol. 19, no. 19, p. 4271, Oct. 2019.

[10] L. Wang and A. Cavallaro, *Deep Learning Assisted Time-Frequency Processing for Speech Enhancement on Drones*, IEEE Transactions on Emerging Topics in Computational Intelligence, vol. 5, no. 6, pp. 871–881, Dec. 2021, Conference Name: IEEE Transactions on Emerging Topics in Computational Intelligence.

[11] Y. Hioka, M. Kingan, G. Schmid, and K. A. Stol, "Speech enhancement using a microphone array mounted on an unmanned aerial vehicle," in *2016 IEEE International Workshop on Acoustic Signal Enhancement (IWAENC)*, Sep. 2016, pp. 1–5.

[12] B. Yen, Y. Hioka, G. Schmid, and B. Mace, *Multi-sensory sound source enhancement for unmanned aerial vehicle recordings*, vol. 189, p. 108 590, Feb. 2022.

[13] B. Yen, Y. Hioka, and B. Mace, "Source enhancement for unmanned aerial vehicle recording using multi-sensory information," in *2020 Asia-Pacific Signal and Information Processing Association Annual Summit and Conference (APSIPA ASC)*, ISSN: 2640-0103, Dec. 2020, pp. 850–857.

[14] M. Souden, J. Benesty, and S. Affes, *A Study of the LCMV and MVDR Noise Reduction Filters*, vol. 58, no. 9, pp. 4925–4935, Sep. 2010, Conference Name: IEEE Transactions on Signal Processing.

[15] Y. Li, B. Yen, and Y. Hioka, *Performance evaluation on multi-channel Wiener filter based speech enhancement for unmanned aerial vehicles recordings*, vol. 263, no. 3, pp. 3584–3594, Aug. 2021.

[16] Y. Hioka, K. Furuya, K. Kobayashi, K. Niwa, and Y. Haneda, *Underdetermined Sound Source Separation Using Power Spectrum Density Estimated by Combination of Directivity Gain*, vol. 21, no. 6, pp. 1240–1250, Jun. 2013.

[17] R. C. Hendriks and T. Gerkmann, *Noise Correlation Matrix Estimation for Multi-Microphone Speech Enhancement*, vol. 20, no. 1, pp. 223–233, Jan. 2012.

**QUIET DRONES**
**Second International e-Symposium**
**on**
**UAV/UAS Noise**
**27th to 30th June 2022**

# Computational aeroacoustics of an urban air mobility vehicle using the acoustic preserved artificial compressibility method

**Yuhong Li[1], Hanbo Jiang[1*], Zhida Ma[1], Siyang Zhong[1**] and Xin Zhang[1,2]**

1. Department of Mechanical and Aerospace Engineering, The Hong Kong University of Science and Technology, Clear Water Bay, Kowloon, Hong Kong SAR, China
2. HKUST-Shenzhen Research Institute, Hi-Tech Park, Nanshan, Shenzhen, 518057, China

## Summary

This work investigates the turbulent flow of an urban air mobility (UAM) vehicle and its far-field acoustic feature. The vehicle is equipped with six propellers, which can generate a total thrust of about 5000 N. Each propeller has a radius of 1 m. The near-field flows are simulated using the acoustic wave preserved artificial compressibility (APAC) method, and the turbulence is modelled through the delayed detached eddy simulations (DDES). The far-field noise is computed by an on-body integral solution of the Ffowcs Williams and Hawkings (FW-H) equations. Results show strong fluctuations in the thrust signal for the vehicle under hovering conditions, which are caused by the interaction between each propeller and its support structure. Such interaction also produces unsteady loadings acting on blade surfaces, leading to considerable tonal noise at the blade passing frequency and its harmonics. The noise directivity is also explored, and the spectra at various observers exhibit visible patterns that are likely attributed to the interference between noise from individual propellers. Additionally, the propeller wake interacts with the vehicle fuselage, changing its propagation direction and causing pressure fluctuations on the fuselage, which can also contribute to noise emissions.

* Email: jianghanbo@ust.hk
** Email: zhongsy@ust.hk

# 1. Introduction

Unmanned aerial vehicles (UAVs), usually referred to as drones, have been widely employed in various civilian applications [1]. For urban air mobility (UAM), the vehicle usually has a larger size than conventional drones and has attracted considerable research interest [2]. However, noise pollution is an essential issue because the vehicles will fly at a relatively low altitude near the populated urban area [3]. The noise exposure could raise annoyance in the community and will possibly limit the development of UAM [4].

The flows around multiple propellers are inherently unsteady and complicated. The complexity is compounded in the presence of a fuselage. Lately, several numerical studies have been conducted on the noise generated by an isolated propeller. Mankbadi et al. [5] studied the radiated noise by an isolated UAV propeller using a hybrid large eddy simulation - unsteady Reynolds averaged Navier-Stokes approach and Ffowcs Williams and Hawkings (FW-H) formulation [6]. Diaz and Yoon [7] conducted numerical simulations for an isolated propeller and quadcopters using an overset grid technique. While many studies focused on the hovering condition, some researchers also investigated the effect of more complex flows. Nardari et al. [8] analysed the confinement effect induced by recirculating flow inside a closed anechoic chamber based on a Lattice-Boltzmann simulation and FW-H solution. The same techniques were also used by Romani et al. [9] to investigate the flow incidence effects on the far-field noise feature. Recently, Jiang and Zhang [10] proposed the APAC method for fast and robust simulations of low-Mach number flows. The method was successfully applied to the propeller noise computations, and their results showed good agreement with experimental measurements.

During forwarding fights, vortices shed from propellers can interact with the vehicle fuselage, affecting aerodynamic noise generation and propagation. To study the influence of the fuselage model on the noise sources, Jia and Lee [11] investigated the acoustics of a quadrotor aircraft using computational fluid dynamics simulations. Lee and Lee [12] conducted numerical using the nonlinear vortex lattice method and acoustic analogy to understand the rotor interactional effect on the aeroacoustics of a multi-rotor system. A similar study was also conducted by Misiorowski et al. [13] to consider the side flight using detached-eddy simulation. Heydari et al. [14] recently studied the noise generated by a biplane quadcopter under various flight conditions. They found that the quadcopter's sound power depends on inflow angle and shows a significantly higher level than the isolated propellers.

In this work, the aerodynamics and aeroacoustics of a hexa-rotor vehicle are investigated using the APAC method. The remainder of this paper is organized as follows. Section 2 introduces the numerical methods. Section 3 presents the simulation results under the design flight condition and relevant discussions. Section 4 summarizes this study.

# 2. Numerical methods

## 2.1 Flow model

The APAC method solves the following equations [10]:

$$\frac{1}{\rho_0 c_0^2}\left(\frac{\partial P}{\partial t} + \nabla\cdot(P\boldsymbol{u})\right) + \nabla\cdot\boldsymbol{u} = 0,$$

$$\frac{\partial \boldsymbol{u}}{\partial t} + \nabla\cdot(\boldsymbol{u}\boldsymbol{u}) - \nabla\cdot(\nu\boldsymbol{u}) = -\nabla P,$$

where $\rho_0$ and $c_0$ are the freestream density and the speed of sound. $P$, $\nu$ and $\boldsymbol{u}$ represent the kinematic pressure, the kinematic viscosity and the fluid velocity, respectively. The Spalart-Allmaras turbulence model [15] is adopted for DDES computations.

## 2.2 Far-field noise model

The numerical implementation of the FW-H solution adopts Farassat's formulations 1A [16], which gives a far-field integral solution by

$$p'(\boldsymbol{x},t) = p'_T(\boldsymbol{x},t) + p'_L(\boldsymbol{x},t),$$

where $p'_T(\boldsymbol{x},t)$ and $p'_L(\boldsymbol{x},t)$ are thickness and loading noise, respectively, with the following expressions:

$$\begin{aligned}4\pi p'_T(\boldsymbol{x},t) = &\int_{f=0}\left[\frac{\rho_0\left(\dot{U}_n + U_{\dot{n}}\right)}{r(1-M_r)^2}\right]_{\text{ret}}\mathrm{d}S \\ &+ \int_{f=0}\left[\frac{\rho_0 U_n\left(r\dot{M}_r + c_0(M_r - M^2)\right)}{r^2(1-M_r)^3}\right]_{\text{ret}}\mathrm{d}S,\end{aligned}$$

$$\begin{aligned}4\pi p'_L(\boldsymbol{x},t) = &\frac{1}{c_0}\int_{f=0}\left[\frac{\dot{L}_r}{r(1-M_r)^2}\right]_{\text{ret}}\mathrm{d}S \\ &+ \int_{f=0}\left[\frac{L_r - L_M}{r^2(1-M_r)^2}\right]_{\text{ret}}\mathrm{d}S \\ &+ \frac{1}{c_0}\int_{f=0}\left[\frac{L_r\left(r\dot{M}_r + c_0(M_r - M^2)\right)}{r^2(1-M_r)^3}\right]_{\text{ret}}\mathrm{d}S.\end{aligned}$$

In the above equations, $f = 0$ denotes the blade surface, $r = |\boldsymbol{x} - \boldsymbol{y}|$ is the distance between the observer $\boldsymbol{x}$ and the source position $\boldsymbol{y}$. $U$ and $M = U/c_0$ are the velocity and Mach number of a source point on the integral surface. $\boldsymbol{L} = p\boldsymbol{n}$ denotes the loading vector where $p = \rho_0 P$ is the gauge pressure and $\boldsymbol{n}$ represents the surface unit normal vector. $[\cdot]_{\text{ret}}$ indicates the retarded time, which means the quantities inside the square brackets should be evaluated at the source time. The subscripts $r$ , $n$ and $M$ indicate the projections in the radiation direction, the surface normal direction and the surface motion direction, respectively. The dot over a variable represents the time derivative.

### 2.3 Computational setup

The vehicle model is designed in the Aerodynamics Acoustics & Noise control Technology Centre (AANTC) at the Hong Kong University of Science and Technology. The geometry parameters of this vehicle are given in Table 1. The designed gross weight is 500 kg. Figure 1(a) introduces the computational setup. The propeller diameter *D* = 2.05 m is used as a reference. The computational domain is a cylindrical volume, featuring a diameter of 20*D* and a height of 20*D*. Six cylindrical zones with a diameter of 1.05*D* and a length of 0.2*D* are defined around propellers, in which the grids move with the rotating propellers. Three propellers rotate clockwise while the other three rotate counter-clockwise to balance the propeller-induced torque. The rotational speed for each propeller is 25 revolutions per second (RPS). An acoustic sponge layer with a thickness of 2.5*D* is adopted to minimize wave reflection from the far-field boundary. The vehicle is in the hovering condition.

| Number of propellers | Propeller diameter | Fuselage length | Fuselage width | Overall length | Overall width |
|---|---|---|---|---|---|
| 6 | 2.05 m | 2.49 m | 1.57 m | 4.15 m | 3.85 m |

Table 1: Geometry parameters of the vehicle.

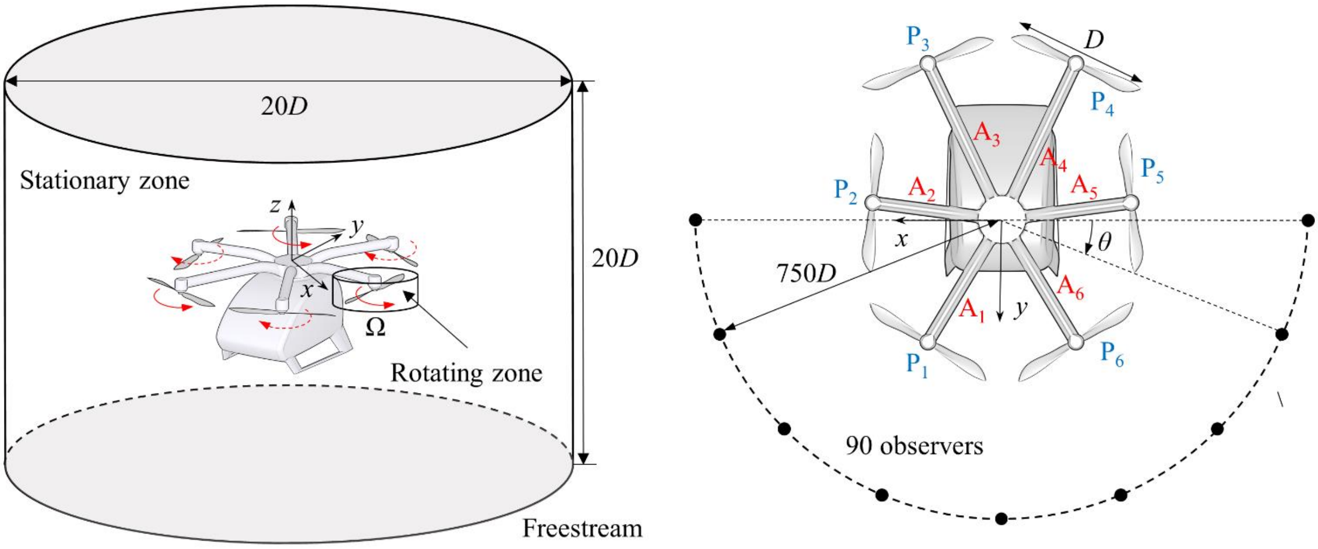


(a) (b)

Figure 1: Sketch of (a) the computational domain and (b) the microphone locations.

For far-field noise computation, all surfaces including propellers, supporting arms and the fuselage, are chosen as the FW-H integral surface. As shown in Fig. 1(b), the six propellers and their supporting arms are referred to as $P_1$ to $P_6$ and $A_1$ to $A_6$, respectively. The observers were located at 750*D* away from the vehicle centre. 90 equally-spaced observers are placed within 180° in the $z = 0$ plane, towards the rear direction of the fuselage. The sampling frequency is 20 kHz, which allows the analysed frequency range up to 10 kHz. The data is collected after 20 propeller revolutions to ensure the near-field flow is fully developed. The total computational time lasts for 25 propeller revolutions.

The computational mesh consists of 44 million hybrid hexahedra and tetrahedra grids. A sectional visualization of the mesh structure is shown in Fig. 2(a). The mesh is refined hierarchically near the vehicle surface. Figure 2(b) presents the mesh on the fuselage and the blade surface. Additional refinement is performed near the trailing edge and tip.

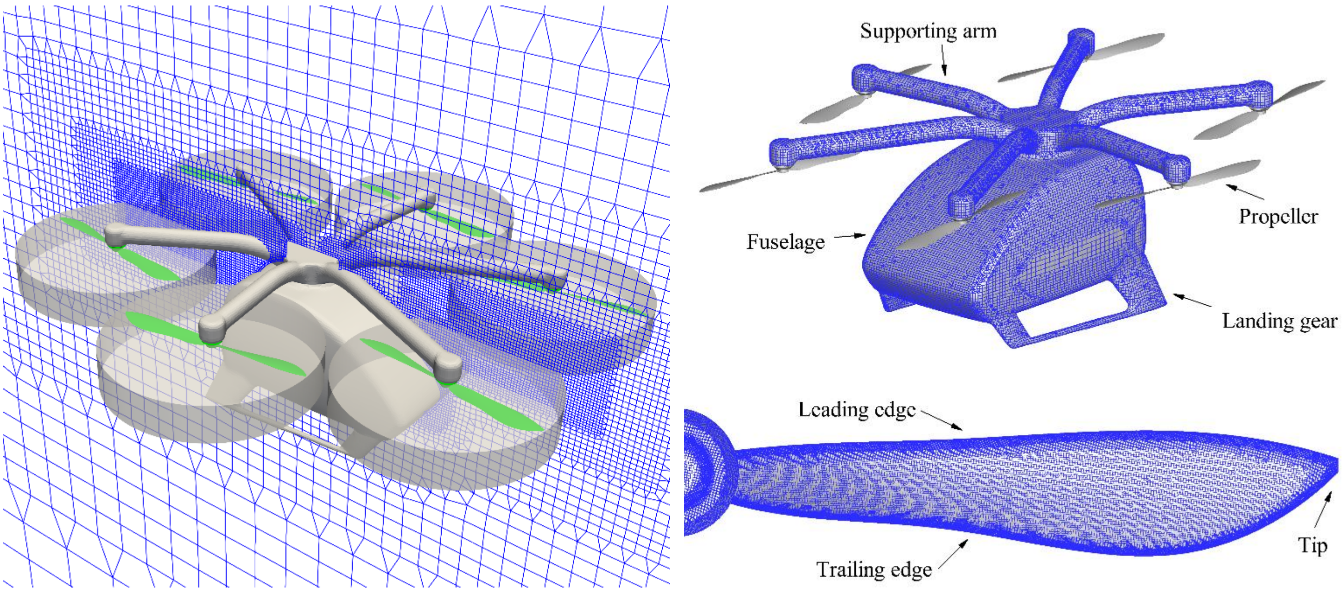


(a) (b)

Figure 2: The computational grids on (a) the cross section of the symmetry plane; (b) the fuselage and blade surface.

# 3. Results and discussion

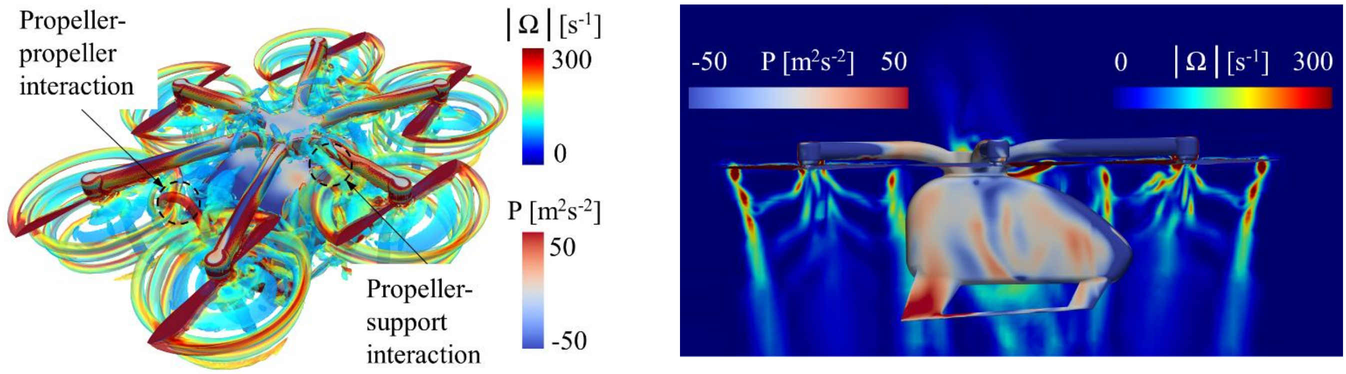


(a) (b)

Figure 3: (a) Iso-surfaces of Q-value coloured by the vorticity magnitude with Q = 1500 $s^{-2}$. (b) Sectional view of the vehicle with contour coloured by the vorticity magnitude. Pressure is shown at the body surfaces for both plots.

Figure 3(a) shows the instantaneous iso-surfaces of Q-value coloured by the vorticity magnitude and the kinematic pressure on the vehicle surface. Strong vortices were shed from the blade tips, interacting with the supporting arms and the fuselage. The interaction between the vortices shed from two neighbour propellers can also be noticed, especially for the two frontal propellers. There are also weak vortices shed from the middle of the blade span. When a propeller approached its supporting arm, the pressure on the arm surface reduced (the two frontal propellers), and when the propeller swept away from the supporting arm, the pressure on the arm surface increased again (the two propellers on both sides of the fuselage), exhibiting a periodic change. Figure 3(b) presents a sectional view of the instantaneous vorticity field near the vehicle. Tip and hub vortices were shed from the propeller, propagating downstream and interacting with the fuselage. Unlike isolated propellers, the wake region shown in Fig. 3(b) is no longer symmetric due to the presence of the fuselage.

Figure 4(a) shows the thrust history during last five propeller resolutions. The thrust is obtained by integrating the aerodynamic forces on the $z$-axis (vertical upward, see Fig. 1(a)). The thrust varies in a small dynamic range, indicating the flow is fully developed. The time-averaged thrust is 5415 N, and the standard deviation is 109.1 N. The thrust spectrum is shown in Fig. 4(b). There are strong peaks at the blade passing frequency (BPF) and its harmonics. These peaks are likely attributed to the blade periodically sweeping through the region below the supporting arm.

Figure 5 is a contour plot coloured by the sound pressure level (SPL). The results contain the spectrum information up to $f$/BPF = 200 and the corresponding directivity at each frequency. There are strong tonal peaks at BPF harmonics, showing different directivity patterns. Unlike the isolated propeller, the tones at up to $f$/BPF = 10 are still strong due to the periodic interactions between the propellers and the supports. The broadband noise shows smaller SPL values than the tonal components and decreases rapidly after $f$/BPF = 100. As for the noise directivity, all BPF tones show symmetry around the observer angle $\theta$ = 90° since the vehicle body is symmetric around the $y$-axis. However, each BPF tone shows a different pattern. For example, at $\theta$ = 90°, the radiated noise level is low at $f$/BPF = 1, and it becomes high for $f$/BPF = 2.

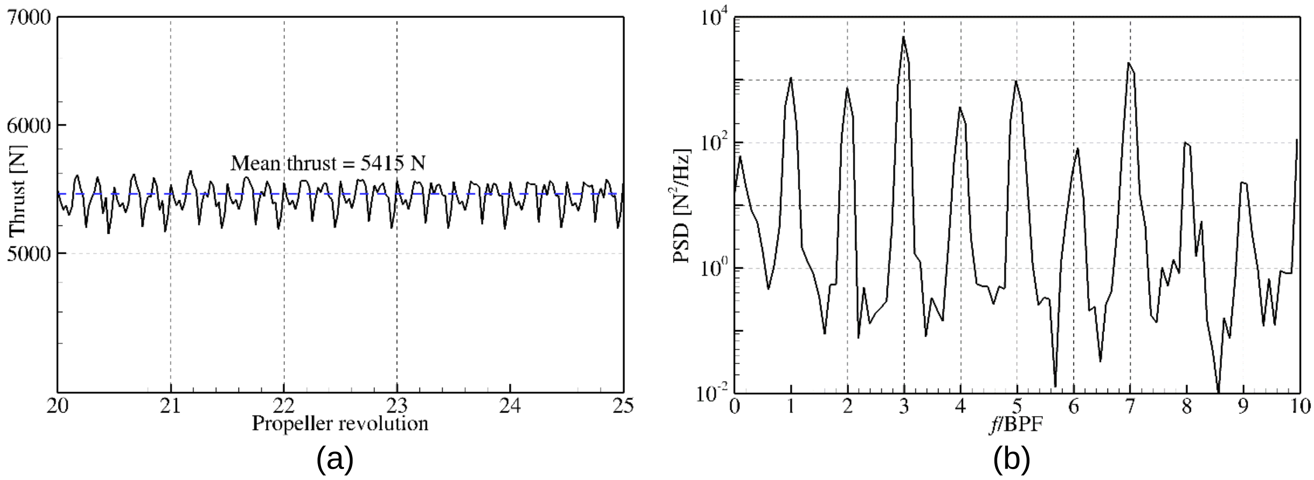


Figure 4: Thrust results. (a) Time history of the last five propeller revolutions. (b) Power spectrum density.

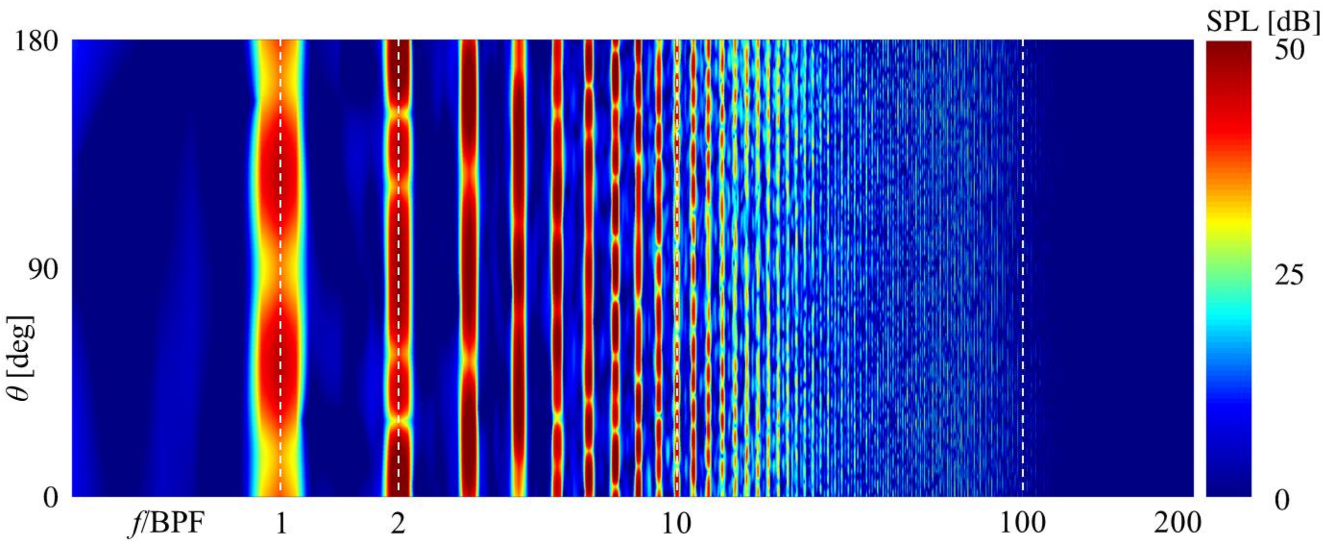


Figure 5: Contour plot of the noise spectra in different radiation directions.

## 4. Conclusions

This paper introduces a computational framework to predict the noise of a UAM vehicle using high-fidelity computational aeroacoustics. The computation is conducted for a configuration with a maximum take-off mass of 500 kg. The DDES computations were conducted using the APAC method, and the far-field noise was calculated using the FW-H formulations. The complex flow interactions between the propellers, the supports and the fuselage are successfully captured. Meanwhile, the total thrust generated by the propellers shows strong periodic characteristics at BPF harmonics due to the propeller-support interaction. Finally, the far-field noise spectrum and directivity are computed. The results indicate that the far-field noise consists of multiple strong tones at BPF harmonics and weaker broadband components. The BPF tones also show different directivity patterns, which are likely due to the interference between noise radiated from individual propellers having different rotational directions.

**Acknowledgements**

This work is funded by the National Key R&D Program of China (Grant No. 2018YFE0183800).

## References


[1] Floreano, D., and Wood, R. J. (2015), *Science, technology and the future of small autonomous drones,* Nature 521(7553), 460–466.

[2] Rajendran, S., and Srinivas, S. (2020), *Air taxi service for urban mobility: a critical review of recent developments, future challenges, and opportunities*, Transportation Research Part E: Logistics and Transportation Review 143, 1–33.

[3] Rizzi, S. A., Huff, D. L., Boyd, D. D., Bent, P., Boeing, R., Louis, S., Henderson, B. S., Snider, R., Flight, B., and Worth, F. (2020), *Urban air mobility noise: current practice, gaps, and recommendations*, NASA/TP–2020-5007433, 1–59.

[4] National Academies of Sciences, Engineering, and Medicine. (2020), *Advancing aerial mobility: a national blueprint*. Washington, DC: The National Academies Press.

[5] Mankbadi, R. R., Afari, S. O., and Golubev, V. V. (2021), *High-fidelity simulations of noise generation in a propeller-driven unmanned aerial vehicle*, AIAA Journal 59(3), 1020–1039.

[6] Ffowcs Williams, J. E., and Hawkings, D. L., (1969), *Sound generation by turbulence and surfaces in arbitrary motion*, Philosophical Transactions of the Royal Society of London. Series A, Mathematical and Physical Sciences 264(1151), 321-342.

[7] Diaz, V. P., and Yoon, S. (2018), *High-fidelity computational aerodynamics of multi-rotor unmanned aerial vehicles*, AIAA Paper 2018-1266.

[8] Nardari, C., Casalino, D., Polidoro, F., Coralic, V., Lew, P.-T., and Brodie, J. (2019), *Numerical and experimental investigation of flow confinement effects on UAV rotor noise*, AIAA Paper 2019-2497.

[9] Romani, G., Grande, E., Avallone, F., Ragni, D., and Casalino, D. (2021), *Computational study of flow incidence effects on the aeroacoustics of low blade-tip Mach number propellers*, Aerospace Science and Technology 120, 107275.

[10] Jiang, H., and Zhang, X. (2021), *An acoustic-wave preserved artificial compressibility method for low-Mach-number aeroacoustic simulations*, Journal of Sound and Vibration 516, 116505.

[11] Jia, Z., and Lee, S. (2019), *Acoustic analysis of a quadrotor eVTOL design via high-fidelity simulations,* AIAA Paper 2019-2631.

[12] Lee, H., and Lee, D. J. (2020), *Rotor interactional effects on aerodynamic and noise characteristics of a small multirotor unmanned aerial vehicle*, Physics of Fluids 32(4).

[13] Misiorowski, M., Gandhi, F., and Oberai, A. A. (2019), *Computational study on rotor interactional effects for a quadcopter in edgewise flight*, AIAA Journal 57(12), 5309–5319.

[14] Heydari, M., Sadat, H., and Singh, R. (2021), *A computational study on the aeroacoustics of a multi-rotor unmanned aerial system*, Applied Sciences 11(20), 9732.

[15] Spalart P, Allmaras S. (1992), *A one-equation turbulence model for aerodynamic flows*, 30th aerospace sciences meeting and exhibit, 439.

[16] Farassat, F. (2007), *Derivation of formulations 1 and 1A of Farassat*, Nasa/TM-2007-214853, 1–25.

QUIET DRONES
Second International e-Symposium
on
UAV/UAS Noise
27th to 30th June 2022

# Acoustic measurement of multi-rotor drones in anechoic and hemi-anechoic chambers

**Zhida Ma[1], Han Wu[1], Hanbo Jiang[1], Siyang Zhong[1,2], Xin Zhang*[1,3].**

**1. Department of Mechanical and Aerospace Engineering, The Hong Kong University of Science and Technology, Hong Kong, China.**

**2. HKUST Institute for Advanced Study, The Hong Kong University of Science and Technology, Hong Kong, China.**

**3. HKUST-Shenzhen Research Institute, Nanshan District, Shenzhen, China.**

## Summary

The rapidly widening applications of drones can cause significant noise pollution issues. There exist needs for drone noise measurements in controllable test facilities. In this paper, we present the outcome of in-flight noise measurements of a quad-rotor drone in an anechoic chamber that can be set up as either a full anechoic configuration or a hemi-anechoic configuration. Flight conditions including hover, cruise, vertical climb and descent were tested. The noise was measured by two linear microphone arrays with a total of 15 free-field microphones. The instantaneous position of the drone was recorded by an optical motion capture system. For each working condition of the drone flight, multiple tests were conducted to reduce the statistical errors and uncertainties in the noise measurement. A criterion about the observer distance to ensure the acoustic far-field condition is proposed and justified using the measurement results. Moreover, by adjusting the drone's position and orientation, i.e., the heading angle, the noise directivity patterns on a spherical surface are obtained, showing a discernible correlation with the drone's airframe geometry and rotor configuration. The comparison between the full anechoic and the hemi-anechoic configurations highlighted the need of using non-reflective facilities for drone noise tests.

* aexzhang@ust.hk

# 1. Introduction

The fast-evolving technologies in consumer electronics and information technology facilitate the development and application of multi-rotor drones [1]. As a public health risk, the noise emission of drones has drawn considerable attention from both the drone industry and the academic community [2][3]. Noise assessment and certification for drones are increasingly being discussed. Several experimental studies have investigated the noise characteristics of multi-rotor drones. Tinney and Sirohi [4] conducted measurements of the multi-rotor drone noise at static thrust in an anechoic chamber and obtained some understanding of the dependence of drone noise on rotor size and operation speed. Outdoor field tests have been performed to investigate the noise characteristics of multi-rotor drones in flight conditions [5][6], which, however, suffered from limited accuracy and repeatability because of the wind gusts, ground reflections, environmental noise and positioning errors [7]. The outdoor experiment by Heutschi et al. [8] showed that for a drone in hover, the variation in the rotation speed of the rotors could reach up to 500 revolutions per minute (RPM) at a windspeed of 4.2 m/s. To reduce the uncertainties in the drone noise measurements, an acoustically qualified environment is necessary for drone noise assessment. Zhou et al. [9] conducted the noise measurements of a flying quad-rotor drone in a large anechoic chamber, providing comprehensive noise characteristics of the drone in real flight conditions.

Anechoic facilities have the advantages of providing a controllable test condition, isolating background noise, and realizing free-field conditions in all directions. However, a standardized drone noise test protocol has not been established. In 2019, the European Commission [10] issued a regulation on the requirements for the design and manufacture of the small unmanned aerial system (sUAS), which specified a test code for the airborne noise of sUAS with a maximum take-off mass (MTOM) below 25 kg. The acoustic measurement follows the ISO 3744:2010 standard and requires the sUAS to hover at 0.5 m above a reflecting plane in an anechoic chamber. The noise metric is the A-weighted sound power level ($L_{WA}$). However, the test method could suffer from several issues. At such a low hover height, the wake from the rotors of the drone can directly impinge the reflecting surface, resulting in an aerodynamic ground effect [11]. The interaction between the rotors and the reflecting surface could affect the acoustic characteristics. Also, the test code does not consider the noise directivity of the sUAS, which is important because observers can perceive the noise of drones operating in a low-altitude urban space from different directions. Moreover, requirements for the measurement distance to satisfy the acoustic far-field condition, which is essential in characterizing the noise sources, are missing.

This work aims at capturing the fundamental properties of noise radiated by multi-rotor drones by measurements in an anechoic chamber. Comprehensive noise tests were conducted for a representative quad-rotor drone under realistic flight conditions, including hover, vertical climb and descent, and horizontal cruise. An advantage of the chamber is that it can be set up as either a full anechoic configuration or a hemi-anechoic one, allowing us to assess the influence of ground reflection on the noise measurement. The remaining part of this paper is arranged as follows. In section 2, the test apparatus and methods are described. In section 3, the results and analysis of the measurements are presented. Section 4 are the conclusions.

# 2. Experimental setup and methods

## 2.1 Test apparatus

The experiments were conducted in the anechoic chamber of the Aerodynamic and Acoustic Facility at the Hong Kong University of Science and Technology. The chamber has a wedge-to-wedge dimension of 8.1 m (L) × 6 m (W) × 5.1 m (H) and a cut-off frequency of 100 Hz in the full anechoic configuration. With the bottom wedges removed, the chamber is in the hemi-anechoic configuration and the height is 5.7 m. Figure 1 shows a schematic of test setup.

An off-the-shelf quad-rotor drone was tested in the experiment. The drone was equipped with four fixed-pitch rotors with a diameter of 0.24 m. It has a diagonal axial distance of 0.35 m and a gross mass of 1.4 kg. An optical motion capture system consisting of nine infrared cameras was deployed to track the positions of the drone. The system provides real-time position data with a resolution of 0.1 mm and a refresh rate of 50 Hz. The position data was recorded in synchronization with the acoustic measurements. During the tests, the position of the drone was remotely controlled by the operator outside the chamber and maintained by the visual sensing module equipped by the drone, and the position drift is within 0.03 m.

Acoustic measurements were made using two linear microphone arrays consisting of fifteen ¼" G.R.A.S. 46BE free-field microphones in total. The two arrays were aligned in a single vertical plane. One with nine microphones was placed vertically near a corner of the chamber. The other one containing the remaining six microphones was mounted horizontally 0.12 m above the bottom wedges. The microphones were separated 0.5 m from the adjacent ones, and all of them were equipped with windscreens to alleviate the measurement noise generated by airflow around the microphone head. A National Instruments PXIe-4497 module with PXIe-1073 chassis was used to record the acoustic data. The sampling rate was 50 kHz, and a record time of 20 s was used for each test. The acquired acoustic data was processed by Welch's method [12] using a Hann window with a 50% overlap and a frequency resolution of 5 Hz.

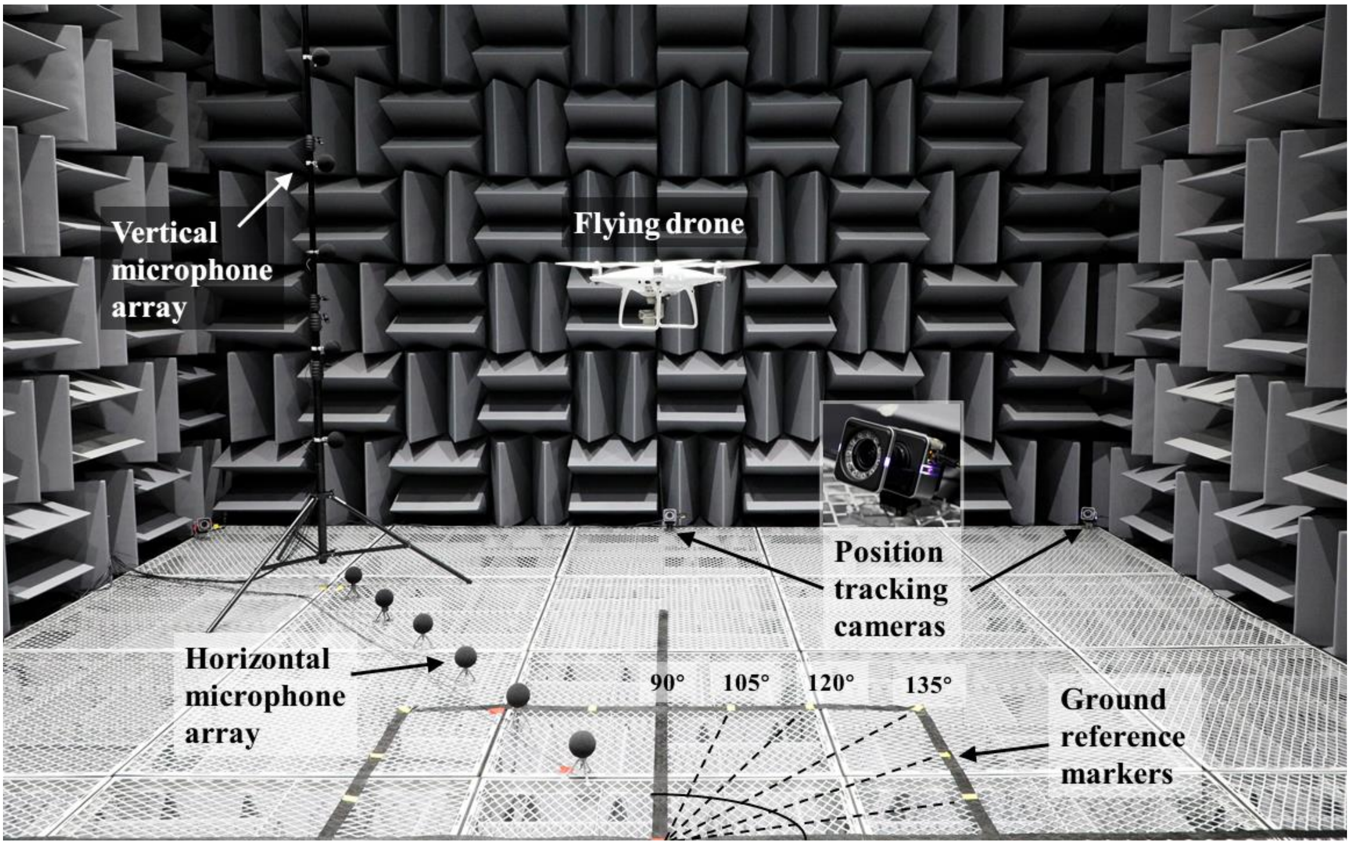


Figure 1: Schematic of test setup in the anechoic chamber.

### 2.2 Reference dimension

The determination of acoustic measurement distance should generally satisfy two requirements. First, the distance should not be too far. Otherwise, the measured sound will be affected by background noise, resulting in a low signal-to-noise ratio (SNR). However, this criterion is not a problem in the current study because the background noise of the anechoic chambers is sufficiently low. Second, the measurement distance should be larger than a critical value to ensure the acoustic far-field condition. In this case, at a given observer angle, the sound level will decrease inversely and follow the inverse square law. So far, the requirements for the drone noise measurement have not been clearly established, especially for drone noise tests.

Here we propose a normalized reference dimension $L$ for the acoustic measurement of a multi-rotor drone:

$$L = d + D, \tag{1}$$

where $d$ is the maximum diagonal axial distance between two rotors and $D$ is the maximum diameter of the rotors. In this way, both the airframe dimension (gross weight dependent) and rotor dimension (propulsive power dependent) are considered. From the perspective of acoustics, the reference dimension $L$ denotes the minimum diameter of a sphere to completely enclose the possible drone noise source regions. For the quad-rotor drone used in this experiment, a reference dimension $L = 0.59$ m. Then, based on our previous experience in measuring the propeller noise, the far-field condition can often be satisfied by a measurement distance larger than 10 times of the rotor radius. Therefore, in this work, we will examine if the far-field condition is met when

$$R \geq 5L, \tag{2}$$

where $R$ is the distance between the observer (microphone) and the centre of the drone.

### 2.3 Hemi-anechoic and full anechoic configurations

Two groups of hover tests were conducted with the chamber in the hemi-anechoic and the full anechoic configurations respectively. Only the data from the vertical microphone array were used to compare the drone noise properties in the lateral directions. As shown in Figure 2, two different reference ground planes were regarded as reflective and non-reflective surfaces and served as the basis ($z = 0$) for height calculation, respectively. One more microphone was mounted to the vertical array due to the extended height of the chamber with the bottom wedges removed.

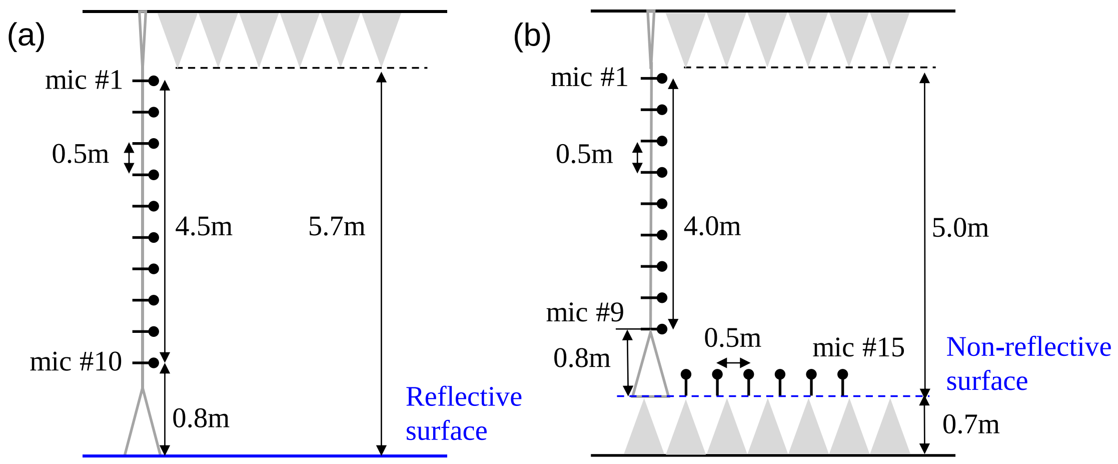


Figure 2: Microphone setups for (a) hemi-anechoic configuration (b) full anechoic configuration.

The top view of the positions of microphone arrays, hover points, and position tracking cameras, as well as the definition of the ground coordinate system, are shown in Figure 3. Five hover points denoted by *a*, *b*, *c*, *d* and *e*, separated by a horizontal interval of $L$, were tested to realize different observer distances. The drone hovered above each hover point, heading +x direction, at a height same as each microphone numbered #2 to #9 in the vertical array. Therefore, a planar grid composed of 40 hover positions is generated for both full anechoic and hemi-anechoic configurations, as shown in Table 1. The two groups of hover tests were each repeated five times.

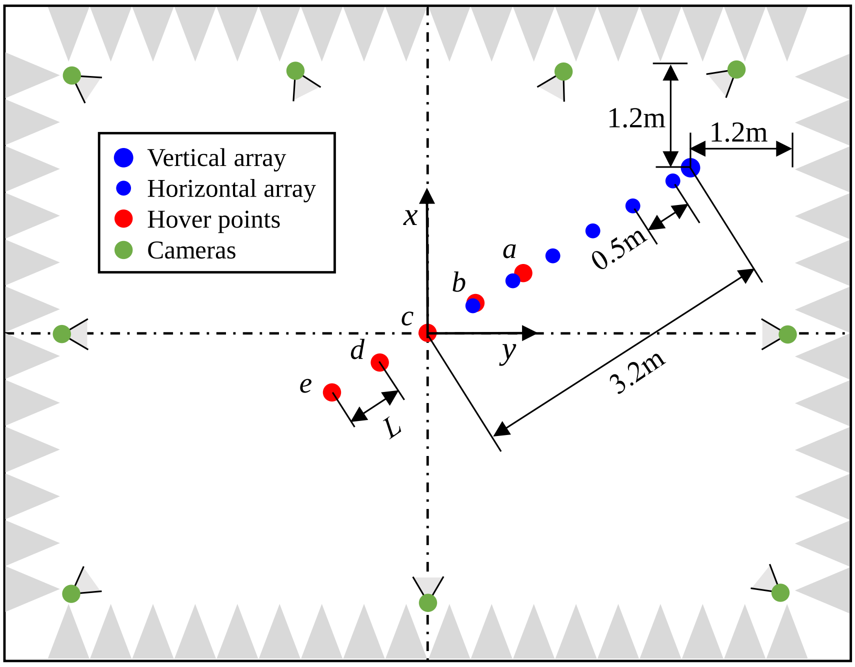


Figure 3: Positions of microphone arrays, hover points and cameras (top view).

| Hover heights | Hemi-anechoic | Full anechoic |
|---|---|---|
| 4.8 m | √ | × |
| 4.3 m | √ | √ |
| 3.8 m | √ | √ |
| 3.3 m | √ | √ |
| 2.8 m | √ | √ |
| 2.3 m | √ | √ |
| 1.8 m | √ | √ |
| 1.3 m | √ | √ |
| 0.8 m | × | √ |

Table 1: Hover heights tested in the two groups of experiments. The cross sign (×) means the corresponding measurements were not conducted due to space limitations.

### 2.4 Noise directivity tests

Since the microphone arrays are fixed while the drone is agile to manoeuvre inside the chamber, the drone was controlled to hover at different heading angles to realize different azimuthal observer angles. A schematic of the definition of the polar observer angle ($\theta$) and azimuthal observer angle ($\varphi$) is shown in Figure 4 (b). Three hover positions in the microphone plane were determined to maximize the measurable polar observer angle as shown in Figure 4 (a). In this case, only data from microphones #1 to #5 were used for the hover positions 2 and 3, detailed coordinates and $\theta$ measurement ranges of these hover positions are specified in Table 2.

The drone was controlled to hover at each position and vary heading directions at an interval of 15°. Precise heading angle adjustment is realized by aligning the real-time image from the onboard camera to the yellow ground reference markers (see Figure 1). The tests were repeated four times, and the four rotors were swapped diagonally between each repeated test group to minimize the influence of their manufacturing differences on the noise directivity measurement.

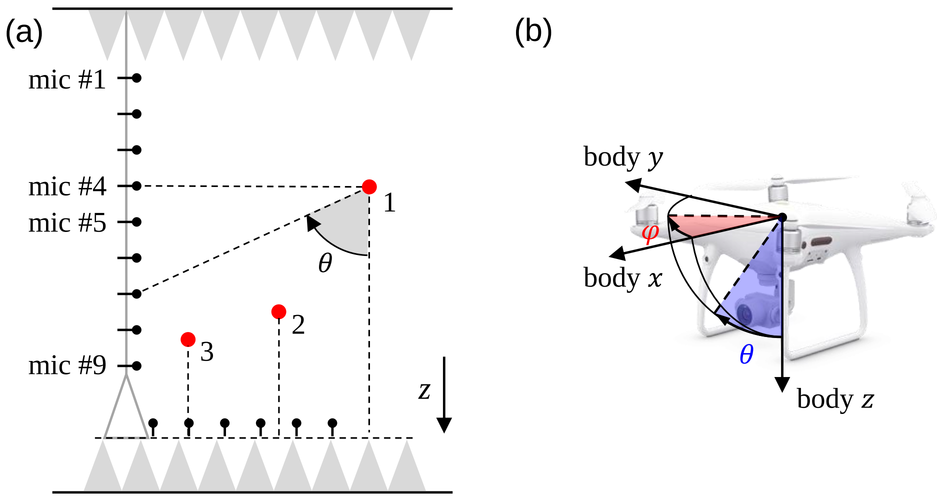


Figure 4: (a) Hover positions for directivity test (b) observer angle definition in body-fixed frame.

| Hover position | $x$ (m) | $y$ (m) | $z$ (m) | $\theta$ range (°) |
|---|---|---|---|---|
| 1 | 0.00 | 0.00 | -3.30 | [8.9,115.5] |
| 2 | 0.70 | 1.00 | -1.60 | [122.0,149.0] |
| 3 | 1.42 | 2.08 | -1.20 | [158.4,170.0] |

Table 2: Coordinates and polar angle measurement range at each hover position.

### 2.5 Dynamic flight test

Vertical climb, descent and cruise flight tests were performed to study the noise characteristics of the drone in dynamic flight conditions. The utilization of the space was maximized with the help of the position tracking system. The cases of dynamic flight tests are illustrated in Table 3.

| Flight condition | Case index | Start position $p_{\text{start}}$ (m) | End position $p_{\text{end}}$ (m) | Flight speed $V$ (m/s) |
|---|---|---|---|---|
| Vertical climb | C1 | [0,0,-0.80] | [0,0,-0.43] | 0.50 |
| | C2 | | | 0.25 |
| Vertical descent | D1 | [0,0,-0.43] | [0,0,-0.80] | 0.50 |
| | D2 | | | 0.25 |
| Cruise | F | [-2.00, 2.90,-3.30] | [2.00,-2.90,-3.30] | 0.50 |

Table 3: Start, end positions and flight speeds of tested dynamic flight conditions.

## 3. Results and discussions

The results are presented in five subsections. The first subsection shows the repeatability of both position and acoustic data. The second subsection gives the comparison between hemi-anechoic and full anechoic configurations, as well as the examination of the far-field criterion in Eq.(2). The third subsection analyses the effect of ground reflection in the hemi-anechoic chamber setup on noise measurements. The fourth subsection presents the reconstructed noise directivity map of the drone in hover. The final subsection presents the results of selected cases from dynamic flight tests described in Table 3.

### 3.1 Repeatability of test data

Although the real-time position data from the tracking system were not used to form an automatic position control system for the time being, the drone's position maintaining capability provided by its visual positioning system was satisfactory. Figure 5 shows the instantaneous position deviations (from nominal values) in three directions of five repeated hover tests. The average position drift, indicated by the maximum deviations, of all hover tests was 0.05 m ($0.085L$) horizontally and 0.026 m ($0.044L$) vertically.

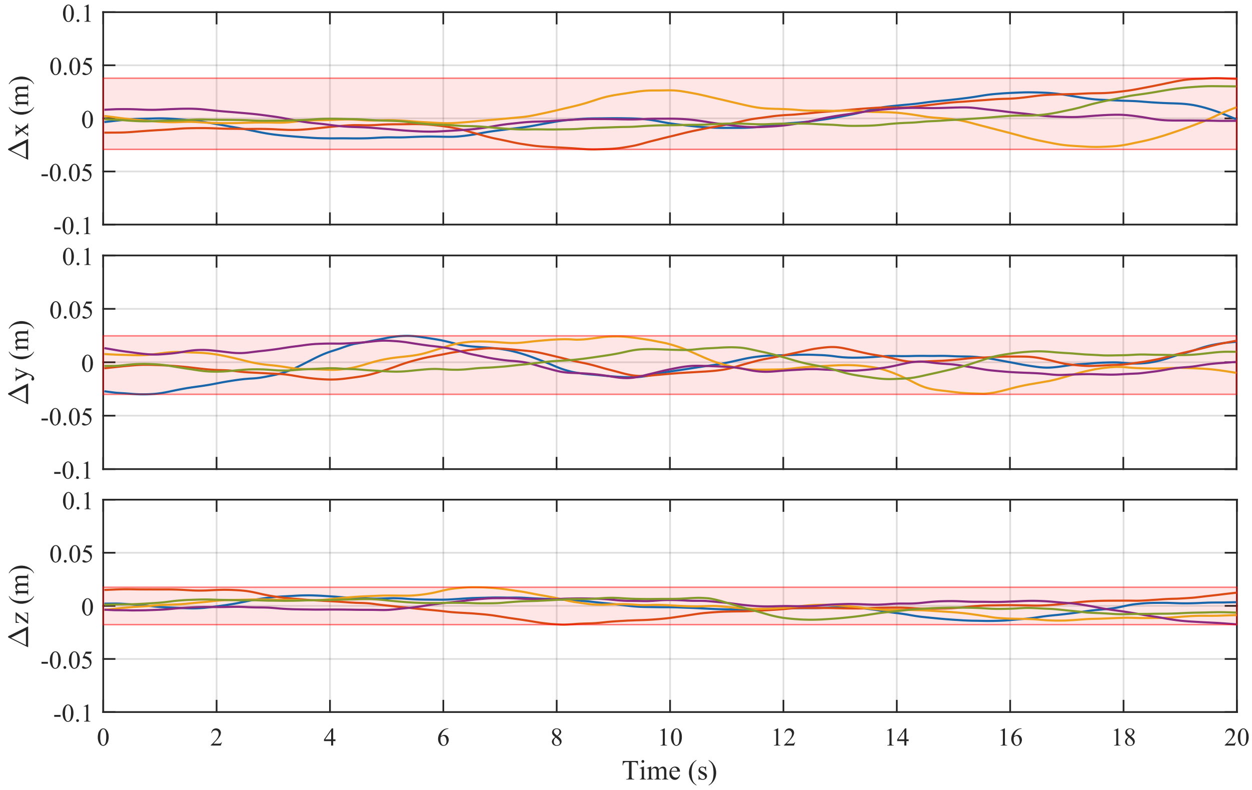


Figure 5: Position deviations from averaged values during five repeated hover tests.

Figure 6 shows the sound pressure level (SPL) spectra of the five repeated hover tests. The spectrum of the background noise in the full anechoic experiment is also plotted. The data is from microphone #4 as the drone hovered 3.3 m above point $c$ (horizontal centre of the chamber). The measured noise surpasses the background noise in the frequency range of interest (100~20000 Hz), the spectrum of each repeated test conforms well with others, and the blade passage frequency (BPF) is at around 182 Hz.

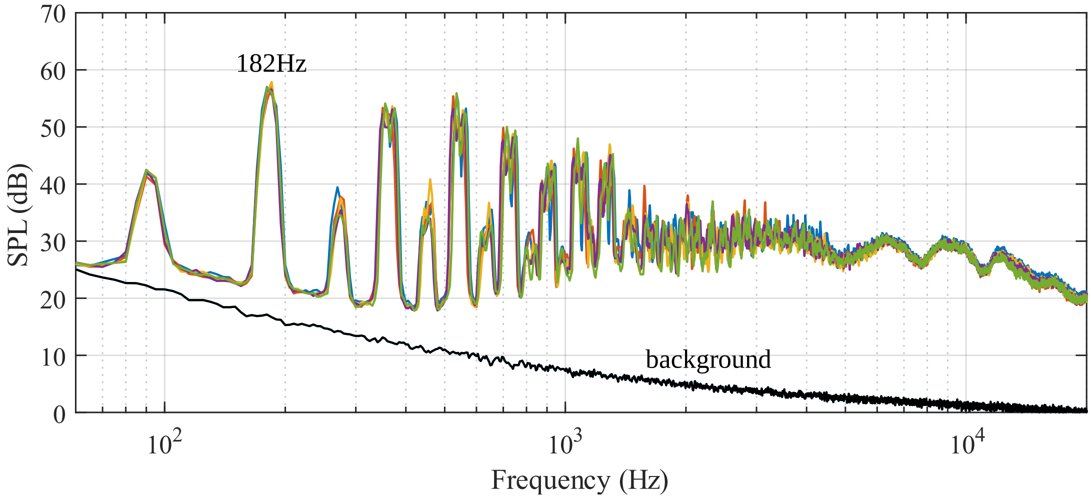


Figure 6: SPL spectra of five repeated tests and background noise.

### 3.2 Acoustic pressure decay with observer distance

Figure 7 shows the overall sound pressure level (OASPL) decay with respect to observer distance (normalized by $L$) when the drone is hovering at different heights in both the full anechoic and the hemi-anechoic configurations. The OASPL is integrated from 100 to 20000 Hz using the data from the microphone at the same height as the drone. Each data point on a single curve, representing the averaged values, corresponds to a hover point described in Figure 3. The error bars indicate the max deviations in the five repeated tests. With the abscissa in logarithmic scale, the gradient of the blue dashed line is a reference of spherical sound pressure decay ($1/R$) based on the inverse square law.

A larger discrepancy can be observed in the results from the hemi-anechoic configuration, as shown in Figure 7 (a). The linearity of curves does not agree well with the spherical decay reference, and the deviations can reach as large as 3 dB. Nevertheless, the error bars of the two groups of results are at a comparable level (0.5 dB), which indicates the high repeatability of both groups of measurements. Therefore, the discrepancy in the hemi-anechoic results is attributed to the presence of the reflective surface.

For the measurements in the full anechoic configuration, the sound pressure decay agrees well with the spherical decay within the measured distance range ($3.4L \sim 7.4L$). In this case, it will be reasonable to scale the acoustic data measured within this distance range to a uniform measurement distance. Moreover, the results justified that the criterion specified in Eq. (2) is sufficient to ensure far-field condition.

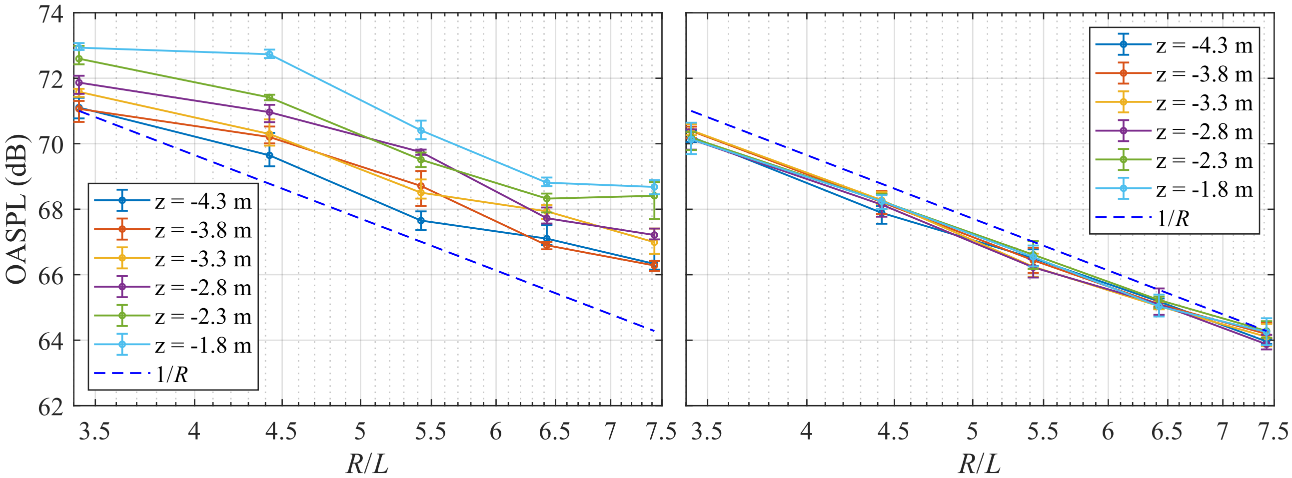


(a) hemi-anechoic (b) full anechoic

Figure 7: OASPL decay with respect to measurement distance at different hover heights.

### 3.3 Effect of ground reflection

This subsection presents the detailed spectral analysis of the ground reflection to illustrate its effect on the noise assessment of multi-rotor drones. Figure 8(a) shows the noise spectra from two adjacent microphones in a hemi-anechoic measurement. A large discrepancy can be found in the low to middle-frequency range. Since the two microphones' observer distance and equivalent angle are close, the acoustic spectral results were expected to be similar. However, in Figure 8 (b), little difference is found for the full anechoic measurement, while a significant difference can be found in the hemi-anechoic test results. At the BPF, which is the dominant tonal contribution, the difference in the measured SPL can be as significant as 10 dB. Therefore, it can be concluded that the ground reflections can change the original spectral characteristics, especially at low frequencies. The results illustrate the need to use a full anechoic facility to measure the drone noise spectra.

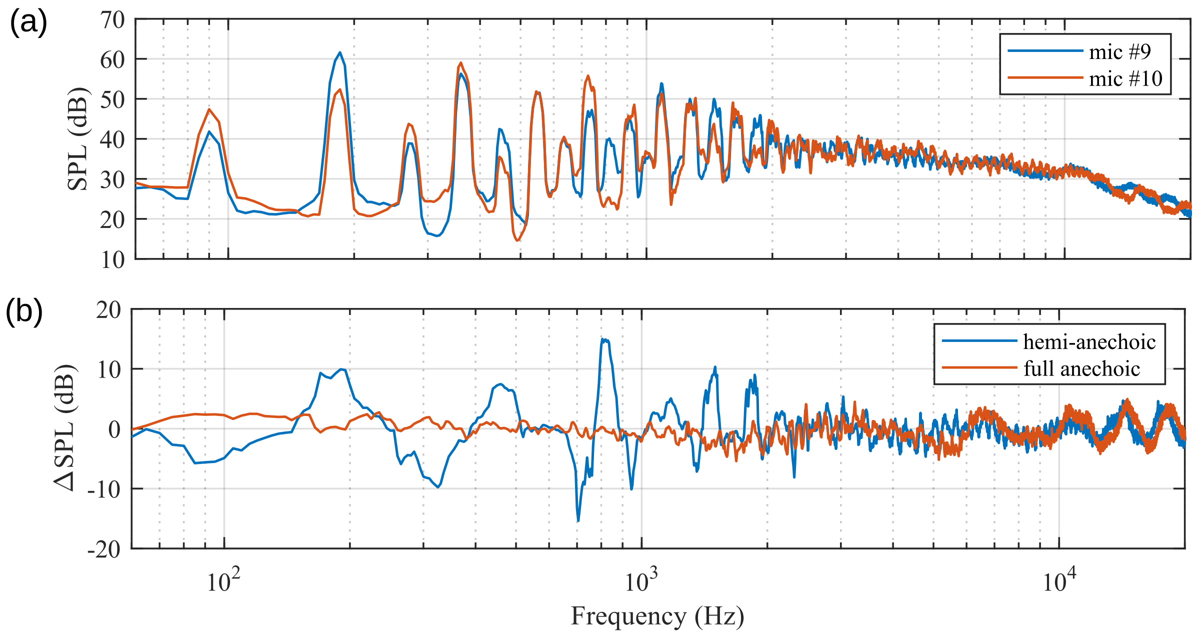


Figure 8: (a) SPL spectra from mic #9 and #10 in a hemi-anechoic test (b) SPL spectral difference between the two near-ground microphones in two chamber configurations.

### 3.4 Noise directivity in hover

Based on the test results, complete spherical directivity maps of the drone were reconstructed in the body-fixed frame for different noise components, as shown in Figures Figure 9 and Figure 10. Linear interpolation and extrapolation were used to estimate the values at the observer angles that were not covered by the measurements. The data were averaged from four groups of repeated tests and scaled to a uniform observer distance of 3.2 m.

Figure 9 shows the directivity of broadband OASPL integrated from 100 to 20000 Hz. The broadband noise generally exhibits a dipole pattern with the peak values in the axial direction of the rotors. A maximum difference of 10 dB can be found between the noise radiated in different directions. As for the tonal components shown in Figure 10, each tone presents significantly different directivity patterns. These patterns exhibit either two or four lobes in the azimuthal direction, possibly caused by rotor-rotor and rotor-airframe interactions.

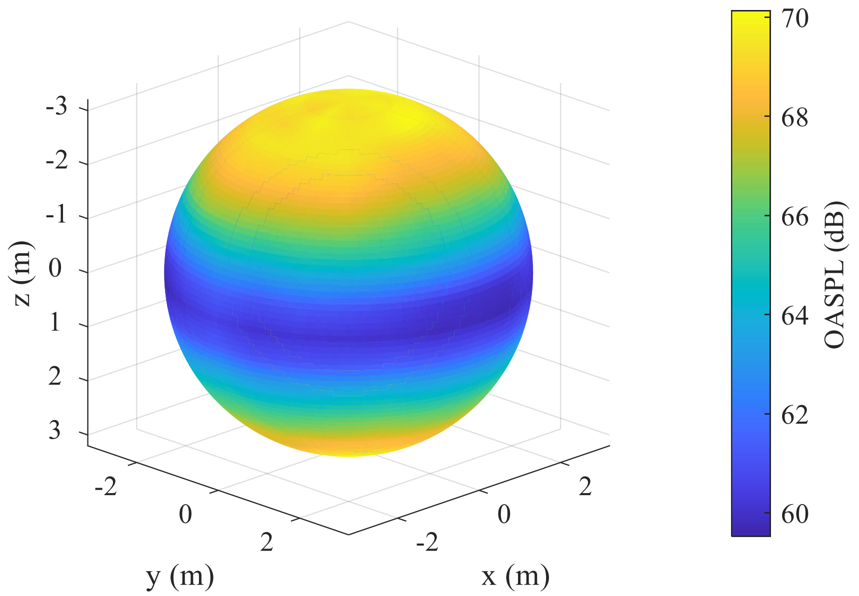


Figure 9: Broadband OASPL directivity.

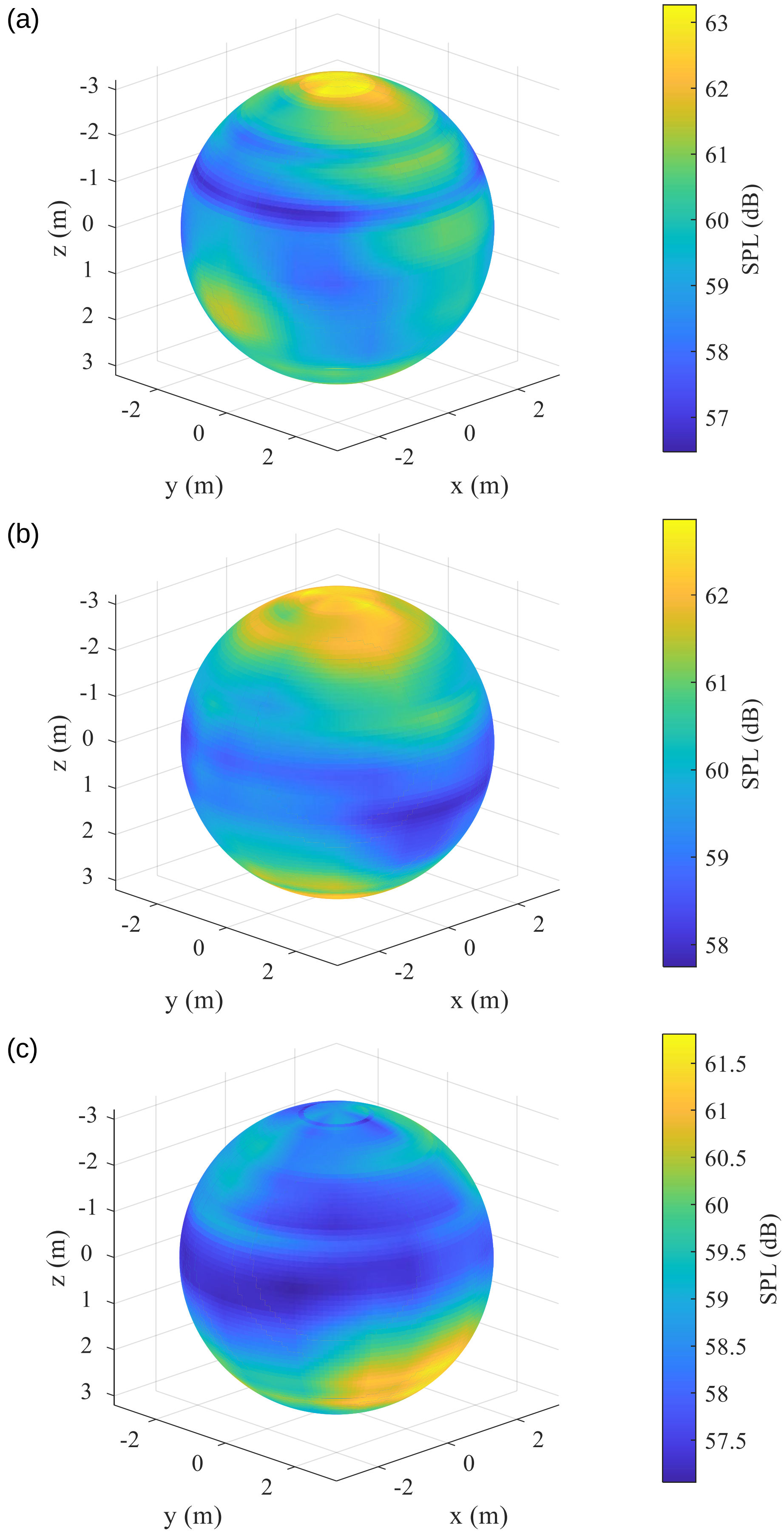


Figure 10: Tonal SPL directivity at (a) 1BPF (b) 2BPF (c) 3BPF.

With the spherical SPL data, the sound power level (PWL) of the drone in hover can be estimated. The calculation follows the procedure specified in ISO 3745-2012 standard [13], the averaged SPL at the measurement surface is expressed by:

$$\overline{L_{\mathrm{pf}}} = 10\log_{10}\left[\frac{1}{4\pi r}\int_{0}^{2\pi}\int_{-\frac{\pi}{2}}^{\frac{\pi}{2}} 10^{0.1L_p(r,\theta,\varphi)}\, r^2 \sin\theta \, d\theta d\varphi\right], \tag{3}$$

where $r$ is the normalized measurement distance, and $L_p(r,\theta,\varphi)$ is the SPL at the corresponding microphone location. Thus, the PWL at a reference sphere which has a 1 m$^2$ surface area is calculated by:

$$L_W = \overline{L_{\mathrm{pf}}} + 10\log_{10}\left(\frac{S_1}{S_0}\right)\mathrm{dB} + C_1 + C_2, \tag{4}$$

where $S_1$ is the area of the test sphere (of radius $r$), $S_0$ is 1 m$^2$, $C_1$ and $C_2$ are two correction terms regarding the barometric pressure during the measurements. The calculated PWL is 91.38 dB, when A-weighting is applied, the A-weighted PWL is 90.52 dBA.

### 3.5 Dynamic flight conditions

As the drone's position varied with time during dynamic flight tests, the short-time Fourier transform (STFT) was applied to the acoustic data to perform time-frequency analysis. The STFT calculation resulted in a frequency resolution of 5 Hz and a time resolution of 0.1 s. To analyze the correlation between the drone's motion and noise radiation, the position tracking data are differentiated to generate the velocity in the primary flight direction and plotted in combination with noise data.

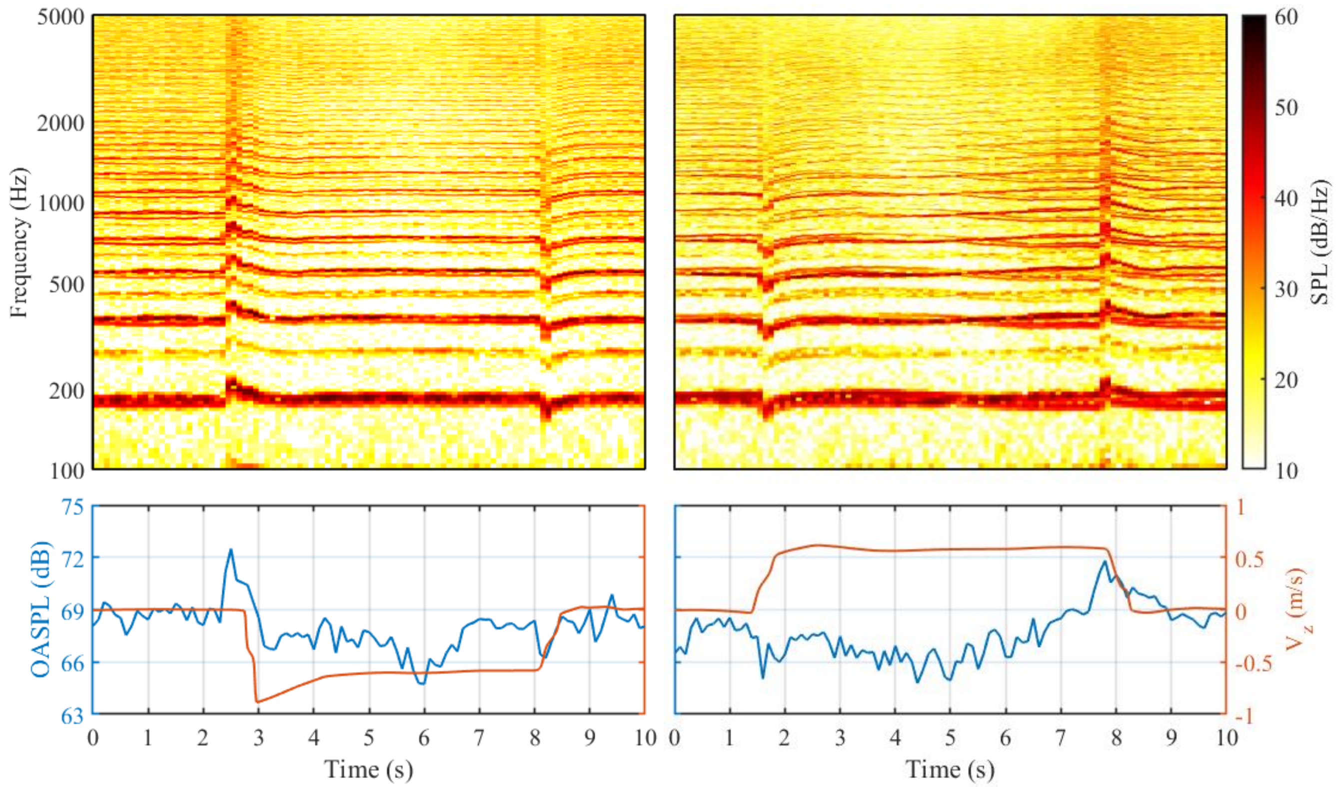


(a) case C1 (b) case D1

Figure 11: Mic #5 SPL spectrogram, OASPL and vertical speed data of flight cases C1 and D1.

Figure 11 presents the SPL spectrogram at the microphone #5 (at the mid-height) of the vertical flight cases C1 and D1. The corresponding OASPL and instantaneous vertical speed data are also plotted, respectively. The results indicate that the acceleration and deceleration in the axial flight direction cause instantaneous rotor speed change, which results in spectral and OASPL variations. Generally, upward (-z) acceleration leads to an increment in OASPL and downward (+z) acceleration leads to a decrease in OASPL. This is a reasonable consequence of the rotor speed change due to lifting power variation. It is worth mentioning that when the drone was at a similar height to microphone #5 in the climb/descent process, a low OASPL was measured, which corresponds to the directivity map illustrated in the last subsection.

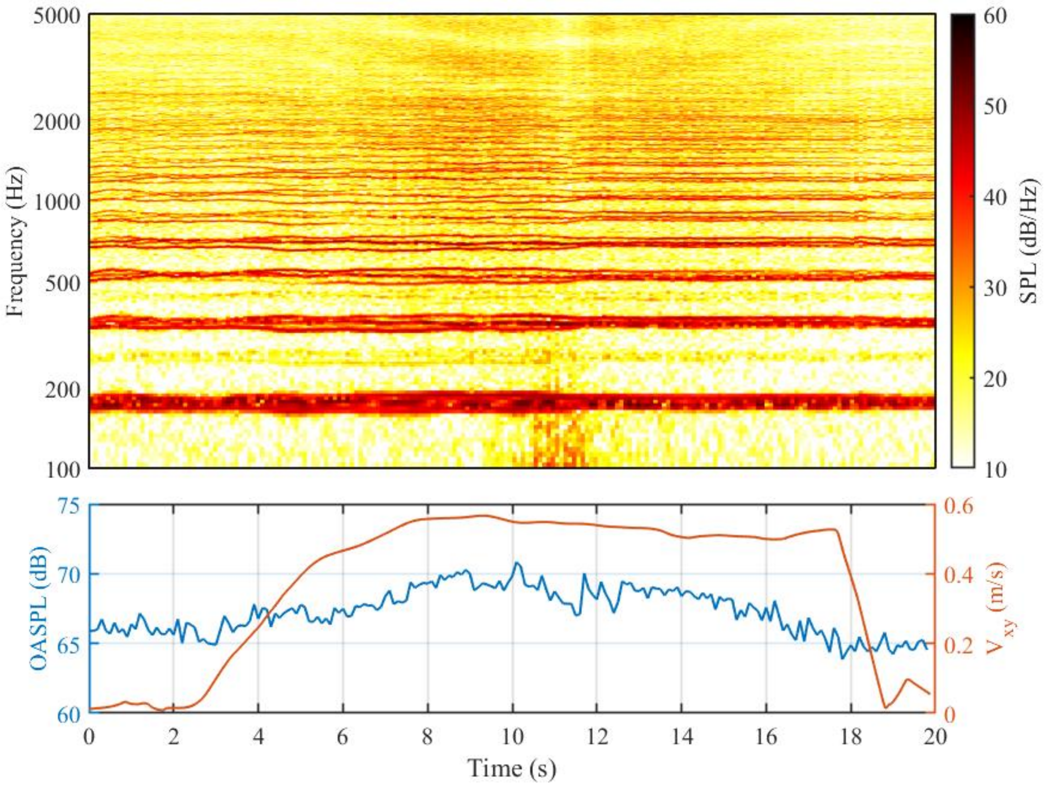


Figure 12: Mic #15 SPL spectrogram, OASPL and horizontal speed data of flight case F.

Figure 12 presents the SPL spectrogram at microphone #15 of the cruise flight case F. The OASPL and instantaneous horizontal speed data are also plotted. Separated tones can be observed from the spectrogram, which indicates the rotor speed difference during cruise flight. At around 11 s, the drone flew over the microphone and generated a prominent pressure fluctuation at low frequencies due to rotor wake. Meanwhile, a decrease in the measured broadband noise occurs.

## 4. Conclusions

Noise measurements of a quad-rotor drone were performed in an anechoic chamber with both full anechoic and hemi-anechoic configurations. Good repeatabilities of both position and acoustic data were obtained. The comparison between the results of the two configurations (full-anechoic and hemi-anechoic) revealed the influence of ground reflection on the drone noise measurement. Moreover, the acoustic interference caused by ground reflection can deviate from the measured spectra, especially at low frequencies. Thus, using a hemi-anechoic chamber could considerably degrade the tonal noise assessment accuracy.

The noise directivity in hover flight condition was measured by adjusting the position and the heading angle of the drone. The spherical directivity of broadband OASPL and different tones were obtained. The directivity patterns show observable correlations with the airframe geometry and rotor configuration, possibly caused by rotor-rotor and rotor-airframe interactions, which requires further investigation. The measurements of dynamic flight cases were analysed in combination with the instantaneous position data, which revealed the noise features of the drone in dynamic flight states.

## References

[1] Floreano, D., & Wood, R. J. (2015). Science, technology and the future of small autonomous drones. Nature, 521(7553), 460-466.

[2] Christian, A. W., & Cabell, R. (2017). Initial investigation into the psychoacoustic properties of small unmanned aerial system noise. AIAA Paper 2017-4051.

[3] Torija, A. J., & Clark, C. (2021). A psychoacoustic approach to building knowledge about human response to noise of unmanned aerial vehicles. International Journal of Environmental Research and Public Health, 18(2), 682.

[4] Tinney, C. E., & Sirohi, J. (2018). Multirotor drone noise at static thrust. AIAA Journal, 56(7), 2816-2826.

[5] Zawodny, N.S., Christian, A., & Cabell, R. (2018). A summary of NASA research exploring the acoustics of small unmanned aerial systems. AHS Paper 20180002208.

[6] Alexander, W. N., Whelchel, J., Intaratep, N., & Trani, A. (2019). Predicting community noise of sUAS. AIAA Paper 2017-2686.

[7] Cabell, R., Grosveld, F., & McSwain, R. (2016). Measured noise from small unmanned aerial vehicles. NOISE-CON Paper 20160010139.

[8] Heutschi, K., Ott, B., Nussbaumer, T., & Wellig, P. (2020). Synthesis of real world drone signals based on lab recordings. Acta Acustica, 4(6), 24.

[9] Zhou, T., Jiang, H., Sun, Y., Fattah, R. J., Zhang, X., Huang, B., & Cheng, L. (2019). Acoustic characteristics of a quad-copter under realistic flight conditions. AIAA Paper 2019-2587.

[10] European Commission. (2019). Commission Delegated Regulation (EU) 2019/945 of 12 March 2019 on unmanned aircraft systems and on third-country operators of unmanned aircraft systems. European Commission.

[11] Sanchez-Cuevas, P., Heredia, G., & Ollero, A. (2017). Characterization of the aerodynamic ground effect and its influence in multirotor control. International Journal of Aerospace Engineering, 2017, 1823056.

[12] Welch, P. (1967). The use of fast Fourier transform for the estimation of power spectra: a method based on time averaging over short, modified periodograms. IEEE Transactions on Audio and Electroacoustics, 15(2), 70-73.

[13] ISO. (2012). ISO 3745:2012, Acoustics — Determination of sound power levels and sound energy levels of noise sources using sound pressure — Precision methods for anechoic rooms and hemi-anechoic rooms. International Organization for Standardization.

QUIET DRONES
Second International e-Symposium
on
UAV/UAS Noise
27th to 30th June 2022

# Development of a Comprehensive UAV Noise Evaluation Platform

**Alex McGinn: almcginn@tcd.ie**
**Trinity College Dublin, the University of Dublin**
**College Green**
**D02 PN40**
**Ireland**
**John Kennedy: jkennedt@tcd.ie**

## Summary

Drones, Unmanned Aerial Vehicles (UAVs) and or Unmanned Aerial Systems (UAS) are set to become more prevalent in our skies over coming years. This project developed and applied a process and test rig for measuring drone noise under the ISO 3744:2010 standard and European Union Aviation Safety Association (EASA) legislation. In the process it also assessed the practicality of the standard and overarching regulation. The potential for environmental pollution resulting from the rapid growth and diversification in drone use has begun to attract regulatory attention. An initial review of applicable standards and regulations was carried out and used to develop a process compliant with ISO 3744:2010 for measuring noise emissions from UAVs. A compact and portable test rig was designed based on the approach of a rotating sound source within a fixed microphone configuration, surrounded by a protective cover and acoustic baffles. The rotating noise source consisted of a base plate, turntable and stepper motor and bracket to which a drone could be secured. The test procedure was executed and refined in three different rooms. As all three of these rooms have a hard reflecting plane for a floor as stipulated in ISO 3744:2010, an approach was adopted of first testing a reference sound source (RSS) and then using these results to develop correction factors for the drone measurement. The refined procedure was then applied to a commercially available drone - DJI Inspire 1 - in the most suitable of the tested rooms. Measurements were taken at 10° intervals. The results obtained showed clear directionality in the noise emitted by the drone as well as confirming that the drone's maximum sound power is above the limit set out by the EASA. Overall, the testing process and rig performed well. The ISO Standard was found to be suitable and applicable and this is discussed in more detail. Suggestions are also made for refining the EASA legislation. Further

work to refine the design of the drone restraint mechanism and containment strategy and to build a database of drone test results is planned.

# 1. Introduction

## 1.1 Drone Market and Usage

UAVs are becoming more prevalent in our skies. Statista predicts that the US drone sales market alone is projected to grow to a value of 1.4 Billion dollars by 2026 [1]. Not only are drone sales for established applications increasing, but the breadth of new applications is expanding. Companies such as Amazon are investing in the drone delivery space with Amazon's own service branded 'Prime Air'. Large scale Volocopter drones are being tested to carry passengers at the Paris Olympics in 2024 [2].Testing for this was carried out in April 2022. In the Irish context drone delivery enterprises are already present with companies such as Manna Aero operating delivery services in both Galway and Dublin and FedEX launching its own package delivery service [3] and a 'Vertiport' is planned to open this year in the Shannon area [4].

## 1.2 Environmental Effects of UAV Noise

With the increase in their use expected over the coming years, a corresponding increase in the level noise of pollution associated with UAVs is inevitable. Furthermore the noise produced by the current generation of UAVs is recognised to be more annoying than noise produced by all forms of 4 wheel transport [5]. Furthermore a study showed that fluctuations in sound level of UAVs were described as producing a more annoying affect to the listener [6]. In addition to annoyance there are clear public health effects from living in a noise polluted environment (e.g. living beside a busy road) which include increased cardiovascular disease as well as hearing loss, tinnitus and loss of cognitive function [7], [8]. WHO Europe state that a third of Europeans are already exposed to harmful traffic noise and a fifth are exposed to sound levels at night that could significantly damage their health [9]. For this reason, it is clear that if UAVs are to become a part of our everyday lives then the noise produced by them must be mitigated and regulated.

## 1.3 European Regulation

To mitigate these issues in 2019 the European Union Aviation Safety Association (EASA) introduced new regulations: the 'Easy Access Rules for Unmanned Aircraft Systems' with the aim of curbing the noise emissions produced by UAS. These regulations categorise UAS, define limits for noise emission by category, create a system of labelling for their maximum sound power and finally aim to reduce these defined limits every two years from the introduction of the regulations i.e. 2021 and 2023. The EASA also identified the ISO standard (3744:2010) to be used to measure noise emission by UAS.

## 1.4 Scope and Research Objectives

This project aimed to create a comprehensive drone testing platform that uses this standard in order to accurately measure the sound power produced by a drone or single motor with a rotor attached to it. This testing platform aims to be both portable and practical. Specifically the detailed objectives were:

1. Assessment of current legislation of the European Union and its impact on current drone design and how the industry will respond to this new impetus for quieter flight systems.
2. Design and construction of a rig to measure the sound power of a UAV or rotor in accordance with ISO 3744:2010 and the EASA regulations.
3. Conduct of a test of the noise emission of a UAV using the ISO 3744:2010 standard.
4. Assessment of the ISO 3744:2010 suitability for the measurement of noise from UAV's.

# 2. Literature Review

## 2.1 UAV Noise and Mitigation

The primary source of drone noise is the rotors, when operating under load to keep the drone airborne. There are two types of noise emitted by a drone rotor blade. The first is a tonal noise caused by a combination of loading noise from the rotor exerting lift and drag forces on the surrounding air and thickness noise originating from the air displaced by the blade[10]. Tonal or harmonic noise occurs at multiples of the Blade Pass frequency (BPF). The other main source is a broadband noise which is random and non-periodic due to turbulent air flow over the rotor blades [11]. Taking cues from research done in the fields such as helicopter, jet engine and wind turbine noise. Technologies such as biomimetics can lead to important reductions in drone noise without necessarily compromising in thrust. Leading edge serrations mimicking an owls wing were found to not only provide a significant reduction in the noise of the drones (up to 4.73 dB) but also increase the thrust performance of the UAV by 3.5% [12]. Furthermore these mimetic technologies are already being implemented in other sectors, namely in wind turbine technology where the Siemens DinoTail employs biomimetic trailing edge serrations to reduce noise [13]. Perforated extensions to the trailing edge of blades coupled with variations in the angle of attack of these blades can contribute to a reduction of up to 2dB in certain frequency bands [14].

While concepts such as contra-rotating rotors can help to increase the thrust output of a UAV, the noise produced by such designs is higher. This is due to the additional noise source created by unsteady loading on the rotor blades as a result of its proximity and interlinked effect on the flow field of the adjacent contra-rotating rotor blade [15]. Furthermore a study undertaken on confined drone flight found that there is up to a 5dBA increase in measured microphone sound pressure from a confined drone. Vortices recirculating were shown to be directly responsible for this increase in sound pressure level through the generation of unsteady loading as well as higher BPF harmonic tonal values [16]. Commercially available systems to reduce drone noise are available such as the Delson Aeronautics motor and blades system where the comparative sound pressure vs thrust is an average of 10dB lower than other models [17]. Other complete UAV systems are also on the market with the AC1 Atlas-T specifically designed for low noise applications. However, due to its cost at a minimum of 16,000$ this technology is prohibited from widespread use in the current market.

## 2.2 ISO 3744:2010

The ISO standard which the EASA has selected for UAVs is ISO 3744:2010 (ISO 3744:2010, 2022). This standard was conceived for measuring the sound power of a wide variety of sound sources on a reflecting plane, not specifically for UAVs. There are a number of configurations for microphone positions and corresponding sound source geometries supplied by the standard. As EASA regulations stipulate a hemispherical measurement surface part 13, Figure *1* displays the chosen strategy of a sound source with a hemispherical measurement surface and microphones rotating around the sound source. The decision was taken by this project to change the rotating component, with the sound-source itself being rotated while the microphone array remains stationary.

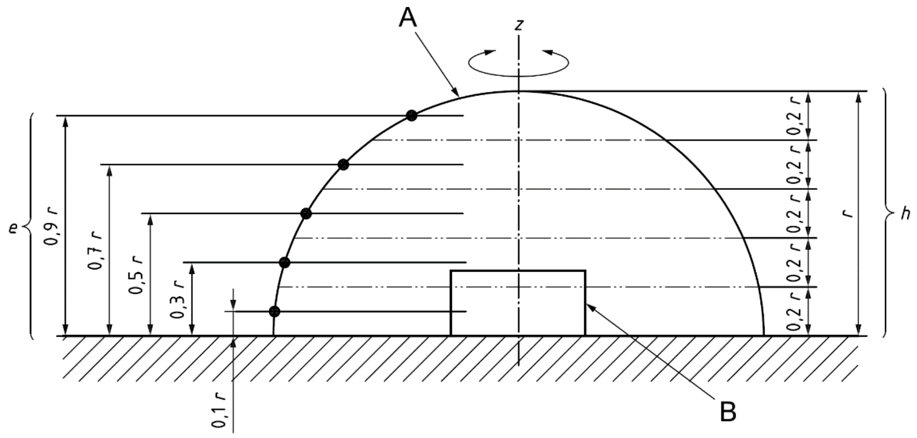


Figure 1 sound source with a hemispherical measurement (ISO 3744:2010)

# 3. Design and Instrumentation

## 3.1 Microphone Stand

An array of microphones at specific positions was required to carry out a sound pressure measurement using the method described in Annex B:5 of the standard. To hold these, a microphone stand and boom were chosen with extenders used to project the microphones to the selected radius. As seen in Figure *2* this setup was achieved and provided for a variety of measurement radii to be used throughout the testing phase of this project. In addition, this setup facilitated quick assembly of the testing space in the room removing the need for a permanent fixture.

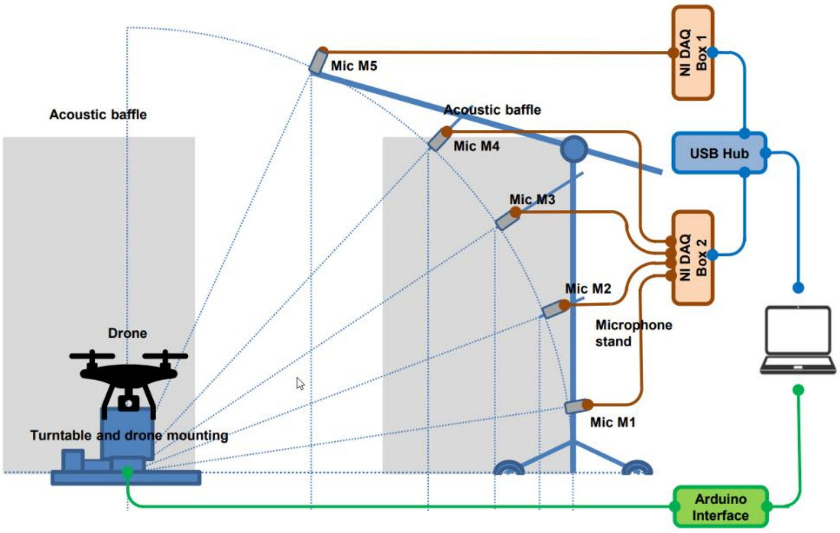


Figure 2 Measurement setup

The microphones were secured to the stand and orientated towards the sound source at the correct radius using an assembly of 3D printed parts. The body into which the microphone or extender is inserted was printed in Flex compared to PLA for the other components. The microphone model used throughout the course of the testing was the GRAS 40PL. The microphones have a frequency response of ±1 dB within 50 - 5,000 Hz, ±2 dB within 5 - 20 kHz and upper limit of the dynamic range of 150dB [19].

## 3.2 Turntable

The turntable incorporated a stepper motor used in conjunction with an Adafruit MotorShield and Arduino Uno. In order to secure the drone to the turntable, a bracket was made that bolted onto the turntable and allowed a drone to be placed on top and strapped to it. To stop a UAV from moving the turntable an approximately 40x40 cm plate of steel 1cm thick with countersunk holes on the underside was bolted to the turntable. A steel plate was chosen as it has similar acoustic characteristics to the reflecting plane of the test space (concrete floor) and provides a low profile so that the noise produced by the UAV is not affected by a complex geometry or any significant difference in surface material close to it.

# 4. Testing of a DJI – Inspire 1

## 4.1 Test Procedure

The base plate was placed on the floor at the centre of the measurement radius of 1.5m. Measurements of 20 seconds were taken with the 5 microphones simultaneously with the DJI motors on and providing thrust. The drone was rotated in 10° intervals for a total of 36 measurement angles. The mean value in each 1/3 octave band at each rotation was obtained and the correction factors $K_1$ and $K_2$ for background noise and room reverberation were calculated for the respective 1/3 octave bands, and deducted from the measured values to obtain the sound power as specified in the standard. $K_1$ cannot be below 6dB(A) and preferably above 15dB(A) and $K_2$ cannot go above 4dB(A) in a specific octave band, otherwise the test space is deemed unsuitable for testing in octave bands below or above the range that falls inside these values. This was best achieved in a large (approx.10mx9.5mx6m), empty room with minimal furnishings and a hard smooth concrete floor. This procedure allowed the directivity of the drone noise emission to be assessed. To mitigate the influence of battery charge on the power output of the motors the battery in the drone was swapped out once it had discharged by half.

## 4.2 Total Sound Power

The total A-weighted sound power averaged across all rotation angles $\mathrm{LW}_{\mathrm{Total\ A}}$ was calculated to be 105dBA. In this case the drones falls into the C2 class of UAVs with a MTOM of 3060g [20]. However, the 0-year limit of the UAV based on this MTOM is 94.8 and decreases to 92.8 and 90.8 for the 2-year and 4-year limits respectively. This shows that using this method of measurement the guaranteed maximum sound power of the DJI Inspire 1 is far above the limit as set out in the EASA legislation - not only for the current time frame, but since the original limit in the legislation was introduced.

## 4.3 Polar Plotting of Directivity

The polar plots below show the directivity of the DJI Inspire 1 at 4 frequency bands as well as an overall directivity for the drone. Table *1* shows that up to 100Hz the microphone stand is less than one wavelength from the emitting sound source, this may explain the variation in directivity seen in Figure *3*. Moving to distances of 1 to 3 wavelengths from the sound source at higher frequencies, the variation in directivity decreases, potentially denoting a move away from nearfield effects. A smoother polar plot is seen in the 500 Hz band. Finally, when the number of wavelengths increases beyond 3, the resultant range of recorded sound power values decreases and stabilises at around 2.2 - 3dB for all subsequent octave bands and can be considered in the far-field. This is reflected in the polar plots for 1000Hz and 2000Hz as well as in the overall polar plot, in which the average sound power at each rotation was obtained.

| 1/3 Octave Bands (HZ) | Range (dB) | Number of λ |
|---|---|---|
| 100 | 14.35951 | 0.437318 |
| 500 | 5.888662 | 2.186589 |
| 1000 | 2.74448 | 4.373178 |
| 2000 | 2.210582 | 8.746356 |

Table 1 Measurement distance expressed in terms of wavelength for a range of frequencies

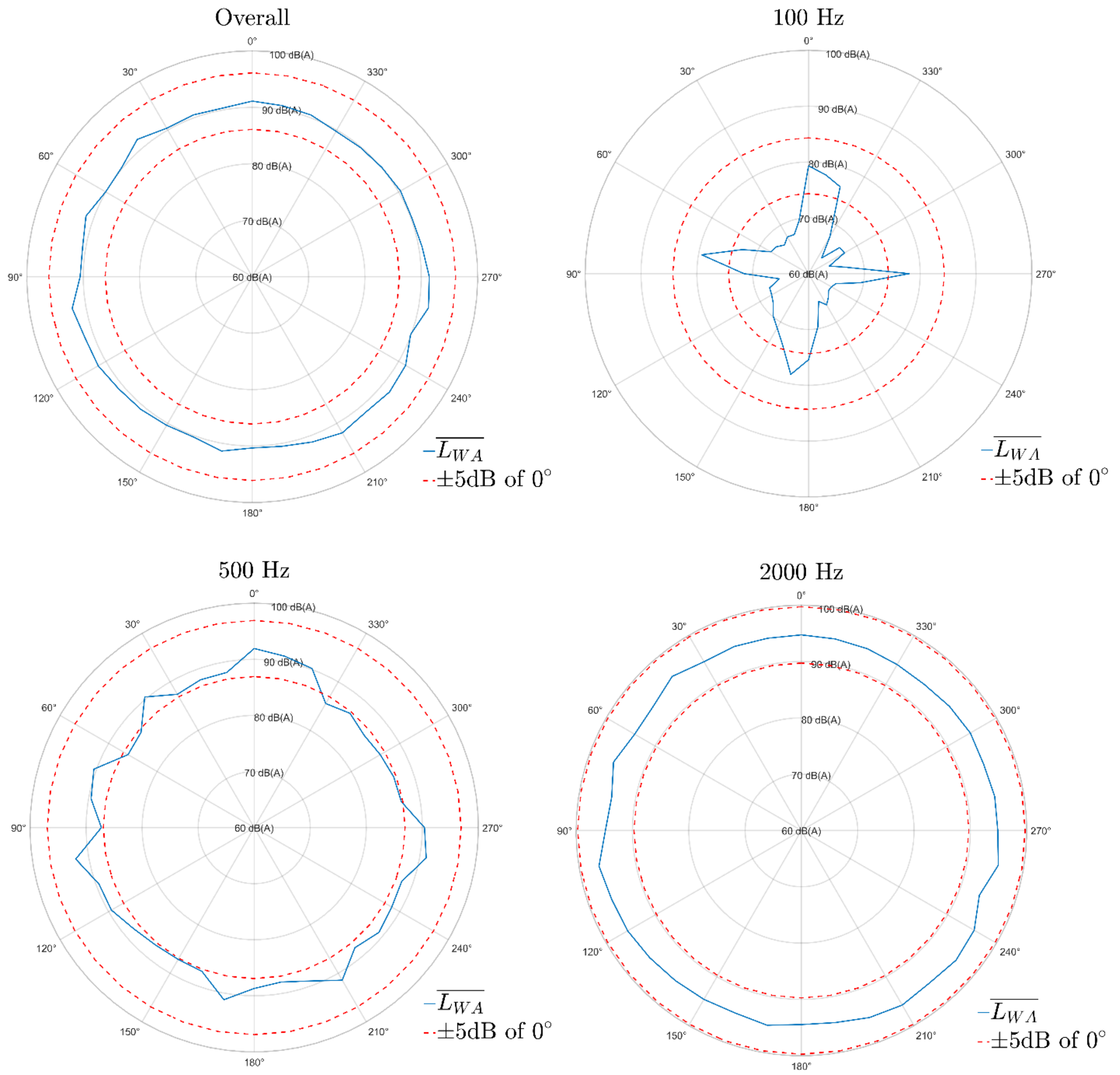


Figure 3 Directivity of UAV noise emission as a function of frequency

### 4.4 Numerical Modelling with iNoise

The data collected through testing was input into the commercial environmental noise modelling software iNoise. The DJI Inspire 1 was simulated as a point source hovering at a height of 30m above a flat surface of 500mx500m. Figure *4* (a) presents the noise maps of average sound power $\overline{\mathrm{L_{W\,A}}}$ of the DJI with no directivity data. Directivity $D^*_{Ii}$ for each rotation was calculated. As iNoise assumes symmetry, an amalgamation of two noise plots is presented for each scenario, with the left hand side being $D^*_{I0-180}$ and the right hand side being $D^*_{I180-360}$. The overall directivity or $\overline{D^*_I}$ averaged across all frequency bands for each microphone position is shown in Figure *4* (b). Furthermore, the directivity from near field of 100Hz, transitional at 500Hz and far field at 2000Hz is shown in Figure *4* (c) to (e). There is a strong directivity in the drone noise. This is true across all the frequency bands assessed with higher frequencies becoming more omnidirectional.

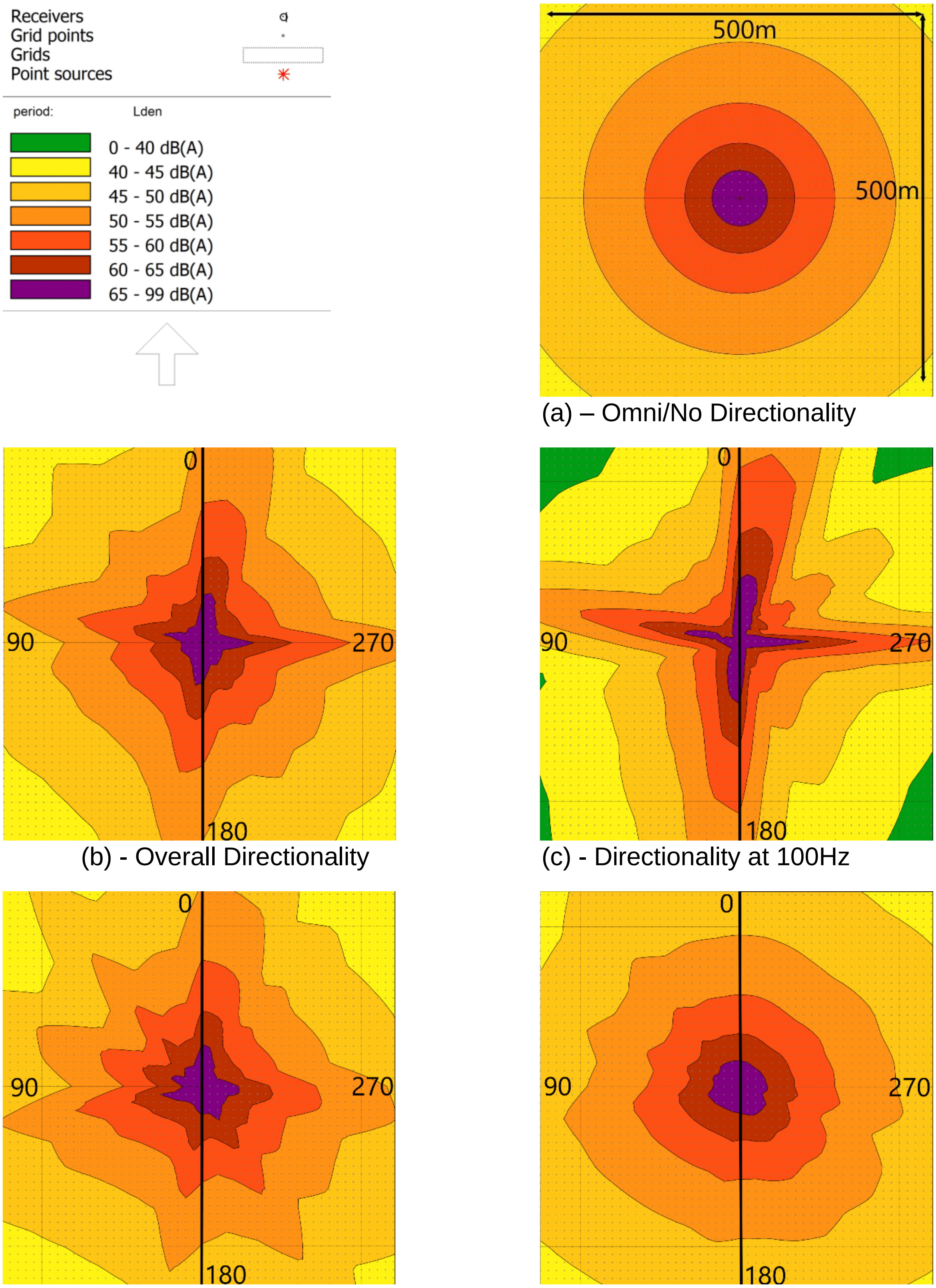


(a) – Omni/No Directionality

(b) - Overall Directionality

(c) - Directionality at 100Hz

(d) - Directionality at 500Hz

(e) – Directionality at 2000Hz

Figure 4 UAV noise emission on the ground for an altitude of 30m and as a function of frequency

# 5. Discussion of Overall Results

## 5.1 Practicality of the Drone Noise Measurement Approach and Equipment Design

The results of this study show that it is practical and effective to measure UAV noise emissions with a compact and portable setup in a variety of test spaces. Therefore, this allows for local or onsite testing of a UAV and does not necessarily require a large permanent installation for measurement. Furthermore, the results show that the measurement radius can be adjusted to suit a range of UAV characteristic dimensions depending on the class of UAV. It can also be adjusted to suit the test space in which the measurements are being taken in order to ensure the minimisation of reverberant noise captured by the microphones and so be located inside the critical distance. If the testing is to be carried out in a room with immovable features (e.g. structural elements or large equipment), such that acoustic baffles are needed to mitigate their sound reflecting effects, then asymmetry in the baffle positioning and distance from the sound source is important.

The nature of the drone restraint (strap) means that the noise measured will always be higher than under likely operating conditions (since the UAV will fight harder to leave the ground as it cannot get airborne). Therefore any labelling resulting from the test is likely to be more accurate as the upper limit of the noise generated by the UAV. However, labelled value will be unnaturally high and so more UAVs tested will fall outside of the desired limit set by EASA. A further "confinement factor" $K$ could be taken into account similar to the flow confinement effects [16] that would account for this higher total sound power. However, even if the maximum of 5dB as found in [16],was deducted from the total sound power measured this value would still fall outside of the least restrictive 0-year calculated limit for the DJI Inspire 1.

It should be noted that drones cannot be reliably flown in a GPS mode indoors, as they can struggle to get a satellite signal. Hence indoors they must be flown without GPS (in an *ATTI* mode in the case of DJI or equivalent). If a UAV only has a GPS mode and the test space does not have the requisite signal or enough satellites cannot be connected then the test space can be deemed unsuitable. This is a difficult balance that will have to be struck as the space must have a low background noise level but by insulating the space this will make it more difficult for satellite signals to penetrate the building. However, it is necessary to carry these acoustic tests out in a controlled environment to gain as accurate a picture of a UAV's noise emission as possible.

## 5.2 Evaluation of the Suitability of ISO 3744:2010 to UAV Noise Measurement

The flexibility of the layout configurations permitted by the standard is its greatest strength as a procedure to be followed. It not only accommodates a variety of set-ups with regards to the floor space (e.g. a flat open space, next to a wall or in a corner), but also provides for a wide variety of source geometries to be tested. Therefore it was sensible for the EASA to choose this standard for the testing of drones, as the standard can accommodate the variety in scale from class C1 to C4 to be tested under the same conditions as well as allow for an easier setup for commercial testing with the geometry and test space in which it can be carried out.

The atypicality of the drone operation during the test is the greatest weakness of the standard. The standard was conceived with ground based sources in mind - i.e. devices being tested under normal operating conditions remain stationary on the floor and assumes that the reference box which encapsulates the source is always on the ground and does not change shape. By its nature a drone being tested at operational rotor RPM would not be on the ground - it would be hovering. Therefore a restraint of some sort is then required to keep it on the ground. The reflective plane integral to the ISO will reflect noise towards the microphones that would normally be emitted in different directions, the drone being airborne. The measurements here demonstrate the high directionality of the drone noise emission, which may not be representative of the in-flight directionality. It is an omission in the standard that nothing makes provision for the use of safety cages or other devices which might be used to stop a drone or UAV from colliding or any debris from a UAV being thrown outwards. As such it is left up to the researcher to implement such a precaution and verify that it does not interfere with the noise measured by microphones.

### 5.3 Effectiveness and Practicality of the EASA Regulations

Given that the standard requires the UAV to be ground based during measurement the EASA legislation which cites the standard makes no specific provision for how to restrain the drone or operate safety during the test and this should be addressed. The legislation does not reflect the flexibility built into the standard and this is a drawback. Specifically, Part 13 of the legislation stipulates a hemispherical measurement surface [21]. Therefore the legislation should be amended to permit the appropriate use of whatever measurement surface is practical under the standard for the UAV geometry.

## 6. Further Work

### 6.1 Changing the approach to securing the drone

It is recommended that the use of a tether is investigated in preference to using a strap to secure the drone. As discussed the use of a strap leads to artificially high noise emissions. Furthermore, UAV's such as the DJI Inspire 1 have different geometries for take-off and flight, this is difficult to test using a strap because once the drone geometry changes the strap loses tension and cannot be readjusted manually since the rotors must be engaged to be in flight mode. In contrast, use of a short tether would allow for this change in geometry to take place and then might possibly have its length adjustable to accommodate the new rotor height and to maintain the same reference box for the testing. Powered tethers can also be used with certain UAVs. These third-party technologies are compatible with a wide array of UAVs and would eliminate the potential for a change in power supply to the motors as the battery discharges. Moreover, it would allow for continuous testing and so accommodate finer resolutions of rotation angle being chosen as the drone can simply be rotated in the air under its own motor power. However, such products could significantly alter the noise measured by the microphones since placing it underneath the UAV would interfere with the reflecting plane as described in ISO 3744:2010. Placing it in a cavity in the floor or under a flat platform could facilitate its use in a more permanent testing facility. Overall, a simple base plate and swivelling cable tether would complement the test rig described in this work. Provided that the tether is short the measurement surface might be considered to remain hemispherical without any required changes. Alternatively, in section 7.2.6 the standard makes provision for measurement surfaces to be combined [18] and so a cylindrical measurement surface could be combined with a hemispherical surface on top to comply with part 13 of the EASA regulations.

### 6.2 Near and Far-field Measurement Radius

In order to more accurately understand the directivity of UAV noise emission at low frequencies the measurement radius should be increased so that the radius as a function of λ is greater than 3 wavelengths. This data would allow for a more accurate description of UAV noise in modelling software such as iNoise. However, this should be balanced against the effects on the environmental correction factor $K_2$ and absorption $A$ of the test space which may be adversely affected by an increase in measurement radius.

### 6.3 Using Either the Current or Further Amended Approach and Equipment to Test a Wide Variety of UAVs

Further research should be undertaken to investigate more UAS. Building a database of noise emission data from a variety of UAS across the industry from hobby flying to commercial delivery to larger scale agricultural and transport drones would allow for a more realistic simulation and prediction of the impact of these UAS in our cities over the coming years. A more comprehensive database would facilitate processes such as planning permission for drone related developments including vertiports. As the Irish government plan to introduce such developments in Ireland and EASA have released new details on the design of landing pads [22].Using this database in iNoise to simulate the effects these developments would have on their surroundings as a function of the number of flights. Furthermore using an indoor test space allows for the controlling of environmental factors. Further investigation into the effects of environmental factors such as constant wind speed, gusting and temperature variability on noise emission should be undertaken. As this data can be input in software it would allow for a more complete description of the effects of possible drone routing in our skies.

### 6.4 Provision for 'Aftermarket' Reconfiguration of a UAV

It is clear that the noise generated by a UAV can potentially be significantly affected by changing certain components from those originally supplied. For example, the largest noise source are the rotors and these are replaceable aftermarket with potentially significant effects on the noise levels. Such aftermarket modifications could provide a means for maintaining older drones within the noise limits defined by the legislation. However, the legislation does not make any provision or give any guidance on such matters. For example, the UAV tested in this study the DJI Inspire 1 is outside of the limit for its total power produced across the range of 1/3 octave bands. However, the possibility exists of retrofitting it with new blades from DJI or a third-party which might resolve this problem. Currently there is no specification under the EASA legislation on whether this model of UAV would then fall under the noise limit. As the limits become more restrictive more drones will fall outside the limit. Some of the questions that such amendments to the legislation would need to consider:

1. If a drone that is above the noise limit is retrofitted with a system such as the Delson motor-blade system, does this satisfy the legislation?

2. Does a drone that is retrofitted with new blades need a new noise emission label?

3. In such a retrofitting scenario could a noise rating be applied to the blades as well as or instead of the drones?

4. As the blades are the primary source of the noise created how much does the geometry of different UAVs affect the noise emitted by the same blades? Further investigation is required into how UAV geometry both in terms of its body design and its spacing of blades affect the noise produced.

5. In the future should manufactures decouple the blades from the UAVs (analogous to the way in which cars can be purchased with different engines in them to produce different levels of performance)? Something similar could be done with UAVs with regards to both thrust and noise emission depending on the intended use of the drone both in terms of its function and environment it will be functioning in.

6. Since noise is viewed as a pollutant and these UAVs are polluting the environment could a similar perspective be taken by legislators as with exhaust pollutants and engine efficiency in cars?

### References

[1] Statista Market Forecast, “Drones - United States | Statista Market Forecast,” *Statista*. https://www.statista.com/outlook/cmo/consumer-electronics/drones/united-states (accessed Apr. 21, 2022).

[2] A. Scerri, “Volocopter participates in acoustic testing at Pontoise Airport,” *evtol.com*. https://evtol.com/opinions/volocopter-participates-uam-acoustic-testing-pontoise-cormeilles-airport/ (accessed Apr. 12, 2022).
[3] Irish Tech News, “Drone Deliveries Take Flight in First-of-its-Kind Trial in Ireland,” Oct. 04, 2021. https://irishtechnews.ie/drone-deliveries-trial-in-ireland/ (accessed Apr. 12, 2022).
[4] W. de Jager, “Ireland to open first first passenger and cargo vertiport in 2022,” *Dronewatch Europe*, May 27, 2021. https://www.dronewatch.eu/ireland-to-open-first-first-passenger-and-cargo-vertiport-in-2022/ (accessed Apr. 12, 2022).
[5] A. W. Christian and R. Cabell, “Initial Investigation into the Psychoacoustic Properties of Small Unmanned Aerial System Noise,” presented at the 23rd AIAA/CEAS Aeroacoustics Conference, Denver, Colorado, Jun. 2017. doi: 10.2514/6.2017-4051.
[6] D. Y. Gwak, D. Han, and S. Lee, “Sound quality factors influencing annoyance from hovering UAV,” *J. Sound Vib.*, vol. 489, p. 115651, Dec. 2020, doi: 10.1016/j.jsv.2020.115651.
[7] M. Basner *et al.*, “Auditory and non-auditory effects of noise on health,” *The Lancet*, vol. 383, no. 9925, pp. 1325–1332, Apr. 2014, doi: 10.1016/S0140-6736(13)61613-X.
[8] WHO Europe, *Environmental noise guidelines for the European Region*. 2018. Accessed: Apr. 20, 2022. [Online]. Available: http://www.euro.who.int/en/publications/abstracts/environmental-noise-guidelines-for-the-european-region-2018
[9] WHO Europe, “Noise Health Effects.” https://www.euro.who.int/en/health-topics/environment-and-health/noise/noise (accessed Apr. 20, 2022).
[10] N. S. Zawodny, D. D. Boyd Jr, and C. L. Burley, “Acoustic characterization and prediction of representative, small-scale rotary-wing unmanned aircraft system components,” in *American Helicopter Society (AHS) Annual Forum*, 2016, no. NF1676L-22587.
[11] S. A. L. Glegg and W. Devenport, *Aeroacoustics of low Mach number flows: fundamentals, analysis, and measurement*. London: Academic Press, 2017.
[12] Y. Wei, F. Xu, S. Bian, and D. Kong, “Noise Reduction of UAV Using Biomimetic Propellers with Varied Morphologies Leading-edge Serration,” *J. Bionic Eng.*, vol. 17, no. 4, pp. 767–779, Jul. 2020, doi: 10.1007/s42235-020-0054-z.
[13] R. Kuilboer, “Low-noise wind turbine design using DinoTails® Next Generation,” p. 10.
[14] C. Sumesh and T. Jothi, “Aerodynamic noise from an asymmetric airfoil with perforated extension plates at the trailing edge,” *Int. J. Aeroacoustics*, vol. 20, no. 1–2, pp. 88–108, Mar. 2021, doi: 10.1177/1475472X20978388.
[15] R. S. McKay, M. J. Kingan, S. T. Go, and R. Jung, “Experimental and analytical investigation of contra-rotating multi-rotor UAV propeller noise,” *Appl. Acoust.*, vol. 177, p. 107850, Jun. 2021, doi: 10.1016/j.apacoust.2020.107850.
[16] C. Nardari, D. Casalino, F. Polidoro, V. Coralic, P.-T. Lew, and J. Brodie, “Numerical and Experimental Investigation of Flow Confinement Effects on UAV Rotor Noise,” in *25th AIAA/CEAS Aeroacoustics Conference*, American Institute of Aeronautics and Astronautics, 2019. doi: 10.2514/6.2019-2497.
[17] Delson Aero, “UAV Blades,” *Delson Aeronautics Ltd.* https://delsonaero.com/uav-blades (accessed Apr. 19, 2022).
[18] “ISO 3744:2010 - Acoustics Determination of sound power levels and sound energy levels of noise sources using sound pressure Engineering methods for an essentially free field over a reflecting plane.” ISO - INTERNATIONAL ORG. FOR STANDARDIZATION, Mar. 10, 2022. [Online]. Available: https://eu-i2-saiglobal-com.elib.tcd.ie/management/display/anchorViaIP/229014
[19] GRAS, “40PL CCP Free-field Array Microphone, High Pressure.” [Online]. Available: https://www.grasacoustics.com/products/special-microphone/array-microphones/product/ss_export/pdf2?product_id=177
[20] DJI, “User Manual DJI I1 V2.0 EN.” [Online]. Available: https://dl.djicdn.com/downloads/INSPIRE+1+series/20171221/INSPIRE_1_V2.0_User_Manual_EN.pdf
[21] EASA, “Easy Access Rules for Unmanned Aircraft Systems (Regulation (EU) 2019/947 and Regulation (EU) 2019/945),” *EASA*. https://www.easa.europa.eu/document-library/easy-access-rules/easy-access-rules-unmanned-aircraft-systems-regulation-eu (accessed Apr. 11, 2022).
[22] EASA, “Prototype Technical Design Specifications for Vertiports,” *EASA*, Mar. 24, 2022. https://www.easa.europa.eu/document-library/general-publications/prototype-technical-design-specifications-vertiports (accessed Apr. 21, 2022).

# QUIET DRONES
# Second International e-Symposium
# on
# UAV/UAS Noise
# 27th to 30th June 2022

## Multirotor UAV turbulence ingestion noise

**Ryan S. McKay, Dotterel Technologies: ryan.mckay@dotterel.com**

**Michael J. Kingan, University of Auckland: m.kingan@auckland.ac.nz**

**Sung Tyaek Go, University of Auckland: sgo587@aucklanduni.ac.nz**

**Summary**

Turbulence ingestion noise (TIN) is an important noise source for multirotor unmanned aerial vehicles (UAVs). TIN is caused by streamwise elongation of ingested turbulent eddies interacting with a propeller and is particularly problematic for hovering UAVs when the propeller interacts with an elongated eddy over multiple blade passages. This generates quasi-tonal noise centred around a multitude of harmonics of the blade passing frequency (BPF). This paper presents predictions using a model previously presented by the authors of a propeller in an anechoic chamber and of a hovering DJI Mavic UAV. These predictions are compared with experimental measurements. A simplified form of the TIN model which has significantly reduced computational costs is also presented. Predictions from this simplified model are compared to the experimental measurements which show slightly worse agreement than the forementioned model.

## 1. Introduction

Turbulence ingestion noise is an important source of multirotor unmanned aerial vehicle (UAV) noise which has not received much attention in the literature. Various authors have investigated steady loading and thickness noise from UAVs (e.g. [1,2]), broadband noise sources (e.g. [1,3–6]), motor noise (e.g. [7–9]) and other minor sources (e.g. [10–12]); however, the cause of the multitude of tones at harmonics of the blade passing frequency (BPF) seen in outdoor experimental measurements (e.g. [13–15]) is rarely discussed. The multitude of tones has however been discussed by several studies investigating the effect of recirculation in anechoic chambers on UAV propellers. Multiple authors [1,16–18] have shown that tones at harmonics of the blade passing frequency (BPF) become apparent in the acoustic spectra several seconds after a propeller starts rotating in an enclosed quiescent space. It is important to note that these tones are seen in outdoor experimental measurements of hovering UAV [13–15] and static propellers [19].

Nardari et al. [20] used a Lattice-Boltzman method CFD code to simulate the noise from a propeller in free-space and compared this to a simulation of the same propeller in an enclosed space. Their results showed an increase in the amplitude of the higher-frequency BPF harmonics which they attributed to the interaction of the propeller blades with the vortical structures convected by the recirculating flow. They also showed elongated turbulence structures present in the inflow of the enclosed propeller.

Hanson [21] investigated the quasi-tonal noise produced by turbulent inflow into a ducted fan (although he noted that his work was also applicable to propellers). He demonstrated that isotropic turbulence can be stretched by a fan/propeller such that it becomes highly anisotropic at the propeller plane. In a flow with relatively low axial velocity, these stretched turbulent structures can be chopped by multiple propeller blade passages which causes partially coherent blade loading. This generates narrow-band random noise at harmonics of the BPF. Figure 1 illustrates this process with a schematic of the streamlines from a propeller with turbulence being distorted.

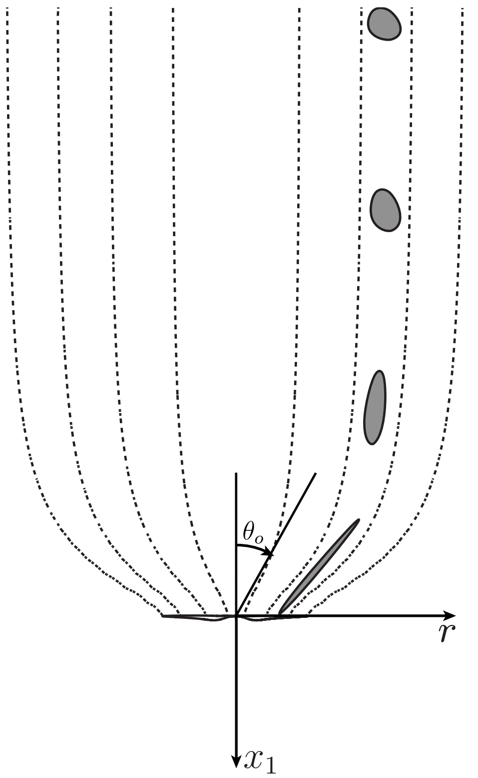


*Figure 1. Illustration of the streamlines of a propeller in a freestream with low velocity. The turbulence is distorted by the mean flow which results in long narrow eddies which can interact with a propeller over multiple revolutions.*

An early method for predicting TIN which incorporates a model for calculating the turbulence distortion caused by a propeller's stream tube contraction was presented by Amiet et al. [22]. Their method incorporates a turbulence distortion model developed by Simonich et al. [23] in which the upstream turbulence was modelled as being isotropic. This noise prediction method uses the following calculation process:

1. Model the atmospheric turbulence (spectrum, integral length scale, mean velocity profile & intensity)
2. Predict the mean flow contraction
3. Predict the turbulence contraction using rapid distortion theory
4. Predict the aerofoil response to the unsteady inflow
5. Perform an acoustic prediction due to the unsteady loading

Majumdar and Peake [24] developed a prediction method for the TIN produced by open rotors which used a similar procedure. Their method assumed that the turbulence upstream was isotropic and well modelled by the von Kármán spectrum. The mean flow through the propeller was predicted using an actuator disk model and rapid distortion theory was used to calculate how the mean flow distorted the upstream turbulence. This work was extended by Robison [25] and Robison and Peake [26] to include asymmetric inflows and a minor correction. Majumdar and Peake, Robison, and Robison and Peake used the LINSUB code [25,26] to predict the blade loading. The LINSUB code predicts the response of a rectilinear cascade of flat plate blades subject to an incident convected harmonic velocity perturbation, which is not suitable for small UAV propellers. They use the blade loading from the LINSUB code to predict the far-field acoustic spectrum using [24, eq. 2.46] which was corrected by Robison to [25, eq. 2.133].

This paper will focus on the noise generated by a static propeller with a turbulent inflow, which is representative of a hovering UAV. The paper will summarise a model developed by the authors which is an extension of the work by Robinson and Peake and is suitable for predicting TIN from a UAV propeller. Predictions from this model are compared to experimental data from anechoic chamber measurements and outdoor measurements. These results are then discussed.

## 2. Model

The model used in this paper is an extension of Robison [25] and Robison and Peake [26]. Unlike those models we have made a compact chord assumption and used isolated blade response functions. Our model is also only valid for axisymmetric mean-flows (unlike Robison and Robison & Peake who considered flows which may be non-axisymmetric). These approximations are generally valid for the small propellers used on small UAVs and result in significant reductions in computational cost. In this section we only present the final set of equations required for implementing the model. The complete model and derivation can be found in [19] and a further extension which includes TIN from ducted propellers can be found in [27].

For an observer located at $\mathbf{x}$ and at frequency, $\omega$, the radiated spectral density is given by

$$\bar{S}_{pp}(\mathbf{x},\omega) = \frac{B^2}{(4\pi R_o)^2 U_\infty} \sum_{n=-\infty}^{\infty} \sum_{m=-\infty}^{\infty} \int_0^{\infty} \int_0^{2\pi} \Phi_{ij}^{\infty}(\mathbf{k}) X_i^{(n,s)} X_j^{(n,s)*} \, k_r \mathrm{d}k_\phi \mathrm{d}k_r \,, \tag{1}$$

where $s = mB - n$, $k_1 = [mB\Omega - \omega]/U_\infty$,

$$X_i^{(n,s)} = \pi\rho_0 \int_{r_h}^{r_t} B^{(n)}(r) U_r(r) c(r) G(\omega - n\Omega, r) Z_i^{(s)}(r, \mathbf{k}) \exp\{-\mathrm{i}k_1 X_1\} \,\mathrm{d}r\,, \tag{2}$$

and

$$Z_i^{(s)}(r, \mathbf{k}) = \frac{1}{2\pi} \sum_{q=-\infty}^{\infty} J_q(k_r R) \exp\left\{\mathrm{i}q\left(k_\phi - \frac{\pi}{2}\right)\right\} \int_0^{2\pi} n_j^{(b)}(r) A_{ji}(\mathbf{x}, \mathbf{k}) \exp\{\mathrm{i}(s-q)\phi_b\} \,\mathrm{d}\phi_b\,. \tag{3}$$

The symbols used in eqs. (1-3) are defined below:

$B$ is the number of blades on the propeller

$R_o$ is the observer distance from the propeller centre

$U_\infty$ is the freestream velocity

$\Phi_{ij}^{\infty}(\mathbf{k})$ is the turbulence spectra which is dependent on wavevector $\mathbf{k}$

$k_r$ is the wavenumber in the radial direction

$k_\phi$ is the wavenumber in the azimuthal direction

$\rho_0$ is the density of the fluid

$r$ is the radial coordinate of the propeller

$U_r = \sqrt{U_1^2 + (\Omega r)^2}$

$c(r)$ is the chord length at radius $r$

$G$ is the blade response function. See Appendix 1 for details

$\Omega$ is the rotational speed of the propeller

$k_1 = \frac{mB\Omega - \omega}{U_\infty}$

$X_1 = U_\infty \Delta$ where $\Delta$ is Lighthill's drift function [28]

$J_q$ is a Bessel function of the first kind of order $q$

$R = \sqrt{2\psi/U_\infty}$ where $\psi$ is the streamfunction. i.e. constant $R$ defines a streamline

$n_j^{(b)}(r)$ is the unit vector aligned with the local lift force

$A_{ji}(\mathbf{x}, \mathbf{k})$ is the distortion amplitude tensor. See [19] or [25] for details

This model typically takes around two hours to run per frequency per core on a workstation which makes it infeasible to use for many design tasks. However, if we assume that the turbulence is not distorted, but instead that the propeller is immersed in anisotropic homogeneous turbulence, the model greatly simplifies and can be run for all audible frequencies within a minute. This can be even further simplified by assuming that the propeller blades are untwisted (i.e. the blades are flat) and that the observer is on the propeller's rotational axis. This allows for predictions to be made within a couple of seconds. The radiated spectral density for this simple case is given by

$$\bar{S}_{pp}(\mathbf{x},\omega) = \frac{l_a l_t^4 \overline{u^2} B^2 \rho_0^2 k_a^2}{4\pi R_O^2 U_\infty} \int_0^\infty \left| \int_{r_h}^{r_t} U_r(r) c(r) G(\omega, r) \sum_{m=-\infty}^{\infty} \frac{J_{mB}(k_r r)}{(1 + l_a^2 k_1^2 + l_t^2 k_r^2)^{3/2}} \mathrm{d}r \right|^2 k_r^3 \mathrm{d}k_r \,, \tag{4}$$

where $l_a$ is the axial turbulence integral length scale, $l_t$ is the transverse turbulence integral length scale, $\overline{u^2}$ is the mean-square fluctuating velocity, $k_a = \omega/c_0$, $c_0$ is the speed of sound, $R_o$ is the observer distance from the propeller centre and $k_1 = (mB\Omega - \omega)/U_\infty$.

### 2.1 Atmospheric turbulence model

In the full model (defined by eqs. 1-3), we use the well-known isotropic von-Karman spectrum which is defined as

$$\Phi_{ij}^{\infty}(\mathbf{k}) = \frac{55 g_1 \overline{u_{1,\infty}^2} l_{1,\infty}^5}{36\pi\left(g_2 + k^2 l_{1,\infty}^2\right)^{\frac{17}{6}}} \left(k^2 \delta_{ij} - k_i k_j\right), \tag{5}$$

where $\overline{u_{1,\infty}^2}$ is the mean-square fluctuating velocity in the axial direction, $l_{1,\infty}$ is the integral length scale in the axial direction far away from the propeller, $k = \|\mathbf{k}\|$, $g_1 \approx 0.1955$ and $g_2 \approx 0.558$.

Note that the simple model (eq. 4) utilises the Gliebe-Kerschen turbulence spectrum [29,30].

## 3. Results

This section compares experimental measurements of a single static propeller tested in an anechoic chamber and of a DJI Mavic in hover to predictions of the TIN noise using the models presented in this paper. Other noise sources, such as steady loading, thickness and trailing edge noise are not included.

TIN appears in experimental spectra as tone-like haystacks at harmonics of the BPF and the width of the haystack increases with increasing frequency. The TIN models also predict narrow 'haystacks' at harmonics of the BPF, as shown in Figure 2. In order to quantify the noise level of each haystack, the power spectral density should be integrated across the width of the haystack and the resulting mean-square pressure converted to a sound pressure level. An example of such a calculation is shown in Figure 2 where the narrow band SPL (1 Hz bandwidth) is compared to the integrated level which is shown by the orange circle centred on the BPF (which corresponds to the peak of the haystack). In the following, some predictions use an × to denote the peak value of the predicted narrow band (1 Hz bandwidth) SPL instead of integrating the haystack due to computational limitations. Further computations will be carried out to predict the integrated sound pressure level of these cases and presented in future work.

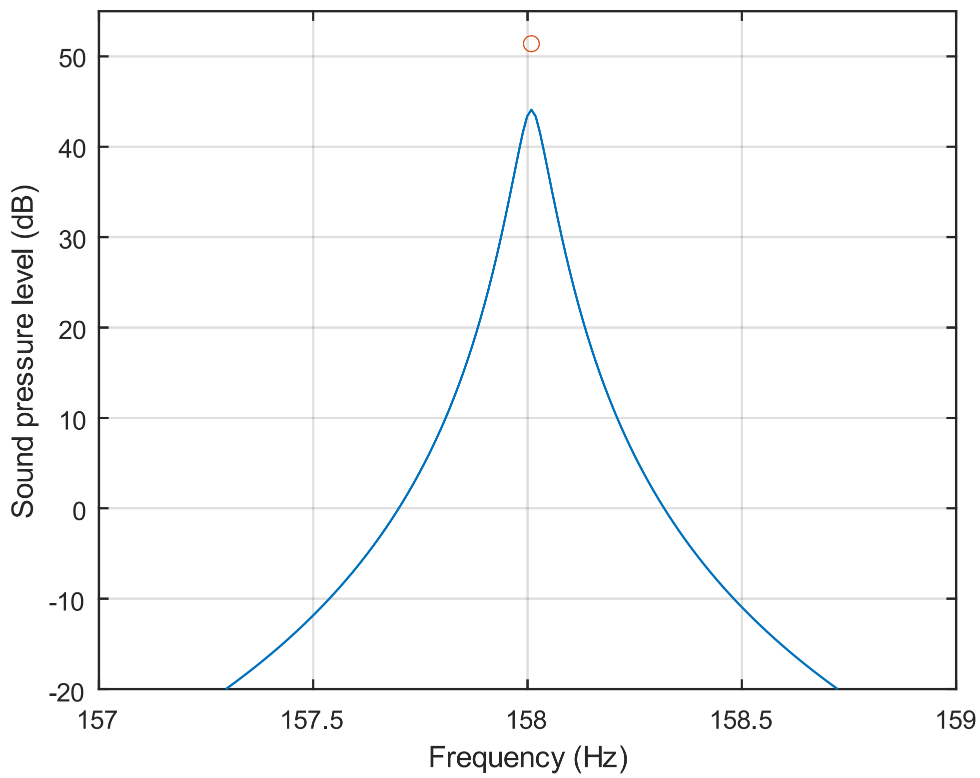


*Figure 2. A prediction of TIN produced by a static propeller showing a single haystack. The integrated sound pressure level is shown by the ○ orange circle.*

### 3.1 Anechoic chamber

The noise from a 15” T-Motor propeller was measured in the University of Auckland anechoic chamber. The propeller was rotating at 4800 rpm. See [19] for further details of these experimental measurements.

Figure 3 shows the acoustic spectra at observer positions of $\theta_o = 0°$ (directly above the propeller), 45° and 85° (slightly above the plane the propeller rotates in). Predictions using the ‘full distorted’ TIN model which includes the effect of the distortion of the inflow turbulence are shown overlaid against the experimental results which show moderately good agreement with the experimental data. Due to the confinement, the flow within the chamber is different from the modelled flow e.g. there is recirculation rather than the inflow being perpendicular to the propeller far upstream. However, the inflow turbulence has been matched to the inflow conditions as well as possible. This result suggests that the multitude of haystacks at harmonics of the BPF which are observed in anechoic chamber test results are likely caused by TIN.

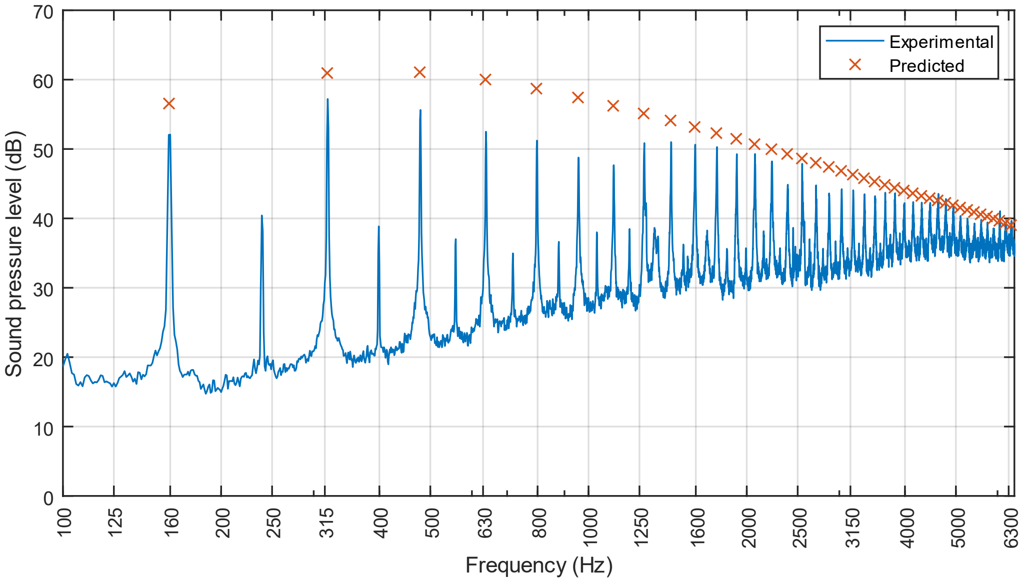


a) $\theta_o = 0°$

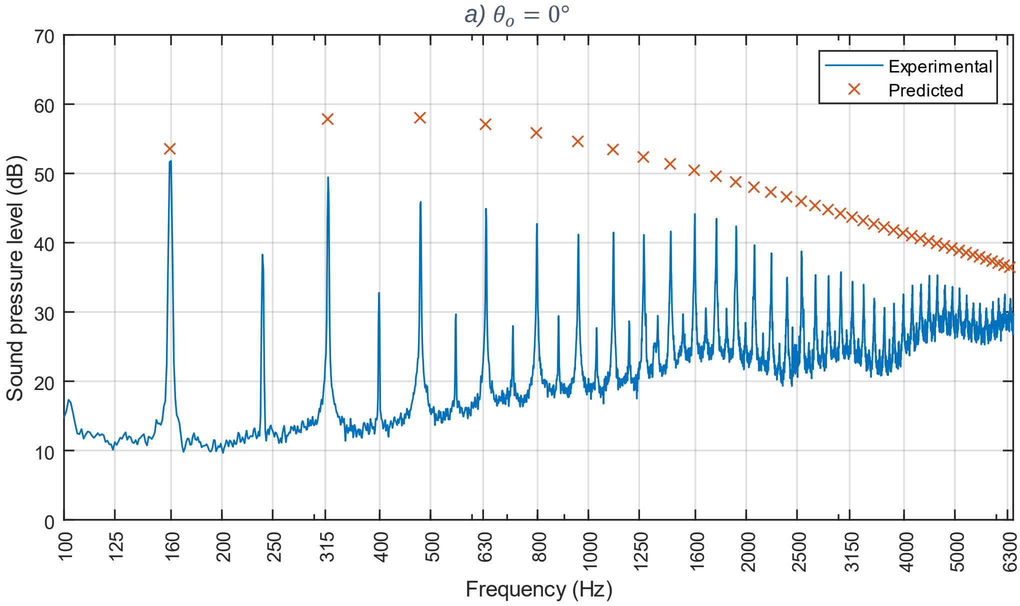


b) $\theta_o = 45°$

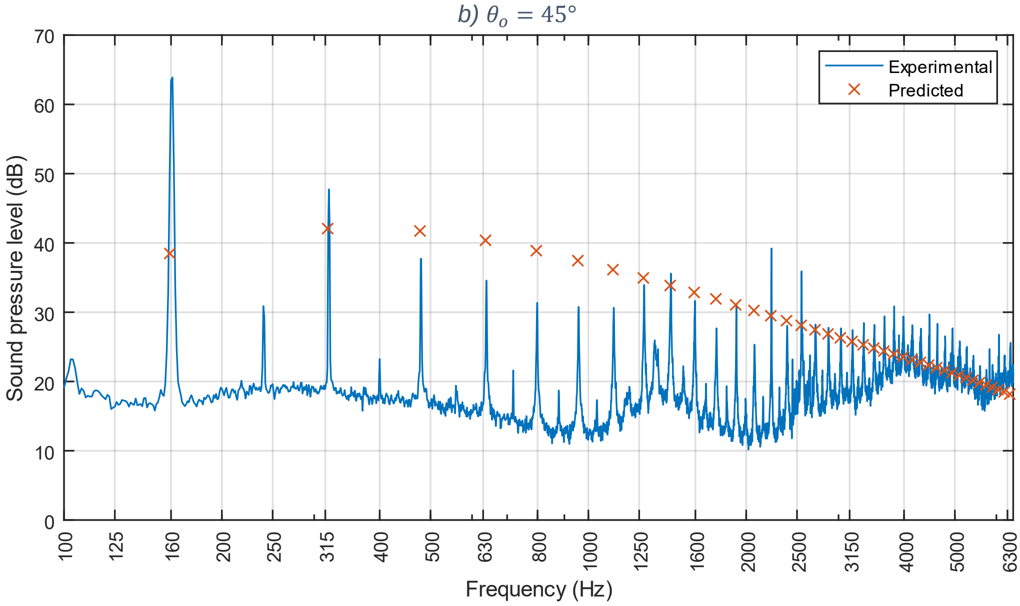


c) $\theta_o = 85°$

*Figure 3. Acoustic measurements of a static 15" T-Motor propeller in an anechoic chamber compared to predictions using the distorted TIN model (eqs. 1-3). The orange crosses denote the peak sound pressure level assuming a 1 Hz bandwidth instead of an integrated value.*

Figure 4 shows the same experimental data compared to predictions made using the simplified model at $\theta_o = 0°$. This model uses measured turbulence properties just above the propeller (see [19] for information on the measurements). The predicted amplitude and rate at which the amplitude of the haystacks decrease is different to the full distorted TIN model; however, the agreement is still moderately good at low frequencies. This prediction took <3 s compared to full distorted TIN model which took >6 h which illustrates the trade-off between accuracy and solution time.

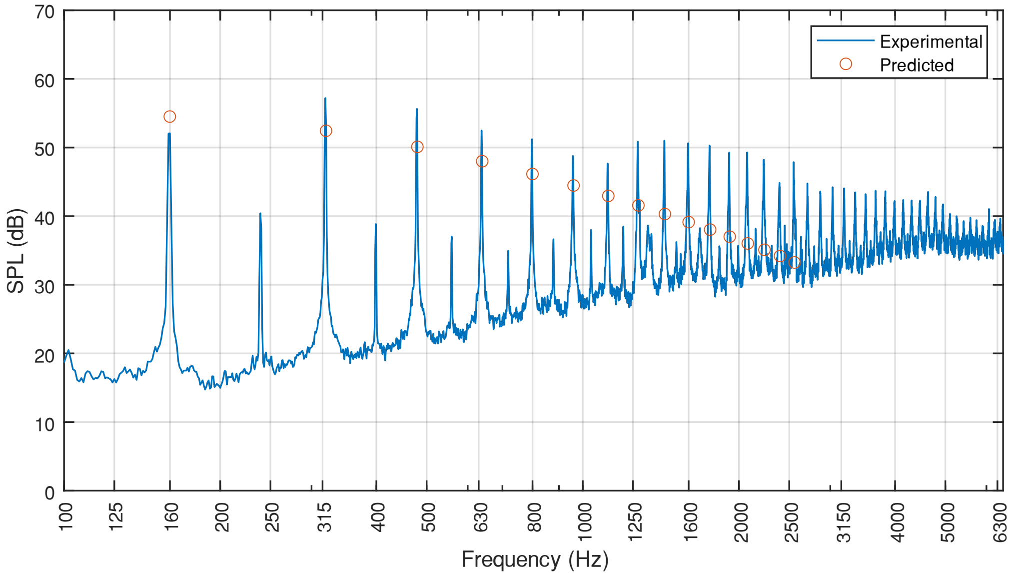


*Figure 4. Acoustic measurements of a static 15" T-Motor propeller in an anechoic chamber compared to predictions using the simplified TIN model (eq. 4) at $\theta_o = 0°$ (directly above the propeller).*

### 3.2 Hovering multirotor UAV

The noise from a hovering DJI Mavic was measured. These measurements are detailed in a Quiet Drones 2022 paper by Kingan et. al [31]. The wind speed during these measurements was around 5 kmph. The turbulence properties of the air were not measured, but an axial integral length scale of 1 m, which is often used by acousticians [25], was used in the predictions. Robison [§3.3.3, 25] provides a more comprehensive discussion on suitable integral length scales. We have used a transverse integral length scale of 0.05 m. The freestream velocity was assumed to be 1 m/s – it is important to note this velocity is generated by the propeller rather than the velocity of the wind. The axial mean square velocity was assumed to be 0.75 m/s.

The experimental spectra contain very broad tones because the propeller speed varied throughout the measurement (which is typical for a hovering UAV). These tones were integrated to get a single value which is comparable to the predicted values. This is denoted with a yellow cross. Figure 5 shows a prediction from the full distorted TIN prediction compared to experimental results taken at $\theta_o = 150°$ (60° below the plane of the propeller) and Figure 6 shows a prediction from the simplified TIN model compared to a measurement directly below the UAV. Although both predictions show good agreement, the full distorted TIN prediction captures the decay of the amplitude of the quasi-tones better than the simplified model.

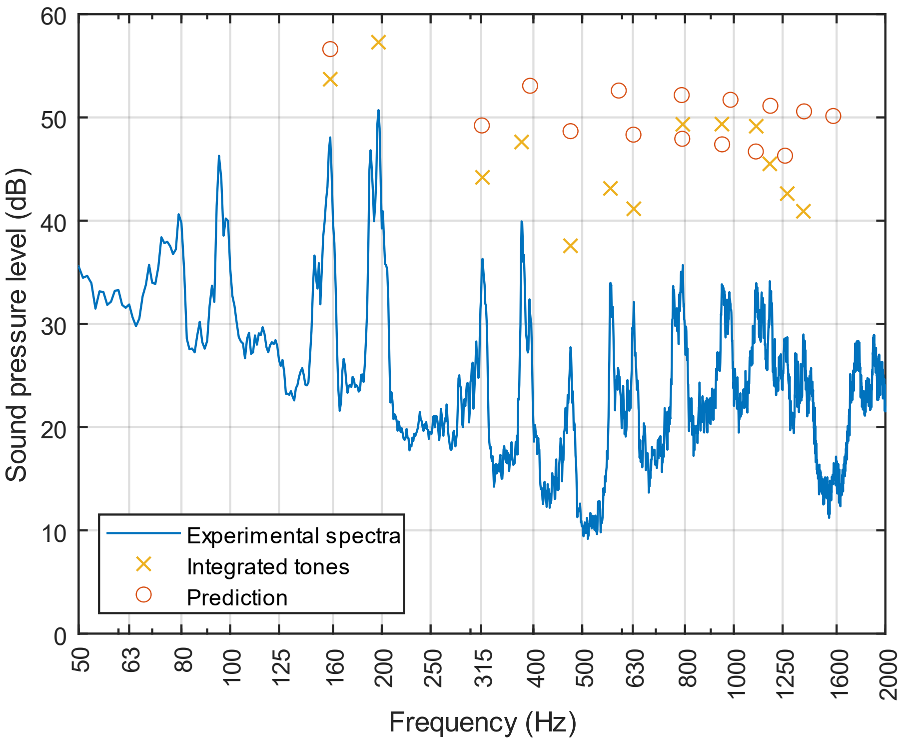


*Figure 5. Experimental results from a hovering DJI Mavic from a microphone located 60° below the plane the propeller rotates in. The × indicate the sound pressure level of the integrated tones and the ∘ the predicted integrated tones using the full distorted TIN model (eqs. 1-3).*

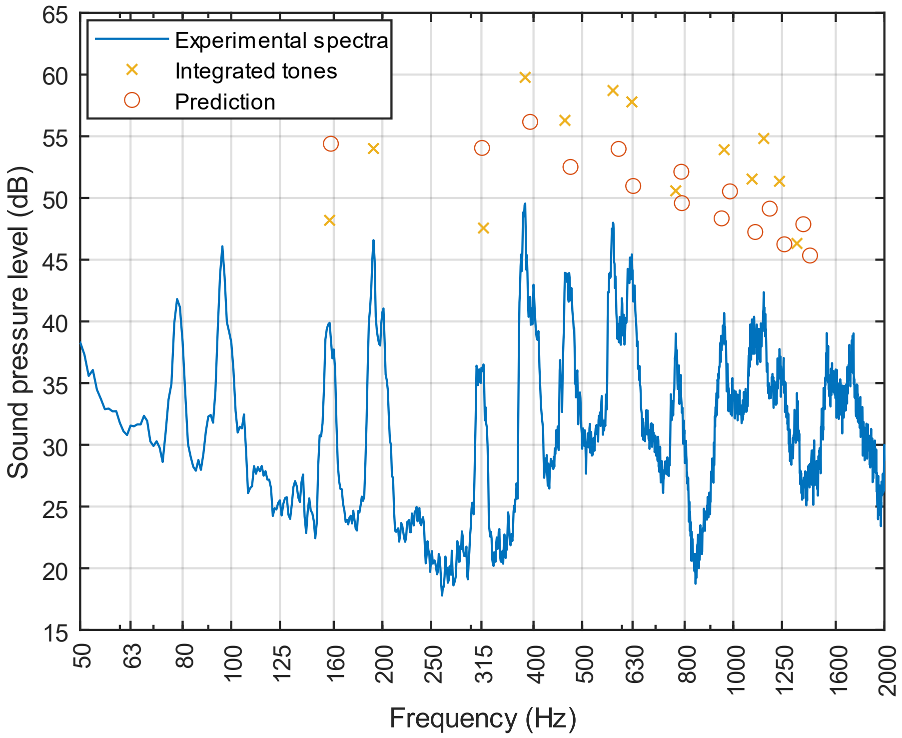


*Figure 6. Experimental results from a hovering DJI Mavic from a microphone located at 180° (directly below the propeller). The × indicate the sound pressure level of the integrated haystacks measured in the experiments and the ∘ indicate the integrated SPL of the haystacks predicted using the simple TIN model (eq. 4).*

## 4. Discussion

The results in the previous section demonstrate that TIN likely causes the multitude of tones seen in experimental spectra of a static propeller in an anechoic chamber and of a hovering quadcopter. The model which predicts the distortion of the turbulence better predicts the decay of the amplitude of the quasi-tones/haystacks which suggests that the inhomogeneity of the distorted turbulence plays a role as the simplified model which relies on a homogeneous anisotropic turbulence model is less able to predict the way the quasi-tones decrease at higher frequencies.

The quasi-tones caused by TIN are a significant source of UAV noise which means it should be considered when designing quiet multirotor UAV propellers. Although the full distorted TIN model better predicts the noise from a propeller, it also has a significant computational expense. The simplified model does not predict the noise as accurately; however, it is able to capture several important properties of a propeller in the predictions whilst having significantly less computational expense. A parameter study by one of the authors using this model showed that increasing the blade number and reducing the rotational speed were two ways of reducing the TIN from a UAV propeller [19].

The quasi-tones generated by TIN are also important to consider when measuring the noise from a static propeller. Various authors have tried to reduce the multitude of BPF harmonics in their experimental measurements by limiting measurement durations to prior to the higher BPF harmonics starting [1] or by using turbulence screens [32]. However, the result in this paper shows that the presence of turbulence in the inflow is the likely cause of these tones rather than specifically recirculation or flow confinement effects. Most multirotor UAVs operate in environments where turbulence is present; therefore, turbulence should be present to measure the noise from a UAV as it would be heard in real operation. This might present difficulty for those developing standards for measuring UAV noise as the TIN is sensitive to inflow conditions which are dependent on factors such as propeller size, propeller loading and anechoic chamber dimensions.

## 5. Conclusions

One of the main benefits of a multirotor UAV over a fixed-wing UAV is its ability to hover. However, in hover, the UAV's propeller interacts with elongated turbulence structures over multiple revolutions which generates a multitude of quasi-tones/haystacks at harmonics of the BPF. This paper summarises a model for predicting the noise generated by a propeller interacting with distorted inflow turbulence. Predictions using this model were compared to experimental measurements of a static propeller in an anechoic chamber and to a hovering UAV and showed moderately good agreement.

A simplified version of this model was also presented which reduced the computational time from several hours to a couple of seconds. Although this model does have moderately good agreement with experimental data, the full model which predicts the distortion of turbulence shows better agreement. An advantage of this simplified model may be in designing quiet propellers where many evaluations of the model could be necessary.

TIN being an important noise source has implications on acoustic measurements of UAV propellers. Testing in a quiescent room and limiting measurements to a period where turbulence is not ingested means that an important noise source is excluded, despite TIN being present in almost all real applications. However, controlling the turbulence within a test space to enable repeatable and comparable testing is difficult. This may pose a challenge for those developing UAV acoustic standards.

## 6. Acknowledgements

The authors would like to thank the University of Auckland, Callaghan Innovation and Dotterel Technologies for funding this research.

## 7. References

[1] Zawodny, N. S., Boyd Jr., D. D., and Burley, C. L. Acoustic Characterization and Prediction of Representative, Small-Scale Rotary-Wing Unmanned Aircraft System Components. 2016.

[2] Tinney, C. E., and Sirohi, J. “Multirotor Drone Noise at Static Thrust.” *AIAA Journal*, Vol. 56, No. 7, 2018, pp. 2816–2826. https://doi.org/10.2514/1.J056827.

[3] Vieira, A., Cruz, L., Lau, F., Mortagua, J. P., and Santos, R. A New Computational Framework for UAV Quadrotor Noise Prediction. 2015.

[4] Alexander, W. N., Whelchel, J., Intaratep, N., and Trani, A. “Predicting Community Noise of SUAS.” No. May, 2019, pp. 1–15. https://doi.org/10.2514/6.2019-2686.

[5] Alvarez, E., Schenk, A., Critchfield, T., Ning, A., Alvarez, E. J., Schenk, A., and Ning, A. “Rotor-on-Rotor Aeroacoustic Interactions of Multirotor in Hover.” *BYU Faculty Publications*, 2020.

[6] Chen, L., and MacGillivray, I. R. “Prediction of Trailing-Edge Noise Based on Reynolds-Averaged Navier-Stokes Solution.” *AIAA Journal*, Vol. 52, No. 12, 2014, pp. 2673–2682. https://doi.org/10.2514/1.J052827.

[7] Huff, D. L. fo., and Henderson, B. S. “Electric Motor Noise for Small Quadcopters: Part 1 – Acoustic Measurements.” *2018 AIAA/CEAS Aeroacoustics Conference*, 2018, pp. 1–20. https://doi.org/10.2514/6.2018-2952.

[8] Henderson, B. S., Huff, D. L., Cluts, J., and Ruggeri, C. “Electric Motor Noise for Small Quadcopters: Part II – Source Characteristics.” *2018 AIAA/CEAS Aeroacoustics Conference*, 2018, pp. 1–20. https://doi.org/10.2514/6.2018-2952.

[9] McKay, R. S., and Kingan, M. J. Multi-Rotor Unmanned Aerial System Noise: Quantifying the Motor’s Contribution. 2018.

[10] McKay, R., and Kingan, M. J. Multirotor Unmanned Aerial System Propeller Noise Caused by Unsteady Blade Motion. 2019.

[11] Wu, Y., Kingan, M. J., and Go, S. T. An Experimental Study of a UAV Propeller and Strut Interaction Noise. 2021.

[12] Zawodny, N. S., and Boyd, D. D. “Investigation of Rotor-Airframe Interaction Noise Associated with Small-Scale Rotary-Wing Unmanned Aircraft Systems.” *Journal of the American Helicopter Society*, Vol. 65, 2020. https://doi.org/10.4050/JAHS.65.012007.

[13] Cabell, R., Mcswain, R., and Grosveld, F. Measured Noise from Small Unmanned Aerial Vehicles. In *Inter-Noise and Noise-Con Congress and Conference Proceedings*, Institute of Noise Control Engineering, 2016, pp. 345–354.

[14] Kloet, N., Watkins, S., and Clothier, R. “Acoustic Signature Measurement of Small Multi-

Rotor Unmanned Aircraft Systems." *International Journal of Micro Air Vehicles*, Vol. 9, No. 1, 2017, pp. 3–14. https://doi.org/10.1177/1756829316681868.

[15] Alexander, N., and Jeremiah, W. Flyover Noise of Multi-Rotor SUAS. 2019.

[16] Weitsman, D., Stephenson, J. H., and Zawodny, N. S. "Effects of Flow Recirculation on Acoustic and Dynamic Measurements of Rotary-Wing Systems Operating in Closed Anechoic Chambers." *The Journal of the Acoustical Society of America*, Vol. 148, No. 3, 2020, pp. 1325–1336. https://doi.org/10.1121/10.0001901.

[17] Stephenson, J. H., Weitsman, D., and Zawodny, N. S. "Effects of Flow Recirculation on Unmanned Aircraft System (UAS) Acoustic Measurements in Closed Anechoic Chambers." *The Journal of the Acoustical Society of America*, Vol. 145, No. 3, 2019, pp. 1153–1155. https://doi.org/10.1121/1.5092213.

[18] Whelchel, J., Alexander, W. N., and Intaratep, N. "Propeller Noise in Confined Anechoic and Open Environments." No. January, 2020, pp. 1–25. https://doi.org/10.2514/6.2020-1252.

[19] McKay, R. S. *Multirotor Unmanned Aerial Vehicle Propeller Noise*. University of Auckland, 2021.

[20] Nardari, C., Casalino, D., Polidoro, F., Coralic, V., Lew, P.-T., and Brodie, J. Numerical and Experimental Investigation of Flow Confinement Effects on UAV Rotor Noise. 2019.

[21] Hanson, D. B. "Spectrum of Rotor Noise Caused by Atmospheric Turbulence." *The Journal of the Acoustical Society of America*, Vol. 56, No. 110, 1974, pp. 110–126. https://doi.org/10.1121/1.1919518.

[22] Amiet, R. K., Simonich, J. C., and Schlinker, R. H. "Rotor Noise Due to Atmospheric Turbulence Ingestion -- Part II - Aeroacoustic Results." *Journal of Aircraft*, Vol. 27, No. 1, 1990, pp. 15–22. https://doi.org/10.2514/3.45891.

[23] Simonich, J. C., Amiet, R. K., Schlinker, R. H., and Greitzer, E. M. "Rotor Noise Due to Atmospheric Turbulence Ingestion - Part I: Fluid Mechanics." *Journal of Aircraft*, Vol. 27, No. 1, 1990, pp. 7–14. https://doi.org/10.2514/3.45891.

[24] Majumdar, S. J., and Peake, N. "Noise Generation by the Interaction between Ingested Turbulence and a Rotating Fan." *Journal of Fluid Mechanics*, Vol. 359, 1998, pp. 181–216. https://doi.org/10.1017/S0022112097008318.

[25] Robison, R. A. V. *Turbulence Ingestion Noise of Open Rotors*. University of Cambridge, 2012.

[26] Robison, R. A. V., and Peake, N. "Noise Generation by Turbulence-Propeller Interaction in Asymmetric Flow." *Journal of Fluid Mechanics*, Vol. 758, 2014, pp. 121–149. https://doi.org/10.1017/jfm.2014.487.

[27] Go, S. T., Kingan, M. J., McKay, R. S., and Sharma, R. N. "Turbulent Inflow Noise Produced by a Shrouded Propeller [In Review]." *Journal of Sound and Vibration*, 2022.

[28] Lighthill, M. J. "Drift." *Journal of Fluid Mechanics*, Vol. 1, No. 1953, 1956, pp. 31–53. https://doi.org/10.1017/S0022112056000032.

[29] Gliebe, P. R., and Kerschen, E. J. *Analytical Study of the Effects of Wind Tunnel Turbulence on Turbofan Rotor Noise*. 1979.

[30] Posson, H., Moreau, S., and Roger, M. "Broadband Noise Prediction of Fan Outlet Guide Vane Using a Cascade Response Function." *Journal of Sound and Vibration*, Vol. 330, No. 25, 2011, pp. 6153–6183. https://doi.org/10.1016/j.jsv.2011.07.040.

[31] Kingan, M. J., McKay, R. S., Wu, Y., Schmid, G., and Mascarenhas, S. "Outdoor UAV Noise Measurement." *Quiet Drones*, 2022.

[32] Weitsman, D., Stephenson, J. H., and Zawodny, N. S. "Effects and Mitigation of Flow Recirculation Patterns Generated by an Open Rotor in a Closed Anechoic Chamber." *The Journal of the Acoustical Society of America (unpublished)*, 2020, pp. 1–12. https://doi.org/10.1121/1.5092213.

[33] Amiet, R. K. "Compressibility Effects in Unsteady Thin-Airfoil Theory." *AIAA Journal*, Vol. 12, No. 2, 1974, pp. 252–255. https://doi.org/10.2514/3.49212.

[34] Landahl, M. T. *Unsteady Transonic Flow*. Pergamon Press, 1961.

[35] Amiet, R. K. "Acoustic Radiation from an Airfoil in a Turbulent Stream." *Journal of Sound and Vibration*, Vol. 41, No. 4, 1975, pp. 407–420. https://doi.org/10.1016/S0022-460X(75)80105-2.

[36] National Institute of Standards and Technology. Error Functions, Dawson's and Fresnel Integrals. *Digital Library of Mathematical Functions*. https://dlmf.nist.gov/7.2. Accessed Mar. 23, 2022.

## Appendix 1: Blade response function

$G(\omega, r)$ is commonly referred to as an aerofoil response function. For low frequency gusts this is defined using Amiet's response function [29, pp. 205-209], and for high frequency gusts using Landahl's response function [30, pp. 27-29] with a switch point recommended by Amiet [31, pp. 407-420]

$$G(\omega, r) = \begin{cases} \dfrac{S\left(\dfrac{\sigma}{\beta_r^2}\right)}{\beta_r}\left[J_0\left(\dfrac{M_r^2\sigma}{\beta_r^2}\right) + \mathrm{i}J_1\left(\dfrac{M_r^2\sigma}{\beta_r^2}\right)\right]\exp\left\{-\mathrm{i}\dfrac{\sigma f(M_r)}{\beta_r^2}\right\}, & \dfrac{|\sigma|M_{r_2}}{\beta_r^2} < \dfrac{\pi}{4}; \\ \dfrac{\exp\left\{-\mathrm{i}\sigma + \mathrm{i}\dfrac{\pi}{4}\right\}}{\pi\sigma}\sqrt{\dfrac{2}{M_r}}E\left(\sqrt{\dfrac{4\sigma M_r}{\pi(1+M_r)}}\right), & \dfrac{|\sigma|M_{r_2}}{\beta_r^2} > \dfrac{\pi}{4}; \end{cases} \tag{A 1}$$

where $E(x) = \int_0^x \exp\{\mathrm{i}(\pi/2)\xi^2\}\,\mathrm{d}\xi$ is a Fresnel integral [32, eq. 7.2.6], $f(M_r) = (1-\beta_r)\ln(M_r) + \beta_r\ln(1+\beta_r) - \ln(2)$, $\sigma = \omega c/2U_r$ is the reduced frequency, $S(\sigma) = \left[-\mathrm{i}\sigma\big(K_0(-\mathrm{i}\sigma) + K_1(-\mathrm{i}\sigma)\big)\right]^{-1}$ is the Sears function, $\beta_r = \sqrt{1-M_r^2}$ is a Prandtl-Glauert factor, $U_r$ is the local Mach number of the blade relative to the fluid and $M_r = U_r/c_0$ is the corresponding Mach number.

QUIET DRONES
Second International e-Symposium
on
UAV/UAS Noise
27th to 30th June 2022

# Small scale rotor aeroacoustics characterization on the interaction noise

**Tiziano Pagliaroli, Università Niccolò Cusano: tiziano.pagliaroli@unicusano.it**
**Paolo Candeloro, Università Niccolò Cusano**
**Fabrizio De Gregorio, Italian Aerospace Research Centre (CIRA)**
**Giuseppe Ceglia, Italian Aerospace Research Centre (CIRA)**

## Summary

In this work, the noise generated by twin rotors for mini drone propulsion was investigated. The experimental study, conducted by varying the speed, distance and phase of the propellers showed that the noise is influenced by all these parameters. An advanced phase control system allowed both to keep constant the rotor-rotor phase and to apply an active noise control technique using a phase randomisation strategy. The control technique developed is very effective when rotors are in close proximity and reduced noise by a maximum of 8 dB.

## 1. Introduction

Unmanned Aerial Vehicle (UAVs) or Micro Aerial Vehicle (MAV) are commonly called drones and are already designed with vertical take-off and landing capabilities, and can be manoeuvred with extremely high versatility and speed. For this reason, MAVs can be easily employed for tactical missions or in urban areas for civil purposes. In both applications, a low noise footprint is mandatory. In fact, for defence applications, a drone with a low noise signature can stealthily approach the target. On the other hand, for civil application in urban areas, drones with low noise emission can more easily obtain the public acceptance.
To give an idea of the public acceptance of large-scale use of delivery drones in residential areas, it would be sufficient to read the title of an article recently published by the Wall Street Journal:" Delivery Drones Cheer Shoppers, Annoy Neighbours, Scare Dogs" [1].

Since the rotors are main source of drone noise, significant efforts are focusing on the aeroacoustic studies of the blades with the aim of understanding the phenomenon and implementing passive control strategies.
In the past, the topic of rotor noise has been extensively addressed also on helicopter, but these studies cannot be directly extended to drone rotors. This aspect is related to the difference in scale of the drone blades compared to helicopter ones. In fact, for the small-scale rotors the Reynolds number assumes smaller values than helicopter and the flow physics results to be completely different [2]. For small scale rotor the aerodynamic filed is characterized by Tollmien-Schlichting instability, laminar recirculation bubble dynamics, transition form laminar to turbulent boundary layer. All of these characteristics of the flow physic play an important in noise generation [3]. Moreover, the tonal noise component emitted by drones results to be less intense, compared to helicopters, and becomes to be of the same order of the broadband component. For these two reasons: transitional aerodynamics and a significant broadband noise component, the topic of the drone noise requires specific experimental studies and the development of dedicated mathematical tools for noise prediction.
In the last years, the scientific community has tackled the study of drone aeroacoustics by focusing the attention on two mainstream topics: *i*) single rotor noise (isolated rotor), and *ii*) drone noise (noise generated by complete quad-, hexa- or octo-copter). The aeroacoustic study of a complete drone is justified by a non-linear noise source related to the proximity of the rotors, which can mutually interact, generating an additional noise component called interaction noise.
In view of its relevance, several of works have been recently published on the aeroacoustic behavior of multi-rotors. Zhou et al. performed an experimental investigation on the impact of the distance between the two rotors [4]. Tinney and Sirohi assessed the aerodynamic performance and the near-field acoustics of an isolated rotor, quad-copter, and hexa-copter to address the effects of the number of rotors [5]. Jia and Lee investigated the interactional aerodynamics and acoustics of the coaxial rotor and quad-rotor [6, 7]. Ko et al. have analysed the noise directivity patterns depending on the diamond and square multi-rotor configuration [8]. Recently, Lee et al. performed an aeroacoustic study of rotor-rotor interaction by varying their mutual distance [2]. Although, several studies on the multi-rotor have been performed, the analysis of the rotor-rotor aeroacoustic interaction is an open issue.
Since, the interaction noise is significantly influenced by the rotor-rotor distance, in the present manuscript, an experimental aeroacoustics characterization of a twin rotors by varying the distance and the rotational regime is reported and discussed.
In addition, an in-depth aeroacoustic investigation was conducted to address the effect of the phase angle between the rotors on the interaction noise source. To our best knowledge, in the context of drones, this subject has never been investigated before. To study the effect of the phase between rotors, a PID based control system was implemented, the performance of this system is described hereafter.

## 2. Experimental setup

Figure 1a show a picture of the test rig and instrumentation employed for the research activity. A couple of three bladed rotors 393.7 mm in diameter (D) (KDE-CF155-TP), two engines (KDE4012XF-400), with two electronic speed controllers (KDEXF-UAS55) were used for the experimental campaign.
The rotor angular position and speed were measured by using two encoders Kubler by 500 ppr (see Figure 1 b). Pressure fluctuations were measured using an arc of microphones.
The experimental campaign was conducted inside the anechoic chamber of the Italian Aerospace Research Centre (CIRA). The chamber is 8.05x6.85x2.62 m in size and has a cut-off frequency of 90 Hz.

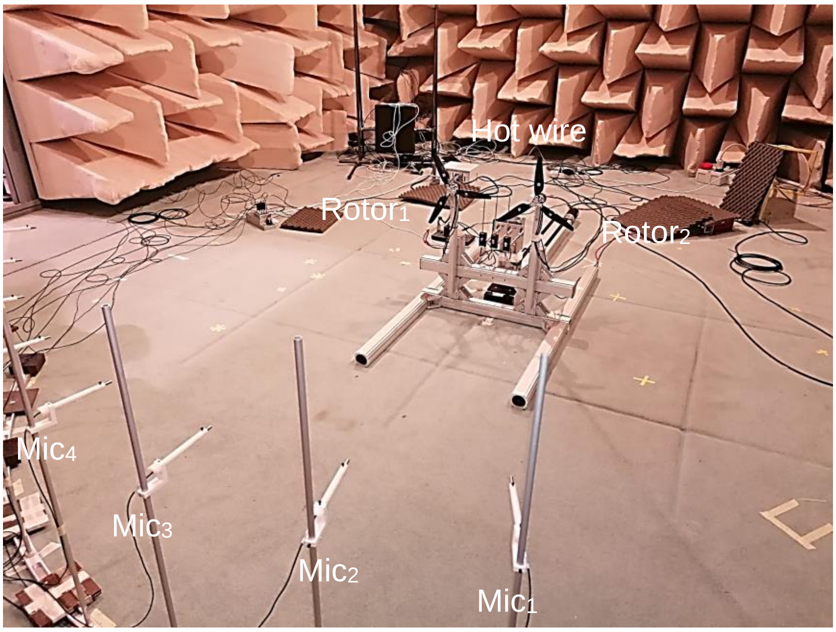


(a) (b)

Figure 1: Picture of the anechoic chamber, the test rig and a portion of the microphone arc (a); close-up photography of the test rig (b).

## 2.1 Aeroacoustic measurements

The 10-microphone array was located on a circular arc at a radial distance r/D=5, from the centreline of the rotor discs, spanning a relative polar angle range $\theta = [0°,\ 90°]$, the polar angle being defined positive in the counter clockwise direction.
Figure 2 shows one of the four possible positions of the microphone arc, located in the first quadrant (I). After each single test, keeping constant all parameters (e.g. speed, rotor-rotor phase and distance), the arc was moved to the other quadrants to cover the angular range $\theta = [0°, 360°]$.
The objective of this procedure is to measure the pressure fluctuation, with an angular resolution of 10°, and provide the complete noise directivity pattern. Pressure fluctuations were measured using 1/8” GRAS microphones.
Time signals were acquired by National Instruments cDAQ-9234 system with a sampling frequency of 51.2 kHz for an acquisition time of 30 s.

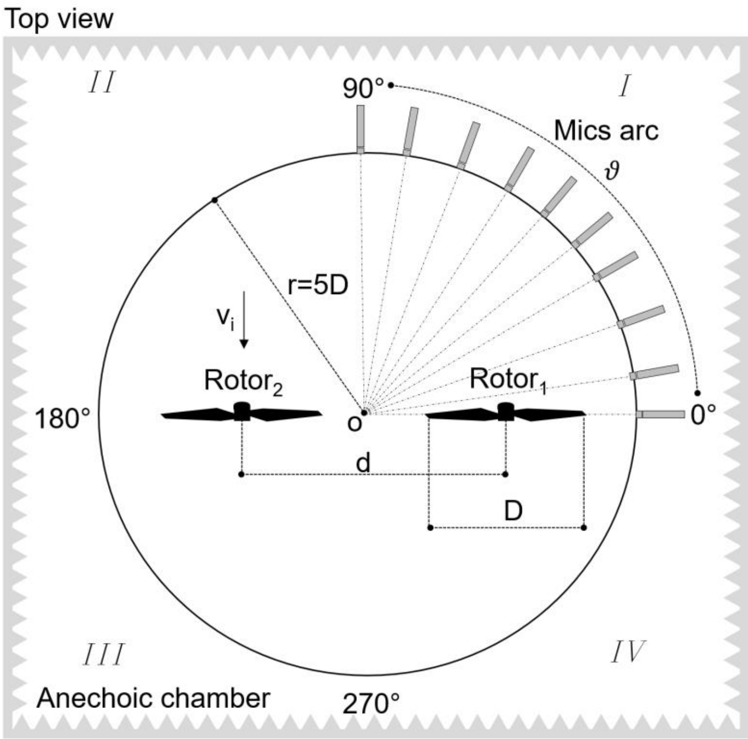

Figure 2: Sketch of the experimental setup: top view.

### 2.2 Synchrophaser

The test rig, using a custom-made control system named *Synchrophaser*, matches the counter clockwise speed between rotors and allow us to set the rotors phase angle, $\psi$ ,defined as shown in Figure 3a. For completeness, two examples of angular configurations between rotors are provided in Figure 2 b and c: $\psi$ =0° and 30° (the phase shift always refers to the slave propeller relative to the master.

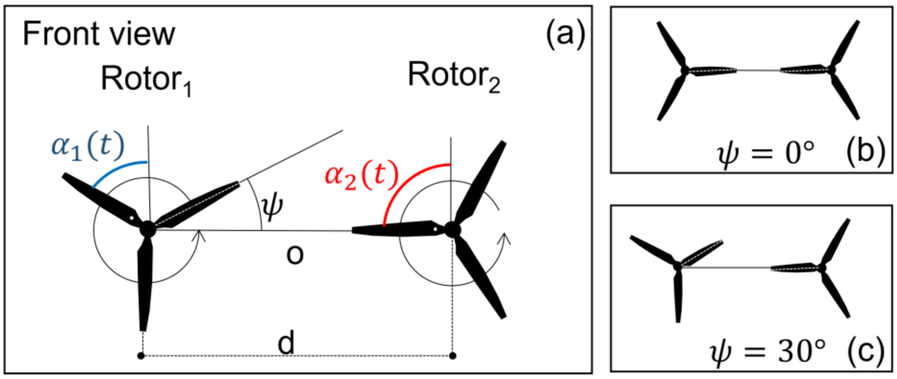


Figure 3: Sketch of the experimental setup front view (a). Example of the rotor-rotor phase configuration: $\psi$=0° (b) and $\psi$=30° (c).

The synchrophaser is based on a PID control system as sketched in Figure 4. The encoders measure the angular position of the motors, using an operator they also measure the phase angle between the rotors which is compared with a set point angle, $\psi_{sp}$. The difference between the two angles is used to calculate the error, which is input to the PID controller. The PID controller generates a change in the control signal of motor 2 ($PWM_2$), named the slave motor.

The slave motor chases the master with a phase angle if it deviates as little as possible from the set point.

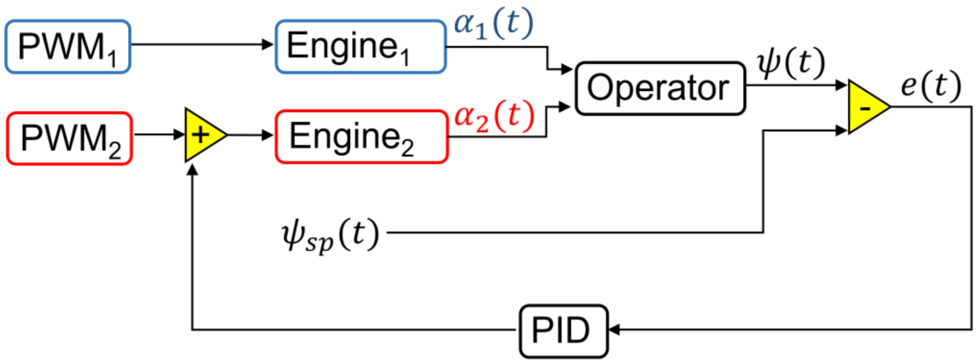


Figure 4: Flow chart representing the control strategy implemented into the synchrophaser.

The system allows variable phase set points to be set. A random phase generator was used to show that a loss of phase coherence has a dominant effect on the interaction noise.

### 2.3 Test matrix

During the tests campaign, the distance (d), the rotational speed (Ω) and the phase angle ($\psi$) of the rotors were varied. The values assumed by these variables are shown in the table below:

| d (mm) | Ω, RPM | $\psi$, deg |
|---:|---:|---:|
| 417 | 3500 | 0° |
| 409 | 4360 | 30° |
| 402 | 5300 | 60° |
| / | / | 90° |
| / | / | |

Table 1: Test matrix.

Each possible combination of the parameters reported in the Table 1 was experimentally investigated for a total of 36 test cases.

## 3. Results

Single rotor noise ($\text{Rotor}_1$) was pre-qualified at three different speeds. Figure *5* shows the directivity of the isolated rotor in terms of Sound Pressure Level (SPL). It is noticeable that the origin of the mics arc is not centred on the rotor disc, but in the centre of the two rotors. The idea is to compare the noise of a single rotor with that generated by the pair of rotors without moving the reference system. For this reason, SPL, in the range $\theta = [150°, 180°]$, assumed smaller value than in the range $\theta = [0°, 30°]$. Furthermore, the aeroacoustic effects of the slipstream affects the range $\theta = [270°, 290°]$, where a significant increase in noise is observed. In general, higher rotational regime leads to an increase in SPL.

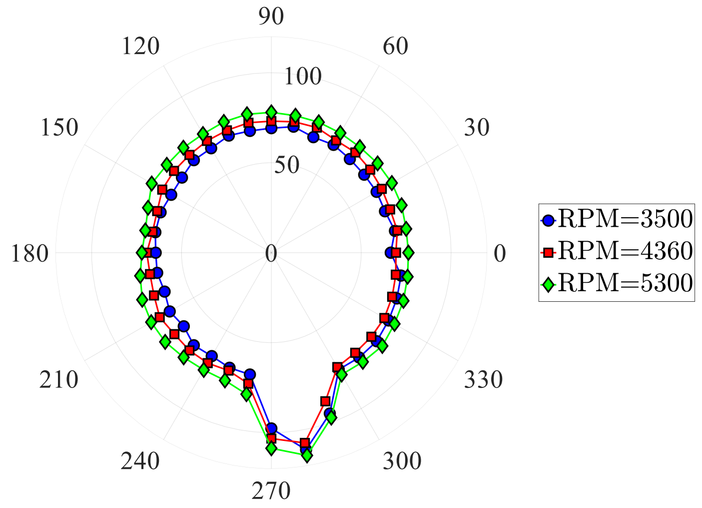


Figure 5 Polar diagram of the sound pressure level radiated by single rotor and measured for different rotational regime: 3500, 4360, and 5300 RPM.

The directivity pattern of two rotors is represented in Figure 6 by varying: rotational speed, phase and distance between the two rotors.
In all cases, the noise emitted by the rotors has a distribution in first approximation constant with the angular position, except for the $\theta = [260°,\ 280°]$, in which a high increase in SPL is observed due to the pressure fluctuations present in the slipstream. The noise in the slipstream becomes greater with increasing velocity (compare for example Figure 6 a, d, g).

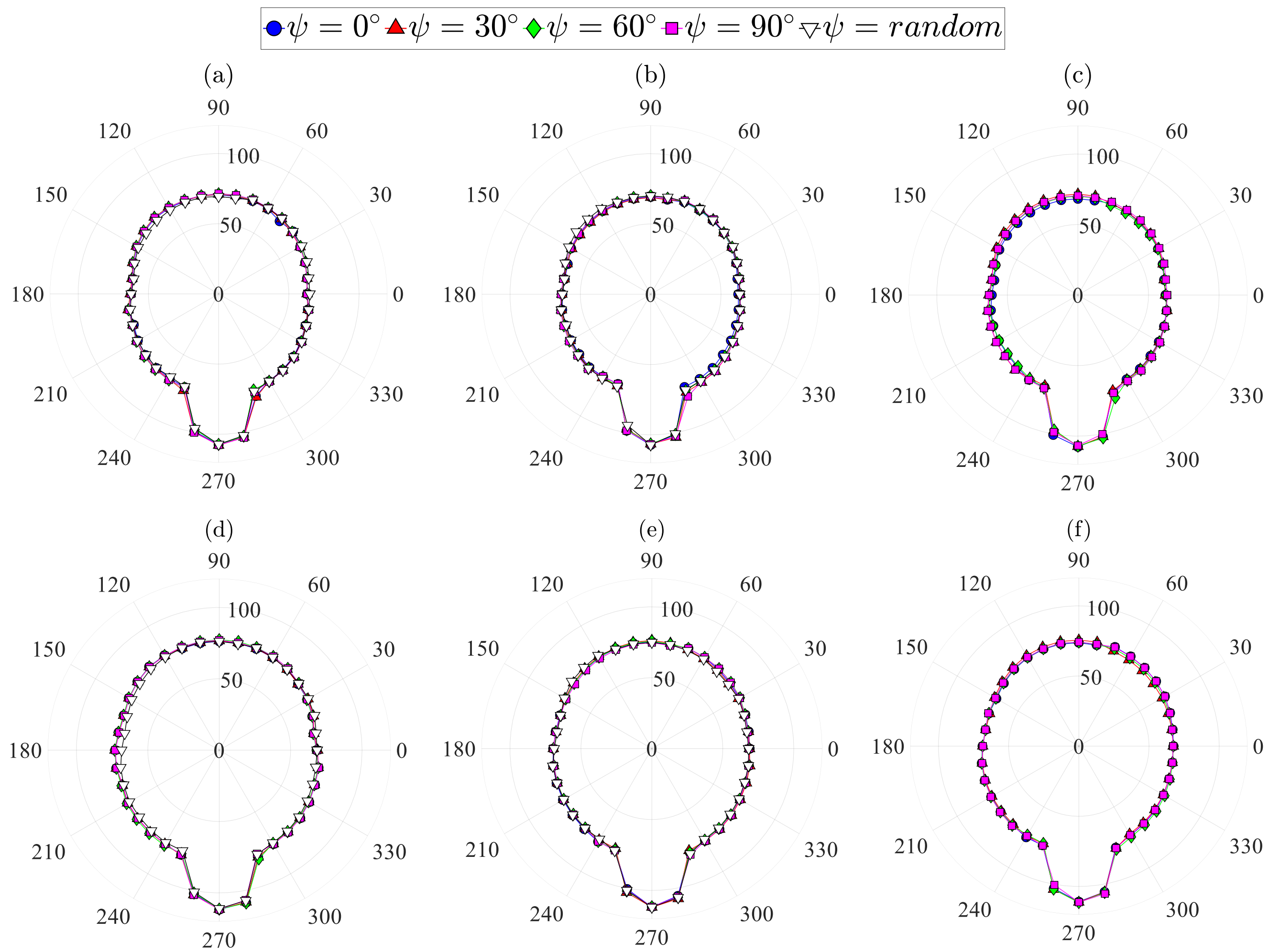

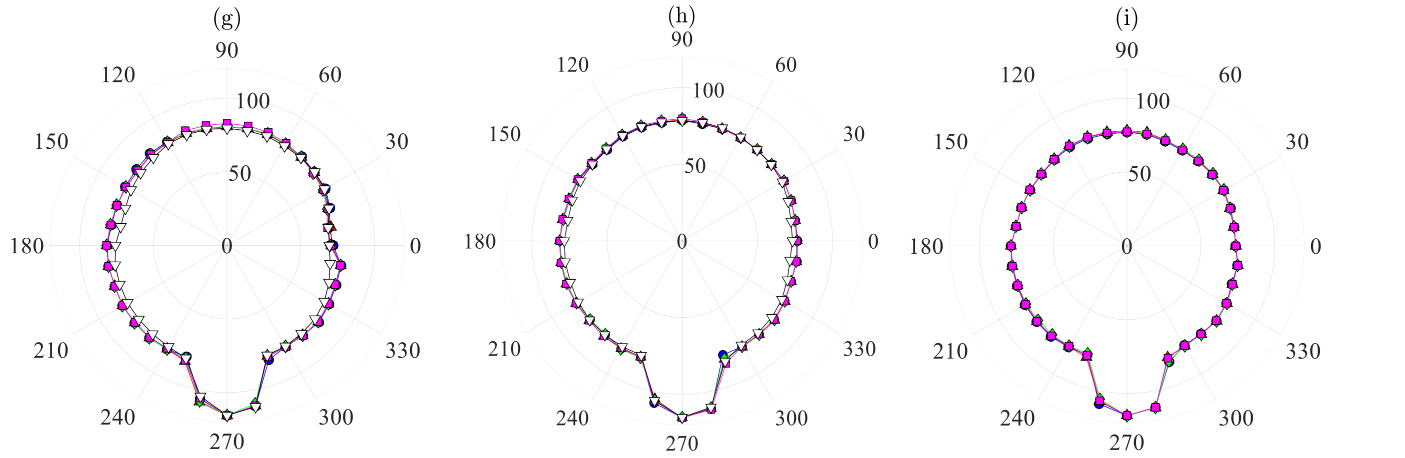


Figure 6: Sound pressure level polar diagram measured for different rotational regime and rotor-rotor distance for co-rotating configuration. For the first row of plot the rotational regime is 3500 RPM and the rotor-rotor distances are 402 mm (a), 409 mm (b) and 417 mm (c) respectively. For the second row of plot the rotational regime is 4360 RPM and the distances are 402 mm (d), 409mm (e), and 417 mm (f). The rotational regime referred to the third row of plot is 5200 RPM, whereas the distance are 402 mm (g), 409mm (h), and 417 mm (i).

Figure 6 gives an overview of the database. The SPL is nearly constant except in the $\theta = [260°, 280°]$ where the microphones are within slipstream and measure larger pressure fluctuations related to turbulent structures. A comparison of Figure 6a-d-g shows that SPL measured in the wake increases upon the rotational regime. Furthermore, in Figure 6adg, for the configuration in which the rotors are closest, it can be seen that the phase randomisation system is very effective as the speed increases.
The SPL versus azimuthal angle in linear scales, for 5200 RPM and d=409mm reported in Figure 7, shows that the phase randomization is very effective in noise reduction for a broad range of angle: in the range $\theta = [50°, 350°]$ the noise radiated by rotors lead by random phase is lower than fixed phase. The reduction achieves a maximum of 8 dB at $\theta = [170°, 180°]$.

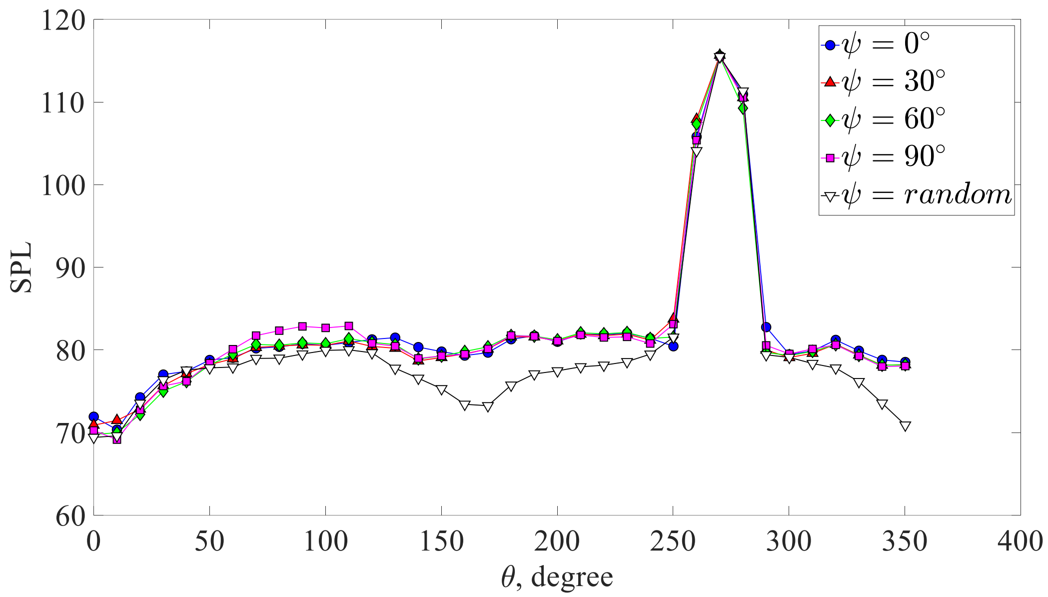


Figure 7: SPL upon azimuthal angle in linear scales, for 5200 RMP and d=409.

To better understand the nature of this noise mitigation, a spectral and statistical analysis was performed on two time series acquired at 180°, where the noise reduction is maximum, and at

270° where there is no reduction in SPL. The spectra are presented in terms of dimensionless frequencies with respect to the blade pass frequency (HBPF).
The phase randomisation system as can be seen in Figure 8a has a two effects: *i*) it reduces the broadband component of the noise in the $HBPF = [1.5,\ 9]$ range while the noise in the wake remains totally unchanged (see Figure 8b); it mitigates the tonal component from the second harmonic (HBPF=2) .

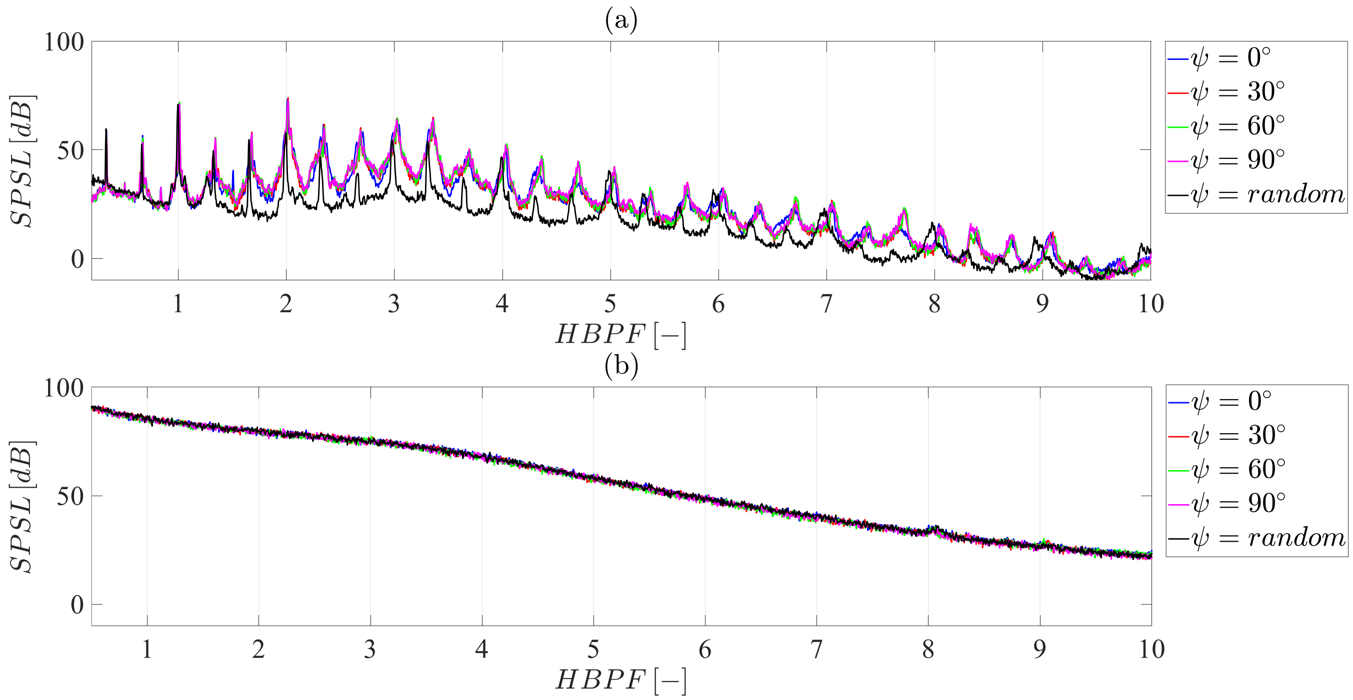


Figure 8: Spectral analysis of the pressure fluctuations time series, for the test case at 5200 RMP and d=409, acquired at two different polar angle: $\theta = 180°$ (a) and $\theta = 270°$ (b).

For the same time series on which the spectral analysis was performed, Probability Density Functions (PDF) were calculated as well. At 180°, the PDF obtained by phase randomisation results to be very different from the others (see Figure 9a), which have a similar shape to each other. Randomisation of the phase gives rise to a left tail indicating the presence of fluctuations of predominant negative amplitude. Phase randomisation, in the statistical sense, introduces fluid expansions that play a key role in mitigating interaction noise. In contrast, it can be seen that no statistical variation due to phase randomisation is introduced in the wake (see Figure 9b). The phenomenon of noise mitigation is therefore local and does not introduce significant effects in the slipstream.

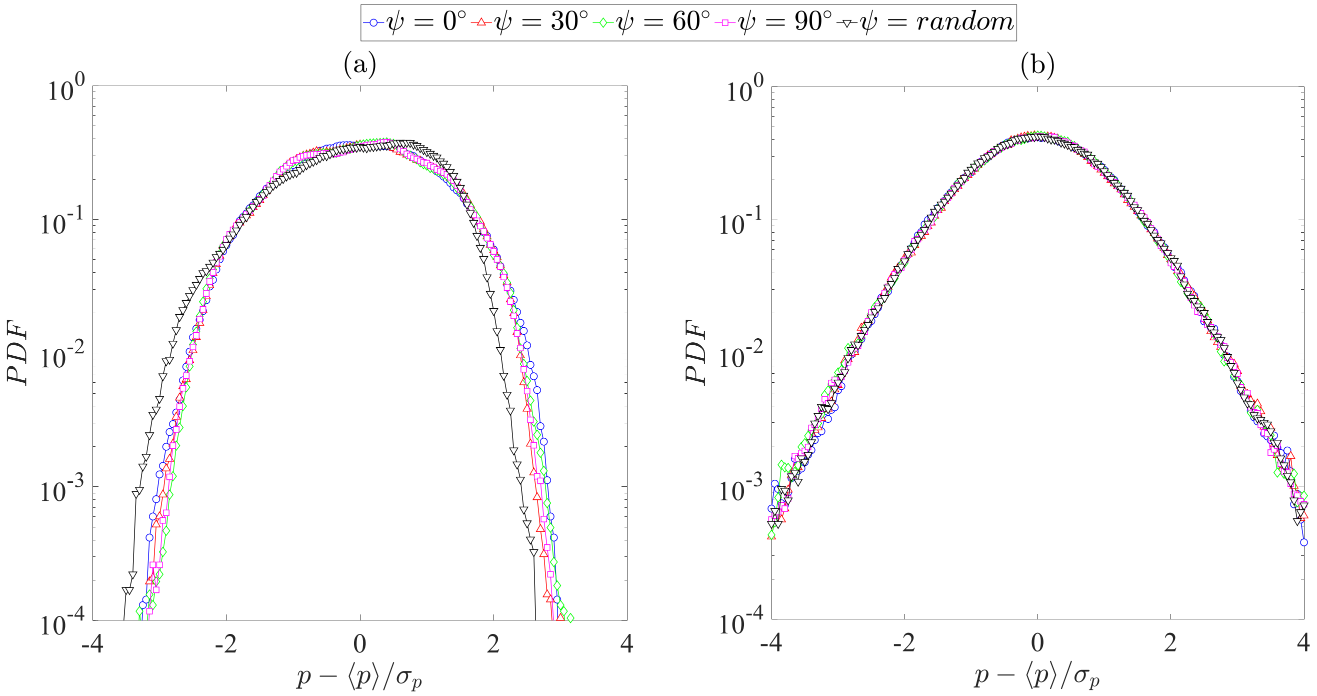


Figure 9: Probability density function of the pressure fluctuations time series, for the test case at 5200 RMP and d=409, acquired at two different polar angle: $\theta = 180°$ (a) and $\theta = 270°$ (b).

## 4. Conclusions

In this work, the noise generated by twin rotors for mini drone propulsion was investigated. The experimental study conducted by varying the speed, distance and phase of the propellers showed that the noise is influenced by all these parameters. An advanced phase control system allowed both to keep constant the rotor-rotor phase and to apply an active noise control technique using a phase randomisation strategy. The control technique developed is very effective when rotors are in close proximity giving a maximum noise mitigation of 8 dB. In addition, the control technique seems to work on both the tonal and the broad band component of the noise. It is also interesting to note that the statistical analysis reveals the presence of an important left tail in the PDF, which indicates the generation of pressure waves of negative amplitude, i.e. expansions, more likely than compression waves.

**References**


1. M Cherney. Delivery drones cheer shoppers, annoy neighbours, scare dogs. Wall Street Journal, 578, 2018.
2. Hakjin Lee and Duck-Joo Lee. Rotor interactional effects on aerodynamic and noise characteristics of a small multirotor unmanned aerial vehicle. Physics of Fluids, 32(4):047107, 2020.
3. Giorgia Sinibaldi and Luca Marino. Experimental analysis on the noise of propellers for small uav. AppliedAcoustics, 74(1):79–88, 2013.
4. Wenwu Zhou, Zhe Ning, Haixing Li, and Hui Hu. An experimental investigation on rotor-to-rotor interactions of small uav propellers. 35th AIAA applied aerodynamics conference, page 3744, 2017.
5. Charles E Tinney and Jayant Sirohi. Multirotor drone noise at static thrust. AIAA Journal, 56(7):2816–2826, 2018.
6. Zhongqi Jia and Seongkyu Lee. Acoustic analysis of urban air mobility quadrotor aircraft. In Vertical Flight Society (VFS) Aeromechanics for Advanced Vertical Flight Technical Meeting, 2020.
7. Zhongqi Jia and Seongkyu Lee. Impulsive loading noise of a lift-offset coaxial rotor in high-speed forward flight. AIAA Journal, 58(2):687–701, 2020.
8. Jeongwoo Ko, Jonghui Kim, and Soogab Lee. Computational study of wake interaction and aeroacoustic characteristics in multirotor configurations. In INTER-NOISE and NOISE-CON Congress and Conference Proceedings, volume 259, pages 5145–5156. Institute of Noise Control Engineering, 2019.

QUIET DRONES
Second International e-Symposium
on
UAV/UAS Noise
27th to 30th June 2022

# A greenery-based solution for low-noise delivery hub for unmanned aerial transport

**Giorgio Palma, Derpartment of Engineering, Roma Tre University, Via Vito Volterra, 62, Roma, 00146, Italy: giorgio.palma@uniroma3.it**
**Claudio Pasquali, Derpartment of Engineering, Roma Tre University, Via Vito Volterra, 62, Roma, 00146, Italy: claudio.pasquali@uniroma3.it**
**Caterina Poggi, Derpartment of Engineering, Roma Tre University, Via Vito Volterra, 62, Roma, 00146, Italy: caterina.poggi@uniroma3.it**
**Lorenzo Burghignoli, Derpartment of Engineering, Roma Tre University, Via Vito Volterra, 62, Roma, 00146, Italy: lorenzo.burghignoli@uniroma3.it**
**Jacopo Serafini, Derpartment of Engineering, Roma Tre University, Via Vito Volterra, 62, Roma, 00146, Italy: jacopo.serafini@uniroma3.it**

## Summary

Unmanned Aerial vehicles are nowadays involved in a wide range of applications, such as surveillance, safety control, scientific research, and commercial activities. The logistics industry, in particular, is showing a substantial interest in a partial transition of the last-mile delivery service from ground to air transport. A key point to make this scenario feasible resides in the design of delivery hubs to serve the surrounding areas, thus overcoming the logistical difficulties of a door-to-door delivery while respecting the strict regulations in terms of noise. The proposed paper deals with the study and design of an urban hub for package delivery that uses natural elements such as hedges to limit the noise footprint associated with drone operations by exploiting the shielding capabilities of natural barriers. Some constraints driving the design are identified, leading to a tentative conceptual design. The acoustic property of a sample hedge is evaluated using an equivalent porous medium approach, informed by parameters estimated by image processing of the external surface of the hedge. Eventually, the model is used in coupled BEM-FEM simulations of simplified designs. Preliminary results show encouraging noise reductions in the areas surrounding the hub.

## 1. Introduction

In the last few years, the constant growth of urban pollution and overcrowding has led to an increasing interest in alternative and sustainable solutions to conventional urban mobility. In this framework, the Urban Air Mobility (UAM) represents a possible solution made viable by the emerging technological innovations in several fields, such as automation or electrification. Nevertheless, many open questions regarding the implementation of UAM transportation networks, such as certification, traffic management, or ground infrastructure requirements, remain answered [1]. Besides, the environmental sustainability of these Urban Aerial Vehicles (UAVs) is a fundamental condition of their entry-into-service, as well testified by the increasingly strict regulations for the whole aviation world in terms of chemical pollution and noise [2]. Many industries are nowadays involved in the design and manufacturing of innovative electric vertical takeoff and landing concepts (eVTOLs) [3]. Furthermore, several tasks, such as surveillance, safety control, and scientific research, have been in the last few years rethought in order to be accomplished by drones [4]. Moreover, UAVs are rapidly being involved in commercial activities. The logistics industry, in particular, is showing a substantial interest in a partial transition of the last-mile delivery service from ground to air transport, and different solutions have been presented by the leading actors who are showing interest in this area [5]. Delivery drones in the sky might become as common as mail trucks on the road in the near future. Nevertheless, to make this suggestive scenario feasible, a new set of infrastructures are necessary for the operations connected to drone flight tasks [6]. A typical mission of a UAV for delivery starts with the pick up of the pack, an autonomous flight ending with a hovering phase over the delivery point, and a vertical descent to drop the pack safely (max altitude 0.15-0.30 m) [7]. It is hard to imagine a drone landing spot for each consumer in the urban context. Thus, a feasible solution could be the realization of delivery hubs serving all surrounding areas. Nevertheless, the noise annoyance produced by intensive operations in localized areas, although of small drones, is a critical issue for developing urban air delivery services. In this scenario, this work deals with the study and design of an urban hub for package delivery that uses natural elements (grass, hedges, trees) to limit the noise footprint associated with drone operations. There is a growing interest in the noise shielding capabilities of natural barriers. Some works can be found in the literature on the acoustic modeling of organic barriers, mainly focused on low growing plants [8, 9, 10, 11]. A common approach considers the greenery as a porous material, presenting a rigid frame (leaves and woody parts) filled with air, which can be, in turn, characterized using different models. In [10] and [11], experiments allowed to perform optimization for the inverse characterization of the equivalent porous medium using the three-parameters Delany-Bazley-Miki model[12]. Specifically, based on the physical and geometrical properties of the plant, some semi-empirical models were derived for equivalent porosity, flow resistivity, and tortuosity. It is there highlighted how trying to measure such parameters for plants and trees directly is not a trivial task, and inverse estimation was explored as a strategy to develop reliable equivalent-medium-based modeling for plants and plant-soil combinations. Some experiments have also been performed on sound attenuation by hedges[13], measuring the insertion loss obtained at a distance of 1m from the hedge for a controlled noise source and numerically reproducing it through an equivalent porous material. It is found that a considerable noise reduction at the receiver can be obtained for hedges of 1.5m of thickness, with an effect comparable to standard acoustic barriers. To this aim, first, the acoustic properties of standard plants are evaluated, and then preliminary simulations to assess the acoustic properties of the hedge shields are performed. In particular, in Sec. 2 the guidelines followed for the delivery hub design are presented; then, in Sec. 3 the strategy followed for the characterization of the acoustic properties of the selected barriers are explained, and the numerical results of the proposed approach for a selected configuration are shown in Sec. 4; finally, some concluding remarks are reported in Sec. 5.

## 2. Design of the Green delivery hub

Operational and environmental constraints influence the design of a delivery hub. A non-exhaustive list of such constraints are:

- internal space sufficient to host a landing spot and an automatic locker;
- enough space for user access and to perform maintenance;
- overall footprint below 10x10 $m^2$ in order to be fitted into parks or unused urban space;
- high capacity;
- possibility to perform non-vertical takeoff to reduce required power;
- good resilience to gusts.

These constraints lead to the definition of a tentative design of the delivery hub, consisting of a number of circular hedges surrounding a landing/take-off platform. The sketch of the proposed hub in multi-hedge configuration is shown in the Fig. 1, including hedges (in green) and the operational platform (in black). Access to the hub is guaranteed by the openings present in the various layers of the hedge (visible in Fig. 1b), which are suitably misaligned to minimize the inevitable loss of acoustic performance. In addition, the hedges are designed with different heights (Fig. 1a) to form an inverted cone-shaped entrance towards the platform. This inverted cone shape is

(a) Side view. (b) Top view.

Figure 1: Sketch of the proposed delivery hub including two layers of hedges (green) and the platform for landing/take-off (black).

| Name | Planform dimensions (mm) | MTOW (kg) | Payload |
|---|---|---|---|
| Wingcopter 198[14] | 1520 x 1980 | 25 | 5 |
| Swoop aero Kite[15, 16] | 2400 x n.a. | n.a. | 5 |
| Alphabet Wing[17] | 1300 x 1000 | 6.4 | 1.2 |
| Amazon prime air[5] | 914 x 914 | 7.8 | 2.3 |
| Dij Matrice 600 Pro[18] | 1668 x 1518 | 15.5 | 5.5 |

Table 1: Delivery drone dimensions.

intended to give good noise shielding performance up to a specific azimuth, allowing, at the same time, an easy and efficient landing with sufficient translational velocity. Indeed, a purely vertical take-off and landing would require more power (due to the absence of translational lift) and drastically reduce hub capacity (hourly throughput) since the maneuver is slow and the descent and climb path coincide. Furthermore, the multi-hedge configuration reduces the loss of shielding effect in the path users follow (avoiding the line of sight between the noise source and observers outside the hub) and optimizes plants' use since the leaf distribution is concentrated in the outer part of the plants. An analysis of dimensions of existing delivery drones, reported in Tab.1, helped in defining the required take-off&landing area extension. It is found that an average delivery drone has a planform that can be contained in a square box of 2.5 m side, hence it is decided that a circular area of radius 2.5m inside the inner hedge circle is needed, in order to ensure sufficient tolerances for the autonomous maneuvers.

Maintenance represents a critical aspect that, especially in a hub based on natural elements such as hedges, must be considered right from the conceptual design stages. In particular, (i) the distance between the various layers of plants must be sufficient not only for the transiting of people and their goods but also to allow the necessary thinning operations; (ii) it is necessary to ensure the presence of an adequate water network for the necessary irrigation. The main requirements that hedges must meet are: (i) they do not drop leaves during the adverse season; (ii) possibility of growing to heights equal or greater than two meters; (iii) high growth rate; (iv) resistance to local climate (extreme) conditions. The first requirement implies that the choice necessarily falls on evergreen plants, commonly used for making hedges. Among these, it is possible to identify some that meet all or part of the above requirements, for example, looking at applications in the Mediterranean and Center Europe, the *Cherry Laurel*, the *Laurel*, the *Cypress*, the *Ligustrum*, the *Pyracantha* and the *Japanese Privet*. For availability reasons, in the present study, the studied hedges is assumed to be made of *Buxus*, even though this species is not one of the most suitable.

## 3. Porous material model for hedges

A modified version of the well known six-parameters Johnson-Champoux-Allard model for porous media has been introduced recently[19], hereby called the JCAH model, reducing the number of independent parameters of the porous domain down to three under the assumption of log-normal distribution of pores' size, namely the porosity $\Phi$, the standard deviation of the pores' size $\sigma_S$, and the size of the median pores $\bar{s}$. Under the mentioned hypothesis, tortuosity $a_\infty$, flow resistivity $\sigma$ and thermal flow resistivity $\sigma'$ are obtained as

$$a_\infty = e^{4(\sigma_S \log 2)^2} \tag{1}$$

$$\sigma = \frac{8\eta a_\infty}{\bar{s}^2\Phi} e^{6(\sigma_S \log 2)^2} \tag{2}$$

$$\sigma' = \frac{8\eta a_\infty}{\bar{s}^2\Phi} e^{-6(\sigma_S \log 2)^2} \tag{3}$$

with $\eta$ being the dynamic viscosity. Expressions for equivalent mass density and bulk modulus can be obtained from these parameters as:

$$\rho(\omega) = \rho_0 \frac{a_\infty}{\Phi}\left(1 + \epsilon_\rho^{-2} F_\rho(\epsilon_\rho)\right) \tag{4}$$

$$B(\omega) = \frac{\Phi}{\gamma p_0}\left(\gamma - \frac{\gamma - 1}{1 + \epsilon_B^{-2} F_B(\epsilon_B)}\right) \tag{5}$$

with

$$\epsilon_\rho = \sqrt{\frac{-i\omega\rho_0 a_\infty}{\Phi\sigma}}, \quad F_\rho(\epsilon_\rho) = \frac{1 + \theta_{\rho,3}\epsilon_\rho + \theta_{\rho,1}\epsilon_\rho^2}{1 + \theta_{\rho,3}\epsilon_\rho} \tag{6}$$

$$\theta_{\rho,1} = \frac{1}{3}, \quad \theta_{\rho,2} = \frac{e^{-\frac{1}{2}(\sigma_S \log 2)^2}}{\sqrt{2}}, \quad \theta_{\rho,3} = \frac{\theta_{\rho,1}}{\theta_{\rho,2}} \tag{7}$$

$$\epsilon_B = \sqrt{\frac{-i\omega\rho_0 \mathrm{Pr}\, a_\infty}{\Phi\sigma'}} \quad F_B(\epsilon_B) = \frac{1 + \theta_{B,3}\epsilon_B + \theta_{B,1}\epsilon_B^2}{1 + \theta_{B,3}\epsilon_B} \tag{8}$$

$$\theta_{B,1} = \frac{1}{3}, \quad \theta_{B,2} = e^{\frac{3}{2}(\sigma_S \log 2)^2}, \quad \theta_{B,3} = \frac{\theta_{B,1}}{\theta_{B,2}} \tag{9}$$

where $\gamma = c_p/c_v$, Pr is the Prandtl number and $p_0$ is the ambient pressure.

In this article, it is proposed that the information required for the definition of the equivalent porous material in terms of $\bar{s}$ and $\sigma_S$ can be obtained by analyzing simple pictures of the hedge, and consequent values obtained for $\sigma$ are comparable to what is predicted using the method in [10], and [11].

### 3.1. Estimation of hedge parameters

As stated above, in this work, an algorithm to estimate $\bar{s}$ and $\sigma_S$ has been developed, which is based on an image processing of the external surface of the hedge. The main idea behind the algorithm comes from direct observation of the hedge. Due to its composition, it is a common experience that, looking at its external surface, one will see a random distribution of clear and dark areas, coming from an overlap of leaves layer which fights together to reach the light. This structure somehow represents a porous surface with a random distribution of holes. The algorithm could be outlined in the following procedure:

i - Calibration - During the first step the pixel-to-meter scaling is obtained from the ruler inserted in the picture,

ii - Binarization - Defining a threshold value, the original RGB or grey scale image is converted to a black and white one.

iii - Image analysis - In the B&W converted image, the white parts represent the holes on the hedge surface. These are extracted by the processing algorithm, identifying ellipses with equivalent radius bigger than a minimum reference value.

iv - Statistics evaluation - The data from the previous step in terms of holes equivalent radius are statistically analyzed and a fitted by a log-normal distribution. Its median $\bar{s}$ and standard deviation $\sigma_S$ are then obtained and used for the characterization of the equivalent porous material.

In Fig. 2 an application of the proposed algorithm is presented: the red ellipses in Fig. 2a represent the holes identified on the b&w image, superimposed on the original picture in Fig. 2. In particular, Fig. 2a clearly shows how the algorithm can correctly identify the equivalent holes of the hedge surface. For the sake of simplicity, the mean of the two ellipse's axes has been chosen as the radius of an equivalent circumference representing each hole. Once the ellipses are identified and their equivalent radii collected, it is possible to analyze and verify the log-normality of their distribution, Fig. 3. The evaluation of the porosity $\Phi$ has been performed starting from some morphological parameters of the plant: the average thickness of a representative leaf $t_f$, the average distance between two leaves along a branch $d_f$ and the surface porosity $\Phi_S = \sum_{j=1}^{n_h} S_j/S_p$, defined as the ratio between the holes surface $S$ measured from the picture and the picture surface $S_p$,

$$\Phi = \frac{d_f + \Phi_S h_f}{d_f + h_f} \tag{10}$$

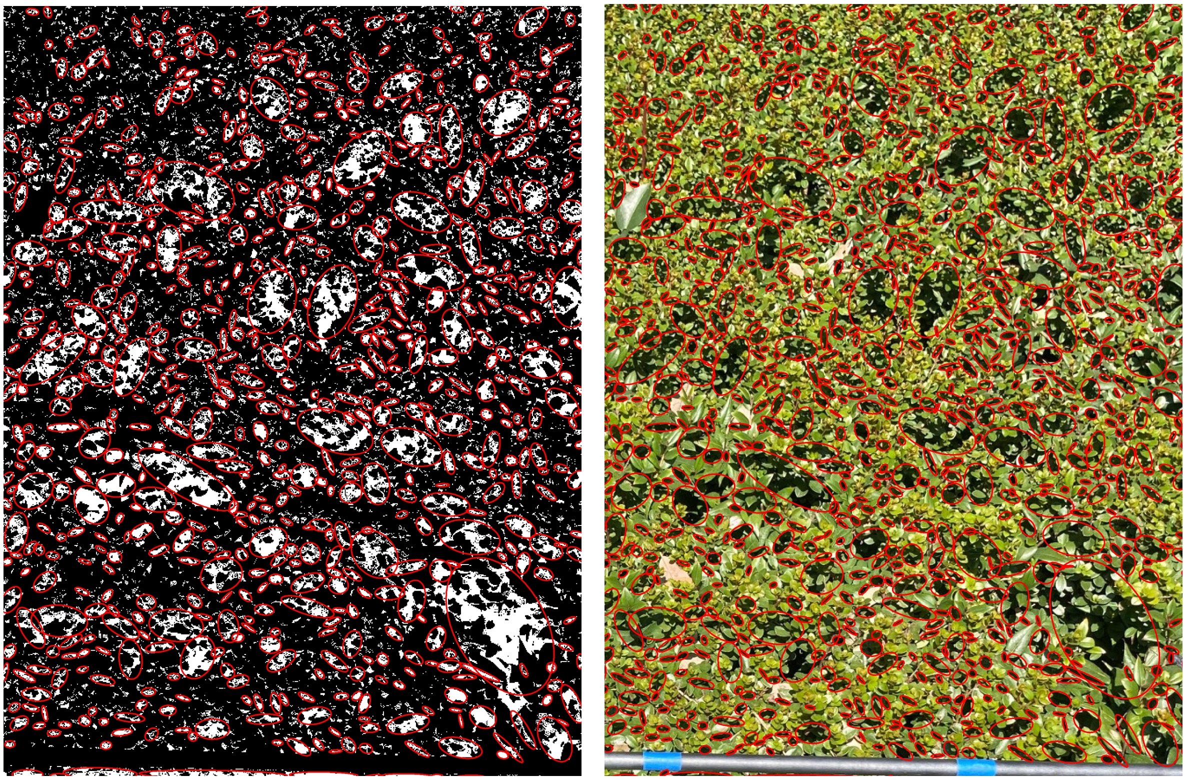

(a) (b)

Figure 2: Binarized image with the identified holes (a). The red ellipses representing the holes are plotted over the original RGB picture (b) to verify the results of the analysis.

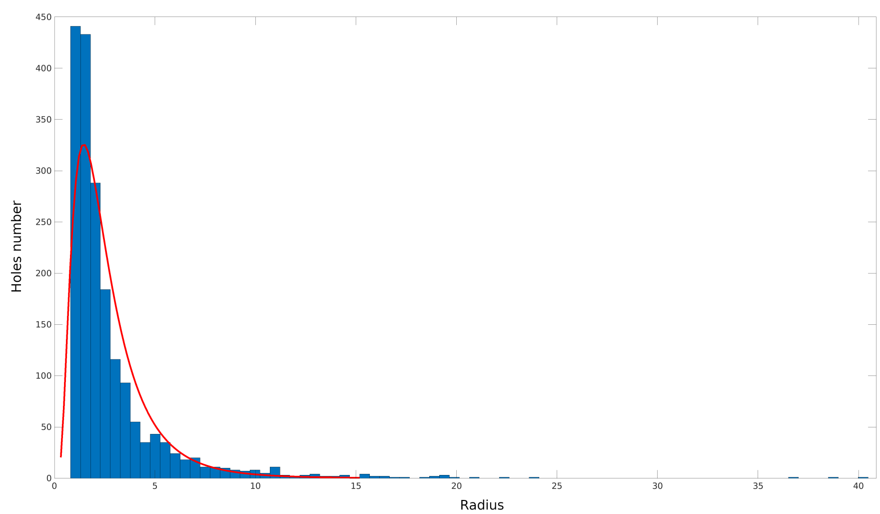


Figure 3: Probability distribution of holes equivalent radii for the Buxus hedge.

The obtained values have been verified with a more classic approach, following the experience reported in [10]. Other morphological parameters of the plants were measured from taken specimens of known sizes: the area of a representative leaf $a_f$ that has been measured with the image processing technique and the number of leaves in the sample $n_f$ that has been directly counted. In this case, starting from the volume of the sample $V_p$ and the volume occupied by the foliage $V_f$, the porosity is evaluated as

$$\Phi_H = 1 - \frac{V_f}{V_p} = 1 - \frac{n_f a_f t_f}{V_p} \tag{11}$$

Values of $\Phi$, $\bar{s}$ and $\sigma_S$ are reported in Tab. 2 for a Buxus hedge The two approaches

| Species | $\Phi$ | $\Phi_H$ | $\bar{s}$ (m) | $\sigma_S$ |
|---|---|---|---|---|
| Buxus | 0.96 | 0.97 | 0.00246 | 0.655 |

Table 2: Plants parameters

for the evaluation of the porosity provided almost identical results for the considered specimens.

## 4. Numerical Results

Some preliminary simulations have been performed on simplified geometries, representative of the proposed design for the green delivery hub using the data from the Buxus hedge. In particular, to acoustically shield the landing area with a radius of 2.5m, we compared a single-layer and a two-layers design of 2m high circular hedge(s). The former has a thickness of 1.5m, placed around a landing area with a radius of 2.5m. The latter is composed of two concentric hedges with a thickness of 0.75m each; a labyrinthine path guarantees access to the landing area inside the inner circle, passing through the annular region in the middle of the two hedges ($r_2 - r_1 = 1m$). To reduce the computational burden, a 2D section is taken as representative of the axially symmetric domains, Fig. 4. Under the quiescent irrota-

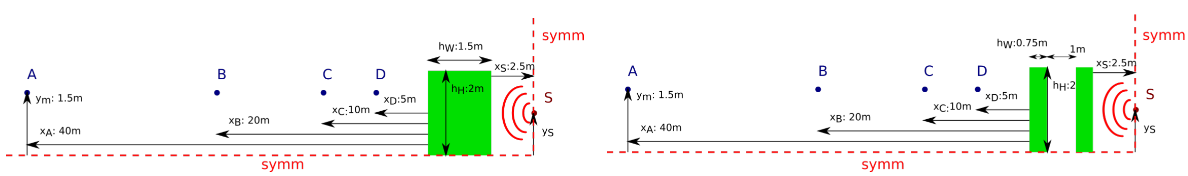


(a) (b)

Figure 4: Single- and two-layer hedges, (a) and (b) respectively, numerical analysis sketch.

tional and homentropic fluid hypothesis, the small amplitude acoustic perturbations are held by the D'Alembert operator ($\Box p = S$). The wave equation is then Fourier-transformed and solved in the frequency domain. A FEM-BEM combined approach is employed in order to set a multi-domain problem, in which the propagation properties of the hedge(s) domain, modeled with the FEM, are obtained from Eqs.(4) and (5), considering $\rho_0 = 1.21$ kg/m$^3$ and $c_0 = 343$ m/s. The use of the BEM for the exterior propagation automatically ensures the non-reflecting condition at infinity. An elementary point acoustic monopole of unitary amplitude is used to model the noise source ($S = \delta(\mathbf{x} - \mathbf{x_S})$). The noise reduction effect of the green barrier is investigated for two vertical positions of the source $y_s$ =1m and 2m, centered in the landing area, at a set of virtual receivers placed 40, 20, 10, and 5 m away from the outer edge of the hedges at 1.5 m from the ground, named A, B, C and D respectively. The application of the method of the images ensures the imposing of the symmetries of the problem. In this way, the ground is considered acoustically hard, as suggested in ISO 9613-2 for low porosity ground surfaces. Although this may be considered an oversimplification of its properties, considering the even remarkable effect by the ground is out of the scope of the present work. An additional set of simulations neglecting the presence of the ground is also performed.

For all the cases, the Insertion Loss is evaluated as

$$\mathrm{IL}(\mathbf{x}) = 10 \log \frac{|p_F(\mathbf{x})|^2}{|p_H(\mathbf{x})|^2} \tag{12}$$

where $p_F$, also called the free field solution, is the result obtained from the free propagation of the monopole, only interacting with the ground when considered, and $p_H$ is the solution in the presence of the green barrier (and the ground). According to simulations, the single- and double-layer hedge barrier behave similarly, see Figs.5 and 6 for both source positions, suggesting that the overall barrier thickness is the driving parameter. A substantial shielding effect, growing with frequency, occurs mainly when the noise source is "inside" the barrier ($y_s = 1$m). Even if not shown in the presented figures, some tests have been performed comparing the JCAH with the classic JCA and the Delany-Bazley-Miki models; the three predict consistent attenuations, with almost identical trends and levels. The trend and the Insertion Loss values achieved in this situation positively compare to the experimental and numerical results shown in [13], where a reduction of around 8-10 dB at 1kHz and 18-30 dB at 10kHz is measured for two different hedges of thickness similar to the one here considered. An even better agreement is seen compared to the single-layer no-ground case, which might be more representative of the experiments cited, where the directivity of the employed acoustic source was intended to avoid the interaction with the soil. The level of match reached is encouraging in terms of validation of the method adopted in the present work for the extrapolation of the equivalent porous medium parameters for the hedges. The presence of the hard terrain introduces some oscillations in the IL graph, typically more severe for the receiver D, closer to the hedge, compatibly to the constructive and destructive interference paths created by the ground reflections. The main reductions in the shielding performance appearing in the IL spectrum are directly correlated to SPL dips in the free field solutions due to the mentioned destructive interference between direct and ground-reflected waves. These effects are intrinsically local in space and, moreover, the presence of a physical delay/attenuation by the ground (*i.e.*, a finite complex-valued ground impedance) in the reflected waves will have a dramatic impact on their importance. As expected, when the monopole source is at the same height as the upper edge of the hedge(s), the noise signal is subject to a less effective shielding effect by the barrier(s), especially for far receivers more also exposed to diffracted sound. However, the predicted attenuations are also remarkable for the less favorable source-receiver positioning, with an average IL of about 10dB.

## 5. Conclusions

The use of natural elements such as hedges and brushes to reduce noise annoyance caused by commercial drone hubs in urban areas has been investigated through a proof-of-concept analysis. An image processing method has been developed to estimate the equivalent porous medium parameters for the evaluation of noise abatement capability of such greenery barriers, allowing the use of the JCAH model. The values obtained for the three driving parameters are in agreement with those present in the literature. The combination of the image processing and JCAH methods, when applied to plants, avoids the need for direct measuring of parameters otherwise hard to be quantified, such as tortuosity, flow resistivity, and the number of leaves. Numerical simulations predict significant noise reductions, growing with frequency up to 10kHz; attenuation around 10dB at 1kHz and up to 30dB from 6kHz and above are obtained. Comparing results from the single- and double-layer designs, it that the driving parameter for the attenuation is the overall thickness of the possibly segmented barrier. Further validations also against experimental results and/or synthetic 3D models are envisaged in the next future for both the porous medium parameters estimation technique and noise reductions from hedges. Furthermore, simulations may be improved by involving more realistic geometries and ground properties, *i.e.* finite complex-valued impedances, at the cost of an increased computational burden.

## References


[1] Straubinger, A, Rothfeld, R, Shamiyeh, M, Büchter, KD, Kaiser, J and Plötner, KO (2020) *An overview of current research and developments in urban air mobility–setting the scene for uam introduction*. Journal of Air Transport Management 87, 101852

[2] Organization, ICA (2008) *Guidance on the balanced approach to aircraft noise management*. Technical report, ICAO

[3] eVTOL news (2022). https://evtol.news/aircraft

[4] Cohen, AP, Shaheen, SA and Farrar, EM (2021) *Urban air mobility: History, ecosystem, market potential, and challenges*. IEEE Transactions on Intelligent Transportation Systems 22(9), 6074–6087

[5] Jung, S and Kim, H (2017) *Analysis of amazon prime air uav delivery service*. Journal of Knowledge Information Technology and Systems 12(2), 253–266. URL http://dx.doi.org/10.34163/jkits.2017.12.2.005

[6] Rajendran, S and Srinivas, S (2020) *Air taxi service for urban mobility: A critical review of recent developments, future challenges, and opportunities*. Transportation research part E: logistics and transportation review 143, 102090

[7] Hasan, S (2019) *Urban air mobility (uam) market study*. Technical report, Crown Consulting, Inc. Washington, DC, United States. URL https://ntrs.nasa.gov/citations/20190026762

[8] Aylor, D (1972) *Noise reduction by vegetation and ground*. The Journal of the Acoustical Society of America 51(1B), 197–205. URL https://doi.org/10.1121/1.1912830

[9] Van Renterghem, T, Botteldooren, D and Verheyen, K (2012) *Road traffic noise shielding by vegetation belts of limited depth*. Journal of Sound and Vibration 331(10), 2404–2425. ISSN 0022-460X. URL https://www.sciencedirect.com/science/article/pii/S0022460X12000260

[10] Horoshenkov, KV, Khan, A and Benkreira, H (2013) *Acoustic properties of low growing plants*. The Journal of the Acoustical Society of America 133(5), 2554–2565. URL https://doi.org/10.1121/1.4798671

[11] D'Alessandro, F, Asdrubali, F and Mencarelli, N (2015) *Experimental evaluation and modelling of the sound absorption properties of plants for indoor acoustic applications*. Building and Environment 94, 913–923. ISSN 0360-1323. URL https://www.sciencedirect.com/science/article/pii/S0360132315300196

[12] Miki, Y (1990) *Acoustical properties of porous materials-generalizations of empirical models-*. Journal of the Acoustical Society of Japan (E) 11(1), 25–28

[13] Horoshenkov, K, Khan, A, Yang, H, Cheal, C, Smyrnowa, J and Kang, J (2012) *In-situ characterization of hedges with a parametric acoustic transducer*. The Journal of the Acoustical Society of America 131(4), 3462–3462. URL https://doi.org/10.1121/1.4709047

[14] *Wingcopter website*. https://wingcopter.com/wingcopter-198#specs. Accessed: 2022-04-29

[15] *Swoop aero receives series a funding to deliver medical goods via drone*. https://dronedj.com/2020/06/24/swoop-aero-receives-series-a-funding-to-deliver-medical-goods-via-drone/. Accessed: 2022-04-29

[16] *Swoop aero website*. https://swoop.aero/kite. Accessed: 2022-04-29

[17] *Wing website*. https://wing.com/how-it-works. Accessed: 2022-04-29

[18] Koiwanit, J (2018) *Analysis of environmental impacts of drone delivery on an online shopping system*. Advances in Climate Change Research 9(3), 201–207. ISSN 1674-9278. URL https://www.sciencedirect.com/science/article/pii/S1674927818300261

[19] Horoshenkov, KV, Hurrell, A and Groby, JP (2019) *A three-parameter analytical model for the acoustical properties of porous media*. The Journal of the Acoustical Society of America 145(4), 2512–2517. URL https://doi.org/10.1121/1.5098778

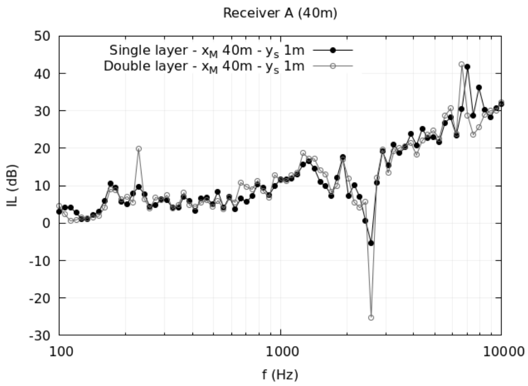


(a) IL at receiver A

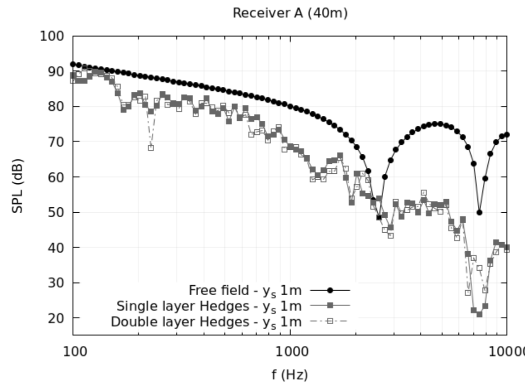


(b) SPL at receiver A

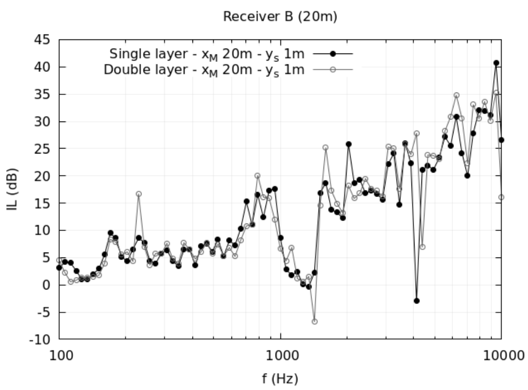


(c) IL at receiver B

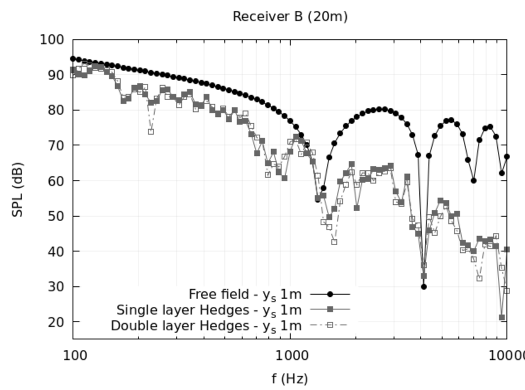


(d) SPL at receiver B

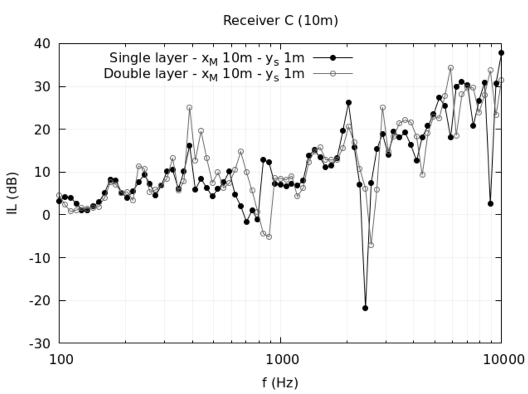


(e) IL at receiver C

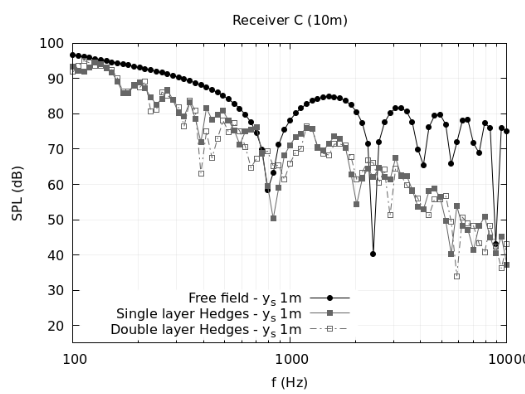


(f) SPL at receiver C

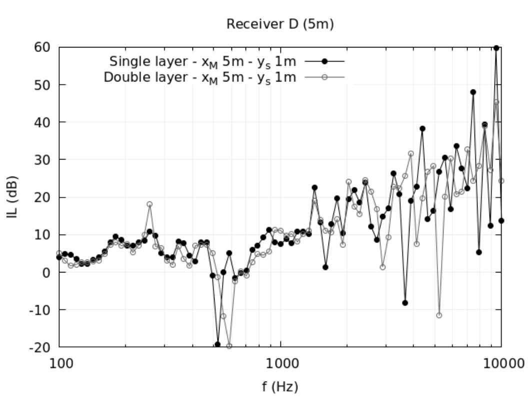


(g) IL at receiver D

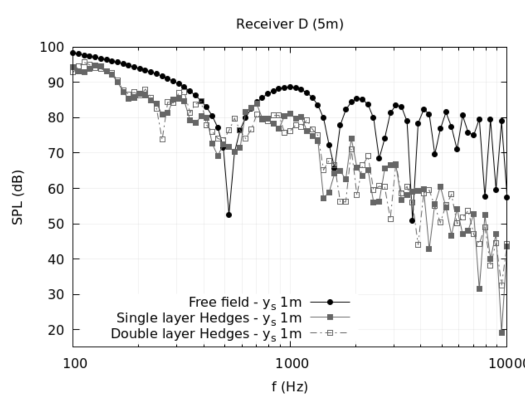


(h) SPL at receiver D

Figure 5: IL and SPL spectra at the virtual receivers, Single vs Double layer design, $y_s = 1m$.

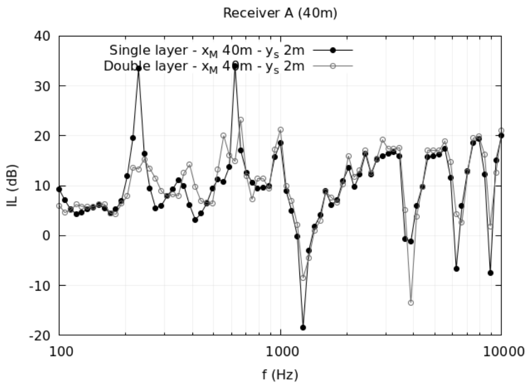


(a) IL at receiver A

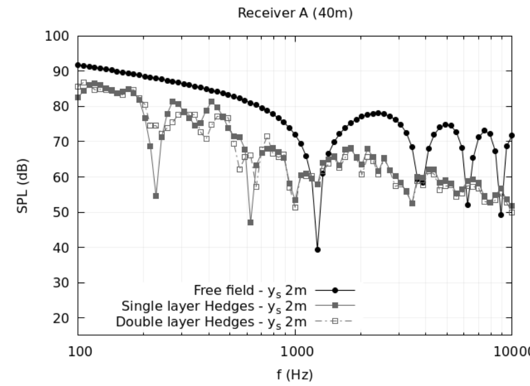


(b) SPL at receiver A

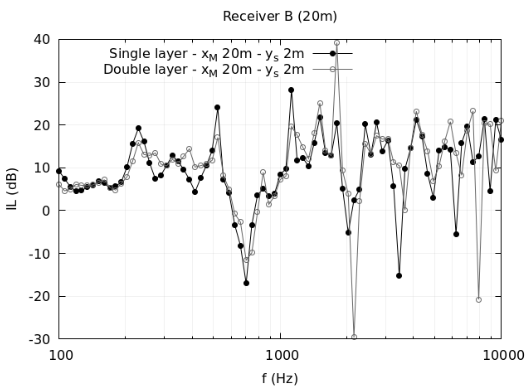


(c) IL at receiver B

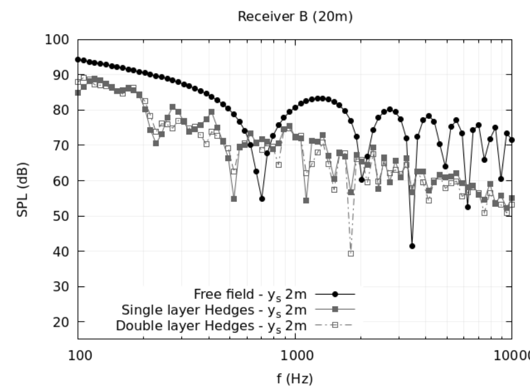


(d) SPL at receiver B

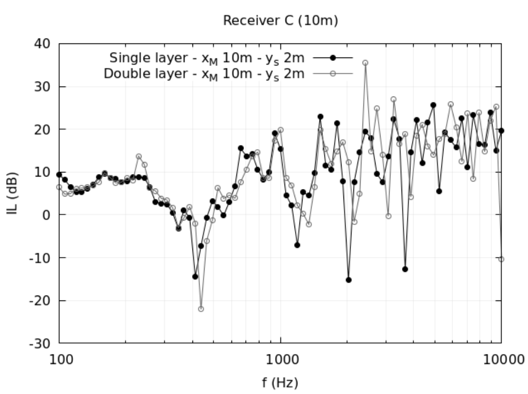


(e) IL at receiver C

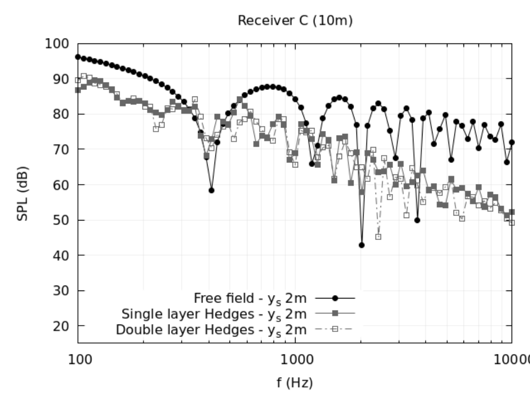


(f) SPL at receiver C

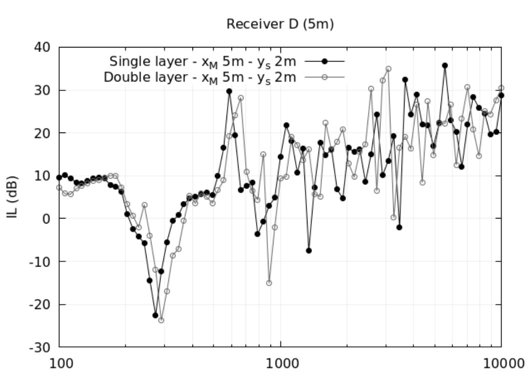


(g) IL at receiver D

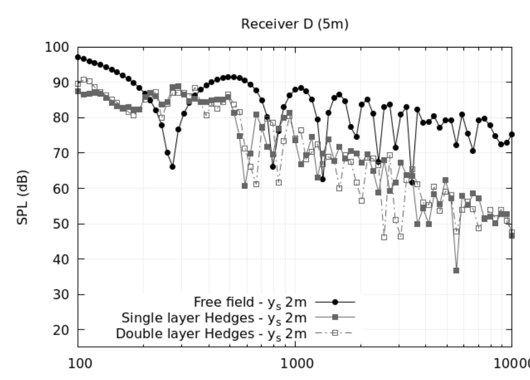


(h) SPL at receiver D

Figure 6: IL and SPL spectra at the virtual receivers, Single vs Double layer design, $y_s = 2m$.

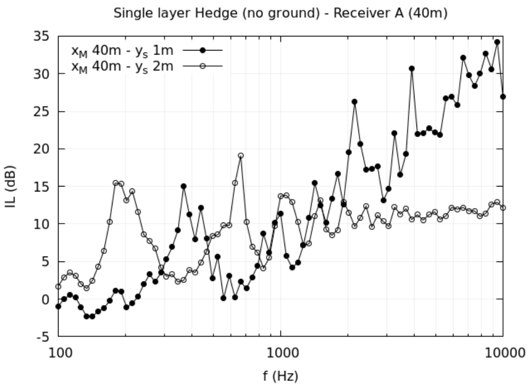


(a) IL at receiver A - no-ground

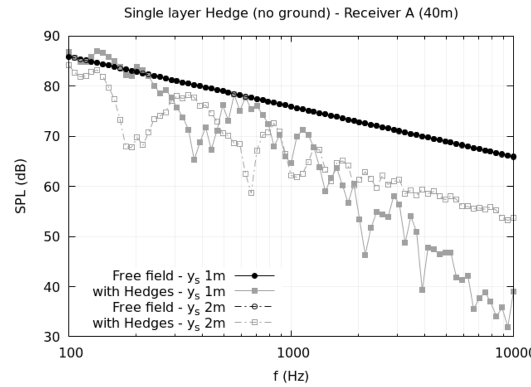


(b) SPL at receiver A - no-ground

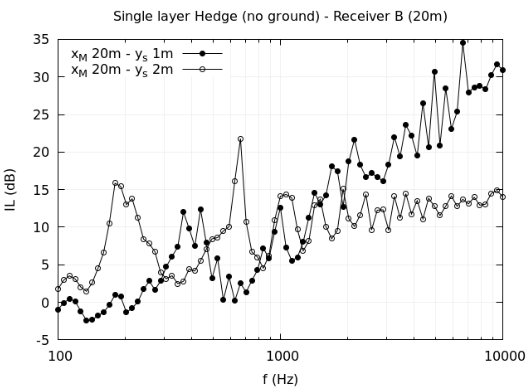


(c) IL at receiver B - no-ground

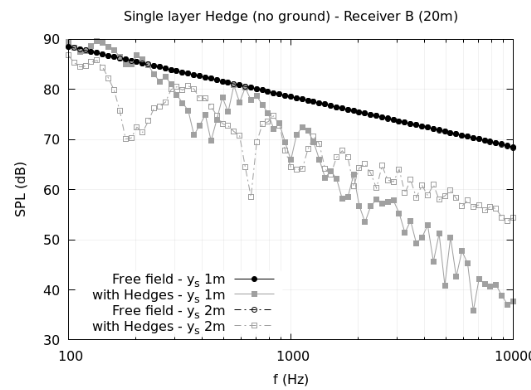


(d) SPL at receiver B - no-ground

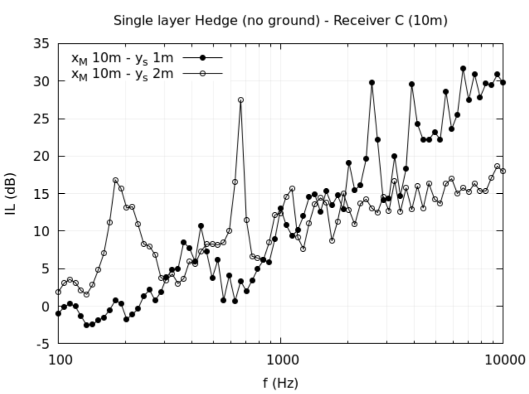


(e) IL at receiver C - no-ground

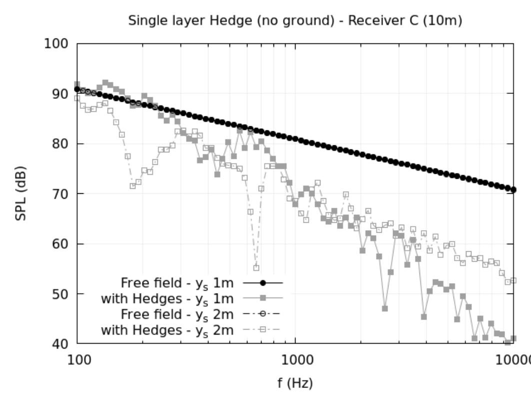


(f) SPL at receiver C - no-ground

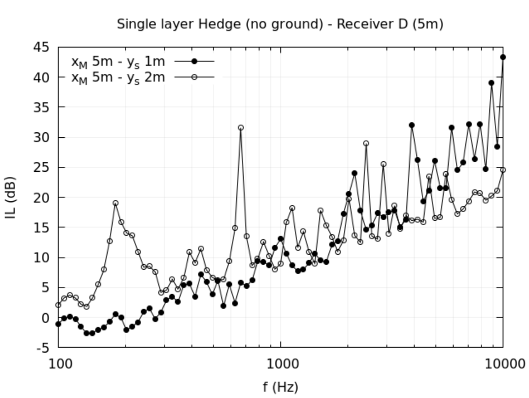


(g) IL at receiver D - no-ground

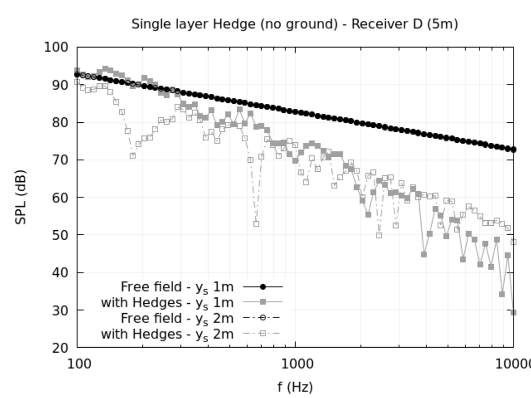


(h) SPL at receiver D - no-ground

Figure 7: IL and SPL spectra at the virtual receivers, Single-layer hedge, no-ground simulations .

QUIET DRONES
Second International e-Symposium
on
UAV/UAS Noise
$27^{th}$ to $30^{th}$ June 2022

# Investigation on lightweight double-leaf cylindrical microperforated-panel structures for motor noise reduction of UAVs

**Yujie Qian,**
**IOT Engineering College, HoHai University, Changzhou, China: 20141923@hhu.edu.cn**
**Jie Zhang,**
**IOT Engineering College, HoHai University, Changzhou, China: 20141931@hhu.edu.cn.**

## Summary

With the ongoing proliferation of unmanned aerial vehicle (UAVs) which usually operate in close proximity to dense populations, their noise is attracting more and more attention and may become great limiting factor for the public acceptability of their operations in urban areas. Although the noise of an electric powered UAV mainly comes from the motors and propellers, previous studies have paid more attention to propeller noise reduction, while neglecting the role of the motors. For this, on the basis of the authors' prophase work related, a noise reduction technique based on lightweight double-leaf cylindrical microperforated-panel (CDMPP) structures is further developed and explored for noise reduction of UAV motors in this paper. Firstly, the theoretical methods for calculating the transmission loss of an CDMPP based on equivalent circuit model are provided. And based on this model, the difference between metallic and non-metallic CDMPP is discussed. Then a case study is performed to evaluate the noise reduction performance and the heat dissipation performance of the proposed CDMPPs for a DC motor of UAVs at different rotating speeds. Results show that our CDMPP is of potential to insulate motor noise at frequency range from 1 kHz to 8 kHz without leading to significant temperature increase.

## 1. Introduction

UAVs are of significant potential for a number of applications such as parcel delivery, monitoring, and surveillance [1-4], which are regarded as a more efficient way to deliver goods than traditional delivery by truck [5]. However, due to their operation in closer proximity to dense populations than other types of aerial vehicles, their noise has led to important public concerns and is considered as a significant limiting factor for the public acceptability of UAV operations in urban areas [6]. Moreover, a recent study shows that the noise of UAVs maybe more annoying than the trucks under the same A-weighted Sound Exposure Level (SELA) [7]. Although a lot of research have been devoted to reducing UAV noise [8-10], most of them are focused on propeller noise with the motor noise being paid so little attention despite of their contribution to the tonal noise (which is considered as an annoying spectrum feature of UAV noise) [11] and total noise level of UAVs [12].

Compared to active noise reduction technology, passive noise reduction technology may be more beneficial to UAVs because of the low cost, simplicity and easy carrying out. Hence in one of our previous study, a passive noise reduction technology based on a single-layer microperforated panel (MPP) (which is regarded as the most promising next-generation absorption material) with and without sound-proof materials for UAV motor has been experimentally investigated [13], Results indicate that a single-layer MPP backed by sound-proof materials (e.g. felt and fibre) does better in overall noise level reduction for a motor than a single-layer MPP with an air cavity behind. However, sound-proof materials may greatly impede the heat dissipation of rotating motor. In fact, compared to a single-layer MPP, it has been proved that a compound double-leaf MPPs with two MPPs arranged in a tandem array have more potential in noise reduction [14]. However, regarding these traditional MPP structures, a rigid backing is usually required. When it comes to UAV motor noise reduction, a rigid backing may be difficult to implement. To remove the limitation of rigid backing and create an absorbing structure without a rigid back wall, Sakagami et al. [15,16] have proposed a double-leaf MPP (DLMPP) absorber, which consists solely of two MPPs without the need of backing wall. Therefore, inspired by Sakagami et al., a lightweight cylindrical double-leaf MPP (CDMPP) structure is proposed and a pilot study on their noise reduction of an UAV motor is initiated in this paper. It is worth noting that one main difference between the current study of CDMPP and the previous study of DLMPP is that this paper focus on the sound insulation performance of CDMPP, whereas the previous study focuses on the absorption performance of DLMPP. Besides this, there are two more concerns for the proposed CDMPP structures in this study: one is that it should be lightweight enough without adding significantly to the UAV's weight since it is weight-sensitive; the other is that it should have good heat dissipation without leading to great temperature rise of UAV motor. Because excessive temperature may have disadvantage effect on both the function and the useful lifespan of the motors.

The present paper is organized as follows. In section 2, the noise reduction performance model in terms of transmission loss of lightweight CDMPP structures is established using the equivalent circuit method. Based on the established model, the difference of the transmission loss between metallic and non-metallic CDMPP is numerically discussed in section 3. Then the proposed CDMPP structure for noise reduction of a brushless DC motor is experimentally tested and their dissipation performance is evaluated in section 4. Finally, concluding remarks are presented in section 5.

## 2. Transmission loss model

To investigate the sound insulation performance of a lightweight CDMPP structure, an analytical model based on the equivalent circuit method to calculate the transmission loss through the structure with an infinite extent is introduced in this section. Fig. 1 shows an idealized arrangement of a CDMPP. Cylindrical MPP1 and MPP2 are placed in parallel with an air-cavity of depth $D$ between them. A sound wave of unit pressure amplitude is assumed to be normally incident upon MPP1 with the source of noise located in the center of the cylinder. The MPP is assumed to be thin and lightweight enough to enable panel-type (or membrane-type) resonance under sound loading. By using electro-acoustic analogy, the acoustic impedance of such a system can be obtained. Basically, the mass-resistance element consists of the MPP and the apertures being connected in parallel. And the mass-resistance elements of MPP1 and MPP2 are coupled through the cavity reactance of the air space. This CDMPP can thus be described by the equivalent electrical circuit model shown in Fig. 2, where $R_P$ and $M_P$ are the specific acoustic resistance and reactance of the panel, respectively; $R_L$ and $M_L$ are the specific acoustic resistance and reactance of the apertures, respectively; the sound wave impinging on the structure is equivalent to a source of sound pressure 2p as produced on the rigid wall and characteristic impedance $\rho c$ as that of air with $\rho$ the air density and $c$ the sound speed in air; $Z_D$ is the impedance of the air cavity.

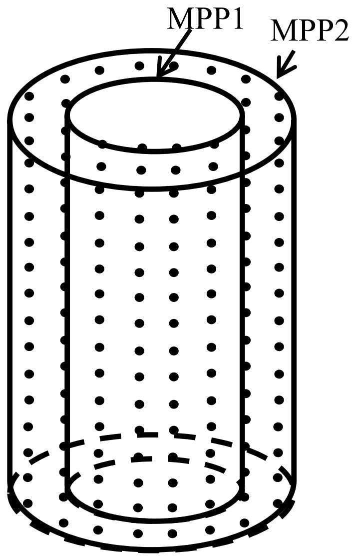


Fig. 1. Model of a CDMPP for theoretical analyses

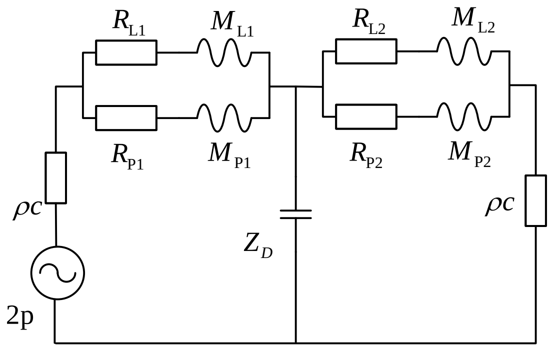


Fig. 2. Electro-acoustical equivalent circuit of a thin CDMPP

Based on the equivalent electrical circuit in Fig. 2, the overall acoustic impedance $Z_{\mathrm{total}}$ of the CDMPP at the surface of MPP1 is given by

$$Z_{\mathrm{total}} = Z_1 + \left(\frac{1}{Z_{\mathrm{D}}} + \frac{1}{Z_2 + \rho c}\right)^{-1} \tag{1}$$

with

$$Z_{1,2} = \left(\frac{1}{Z_{\mathrm{P}1,2}} + \frac{1}{Z_{\mathrm{L}1,2}}\right)^{-1} \tag{2}$$

$$Z_{\mathrm{P}1,2} = R_{\mathrm{P}1,2} + j\omega M_{\mathrm{P}1,2} \tag{3}$$

$$Z_{\mathrm{L}1,2} = R_{\mathrm{L}1,2} + j\omega M_{\mathrm{L}1,2} \tag{4}$$

$$Z_{\mathrm{D}} = -j\rho c \operatorname{ctg}(\omega D / c) \tag{5}$$

Where $\omega=2\pi f$, $f$ is the frequency (Hz). The subscripts 1 and 2 denote association with MPP1 and MPP2, respectively. Consider the normal specific acoustic impedance of the panel normalized by $\rho c$ firstly, which can be calculated by

$$z_{\mathrm{P}} = \frac{R_{\mathrm{P}} + j\omega M_{\mathrm{P}}}{\rho c} = r_{\mathrm{P}} + j\omega m_{\mathrm{P}} \tag{6}$$

Where $r_{\mathrm{P}}$ is the normalized specific acoustic resistance of the panel depending mainly on mounting conditions; $m_{\mathrm{P}}=M_{\mathrm{P}}/\rho c$, $M_{\mathrm{P}}$ is the surface density of the panel (kg/m$^2$). Consider secondly the normal normalized specific acoustic impedance of the apertures, which can be calculated by

$$z_{\mathrm{L}}=\frac{R_{\mathrm{L}}+j\omega M_{\mathrm{L}}}{\rho c}=r_{\mathrm{L}}+j\omega m_{\mathrm{L}} \tag{7}$$

with

$$r_{\mathrm{L}}=\frac{\mathrm{g}_1 t}{\sigma d^2}k_r,\ k_r=\sqrt{1+\frac{k^2}{32}}+\frac{\sqrt{2}k}{8}\frac{d}{t} \tag{8}$$

$$m_{\mathrm{L}}=\frac{0.294\times10^{-3}t}{\sigma}k_m,\ k_m=1+1/\sqrt{3^2+\frac{k^2}{2}}+0.85\frac{d}{t} \tag{9}$$

$$k=\mathrm{g}_2 d\sqrt{f} \tag{10}$$

where $t$ is the panel thickness, $d$ is the perforation diameter, $\sigma$ is the perforation ratio of the panel (the ratio of surface area of the perforations to the total surface area of the panel), $k$ is the MPP*'s* constant. For a metallic material, $g_1$=0.335 and $g_2$=0.21. For a non-metallic material, $g_1$=0.147 and $g_2$=0.316. The normalized specific acoustic impedance of the air cavity between the two leaves is calculated by

$$z_{\mathrm{D}}=-j\mathrm{ctg}(\omega D/c) \tag{11}$$

Then the total normalized acoustic impedance of an CDMPP can be given by

$$z_{\mathrm{total}}=\left(\frac{1}{z_{\mathrm{P1}}}+\frac{1}{z_{\mathrm{L1}}}\right)^{-1}+\left(\frac{1}{z_{\mathrm{D}}}+\frac{1}{\left(\frac{1}{z_{\mathrm{P2}}}+\frac{1}{z_{\mathrm{L2}}}\right)^{-1}+1}\right)^{-1} \tag{12}$$

The sound transmission coefficient, $\tau$, is given by the power consumed at the resistor $\rho c$ behind the MPP2 [15], which is calculated by

$$\tau=\left|\frac{2}{z_{\mathrm{total}}+1}\frac{z_{\mathrm{total}}-\left(\frac{1}{z_{\mathrm{P1}}}+\frac{1}{z_{\mathrm{L1}}}\right)^{-1}}{\left(\frac{1}{z_{\mathrm{P2}}}+\frac{1}{z_{\mathrm{L2}}}\right)^{-1}+1}\right|^2 \tag{13}$$

The normal transmission loss can be given by

$$TL=10\log\left(\frac{1}{\tau}\right) \tag{14}$$

## 3. Influence of material type

Numerical examples of the calculated results are shown in order to discuss the sound insulation performance of a typical CDMPP structure made of metallic materials and non-metallic materials, respectively.

Fig. 3 shows the calculated results of the transmission loss under normal incidence and a cavity depth of 50 mm. The parameters of aluminum MPP1 and MPP2 are an aperture diameter of 0.3 mm, 3 mm distance between the apertures, a 0.785% perforation ratio, 0.1 mm thickness, 2700 kg/m$^3$ density. The PVC MPP1 and MPP2 has identical structure parameters as aluminum ones, except for the density, which is 1380 kg/m$^3$. It can be seen from Fig. 3 that the sound insulation performance of the proposed CDMPP structure is not very good below 1000 Hz. But the peaks emerge around the antiresonance frequency from 1.7 to 16 kHz which improve the transmission loss. The dips around 4 kHz and 14 kHz are due to the cavity resonances which occur at around the corresponding acoustic wavelength of $n\lambda$ = 2D with $n$ is any non-zero positive integer [17]. Also interesting is that the metallic CDMPP is slightly different from its non-metallic counterpart in terms of transmission loss although with identical structure parameters except for the density. To make it clear that whether such difference is simply caused by the different densities rather than material type, we assume that there being non-metallic and metallic CDMPPs have the same structure parameters and density with each other. Their calculated transmission loss is shown in Fig. 4. It shows that the density is not the only factor that causes the difference in transmission loss between the metallic and non-metallic

CDMPPs. It is reasonable since for metallic materials the energy dissipated by heat conduction should also be considered.

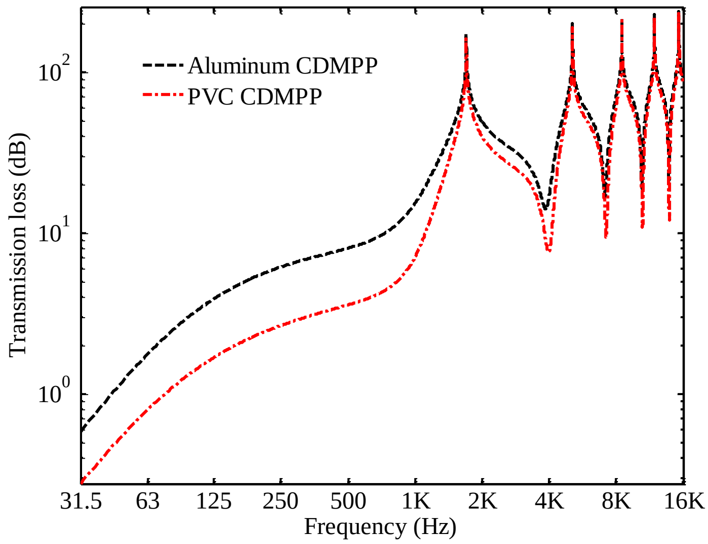


Fig. 3. Calculated transmission loss of the proposed CDMPP of different materials with different density

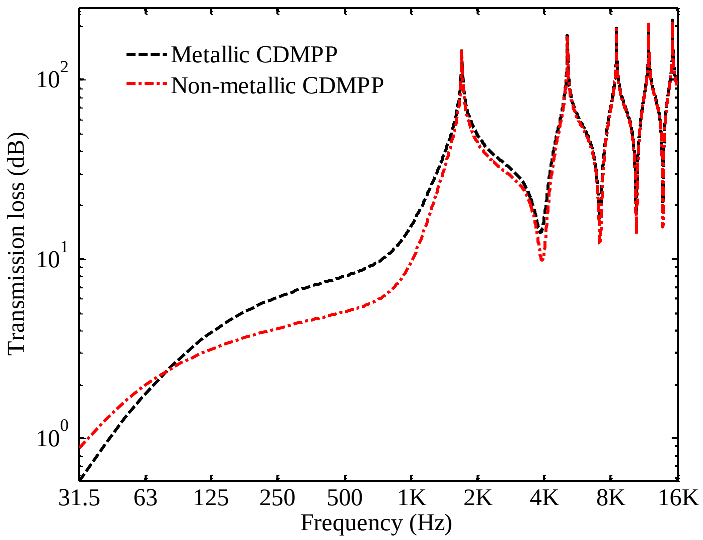


Fig. 4. Calculated transmission loss of the proposed CDMPP of different materials with identical density

# 4. Case study

## 4.1 Sound insulation performance

The sound insulation performance of the proposed CDMPP structures with different structure parameters for a DC motor that is usually used in unmanned aerial vehicles (UAVs) are tested experimentally in this section. The aluminum is adopted for the tested specimen because it not only has good heat conduction, but also it is lightweight compared to other metallic materials. The parameters of the tested specimens are shown in Tab. 1, where $d_1$, $t_1$ and $b_1$ are the hole diameter, panel thickness and distance between adjacent holes of MPP1, respectively; $d_2$, $t_2$ and $b_2$ are the hole diameter, panel thickness and distance between adjacent holes of MPP2, respectively; and $D$ is the cavity depth between MPP1 and MPP2. One of the pictures of specimen #2 is shown in Fig. 5. The experimental setup is the same as our previous study [13], as shown in Fig.6.

Tab.1. The material and structural parameters of CDMPPs

| Specimen | Material | $d_1$(mm) | $d_2$(mm) | $t_1$(mm) | $t_2$(mm) | $b_1$(mm) | $b_2$(mm) | $D$ (mm) |
|---|---|---|---|---|---|---|---|---|
| #1 | Aluminium | 0.1 | 0.1 | 0.1 | 0.1 | 1 | 1 | 10 |
| #2 | Aluminium | 0.3 | 0.3 | 0.1 | 0.1 | 3 | 3 | 10 |
| #3 | Aluminium | 0.5 | 0.5 | 0.1 | 0.1 | 5 | 5 | 10 |

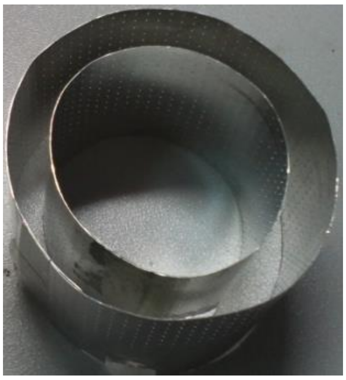

Fig. 5. An example of the experimental specimen

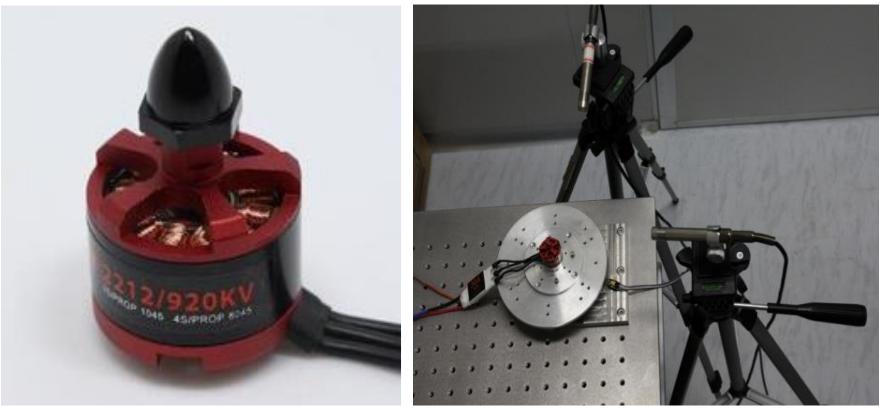


(a) DC motor (b) Testing platform

Fig. 6. A small DC motor and its noise testing platform

The test results at different rotating speeds of 3000 r/min, 4000 r/min, 5000 r/min, 6000 r/min, 7000 r/min and 8000 r/min are ploted with the 1/3-octave bands in Fig. 7. As shown, under different rotating speeds, the noise reduction performance of the proposed CDMPP is undesirable below 1000 Hz, which conforms with the numerical findings in section 3. However, at a frequency range from 1 to 8 kHz, the CDMPP exhibits relatively good sound insulation performance. On the whole our proposed CDMPP has potential to be used as a sound insulation barrier that can meet needs of simple structure and light weight.

### 4.2 Heat dissipation performance

As mentioned earlier, apart from sound insulation performance, the heat dissipation performance of the proposed CDMPP structures is another important concern for UAV motor. For evaluating the heat dissipation, the rise in motor temperature with and without CDMPP specimens are tested at the rotating speed of 6000 r/min, as shown in Fig. 8. It can be seen that the maximum temperature of the rotating motor with surrounded CDMPPs of different structure parameters are not significantly different, which are approximately 47.2 ℃. And compared to motor without the CDMPP structures, its maximum temperature reaches approximately 45.1℃, which means that the proposed CDMPP doesn't result in a significant rise in temperature of motor.

## 5. Conclusions

A lightweight cylindrical double-leaf micro-perforated panel (CDMPP) structure is presented and investigated for noise reduction of UAV motor in this paper. Firstly, the difference in the transmission loss between metallic and non-metallic CDMPPs is discussed based on the established transmission loss model of CDMPPs. It shows that the metallic CDMPP outperforms the nonmetallic CDMPP in terms of sound insulation performance. Then to evaluate the noise reduction performance and the heat dissipation performance of the proposed CDMPP structure for a UAV motor, a case study is performed in which

CDMPPs are adopted. Results show that the noise reduction performance of the proposed CDMPPs are undesirable below 1000 Hz for motor noise at different rotating speeds, however they exhibit good performance to insulate motor noise at frequency range from 1 kHz to 8 kHz; regarding heat dissipation, results show that the proposed CDMPPs won't cause significant temperature rise for rotating motor. In summary, CDMPPs are of potential to insulate motor noise.

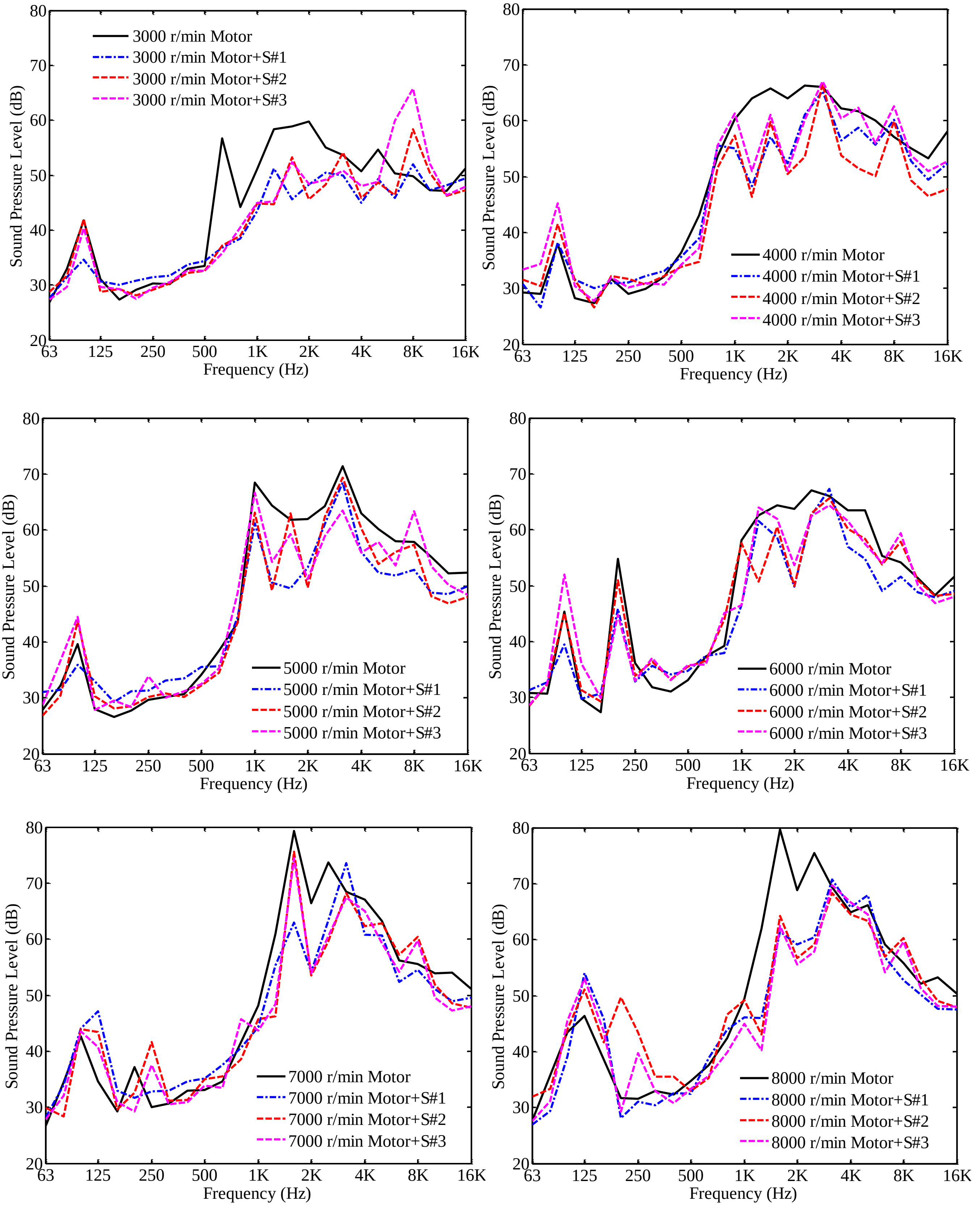


Fig. 7. Experiments of noise reduction performance of CDMPPs with different parameters

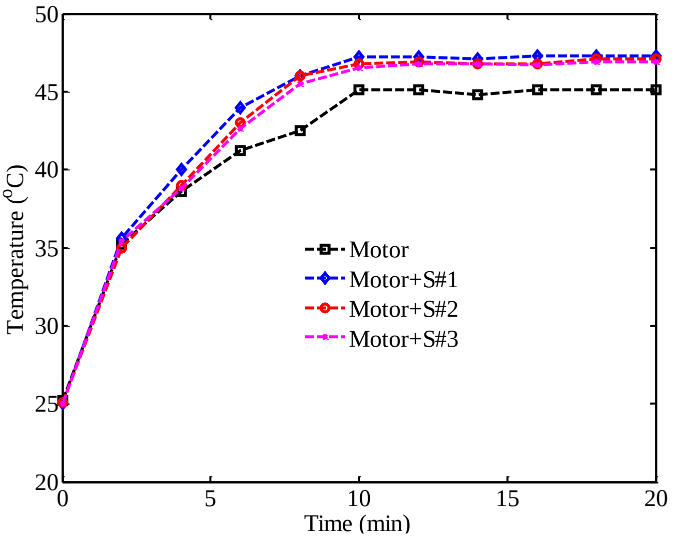

Fig. 8. Comparison of changes in temperature of motor with and without CDMPP specimens

**Acknowledgement**

This research was supported by the Fundamental Research Funds for the Central Universities (No. B210202084) and Changzhou Foundation of Science and Technology (No. CJ20210144).

## References

[1] S. Hayat, E. Yanmaz and R. Muzaffar (2016), Survey on Unmanned Aerial Vehicle Networks for Civil Applications: A Communications Viewpoint. IEEE Communications Surveys & Tutorials 18(4), 2624-2661.

[2] S. Sreenath, H. Malik, et al. (2020), Assessment and Use of Unmanned Aerial Vehicle for Civil Structural Health Monitoring, Procedia Computer Science 170, 656-663.

[3] X. Li, N. Levin, J.L. Xie, D.R. Li (2020), Monitoring hourly night-time light by an unmanned aerial vehicle and its implications to satellite remote sensing. Remote Sensing of Environment 247, 1-20.

[4] S. Sawadsitang, D. Niyato, P. Tan and P. Wang (2019), Joint Ground and Aerial Package Delivery Services: A Stochastic Optimization Approach. IEEE Transactions on Intelligent Transportation Systems 20(6), 2241-2254.

[5] W. Yoo, E. Yu and J. Jung (2018), Drone delivery: Factors affecting the public's attitude and intention to adopt. Telematics and Informatics 35, 1687-1700.

[6] C. R. Theodore (2018), A summary of the NASA Design Environment for Novel Vertical Lift Vehicles (DELIVER) project. In: Proceedings of the AHS International Technical Conference on Aeromechanics Design for Transformative Vertical Flight 2018, San Francisco, CA, USA.

[7] A. Christian and R. Cabell (2017), Initial investigation into the psychoacoustic properties of small unmanned aerial system noise. In: Proceedings of the 17th AIAA Aviation Technology, Integration, and Operations Conference (AVIATION 2017), Denver, CO, USA.

[11] S. Z. Nikolas, C. Randolph (2018), A Summary of NASA Research Exploring the Acoustics of Small Unmanned Aerial Systems. AHS Specialists' Conference on Aeromechanics Design for Transformative Vertical Flight.

[12] R. S. McKay, M. J. Kingan (2018), Multi-rotor unmanned aerial system noise: Quantifying the motor's contribution. XXIVth Biennial Conference of the Acoustical Society of New Zealand, Auckland, New Zealand, 12-14 November 2018.

[13] Y.J. Qian, Y.L. Wei, D.Y. Kong, H. Xu (2021), Experimental investigation on motor noise reduction of Unmanned Aerial Vehicles. Appl Acoust 176, 1-6.

[14] D. Y. Maa (1987), Microperforated panel wide-band absorber. Noise Control Eng. J. 29, 77–84.

[15] K. Sakagami, M. Morimoto, W. Koike (2006), A numerical study of double leaf microperforated panel absorbers, Appl Acoust 67, 609–619.
[16] K. Sakagami, T. Nakamori, et. al. (2009), Double-leaf microperforated panel space absorbers: A revised theory and detailed analysis. Appl Acoust 70(5), 703-709.
[17] T. Dupont, G. Pavic, B. Laulagnet (2003), Acoustic properties of lightweight micro-perforated plate systems. Acta Acustica/ Acustica 89(2), 201–212.

QUIET DRONES
Second International e-Symposium
on
UAV/UAS Noise
27th to 30th June 2022

# Estimation of noise exposure due to drone operations.

**Carlos Ramos-Romero - Acoustics Research Centre, University of Salford, M5 4WT, UK: C.A.RamosRomero@salford.ac.uk**
**Nathan Green - Acoustics Research Centre, University of Salford, M5 4WT, UK: N.Green7@edu.salford.ac.uk**
**Seth Roberts - Hayes McKenzie Partnership Ltd, Unit 3 Oakridge Office Park, Salisbury SP5 3HT, UK: seth@hayesmckenzie.co.uk**
**Charlotte Clark - Population Health Research Institute, St George's University of London, SW17 0RE, UK: chclark@sgul.ac.uk**
**Antonio J. Torija - Acoustics Research Centre, University of Salford, M5 4WT, UK: A.J.TorijaMartinez@salford.ac.uk**

## Summary

Drone operations have significantly grown during the last few years and are expected to inundate our skies with innovative aerial transportation projects. If this scenario materialises, drones will become an important source of environmental noise pollution. Although substantial investigation has been carried out to develop our understanding of the sound source generation mechanisms and noise reduction technologies for drones, still there are important questions regarding the requirements for operational procedures and regulatory framework.

An important issue is that drones operate closer to communities, owing to the lower operating altitudes, than conventional aircraft or rotorcraft. In addition, the noise produced is highly tonal and with important high-frequency content which may cause significant impacts on exposed communities, due to adverse effects such sleep disturbance.

This paper presents the results of the estimation of the maximum A-weighted Sound Pressure Level $LA_{max}$ and Sound Exposure Level $SEL$ as received in typical indoor residential environments. To do this, a series of drone sounds recorded during in-situ operations in free field have been filtered to simulate the external to internal transmission loss associated with sound propagation through a typical partition which includes a standard glazing configuration.

This estimation of drone noise exposure indoors is highly relevant to inform operational constraints, such as the optimal distance to minimise noise annoyance and sleep disturbance.

## 1. Introduction

One of the most important changes in urban mobility is the rapid expansion of Unmanned Aerial Vehicles (UAVs) - also known as drones, which is a sector for some daily activities, such as delivery, blue light services, photography and research. Although these new vehicles can bring substantial economic, environmental, and social benefits, they are also new and unconventional sound sources which operate at closer distances to communities than other traditional noise sources e.g., standard aircraft or road traffic noise.

Some of the recommended noise levels for conventional urban noise sources are based on existing evidence derived from the effects of other sources of transportation noise on sleep quality and well-being (Basner & McGuire, 2018). As discussed by Torija and Clark (2021), it is uncertain whether the current noise metrics, evidence on human response to transportation noise and regulation are appropriate for the specific case of drone noise. Among other research gaps, Torija and Clark (2021) state that traditional research is needed to define acceptable levels for drones; and to inform best operational practices for drones with regard to noise profiles.

Although drone noise has specific characteristics unlike other sources of noise people are familiar with, they are probably not accounted for current noise metrics (e.g., large content of complex tonal noise, substantial content of high frequency noise) (Torija & Nicholls, 2022), this paper will assess noise requirements for drone operations on the basis of $LA_{max}$ and $SEL$ metrics. The noise criteria considered within this research are based on WHO guidelines, i.e., the noise levels recommendations for “Sleep Quality – Waking up in the night and/or too early in the morning” (Hurtley, 2009).

This paper presents a modelling framework to recommend a minimum operational distance between the drone and the façade to ensure low noise impact on receivers in residential properties. The modelling framework accounts for the drone noise characteristics, operational variables such as velocity and distance from receivers, factors affecting drone sound propagation (outdoors) and factors affecting the sound transmission through the façade (outdoors-to-indoor). Once all these parameters are known, and the specific noise target (to minimize impact on residents’ health and well-being) has been set, the framework calculates the recommended minimum distance between the drone and the residential property’s façade.

## 2. Drone Sound Signals

A number of different flying operations for different types of UAVs were recorded and reported within free-field conditions by Read et al. (2020). From the referenced report, the analysed signal corresponds to flying over operations at high horizontal vehicle speed. From this database it was possible to analyse the acoustical footprint of the drones’ sound events by 1/3 octave band [Hz].

Figure 1 (left) describes the measurement setup with the inverted ground microphone located at 150 feet ($height \sim 47.5$ m) below the drone flightpath. From the $LA_{max}$ amplitude registered during the one of the flying over procedure executed by the drone model Yuneec Typhoon Figure 1 (right) ($speed{\sim}12.5\ \mathrm{m}/s$), it is possible to visualize the noise emission, with important content in the low frequency range (due to the fundamental frequencies of the rotors), mid frequency ( due to high harmonics of the rotors' fundamental frequencies), and high frequencies (due to electric motor noise) (Torija et al., 2019).

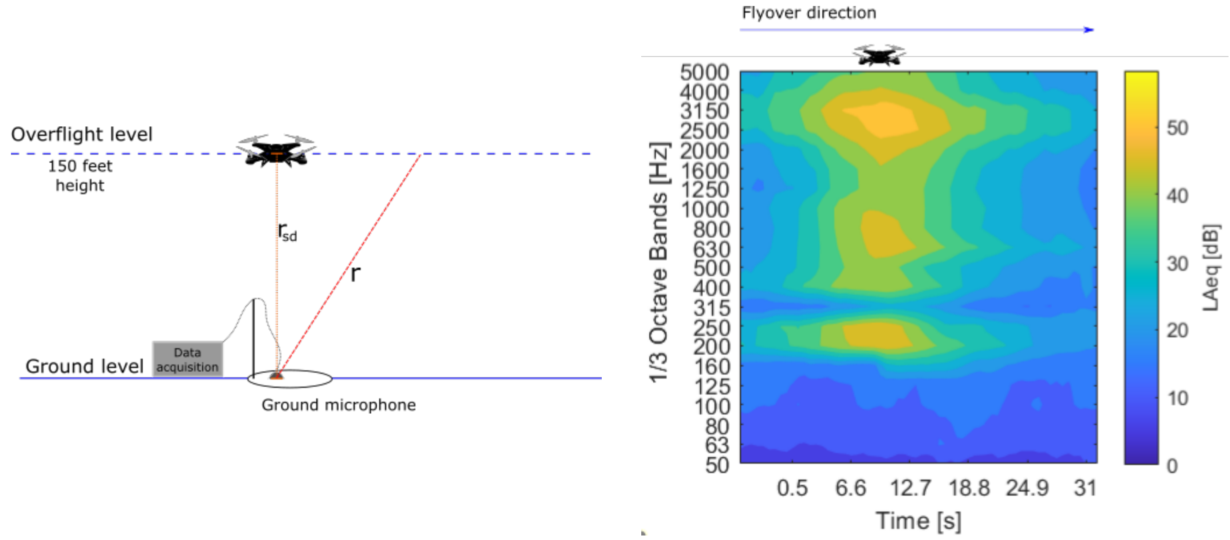

Figure 1. Experimental setup (Read et al., 2020) (left) and flyover noise footprint (right).

From a noise perception point of view, an interesting phenomenon can occur when a given maximum drone noise emission footprint (tonal components) coincides in the frequency range where the Apparent Sound Reduction Index $R'$ of a façade-window configuration is lowest, i.e., at the resonance and coincidence frequencies. This effect is depicted by the tonal components at low ($\sim 250\ Hz$) and high frequency ($\sim 4000\ Hz$) of the Figure 1 (right), and the $R'$ reported for a window configuration in the Figure 2.

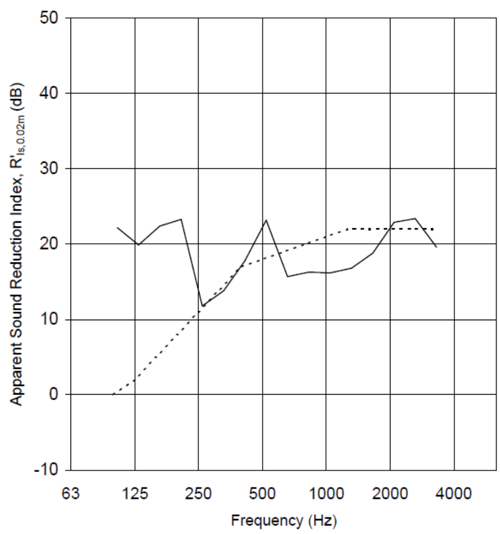

Figure 2. Measured $R'$ of a 70 mm PVC-U bottom hung inward tilt window 4-16-4 mm.
Non-diffuse source field to replicated domestic environment.
Reported by Waters-Fuller and Lurcock (2007).

## 3. Drone Noise Modelling Framework

The modelling framework for the estimation of the noise metrics inside the receiver room and the approach for setting drone operation constrains are presented in Figure 3.

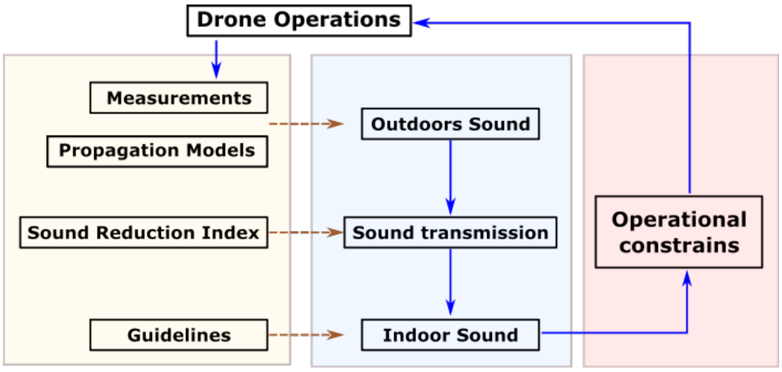

Figure 3. Framework for the application of noise annoyance guidelines to the drone operations.

Using the process outlined in the flowchart above, the indoor sound levels can be estimated from the drone noise (generated outside during the flying operation) by simulating the transmission loss during the propagation from drone to the façade, and then during the transmission external to the façade into the receiver room. Once the sound levels indoors are estimated, the drone operational constrains can be set to comply with the guidelines of noise exposure on the receiver side, for instance in terms of Drone/façade distance.

### 3.1 Outdoor Sound

The sound levels at outdoors are a function of the environmental conditions and flight manoeuvres and can be obtained by actual measurements either on-field or in-laboratory conditions, or even by sound emission and propagation models.

From the reviewed measuring campaigns (Read et al., 2020), it is possible to obtain data of actual sound levels from a group of drones at the microphone distances $r$. Some of the usual drone operations have been explored, such as flyover, take-off, landing and hovering. The drone noise database available provides the sound pressure levels only at distances equal or longer to the Slant distance $r_{sd}$ (straight line between the microphone and the sound source), see Figure 1.

From the data available, the sound pressure levels at shorter distances can be estimated implementing state-of-the-art sound propagation models, which are described below. It is important to note that the sound propagation models can be applied to estimate the sound level at any distance needed in the analysis.

There are several acoustics considerations for a comprehensive model of sound propagation, they can be expressed in the generic Eq. 1; where $L_p$ is the sound pressure level in terms of the sound power level $L_w$ and the combination of modifying factors $A_i$ that attenuate or increase the transmission of sound energy during its propagation from the source to the receiver (Kapoor et al., 2018).

$$L_p = L_w + \Sigma_i A_i \qquad \text{Eq. 1}$$

For this paper, a simplified model was applied with the distance $r$ and atmospheric sound absorption coefficient $\alpha$ as the principal contributors to estimate sound levels at shorter drone operation distances (Eq. 2).

$$L_p(r, \alpha) = L_w + A_r + A_{\alpha,r} \qquad \text{Eq. 2}$$

The measured sound level $L_m$ at a reference distance $r_m = r_{sd}$ from the drone includes the effect of the mentioned contributors (Eq. 3).

$$L_m = L_w + A_{r_m} + A_{\alpha,r_m} \qquad \text{Eq. 3}$$

Therefore, for other values of distance usually higher than to $1m$ to reduce the effects of the near field (Hansen, 2001), the sound pressure level at different distance $r$ could be obtained by the Eq. 4.

$$L_p(r) = L_m - 20\log_{10}\left(\frac{r}{r_m}\right) - L_{atm} \qquad \text{Eq. 4}$$

The effect on the sound levels where due the atmospheric sound absorption $L_{atm}$ was included by the Eq. 5, where $\alpha$ is the attenuation coefficient for air absorption, which is remarkable at high frequencies (Kapoor et al., 2021; Kinsler et al., 2000).

$$L_{atm} = 10\log_{10} e^{2\alpha r} \qquad \text{Eq. 5}$$

Furthermore, once the maximum sound level $LA_{max}$ has been determined, it would be possible to estimate the sound exposure level $SEL$ with an effective time $t_e$ by the Eq. 6 (Kapoor et al., 2021). A graphical relation between $LA_{max}$ and $SEL$ is depicted in the Figure 4 (Min et al., 2015).

$$SEL = LA_{max} + 10\log_{10}\left(\frac{t_e}{t_0}\right); t_0 = 1s. \qquad \text{Eq. 6}$$

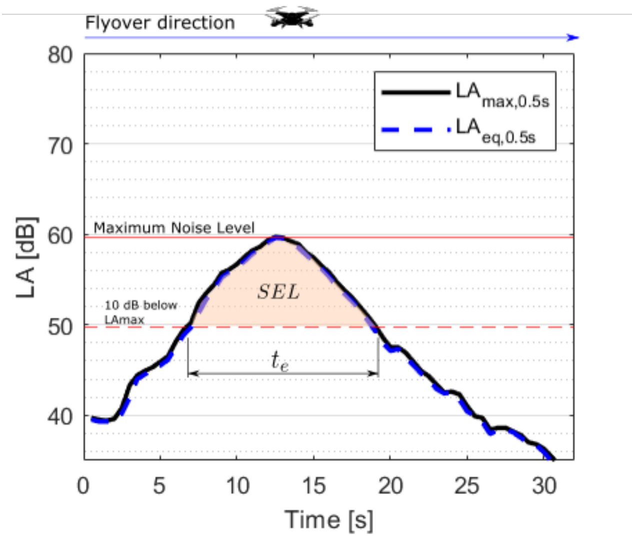


Figure 4. Overall sound level values during a flyover.

From Figure 4, the recorded noise amplitude shows a stable sound signal during the flyover, i.e., the amplitudes of $LA_{max}$ and $LA_{eq}$ registered each $0.5\ second$ remains almost equals during this particular operation. This effect may not always be present in other flight operations with possible sudden amplitude fluctuation due to changes in rotors' thrust for specific manoeuvres.

### 3.2 Sound Transmission

The next step is to incorporate the effects of the sound attenuation through the façade of a building, in this example a typical residential façade configuration has been assumed. The transmission loss due the façade could be estimated by either experimental methods or constructive solutions modelling.

The Sound Reduction Index $R$ (Eq. 7) compares the average sound levels between two rooms. i.e., the source $L_S$ and receiving $L_R$; also considering the surface $S$ of the partition and the sound absorption provided by the interior of the receiving room $A_R$.

$$R = L_S - L_R + 10\log_{10}\left(\frac{S}{A_R}\right) \qquad \text{Eq. 7}$$

In theory, the $R$ index does not depend on the façade elements installation. However, the effects of the different wave paths shall be reflected on the results of experimental tests (Asdrubali & Desideri, 2019) and can be reported by the Apparent Sound Reduction Index $R'$.

### 3.3 Indoor Sound

It is feasible to consider a receiver room with volume $V$ and reverberation time $T$, where the sound signal inside is attenuated mainly by the façade. From this perspective, it is possible to calculate the sound pressure level in the receiving room $L_{inside}$ (Eq. 8) by deriving the equation 4 of the standard (BSI, 2017) for the Apparent Sound Reduction Index $R'$.

$$L_{inside} = L_{outside,2m} - R' + 10\log_{10}\left(\frac{TS}{0.16V}\right) \qquad \text{Eq. 8}$$

Finally, the estimated sound level at the receiver environment allows setting operational constrains based on recommended sound metrics at the receiver. In this regard, the drone operating conditions such as, distance, speed, or operation can be informed on the bases of the acoustics objective.

For instance, the WHO guidelines for sleep quality effects can be used to set these acoustic requirements. These WHO guidelines, sets the threshold of the $LA_{max,inside}$ at 42 dB for “Waking up at night and/or too early in the morning” (Hurtley, 2009). In addition, the number of drones in operation could be considered as a variable to adjust the model to recurrent flight events.

## 4. Case Study

The developed modelling framework is illustrated considering the specific acoustics and operating conditions of a multicopter type Yuneec Typhoon during a fast speed flyover ($speed{\sim}12.5\ \mathrm{m}/s$). The sustained flying conditions remained stable during the whole exercise, i.e., flight path and speed of the drone.

Firstly, the drone is considered as a noise source operating outdoors. Then, the amplitude of the sound inside was estimated considering a façade configuration located at the source-receiving interface.

The Figure 5 shows the amplitude of $LA_{max}$ as a function of the Drone/Façade distance $DFd$ in the receiver environment without (left) and with (right) the hypothetical installation of the partition with the window considering an open area, in this case $0.05m^2$.

The assumed façade’s third-octave band $R'$ index which includes a standard glazing element was evaluated experimentally and reported by Waters-Fuller and Lurcock (2007). In particular, the $R'$ of the wall with an inward lateral rotation window with standard glazing type $4-16-4\ mm$ was applied on this document (Figure 5 - middle).The sound signal obtained at the receiver shows that the attenuation at high frequencies is not great, considering the significant emission of the drone on this range of frequencies.

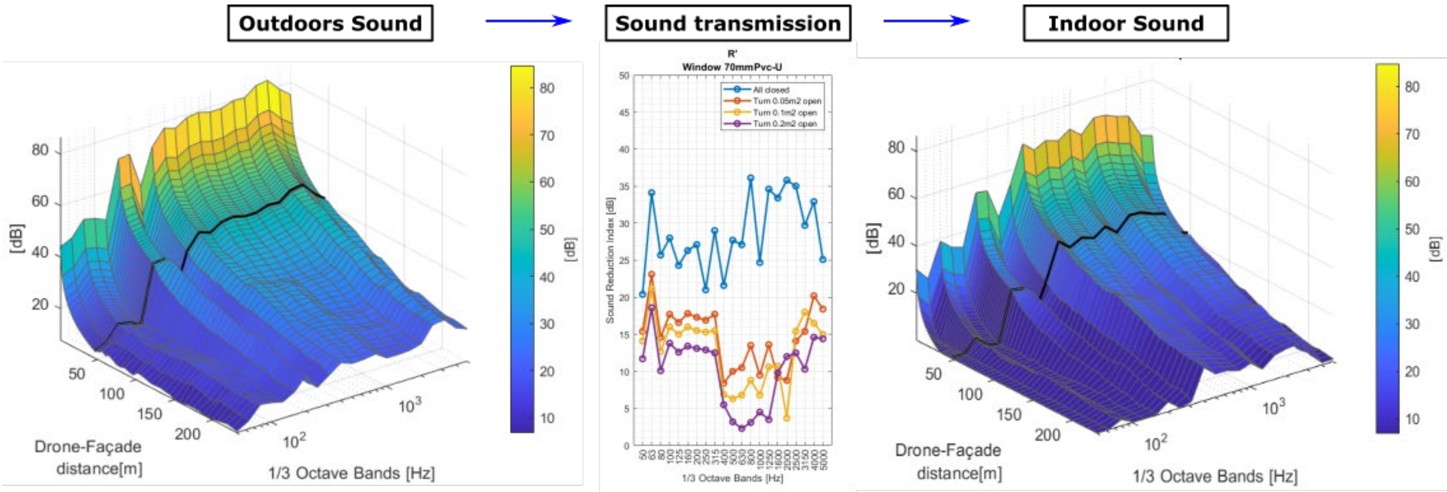


Figure 5. $LA_{max}$ by frequency as a function of the distance $r$, without (left) and with (right) the partition located in the sound wave path ($0.05m^2$ window open area). The Apparent Sound Reduction Index $R'$ of the partition due the glazing open area is included (middle).

The waterfall plots are highlighted at the $r_{sd}$ to show the sound amplitudes obtained at a distance $r$ from the source, by both actual measurements ($r \geq r_{sd}$) and modelled propagation ($1m < r < r_{sd}$). Then, it is possible to obtain the total value $LA_{max}$ as a function of the distance $r$ through the signal amplitude on each frequency band.

Finally, a fitting curve model (Figure 6) was estimated to establish a minimum $DFd$ from the recommended values of $LA_{max,inside}$ due to a specific flyover operation.

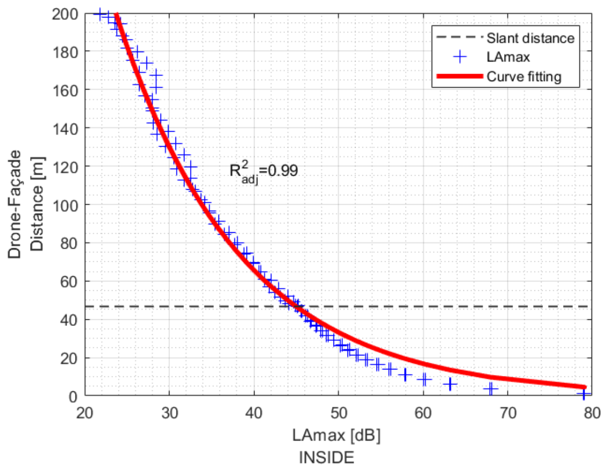


Figure 6. Drone/Façade distance fitting curve.

As is depicted in the Figure 7 (left), it is possible to obtain a particular fitting curve for each combination of drone flyover operation and receiver room configuration, from which to establish an acoustic objective indoors.

Consequently, it is possible to find the recommended Drone/Façade distance $DFd$ to comply, for instance, with the Sleep quality guidelines as reported by WHO (Hurtley, 2009). These obtained $DFd$ values depend on the window configurations and are tabulated in the Table 1. Therefore, the lowest values of $DFd$ are recommended when the window setup have highest performance of sound isolation.

The recommendations for the $DFd$ could be based on certain reference value of $SEL_{inside}$. The recommended Drone/Façade distance ($DFd$) to comply the guidelines based on $SEL$ values is showed in the Figure 7 (right).

Table 1. Estimation of the optimal Drone/Façade distance $DFd$ for a drone fast flyover operation near to a façade with a conventional window configuration.

| Drone | Operation | Glazing configuration | DFd [m] | Curve fitting | | |
|---|---|---|---|---|---|---|
| | | 4-16-4 mm 70mmPVC internal tilt &turn (Waters-Fuller & Lurcock, 2007) | Aim: **42dB** $LA_{max,inside}$ Sleep quality. Waking up in the night and/or too early in the morning (Hurtley, 2009). | Drone/Façade distance $DFd = a\, e^{-bLA_{max}}$ | | |
| | | | | $a$ | $b$ | $R^2_{adj}$ |
| Yuneec Typhoon | Fast flyover $speed \sim 12.5\ \mathrm{m/s}$ (Read et al., 2020) | Fully open | 131.6 | 2473 | -0.0698 | 0.98 |
| | | Open 0.20 m2 | 80.5 | 1556 | -0.0705 | 0.98 |
| | | Open 0.10 m2 | 67.8 | 1191 | -0.0682 | 0.99 |
| | | Open 0.05 m2 | 57.3 | 1007 | -0.0682 | 0.99 |
| | | Closed | 15.8 | 389 | -0.0762 | 0.99 |

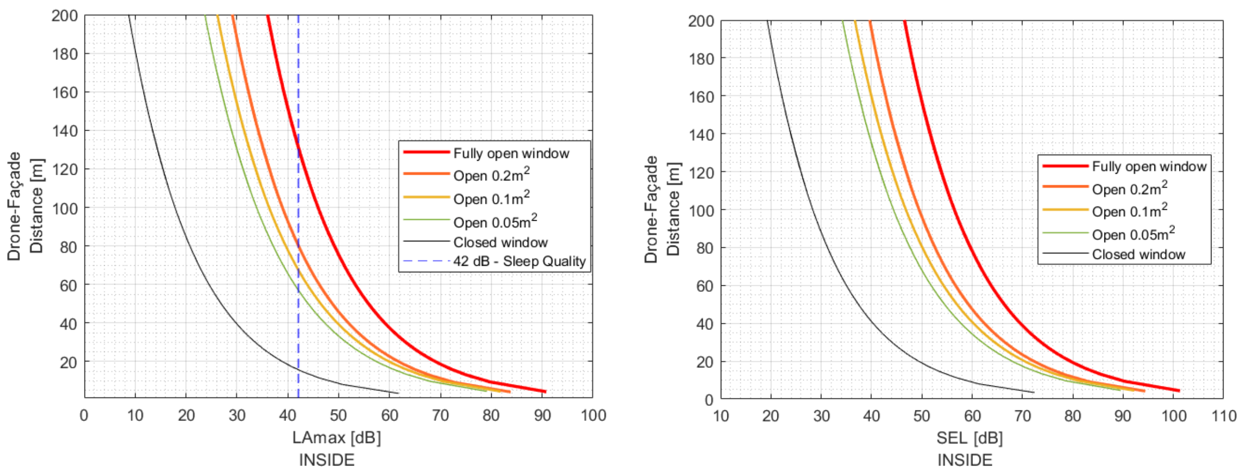


Figure 7. Recommended Drone/Façade distance based on the $LA_{max,inside}$ (left) and $SEL_{inside}$ (right).

## 5. Conclusions

This paper presents a modelling framework for the estimation of indoor noise exposure due to drone operations and allows operational restrictions settings to meet specific recommended noise levels to avoid significant acoustic impact on communities inside dwellings. This framework is based on the measured drone noise signature and the sound propagation outdoors. The method also includes the effects of the sound attenuation provided by masonry and glazing elements during the sound transmission into the receiver room.

The application of this modelling framework is illustrated with a case of study, where the minimum distance from a given drone to a typical residential building is defined to comply with the noise requirements to avoid the sleep disturbance.

The objective of this modelling framework was to provide a tool to establish technical recommendations of the variables of the drone operation (i.e., Drone/Façade distance). However, it is important to note that the presented modelling framework can be extended to analyse the estimated indoor noise through the application of other state-of-the-art acoustic technologies, including auralisations, sound virtual reality, sound quality metrics, etc. With this perspective, it is possible to establish a growing scope in the drone noise exposure analysis.

## 6. Acknowledgements

Dr Ramos-Romero, Mr Green and Dr Torija Martinez would like to acknowledge the funding provided by the UK Engineering and Physical Sciences Research Council for the DroneNoise project (EP/V031848/1).

**References**

Asdrubali, F., & Desideri, U. (2019). Chapter 6 - Building Envelope. In F. Asdrubali & U. Desideri (Eds.), *Handbook of Energy Efficiency in Buildings* (pp. 295-439). Butterworth-Heinemann. https://doi.org/10.1016/B978-0-12-812817-6.00039-5

Basner, M., & McGuire, S. (2018). WHO Environmental Noise Guidelines for the European Region: A Systematic Review on Environmental Noise and Effects on Sleep. *International Journal of Environmental Research and Public Health*, *15*(3), 519. https://doi.org/10.3390/ijerph15030519

BSI. (2017). BS EN ISO 12354-3:2017 Building acoustics - Estimation of acoustic performance of buildings from the performance of elements. In *Part 3: Airborne sound insulation against outdoor sound*.

Hansen, C. H. (2001). Fundamentals of acoustics. *Occupational Exposure to Noise: Evaluation, Prevention and Control. World Health Organization*, 23-52.

Hurtley, C. (2009). *Night noise guidelines for Europe*. WHO Regional Office Europe.

Kapoor, R., Kloet, N., Gardi, A., Mohamed, A., & Sabatini, R. (2021). Sound Propagation Modelling for Manned and Unmanned Aircraft Noise Assessment and Mitigation: A Review. *Atmosphere*, *12*(11), 1424. https://doi.org/10.3390/atmos12111424

Kapoor, R., Ramasamy, S., Gardi, A., Schyndel, R. V., & Sabatini, R. (2018). Acoustic sensors for air and surface navigation applications. *Sensors*, *18*(2), 499. https://doi.org/10.3390/s18020499

Kinsler, L. E., Frey, A. R., Coppens, A. B., & Sanders, J. V. (2000). *Fundamentals of acoustics*. John wiley & sons.

Min, S., Lim, D., & Mavris, D. N. (2015). Aircraft Noise Reduction Technology and Airport Noise Analysis for General Aviation Revitalization. 15th AIAA Aviation Technology, Integration, and Operations Conference,

Read, D. R., Senzig, D. A., Cutler, C. J., Elmore, E., & He, H. (2020). *Noise Measurement Report: Unconventional Aircraft-Choctaw Nation of Oklahoma: July 2019*.

Torija, A. J., & Clark, C. (2021). A psychoacoustic approach to building knowledge about human response to noise of unmanned aerial vehicles. *International Journal of Environmental Research and Public Health*, *18*(2), 682. https://doi.org/10.3390/ijerph18020682

Torija, A. J., & Nicholls, R. K. (2022). Investigation of Metrics for Assessing Human Response to Drone Noise. *International Journal of Environmental Research and Public Health*, *19*(6), 3152. https://doi.org/10.3390/ijerph19063152

Torija, A. J., Self, R. H., & Lawrence, J. L. (2019). Psychoacoustic characterisation of a small fixed-pitch quadcopter. INTER-NOISE and NOISE-CON Congress and Conference Proceedings,

Waters-Fuller, T., & Lurcock, D. (2007). NANR116:'Open/Closed Window Research'sound insulation through ventilated domestic windows. *Dep Environ Food Rural Aff*.

QUIET DRONES
Second International e-Symposium
on
UAV/UAS Noise
27th to 30th June 2022

# Accurate measurement of Drone Noise on the ground

**Per Rasmussen – Acoustic consultant: pr@grasacoustics.com**
**Lars Winberg – Business Development Manager: lw@grasacoustics.com**

## Summary

Accurate measurement of noise from smaller unmanned aerial vehicles/systems (UAVs/UASs) can be performed in anechoic chambers, but larger types need to be tested in outdoor environments. This will introduce ground reflections that may disturb the measurements if microphones are mounted above the ground. By placing the measurement microphone on a fully reflecting ground board, the influence of the reflection becomes well defined and will result in a simple pressure doubling. By using flush-mounted microphones in the ground board, the frequency range of the system may be extended to cover the full audible range up to 20 kHz.

## 1. Introduction

With an increasing number of lightweight and small multirotor unmanned aerial systems (UASs), the need for assessing the methods used for accurate UAS noise measurements is increasing. The characteristics of noise from lightweight and small multirotor UASs differ from jet and propeller-driven airplanes in frequency and tonality. Also, large jet airplanes typically fly in predefined air corridors, different from smaller propeller-driven airplanes flying at lower altitudes, while lightweight and small multirotor UASs normally operate even closer to habitable areas, sometimes hovering and thereby constituting a stationary noise source.

Traditionally, two methods have been used for measuring noise from airplanes on the ground: 1) Pole-mounted microphones and 2) inverted microphones over a reflecting pane. This paper evaluates these methods and investigates new standards for measuring noise from UASs.

The noise from smaller hovering UASs can be measured and studied in anechoic chambers, which will provide a well-defined free field acoustic environment. For larger UASs, the size of most anechoic chambers may be too small and may incur problems with recirculation and safety. It may therefore be necessary to perform the measurements at an outdoor test site where it will not be possible to obtain a free field as in the anechoic chamber because the ground will act as a reflecting plane.

Traditional aircraft noise measurements as, for example, described in ICAO Annex 16 [1] or ISO 20906 [2], are performed with a microphone mounted at some distance above the ground, and the results from such measurements will be influenced by the reflections from the ground impedance. This may provide a good estimate of the overall A-weighted sound pressure level for an aircraft flying over the measurement position. However, for detailed studies of the frequency content and for hover conditions, this method may lead to considerable errors.

This issue has been recognized in ICAO Annex 16 [1], as the method for helicopter test is performed with a microphone mounted on a plate with a well-defined impedance. The inverted microphone technique described in ICAO Annex 16 [1] is, however, limited to frequencies below 10 kHz. This may be relevant for traditional aircraft, which are typically operated at relatively large distances from observers, and the attenuation of high frequencies by the air will eliminate the problem with high frequencies. However, many UASs are intended for operation closer to observers and high frequencies may not be attenuated before reaching an observer and therefore need to be considered.

## 2. Aircraft noise measurements

### 2.1 Microphone over a reflecting plane

Traditional aircraft noise measurements are performed with a microphone positioned at a height of 1.2 m, as described in for example ICAO Annex 16 Volume 1 Appendix 1, 3.5.1 [1], illustrated in Figure 1.

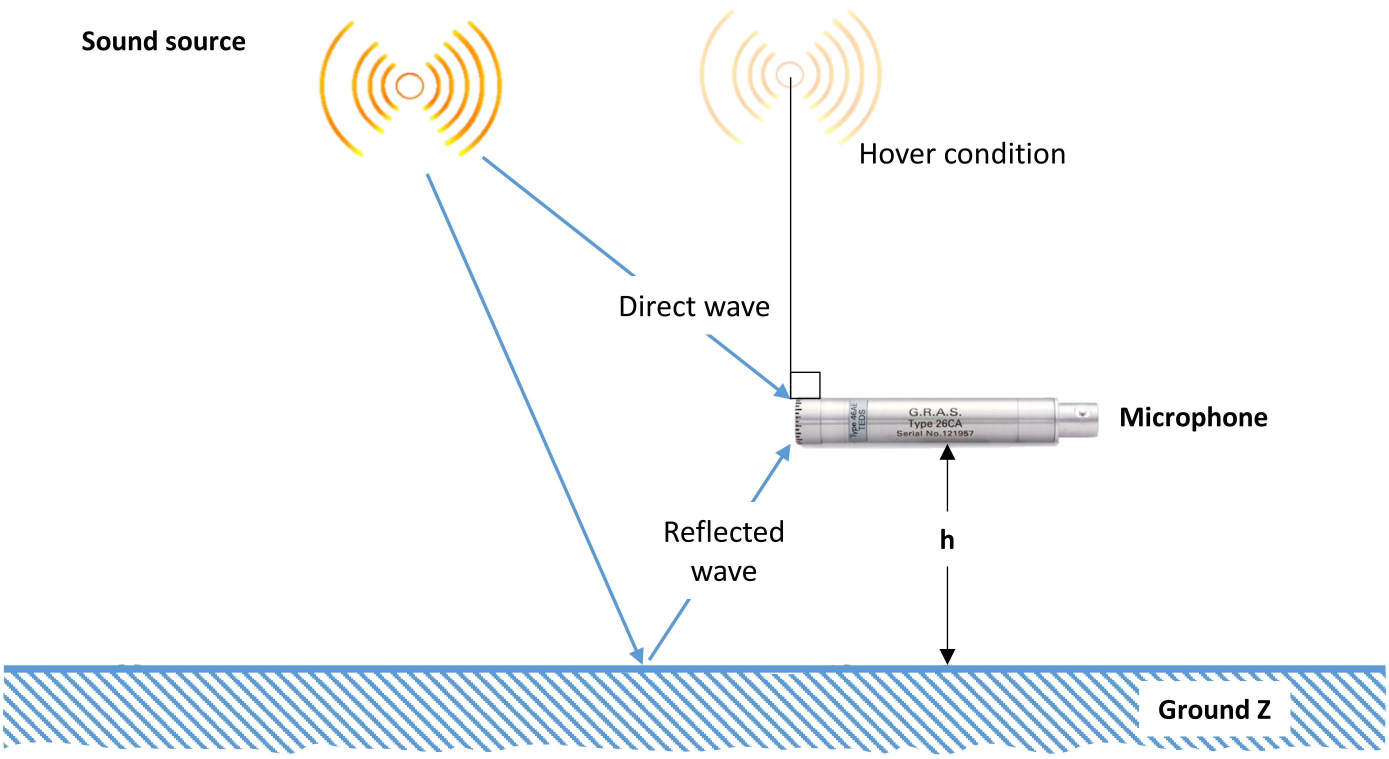


*Figure 1. Microphone at height h with sound source above*

This introduces interference between the direct wave and the reflected wave at the microphone position [3]. If the sound source emits pink noise and is directly above the microphone, the resulting spectra at the microphone position will be as shown as the orange curve in Figure 2, where the blue curve indicates the corresponding free-field level at the microphone position with no ground reflection. (It should be noted that the following calculations are idealized simulations and that actual measurements would give less well-defined effects at high frequencies due to scattering, impedance changes and other factors resulting in lower spatial correlation).

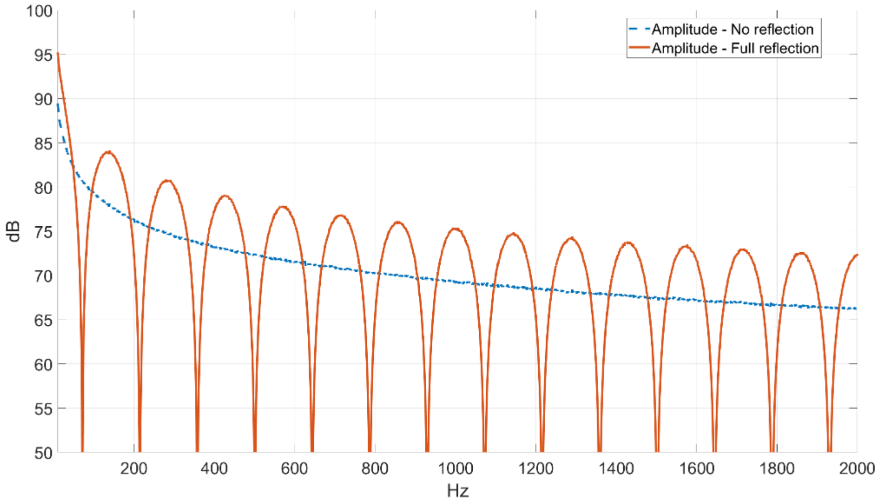


*Figure 2. FFT spectra for pink noise source directly above microphone (hover conditions)*

The interference of the direct wave and the reflected wave at the microphone position is like a comb filter, with the first minimum at the frequency where the microphone height 1.2 m equals ¼ of the wavelength:

$$f_0 = \frac{c}{4 * l} \approx 71.4\ Hz$$

And the first maximum at

$$f_1 = \frac{c}{2 * l} \approx 143\ Hz$$

This can be seen more clearly using 1/24-octave filtering as in Figure 3:

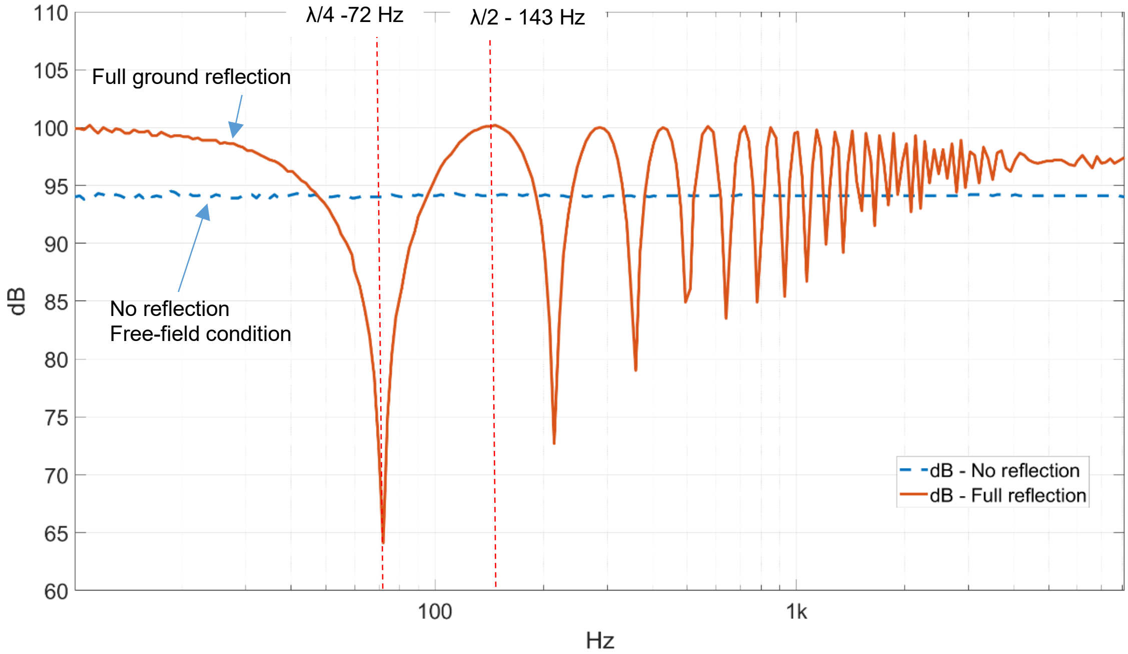


*Figure 3. 1/24-octave spectra for pink noise source directly above microphone (hover conditions)*

Using 1/3-octave filtering, the effect of the comb-filtering will be further smoothed at higher frequencies, as shown in Figure 4. This shows a 1/3-octave spectra for pink-noise source directly above the microphone (hover conditions), where the frequencies coincident with the comb-filter minima are reduced by more than 20 dB, and the frequencies coincident with the comb-filter maxima are amplified by 6 dB. It may be possible to correct the frequencies amplified by the maxima, but it is more difficult to correct the frequency components reduced by the comb filter, as they often may be reduced below the general broadband noise level.

It should be noted that the overall sound pressure level measured at 1.2 m height will be 3 dB higher than the corresponding level measured in a full free field as for example inside an anechoic chamber; therefore, it is important to consider the specific circumstances of the actual measurement before comparing levels.

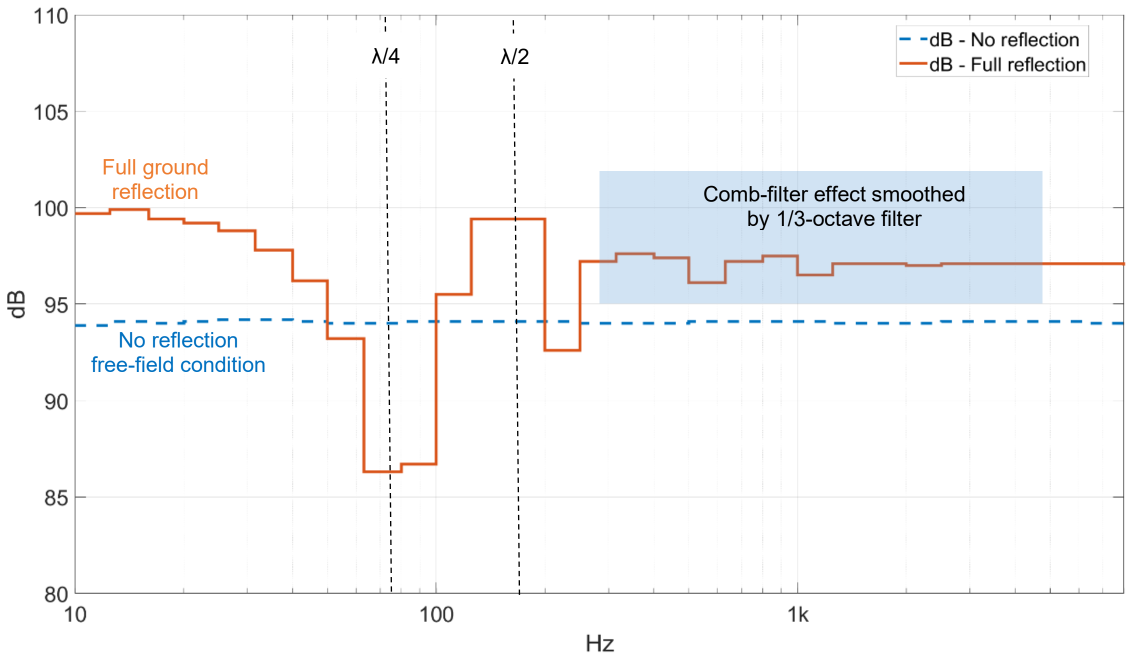


*Figure 4. 1/3-octave spectra for pink-noise source directly above microphone (hover conditions)*

In practice it may be possible to correct the data for the comb-filtering effect as long as the source signal is broadband noise. However, if the source signal contains pure tone components, it will not be possible to do this correction. Figure 5 shows an example where the source signal contains pure tone frequencies at 72 Hz and higher harmonics.

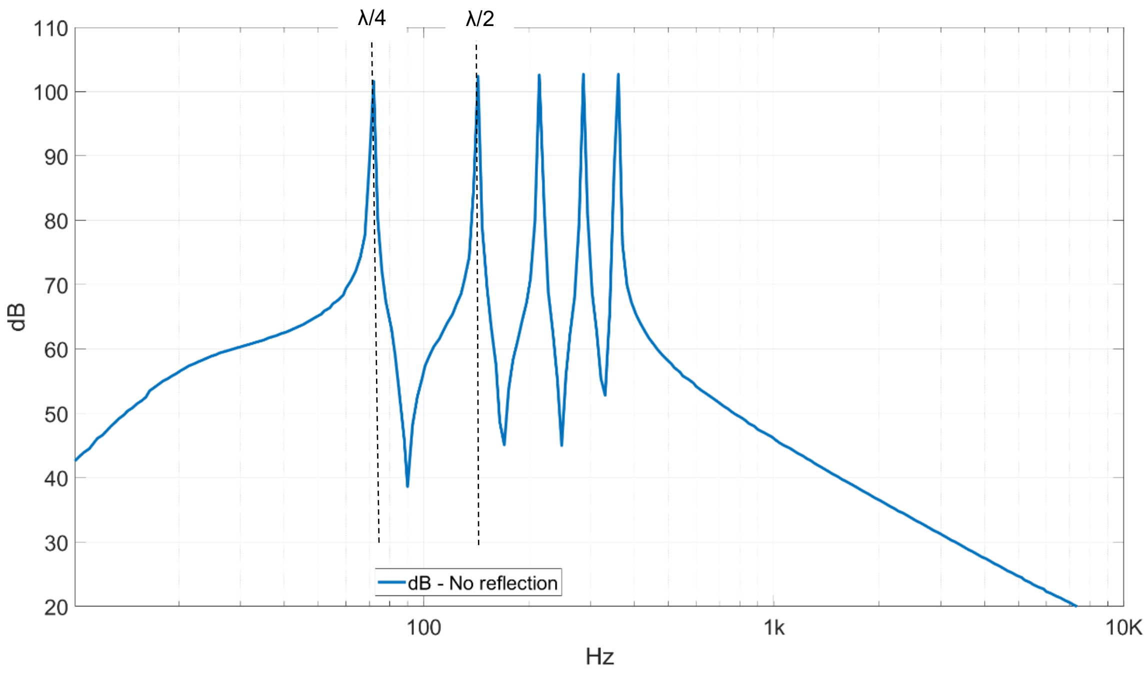


*Figure 5. 1/24-octave spectra of 72 Hz, 143 Hz, 215 Hz, 286 Hz and 357 Hz in free field*

When this signal is filtered by the comb filter created by the 1.2 m height interference, the resulting spectra will be as seen in Figure 6.

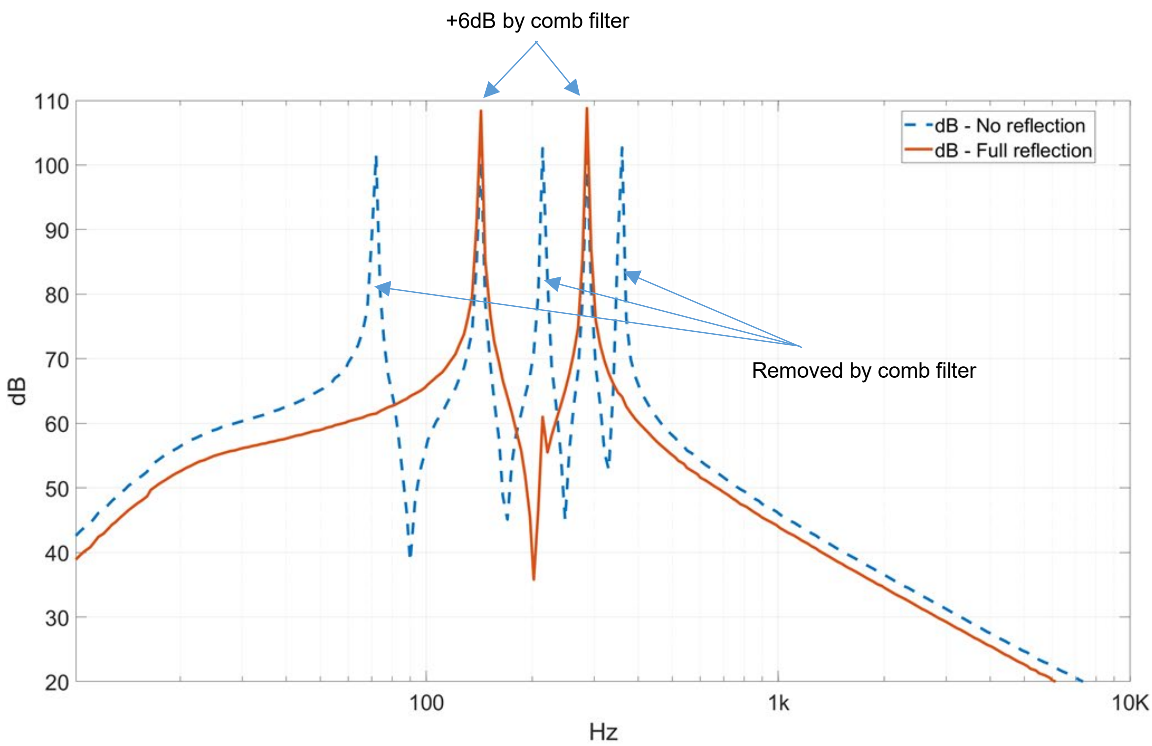


*Figure 6. 1/24-octave spectra for pure tone source directly above microphone (hover conditions), blue curve: free field, orange curve: ground reflection 1.2 m*

The examples above have assumed a perfectly reflecting ground surface, and this condition may be fulfilled inside a semi-anechoic room with hard concrete floor or in an outside site with similar hard reflecting ground surface. Many outdoor measurement sites may have ground surfaces like gravel, grass or hard soil—not perfectly reflecting. The ground impedance can be modelled as a porous layer (Delany-Bazley-Miki) [4] with flow resistivity between 30 kPa*s/$m^2$ and 30 MPa*s/$m^2$. Figure 7 shows the simulation (COMSOL BEM) of the sound field above reflecting ground surfaces with different flow resistivity.

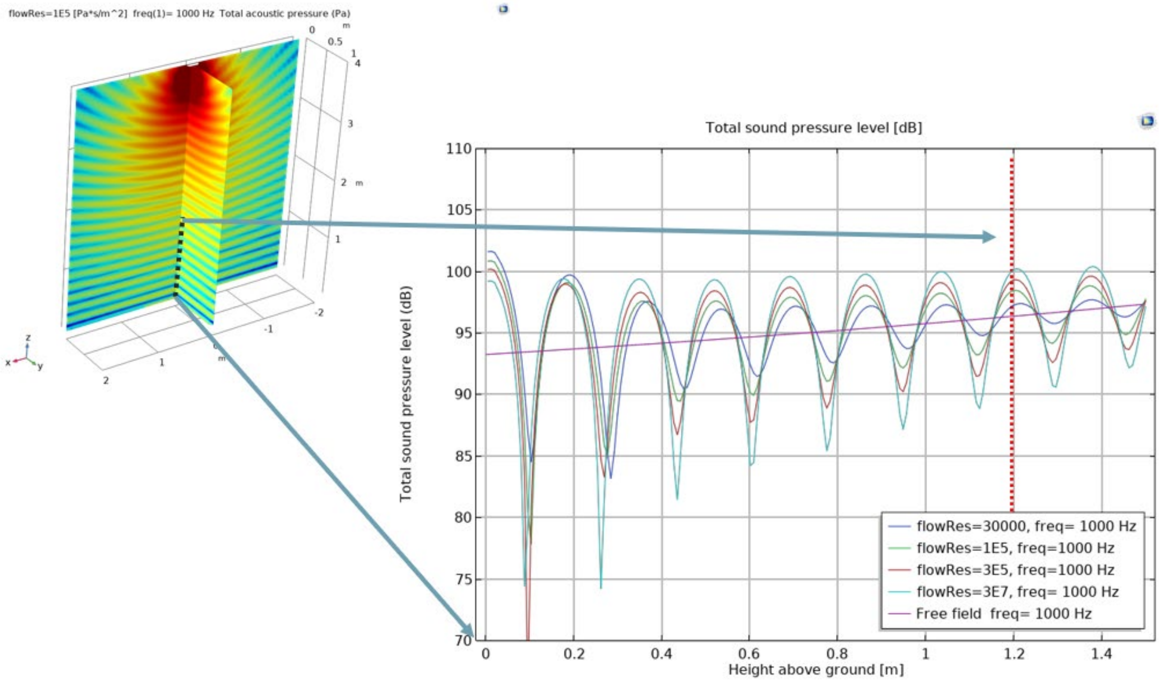


*Figure 7. Sound pressure level above ground for different flow resistivities at 1 kHz*

At 1.2 m height the influence of the ground reflection is considerable even with a ground flow resistivity of 30 kPa*s/$m^2$ corresponding to something like very soft forest ground covered with moss. It can also be seen that moving the microphone closer to the ground surface will further increase the influence of the ground reflection, and even very soft ground surfaces will not prevent the interference.

The hover situation, with the sound source directly above the microphone position, is the worst as far as interference between the direct and reflected wave. For a fly-by measurement, the elevation angle as defined in Figure 8 will vary continuously from 0° to 180°, with 90° corresponding to the source being right above the microphone, as in the hover example above.

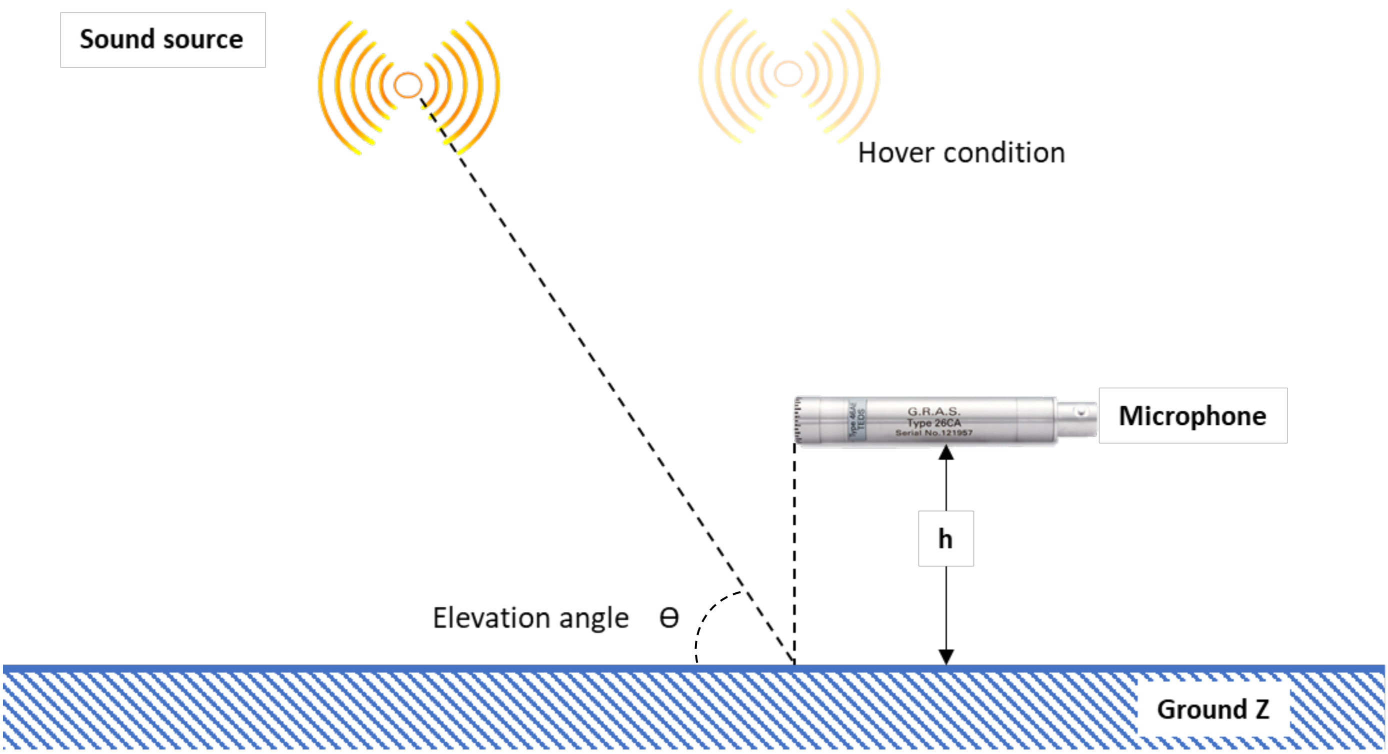


*Figure 8. Elevation angle for source over microphone*

As the angle varies, the distance travelled by the direct and the reflected wave will change, and this will change the comb-filter effect as illustrated in Figure 9.

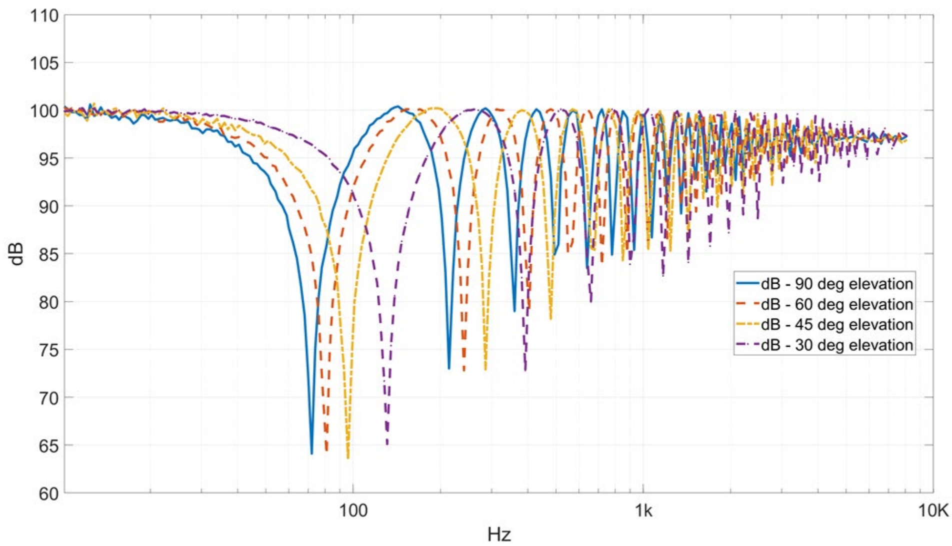


*Figure 9. Comb-filtering effect for different elevation angles for microphone height 1.2m and source height 10 m.*

## 2.2 Ground board measurements with inverted microphone

ICAO Annex 16 Volume I, Appendix 6 [1] for propeller-driven airplanes not exceeding 8,618 kg, uses a ground board microphone configuration as shown in Figure 10. This is explained further in ICAO Environmental Technical Manual, Volume I, Procedures for the Noise Certification of Aircraft: *"The specified ground plane microphone configuration greatly minimizes the interference effects of reflected sound waves inherent in pole-mounted microphone installations. For a 1.2 m*

*(4 ft) microphone, such effects typically occur in the frequency region that is most significant for propeller-driven aircraft noise".* [5]

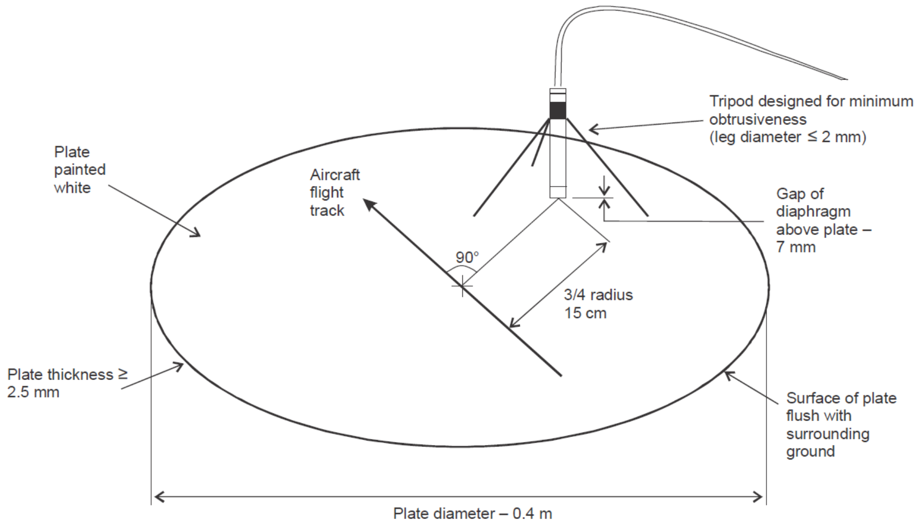


*Figure 10. ICAO ground plane microphone configuration*

The resulting sound field on the surface of the ground plate depends on the impedance of the surrounding ground and the angle of incidence for the incoming sound waves [6]. For a 90° elevation, where the sound source is directly above the plate, the pressure distribution on the plate is as shown in Figure 11.

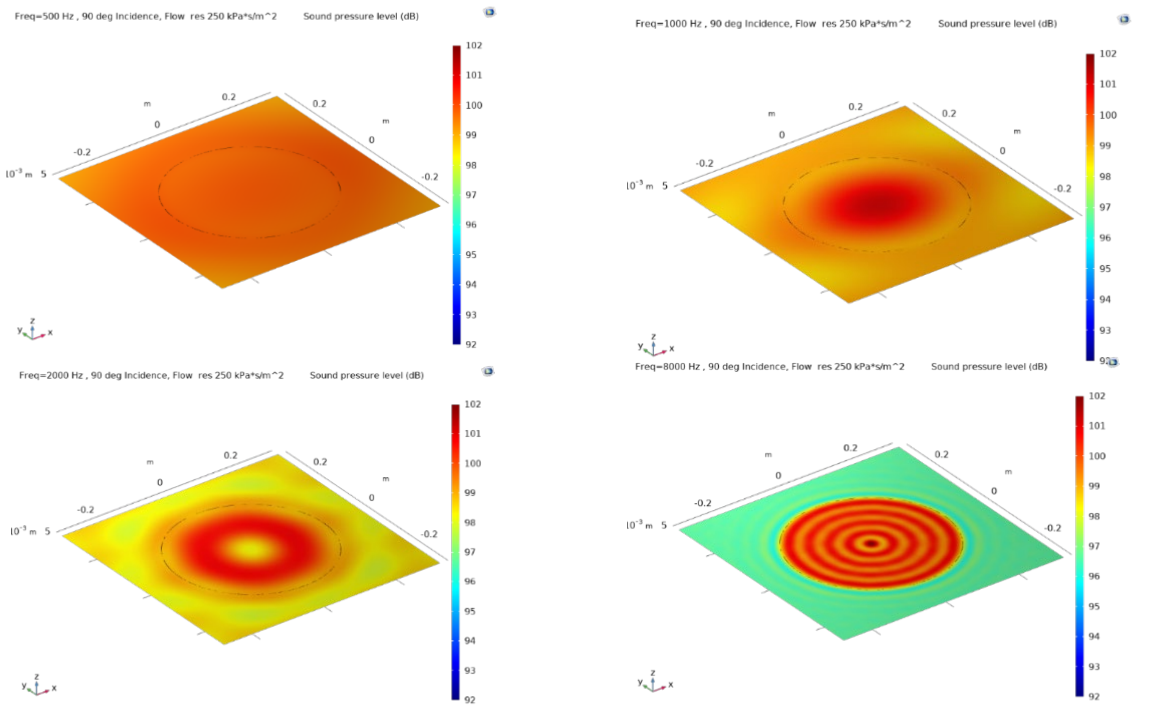


*Figure 11. SPL on plate and surrounding ground for 90° incidence with 250 kPa's/m2 (a) 500 Hz, (b) 1 kHz, (c) 2 kHz) and (d) 8 kHz*

The SPL pressure distributions on the ground board was calculated for a free-field sound pressure level of 94 dB, and it can be seen that while the SPL on the ground surface decreases at higher frequencies due the absorption, the pressure on the plate is almost constant at 100 dB, corresponding to a pressure doubling from the free-field condition. It can also be seen that the center point of the plate is not the optimum position. Figure 12 shows the spectra calculated in the center position (blue curve) compared to the spectra in the microphone position at r=0.15 m, as specified in Figure 10.

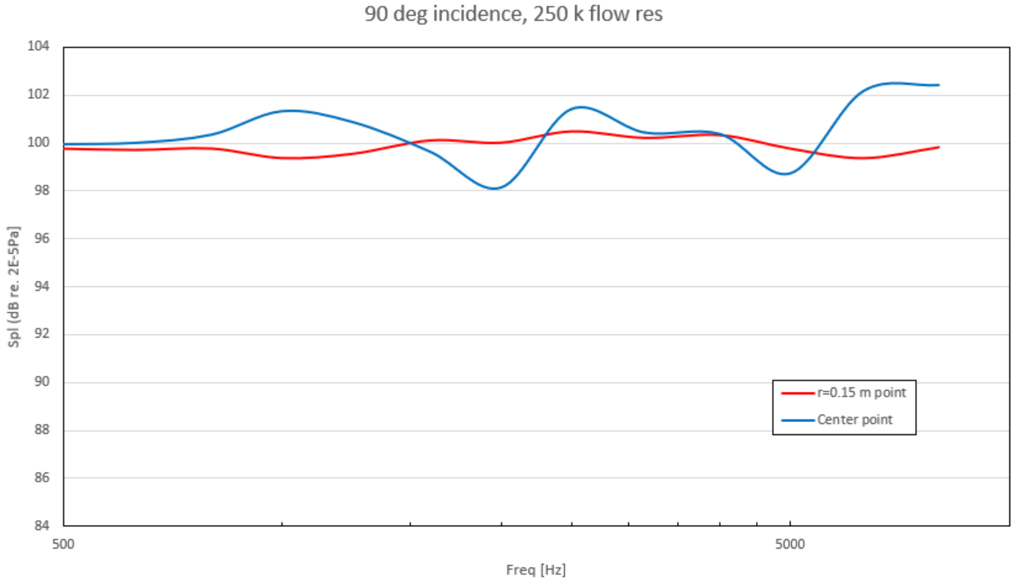


*Figure 12. Frequency response for 90° incidence at center point and at a point at r=0.15 m*

The ICAO microphone configuration used for propeller-driven aeroplanes not exceeding 8,618kg in Figure 10 has the draw-backs in that it is very sensitive to changes in the distance between the ground plate and the microphone diaphragm as shown in Figure 13. This might be problematic in the field when a last-minute calibration is required to validate the measurement chains.

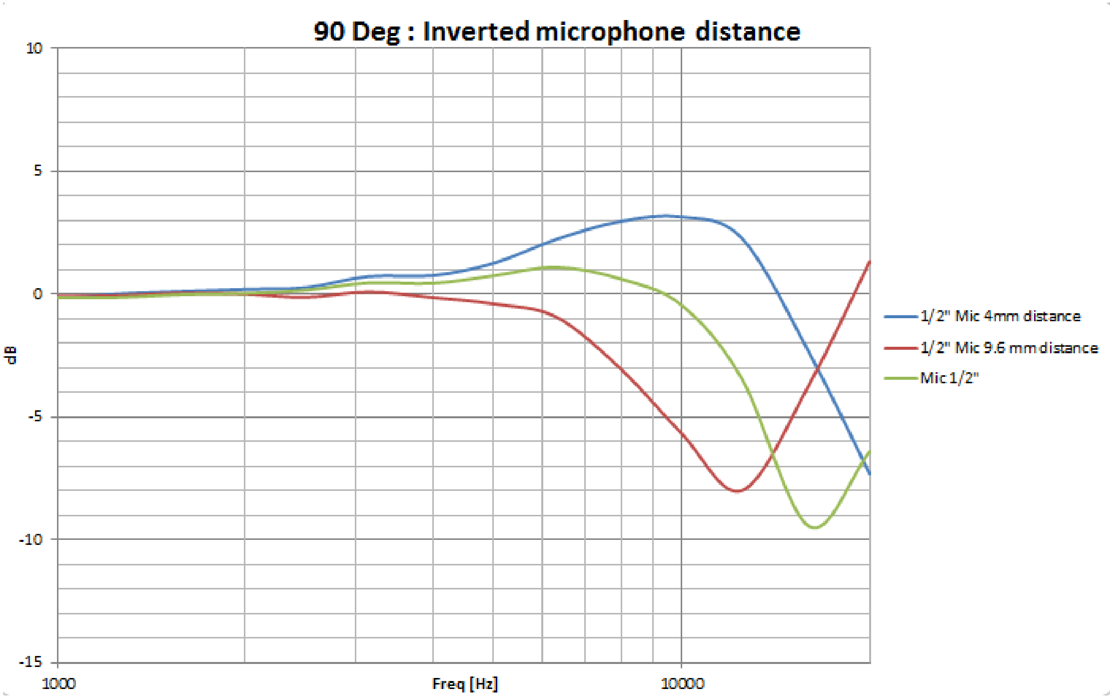


*Figure 13. ½" Inverted microphone over ground plate with 7 mm distance (green curve), 4 mm distance (blue curve) and 9.6 mm distance (red curve)*

Secondly, the inverted microphone mounted on top of the reflecting plate disturbs the measurements above 10 kHz. The influence of different-sized microphones can be seen from Figure 14. The graph shows the influence of different-sized microphones mounted upside-down above the ground plate compared to a reference microphone mounted flush on the plate.

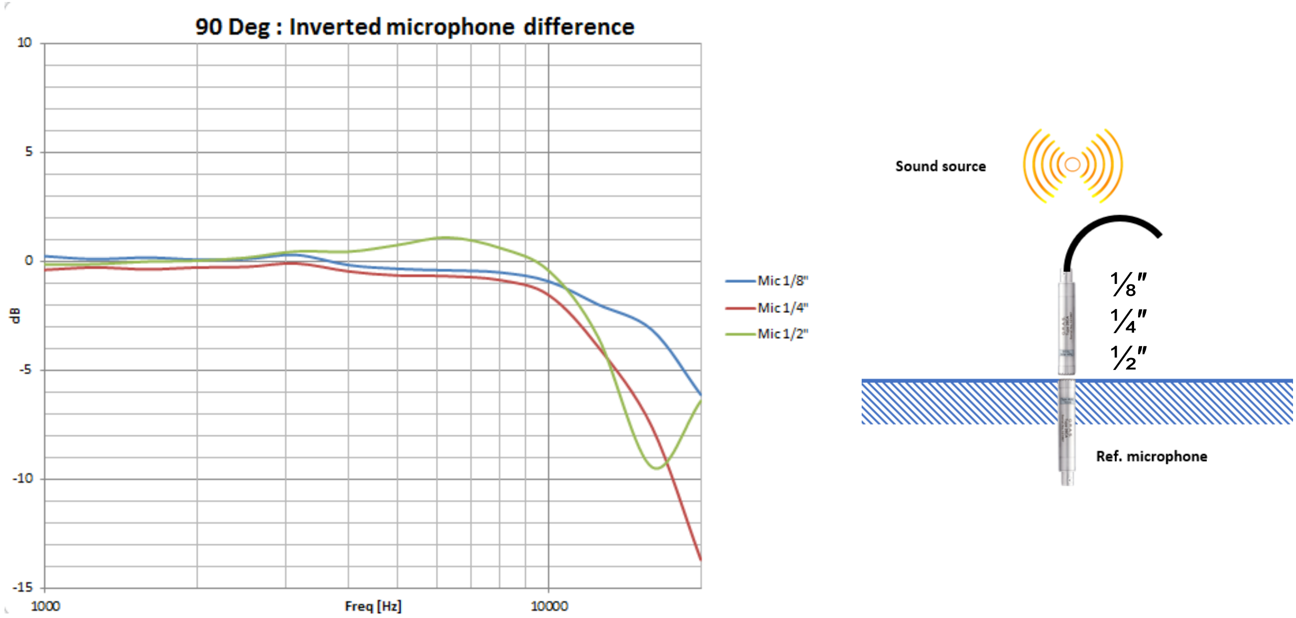


*Figure 14. Influence of ⅛", ¼" and ½" microphones mounted upside-down above the ground plate compared to a reference microphone mounted flush on the plate*

### 2.3 Ground board measurements with flush-mounted microphones

For traditional aircraft, the high-frequency content above 10 kHz may not be of particular interest, as the aircraft are normally far away, where the atmospheric absorption will reduce the high frequencies before they reach an observer. Typical drones may however be operated closer to observers, and it may not be justified to ignore the high-frequency content. To configure a setup where the ground reflections are avoided and where no inverted microphone disturbs the measurements above 10 kHz, the microphone must be flush mounted with the plate surface, as shown in Figure 15. This will increase the frequency range up to 20 kHz and thus allow measurement of the high-frequency content.

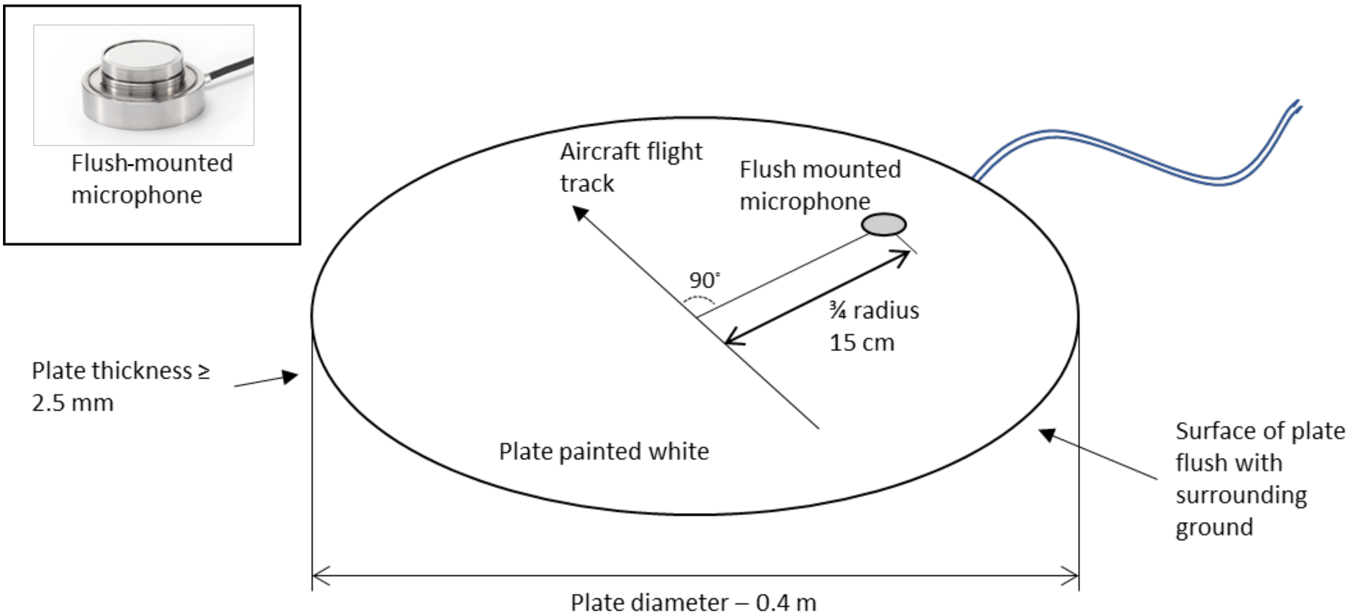


*Figure 15. Ground board plate with flush-mounted microphone*

Conclusions

A free-field measurement in a fully anechoic chamber enables accurate measurements of the full spectral content of the device under test for both broadband noise sources and for noise sources containing pure tone sources. For outdoor measurements, which include ground reflections, and for semi-anechoic chamber measurements, the overall level of a broadband noise source can be obtained, with microphones at a certain height, but in general the level obtained with this method will be 3 dB higher than the free-field condition.

If the microphone, instead of mounted at a certain height, is flush mounted with a fully reflecting ground, both broadband noise sources and pure tone sources can be measured, but with a 6 dB higher level than for the free-field situation.

As larger jet airplanes move along a flight track at almost constant speed at a considerable distance from the measurement point, the tonal content of the noise is reduced due to the distance, and the constant movement of the source minimizes the comb effect. The interference from the reflecting wave is therefore neglectable, and the measurements are repeatable for this kind of noise source.

As lighter aircraft do not follow the same predefined flight tracks and as they fly at lower altitudes, the interference from the ground is no longer neglectable, and a ground plate with an inverted microphone should be used. This ensures a repeatable measurement for frequencies below 10 kHz. As the inverted microphone is mounted in the sound field, the sensor influences measurements above 10 kHz, and it is therefore not suitable for lightweight and small multirotor unmanned aerial systems.

As some of the characteristics of the noise from UAVs/UASs are different from noise from larger airplanes in relation to tonal content and higher frequency as well as lower altitude and stationary source, the current standards for accurate measurement of noise on the ground are not optimal, and a flush-mounted microphone on a ground plate is preferable. This configuration is useful for stationary and non-stationary noise sources with frequencies up to 20 kHz, where the noise contains tones.

**References**


1. *ICAO Annex 16 to the Convention on International Civil Aviation: Environmental Protection: Volume 1—Aircraft Noise*, International Civil Aviation Organization, July 2017.
2. *ISO 20906: Acoustics—Unattended monitoring of aircraft sound in the vicinity of airports*, ISO, 2009.
3. T.D. Norum and C.H. Liu, “Point source moving above a finite impedance reflecting plane—experiment and theory,” *The Journal of the Acoustical Society of America*, vol. 63, 1069, 1978, doi: 10.1121/1.381839
4. K. Attenborough, I. Bashir and S.Taherzadeh, “Outdoor ground impedance models,” *The Journal of the Acoustical Society of America*, vol. 129, 2806, 2011, doi: 10.1121/1.3569740
5. *ICAO Environmental Technical Manual, Volume I, Procedures for the Noise Certification of Aircraft*, International Civil Aviation Organization, 2015.
6. W.L. Willshire, Jr. and P. Nystrom, “Investigation of Effects of Microphone Position and Orientation on Near-ground Noise Measurements,” *NASA Technical Paper*, NASA, April 1982.

**QUIET DRONES**
**Second International e-Symposium**
**on**
**UAV/UAS Noise**
**27th to 30th June 2022**

# Numerical Investigation of Noise Emissions from a Cargo eVTOL UAV

**Michael Schmähl, Technical University of Munich, michael.schmaehl@tum.de**
**Marcus Gnoth, Phoenix-Wings GmbH, marcus.gnoth@phoenix-wings.de**
**Mirko Hornung, Technical University of Munich, mirko.hornung@tum.de**

## Abstract

Urban air mobility (UAM) applications such as cargo electric vertical take-off and landing (eVTOL) unmanned aerial vehicles (UAVs) promise additional transportation capacities for congested urban areas. A major drawback facing UAM operations in future is that the new aerial vehicle movements are bound to lead to additional traffic noise emissions affecting urban areas. Minimum noise designs are therefore essential for UAM aircraft. This paper presents a numerically based computational fluid dynamics (CFD)/Ffowcs Williams-Hawkings (FW-H) model of the noise emissions generated by a cargo eVTOL UAV with separate hover and cruise propellers and focuses on the cruise flight. Installation effects play a predominant role in the noise generation of this highly integrated aerial vehicle configuration. The numerical results of the vehicle's base configuration are validated by inflight noise measurement data. The noise results are split into propeller and airframe components. Alternative tail and propeller configurations are simulated to identify noise reduction potentials that stem from the effects of decreased aerodynamic interaction. It is envisaged that these investigations should form the groundwork for future numerical noise optimizations of the before mentioned base configuration, which explicitly consider the effects of aerodynamic interaction on noise emissions. The noise reduction potentials identified in this study support the idea of parallel rotor and airframe optimization.

## 1. Introduction

Urban air mobility (UAM) comprises applications such as air taxis or cargo drones and is currently the subject of intensive research within the aerospace community. A study of the societal acceptance of UAM published by the EASA in 2021 reveals that many people have "a positive initial attitude to UAM" [1, p. 7] but also that noise is one of the main concerns expressed by people in the EU [1, p. 10]. It is therefore clear that research in the field of UAM must also address noise issues.

One of the main focuses of research is on the design of aerial vehicles. A vertical takeoff and landing (eVTOL) configuration is often chosen for UAM aircraft. Many of these configurations are both novel and highly integrated in terms of function, necessitating careful consideration of noise emissions generated throughout the different flight phases. For single rotors with negligible effects stemming from aerodynamic interaction (like it is the case for conventional tractor single propeller configurations), low noise levels can be achieved by reducing blade tip Mach numbers and increasing blade counts (for example, as demonstrated by the acoustic propeller optimization findings published in [2]). However, any noise reductions brought about by these measures come at the cost of aerodynamic efficiency ( [3, p. 7]). A theoretical alternative to altering blade number and propeller diameter to achieve noise improvements would be to modify the shape of the blade. However, according to blade element momentum theory (BEMT), there is a distinct chord and twist distribution for which the aerodynamic efficiency of a given propeller is optimal [3, p. 10]. Consequently, any noise improvements achieved through blade shape modifications are at the cost of aerodynamic efficiency.

The overall noise emissions of highly integrated eVTOL configurations can differ significantly from the mere sum of the single propeller's noise contributions (that are regarded as isolated propellers). This is partly due to the effects of the aerodynamic interaction between the different rotors or between the rotor and the airframe, which are, to a certain extent, unavoidable. Another reason is scattering of propeller noise on the airframe [4], which, depending on the size, shape and dominant sound wavelength of the aircraft, leads to interference at far-field observer positions. Optimal noise designs are therefore not necessarily bound to the concept of aerodynamic efficiency versus noise interdependence, in which noise improvements are only possible at the cost of efficiency.

The authors suggest the idea of optimizing the shape parameters of rotors and airframe structures that interact aerodynamically with the rotor in parallel. To assess the potential of such an approach a computational fluid dynamics (CFD)/ Ffowcs Williams-Hawkings (FW-H) model of a pusher propeller cargo eVTOL UAV is set up and validated with in-flight noise measurement data in this paper. The aircraft's noise emissions in cruise flight are significantly impacted by aerodynamic interaction between tail structures and the pusher propeller. In a second step, modifications in the tail/propeller region are then implemented in the model. The aim of the modifications is to influence the aerodynamic interaction in this region while maintaining controllability of the overall aircraft system. Subsequently, the influence of these modifications on noise emissions is assessed.

## 2. Validation of the CFD/FW-H Noise Model

In this chapter the validation of the CFD/FW-H noise model of the cargo UAV under consideration is presented. It begins with a description of the noise metrics and the noise measurement data which the validation is based upon. Subsequently, the model is introduced and a comparison of simulation and measurement data is given.

### 2.1 Definition of Noise Metrics

All sound pressure levels (SPL) given in this paper are A-weighted. This reflects the sensitivity of the human ear with respect to the audible frequency spectrum and applies both to instantaneous SPLs, which measure the sound pressure at specific points, and to sound power levels, which are a measure of the overall power of a sound source.

## 2.2 Noise Measurement Data

The noise measurement data of the cargo UAV considered here was acquired with three ground microphones during an in-flight measurement campaign. In this campaign the aircraft performed a sequence of microphone flyovers and flybys (see Figure 1) such that noise emissions were measured for various aircraft noise emission directions. The noise measurement data were subsequently synchronized with the aircraft log data. The relative velocities between the microphones and the aircraft were then computed and the noise data de-dopplerized on the basis of the relative velocity information. Through this treatment the synchronized noise measurement data is made directedly comparable to the FW-H noise simulation data which is free-field noise without Doppler-frequency shifts. For a more detailed description of the noise data acquisition and processing, refer to [5].

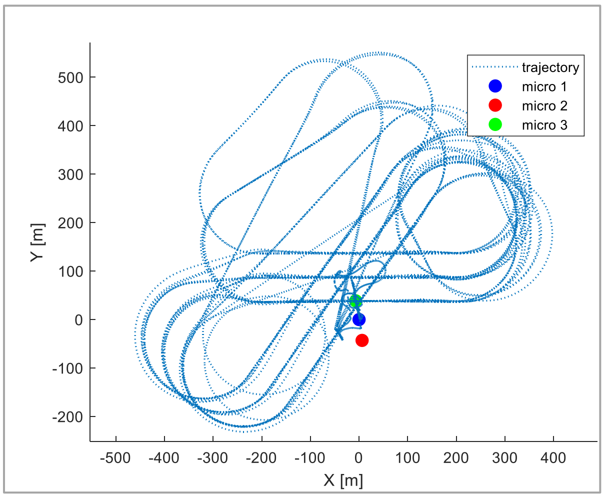

*Figure 1: **Left:** flight trajectory and microphone positions; **right:** cargo eVTOL UAV "Manta Ray" by Phoenix-Wings GmbH*

## 2.3 Numerical Noise Model

The numerical noise model in this paper adopts a hybrid CFD/FW-H approach. 'Hybrid' in this context means that the approach comprises one step for the numerical CFD solution of the aeroacoustic sound sources, and a separate step for the projection of this source information to the far-field noise receiver points. Both parts of the model are implemented in the starCCM+ CFD software product. For a deeper discussion of the CFD/FW-H noise model setup for UAV-size aircraft, refer to [6].

The meshing in the CFD component of the modelling process is based on CAD models of the airframe and the pusher propeller. Whereas the CAD models on which the closed surface model of the airframe is based were provided by Phoenix-Wings, the propeller was reconstructed from scan data. Potential aeroelastic deformations of the airframe are neglected and the elevator is assumed to be undeflected in the model. The unstructured polyeder mesh consists of *13.0* million cells in the environment domain and *4.6* million cells in the rotating propeller domain. A compressible fluid model is applied which, in combination with a volume mesh not exceeding a maximum cell size of *25 mm* in the area around the propeller and tail, is suitable for resolving the acoustic near field in this source region. An unsteady Reynolds Averaged Navier Stokes (uRANS) approach is applied to model the effect of turbulence in the flow. As turbulent vortices are not explicitly resolved by a uRANS approach, aeroacoustic broadband noise sources are not resolved by the flow simulation. This means that the noise solution is only able to resolve broadband noise to a limited extent.

The acoustic component of the model applies Farassat's formulation 1A of the FW-H integral. All propeller and airframe surfaces are utilized as integration surfaces for the FW-H solver, though relevant aeroacoustic sources are to be expected only in the vicinity of the propeller and tail. This ensures that all relevant source contributions from the airframe are considered, which is necessary, as the airframe surface data contains pressure fluctuations that originate from sound waves emitted by the propeller. Hence, sound scattering on the airframe is considered by including all airframe surfaces in the FW-H integration surface. The receiver points are located in a sphere with a radius of *30 m* around the center of the propeller.

### 2.4 Validation of Noise Results

Cruise flight at an airspeed of *25 m/s* and a propeller angular speed of *4150 rpm* is taken as the validation operating point. A comparison of lower sound hemisphere plots for measurement and CFD/FW-H simulation data is given in Figure 2. See the appendix in Figure 17 for a schematic sound hemisphere with an explanatory illustration of the sound emission angles. For the measurement data noise sphere, all measurement samples are converted to a reference distance of *30 m* in order to establish comparability to the simulation data sphere. Measurement and simulation data are in high agreement, both, regarding directivity and magnitude of SPLs. Similarly, the emitted SPL magnitudes exhibit a minimum value of approx. *50 dB(A)* for sound emissions towards the ground (elevation = *-90*°) and a maximum value of approx. *70 dB(A)* for horizontal sideward sound emission (elevation = *0*°, azimuth = ±*90*°).

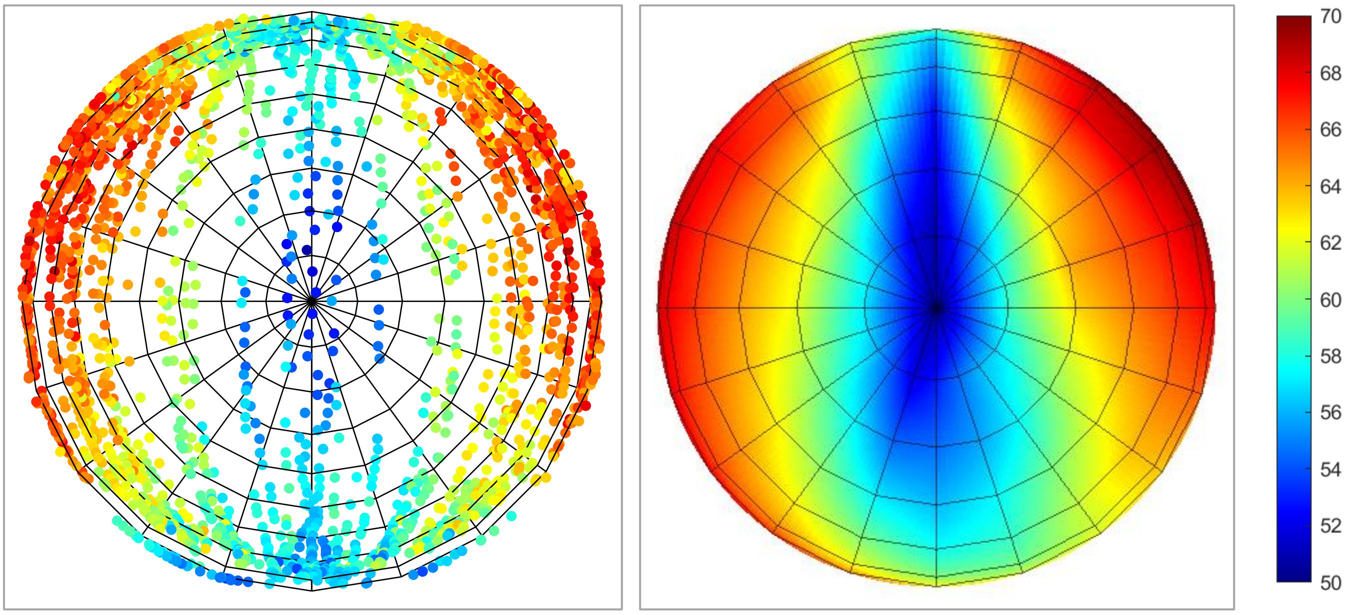


*Figure 2: Measurement (left) and simulation (right) over all sound pressure levels (OASPL) [dB(A)], sphere radius: 30 m; grid nodes in simulation hemisphere correspond to receiver points; top: azimuth = 0°, right: azimuth = 90°*

Next, the sound spectra of the two noise emission directions are compared. Figure 3 corresponds to noise emission direction towards the ground (elevation = -*90*°) and Figure 4 corresponds to an emission direction inside the propeller plane (elevation = -*30*, azimuth = *90*°) which lies within one of the two noise lobes. Both plots show the blade passing frequency (BPF) tone, which has a frequency of *138.3 Hz*, and a number of BPF harmonics appearing as peaks in the SPL curve.

For noise emission towards the ground, the simulation data is in line with the measurement data, with the BPF showing the highest peak. Compared with the neighboring peaks, the harmonic peaks exhibit smaller SPLs for *n = 3, 9, 14* and higher ones for *n = 6, 11* (peak frequencies described by n*BPF). For sideward noise emissions, the simulation data peaks are in good agreement for *n = 1* to *n = 7*. Concordantly, the peak values are located between *n = 5* and *n = 12*. For frequency peaks higher than *n = 7*, the simulation data over pronounces the SPL peaks. In summary, measurement and simulation spectra are in fair agreement in both emission directions in terms of harmonic tones.

For broadband noise, however, the situation is different. For both emission directions, the CFD/FW-H simulation data does not follow the trend of the broadband noise component in the measurement data. There are two main reasons for this discrepancy. First, the significantly higher broadband in the measurement data for low frequencies can be attributed to background noise, which is not covered by the simulation data. Second, the CFD/FW-H simulation in this study does not explicitly resolve turbulence, and broadband noise can therefore only be resolved to a limited extent.

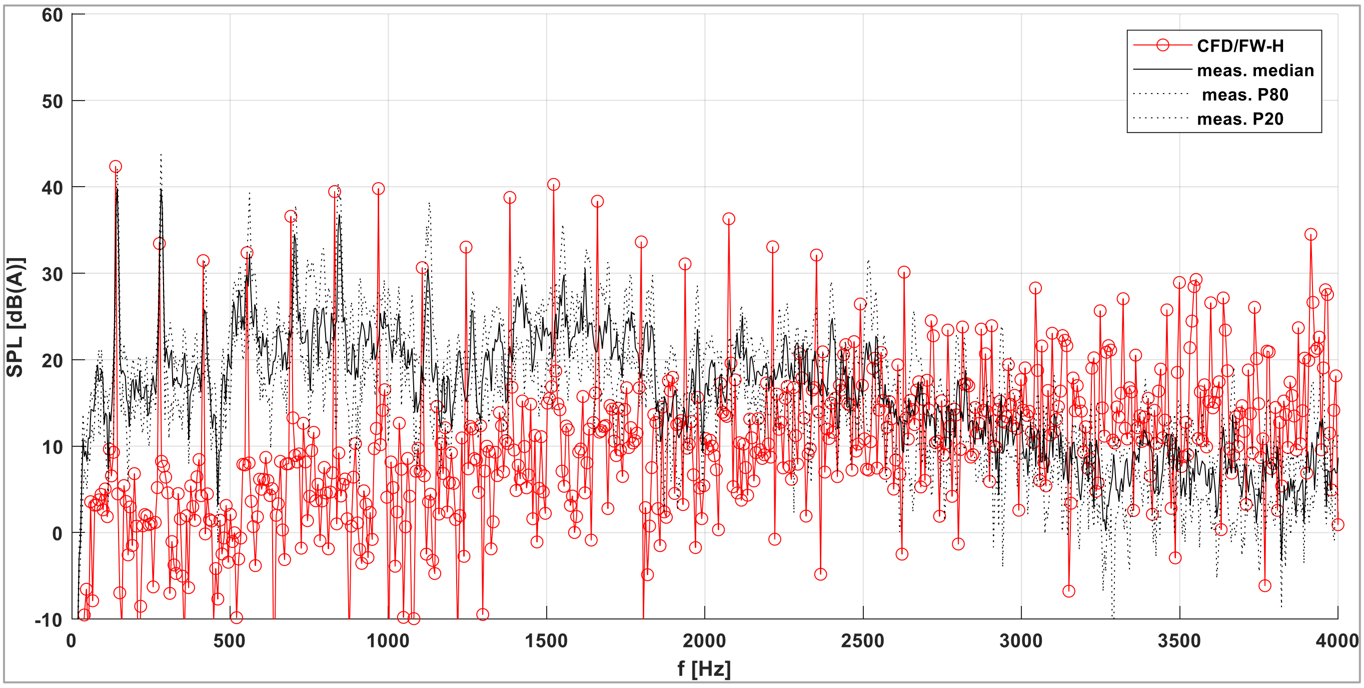


*Figure 3: SPL spectrum; noise emission direction: elevation = -90°; median, 20% and 80% percentile curve for measurement data displayed*

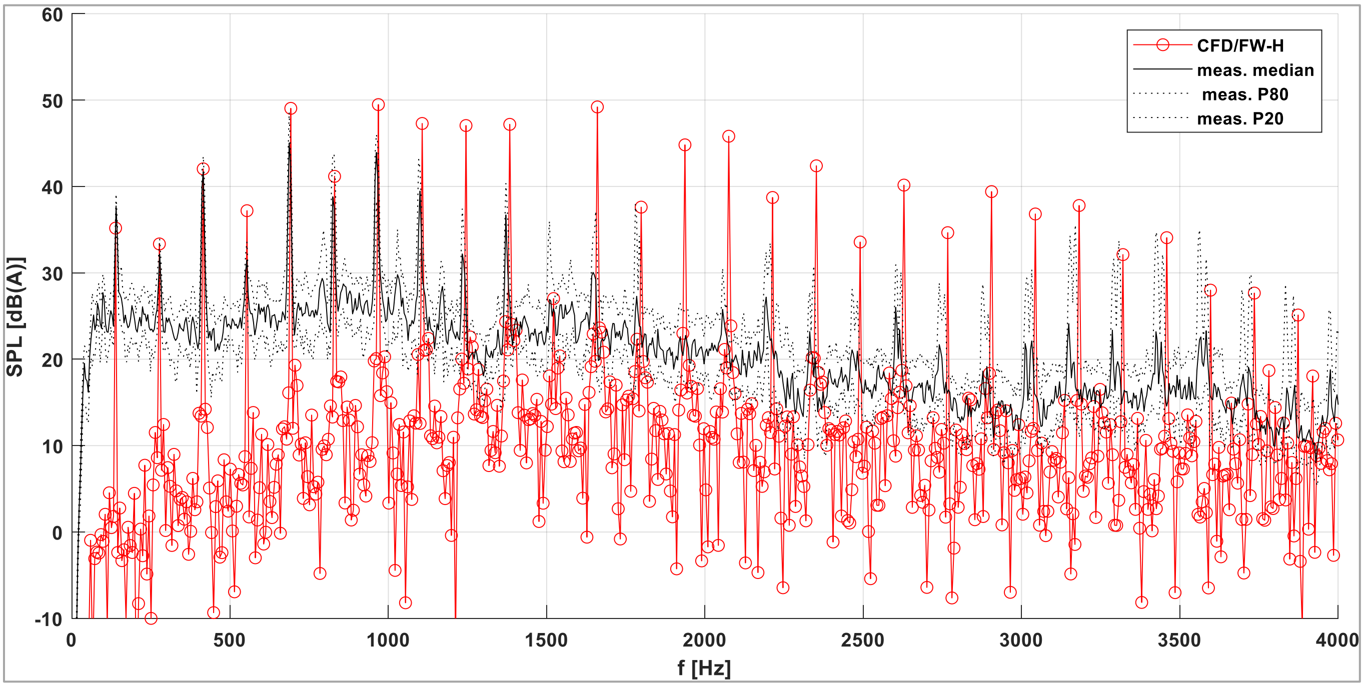


*Figure 4: SPL spectrum; noise emission direction: elevation = -30°, azimuth = 90°; median, 20% and 80% percentile curve for measurement data displayed*

One way of determining the extent to which the different FW-H surface regions contribute to the overall noise is to split the latter into components corresponding to the various FW-H surfaces.

Figure 5 displays the noise hemisphere, divided into the propeller, the airframe, and the sum of both. Unlike Figure 2, the color scale here is adjusted to give low SPL values a higher visibility. The propeller hemisphere is symmetric with the propeller's rotational axis, which is in accordance with theory [7]. The SPL maxima at azimuth *0°* and *180°* can be attributed to interaction noise. The airframe hemisphere exhibits a clear dipole characteristic, with a minimum in the x, z plane. A comparison of the two components with the hemisphere of both components reveals that the contribution of the airframe to the overall sound emission clearly dominates for most emission directions. Only in the x, z-plane, where the airframe component is at its minimum, does the propeller component contribute significantly to the overall sound emissions.

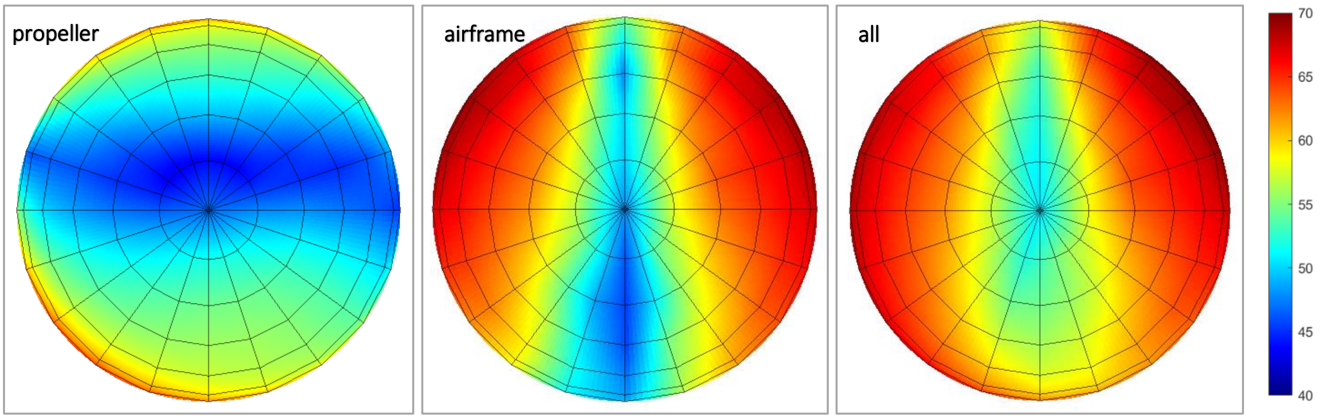


*Figure 5: Simulation data noise hemispheres in [dB(A)]; **left**: propeller only, **center**: airframe only; **right**: all surfaces used for FW-H integration; top: azimuth = 0°, right: azimuth = 90°*

## 3. Evaluation of Design Modifications

This chapter presents three tail design modifications, the goal of which is to influence the aerodynamic interaction between the airframe and propeller and in turn impact the noise emissions of the overall UAV system. These modifications are implemented in the base CFD/FW-H model and evaluated. This is followed by the CFD/FW-H results, which show the effects of the modifications on aerodynamic interactions and the aeroacoustic noise generation.

### 3.1 Conception of Design Modifications

Figure 6 and Figure 7 below show all the design modifications. In modification M1, the axial distance between the propeller and tail has been increased by *6 cm*. This increases the absolute tail/propeller distance from approx. *2 cm* to approx. *8 cm*. The aim is to reduce the interaction between the horizontal stabilizer and the propeller by increasing the distance between the two components. In modification M2, the T-tail is replaced by a conceptual V-tail which consists of two NACA0012 profiles. In order to maintain the function of the base tail, the wetted area of the V-tail remains constant in relation to the base tail [8]. Finally, in modification M3, the same profiles as in M2 are rearranged to form an inverse V-tail, which is connected to the hover booms. The design intention of modifications M2 and M3 is to influence the aerodynamic interactions between the tail and propeller by varying the tail type but without to vary the axial positions of the tail surfaces. Essentially, M2 and M3 affect whether or not the tail wakes flow across the propeller disk and, if so, at which propeller disk position the tail wakes interact with the propeller. However, in contrast to M1, they do not significantly affect the strength of the wakes, as the distance between the tail and propeller is kept constant in relation to the base configuration.

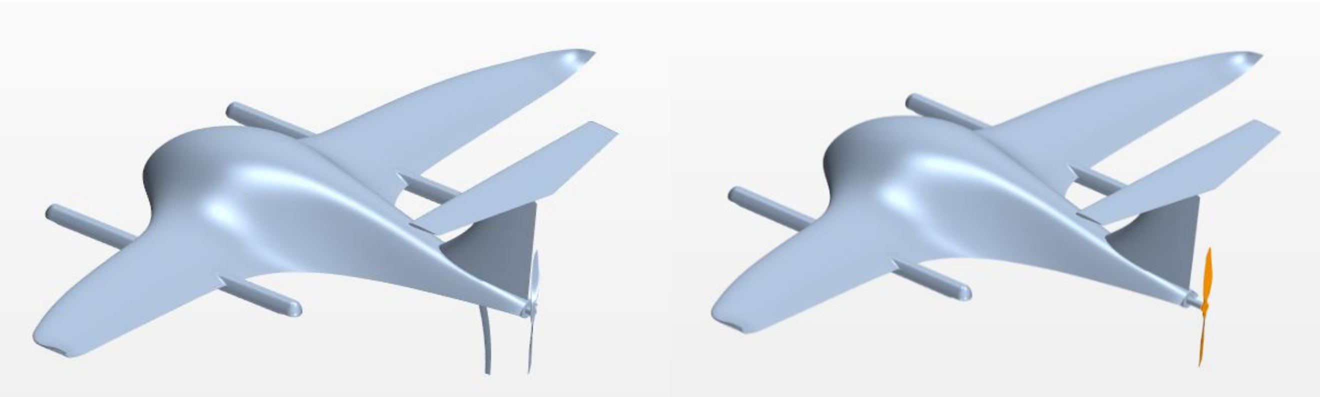

*Figure 6: **Left**: base design; **right**: pusher distance axis distance increased by 6 cm (M1)*

*Figure 7: **Left**: V-tail (M2); **right**: inverted V-tail (M3)*

### 3.2 Numerical Evaluation of Tail Modifications

Taking a hybrid CFD/FW-H approach, noise predictions are based on the aerodynamic results obtained with the CFD solution. Hence, the evaluation of the tail modifications begins with an assessment of the CFD results and then continues with the FW-H results.

#### 3.2.1 Aerodynamic Results

The extent of the aerodynamic interaction between the flow around the airframe and the propeller tends to be high in pusher propeller configurations. In particular, wakes are present in the flow downstream airframe structures that disturb the propeller inflow. Figure 8 and Figure 9 display the velocity magnitude in a section plane located in the middle between the tail and the propeller, relative to the base configuration, for all four investigated cases. Common to the base configuration and all three modifications is that they show a pronounced horizontal wake due to wing downwash and a comparatively weak vertical wake structure due to the rear landing gear leg. The third wake structure, which leads to the most pronounced velocity deficits compared to the mean flow, is the one caused by the tail. As M1 does not affect the tail, the tail wake of M1 is identical to that of the base. For M3, the propeller does not directly interact with the tail wake. As the inverted V-tail surfaces are located above the propeller, the tail wakes do not flow across the propeller disk.

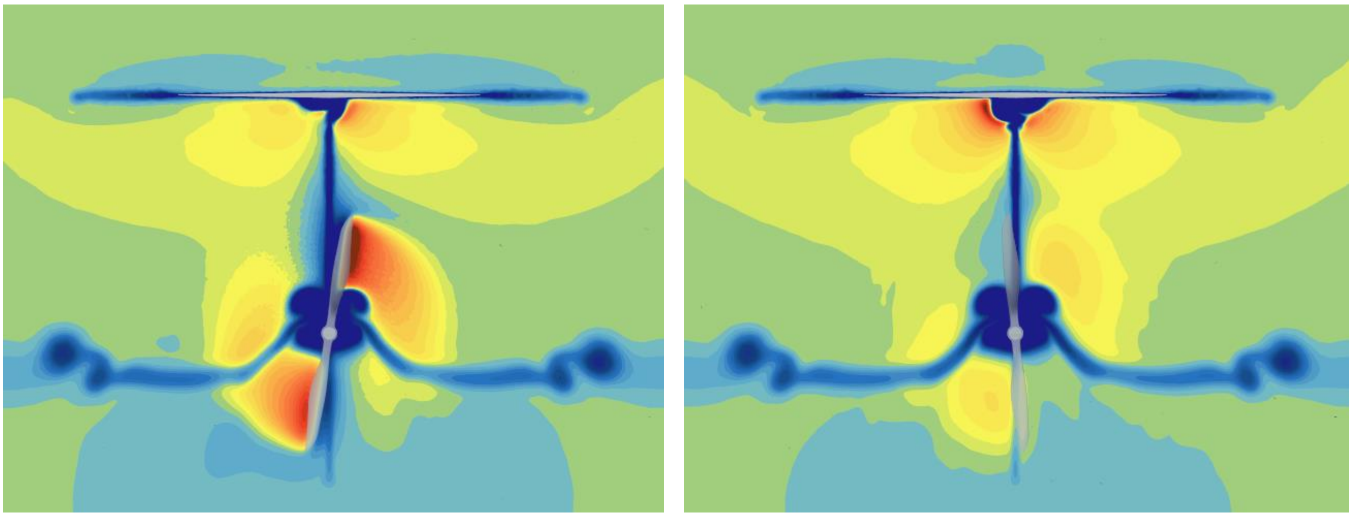

*Figure 8: Velocity magnitude on section between tail and propeller; red: 30 m/s and above, blue: 20 m/s and below;* ***left:*** *base configuration,* ***right:*** *M1*

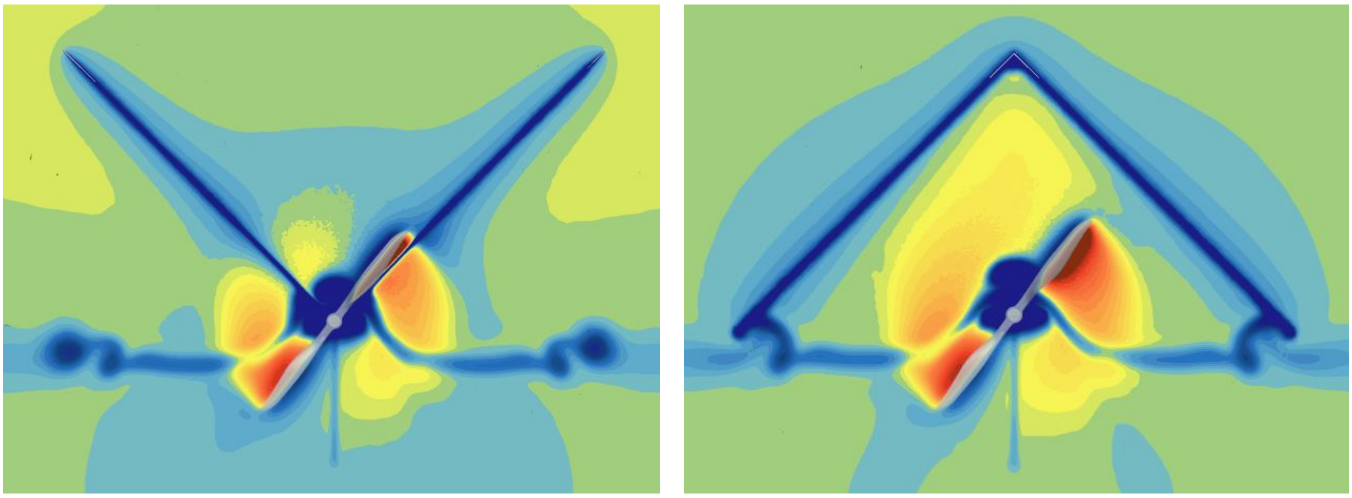

*Figure 9: Velocity magnitude on section between tail and propeller; red: 30 m/s and above, blue: 20 m/s and below;* ***left:*** *M2****, right:*** *M3*

The aforementioned aerodynamic interaction leads to variations in the velocity and angle of attack of the propeller inflow that affect the propeller thrust. Figure 10 (left) displays the thrust curves of all four simulated cases for one propeller rotation. At *t=0 s,* the two-blade propeller is aligned with the vertical axis. The corresponding FW-H sound pressure result for a receiver point located *30 m* downstream on the propeller axis is displayed on the right-hand side of Figure 10. The time shift between the two diagrams is *0.0889 s,* which equals the sound propagation time for a distance of *30 m*. The effect of the wing and landing gear wakes, which are identical in all cases, is most easily recognizable in the thrust curve of M3, but is present in the other curves as well. While the wing wakes lead to two close peaks, which occur twice per rotation, the landing gear wake leads to thrust peaks that occur right in the middle and at the end of each propeller rotation. For the base configuration and for M1 and M2, the interaction of the propeller with the tail wake adds further peaks to the thrust curve. Since, for a two-blade propeller, the interaction with the vertical stabilizer of the base tail coincides exactly with the one with the landing gear, the tail wake peak of the base configuration is apparently further amplified in relation to the V-tail. The sound pressure diagram on the right of Figure 10 shows that all thrust peaks at emission time coincide with the sound pressure pulses at the respective sound immission times. The strongest sound pressure pulses are caused by the interactions with the tail wakes. It is because of the coincidence of the tail and landing gear interaction in the base configuration that the two tail wake sound pressure pulses of the base configuration are stronger in magnitude than the respective four pulses of M2.

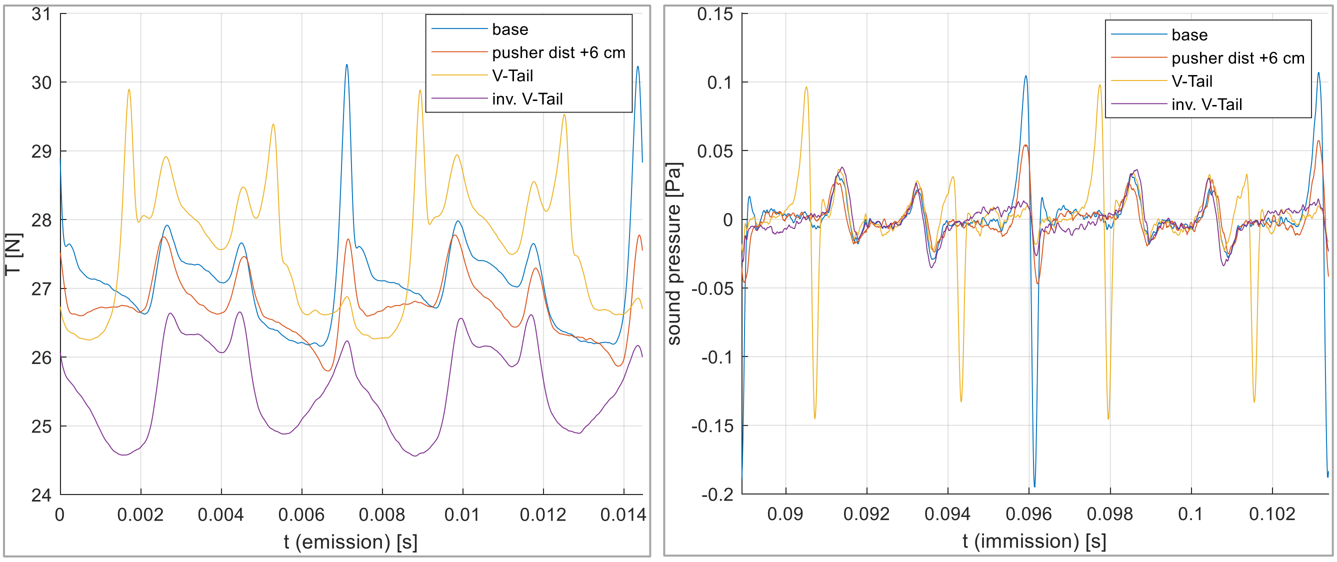


*Figure 10: **Left**: propeller thrust at emission time (for one propeller rotation); **right**: fluctuating component of sound pressure at sound immission time (for one propeller rotation)*

### 3.2.2 Aeroacoustic Results

This section discusses the lower sound hemisphere representations of the CFD/FW-H noise results obtained for all modifications (Figure 11, Figure 12 and Figure 13) and the corresponding sound power levels (Figure 14). In this analysis, the sound power level of the lower noise hemisphere is chosen as a scalar noise metric. As the noise perception of an observer on the ground is dominated by the lower half of the noise hemisphere, the computation of the sound power level is based on the lower noise hemisphere data.

Figure 11 shows that the axial distance increase in M1 leads to a significant noise reduction compared to the base (see Figure 5), which translates to a sound power level reduction of *11.3 dB(A)*. While the directivity of the M1 propeller noise component in relation to the base is unaffected by this modification, that of the airframe component is significantly changed. Furthermore, the sound power level reduction of the airframe component resulting from M1 (*15.5 dB(A)*) is significantly higher than that of the propeller component (*4.6 dB(A)*). Thus, in contrast to the base configuration, the propeller component dominates the overall sound power level for M1. As in the case of M1, the inverted V-tail of M3 also causes an overall reduction in noise emissions compared to the base configuration. A close examination of the sound power levels and noise hemispheres shows that, as with M1, the inverted V-tail of M3 results in a considerable reduction in the airframe noise component, such that the propeller component dominates the overall aircraft noise emissions of M3. While M1 leads to a reduction in the aerodynamic interaction of the tail wake and the propeller, M3 completely avoids direct interaction of tail wake and propeller. It can be concluded from this comparison that the more aerodynamic interaction is reduced, the less sound power is generated overall by the aircraft.

The V-tail shape in M2 results in a twofold increase in the number of circumferential positions in which a propeller blade interacts with a tail wake. As a consequence, the sound power level of the lower hemisphere increases by *2.0 dB(A)*, due to the increased interaction of the V-tail. As with all other modifications, the directivity of the propeller noise contribution remains similar to the base, while that of the airframe changes significantly.

No significant destructive sound interference effects are found in any of the four simulated cases. In none of the cases is the overall sound emission from the aircraft reduced in relation to the sound emission of the dominant component (propeller or airframe).

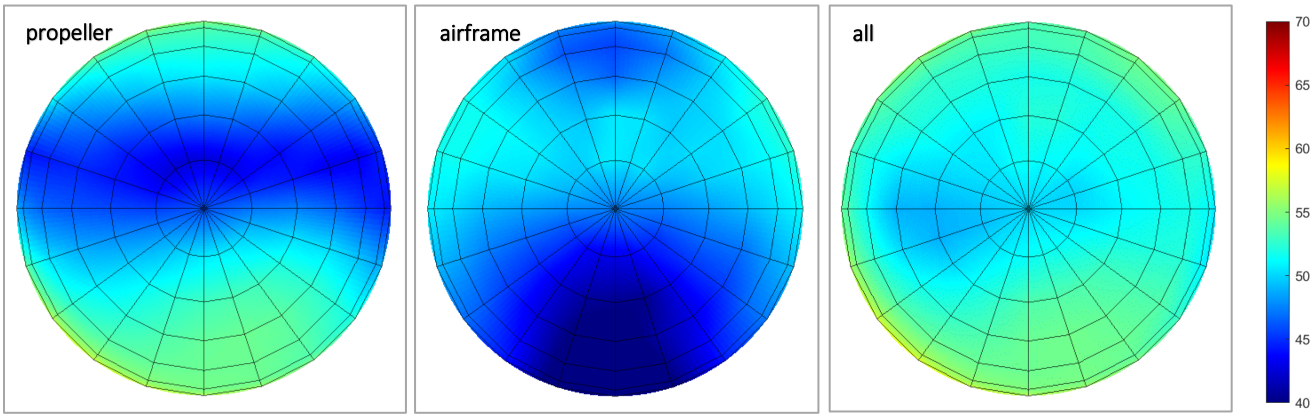


*Figure 11: M1 noise hemispheres in [dB(A)]; **left**: propeller only, **center**: airframe only; **right**: all surfaces used as FW-H integration surfaces; top: azimuth = 0°, right: azimuth = 90°*

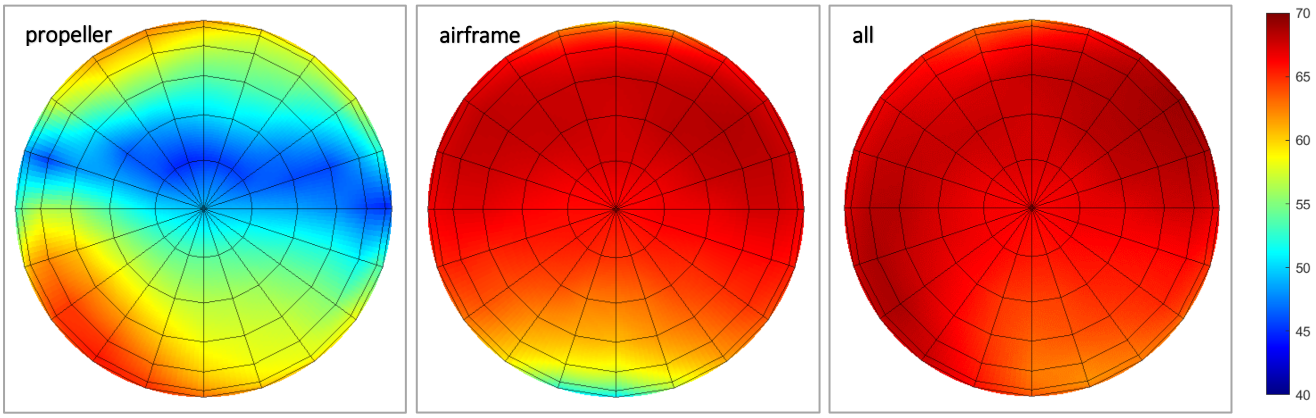


*Figure 12: M2 noise hemispheres in [dB(A)]; **left**: propeller only, **center**: airframe only; **right**: all surfaces used as FW-H integration surfaces; top: azimuth = 0°, right: azimuth = 90°*

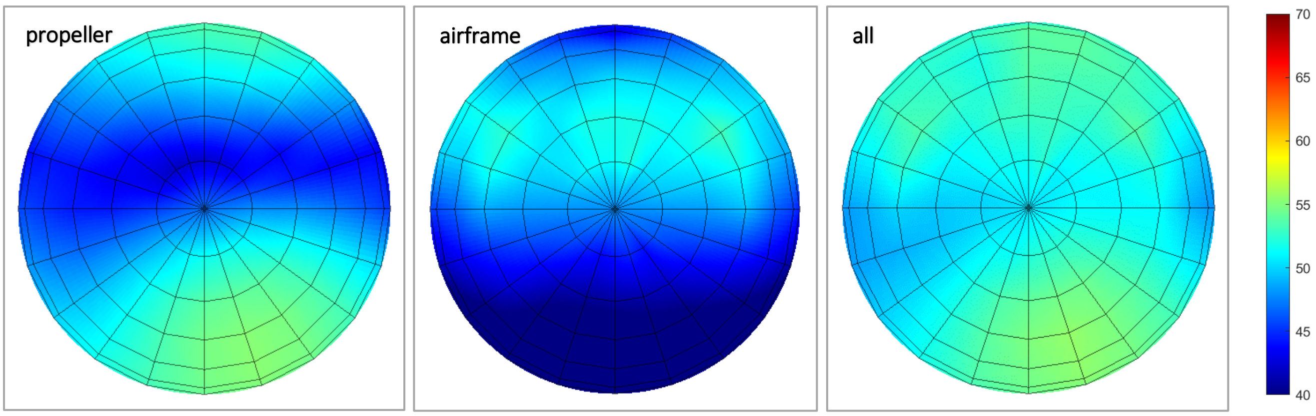


*Figure 13: M3 noise hemispheres in [dB(A)]; **left**: propeller only, **center**: airframe only; **right**: all surfaces used as FW-H integration surfaces; top: azimuth = 0°, right: azimuth = 90°*

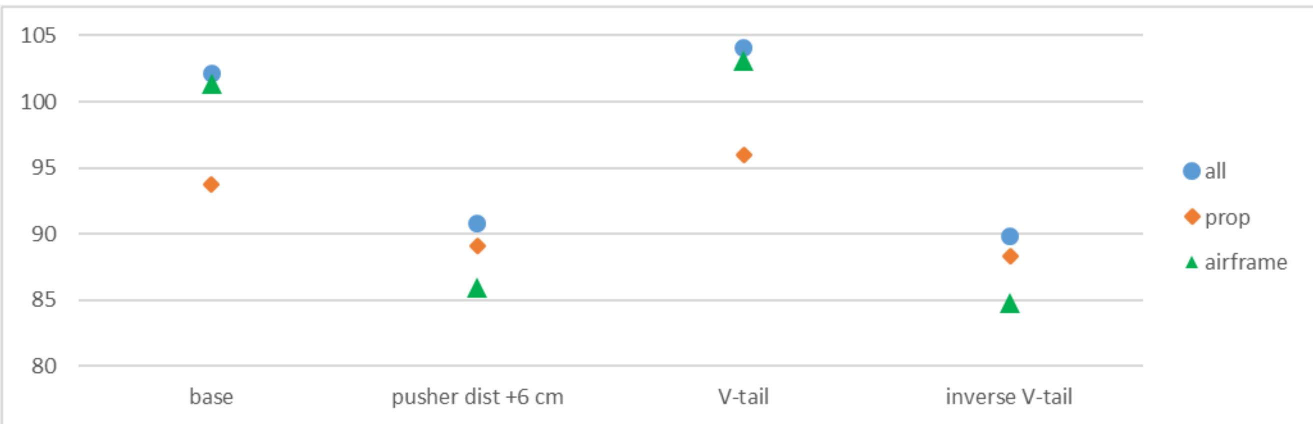


*Figure 14: Sound power levels in [dB(A)] for lower hemispheres and UAV variants (base + modifications), divided into contributing surfaces*

### 3.2.3 Airframe Noise

The interaction noise generation mechanism affecting the propeller noise component was considered in section 3.2.1, and this section now discusses the aeroacoustic source mechanism of the airframe component. The base configuration airframe noise component (see Figure 5) exhibits a dipole characteristic, with its plane of symmetry being identical to the orientation of the vertical stabilizer. This observation suggests that the airframe noise is due to fluctuating forces that act on the tail surfaces which are caused by the rotating propeller. Curle's formulation of Lighthill's acoustic analogy can be used to predict the noise emitted from stationary surfaces in an aeroacoustic source region (see [9], [10] and [11]). It is therefore suitable for calculating noise originating from the above source mechanism. If the observer is located in the far-field and the sound source is acoustically compact, the term of the Curle integral that considers fluctuating forces as sound sources can be simplified to:

$$(1) \qquad p'(\vec{x},t) \approx -\frac{1}{4\pi c_0^2|\vec{x}|} \cdot \frac{x_i}{|\vec{x}|} \cdot \frac{\partial}{\partial t} F_i\left(t - \frac{|\vec{x}|}{c_0}\right)$$

where $p'$ is the sound pressure fluctuation, $c_0$ is the speed of sound, $|\vec{x}|$ is the point source to observer vector, and $F_i$ is the force vector (where the index $i$ represents Cartesian spatial directions). Acoustic compactness means that the sound wavelength is significantly larger than the source dimension. This assumption is justified for harmonic noise radiating from the tail surfaces, because the BPF wavelength, which is *2.43 m,* is one order of magnitude greater than the chord lengths of the tail surface. Consequently, each of the two tail surfaces in both the base configuration and M2 can be reduced to a point source model according to (1), whose strength is proportional to the time derivative of the respective fluctuating aerodynamic forces. The results of (1) are displayed in the propeller plane in Figure 15. In the base configuration, the vertical stabilizer dipole is significantly stronger than the horizontal one, which is the root cause of the pronounced dipole characteristic in the base configuration. In M2, the dipoles of the two V-tail surfaces superposition in such a way that the dipole directivity pattern cancels out. The full FW-H noise results agree well with the results obtained from (1), which validates this Curle-based tail noise model.

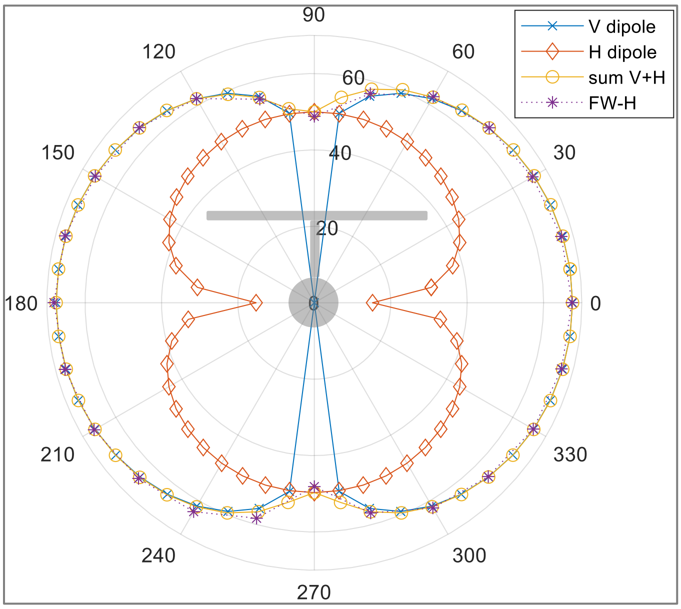


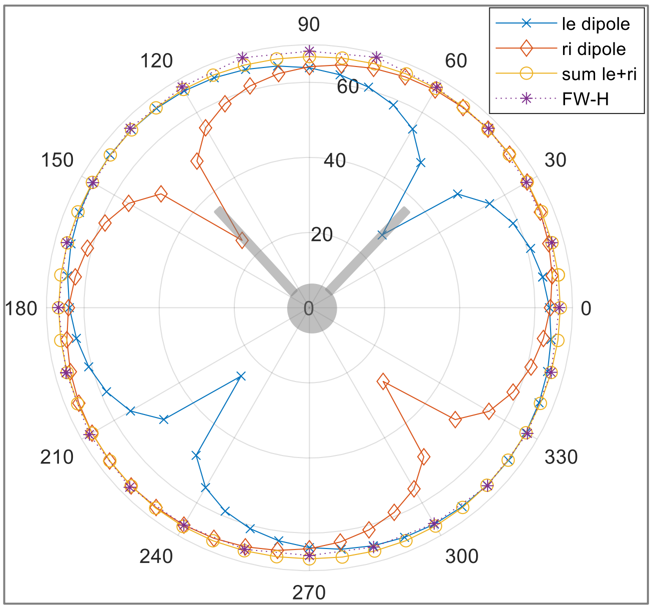


*Figure 15: Polar diagrams in [dB(A)] in propeller plane;* ***left****: base configuration,* ***right****: V-tail (M2)*

### 3.2.4 Propeller Performance

Figure 16 shows a plot of the sound power levels over aerodynamic propeller performance for all four cases. The four data points exhibit a basic sound power level versus efficiency correlation. All cases with higher aerodynamic efficiency also have a higher sound power level than the other cases. This behavior is similar to the noise-efficiency correlation stated for isolated propellers in [3], according to which noise reductions are only possible at the cost of aerodynamic efficiency. Although the correlation does not necessarily hold if noise emissions are dominated by interaction effects, none of the three tail region modifications investigated in this paper manages to reduce noise without decreasing aerodynamic efficiency, and vice versa.

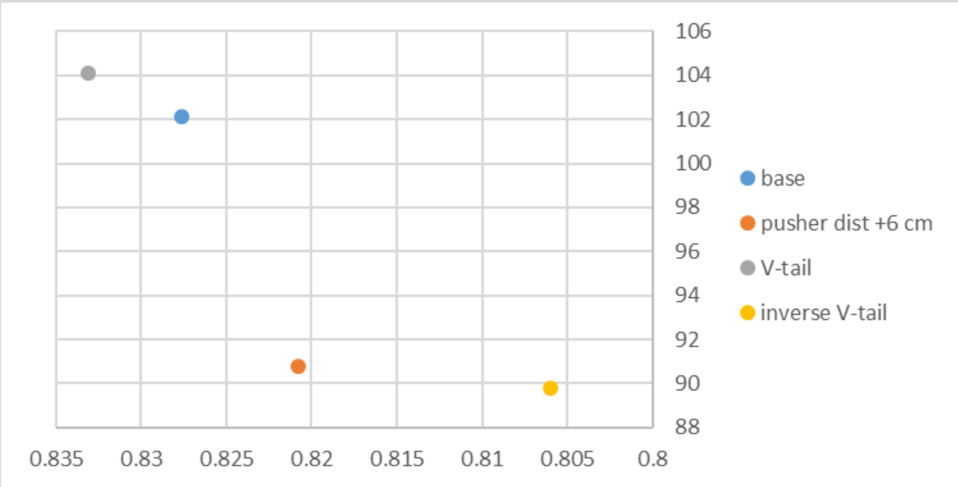


*Figure 16: Sound power level [dB(A)] over aerodynamic efficiency [-]*

## 4. Conclusion and Outlook

This paper assesses design modifications in the tail region of an integrated pusher propeller cargo eVTOL UAV. The purpose of the study is to identify noise optimization potentials for propeller-driven UAVs. First, a CFD/FW-H noise model of a cargo UAV is created and validated using in-flight noise measurement data. The lower noise hemispheres and the sound spectra comparison for two representative noise emission directions shows agreement between the measurement and simulation data. Second, design alternatives affecting the main aeroacoustic source region are suggested; these are implemented in the CFD/FW-H model and assessed numerically. The results of this simulation campaign show that noise generation is reduced by decreasing the aerodynamic interaction between the tail wakes and the propeller.

All in all, this study has identified significant noise reduction potential, supporting the idea of simultaneous optimization of the propeller and airframe. Potential for acoustic optimization can be particularly found in highly integrated configurations in which aerodynamic interactions are unavoidable, as is the case with the UAV considered in this paper. The work presented in this paper only considers airframe modifications but elaborate modifications of both, airframe and propeller, can lead to further reductions in noise.

This study employs a high-fidelity CFD model to obtain a reliable data base with which to assess the acoustic effects of the design modifications in the tail region. A major drawback of this approach is the high computational cost. Future design optimization necessitates a high number of model evaluation. Consequently, a computationally more efficient medium-fidelity CFD approach that is sufficiently accurate to resolve the effects of aerodynamic interaction will be required in future optimizations. To achieve this, the authors suggest using an unsteady BEMT in future work.

## 5. Appendix

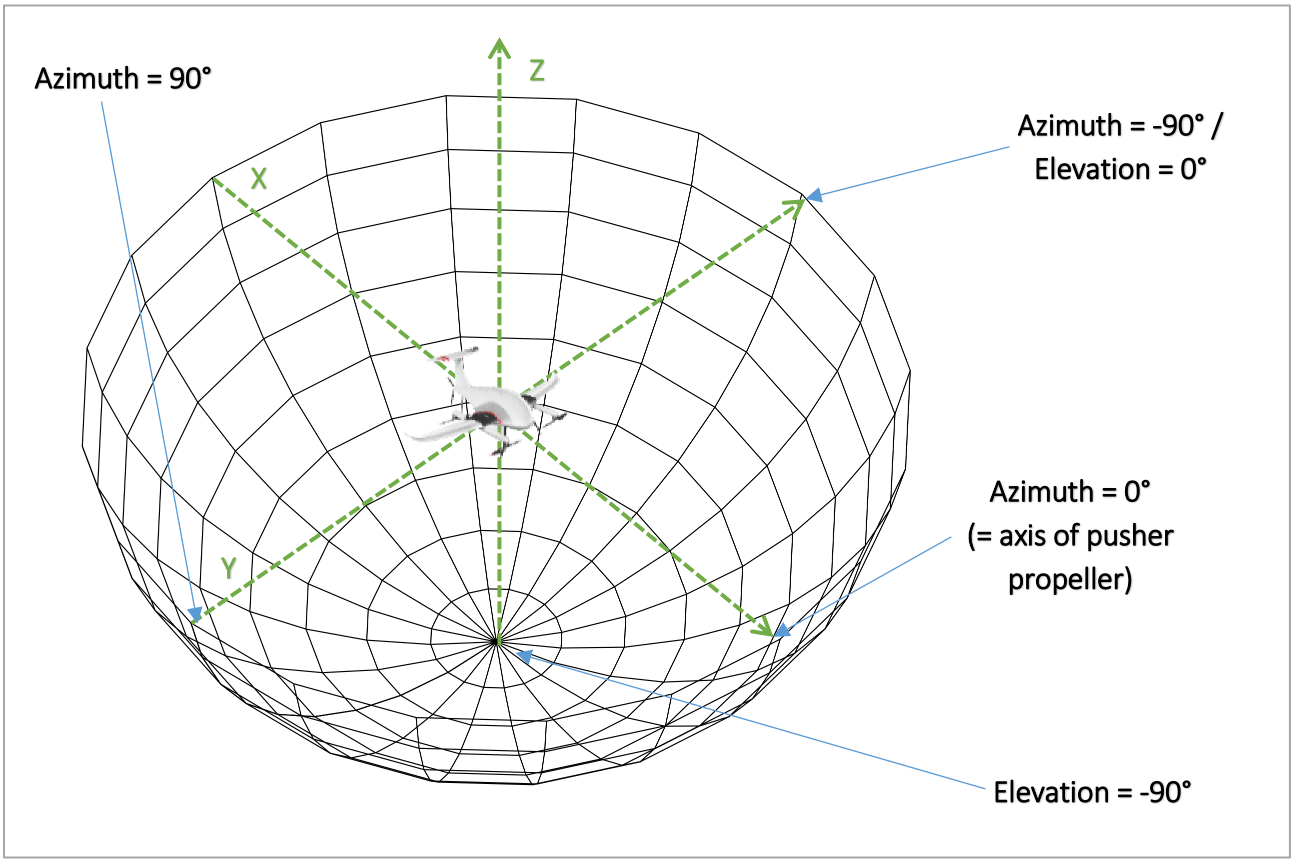


*Figure 17: Lower sound hemisphere sketch showing sound emission directions*

### References


[1] EASA, "www.easa.europa.eu," 2021. [Online]. Available: https://www.easa.europa.eu/sites/default/files/dfu/uam-full-report.pdf. [Accessed 4th of November 2021].

[2] S. Speck, J. Pfefferkorn, K. Kicker and M. Hornung, "Methoden zur Bewertung und Minimierung der Signatur von unbemannten Flugzeugen," in *Deutscher Luft- und Raumfahrtkongress*, Stuttgart, 2013.

[3] A. M. Stoll, "Design of Quiet UAV Propellers," Stanford University, Stanford, CA, 2012.

[4] J. Yin and A. Stürmer, "Coupled uRANS and FW-H Analysis of Installed Pusher Propeller Aircraft Configurations," Miami, Florida, 2009.

[5] M. Schmähl, C. Rieger, S. Speck and M. Hornung, "Semi-empiric noise modeling of a Cargo eVTOL UAV by means of system identification from flight noise measurement data," *CEAS Aeronautical Journal,* pp. 85-96, 01 01 2022.

[6] M. Schmähl, S. Speck and M. Hornung, "Numeric Modeling of the Noise Emission of a Pusher Propeller UAV Configuration," in *AIAA SCITECH 2022 Forum*, San Diego, CA, 2022.

[7] J. E. Marte and D. W. Kurtz, "A Review of Aerodynamic Noise From Propellers, Rotors, and Lift Fans," NASA, Washington, D.C., 1970.

[8] D. Raymer, Aircraft design: a conceptual approach., American Institute of Aeronautics and Astronautics, Inc., 2012.

[9] M. J. Lighthill, "Lighthill, Michael James. "On sound generated aerodynamically I. General theory.," *Proceedings of the Royal Society of London. Series A. Mathematical and Physical Sciences,* vol. 211, no. 1107, pp. 564-587, 1952.

[10] M. J. Lighhill, "Lighthill, Michael James. "On sound generated aerodynamically II. Turbulence as a source of sound.," *Proceedings of the Royal Society of London. Series A. Mathematical and Physical Sciences,* vol. 222, no. 1148, pp. 1-32, 1954.

[11] N. Curle, "The influence of solid boundaries upon aerodynamic sound.," *Proceedings of the Royal Society of London. Series A. Mathematical and Physical Sciences ,* vol. 231, no. 1187, pp. 505-514, 1955.

QUIET DRONES
Second International e-Symposium
on
UAV/UAS Noise
27th to 30th June 2022

# Community noise assessment of a delivery drone based on a flight simulation and noise assessment platform

**Qichen Tan[a], Haoyu Bian[a], Hanbo Jiang[a,1] , Siyang Zhong[a,2], Hong Kam Lo[c], Xin Zhang[a,b,3]**

a. **Department of Mechanical and Aerospace Engineering, The Hong Kong University of Science and Technology, Clear Water Bay, Kowloon, Hong Kong SAR, China.**
b. **HKUST Shenzhen Research Institute, Nanshan District, Shenzhen, China.**
c. **Department of Civil and Environmental Engineering, The Hong Kong University of Science and Technology, Clear Water Bay, Kowloon, Hong Kong SAR, China.**

## Abstract

Drones are promising transport means for the last-mile deliveries in urban communities. However, the low-altitude flights can cause severe noise pollution, requiring rational operational strategies to minimize noise emissions. In this work, the noise emission of delivery drones in an urban community is investigated using a flight simulation and noise assessment platform. Both the tonal and broadband noise components are considered via analytical and semi-analytical prediction methods. The noise propagation in the urban environment is computed by an efficient Gaussian beam tracing method. A systematic study is made for a representative community by considering a drone under different operational conditions. The influence of flight speed and payload on noise emission is studied, and various flight strategies are also explored. This study suggests that the flight simulation and noise assessment platform could be a cost-effective approach for the low-noise path planning of drones in practical urban applications.

[1] jianghanbo@ust.hk
[2] zhongsy@ust.hk
[3] aexzhang@ust.hk

## 1. Introduction

The last-mile delivery in the urban environment has been an emerging and fast-growing sector in recent years [1]. The demand for urban parcel transportation has increased considerably as a result of urbanization and demographic growth, along with the increased diffusion of e-commerce and pervasive technologies [2]. Drones or unmanned aerial vehicles (UAVs) are therefore developed to alleviate ground traffic congestion in future transportation.

In recent years, drones with diverse capabilities for civilian applications have been used in various domains [3], such as food delivery, postal delivery, healthcare delivery, etc. However, some studies have suggested that noise could be a severe environmental problem in urban regions, potentially causing health impairment, annoyance, and learning disorders [4]. Regulations and guidelines are needed to limit noise impact in the community [5][6]. Although the noise requirements for UAVs have not been well established, efforts are still expected with the flourishing of the industry. Numerous endeavours are being devoted to reducing drone noise generation, relying on accurate and high-quality measurements in anechoic facilities [8] and numerical simulations [9]. Operational strategy optimization regarding payload, flight speed, and flight path is another approach to reducing noise.

Accurate modelling of the UAV noise is critical and essential, which is challenging because there is a large variety in UAV designs. Among them, the multirotor configurations have the advantage of realizing vertical take-off and landing capabilities. The thrust is produced by rotors, which generate tonal and broadband noise [10][11]. Many drone noise experiments have been conducted to understand the noise characteristics of isolated rotors or UAVs under different operational conditions [12]-[17]. The prediction of UAV noise calls for efficient and cost-effective approaches. Additionally, the low-altitude operation of UAVs can potentially cause continuous and severe noise pollution in all flight phases. To address these issues, Bian *et al.* [20]-[24] developed a Gaussian beam tracing method to compute the UAV noise impact in a complex urban environment. The established simulation platform also enables investigating the effects of flight paths, noise sources, and acoustic boundary conditions on the nearby buildings.

Figure 1 depicts a typical community delivery scenario in which several packages need to be delivered to the target residents. Due to the limitation of maximum payload, UAVs need to make multiple trips to deliver large volumes of parcels. A short flight with a heavy parcel payload can improve transport efficiency and reduce noise duration; however, a higher thrust is needed to overcome the increased aerodynamic drag, resulting in an increased instantaneous noise level [10][11]. By contrast, a slow flight with a low payload can reduce instantaneous noise emission, but the flight time will be longer. Therefore, efforts are needed to compromise payload and flying speed regarding noise emission.

The community model includes residential buildings, roads, terrain, and a lake. The baseline landscape is at sea-level, with an average building height of $70\ \mathrm{m}$. The speed of sound in the atmosphere is assumed to be constant at $340\ \mathrm{m/s}$. The sea-level atmospheric temperature and ambient pressure are $15\ ℃$ and $101.325\ \mathrm{kPa}$, respectively. According to the impedance model and sound propagation principle [18][19], the flow resistivities $\sigma$ can be used to determine sound attenuation and reflection on environmental boundaries.

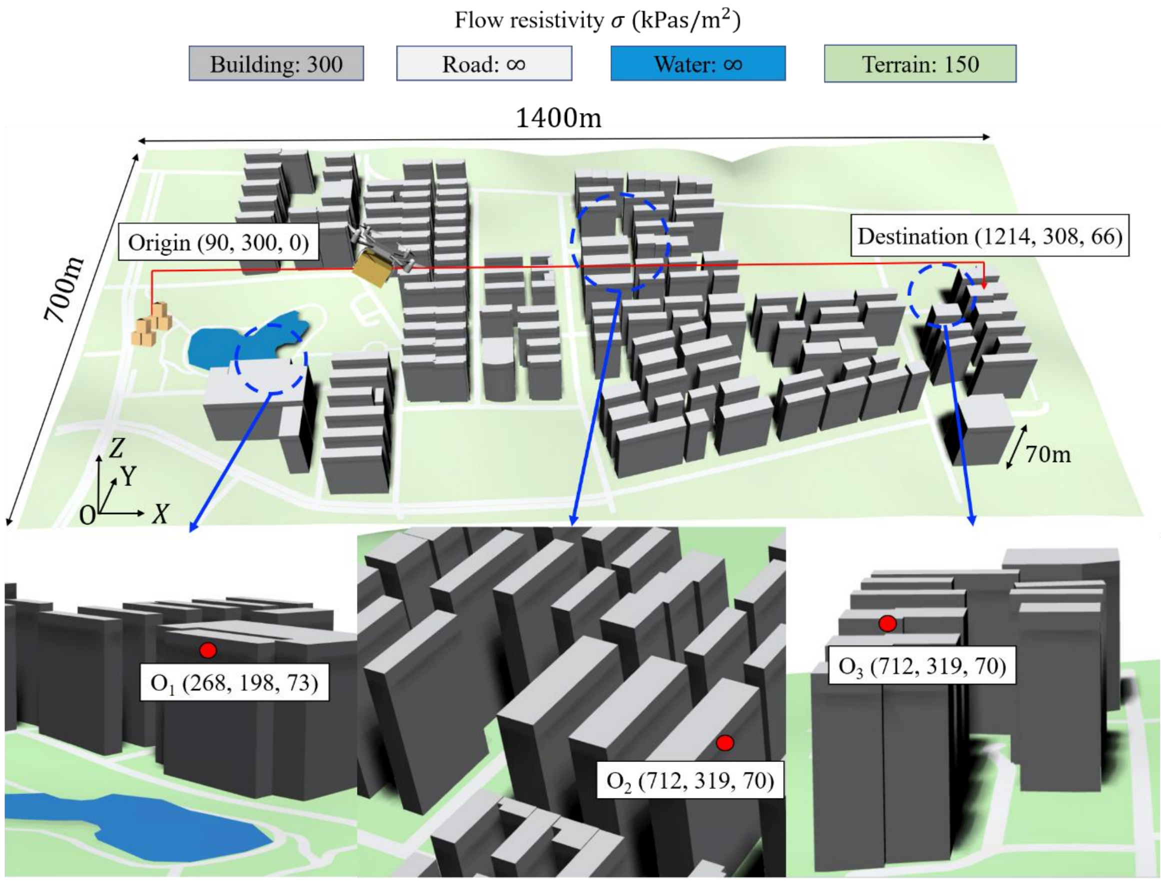

Figure 1: The schematic of UAV delivery in the community.

A typical flight track of the case study is indicated by the red line in Figure 1. The UAV first takes off from the parcel station and then cruises through the neighbourhood at the altitude of $100\ \mathrm{m}$. Finally, the UAV lands on the top of the target building. The sound level caused by the operating UAV is monitored at three observers $\mathrm{O}_1 - \mathrm{O}_3$, as illustrated in Figure 1, which measures the noise emission during three flight phases.

## 2. Methodology

The UAV flight simulation and noise assessment platform includes four main modules: flight dynamics, sound source modelling, sound propagation, and community noise assessment [21]-[24]. Through flight dynamics modelling, the required propeller speed is determined. The propeller noise modelling module can compute the sound source intensities and directivities. Then, the Gaussian beam tracing module computes the sound propagation in the complex urban environment with atmospheric and boundary absorption effects included. Finally, a post-processing module is applied to analyse the noise emission on the environment. A summary of the procedures is shown in Figure 2.

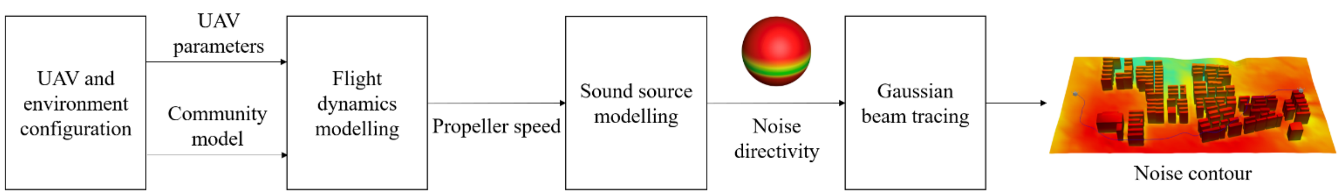

Figure 2: The UAV flight simulation and noise assessment platform.

### 2.1 Flight dynamics modelling

The flight dynamics model of a quadrotor is developed for a symmetric fuselage with rigid propellers. The thrust and the drag are assumed to be proportional to the square of the propeller speed, and the ground effect is neglected. The rotational speed of each propeller is expressed by $f_i$, and the total thrust generated by the four propellers is defined by $F$ as follows: $F = \sum_{i=1}^{4} f_i$. For simplicity, the flying speed remains constant, and the thrust of each propeller is assumed to be the same, satisfying $f_1 = f_2 = f_3 = f_4 = F_1$.

To balance weight, the desired thrust and rotational speed of each propeller are determined. Herein, the rotational speed is inversely calculated using a blade element and momentum theory (BEMT) method [25]. Especially, the thrust $F_0$ of a propeller is estimated from the guessed initial rotational speed $\Omega_0$. Usually, $F_0$ is likely different from the target value $F_1$. In this case, the rotational speed is updated as $\Omega_0^* = \Omega_0\sqrt{F_1/F_0}$, based on which the thrust $F_0^*$ is again estimated using the BEMT solver. The solver iteratively runs until the given error tolerance of thrust is satisfied, i.e., $\epsilon_l \leq \epsilon$, where $\epsilon$ is the stopping criterion, and $\epsilon_l$ is the error between the computed thrust and the target value after $l$ iteration steps. In this work, $l = 4$ could achieve converged results for an accuracy of $\epsilon = 10^{-3}$.

## 2.2 Sound source modelling

In this work, sound source directivities of both tonal and broadband noise are computed at observers on a spherical surface, as shown in Figure 3. The distance from the observers to the UAV center is $1\ \mathrm{m}$. Figure 3 also shows a typical noise directivity result, which will be studied in Section 3.

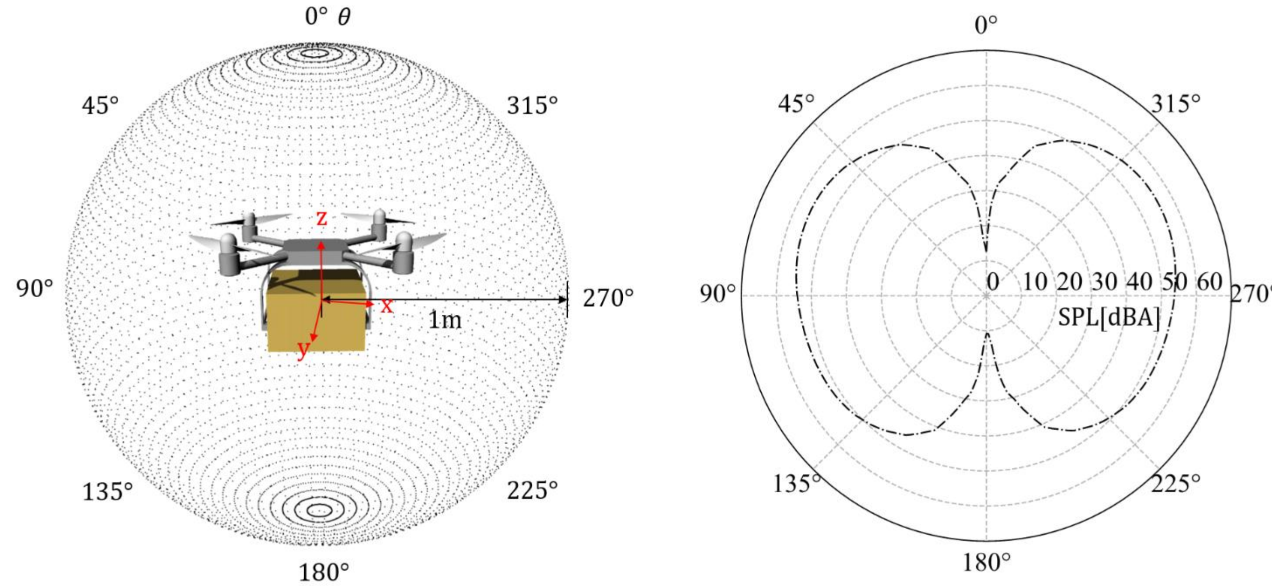


Figure 3: (Left) The global coordinate system for the drone and observers; (Right) A typical noise directivity result.

## 2.3 Gaussian beam tracing

A Gaussian beam tracing method is used to compute sound propagation in complex environments at a low computational cost with satisfactory accuracy [20]-[23]. It considers different acoustic processes. For instance, sound refraction and attenuation effects characterized by the literature [27] are considered during the propagation in the air (a non-turbulent and inhomogeneous medium [21]). In addition, the sound reflection effect caused by impedance boundaries is also robustly modelled. For the sound source, generic source directivities with multiple frequencies can be efficiently modelled [23]. The simulation tool has been previously adopted for multi-rotor flying vehicle noise assessment [22][28].

### 2.4 Noise metrics

In this work, the sound pressure level (SPL) and equivalent sound level ($\mathrm{L_{eq}}$) are used to measure the community noise [5]. A-weighting is applied to instrument-measured sound levels to account for the relative loudness perceived by human ears. The SPL is defined as:

$$\mathrm{SPL} = 10\log_{10}\left(\frac{p}{p_{ref}}\right)^2 ,$$

where $P_{ref} = 2 \times 10^{-5}$ Pa is the reference sound pressure, $p$ is the effective sound pressure. In this work, the sound pressure $p$ is computed using the Gaussian beam tracing solver. The physical effects of a moving sound source are neglected in this work because the UAV's flying speed is much slower than the sound speed.

$\mathrm{L_{eq}}$ quantifies the continuous noise emission and measures the average acoustic energy over a period $T$. It follows:

$$\mathrm{L_{eq}} = 10\log_{10}\left(\frac{1}{T}\int_0^T \frac{p^2}{p_{ref}^2}\,dt\right),$$

where $T$ is the noise measurement duration determined by the duration of one or multiple noise events.

## 3. Result and discussion

### 3.1 Influence of UAV flying speed

In this section, the noise emission under various speed conditions is studied. The take-off and landing speed varies from 1 m/s to 5 m/s, and the cruise speed changes from 5 m/s to 15 m/s. The payload is configurated as 3 kg, and the total weight of the UAV is 7 kg.

#### 3.1.1 Influence of take-off and landing speed

Figure 4 and Figure 5 show the sound source directivities of a UAV at different speeds during take-off and landing, respectively. The tilt angle of the UAV is kept at 0°, as the UAV is only subjected to vertical gravity, air resistance, and thrust. The tonal noise mainly concentrates on the propeller plane, while the broadband noise concentrates on the perpendicular plane. In the take-off phase, the average tonal noise increases by about 2 dBA from 1 m/s to 5 m/s, while the broadband noise only shows a 0.2 dBA increment. In the landing phase, the directivity patterns are similar to those of the take-off phase. However, as the speed increases, the noise intensity falls slightly since a slower landing takes a higher upward thrust to support. The tonal noise drops by around 2.1 dBA from 1 m/s to 5 m/s, and the broadband noise decreases by 0.5 dBA, with the decline of upward thrust from 68.5 N to 65.2 N.

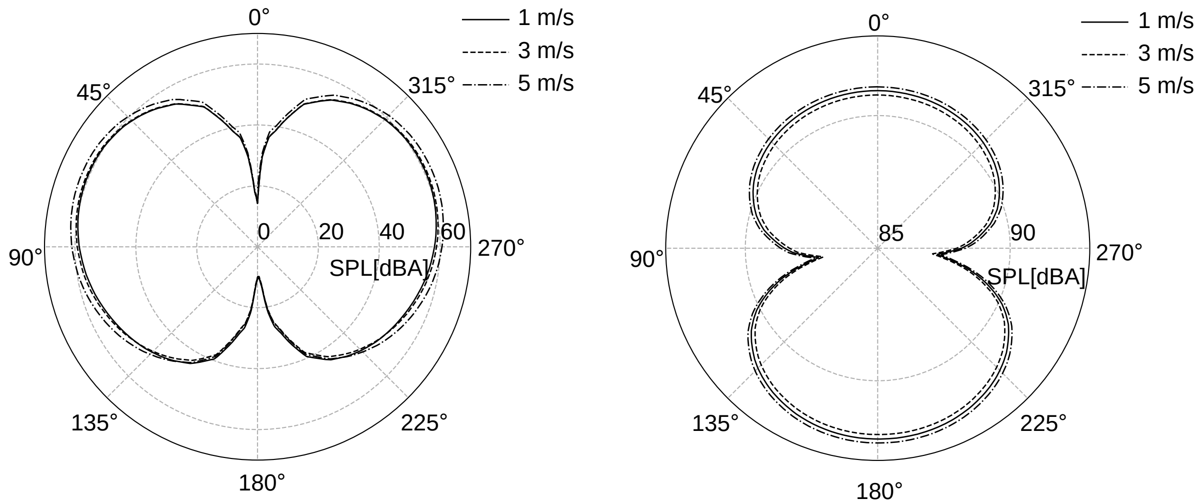


Figure 4: Sound source directivities of a UAV with different speeds during take-off: (left) tonal noise; (right) broadband noise.

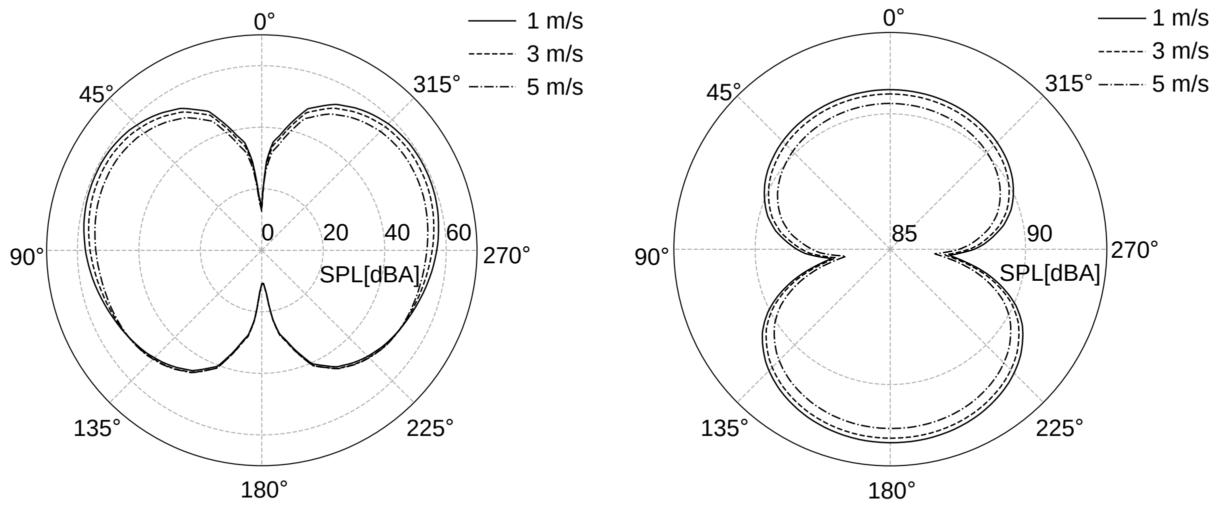


Figure 5: Sound source directivities of a UAV with different speeds during landing: (left) tonal noise; (right) broadband noise.

The SPL variations in the take-off and landing phase are illustrated in Figure 6 at observes $\mathrm{O}_1$ and $\mathrm{O}_3$. Table 1 compares the continuous noise level $\mathrm{L}_{\mathrm{eq}}$. The measurement duration $T$ is 100 s and 34 s in two phases. During the take-off phase, the $\mathrm{L}_{\mathrm{eq}}$ decreases by 5.1 dBA when the speed increases from 1 m/s to 5 m/s. During the landing phase, there is a 7.9 dBA decrement of $\mathrm{L}_{\mathrm{eq}}$ from 1 m/s to 5 m/s. The results suggest that full-speed take-off and landing are favourable combinations regarding continuous noise emission.

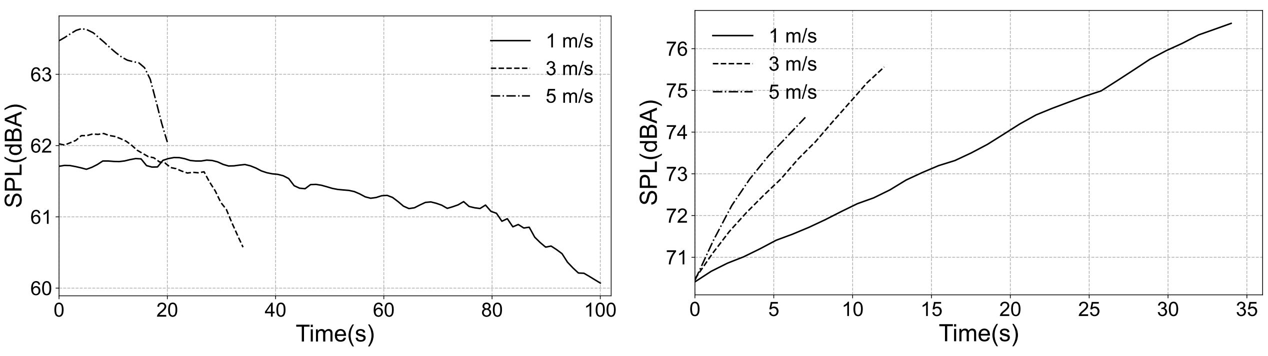


Figure 6: SPL variation under different speed conditions during: (left) take-off; (right) landing.

Table 1: The $L_{eq}$ of the UAV at different speeds during take-off and landing.

| Speed (m/s) | Take-off | | Landing | |
|---|---|---|---|---|
| | Duration (s) | $L_{eq}(100s)$ (dBA) | Duration (s) | $L_{eq}(34s)$ (dBA) |
| 1 | 100 | 61.35 | 34 | 73.91 |
| 3 | 33 | 57.08 | 11 | 68.87 |
| 5 | 20 | 56.25 | 7 | 65.98 |

### 3.1.2 Influence of cruise speed

Figure 7 shows the sound source directivities of the UAV at different cruise speeds. For these cases, the UAV has tilt angles to balance both weight and aerodynamic drag. When the flying speed changes from 5 m/s to 15 m/s, the tilt angle varies from $5°$ to $37°$, causing a significant difference in the directivity. As the cruise speed increases, the thrust grows from 68.8 N to 85.4 N. The noise level is also increased significantly by about 10 dBA for the tonal noise and 1.5 dBA for the broadband noise.

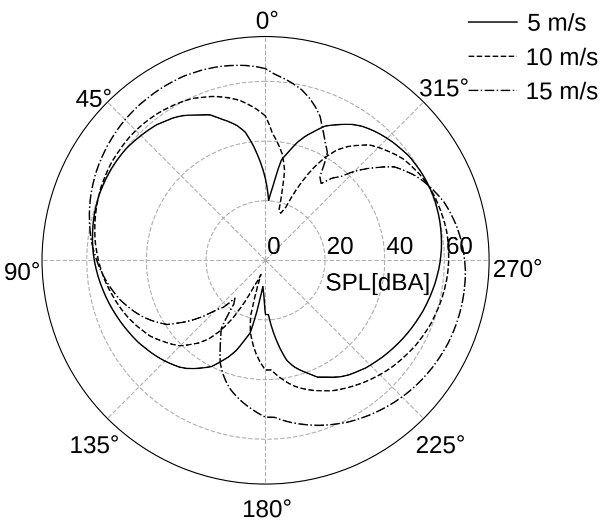


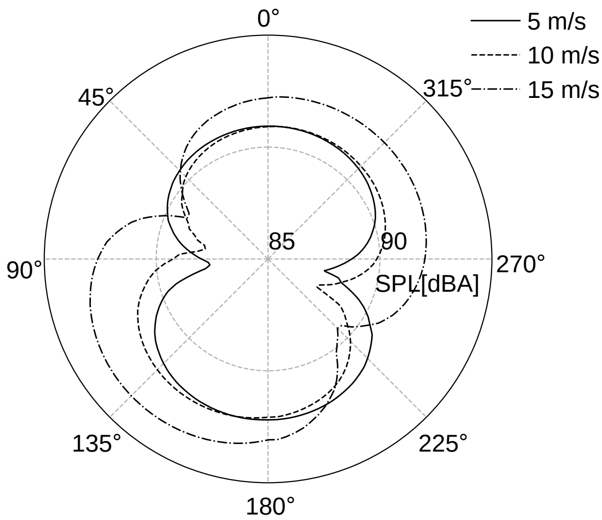


Figure 7: Sound source directivities of a UAV with different speeds during cruising: (left) tonal noise; (right) broadband noise.

Figure 8 demonstrates the SPL variation at the observer location $O_2$, and Table 2 compares the $L_{eq}$ during cruising. The measurement duration is $T = 226\ s$. The SPL rises dramatically with the cruise speed from 10 m/s to 15 m/s. However, from 5 m/s to 10 m/s, there is no significant increase in the maximum SPL value, indicating that the 10 m/s-cruise can halve the noise duration without increasing the average instantaneous noise level. Table 2 shows that the minimum $L_{eq}$ value is obtained at the speed of 10 m/s.

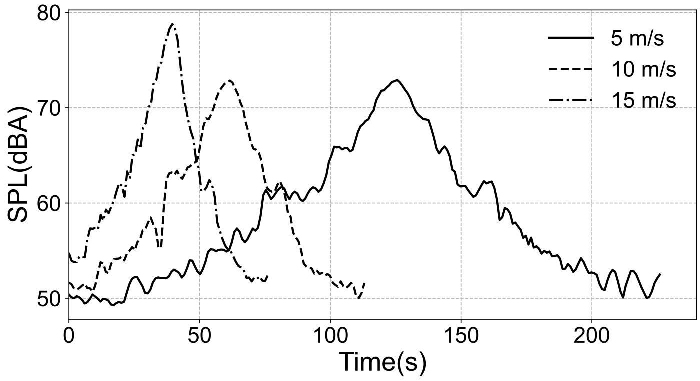


Figure 8: SPL variation under different speed conditions during cruising.

Table 2: The $\mathrm{L_{eq}}$ of the UAV at different speeds during cruising.

| Speed (m/s) | Cruise | |
|---|---|---|
| | Duration (s) | $\mathrm{L_{eq}}(226s)$ (dBA) |
| 5 | 226 | 63.46 |
| 10 | 75 | 61.31 |
| 15 | 45 | 64.39 |

### 3.2 Influence of UAV payload

In this section, we investigate the noise emission of different payloads. We compare the UAV noise emissions under three payload configurations: 0 kg, 1 kg, and 3 kg. The flying speed constantly keeps at 5 m/s during take-off/landing and 10 m/s during cruising. To explore the optimal payload configuration for different cargo demands, both the $\mathrm{L_{eq}}$ of a single trip and the $\mathrm{L_{eq}}$ caused by multiple trips when completing a 30 kg cargo delivery assignment are compared.

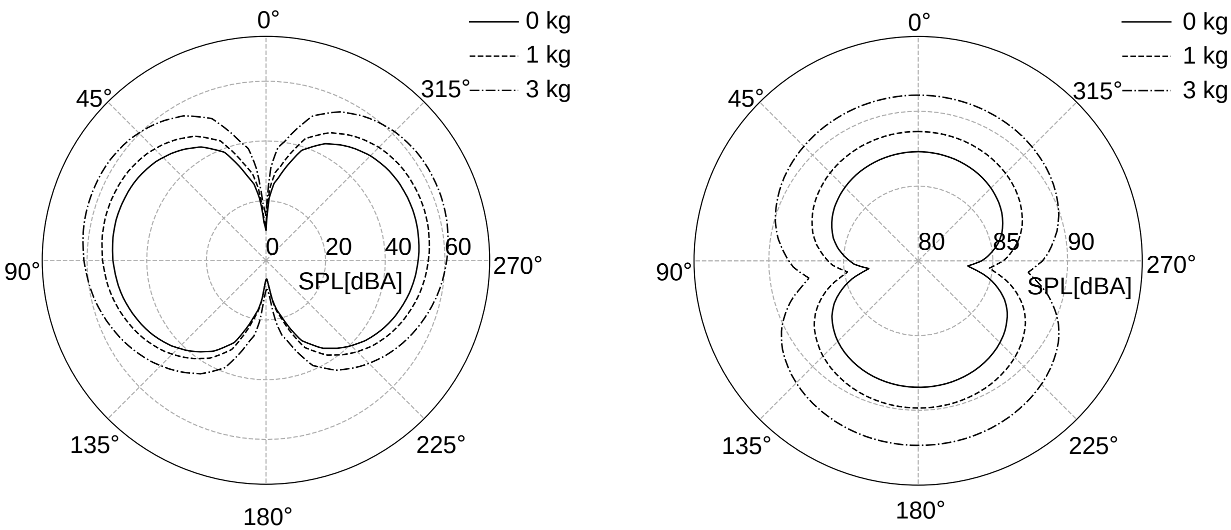


Figure 9: Sound source directivities of a UAV with different payloads during take-off: (left) tonal noise; (right) broadband noise.

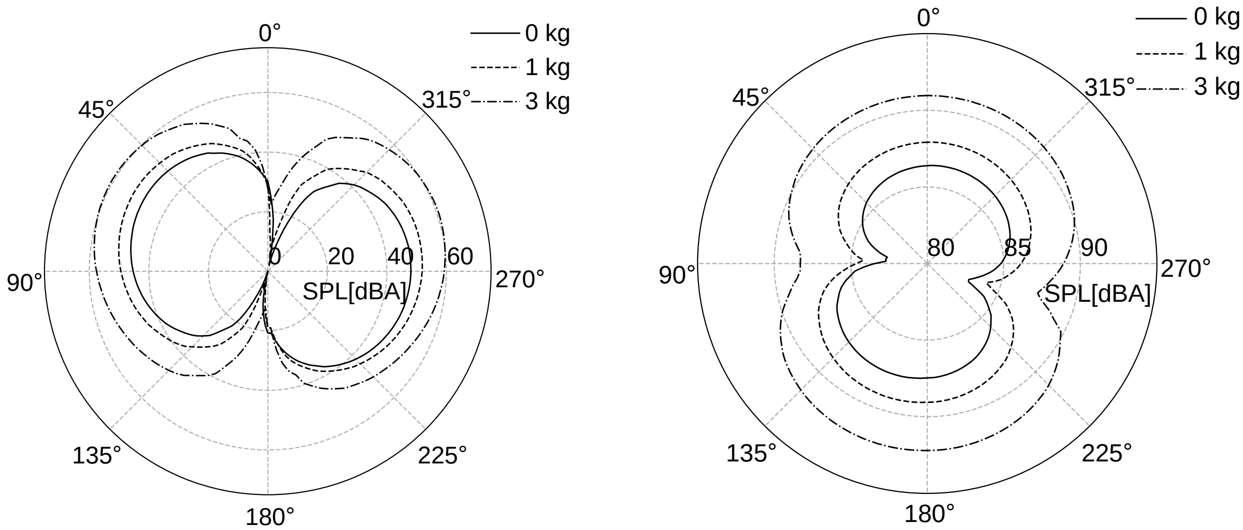


Figure 10: Sound source directivities of a UAV with different payloads during cruising: (left) tonal noise; (right) broadband noise.

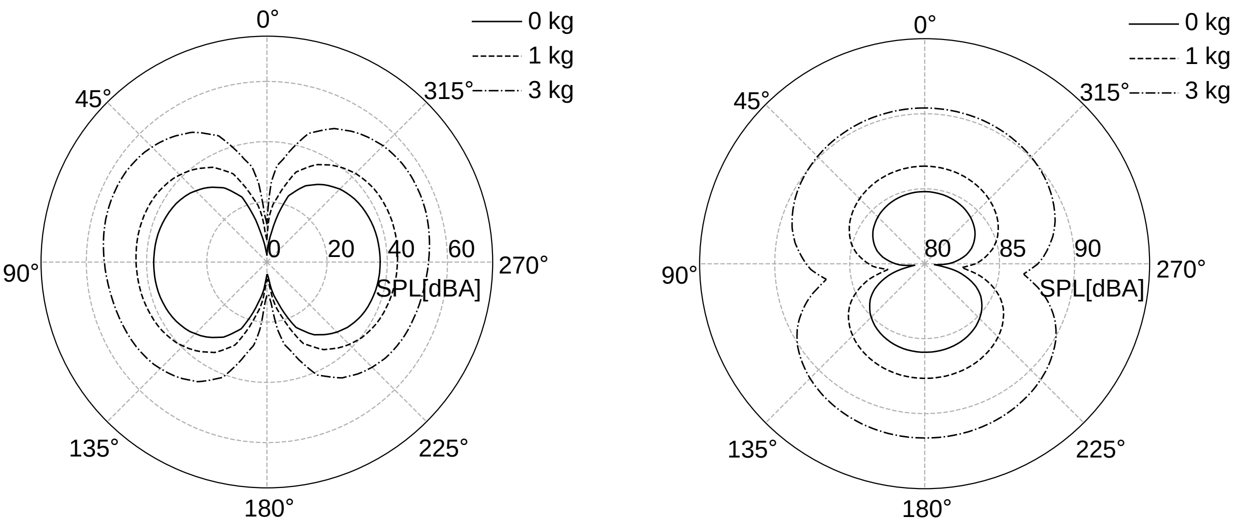


Figure 11: Sound source directivities of a UAV with different payloads during landing: (left) tonal noise; (right) broadband noise.

Figure 9, Figure 10, and Figure 11 present the sound source directivities of a UAV with different payloads during three flight phases. In the take-off and landing phases, the tilt angle of the UAV is kept at $0°$. Both the tonal and broadband noise has a significant increase with the payload. In the take-off phase, the tonal noise increases by around 10 dBA from 0 to 3 kg, while the broadband noise increases by about 4 dBA, due to the change of upward thrust from 42.6 N to 72 N. In the landing phase, the tonal noise increases by approximately 15 dBA, while the broadband noise shows a 5 dBA growth due to the increased upward thrust from 35.8 N to 65.2 N. During the cruise phase, the UAV tilts forward, leading to the change of directivity pattern. The tilt angle decreases from $19°$ to $11°$ with the rise of the payload. The tonal and broadband noise has a 15 dBA and 5 dBA increment, respectively.

Figure 12 illustrates the SPL variation under different payloads during three flight phases. Table 3 compares the $\mathrm{L_{eq}}$ measured by a single trip and multiple trips, respectively. The single trip $\mathrm{L_{eq}}$ indicates the continuous noise of a single-trip delivery assignment, with the measurement duration $T$ of 20 s, 113 s, and 7 s in three flight phases. The result shows that the single trip $\mathrm{L_{eq}}$ increases with the payload, in which the minimum value is obtained at 0 kg during each phase. The multiple trips $\mathrm{L_{eq}}$ indicates the continuous noise emission of a mass delivery assignment. For a 30 kg delivery assignment, the measurement duration $T$ is 600 s, 3390 s, and 210 s in three flight phases, respectively. In all three phases, the multiple trips $\mathrm{L_{eq}}$ of the 3 kg payload UAV is less than that of the 1 kg payload UAV, especially in the cruise phase, with a noise reduction of 2.8 dBA.

Table 3: $\mathrm{L_{eq}}$ on observers due to UAV flights with different payloads during three phases.

| Payload (kg) | Take-off | | Cruise | | Landing | |
|---|---|---|---|---|---|---|
| | $\mathrm{L_{eq}}(20s)$ (dBA) | $\mathrm{L_{eq}}(600s)$ (dBA) | $\mathrm{L_{eq}}(113s)$ (dBA) | $\mathrm{L_{eq}}(3390s)$ (dBA) | $\mathrm{L_{eq}}(7s)$ (dBA) | $\mathrm{L_{eq}}(210s)$ (dBA) |
| 0 | 56.99 | - | 62.05 | - | 69.05 | - |
| 1 | 58.86 | 58.86 | 62.64 | 62.64 | 70.03 | 70.03 |
| 3 | 63.53 | 58.75 | 64.61 | 59.84 | 73.88 | 69.11 |

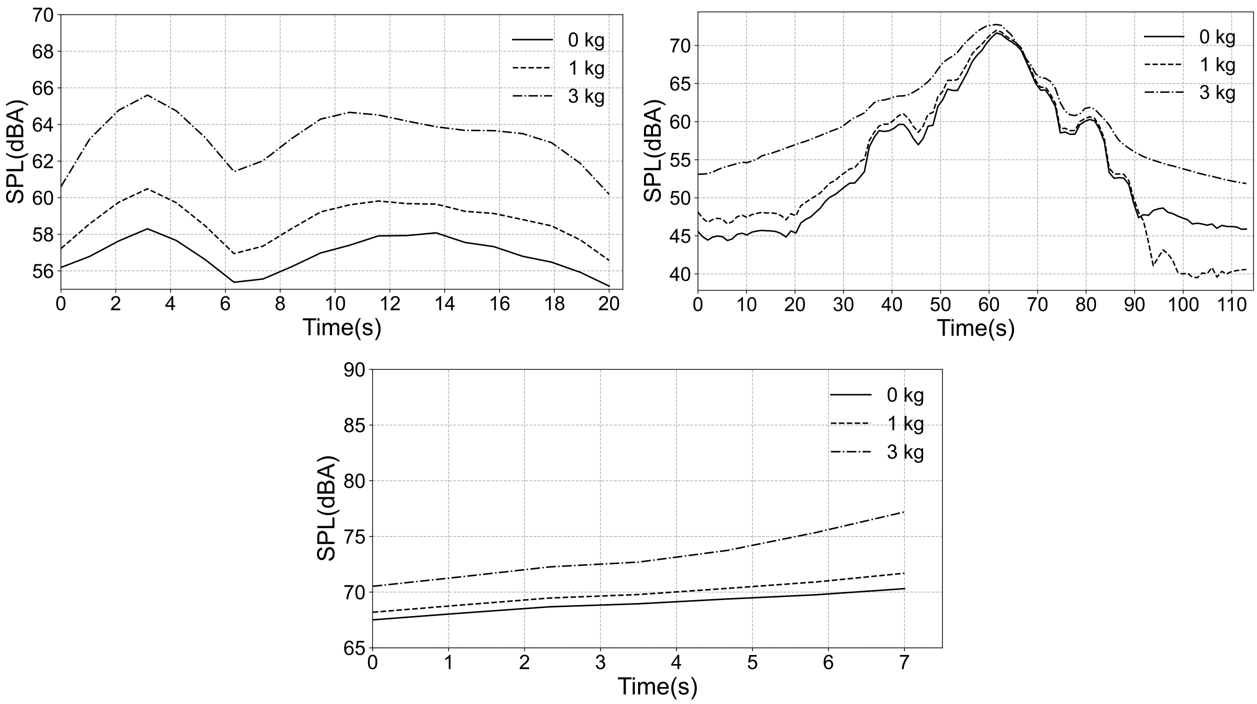

Figure 12: SPL variation under different speed conditions during: (upper left) take-off; (upper right) cruise; (bottom) landing.

## 4. Conclusions

The impact of UAV noise on the community is investigated in this study. A flight simulation and noise assessment platform with flight dynamics, aeroacoustic performance, sound source, and Gaussian beam tracing modules are used to assess the noise emissions for various flying speeds and payloads. Two noise metrics of SPL and $L_{eq}$ are used to quantify the instantaneous and continuous noise emissions. Results show that reducing speed and payload is beneficial for instantaneous noise control in all flight phases. In the mass delivery assignment, the continuous noise emission is sensitive to flying speeds and payloads. Nevertheless, it is still possible to develop low-noise operational strategies by properly balancing time cost and noise emission.

### Acknowledgement

The study is supported by the National Key R&D Program of China (2018YFE0183800). Qichen Tan thanks the Hong Kong University of Science and Technology (Guangzhou) for supporting his Ph.D. thesis research.

### References

[1]. Perboli, G., De Marco, A., Perfetti, F., & Marone, M. (2014). A new taxonomy of smart city projects. Transportation Research Procedia, 3, 470-478.
[2]. Perboli, G., & Rosano, M. (2019). Parcel delivery in urban areas: Opportunities and threats for the mix of traditional and green business models. Transportation Research Part C: Emerging Technologies, 99, 19-36.
[3]. Hassanalian, M., & Abdelkefi, A. (2017). Classifications, applications, and design challenges of drones: A review. Progress in Aerospace Sciences, 91, 99-131.
[4]. Kaltenbach, M., Maschke, C., Heb, F., Niemann, H., & Führ, M. (2016). Health impairments, annoyance and learning disorders caused by aircraft noise. International Journal of Environmental Protection, 6(1), 15-46.
[5]. Berglund, B., Lindvall, T., Schwela, D. H., Organization, W. H. (1999), Guidelines for community noise, WHO.
[6]. Hurtley, C. (Ed.). (2009). Night noise guidelines for Europe. WHO Regional Office Europe.
[7]. International Civil Aviation Organization (ICAO): Guidance on the Balanced Approach to Aircraft Noise Management (2008). ICAO Doc.9829, 2nd edition.

[8]. Wu, H., Zheng, C., Zhou, P., Fattah, R., Zhang, X., Zhou, G., & Chen, B. (2021). The multi-functional rotor aerodynamic and aeroacoustic test platform at HKUST. NOISE-CON Paper 4410-4417.
[9]. Jiang, H., Zhang, X., & Huang, X. (2019). Reduced-basis boundary element method for efficient broadband acoustic simulation. Journal of Sound and Vibration, 456, 374-385.
[10]. Hanson DB, Parzych DJ. (1993). Theory for noise of propellers in angular inflow with parametric studies and experimental verification. NASA Contractor Report TP-4499.
[11]. Brooks, T. F., Pope, D. S., and Marcolini, M. A. (1989). Airfoil Self-Noise and Prediction, NASA RP 1218.
[12]. Wu, H., Chen, W., Fattah, R., Fang, Y., Zhong, S., & Zhang, X. (2020). A rotor blade aeroacoustics test platform at HKUST. NOISE-CON Paper 2476-2484.
[13]. Fattah, R. J., Chen, W., Wu, H., Wu, Y., & Zhang, X. (2019). Noise measurements of generic small-scale propellers. AIAA Paper 2019-2498.
[14]. Wu, H., Zhou, P., Zhong, S., Zhang, X., & Luo, K. (2021). Experimental assessment of the noise characteristics of propellers for commercial drones. NOISE-CON Paper 4418-4425.
[15]. Torija, A. J., Li, Z., & Self, R. H. (2020). Effects of a hovering unmanned aerial vehicle on urban soundscapes perception. Transportation Research Part D: Transport and Environment, 78, 102195.
[16]. Intaratep, N., Alexander, W. N., Devenport, W. J., Grace, S. M., & Dropkin, A. (2016). Experimental study of quadcopter acoustics and performance at static thrust conditions. AIAA Paper 2016-2873.
[17]. Christian, A. W., & Cabell, R. (2017). Initial investigation into the psychoacoustic properties of small unmanned aerial system noise. AIAA Paper 2017-4051.
[18]. Delany, M. E., & Bazley, E. N. (1970). Acoustical properties of fibrous absorbent materials. Applied Acoustics, 3(2), 105-116.
[19]. Chessell, C. I. (1977). Propagation of noise along a finite impedance boundary. The Journal of the Acoustical Society of America, 62(4), 825-834.
[20]. Bian, H., Fattah, R. J., Sun, Y., & Zhang, X. (2019). Noise prediction of drones in urban environments. AIAA Paper 2019-2685.
[21]. Bian, H., Fattah, R., Zhong, S., & Zhang, X. (2020). An efficient rectilinear Gaussian beam tracing method for sound propagation modelling in a non-turbulent medium. The Journal of the Acoustical Society of America, 148(6), 4037-4048.
[22]. Bian, H., Tan, Q., Zhong, S., & Zhang, X. (2021). Assessment of UAM and drone noise impact on the environment based on virtual flights. Aerospace Science and Technology, 118, 106996.
[23]. Bian, H., Fattah, R., Zhong, S., & Zhang, X. (2021). On the efficient modeling of generic source directivity in Gaussian beam tracing. The Journal of the Acoustical Society of America, 149(4), 2743-2751.
[24]. Bian, H., Zhong, S., and Zhang, X. (2021). Assessment of UAM noise impact on the environment based on virtual flights with realistic sources. DICUM 2021.
[25]. Zhong, S., Zhou, P., Fattah, R., & Zhang, X. (2020). A revisit of the tonal noise of small rotors. Proceedings of the Royal Society A, 476(2244), 20200491.
[26]. Goldstein, M. (1974). Unified approach to aerodynamic sound generation in the presence of solid boundaries. The Journal of the Acoustical Society of America, 56(2), 497-509.
[27]. ISO 9613-1: Acoustics–Attenuation of Sound During Propagation Outdoors–Part1: Calculation of the Absorption of Sound by the Atmosphere (International Organization for Standardization, Geneva, Switzerland, 1993).
[28]. Zhong, S., and Zhang, X. (2020), Multi-rotor powered drone noise assessment. Quiet Drones 2020: International e-Symposium on Noise of UAV/UAS.

**QUIET DRONES**
**Second International e-Symposium**
**on**
**UAV/UAS Noise**
**27th to 30th June 2022**

# Application of Acoustic-Vortex Decomposition for Numerical Simulation of Drone Propeller Noise

**Sergey Timushev, Petr Moshkov, Alexey Yakovlev, Dmitry Klimenko, Sergey Fedoseev - Moscow Aviation Institute (NRU) irico.harmony@gmail.com**
**Andrey Aksenov - Tesis LLC**

## Summary

Over the past ten years, there has been a sharp increase in the use of quadcopters for various purposes. Quadcopters have become extremely popular and are used in areas ranging from monitoring traffic or fire conditions to distributing the Internet or cold drinks. Soon, legislation to limit drone noise is adopted in developed countries in Europe and the United States. In the European Union, in 2020, requirements were developed for the maximum permissible noise levels on the terrain of multi-copter UAVs for two ranges of takeoff weights - up to 900 g and from 900 to 4000 g. Therefore, the noiselessness and efficiency of a propeller propulsion system are critical aspects of modern unmanned aerial vehicles. The development of this area of aviation technology in the context of tightening noise standards is impossible without effective optimization methods that work in conjunction with computer-aided design systems. Such a challenge requires the development of theoretical approaches to the numerical simulation of sound generation mechanisms by propellers of quadcopters and the corresponding software. This article discusses software based on a method for calculating sound generation and noise emission by a drone propeller, taking into account the decomposition of the vortex and acoustic modes in a subsonic isentropic flow. The development of this method makes it possible to consider the influence of flow inhomogeneity and turbulence, rotor interference, sound diffraction by airframe elements, impedance characteristics of the hull coating, and other factors while ensuring accuracy and speed of calculations. For preliminary analyses, software based on a single-processor version of FlowVision 2.5 was used, which implements this method in the time domain for propeller blade passing frequency harmonics. Estimates are made about the influence of the grid on the calculated sound power and the distribution of the oscillation amplitude in the near acoustic field. It is demonstrated that in the plane of rotation of the propeller, the sound field is formed by

the quasi-potential of two rotating vortices generating a pressure field with a spiral shape of the wavefronts. The possibilities of the method are demonstrated in the examples of a separate rotor and quadra, Hexa and Hexa-2 configurations with coaxial propellers in the mode of hovering above the ground. Comparing different designs with the same propeller geometry in terms of emitted sound power and aerodynamic parameters are presented.

## 1. Introduction

Small unmanned air systems (SUAS), also known as quadcopters (drones), are becoming increasingly useful for commercial and private activities. Despite its utility, drones create a noise that annoys the population [1,2,3,4]. Surprisingly, for unmanned aerial vehicles, there are no proper rules for safety and noise [5]. Given the need to reduce the noise and develop relevant standards, new research is needed to understand the nature of the generation of noise drones and develop new control methods. [6]. In, drones prevail the noise of the propeller is used as part of its motor installation. The spectrum of the acoustic signal consists of powerful harmonics that are manifested at the frequencies of blade passing frequency (BPF), as well as the broadband component [7, 8]. A sharp increase in the SUAS market for civil and military purposes shows that the noise level and efficiency of the drone propulsion are key aspects in the design of modern aircraft and can very often lead to the success or failure of the project [9]. On the other hand, the acoustic characteristics of commercial propeller aircraft are becoming a key constructive parameter, since airlines are transferred from turbojet engines to turboprop motors for flights on local lines, and noise restrictions Pollution surrounding airports becomes more stringent. The new standard of the noise of the international organization of civil aviation in Appendix 16, Vol. 1, Chapter 14 is a decrease in the effective perceived noise level by 7 dB and will be applied to aircraft with air propellers weighing up to 55 tons in 2020 [10]. Propeller noise also has a direct impact on the health of people living or working near airports [11,12]. The propeller is an open rotor with blades with a fixed or adjustable step. The blades are designed to create a low-pressure area on one side and high pressure on the other. The resulting forces cause air movement in front and repel it back, which leads to a pull. Since the air propellers transmit a relatively small airspeed of a large mass of air, their effectiveness is high. To further improve the efficiency behind the propeller, the second rotor can be added, which rotates in the opposite direction. The noise of a propeller can be divided into three types: harmonic noise, broadband noise and narrowband random noise [13]. Harmonic resulting noise appears in the form of a signal with the main BPF component. Typically, the generated noise signal is not a pure sinusoid, therefore there are a lot of harmonics at the frequencies, multiple of the main frequency. The first harmonic is the main, the second harmonic is occurring with a doubled fundamental frequency, etc. Testing and predicting the noise of the propeller are very important and active areas of research using different methods. This article discusses the harmonic noise of the propeller in the hover mode.

## 2. Acoustic-Vortex Decomposition and Main Equations

The first successful acoustic theory was developed by Gutin in 1936, when he represented stationary aerodynamic forces on the propeller in the form of a ring of Acoustic dipole sources operating at some effective radius [14]. The theory of Gutin, however, was limited to the noise of the load for propellers with the axial flow, a simple geometry, the low circumferential speed at the tips of the blades and the lack of speed forward. Since then, significant success has been achieved in acoustic theory due to the work of many researchers who removed these restrictions [15,16,17]. A thorough review of the methodology for predicting the noise of the propeller, detailed these achievements, was published by several authors [18,19,20].
The physical mechanisms for generating aerodynamic noise in blade machines are quite well studied, in particular in the example of the fans [21], where it was noted that the spectrum of

the noise of fans consists of broadband noise and tonal components at frequencies multiple BPF. Various analytical and semi-empirical methods for calculating broadband fan noise takes into account physical phenomena, such as turbulence at the rotor inlet, turbulent border layer on the blades, the effect of the output edge of the blade, Dry in the radial gap on the periphery of the rotor and the flow of the flow on the blades. With the development of computational hydrodynamics, methods were developed for calculating pressure pulsations in blades, based on solving RANS [22, 23], equations, as well as combined methods with a solution of a wave equation and use of experimental data. Modern methods, using parallel computing, allow to carry out calculations on nets consisting of hundreds of millions of nodes, while simultaneously involving hundreds of thousands of processor cores of modern supercomputers develop [24]. Current approaches to the noise modelling of blade machines are based mainly on the use of the Lighthill equation [25]. Later in the works of Kerl [26], Flowcs-Williams and Hawkins [27], theoretical foundations were formulated for the development of methods for calculating the aerodynamic noise of blade machines based on the so-called aeroacoustic analogy, as well as the use of the Kirchhoff theorem [28].

In Russia, semi-empirical [29]], analytical [30] and numerical methods [31,32,33], which are currently being actively developed, are used to assess the acoustic field of propellers. The results of the assessment of the air propeller fields are then used to estimate noise on Earth in specialized software packages [34, 35], which take into account the atmospheric and surface attenuation of sound, the Doppler effect and the interference of sound waves at the observation point. Additional directions of numerical modelling in the area of propeller acoustics are the calculated estimates of the effect of the air propeller parameters and its design [36, on the expected levels of the noise of drones on Earth.

The lack of most methods, which leads to a significant modelling error of up to 10 dB and more, is associated with an inaccurate solution to the decomposition problem - separation of acoustic and vortex (pseudo-operating) models in the field of oscillation source. It should also be noted that the Lighthill equation was obtained in the assumption of small oscillations in the turbulent stream of the compressible medium, while in the paddle pressure pulsation machines and the generation of the radiated sound occurs in a wide The range of wave numbers when large-scale vortex perturbations disintegrate in the cascade process, and in this process, the generation of acoustic waves occurs. When developing the calculated method, it is taken into account that the oscillations of the main flow parameters cause the appearance of acoustic perturbations spreading at the speed of sound in the working environment. At the same time, the perturbation of the main flow spreads with the velocity of airflow. The latter form of non-stationary motion is called "pseudo-sound" [37] or vortex mode [38 39 40]. The method is based on the theoretical approach of Blochintsev, Landau, and Artamonov. The proposed approach of decomposition of the field of velocity and pressures on the vortex (pseudo) and acoustic mode is based on the linearization of the compressible media equations, taking into account the low Mach number and isentropic flow.

We write down the speed field in the form

$$\mathbf{V} = \mathbf{U} + \nabla\varphi = \mathbf{U} + \mathbf{V}_a \quad (1)$$

Here $\mathbf{U}$ - vortex mode velocity, $\varphi$ - the acoustic potential, $\mathbf{V}_a$ - acoustic speed.

Linearizing the equations of a compressible medium, one can obtain an inhomogeneous wave equation relative to the enthalpy oscillations of flow ($a$ - the sound speed in the unperturbed medium):

$$\frac{1}{a^2}\frac{d^2h}{dt^2} - \Delta h = -\Delta H \quad (2)$$

the perturbing function in the right-hand side Equations (2) can be expressed through the field of vortex mode velocities:

$$-\Delta H = S = \nabla\left(\mathbf{U}\nabla\mathbf{U}\right) = \nabla\left(\tfrac{1}{2}\nabla U^2 - \mathbf{U}\times\nabla\times\mathbf{U}\right) \quad (3)$$

In the acoustic-vortex method, the noise source can be represented as the function of the speed of the vortex mode. This approach largely eliminates the arbitrariness and conventions of the aeroacoustic analogy, determining the source, pressure pulsations and noise propagation in the near field, as a direct result of numerical modelling. Neglecting convective members in the time derivative of the equation, one obtains:

$$\frac{1}{a^2}\frac{\partial^2 h}{\partial t^2}-\frac{\partial^2 h}{\partial x^2}-\frac{\partial^2 h}{\partial y^2}-\frac{\partial^2 h}{\partial z^2}=s \tag{4}$$

through $s=-\nabla g$ the nonstationary part of the function $S$, which, taking into account the continuity equation for the vortex mode, will be equal to

$$S=2\left(\frac{\partial U_y}{\partial x}\cdot\frac{\partial U_x}{\partial y}+\frac{\partial U_z}{\partial x}\cdot\frac{\partial U_x}{\partial z}+\frac{\partial U_z}{\partial y}\cdot\frac{\partial U_y}{\partial z}-\frac{\partial U_x}{\partial x}\cdot\frac{\partial U_y}{\partial y}-\frac{\partial U_x}{\partial x}\cdot\frac{\partial U_z}{\partial z}-\frac{\partial U_y}{\partial y}\cdot\frac{\partial U_z}{\partial z}\right) \tag{5}$$

using the local Integrated specific acoustic impedance Z, the boundary condition for $k$-th BPF harmonic ( $n$ – the normal to the boundary, $g$ – the oscillations of the enthalpy of the vortex mode) can be represented in a form

$$\frac{\partial (h_k-g_k)}{\partial n}=-\frac{1}{aZ}\frac{\partial (h_k-g_k)}{\partial t} \tag{6}$$

где $k$ - номер ЧСЛ гармоники, нормаль к границе, колебания энтальпии вихревой моды.
For the vortex mode, unsteady Navier - Stokes equations are solved using the standard k-ε turbulence model. Experience shows that such an approach gives successful results when modelling BPF oscillations for the steady mode. The iterative procedure is developed before obtaining convergence to a periodic oscillatory solution with the subsequent definition of the source function $s$.
The finite-difference scheme of differential equations in the Cartesian coordinate system is obtained by integrating the acoustic-wave equation in space and time with the introduction of finite volumes. The method was tested in detail based on the experimental model - the air pump [41]. The data was obtained on the efficiency and accuracy of the method for calculating pressure pulsations at the BPF frequency and its higher harmonics. A single-processor version of the software implements a similar method for three-dimensional flow in the blades machines. The calculation results were obtained for discrete components of the BPF in the axial fan [42,43] and centrifugal pump [44].

## 3. Computational research

### 3.1 Research Subject

Research conducted for propeller (Figure 1) Parrot Mambo Drone (http://www.thingiverse.com/ting: 315340). The diameter of the propeller is 70 mm, the rotational speed is 12000 rpm. The purpose is to identify the possibility of using an acoustic-vortex method for modelling the mechanism of generating and propagating acoustic oscillations for open rotors. One- processor core is used --device software created based on the FlowVision2.5X package.

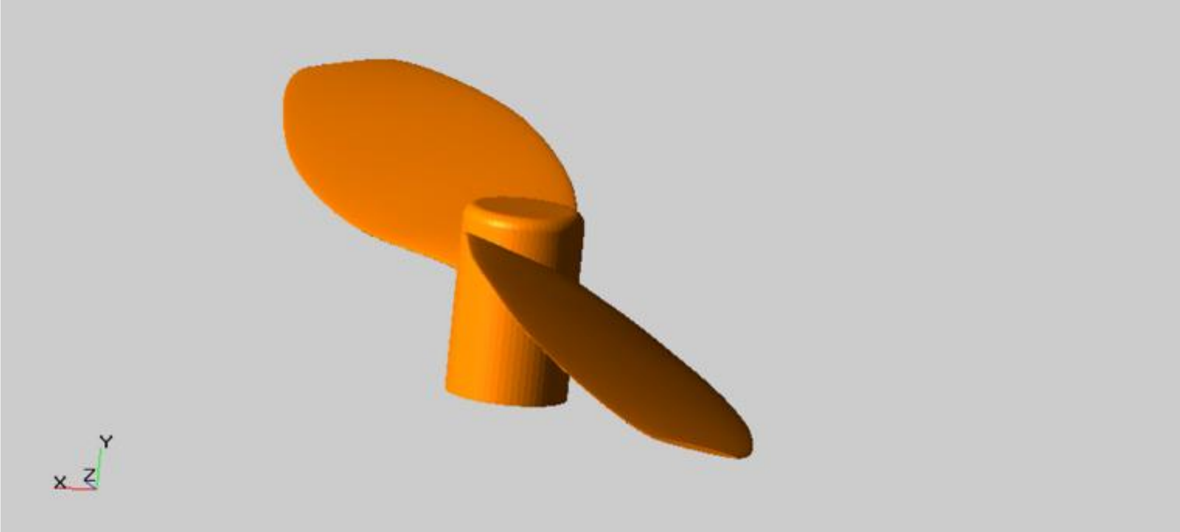


Рисунок 1 Separate propeller

A separate propeller is considered in the hover mode and several configurations with 4 and 6 propellers. The propellers are placed in the computational domain in the form of a hemisphere with a radius of 5 m. The lower part of the hemisphere models a solid reflective surface.

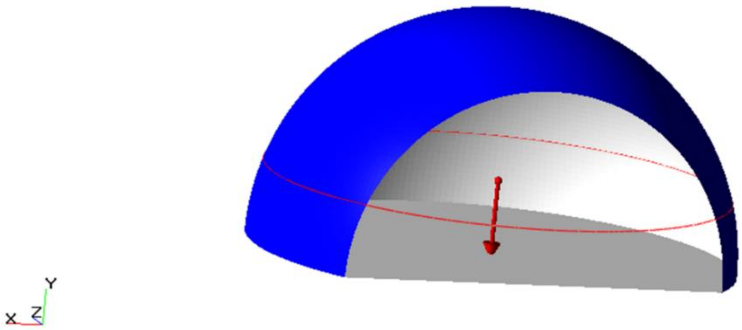


Рисунок 2 Computational domain

The propeller rotation plane shown in red in Figure 2 is located at a distance of 1.5 m from the solid surface. Along with a separate propeller, the configuration of four (Quadro), six propellers (Hexa) and six propellers located in two levels (Hexa2) are considered. For Hexa2, the distance between the propellers is preserved in the plan, as for Hexa. For all these parameters, the geometry of the propeller and its work parameters are stored unchanged. The HEXA2 configuration is shown in Figure 3-distance between the layers is equal to the distance between the rotors in the Quadro scheme.

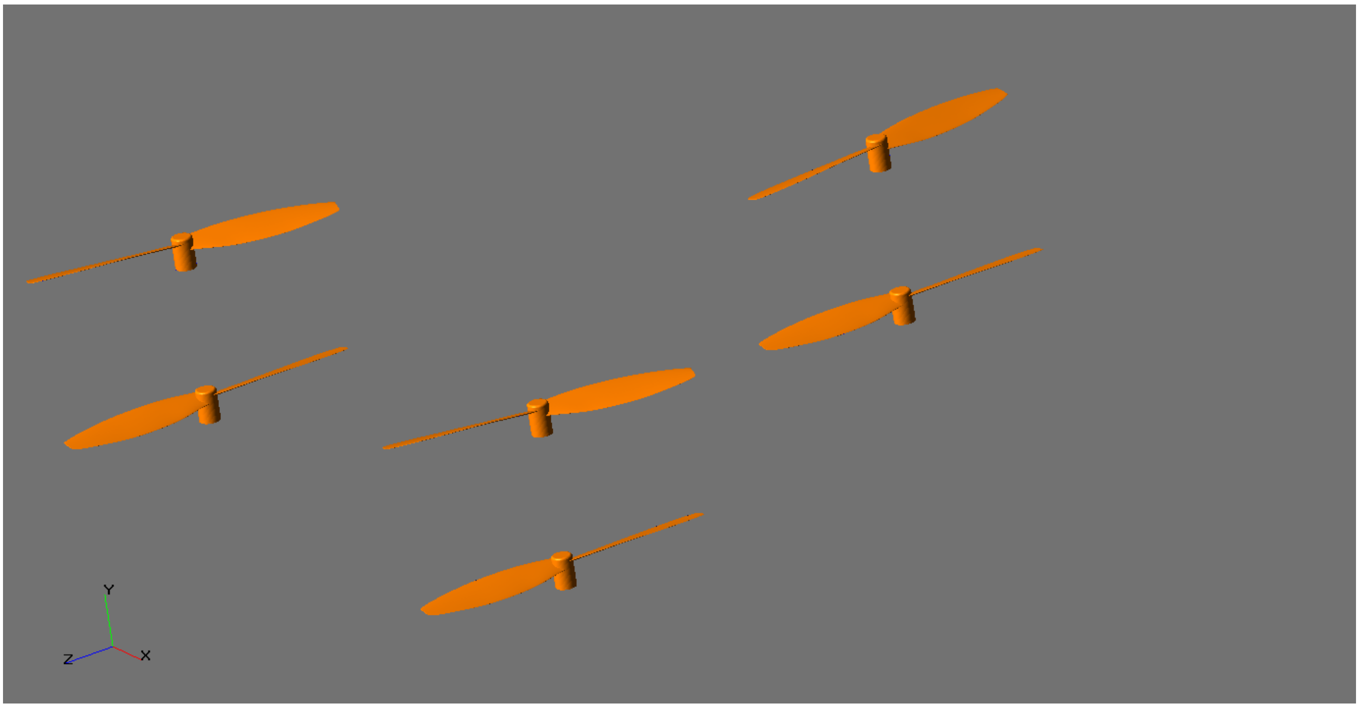

Рисунок 3 Схема Hexa2

### 3.2 Computational Mesh and Boundary Conditions

The initial grid is formed by rectangular (cubic) cells with a face size of 0.1667 m. This size provides over five mesh cells for the wavelength of the first Harmonics of the BPF of the propeller. Near the propeller is carried out adaptation (grinding) of the grid nodes, and each cell of the original grid is divided into eight cells, forming the grid of the first level.

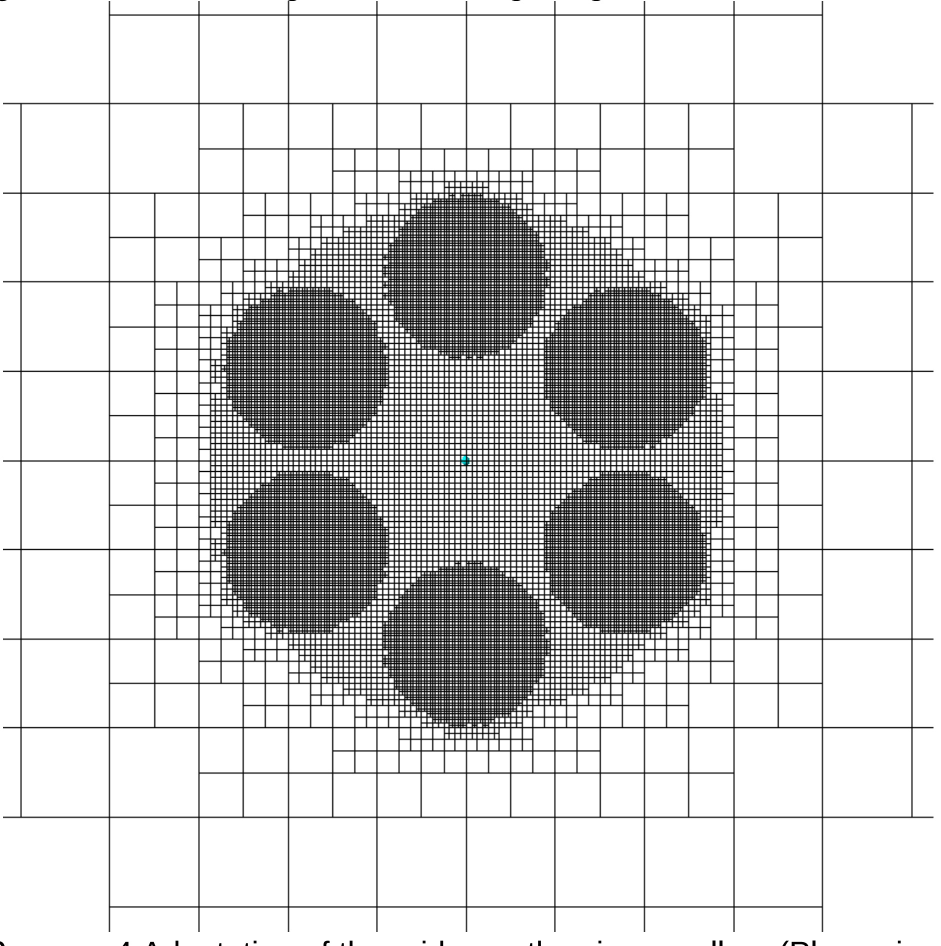
Рисунок 4 Adaptation of the grid near the six propellers (Plane view)

Further grinding leads to a second-level grid, etc. This paper used grids to the 7th level of adaptation near the propeller. Figure 4 for example shows an adapted grid for the HEXA configuration. The "air" border of the hemisphere is given by the condition of zero pressure (relative to the "reference" atmospheric pressure) and zero speed gradients. On the "solid" boundary, a logarithmic range of speeds during roughness of 1000 microns is given. The surface of the propeller is also given a logarithmic law for a speed profile with zero roughness. An endless acoustic impedance is set on the solid boundary. At the air border, the acoustic impedance is equal to acoustic resistance $Z = \rho \cdot a$.

## 4. Computational results of the vortex mode parameters

Computations were carried out by the "moving body method" - in the process of calculating the propeller turns, simulating the real rotation. The following is the characteristic distribution of the instantaneous field of pressure and speed in the plane,

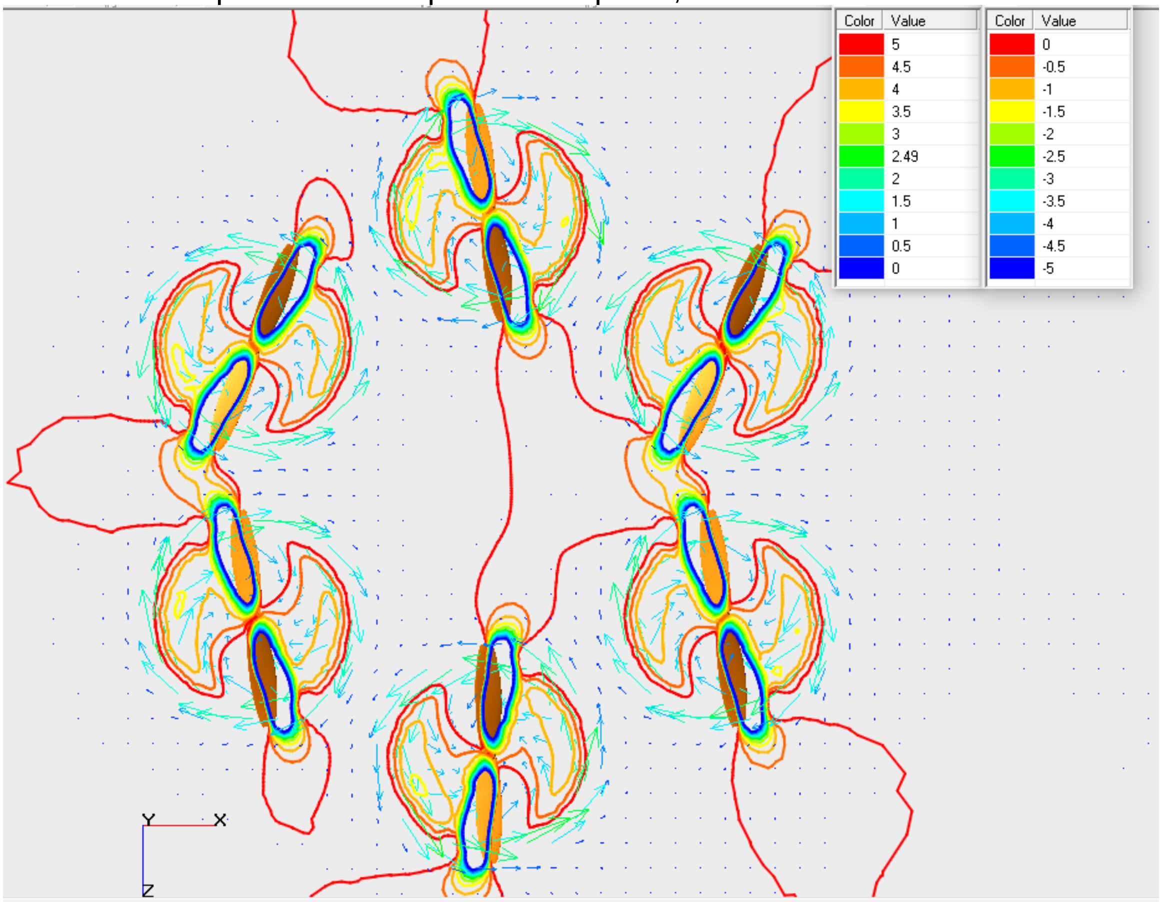


Рисунок 5 Instant pressure field and velocity over the rotation plane for the Hexa, m/s, Pa, scheme Hexa

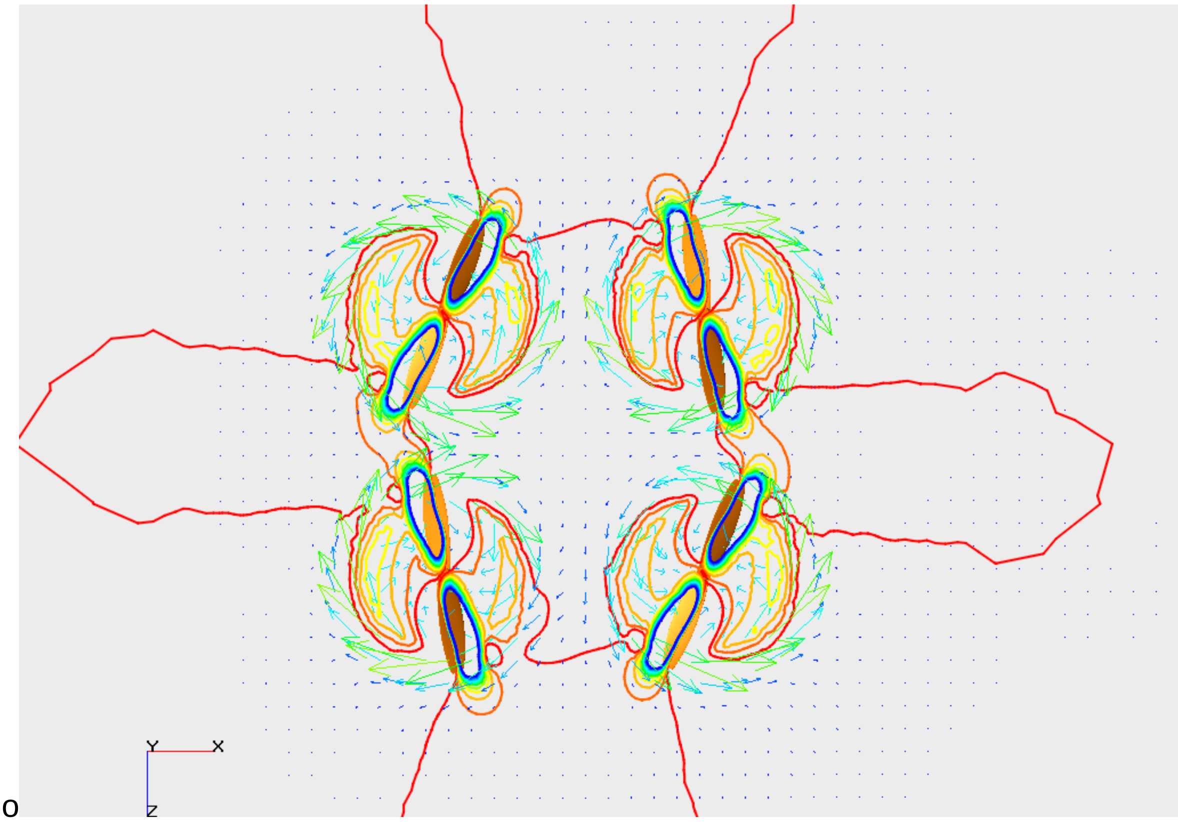


Рисунок 6 Instant pressure field and velocity over the rotation plane for the Quadro, the scale is the same as in figure 5 m/c, Па

adjacent to the rotation plane (7 mm above the propeller blades) for the HEXA, Quadro configuration, which shows a significant heterogeneity of the pressure due to the vortex character of the blade flow. An instantaneous field of pressure in the meridional plane has an inhomogeneity of two orders of magnitude lower than in the rotation plane, therefore the source of harmonic pulsations of the BPF is determined mainly by the pressure distribution on the propeller blades. The structure of the source, which is determined by the formula (5), was previously described: the source function of the Harmonic noise of BPF is two coaxial, rotating with the rotor, the vortex zones[45]. The analysis of non-stationary pressure fields shows that the generation of noise should be the essential influence of the hydrodynamic interaction of the rotors, taking into account their mutual position, should be a significant effect, but it is not studied here [46,47].

## 5. Results of calculating the parameters of the acoustic mode

The acoustic field of the first BPF harmonic of the separate propeller is shown in Figure 7 and Figure 8 in the plane of rotation of the propeller and the meridional plane, respectively. It is important to note that a stable structure of the field in the form of quasi-spiral modes of a quadrupole type is recorded in the rotation plane.

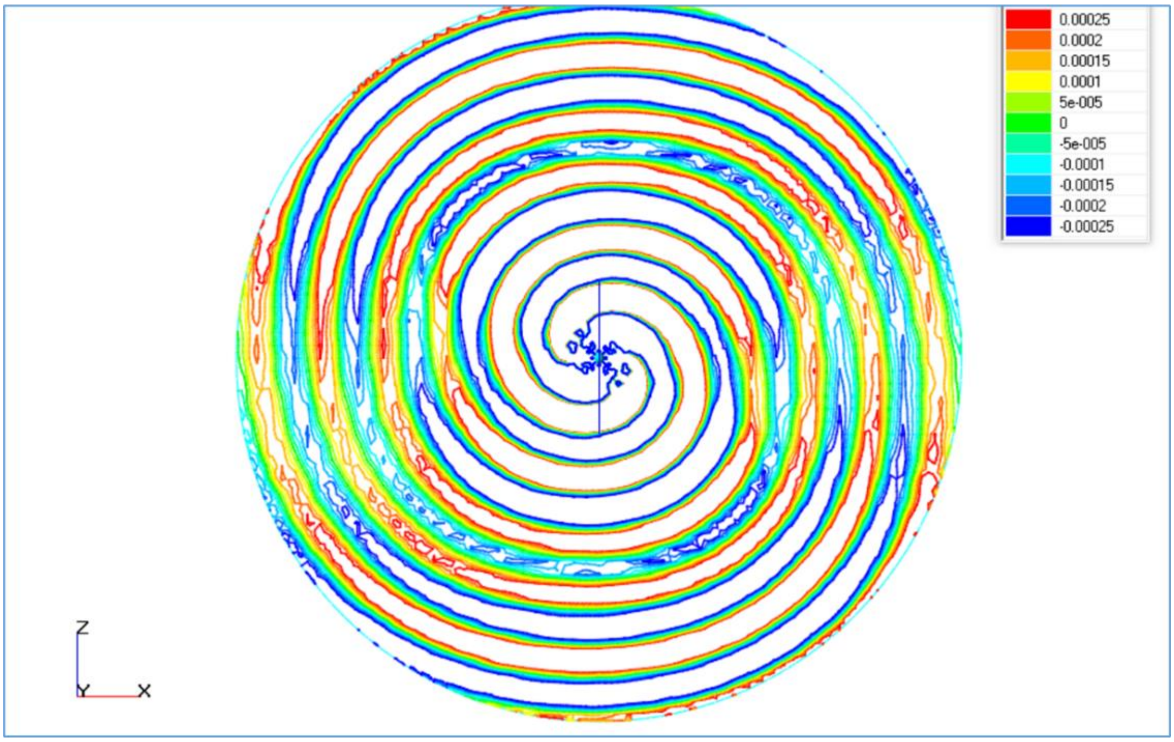

Рисунок 7 Instant field of acoustic pressure of the first BPF harmonic, PA

In the meridional plane, there is a noticeable effect of the solid border

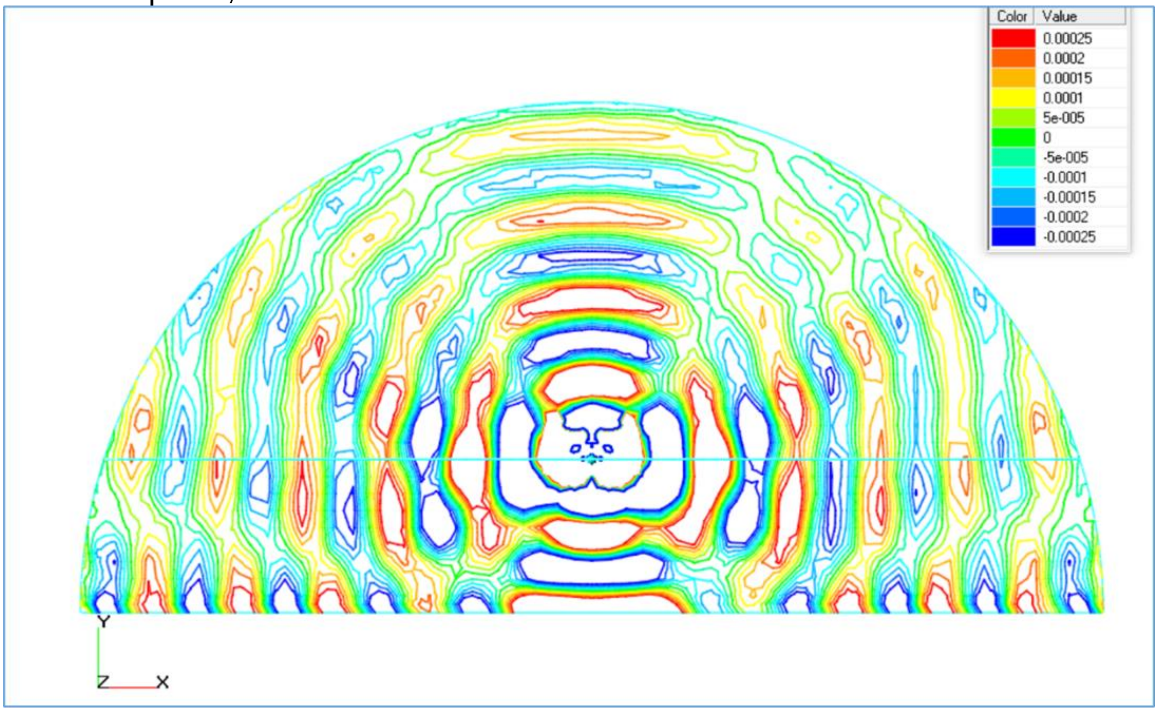

Рисунок 8 Instantaneous field of acoustic pressure of the first BPF harmonic, Pa

, with directivity that gives a higher radiation intensity on the side surface of the sphere. This can be seen in Figure 9, where the form of the plan shows the distribution of amplitude.

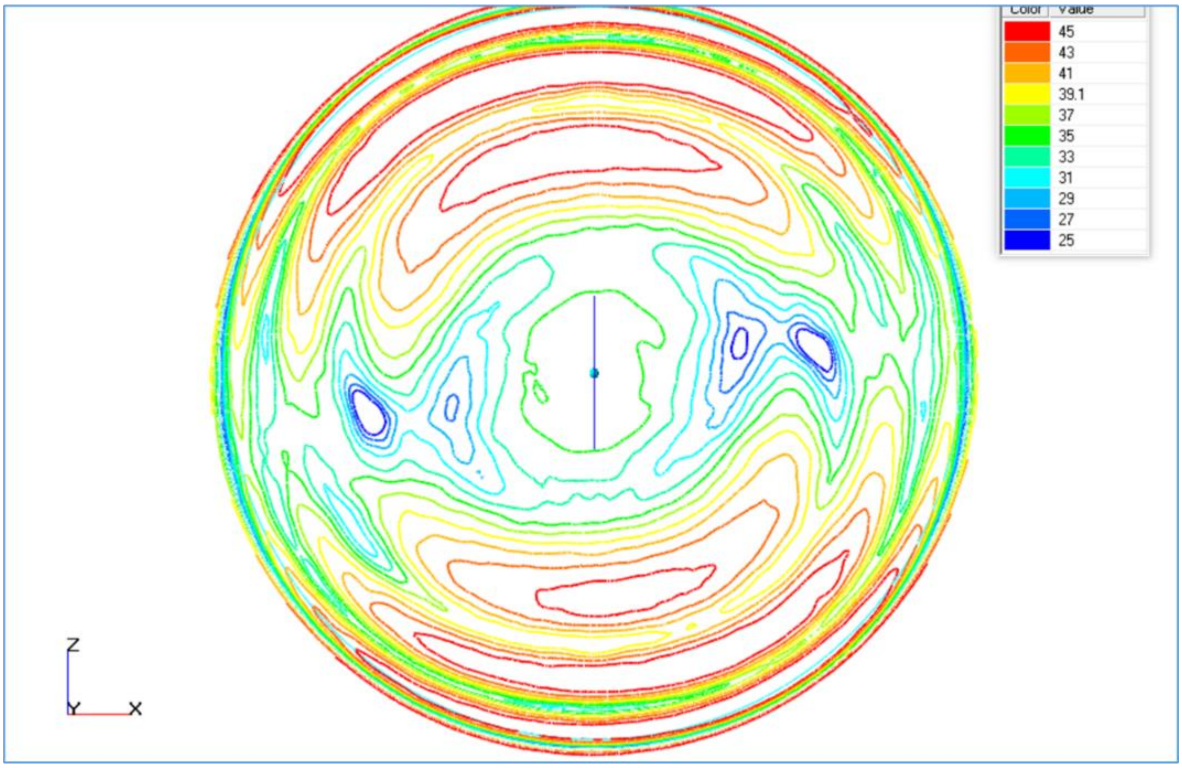


Рисунок 9 Sound level on the surface of the sphere, dB

patterns of change of amplitude near the propeller and in the near field, as well as the influence of the finite-difference grid previously considered [48].

## 6. Computation results for different configurations

The results of the calculation of the amplitude of the first BPF harmonic on the spherical surface are shown in Figures 10 - Figure 13 for different configurations.

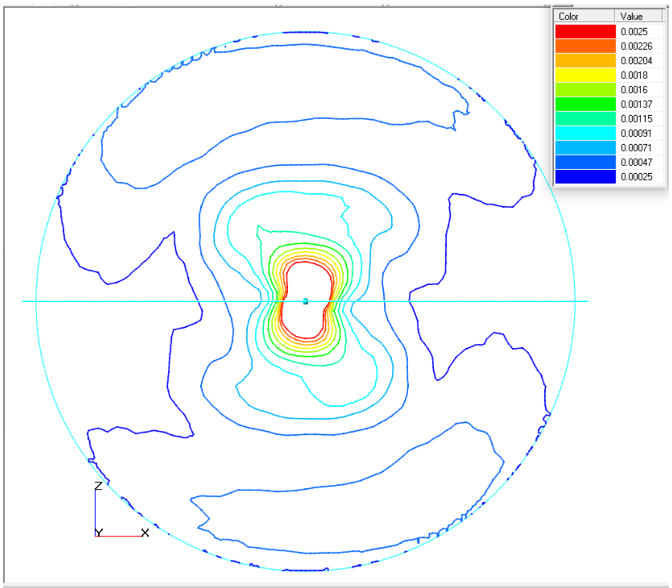


Рисунок 10 Single. The BPF amplitude on the surface of the sphere, dB

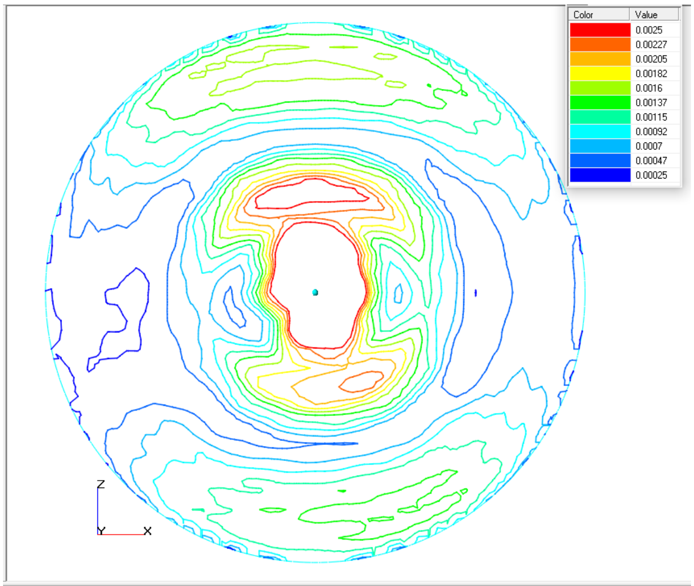

Рисунок 11 Quadro. The BPF amplitude on the surface of the sphere, dB

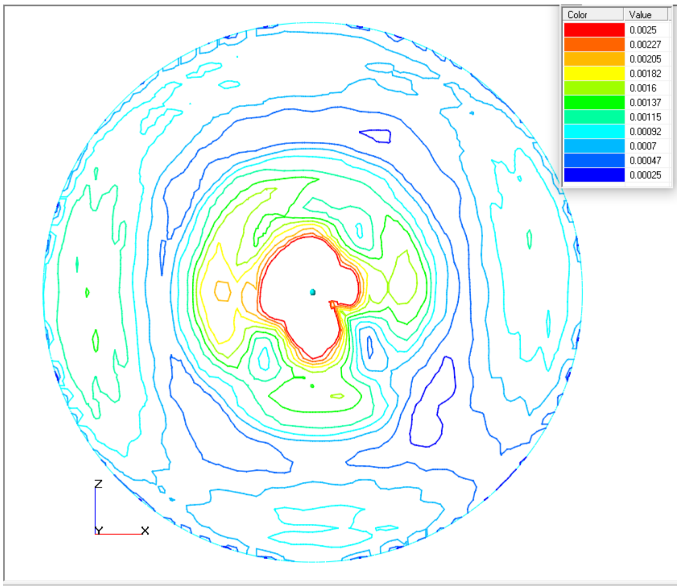

Рисунок 12 Hexa. The BPF amplitude on the surface of the sphere, dB

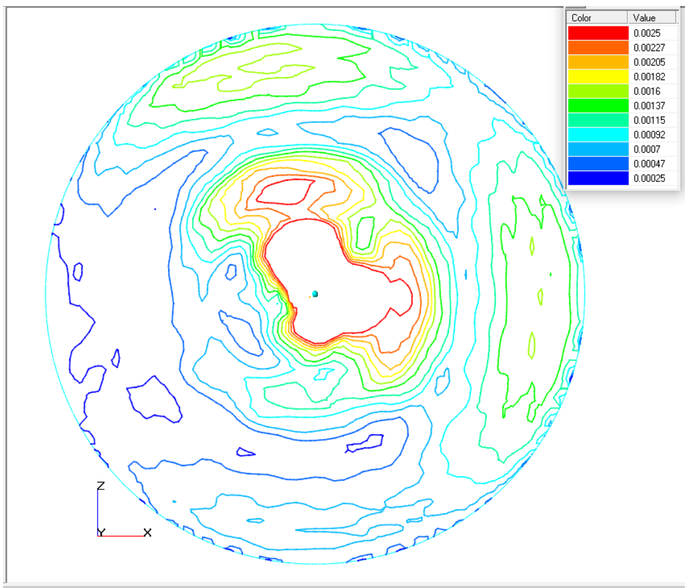

Рисунок 13 Hexa2. The BPF amplitude on the surface of the sphere, dB

The results of sound power calculation for the studied configurations are outlined in table 1.

*Table 1 Computed Sound power*

| Rotor | Sound Pressure, W | Sound Pressure, dB |
|---|---|---|
| Single | 2.53323E-08 | 4.80735E+01 |
| Quadro | 1.70537E-07 | 6.46364E+01 |
| Hexa | 1.08970E-07 | 6.07461E+01 |
| Hexa2 | 1.32281E-07 | 6.24299E+01 |

All multi-rotor schemes give an increase in the sound power of the first BPF harmonic by 12 -16 dB. At the same time, the Quadro scheme has the worst result. Perhaps this circumstance is since this study did not consider optimization of the mutual position of the propellers.

## 7. Conclusion

1. The use of acoustic-vortex decomposition is demonstrated with a solution of the wave equation by a direct method for modelling the noise of the drone propellers in the hover mode.
2. The field of acoustic pressure in the propeller rotation plane reveals the quasi-spiral structure of the acoustic field from the source of the quadrupole type.
3. All multi-rotary schemes provide an increase in the sound power of the first BPF harmonic by 12 -16 dB compared to the separate rotor. At the same time, the Quadro scheme has the worst result.

**References**


1 “ABCNews: Whining drones bringing burritos and coffee are bitterly dividing Canberra residents.”https://www.abc.net.au/news/2018-11-09/noise-from-drone-delivery-service-divides-canberra-residents/10484044. Accessed:11-03-2019.
2 “BBC News: Why your pizza may never be delivered by drone.”https://www.bbc.com/news/business-46483178. Accessed: 11-03-2019.
3 P.A Moshkov., V.F. Samokhin, A.A. Yakovlev «Selection of an audibility criterion for propeller driven unmanned aerial vehicle» // Russian Aeronautics. 2018. Vol. 61. No. 2. pp. 149-155. DOI: 10.3103/S1068799818020010
4 P. Moshkov, N. Ostrikov, V. Samokhin, A. Valiev «Study of Ptero-G0 UAV Noise with Level Flight Conditions» // 25th AIAA/CEAS Aeroacoustics Conference. 2019. AIAA Paper No. 2019-2514. https://doi.org/10.2514/6.2019-2514
5 N. Kloet, S. Watkins, and R. Clothier «Acoustic signature measurement of small multi-rotor unmanned aircraft systems» International Journal of Micro Air Vehicles, vol. 9, pp. 3–14, Feb. 2017.
6 Abhishek Kumar Sahai “Consideration of aircraft noise annoyance during conceptual aircraft design” (PhD thesis) June 2016 http://publications.rwth-aachen.de/record/668901. Accessed: 27-02-2020.
7 C. E. Tinney and J. Sirohi “Multirotor Drone Noise at Static Thrust,”AIAA Journal, vol. 56, pp. 2816–2826, July 2018
8 .N. Intaratep, W. N. Alexander, W. J. Devenport, S. M. Grace, and A. Dropkin, “Experimental Study of Quadcopter Acoustics and Performance at Static Thrust Conditions,”22nd AIAA/CEAS Aeroacoustics Conference, June 2016

9 Giorgia Sinibaldi, Luca Marino, “Experimental analysis on the noise of propellers for small UAV,” Applied Acoustics Volume 74, Issue 1, January 2013, Pages 79-88
10 C. Holsclaw, “Stage 5 Airplane Noise Standards,” Federal Aviation Administration, Federal Register, Vol. 81, No. 1923, Washington, D.C., Jan. 2016.
11 E. Franssen, Van C.Wichen, N. Nagelkerke and E. Lebret, “Aircraft Noise Around a Large International Airport and Its Impact on General Health and Medication Use,” Occupational and Environmental Medicine, Vol. 61, No. 5, 2004, pp. 405–413.
12 H. Swift,“A Review of the Literature Related to Potential Health Effects of Aircraft Noise,” Partnership for Air Transportation Noise and Emissions Reduction, Massachusetts Inst. of Technology PARTNERCOE-2010-003, Cambridge, MA, July 2010.
13 B. Magliozzi, D. B. Hanson, and R. K. Amiet, “Propeller and Propfan Noise,” Aeroacoustics of Flight Vehicles: Theory and Practice, edited by H. H. Hubbard, Vol. 1, NASA Reference Publ. 1258, Hampton, VA, 1991, pp. 1–64.
14 L. Gutin, “On the Sound Field of a Rotating Propeller,” NACA TM-1195, Oct. 1948.
15 A. F. Deming, “Noise from Propellers with Symmetrical Sections at Zero Blade Angle II,” NACA TN-679, Dec. 1938.
16 D. B. Hanson, “Helicoidal Surface Theory for Harmonic Noise of Propellers in the Far Field,” AIAA Journal, Vol. 18, No. 10, 1980, pp. 1213–1220. doi:10.2514/3.50873
17 D. B. Hanson, “Sound from a Propeller at Angle of Attack: A New Theoretical Viewpoint,” Proceedings: Mathematical and Physical Sciences, Vol. 449, No. 1936, 1995, pp. 315–328.
18 C. L. Morfey, “Rotating Blades and Aerodynamic Sound,” Journal of Sound and Vibration, Vol. 28, No. 3, 1973, pp. 587–617. doi:10.1016/S0022-460X(73)80041-0
19 B. Magliozzi, F. B. Metzger, W. Baush, and R. J. King, “A Comprehensive Review of Helicopter Noise Literature,” Federal Aviation Administration Rept. FAA-RD-75-79, June 1975.
20 F. Farassat and G. P. Succi, “A Review of Propeller Discrete Frequency Noise Prediction Technology with Emphasis on Two Current Methods for Time Domain Calculations,” Journal of Sound and Vibration, Vol. 71, No. 3, 1980, pp. 399–419.doi:10.1016/0022-460X(80)90422-8
21 A. Guédel Acoustique des ventilateurs. CETIAT. PYC LIVRES, 1999
22 D. Croba, J.L. Kueny Unsteady flow computation in a centrifugal pump coupling of the impeller and the volute. Fan Noise. An International INCE Symposium. Senlis (France). Proceedings, 1992.
23 S. Chu, R. Dong, J. Katz The effect of blade-tongue interactions on the flow structure, pressure fluctuations and noise within a centrifugal pump. Pump noise and vibrations. 1st International Symposium, Clamart (France), 1993.
24 В. Г. Бобков, И. В. Абалакин, Т. К. Козубская, “Методика расчета аэродинамических характеристик винтов вертолета на основе реберно-ориентированных схем в комплексе программ NOISEtte”, Компьютерные исследования и моделирование, 12:5 (2020), 1097–1122
25 M.J. Lighthill 1952 Proceedings of the Royal Society, London A 211, 564-587. On sound generated aerodynamically. Part I. General Theory
26 N. Curle The influence of solid boundaries upon aerodynamic sound. Proc. Royal Soc. A 231, p.505-514, 1955
27 J. E. Ffowcs Williams and D. L.Hawkings , “Sound Generation by Turbulence and Surfaces in Arbitrary Motion,”Philosophical Transactions of the Royal Society of London, Series A: Mathematical and Physical Sciences, Vol. 264, No. 1151, 1969, pp. 321–342. doi:10.1098/rsta.1969.0031
28 F. Farassat and M.K. Myers «Extension of Kirchhhoff’s formula to radiation from moving surfaces». Journal of Sound and Vibration 123, 451-461 1988.
29 P.A. Moshkov V.F. Samokhin Integral model of noise of an engine-propeller power plant // Journal of Engineering Physics and Thermophysics. 2018. vol. 91, no. 2, pp. 332–338. DOI: 10.1007/s10891-018-1753-8

30 V. Samokhin, P. Moshkov, A.Yakovlev Analytical model of engine fan noise // Akustika. 2019. Vol. 32. pp. 168–173.
31 V.F.Kopiev, V.A.Titarev, I.V. Belyaev Development of a methodology for propeller noise calculation on high-performance computer // TsAGI Science Journal. 2014. Vol. 45. No. 3-4. pp. 293-327. DOI: 10.1615/TsAGISciJ.2014011857
32 I.V.Abalakin, P.A.Bakhvalov, V.G.Bobkov, T.K.Kozubskaya, V.A. Anikin Numerical investigation of the aerodynamic and acoustical properties of a shrouded rotor // Fluid Dynamics. 2016. Vol. 51. No. 3. pp. 419-433.
33 V.A.Titarev, G.A.Faranosov, S.A.Chernyshev, A.S. Batrakov Numerical modeling of the influence of the relative positions of a propeller and pylon on turboprop aircraft noise // Acoustical Physics. 2018. Vol. 64. No. 6. pp. 760-773.
34 A. Filippone Aircraft noise prediction // Progress in Aerospace Sciences. 2014. Vol. 68. pp. 27–63.
35 V.G. Dmitriev, V.F. Samokhin Complex of algorithms and programs for calculation of aircraft noise // TsAGI Science Journal. 2014. Vol. 45. No. 3-4. pp. 293-327. DOI: 10.1615/TsAGISciJ.2014011838
36 N.N. Ostrikov, S.L. Denisov Airframe shielding of noncompact aviation noise sources: theory and experiment // 21st AIAA/CEAS Aeroacoustics Conference. 2015. AIAA Paper No. 2015-2691. https://doi.org/10.2514/6.2015-2691
37 Д. И. Блохинцев Акустика неоднородной движущейся среды. М.: Наука, 1986.
D. I. Blohincev Akustika neodnorodnoj dvizhushchejsya sredy. M.: Nauka, 1986.
38 М.Е. Голдстейн Аэроакустика. М.: Машиностроение, 1981.
Marvin E. Goldstein Aeroacoustics. McSRAW-HILL International Book Company, 1976
39 Е.П. Столяров Возбуждение звука малыми возмущениями энтропии и завихренности в пространственно неоднородных течениях сжимаемого идеального газа.- В кн.  Акустика турбулентных потоков. М.: Наука, 1983.
E.P. Stolyarov Vozbuzhdenie zvuka malymi vozmushcheniyami entropii i zavihrennosti v prostranstvenno neodnorodnyh techeniyah szhimaemogo ideal'nogo gaza.- V kn.  Akustika turbulentnyh potokov. M.: Nauka, 1983.
40 S.C. Crow Aerodynamic Sound Emission as a Singular Perturbation Problem.- Studies in Applied Mathematics, 1970, vol. XLIX, No.1.
41 S. Timouchev, J. Tourret, Numerical Simulation of BPF Pressure Pulsation Field In Centrifugal Pumps. 19th International Pump Users Symposium, Houston, Texas (USA) 25-28 Feb 2002. Proceedings, pp.85-105
42 Serguei Timouchev, Anatoly Nedashkovsky, Goran Pavic Experimental Validation of Axial Fan 3D Acoustic-Vortex Method CFD-CAA Study. Proceedings of 3rd International symposium on Fan Noise 2007, 19-21 September 2007, Lyon, France
43 A.A. Aksenov, V.N. Gavrilyuk, S.F. Timushev «Numerical simulation of tonal fan noise of computers and air conditioning systems». Acoustical Physics, 62, 4, 447-455, 2016, Pleiades Publishing
44 Sergey F Timushev, Dmitry V Klimenko, «Computation of BPF pressure pulsations in the LRE propeller-centrifugal pump with 3D acoustic-vortex method», INTER-NOISE and NOISE-CON Congress and Conference Proceedings,255,3,4157- 4165, 2017, Institute of Noise Control Engineering.
45 Timushev, S.; Klimenko, D.; Aksenov, A.; Gavrilyuk, V.; Li, J. On a new approach for numerical modeling of the quadcopter rotor sound generation and propagationProceedings of 2020. International Congress on Noise Control Engineering, INTER-NOISE 2020
46 Richard Healy Matthew Misiorwoski Farhan Gandhi A Systematic CFD-Based Examination of Rotor-Rotor Separation Effects on Interactional Aerodynamics for Large eVTOL Aircraft. Presented at the Vertical Flight Society 75th Annual Forum &Technology Display, Philadelphia, Pennsylvania, May 13–16, 2019.

47 Brendan Smith, Farhan Gandhi, Robert Niemiec A Comparison of Multicopter Noise Characteristics with Increasing Number of Rotors/ Presented at the Vertical Flight Society's 76th Annual Forum & Technology Display, Virginia Beach, Virginia, October 6-8, 2020.
48 А.А. Аксенов, С.Ф. Тимушев, Д.В.Клименко,С.Ф. Федосеев Применение акустико-вихревого метода для моделирования шума пропеллера квадрокоптера. Математическое моделирование. Будет опубликовано в 2022

QUIET DRONES
Second International e-Symposium
on
UAV/UAS Noise
27th to 30th June 2022

# Sound source localization and enhancement in 3D space from a flying drone

Lin Wang, Centre for Intelligent Sensing, Queen Mary University of London: lin.wang@qmul.ac.uk
Andrea Cavallaro, Centre for Intelligent Sensing, Queen Mary University of London: a.cavallaro@qmul.ac.uk

## Summary

The ego-noise generated from rotating motors and propellers as well as the movement of the drone impose significant challenges to drone audition, which aims to sense the acoustic environment with onboard microphones mounted on a flying drone. As a state-of-the-art framework for sound processing on drones, time-frequency spatial filtering (TFS) exploits the time-frequency sparsity of the acoustic signals and their correlation at multiple microphones to localize and enhance a target sound in the presence of strong ego-noise. The original TFS framework was proposed with a 2D coordinate system considering azimuth only in the horizontal plane. We extend the TFS framework to a 3D coordinate system for the microphone array considering both azimuth and elevation. We validate the proposed framework with data from a flying drone, and the proposed algorithm significantly outperforms the baseline SRP-PHAT algorithm.

## 1. Introduction

With a drone being able to fly around and hover above a ground terrain, drone audition has found wide applications in search and rescue, aerial filming, monitoring and surveillance, and autonomous human-drone interaction [1-6]. However, acoustic sensing based on the signals captured by airborne microphones is a very challenging task, mainly due to three reasons [7]. First, the rotating motors and propellers generate strong ego-noise that leads to extremely low signal-to-noise ratios (SNR can be lower than -15 dB) at onboard microphones, which are located much closer to motors and propellers than target sound sources around the drone. The ego-noise typically consists of full-band and harmonic components, whose spectrum changes dynamically with the rotating speed of the motors and the flight status of the drone. Second, the wind from the rotating propellers and in the natural environment add a strong noise component and further lower the SNR at onboard microphones. Third, the movement of the drone creates dynamic transmission paths between the target sound sources and onboard microphones, and further increases the challenge of acoustic sensing from the drone.

Microphone arrays have been widely used on ground robots to improve acoustic sensing performance in noisy environments [8]. However, the performance of existing microphone array techniques degrades significantly on drone platforms [9]. In recent years, dedicated methods have been proposed for sound source localization and sound enhancement on drones [11-24]. These methods can be categorized into uni-modal and multi-modal approaches. Uni-modal approaches are based on the microphone signals only [12-16, 19, 21, 27]. To cope with the strong ego-noise, some works optimize microphone array placement and develop algorithms for specific hardware setups [13, 15]. Multi-modal approaches utilize additional sensors to improve acoustic sensing performance. Motor speed sensors can be employed to assist in predicting the ego-noise received at onboard microphones; the prediction is subsequently incorporated into microphone array algorithms for improved robustness to the ego-noise [11, 15]. Onboard cameras can be employed to detect pre-defined sound sources (e.g. human speakers in the application of human-drone interaction) with computer vision algorithms, which are not affected by acoustic noise and thus provides guidance for sound processing [14, 18]. The requirement of additional sensors increases the cost and complexity when applying drone audition in practice.

Time-frequency spatial filtering (TFS) is a recently established framework for sound processing on drones [17-24]. The ego-noise and the target sound (e.g. human speech) typically consist of harmonic components that have concentrated energy at isolated time-frequency bins. Based on this observation, the TFS framework proposed to estimate the directional of arrival (DOA) at each time-frequency bin with the microphone array, based on which a set of spatial filters are formulated to estimate the location of the target sound and to suppress the ego-noise. By exploiting the time-frequency sparsity of the signal (see an example in Fig. 5(b)), TFS effectively improves the acoustic sensing performance in the presence of ego-noise, and achieves state-of-the-art performance for microphone array processing on drones [19, 21]. TFS enables both sound enhancement and sound source localization. The sound enhancement performance was further improved in combination with deep learning [23] and blind source separation [24]. A multi-modal analysis framework was proposed that jointly exploits audio and video to enhance the sounds of multiple targets captured from a drone equipped with a microphone array and a video camera [18]. An audio-visual drone sound recording dataset is made public available to encourage research in the field [22].

A limitation of the current TFS framework is that the algorithm was originally proposed with a 2D circular array and thus works only for a 2D coordinate system considering azimuth only in the plane defined by the array. To encourage a more general application of the algorithm, we extend the TFS framework to a 3D coordinate system that considers both azimuth and elevation. We evaluate the performance of the proposed algorithm with the DREGON dataset [25], which consists of recordings made by a 3D array mounted on a flying quadcopter.

The remaining part of the paper is organized as follows. Sec. 2 formulates the problem. Sec. 3 and Sec. 4 present the time-frequency spatial filtering framework for sound enhancement and sound source localization in 3D space, respectively. Sec. 5 presents experimental results. Finally, we draw conclusions in Sec. 6.

## 2. Problem formulation

Let a microphone array mounted on a quadcopter consist of $I$ microphones arranged in an arbitrary shape. Considering a general 3D coordinate system, the locations of the microphones are denoted as $\boldsymbol{R} = [\boldsymbol{r}_1, \cdots, \boldsymbol{r}_I]$, where $\boldsymbol{r}_m = \left[r_{mx}, r_{my}, r_{mz}\right]^{\mathrm{T}}$ is the position of the $m$-th microphone, and the superscript $(\cdot)^{\mathrm{T}}$ denotes the transpose operation. A target sound source in the far field emits sound with a direction of arrival (DOA) $\boldsymbol{\theta}_d = (\alpha_d, \beta_d)$ with respect to the microphone array, where $\alpha_d$ and $\beta_d$ represent the azimuth and elevation, respectively (Fig. 1).

(a)

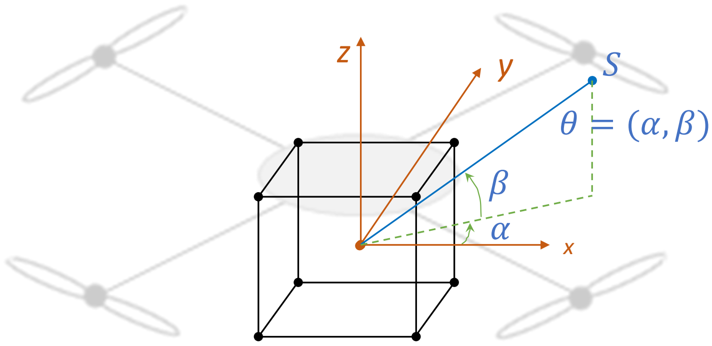


(b)

*Figure 1. A microphone array mounted underneath a drone and the 3D coordinate system. (a) Hardware used in the DREGON dataset (image from [25]). (b)The 3D coordinate system.*

The microphone array signal $\boldsymbol{x}(n) = [x_1(n), \cdots, x_I(n)]^{\mathrm{T}}$ consists of the target sound $\boldsymbol{s}(n) = [s_1(n), \cdots, s_I(n)]^{\mathrm{T}}$ and the ego-noise $\boldsymbol{v}(n) = [v_1(n), \cdots, v_I(n)]^{\mathrm{T}}$. This is expressed in the time domain as

$$\boldsymbol{x}(n) = \boldsymbol{s}(n) + \boldsymbol{v}(n), \tag{1}$$

and in the time-frequency domain as

$$\boldsymbol{X}(k,l) = \boldsymbol{S}(k,l) + \boldsymbol{V}(k,l), \tag{2}$$

where $k$ and $l$ denote the frequency and frame indices, respectively. Let $K$ and $L$ be the total number of frequency bins and time frames, respectively.

Given $\boldsymbol{x}(n)$ and $\boldsymbol{R}$, our goal is to estimate the DOA of the target sound $\hat{\theta}_d = (\hat{\alpha}_d, \hat{\beta}_d)$ and to design a spatial filter $\boldsymbol{w}(k,l) = [w_1(k,l), \cdots, w_I(k,l)]^{\mathrm{T}}$ to extract the target sound from the microphone array signal via

$$y(k,l) = \boldsymbol{w}^H(k,l)\boldsymbol{x}(k,l), \tag{3}$$

where the superscript $(\cdot)^{\mathrm{H}}$ denotes the Hermitian transpose.

## 3. Time-frequency spatial filtering for Sound enhancement

Given the microphone signal $\boldsymbol{X}(k,l)$, the microphone location $\boldsymbol{R}$**,** we aim to extract the sound coming from the target direction $\boldsymbol{\theta_d}$. The basic idea of the algorithm is to compute the instantaneous DOA of the sound at each time-frequency bin, which is subsequently utilized to compute the correlation matrix of the target sound and the corresponding spatial filter.

We first estimate the instantaneous DOA of the sound at each time-frequency bin. This is achieved by computing a local spatial likelihood function as

$$\gamma_{TF}(k,l,\boldsymbol{\theta}) = \mathcal{R}\left\{ \sum_{\substack{m_1,m_2=1 \\ m_1 \neq m_2}}^{I} \frac{X_{m_1}(k,l)X_{m_2}^*(k,l)}{|X_{m_1}(k,l)X_{m_2}(k,l)|} e^{j2\pi f_k \tau(m_1,m_2,\boldsymbol{\theta})} \right\} \tag{4}$$

where $f_k$ denotes the frequency at the $k$-th bin, the superscript $(\cdot)^*$ denotes the complex conjugation, and the operator $\mathcal{R}(\cdot)$ denotes the real component of the argument. The term $\tau(m_1, m_2, \boldsymbol{\theta})$ denotes the delay between two microphones $m_1$ and $m_2$ with respect to the sound coming from a candidate direction $\boldsymbol{\theta} = (\alpha, \beta)$, and can be approximated as

$$\tau(m_1, m_2, \boldsymbol{\theta}) = \frac{|r_{m_1} - r_\theta| - |r_{m_2} - r_\theta|}{c}, \tag{5}$$

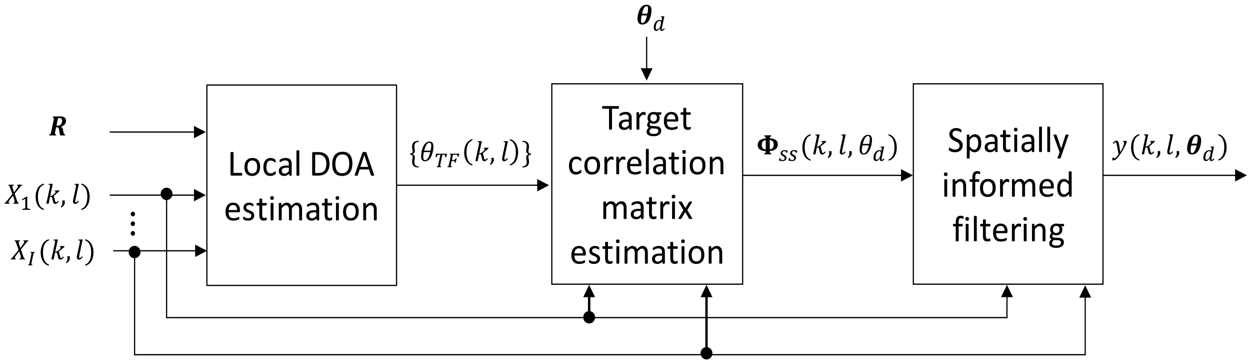


*Figure 2. Time-frequency spatial filtering for sound enhancement, which aims to extract the target sound coming from direction $\boldsymbol{\theta}_d$.*

where $\boldsymbol{r}_{m_1} = [x_{m_1}, y_{m_1}, z_{m_1}]$ and $\boldsymbol{r}_{m_2} = [x_{m_2}, y_{m_2}, z_{m_2}]$ denotes the locations of the two microphones; and

$$\boldsymbol{r}_{\boldsymbol{\theta}} = \left[\widetilde{D}\, cos\,(\alpha)\, cos\,(\beta)\,,\ \widetilde{D}\, cos(\alpha)\, sin(\beta)\,,\ \widetilde{D}\, sin(\beta)\right] \tag{6}$$

with $\widetilde{D} \approx 20$ meters representing a sound source in the far field.

The DOA of the sound at each time-frequency bin $\boldsymbol{\theta}_{TF}(k,l) = \{\alpha_{TF}(k,l), \beta_{TF}(k,l)\}$ is then computed as

$$\boldsymbol{\theta}_{TF}(k,l) = \underset{\boldsymbol{\theta}}{argmax}\, \gamma_{TF}(k,l,\boldsymbol{\theta}). \tag{7}$$

Assuming the target sound comes from the direction $\boldsymbol{\theta}_d = (\alpha_d, \beta_d)$, we define a confidence measure to indicate the target sound presence probability at each time-frequency bin, i.e.

$$c_d(k,l,\theta_d) = exp\left(-\frac{|\boldsymbol{\theta}_{TF}(k,l) - \boldsymbol{\theta}_d|}{2\sigma^2}\right), \tag{8}$$

where

$$|\boldsymbol{\theta}_{TF}(k,l) - \boldsymbol{\theta}_d| = \sqrt{(\alpha_{TF}(k,l) - \alpha_d)^2 + (\beta_{TF}(k,l) - \beta_d)^2} \tag{9}$$

denotes the distance between $\boldsymbol{\theta}_{TF}$ and $\boldsymbol{\theta}_d$; and $c_d \in [0,1]$. Here we assume the DOA estimate to be Gaussian-distributed with mean $\boldsymbol{\theta_d}$ and standard deviation $\sigma$. The higher $c_d$, the closer the local DOA $\boldsymbol{\theta}_{TF}(k,l)$ to the direction $\boldsymbol{\theta}_d$.

Given this confidence measure, we can compute the correlation matrix of the target sound as

$$\boldsymbol{\Phi}_{ss}(k,l,\boldsymbol{\theta}_d) = \frac{1}{L}\sum_{l=1}^{L} c_d(k,l,\boldsymbol{\theta}_d) x^{\mathrm{H}}(k,l) x(k,l), \tag{10}$$

where $c_d$ can be interpreted as the contribution of each time-frequency bin to the target correlation matrix. With this target correlation matrix, we can formulate a spatial filter pointing at direction $\boldsymbol{\theta}_d$. We use a standard Multi-channel Wiener filter (MWF) that is defined as [9]

$$\boldsymbol{w}_{TF}(k,l,\boldsymbol{\theta}_d) = \boldsymbol{\Phi}_{xx}^{-1}(k,l)\Phi_{ss1}(k,l,\boldsymbol{\theta}_d), \tag{11}$$

where $\Phi_{ss1}(k,l,\boldsymbol{\theta}_d)$ is the first column of $\boldsymbol{\Phi}_{ss}(k,l,\boldsymbol{\theta}_d)$, and $\boldsymbol{\Phi}_{xx}(k,l)$ is the correlation matrix of the microphone signal, which can be estimated directly using $\boldsymbol{\Phi}_{xx}(k,l) = \frac{1}{L}\sum_{l=1}^{L} \boldsymbol{x}^{\mathrm{H}}(k,l)\boldsymbol{x}(k,l)$.

Finally, the sound coming from $\boldsymbol{\theta}_d$ is extracted as

$$y_{TF}(k,l,\boldsymbol{\theta}_d) = \boldsymbol{w}^{\mathrm{H}}(k,l,\boldsymbol{\theta}_d)\boldsymbol{x}(k,l). \tag{12}$$

The computation procedure is illustrated in Fig. 2. For sound enhancement, TFS requires to know the target direction $\boldsymbol{\theta}_d$, which can be estimated with the algorithm described in the next section.

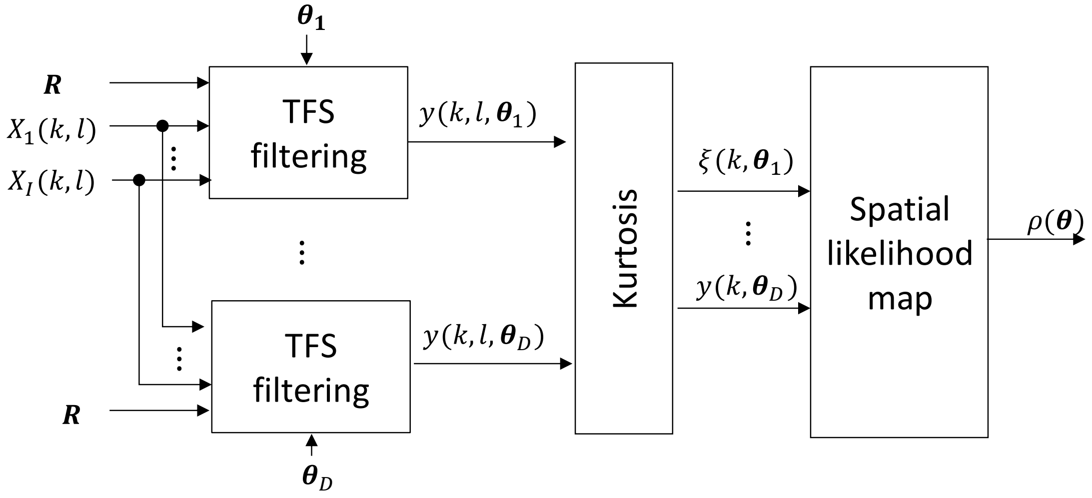


*Figure 3. Time-frequency spatial filtering for sound source localization, which aims to compute a spatial likelihood function $\rho(\boldsymbol{\theta})$ in the search space $\boldsymbol{\theta} \in \{\boldsymbol{\theta}_1, \cdots, \boldsymbol{\theta}_D\}$.*

## 4. Time-frequency spatial filtering for sound source localization

The basic idea of TFS for sound source localization is to formulate a set of spatial filters pointing at candidate directions:

$$\{\boldsymbol{\theta}_1, \cdots, \boldsymbol{\theta}_D\} = \{(\alpha_1, \beta_1), (\alpha_2, \beta_2), \cdots, (\alpha_D, \beta_D)\}, \tag{13}$$

where $D$ is the total number of candidate directions in a grid search space in azimuth and elevation. We then use the kurtosis of the spatial filtering outputs to indicate the spatial likelihood of the target sound. The target location typically presents a high kurtosis value once the target sound is extracted and the ego-noise is suppressed.

For each candidate direction $\boldsymbol{\theta}_i \in \{\boldsymbol{\theta}_1, \cdots, \boldsymbol{\theta}_D\}$, we compute a TFS filter and extract the sound coming from the direction $\boldsymbol{\theta}_i$ as

$$y_{TF}(k, l, \boldsymbol{\theta}_i) = \boldsymbol{w}^{\mathrm{H}}(k, l, \boldsymbol{\theta}_i)\boldsymbol{x}(k, l), \tag{14}$$

We calculate the kurtosis value $\xi(k, \boldsymbol{\theta}_i)$ of the time sequence in each frequency bin:

$$\xi(k, \boldsymbol{\theta}_i) = \mathcal{K}(\tilde{\boldsymbol{y}}_{TF}(k, \boldsymbol{\theta}_i)), \tag{15}$$

where $\tilde{\boldsymbol{y}}_{TF}(k, \boldsymbol{\theta}_i)$ denotes the time sequence $|y_{TF}(k, :, \boldsymbol{\theta}_i)|$ and $\mathcal{K}(\cdot)$ denotes the kurtosis value of the sequence. The spatial likelihood of the target sound at $\boldsymbol{\theta}_i$ is represented as the average of the kurtosis value over the whole frequency band, i.e.

$$\rho(\boldsymbol{\theta}_i) = \frac{1}{K}\sum_{k=1}^{K} \xi(k, \boldsymbol{\theta}_i) \tag{16}$$

Repeating this procedure for $\{\boldsymbol{\theta}_1, \cdots, \boldsymbol{\theta}_D\}$, we get the spatial likelihood function over the whole search space. The location of the sound source is then estimated as the location with the highest peak, i.e.

$$\hat{\boldsymbol{\theta}} = \underset{\boldsymbol{\theta} \in \{\boldsymbol{\theta}_1, \cdots, \boldsymbol{\theta}_D\}}{\operatorname{argmax}} \{\rho(\boldsymbol{\theta})\}. \tag{17}$$

The whole computation procedure is illustrated in Fig. 3.

## 5. Experimental results

We use the DREGON dataset [25] to validate the performance of the TFS algorithm in 3D scenario. The dataset provides 8-channel recordings made via a cubic microphone array (with side length roughly 10 cm) mounted on the bottom side of a MikroKopter drone, which can fly

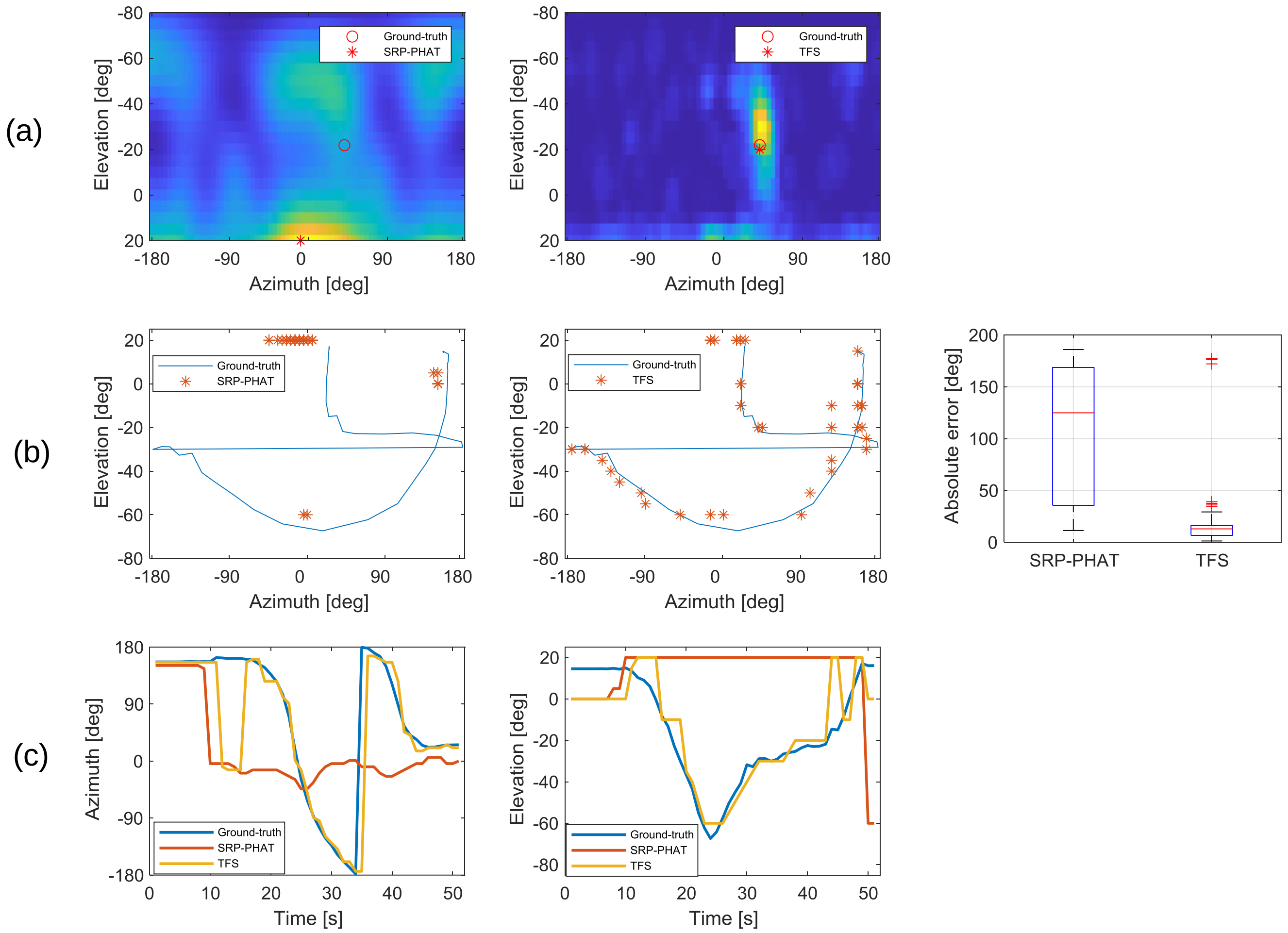


*Figure 4. Sound source localization with SRP-PHAT and TFS. (a) Spatial likelihood map of one sample segment. (b) Scatter plot of the estimation and boxplot of the absolute estimation error. (c) Azimuth and elevation trajectory.*

freely (Fig. 1). A loudspeaker placed on a desk emits speech signals when the drone is flying. The ground-truth location between the sound source and the moving drone was measured with a Vicon motion tracking system. The distance between the drone and the loudspeaker varies between 2 to 4 meters. We use the testing segment “Free Flight – Speech Source at High Volume (Room 1)”. The duration of the recording is about 110 seconds. Based on the description in [25], the SNR of the recording is roughly -12.8 dB.

When applying the TFS algorithm, we set within a space with a grid of $5°$at azimuth $\alpha \in [-179°, 180°]$ and a grid $5°$ at elevation $\beta \in [-90°, 20°]$. This generates 1656 candidate locations in total. We set FFT length 1024 and set $\sigma = 10°$. We employ a block-wise processing scheme to process the signal continuously, i.e. using a processing block of size 2 seconds with half overlap. In this way, we have 51 processing blocks. We apply a medial filter among 3 processing blocks to remove the estimation outliers and to improve the localization accuracy.

We compare with the performance of a baseline algorithm steered response with phase transform (SRP-PHAT) [26], with FFT length 1024. For performance evaluation, we compare the estimated azimuth and elevation with the ground truth, and compute the absolute error as the Euclidean norm of the azimuth and elevation errors.

Fig. 4 shows the sound source localization results by SRP-PHAT and TFS. Fig. 4(a) compares the spatial likelihood map produced by the two algorithms. for one sample segment of 2 seconds. Due to the influence of the ego-noise, SRP-PHAT does not estimate the sound source location correctly. On the other hand, TFS can estimate the sound source location correctly, with a peak clearly observed in the spatial likelihood map. Fig. 4(b) scatterplots the ground-truth location and

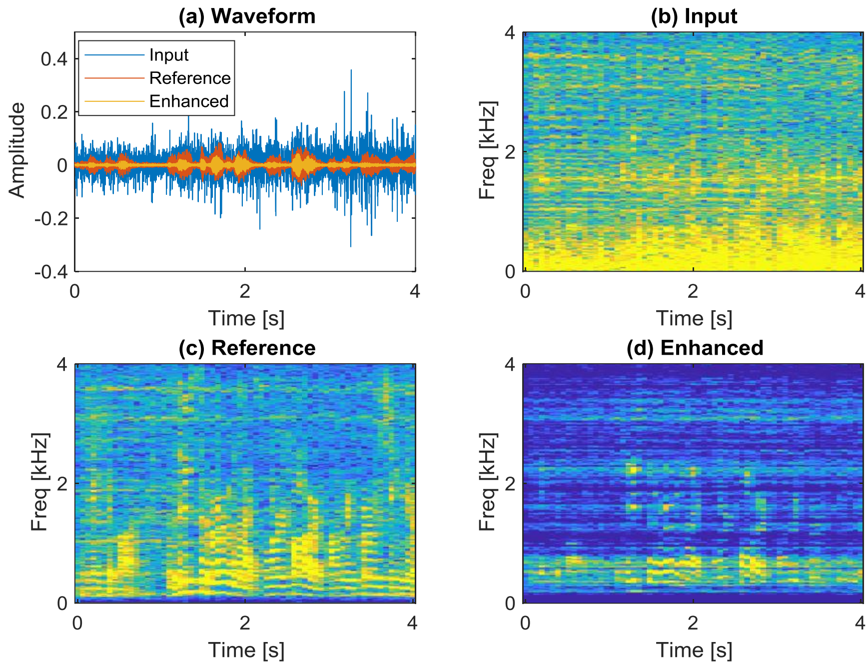


*Figure 5. Sound enhancement results with TFS for a sample segment. (a) Time-domain waveforms of the noisy input, clean reference and enhanced output. (b)-(d) Time-frequency spectrograms of the noisy input, clean reference and enhanced output.*

the estimated locations by the two algorithms in the azimuth-elevation plane. The source locations estimated by SRP-PHAT deviate significantly from the ground-truth while the ones estimated by TFS situate closely to the ground-truth. Fig. 4(b) also boxplots the absolute error across all processing blocks achieved by the two algorithms. SRP-PHAT achieves a median error of $125^\circ$ while TFS achieves a median error of $13^\circ$. Finally, Fig. 4(c) visualizes the azimuth trajectory and elevation trajectory estimated by the two algorithms. The azimuth and elevation of the drone vary dynamically during the flight. TFS algorithm can track the trajectory very well in comparison to SRP-PHAT.

Fig. 5 shows sound enhancement results for one sample segment of 4 seconds (19-23th second in the recording). We use the estimated source location at the 21st second (see Fig. 4) as the target location in this segment. For sound enhancement, we choose a processing segment length of 4 seconds and extract the sound from the target location. In Fig. 5, we show the time-domain waveforms and the time-frequency spectrogram of the noisy input, the clean reference (which was provided by an external camera capturing the whole scene), and the enhanced output by TFS. From the spectrogram in Fig. 5(b), the noisy input contains the ego-noise, which consists of full-band and harmonica components, the wind noise, which dominates the low frequency band, and the speech component, which is hardly distinguished. From Fig. 5(d), the speech component is clearly observed after TFS enhancement, although with certain distortion in comparison with the clean reference in Fig. 5(c).

## 6. Conclusions

We presented a time-frequency spatial filtering framework for sound processing on drones. We extended the TFS filtering framework [19, 21] to a more general 3D scenario and validated the performance with a public dataset for sound source localization from a flying drone. Future work includes optimizing the algorithm for real-time computation.

### Acknowledgement

The work is partly supported by the Pilot Research Fund of UK Acoustics Networks (UKAN+).

## References


[1] M. Basiri, F. Schill, P. U. Lima, and D. Floreano, “Robust acoustic source localization of emergency signals from micro air vehicles,” in *Proc. IEEE/RSJ Int. Conf. Intell. Robot. Syst.*, Vilamoura-Algarve, Portugal, 2012, pp. 4737-4742.

[2] K. Nakadai, M. Kumon, H. G. Okuno, et al., “Development of microphone-array-embedded UAV for search and rescue task,” in *Proc. IEEE/RSJ Int. Conf. Intell. Robot. Syst.*, Vancouver, Canada, 2017, pp. 5985-5990.

[3] Deleforge, D. Di Carlo, M. Strauss, R. Serizel, and L. Marcenaro, “Audio-based search and rescue with a drone: highlights from the IEEE signal processing cup 2019 student competition,” *IEEE Signal Process. Mag.,* vol. 36, no. 5, pp. 138-144, Sep. 2019.

[4] S. Yoon, S. Park, Y. Eom, and S. Yoo, “Advanced sound capturing method with adaptive noise reduction system for broadcasting multicopters,” in *Proc. IEEE Int. Conf. Consum. Electron.*, Las Vegas, USA, 2015, pp. 26-29.

[5] F. G. Serrenho, J. A. Apolinario, A. L. L. Ramos, and R. P. Fernandes, “Gunshot airborne surveillance with rotary wing UAV embedded microphone array,” *Sensors*, vol.19, no. 4271, pp. 1-26, 2019.

[6] Michez, S. Broset, and P. Lejeune, “Ears in the sky: Potential of drones for the bioacoustic monitoring of birds and bats,” *Drones*, vol. 5, no. 9, pp. 1-19, 2021.

[7] L. Wang and A. Cavallaro, “Ear in the sky: Ego-noise reduction for auditory micro aerial vehicles”, in *Proc. Int. Conf. Adv. Video Signal Based Surv.*, Colorado Springs, USA, 2016, pp. 1-7.

[8] H. G. Okuno and K. Nakadai, “Robot audition: Its rise and perspectives,” in *Proc. IEEE Int. Conf. Acoust, Speech Signal Process.*, Brisbane, Australia, 2015, pp. 5610-5614.

[9] S. Doclo and M. Moonen, “GSVD-based optimal filtering for single and multimicrophone speech enhancement,” *IEEE Trans. Signal Process.*, vol. 50, no. 9, pp. 2230-2244, Sep. 2002.

[10] A. Schmidt, H. W. Lollmann, and W. Kellermann, “Acoustic self-awareness of autonomous systems in a world of sounds,” *Proceedings of IEEE*, vol. 108, no. 7, pp. 1127-1149, Jul. 2020.

[11] K. Furukawa, K. Okutani, K. Nagira, T. Otsuka, K. Itoyama, K. Nakadai, and H. G. Okuno, “Noise correlation matrix estimation for improving sound source localization by multirotor UAV,” in *Proc. IEEE/RSJ Int. Conf. Intell. Robot. Syst.*, Tokyo, Japan, 2013, pp. 3943-3948.

[12] P. Misra, A. A. Kumar, P. Mohapatra, and P. Balamuralidhar, “Aerial drones with location-sensitive ears,” *IEEE Commun. Mag.*, vol. 56, no. 7, pp. 154-160, Jul. 2018.

[13] D. Salvati, C. Drioli, G. Ferrin, and G. L. Foresti, “Acoustic source localization from multirotor UAVs,” *IEEE Trans. Industrial Electronics*, vol. 67, no. 10, pp. 8618-8628, 2019.

[14] Y. Masuyama, Y. Bando, K. Yatabe, Y. Sasaki, M. Onishi, and Y. Oikawa, “Self-supervised neural audio-visual sound source localization via probabilistic spatial modeling,” in *Proc. IEEE/RSJ Int. Conf. Intell. Robot. Syst.*, Las Vegas, USA, 2020, pp. 4848-4854.

[15] B. Yen, Y. Hioka, G. Schmid, and B. Mace, “Multi-sensory sound source enhancement for unmanned aerial vehicle recordings,” *Applied Acoustics*, vol. 189, no. 108590, pp. 1-22, 2022.

[16] W. N. Manamperi, T. D. Abhayapala, J. A. Zhang, and P. Samarasinghe, “Drone audition: Sound source localization using onboard microphones,” *IEEE/ACM Trans. Audio, Speech, Lang. Process.*, vol. 30, pp. 508-519, 2022.

[17] L. Wang and A. Cavallaro, "Time-frequency processing for sound source localization from a micro aerial vehicle," *Proc. IEEE Int. Conf. Acoustics, Speech Signal Process.*, New Orleans, USA, 2017, pp. 496-500.

[18] L. Wang, R. S. Matilla, and A. Cavallaro, "Multi-modal localization and enhancement of multiple sound sources from a micro aerial vehicle," *Proc. ACM Multimedia 2017*, pp. 1591-1599, Mount View, USA, 2017.

[19] L. Wang and A. Cavallaro, "Microphone-array ego-noise reduction for auditory micro aerial vehicles," *IEEE Sensors Journal*, vol. 17, no. 8, pp. 2447-2455, Apr. 2017.

[20] L. Wang, R. S. Matilla, and A. Cavallaro, "Tracking a moving sound source from a multi-rotor drone," in *Proc. IEEE/RSJ Int. Conf. Intell. Robot. Syst.*, Madrid, Spain, 2018, pp. 2511-2516.

[21] L. Wang and A. Cavallaro, "Acoustic sensing from a multi-rotor drone," *IEEE Sensors Journal*, vol. 18, no. 11, pp. 4570-4582, Jun. 2018.

[22] L. Wang, R. S. Matilla, and A. Cavallaro, "Audio-visual sensing from a quadcopter: dataset and baselines for source localization and sound enhancement," *Proc. IEEE/RSJ Int. Conf. Intell. Robot. Syst.*, Macau, China, 2019, pp. 5320-5325.

[23] L. Wang and A. Cavallaro, "Deep learning assisted time-frequency processing for speech enhancement on drones," *IEEE Trans. Emerging Topics in Computational Intelligence*, vol. 5, no. 6, pp. 871-881, Dec. 2021.
[24] L. Wang and A. Cavallaro, "A blind source separation framework for ego-noise reduction on multi-rotor drones," *IEEE/ACM Trans. Audio, Speech, Lang. Process.*, vol. 58, pp. 2523-2537, Aug. 2020.
[25] M. Strauss, P. Mordel, V. Miguet, and A. Deleforge, “DREGON: dataset and methods for UAV-embedded sound source localization,” in *Proc. IEEE/RSJ Int. Conf. Intell. Robot. Syst.*, Madrid, Spain, 2018, pp. 5735-5742.
[26] L. Wang, T. Hon, J. D. Reiss, and A. Cavallaro, “An iterative approach to source counting and localization using two distant microphones,” *IEEE/ACM Trans. Audio, Speech, Lang. Process.*, vol. 24, no. 6, pp. 1079-1093, Jun. 2016.
[27] Y. Hioka, M. Kingan, G. Schmid, R. McKay, and K. A. Stol, “Design of an unmanned aerial vehicle mounted system for quiet audio recording,” Applied Acoustics, vol. 155, pp.423-427, 2019.

QUIET DRONES
Second International e-Symposium
on
UAV/UAS Noise
27th to 30th June 2022

# Identification of deterministic components of propeller noise

**Han Wu[1], Hanbo Jiang[1], Peng Zhou[1], Siyang Zhong[1] and Xin Zhang[1,2*]**

**1. Department of Mechanical and Aerospace Engineering, The Hong Kong University of Science and Technology, Clear Water Bay, Kowloon, Hong Kong SAR, China**
**2. HKUST-Shenzhen Research Institute, No.9 Yuexing First Road, South Area, Nanshan, Shenzhen, 518057, China**

## Summary

This study focuses on methods of processing the noise data of propulsive propellers commonly found on ubiquitous multi-rotor flying vehicles. The noise signals recorded in experiments typically contain both periodic tonal and random broadband components produced by rotational motion of the propellers, interaction between the propellers and turbulence, and other random factors. Factors such as unsteady rotational speed, manufacturing tolerance and flow disturbance can exist, leading to time-varying characteristics of the noise signals. In this study, we made assessments of methods to identify the deterministic components of the noise signals of propellers. Considering that the different noise patterns within two adjacent periods (due to the rotation) are similar, we applied averaging methods to remove the random components iteratively. A total of three methods were employed in this work: simple averaging, exponentially weighted moving averaging, and Kalman filter averaging. The exponentially weighted moving averaging method uses a constant weight while the weighting parameter based on the Kalman filter approach is iteratively adjusted. The methods are applied to results obtained using computational aeroacoustic simulations and laboratory experiments, demonstrating the capabilities of the methods to remove the random components. Some characteristics of the noise signals are identified.

[*] Email: aexzhang@ust.hk

## 1. Introduction

The market for drones has emerged rapidly over the past decade. The applications lie across multiple industries and disciplines, such as photography, detection, rescue, and agriculture [1–3]. The recent development of urban air mobility (UAM) is also of interest due to the ability for short-haul domestic commute [4]. The most widely employed propulsive systems for drones and UAMs are propeller-based ones since they can provide flexibility and manoeuvrability in hovering and flights. An important factor influencing the public and regulatory acceptance of drones and UAMs is noise pollution, as these flying vehicles are often operated in populated urban regions. The interaction between the propellers and the surrounding aerodynamic flow is a major noise source of the vehicles, requiring systematic assessment and mitigation.

Considerable efforts have been made to study the propeller noise. Experimentally, acoustic measurements have been conducted by researchers to study the noise characteristics of propellers in recent years. The essential noise characteristics of a single propeller are examined via static testing in anechoic chambers [5–8]. Measurements were also made of dual propellers [9, 10], contra-rotating propellers [11] and multiple rotor configurations [12]. Rotor-airframe interaction is found to generate significant tonal noise at higher blade passing frequency (BPF) harmonics [13]. Equally important, high-fidelity computational aeroacoustic simulations are also sued to simulate the propeller noise [14, 15].

In general, the types of propeller noise can be broadly classified as thickness noise and loading noise [16]. The noise locations vary with time due to the motion of the rotating blades, leading to tonal noise at harmonics of the blade passing frequency (BPF) [17]. Broadband noise is produced because of the interaction between the blades and the surrounding turbulent flows [18]. Both broadband noise [19] and tonal noise [20] can significantly affect human health. There are uncertainty factors that can make the propeller noise characteristics complicated. First, the electric motors commonly used in drones are found to have torque ripples, which could lead to speed fluctuations [21]. A theoretical study conducted by Zhong et al. [22] highlights the tonal noise generation due to speed variation. Kim et al. [23] quantified the fluctuation of propeller rotation as a random variable. Second, shaft-order tones are found in several experiments [5–8, 24], which are barely seen in numerical simulations [14, 15]. The shaft-order tones are likely caused by geometrical differences, as suggested by Zawodny et al. [6]. The geometrical imperfection could cause blade vibration and extra noise [25], and it can exist in practice due to manufacturing tolerance. These factors make the measured propeller noise signal time-dependent, even for the relatively well-controlled experiments in anechoic chambers. Recently, several studies reported that the propeller noise could also be impacted by the flow recirculation effect [6, 8, 10, 26] such that the noise spectra can be altered, depending on the anechoic chamber size.

In this work, we assessed three different averaging methods, namely, simple averaging (SA) method, exponentially weighted moving averaging (EWMA) method, and Kalman filter averaging (KFA) method, to separate the deterministic and random components in noise signals. The noise components due to uncertainty factors in practice can be identified from the overall noise spectrum.

The remaining part of this paper is structured as follows. Section 2 shows the formulations of different averaging methods. Section 3 presents the applications of CAA and experimental results for propeller noise. Section 4 is the conclusion.

## 2. Formulations

The time sequence of the measured sound signal is denoted as $v(t)$, where $v$ is the sound pressure and $t$ is the time. The signal is discrete, and the time step is $\Delta t$. We assume that the process has a period $T_0$, which corresponds to one propeller revolution for our case. We then can divide the signal $v(t)$ to $n$ data blocks sequentially, as shown in Figure 1.

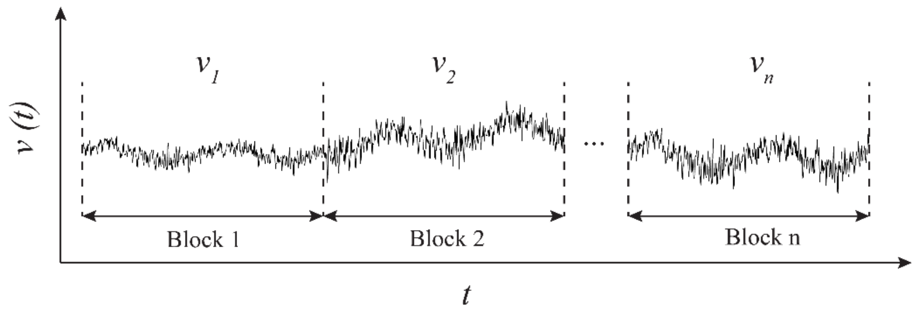


Figure 1: The schematic of signal subdivision. The time-domain noise signal is divided into $n$ blocks.

Our aim is to estimate the deterministic components, which are expected to repeat across the blocks. The target deterministic signals are denoted as $\hat{v}_1, \hat{v}_2, \cdots, \hat{v}_n$, and they are linked to the actual measured signals as

$$v_n = \hat{v}_n + \omega_n,$$

where $\omega$ denotes the random components in measurements.

### 2.1 Simple averaging (SA)

To remove $\omega_n$, a straightforward approach is to perform averages of the existing data blocks. The procedures can be expressed as follows. For a measured data segment containing $n$ blocks, the estimated data is calculated as

$$v_n^s = \frac{1}{n}\sum_{\mu=1}^{n}\left(\hat{v}_\mu + \omega_\mu\right),$$

where the superscript $s$ denotes the values estimated using the SA method. With the increase of $n$, it is straightforward to see the effect of random components, $\omega_n$, can be reduced statistically.

### 2.2 Exponentially weighted moving averaging (EWMA)

In practice, the patterns of noise signals might vary with time due to various uncertainty factors. In this case, we wish to capture the major noise features during one period $T_0$. To meet the requirement, an exponentially weighted moving average (EWMA) method is employed [27]. A weighting parameter $0 \le \beta \le 1$ is introduced to account for the effect of historical and current data, i.e., the data in block $n$ is estimated as

$$\hat{v}_n^W = \begin{cases} 0, & n = 0; \\ \beta \hat{v}_{n-1}^W + (1-\beta) v_n, & n > 1. \end{cases}$$

Here, the superscript $W$ indicates that the values are estimated using the EWMA method. When $\beta$ approaches 1, the updated value $\hat{v}_n^W$ is mainly dependent on that in the historical estimation $\hat{v}_{n-1}^W$.

### 2.3 Kalman filter averaging (KFA)

To capture the dynamic state of the noise signal variation, a Kalman filter [28] is employed in this work. Being different from the EWMA method where the weighting parameter is fixed, an adaptive weighting is employed on account of both estimation and observation uncertainties. The states variables are estimated as

$$\hat{v}_n = \hat{v}_{n-1} + K_n(v_n - \hat{v}_{n-1}),$$

where $K_n$ is called the Kalman gain matrix, and it is estimated as

$$K_n = p_{n-1}/(p_{n-1} + r),$$

where $r$ is the covariance matrix of the measurement error $\omega_n$. $p$ is a matrix estimating the error, and it is updated using

$$p_n = (1 - k_n)p_{n-1} + q,$$

where $q$ is the covariance matrix due to the estimation error.

# 3. Applications

## 3.1 Application on CAA results

The performances of the averaging methods are examined using the data obtained from a high-fidelity CAA computation of a small-scale propeller. The details of the CAA simulation can be found in reference [15]. The accuracy of the numerical simulations has been validated against propeller experiments in an anechoic chamber [15]. The propeller model implemented in the CAA simulation is a custom-designed propeller [29, 31]. The propeller is in a hover state, and the rotation speed is 90 revolutions per second (RPS). The sampling frequency for acoustic data is 20 kHz. The length of the aeroacoustic simulation is 0.5s. For this problem, the rotation period is $T_0$ = 1/90s, and the perturbed pressure signal is thus divided evenly into 45 blocks.

The CAA results at two observer positions are implemented. The relative positions between the microphones and the propeller are shown in Figure 2. The observer angle $\theta$ of the observers are $30^{\circ}$(upstream) and $90^{\circ}$ (rotational plane), respectively. The observer distance to the propeller centre is 1500m to ensure that the acoustic far-field condition is met. The time-domain noise signals and the results of different averaging methods are shown in Figure 3. The total noise signal contains random pressure fluctuations compared to the average. The random pressure fluctuations are relatively more significant for $\theta = 30^{\circ}$. It can also be seen that the averaged noise signal exhibits a repetitive pattern, which corresponds to the periodic rotation of the rotor blade.

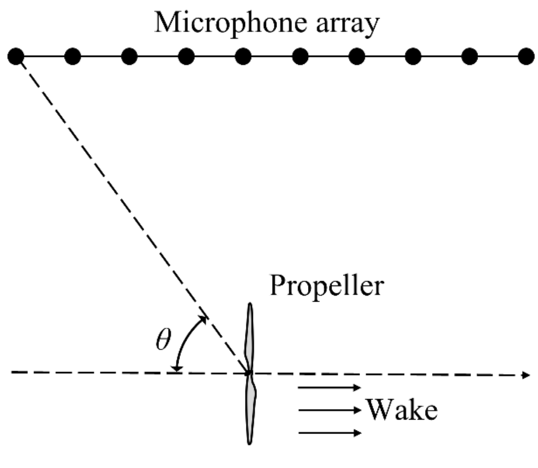


Figure 2: The schematic of the propeller aeroacoustic simulation. $\theta$ is the observer angle.

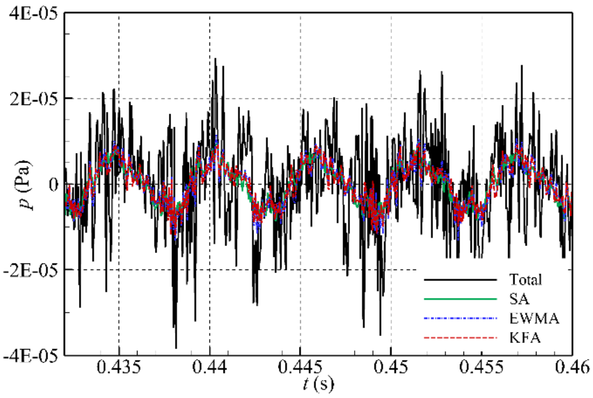


(a) $\theta = 30^{\circ}$.

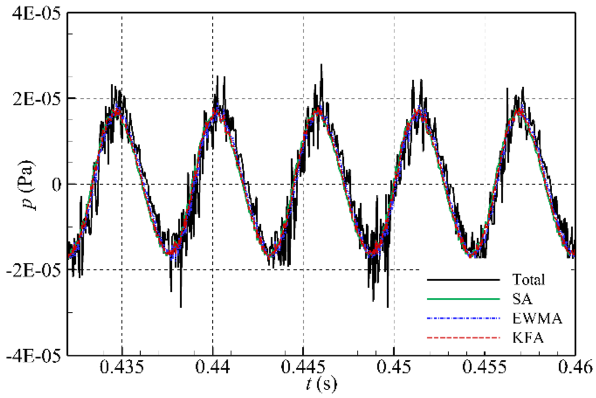


(b) $\theta = 90^{\circ}$.

Figure 3: A comparison of CAA and filtered noise signals of a propeller operating at 90 RPS.

The narrow-band frequency spectra of the total noise signal and the averaging results are plotted in Figure 4. The essential noise features of small-scale propellers can be simulated by the CAA computation, indicated by the solid black lines. In the low-frequency range, the noise spectrum is dominated by the tonal noise at BPF and its harmonics. The broadband noise is the dominant component at higher frequencies. The averaging results only contribute to the tonal components at the shaft-harmonics, as they repeat with rotor revolutions in the time domain. Most of the acoustic energy concentrates around the primary BPF tone. The averaging results can also capture the noise components at higher harmonics of BPF. For example, all the given methods can extract the second BPF tone for $\theta = 90^{\circ}$. There are also tones at higher frequencies, which are generally less significant than the broadband noise. Hence, the total noise spectrum only shows the broadband noise at high frequencies. The excellent match of the essential BPF tones indicates that the filtering methods can be implemented for propeller noise to capture the predominant tonal components.

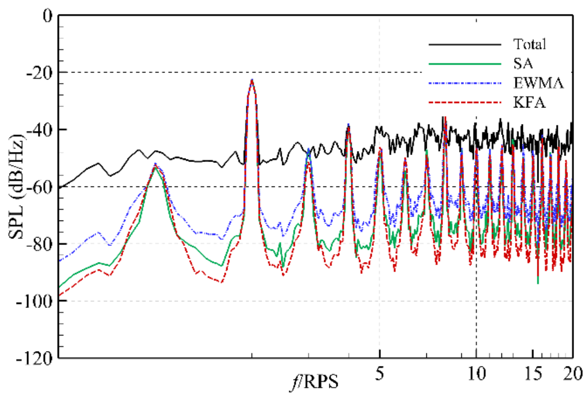


(a) $\theta = 30^{\circ}$.

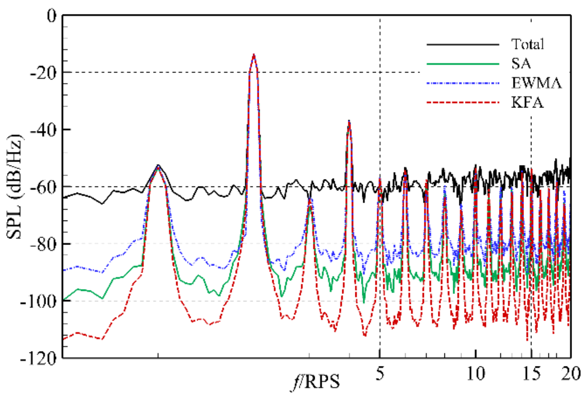


(b) $\theta = 90^{\circ}$.

Figure 4: A comparison of CAA and filtered noise spectra of a propeller operating at 90 RPS.

### 3.2 Application on experimental results

The averaging methods are further applied to propeller noise data recorded in an anechoic chamber test. The details of the experiment can be found in references [8,30]. The data used in this study was obtained at a hovering state of 110RPS. The time-domain noise signal is given in Figure 5(a). As reported by Stephenson et al. [26], the flow recirculation could occur during an anechoic chamber test and change the noise features. Therefore, the recorded data are split into two parts, pre-recirculation, and post-recirculation periods, which correspond to the first and the second half of the measurement. As can be seen from Figure 5(a), the amplitudes of random fluctuations start to increase after $t = 5$s instead of remaining at a certain level. The noise spectra are also compared in Figure 5(b). The flow recirculation leads to an enhancement in the high-order BPF tones and extra high-frequency broadband noise.

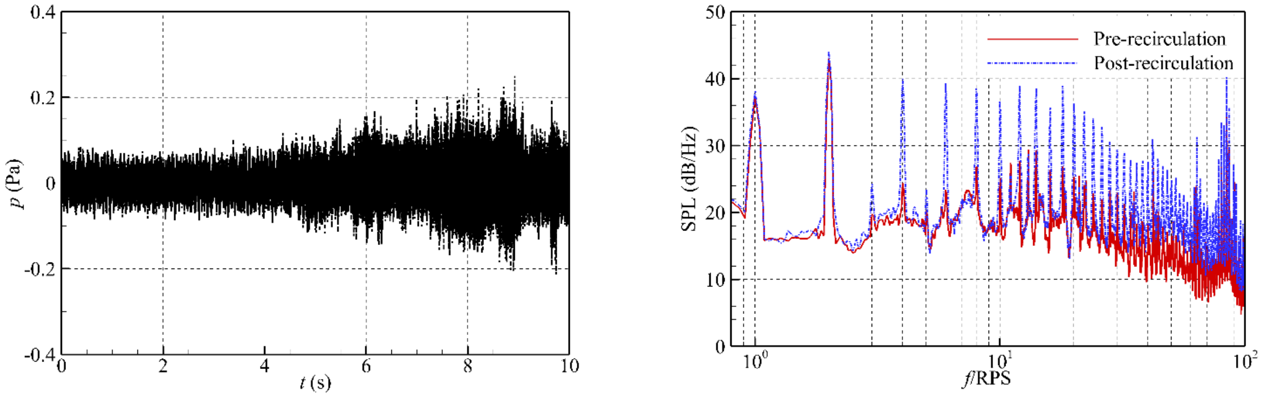


(a) Time signal. (b) Noise spectra.

Figure 5: The measured noise signal and comparison of spectra for different time periods. The noise data is acquired at $\theta = 30^{\circ}$.

The averaging methods are applied to the noise data to obtain the averaging results on the whole measurement period. The noise spectra are computed for both pre-recirculation and post-recirculation periods, respectively. The spectral properties are plotted in Figures 6 and 7. The EWMA and KFA filters can capture some essential tonal components, while the SA filter result does not agree with the total noise. As reported by Huff and Henderson [32], the motor noise is related to its vibration modes and manifests at the multiples of the rotational speed. In addition, the motor noise can be amplified by the propeller loading. In this study, the electric motor generates discrete tones near the 14×RPS and 42×RPS. The motor noise is more distinct before the onset of the flow recirculation, as the high-order BPF tones are not yet increased. As shown in Figure 6, the motor noise cannot be fully captured by the averaging methods. The random fluctuations of the rotating motion could result in random vibrations of the motor, leading to amplification of the motor noise. The shaft-order tones (e.g., $1\times, 3\times$ RPS, etc.) are also captured by the EWMA and KFA filters. Zawodnay et al. [6] state that the shaft-order tones are caused by the geometrical difference. The averaging results show that the shaft-order tones are deterministic. Additionally, there are discrete tones at the high frequencies ($f$/RPS > 50). As demonstrated by the averaging results, these tones could be contributed by the random noise sources since the averaging results contain little acoustic energy at the high frequency during the whole measurement period.

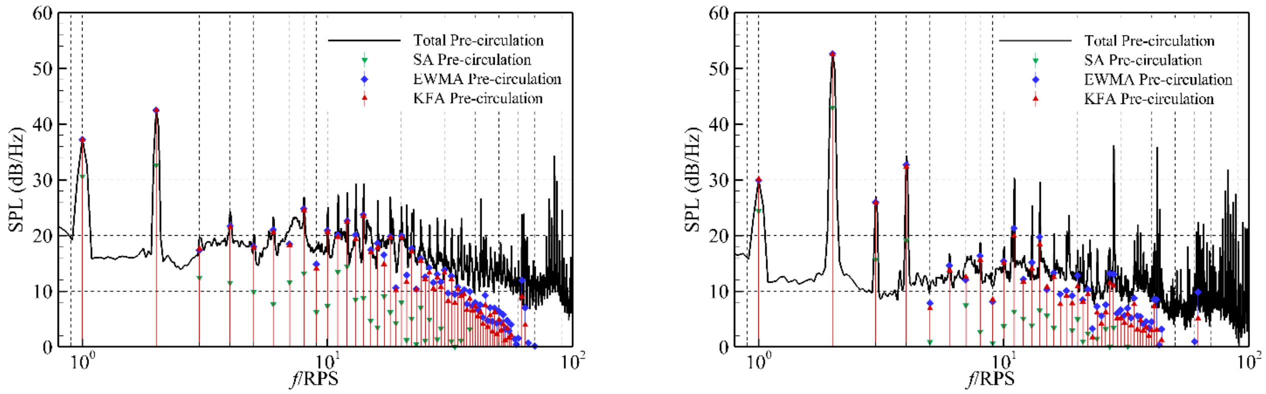


(a) $\theta = 30^{\circ}$. (b) $\theta = 90^{\circ}$.

Figure 6: A comparison of the experimental and filtered noise spectra of the propeller (pre-recirculation).

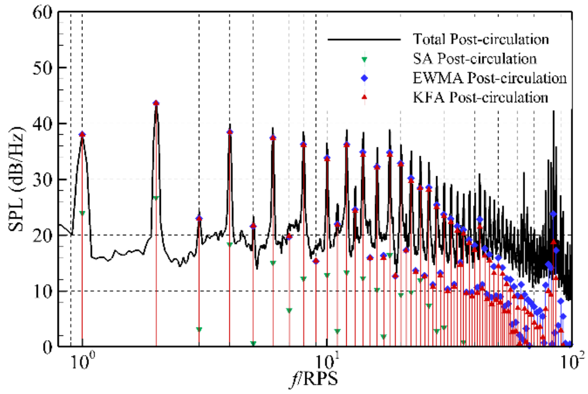


(a) $\theta = 30^{\circ}$.

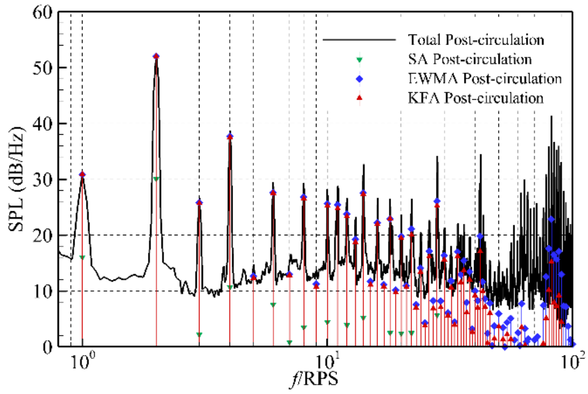


(b) $\theta = 90^{\circ}$.

Figure 7: A comparison of the experimental and filtered noise spectra of the propeller (post-recirculation).

The noise spectra of the post-recirculation case contain more tonal components at the BPF harmonics, as shown in Figure 7. Most of the BPF harmonics, especially those at low frequencies ($f$/RPS < 20), can be captured by the EWMA and KFA filters. The averaging results show that the unsteady flow disturbances can affect the deterministic noise components at the BPF harmonics. The high-frequency tones are also amplified by the flow recirculation, indicating that the flow disturbances can also impose random effects on the noise signatures. As suggested by Zhong et al. [22], the impact of unsteady loading will cause rotational speed fluctuations. The noise features under flow disturbances might increase the randomness in rotating motion. This study suggests the unsteady motion should be further considered in aeroacoustic investigations of the propellers.

## 4. Conclusions

The noise signal of propellers contains both deterministic and random components. In practical operations, the propeller noise can inevitably be affected by uncertainty factors. In this work, three averaging methods are applied to the propeller noise problem to remove the randomness and estimate the averaging state of the noise data. The data obtained from a CAA simulation and an anechoic chamber test are employed. The essential deterministic noise signal can be obtained by removing the randomness in the total signal. Results show that the averaging methods can extract the deterministic components for a given signal, indicating the potential for studying realistic propeller noise problems. For the experimental results, the overall pattern of the propeller noise signal might be randomly fluctuating over time. The EWMA and KFA methods have been shown to give a reasonable estimation of the deterministic noise components for the measured results. The methods can capture the canonical noise component with the overall time-domain trend of the signal.


### Acknowledgement

This work is supported by the Hong Kong Research Grant Council (RGC 16202520) and the National Natural Science Foundation of China (NSFC 11972029).


### References


[1] Motlagh, N. H., Bagaa, M., & Taleb, T. (2017). UAV-based IoT platform: a crowd surveillance use case. IEEE Communications Magazine, 55(2), 128-134.

[2] Tomic, T., Schmid, K., Lutz, P., Domel, A., Kassecker, M., Mair, E., Grixa, I. L., Ruess, F., Suppa, M., & Burschka, D. (2012). Toward a fully autonomous UAV: research platform for indoor and outdoor urban search and rescue. IEEE Robotics & Automation Magazine, 19(3), 46-56.

[3] Zhang, C., & Kovacs, J. M. (2012). The application of small unmanned aerial systems for precision agriculture: a review. Precision Agriculture, 13(6), 693-712.
[4] Donateo, T., De Pascalis, C. L., Strafella, L., & Ficarella, A. (2021). Off-line and on-line optimization of the energy management strategy in a hybrid electric helicopter for urban air-mobility. Aerospace Science and Technology, 113, 106677.
[5] Sinibaldi, G., & Marino, L. (2013). Experimental analysis on the noise of propellers for small UAV. Applied Acoustics, 74(1), 79-88.
[6] Zawodny, N. S., Boyd Jr, D. D., & Burley, C. L. (2016). Acoustic characterization and prediction of representative, small-scale rotary-wing unmanned aircraft system components. AHS Paper 0009054.
[7] Fattah, R. J., Chen, W., Wu, H., Wu, Y., & Zhang, X. (2019). Noise measurements of generic small-scale propellers. AIAA Paper 2019-2498.
[8] Wu, H., Chen, W., Fattah, R., Fang, Y., Zhong, S., & Zhang, X. (2020). A rotor blade aeroacoustics test platform at HKUST. InterNoise Paper 2476-2484.
[9] Zhou, T., & Fattah, R. (2017). Tonal noise characteristics of two small-scale propellers. AIAA Paper 2017-4054.
[10] Bu, H., Wu, H., Bertin, C., Fang, Y., & Zhong, S. (2021). Aerodynamic and acoustic measurements of dual small-scale propellers. Journal of Sound and Vibration, 511, 116330.
[11] McKay, R. S., Kingan, M. J., Go, S. T., & Jung, R. (2021). Experimental and analytical investigation of contra-rotating multi-rotor UAV propeller noise. Applied Acoustics, 177, 107850.
[12] Tinney, C. E., & Sirohi, J. (2018). Multirotor drone noise at static thrust. AIAA Journal, 56(7), 2816-2826.
[13] Zawodny, N. S., & Boyd, D. D. (2020). Investigation of rotor–airframe interaction noise associated with small-scale rotary-wing unmanned aircraft systems. Journal of the American Helicopter Society, 65(1), 1-17.
[14] Nardari, C., Casalino, D., Polidoro, F., Coralic, V., Lew, P. T., & Brodie, J. (2019). Numerical and experimental investigation of flow confinement effects on UAV rotor noise. AIAA Paper 2019-2497.
[15] Jiang, H., & Zhang, X. (2022). An acoustic-wave preserved artificial compressibility method for low-Mach-number aeroacoustic simulations. Journal of Sound and Vibration, 516, 116505.
[16] Brentner, K. S., & Farassat, F. (1998). Analytical comparison of the acoustic analogy and Kirchhoff formulation for moving surfaces. AIAA Journal, 36(8), 1379-1386.
[17] Brooks, T. F., Jolly Jr, J. R., & Marcolini, M. A. (1988). Helicopter main-rotor noise: Determination of source contributions using scaled model data. NASA Technical Paper 2825.
[18] Hubbard, H. H. (Ed.). (1991). Aeroacoustics of flight vehicles: theory and practice. NASA Office of Management, Scientific and Technical Information Program.
[19] Burkard, R., & Hecox, K. (1983). The effect of broadband noise on the human brainstem auditory evoked response. I. rate and intensity effects. The Journal of the Acoustical Society of America, 74(4), 1204-1213.
[20] Landström, U., Åkerlund, E., Kjellberg, A., & Tesarz, M. (1995). Exposure levels, tonal components, and noise annoyance in working environments. Environment International, 21(3), 265-275.
[21] Piccoli, M., & Yim, M. (2014). Cogging torque ripple minimization via position based characterization. In Robotics: Science and Systems.
[22] Zhong, S., Zhou, P., Fattah, R., & Zhang, X. (2020). A revisit of the tonal noise of small rotors. Proceedings of the Royal Society A, 476(2244), 20200491.
[23] Kim, D., Ko, J., Saravanan, V., & Lee, S. (2021). Stochastic analysis of a single-rotor to quantify the effect of RPS variation on noise of hovering multirotors. Applied Acoustics, 182, 108224.

[24] Intaratep, N., Alexander, W. N., Devenport, W. J., Grace, S. M., & Dropkin, A. (2016). Experimental study of quadcopter acoustics and performance at static thrust conditions. AIAA Paper 2016-2873.
[25] Semke, W. H., Zahui, D. K., & Schwalb, J. (2021). The vibration and acoustic effects of prop design and unbalance on small unmanned aircraft. Sensors and Instrumentation, Aircraft/Aerospace, Energy Harvesting & Dynamic Environments Testing, Volume 7, 9-16.
[26] Stephenson, J. H., Weitsman, D., & Zawodny, N. S. (2019). Effects of flow recirculation on unmanned aircraft system (UAS) acoustic measurements in closed anechoic chambers. The Journal of the Acoustical Society of America, 145(3), 1153-1155.
[27] Meyers, R. A. (2002). Encyclopedia of physical science and technology. Academic.
[28] Kalman, R. E. (1960). A new approach to linear filtering and prediction problems. Journal of Basic Engineering, 82 (1), 35–45.
[29] Jiang, H., Wu, H., Chen, W., Zhong, S., & Zhang, X. (2022). Simulation-aided design of low-noise blade and experimental validation. AIAA Paper, accepted.
[30] Yi, W., Zhou, P., Fang, Y., Guo, J., Zhong, S., Zhang, X., Huang, X., Zhou, G., & Chen, B. (2021). Design and characterization of a multifunctional low-speed anechoic wind tunnel at HKUST. Aerospace Science and Technology, 115, 106814.
[31] Jiang, H., Zhong, S., Wu, H., Zhang, X., Huang, X., Zhou, G., & Chen, B. (2022). Radiation modes of propeller tonal noise. Journal of Vibration and Acoustics, 144(2).
[32] Huff, D. L., & Henderson, B. S. (2018). Electric motor noise for small quadcopters: part 1–acoustic measurements. AIAA Paper 2018-2952.

**QUIET DRONES**
**Second International e-Symposium**
**on**
**UAV/UAS Noise**
**27th to 30th June 2022**

# Airport regions authorities dealing with drones

**Sergi Alegre Calero (Airport Regions Council).**

Drones noise impact is one of the most important challanges of their massive use. On the other hand, drones explotation will be linked with aviation activities at airports. Therefore, Airport Regions Council, the European association of public administrations of cities and regions with an airport in their territory is working since so time ago, to promote the proper conditions of the use of drones in order to avoid/minimize/manage the noise impact to the citizens in order to have a peaceful development of this sector. As the administrations/citizens that have dealt more with air noise, we understand that our collaboration can be key in this matter.

# ARC: an organisation for inter-regional cooperation, EU representation,  knowledge exchange & a legitimate partner for European projects

**Sergi Alegre Calero| Airport Regions Council**
Director General

# Airport Regions Council

Who are we ?

30 member regions

Regions with hubs: Frankfurt, Paris, Barcelona, Vienna,….

Regions with middle airports: Prague, Dublin, Gotheborg,….

Regions with small airports: Eilat, Iasi, Rotterdam,…

# Airport Regions Council

## What do we do?

Studies

Projects

MEMBERS

Representation

Communication

# Airport Regions Council

## Projects

ANIMA
Aviation Noise Impact Management through Novel Approaches

Interreg CENTRAL EUROPE
European Union
European Regional Development Fund
LAirA

DREAM
DEVELOPMENT OF REGIONAL EMPLOYMENT AND AIRPORT AREAS MANPOWER

dAIR

# Airport Regions Council

## Studies




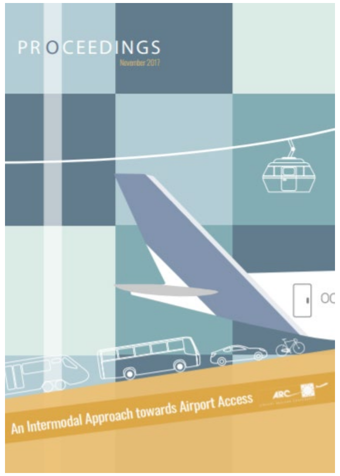

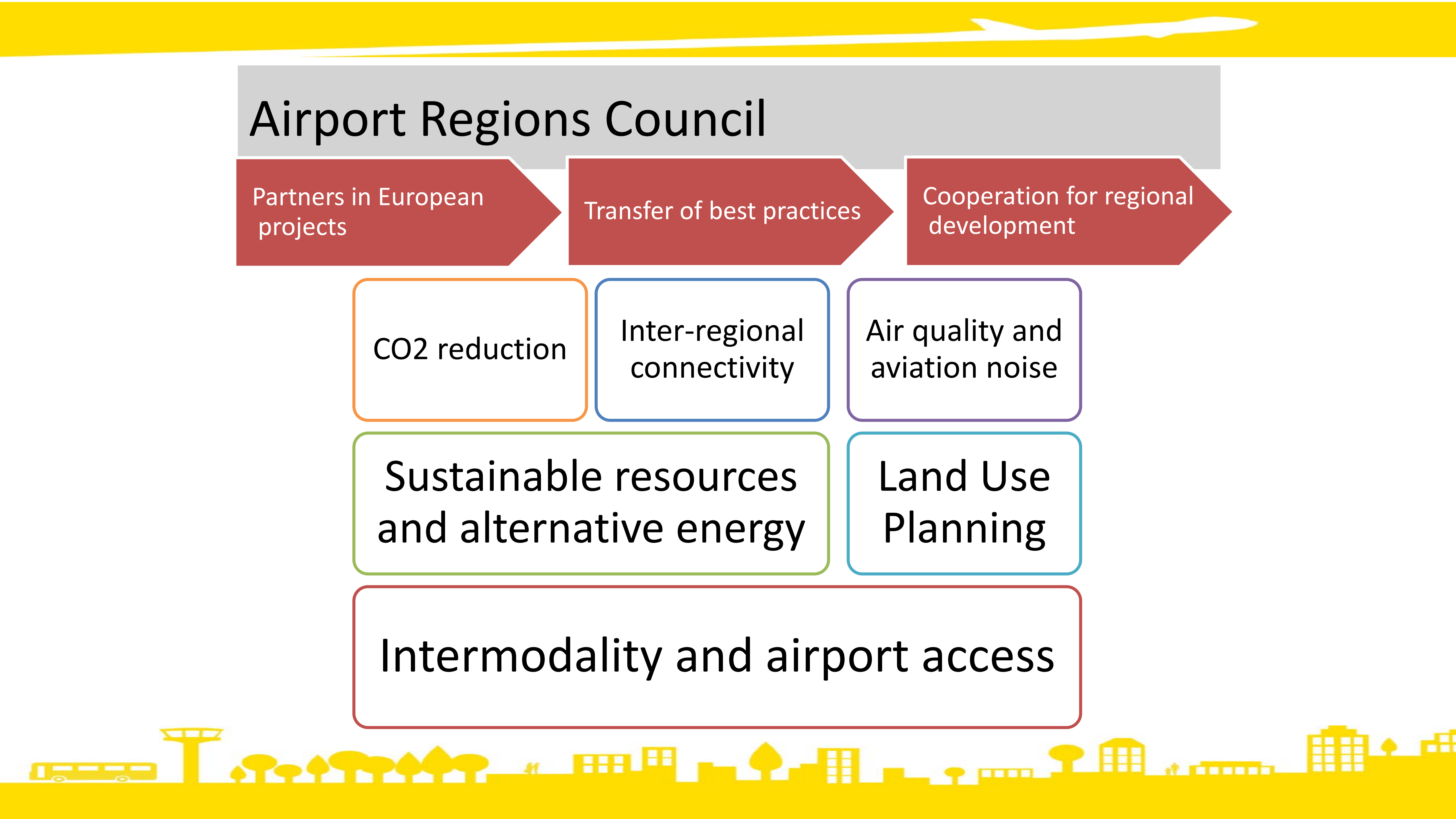
Airport Regions Council
Partners in European projects
Transfer of best practices
Cooperation for regional development
CO2 reduction
Inter-regional connectivity
Air quality and aviation noise
Sustainable resources and alternative energy
Land Use Planning
Intermodality and airport access

- ✓ At European level, it is quite clear that the main issue slowing down the intensive use of drones and other unmanned air vehicles are the social and their consequent political preventions.
- ✓ These preventions have four main aspects:

  . Security - ‘what if a drone falls?’

  . Privacity - ‘what if a drone has a camera -a gun?- and stays in front/over of my house?’

  . Noise - ‘will drones disturb me?’

  . Governance – ‘who can I complain to, if I want to/need to?’, ‘by whom, how and when will the conditions/rules/norms be fixed?, ‘who is responsible of controlling if conditions are met and how?‘

At the present moment, the European Commission, via EASA (European Aviation Safety Agency), is in the process of building the European governance architecture but there is still a long way to go.

Regarding drones, Airport Regions Council has committed itself to be involved in all aspects of the development and specially for noise.  On this respect we consider that :

- ✓ noise could become the most common problem (no one can imagine drones falling down daily), so much attention must be paid
- ✓ we ask all authorities and the drone industry to take note of the know-how and the accumulated experience developed by the aviation/airport authorities, local authorities and citizens associations in dealing with "air noise". We are talking about: information, monitoring, limits, etc.
- ✓ the issue of noise can be very easly avoided if altitudes where air vehicles operate are high enough over the cities (100m/200m)
- ✓ a prevention policy must be developed in all aspects but especially for noise. Therefore, all systems of control, and measurement must be fixed and tested and all the administrative architecture (including the complain and denounce procedures) must be settled before the deployement of drones.

- ✓ UAM cannot increase by any means the base noise of cities. At a moment when noise is identified as one of the biggest annoyances of city life, no one could imagine an increase in social acceptance of noise
- ✓ Before the deployment of drones, as the ‘problematic’ phases of drones activities regarding noise will be the ascent and descent phases, the areas where they can ascent and descent should be determinated and should be monitored with special intensity and the responsible vertiports will have to take the responsability of isolating, if necessary, the surrounding buildings
- ✓ It is necessary to develop a transparent and massive information policy regarding drones, including the noise issue, addressed by all segments of society

QUIET DRONES
Second International e-Symposium
on
UAV/UAS Noise
$27^{th}$ to $30^{th}$ June 2022

# Small scale rotor aeroacoustics characterization on the interaction noise

**Tiziano Pagliaroli, Università Niccolò Cusano: tiziano.pagliaroli@unicusano.it**
**Paolo Candeloro, Università Niccolò Cusano**
**Fabrizio De Gregorio, Italian Aerospace Research Centre (CIRA)**
**Giuseppe Ceglia, Italian Aerospace Research Centre (CIRA)**

## Summary

In this work, the noise generated by twin rotors for mini drone propulsion was investigated. The experimental study, conducted by varying the speed, distance and phase of the propellers showed that the noise is influenced by all these parameters. An advanced phase control system allowed both to keep constant the rotor-rotor phase and to apply an active noise control technique using a phase randomisation strategy. The control technique developed is very effective when rotors are in close proximity and reduced noise by a maximum of 8 dB.

## 1. Introduction

Unmanned Aerial Vehicle (UAVs) or Micro Aerial Vehicle (MAV) are commonly called drones and are already designed with vertical take-off and landing capabilities, and can be manoeuvred with extremely high versatility and speed. For this reason, MAVs can be easily employed for tactical missions or in urban areas for civil purposes. In both applications, a low noise footprint is mandatory. In fact, for defence applications, a drone with a low noise signature can stealthily approach the target. On the other hand, for civil application in urban areas, drones with low noise emission can more easily obtain the public acceptance.
To give an idea of the public acceptance of large-scale use of delivery drones in residential areas, it would be sufficient to read the title of an article recently published by the Wall Street Journal:" Delivery Drones Cheer Shoppers, Annoy Neighbours, Scare Dogs" [1].

Since the rotors are main source of drone noise, significant efforts are focusing on the aeroacoustic studies of the blades with the aim of understanding the phenomenon and implementing passive control strategies.
In the past, the topic of rotor noise has been extensively addressed also on helicopter, but these studies cannot be directly extended to drone rotors. This aspect is related to the difference in scale of the drone blades compared to helicopter ones. In fact, for the small-scale rotors the Reynolds number assumes smaller values than helicopter and the flow physics results to be completely different [2]. For small scale rotor the aerodynamic filed is characterized by Tollmien-Schlichting instability, laminar recirculation bubble dynamics, transition form laminar to turbulent boundary layer. All of these characteristics of the flow physic play an important in noise generation [3]. Moreover, the tonal noise component emitted by drones results to be less intense, compared to helicopters, and becomes to be of the same order of the broadband component. For these two reasons: transitional aerodynamics and a significant broadband noise component, the topic of the drone noise requires specific experimental studies and the development of dedicated mathematical tools for noise prediction.
In the last years, the scientific community has tackled the study of drone aeroacoustics by focusing the attention on two mainstream topics: *i*) single rotor noise (isolated rotor), and *ii*) drone noise (noise generated by complete quad-, hexa- or octo-copter). The aeroacoustic study of a complete drone is justified by a non-linear noise source related to the proximity of the rotors, which can mutually interact, generating an additional noise component called interaction noise.
In view of its relevance, several of works have been recently published on the aeroacoustic behavior of multi-rotors. Zhou et al. performed an experimental investigation on the impact of the distance between the two rotors [4]. Tinney and Sirohi assessed the aerodynamic performance and the near-field acoustics of an isolated rotor, quad-copter, and hexa-copter to address the effects of the number of rotors [5]. Jia and Lee investigated the interactional aerodynamics and acoustics of the coaxial rotor and quad-rotor [6, 7]. Ko et al. have analysed the noise directivity patterns depending on the diamond and square multi-rotor configuration [8]. Recently, Lee et al. performed an aeroacoustic study of rotor-rotor interaction by varying their mutual distance [2]. Although, several studies on the multi-rotor have been performed, the analysis of the rotor-rotor aeroacoustic interaction is an open issue.
Since, the interaction noise is significantly influenced by the rotor-rotor distance, in the present manuscript, an experimental aeroacoustics characterization of a twin rotors by varying the distance and the rotational regime is reported and discussed.
In addition, an in-depth aeroacoustic investigation was conducted to address the effect of the phase angle between the rotors on the interaction noise source. To our best knowledge, in the context of drones, this subject has never been investigated before. To study the effect of the phase between rotors, a PID based control system was implemented, the performance of this system is described hereafter.

## 2. Experimental setup

Figure 1a show a picture of the test rig and instrumentation employed for the research activity. A couple of three bladed rotors 393.7 mm in diameter (D) (KDE-CF155-TP), two engines (KDE4012XF-400), with two electronic speed controllers (KDEXF-UAS55) were used for the experimental campaign.
The rotor angular position and speed were measured by using two encoders Kubler by 500 ppr (see Figure 1 b). Pressure fluctuations were measured using an arc of microphones.
The experimental campaign was conducted inside the anechoic chamber of the Italian Aerospace Research Centre (CIRA). The chamber is 8.05x6.85x2.62 m in size and has a cut-off frequency of 90 Hz.

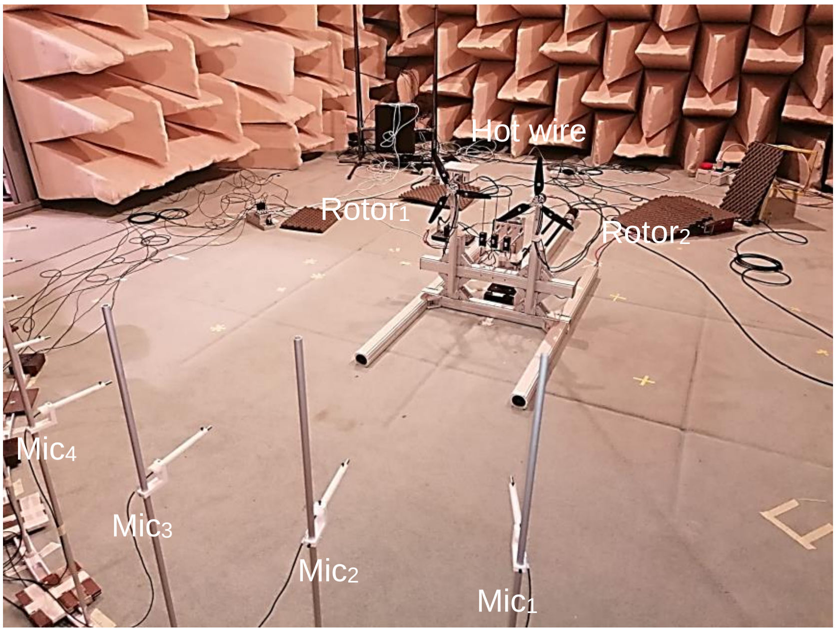

(a)


(b)

Figure 1: Picture of the anechoic chamber, the test rig and a portion of the microphone arc (a); close-up photography of the test rig (b).

### 2.1 Aeroacoustic measurements

The 10-microphone array was located on a circular arc at a radial distance r/D=5, from the centreline of the rotor discs, spanning a relative polar angle range $\theta = [0°,\ 90°]$, the polar angle being defined positive in the counter clockwise direction.
Figure 2 shows one of the four possible positions of the microphone arc, located in the first quadrant (I). After each single test, keeping constant all parameters (e.g. speed, rotor-rotor phase and distance), the arc was moved to the other quadrants to cover the angular range $\theta = [0°, 360°]$.
The objective of this procedure is to measure the pressure fluctuation, with an angular resolution of 10°, and provide the complete noise directivity pattern. Pressure fluctuations were measured using 1/8" GRAS microphones.
Time signals were acquired by National Instruments cDAQ-9234 system with a sampling frequency of 51.2 kHz for an acquisition time of 30 s.

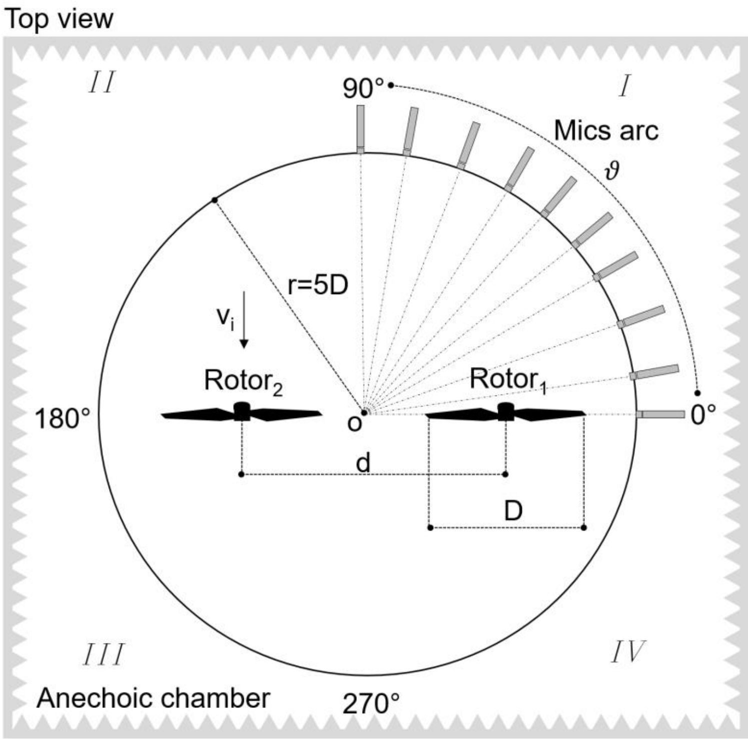

Figure 2: Sketch of the experimental setup: top view.

## 2.2 Synchrophaser

The test rig, using a custom-made control system named *Synchrophaser*, matches the counter clockwise speed between rotors and allow us to set the rotors phase angle, $\psi$ ,defined as shown in Figure 3a. For completeness, two examples of angular configurations between rotors are provided in Figure 2 b and c: $\psi$ =0° and 30° (the phase shift always refers to the slave propeller relative to the master.

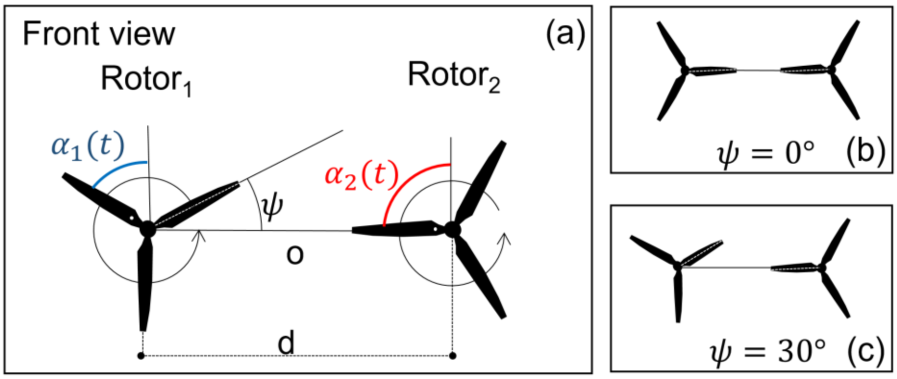


Figure 3: Sketch of the experimental setup front view (a). Example of the rotor-rotor phase configuration: $\psi$=0° (b) and $\psi$=30° (c).

The synchrophaser is based on a PID control system as sketched in Figure 4. The encoders measure the angular position of the motors, using an operator they also measure the phase angle between the rotors which is compared with a set point angle, $\psi_{sp}$. The difference between the two angles is used to calculate the error, which is input to the PID controller. The PID controller generates a change in the control signal of motor 2 ($PWM_2$), named the slave motor.

The slave motor chases the master with a phase angle if it deviates as little as possible from the set point.

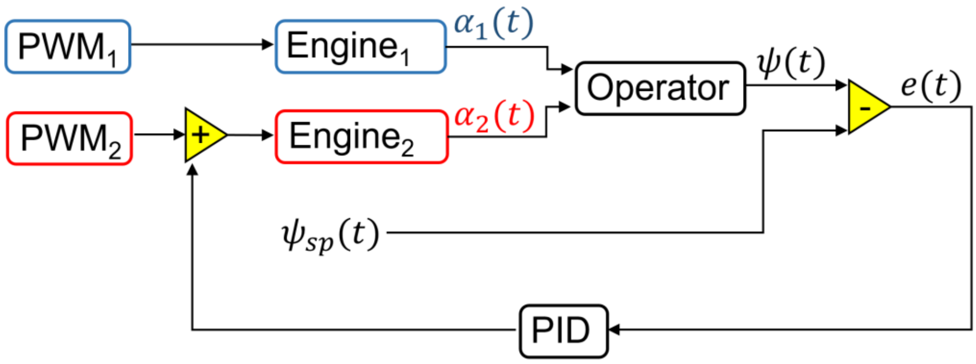


Figure 4: Flow chart representing the control strategy implemented into the synchrophaser.

The system allows variable phase set points to be set. A random phase generator was used to show that a loss of phase coherence has a dominant effect on the interaction noise.

### 2.3 Test matrix

During the tests campaign, the distance (d), the rotational speed (Ω) and the phase angle ($\psi$) of the rotors were varied. The values assumed by these variables are shown in the table below:

| d (mm) | Ω, RPM | $\psi$, deg |
|---|---|---|
| 417 | 3500 | 0° |
| 409 | 4360 | 30° |
| 402 | 5300 | 60° |
| / | / | 90° |
| / | / | |

Table 1: Test matrix.

Each possible combination of the parameters reported in the Table 1 was experimentally investigated for a total of 36 test cases.

## 3. Results

Single rotor noise ($Rotor_1$) was pre-qualified at three different speeds. Figure *5* shows the directivity of the isolated rotor in terms of Sound Pressure Level (SPL). It is noticeable that the origin of the mics arc is not centred on the rotor disc, but in the centre of the two rotors. The idea is to compare the noise of a single rotor with that generated by the pair of rotors without moving the reference system. For this reason, SPL, in the range $\theta = [150°, 180°]$, assumed smaller value than in the range $\theta = [0°, 30°]$. Furthermore, the aeroacoustic effects of the slipstream affects the range $\theta = [270°, 290°]$, where a significant increase in noise is observed. In general, higher rotational regime leads to an increase in SPL.

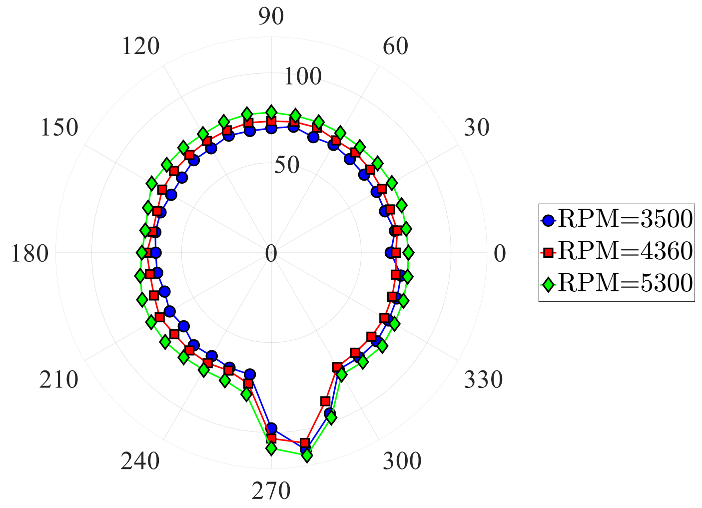


Figure 5 Polar diagram of the sound pressure level radiated by single rotor and measured for different rotational regime: 3500, 4360, and 5300 RPM.

The directivity pattern of two rotors is represented in Figure 6 by varying: rotational speed, phase and distance between the two rotors.
In all cases, the noise emitted by the rotors has a distribution in first approximation constant with the angular position, except for the $\theta = [260°,\ 280°]$, in which a high increase in SPL is observed due to the pressure fluctuations present in the slipstream. The noise in the slipstream becomes greater with increasing velocity (compare for example Figure 6 a, d, g).

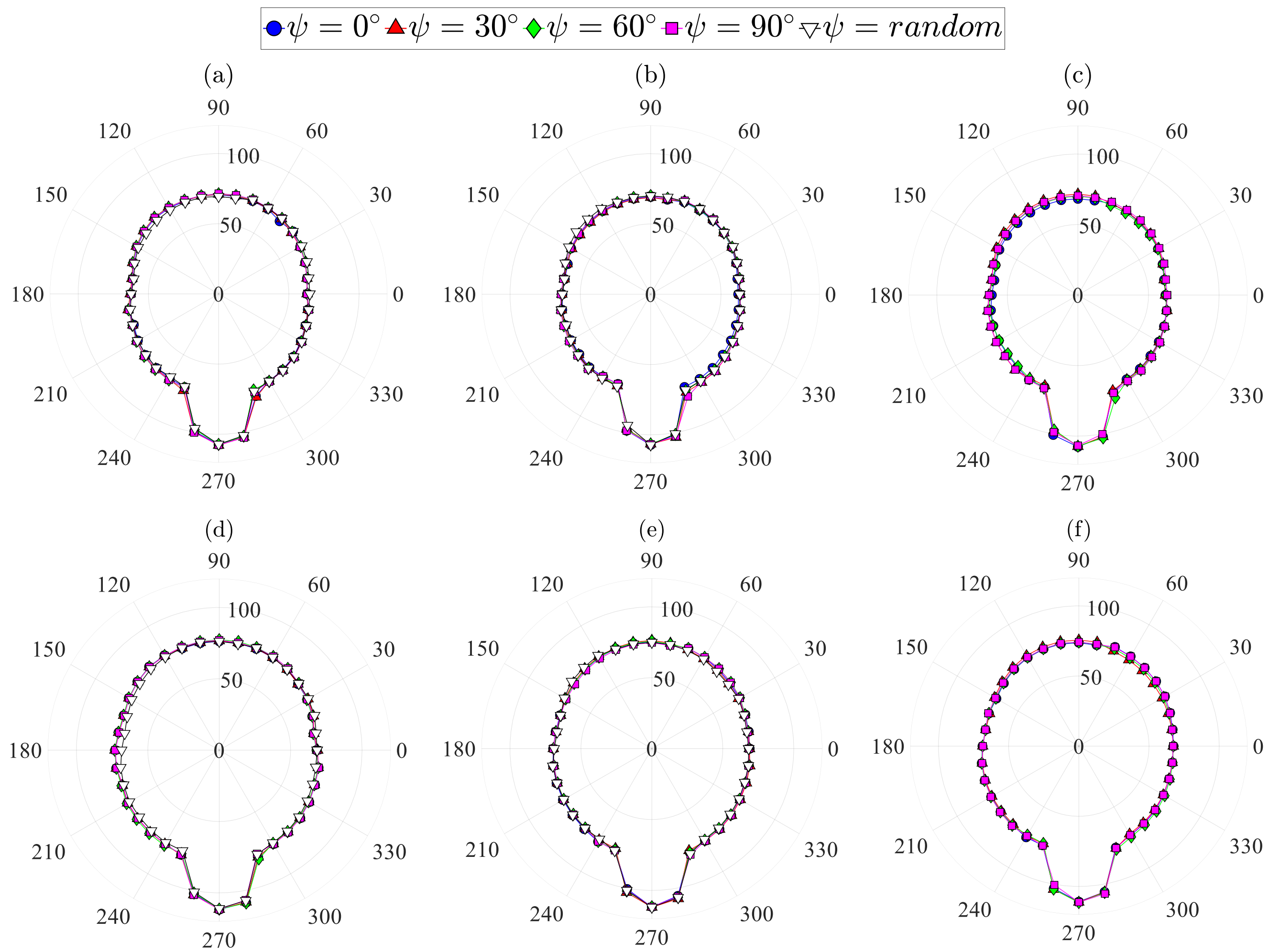

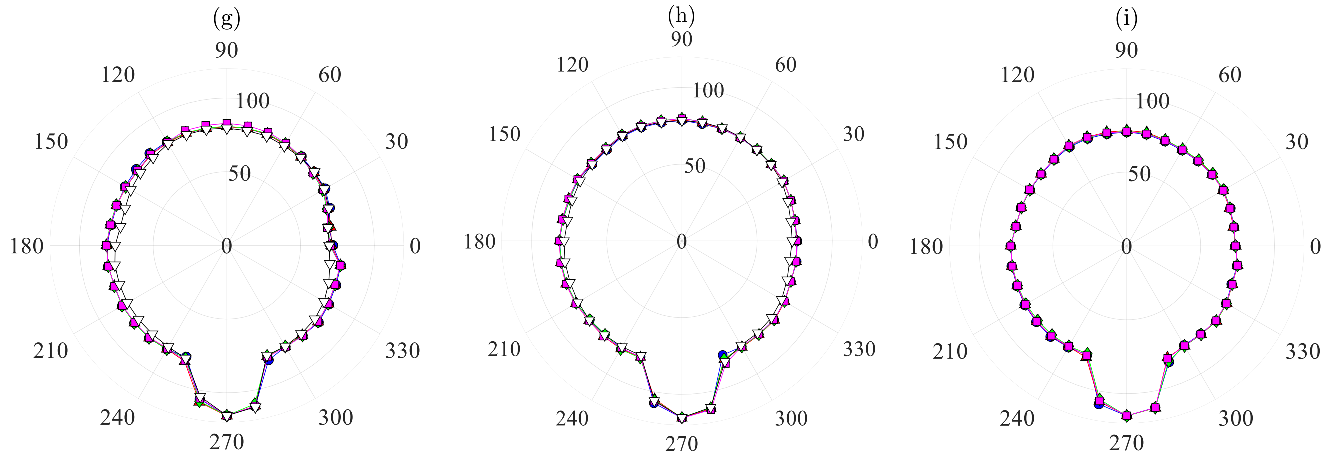


Figure 6: Sound pressure level polar diagram measured for different rotational regime and rotor-rotor distance for co-rotating configuration. For the first row of plot the rotational regime is 3500 RPM and the rotor-rotor distances are 402 mm (a), 409 mm (b) and 417 mm (c) respectively. For the second row of plot the rotational regime is 4360 RPM and the distances are 402 mm (d), 409mm (e), and 417 mm (f). The rotational regime referred to the third row of plot is 5200 RPM, whereas the distance are 402 mm (g), 409mm (h), and 417 mm (i).

Figure 6 gives an overview of the database. The SPL is nearly constant except in the $\theta = [260°, 280°]$ where the microphones are within slipstream and measure larger pressure fluctuations related to turbulent structures. A comparison of Figure 6a-d-g shows that SPL measured in the wake increases upon the rotational regime. Furthermore, in Figure 6adg, for the configuration in which the rotors are closest, it can be seen that the phase randomisation system is very effective as the speed increases.
The SPL versus azimuthal angle in linear scales, for 5200 RPM and d=409mm reported in Figure 7, shows that the phase randomization is very effective in noise reduction for a broad range of angle: in the range $\theta = [50°, 350°]$ the noise radiated by rotors lead by random phase is lower than fixed phase. The reduction achieves a maximum of 8 dB at $\theta = [170°, 180°]$.

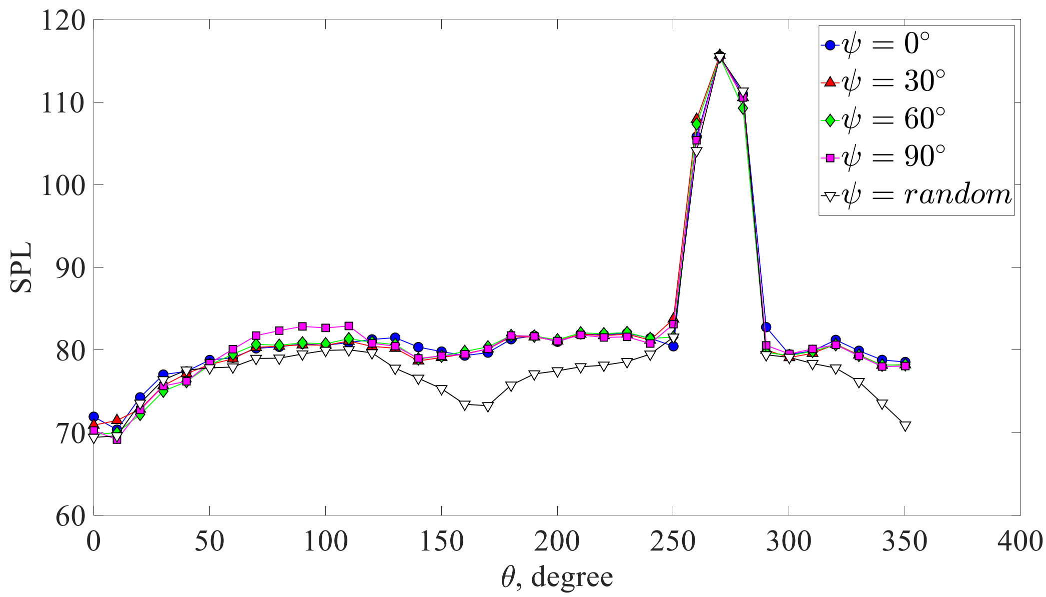


Figure 7: SPL upon azimuthal angle in linear scales, for 5200 RMP and d=409.

To better understand the nature of this noise mitigation, a spectral and statistical analysis was performed on two time series acquired at 180°, where the noise reduction is maximum, and at

270° where there is no reduction in SPL. The spectra are presented in terms of dimensionless frequencies with respect to the blade pass frequency (HBPF).
The phase randomisation system as can be seen in Figure 8a has a two effects: *i*) it reduces the broadband component of the noise in the $HBPF = [1.5,\ 9]$ range while the noise in the wake remains totally unchanged (see Figure 8b); it mitigates the tonal component from the second harmonic (HBPF=2) .

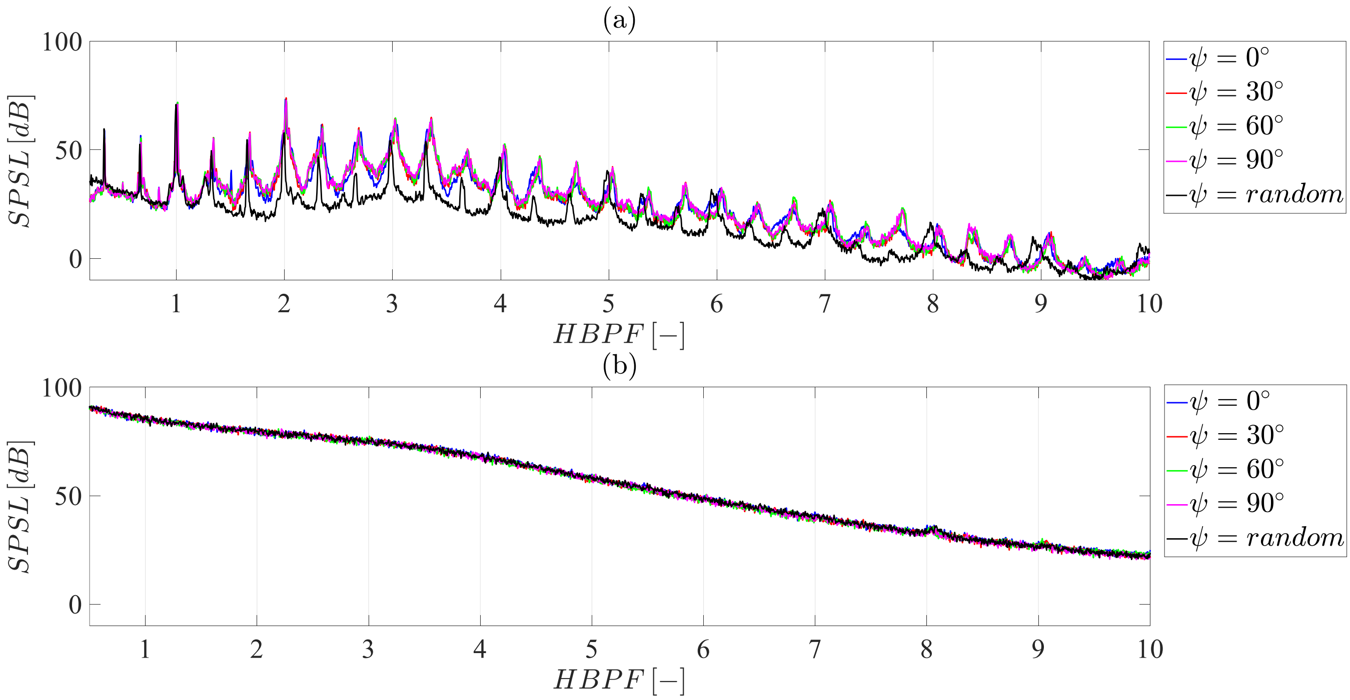


Figure 8: Spectral analysis of the pressure fluctuations time series, for the test case at 5200 RMP and d=409, acquired at two different polar angle: $\theta = 180°$ (a) and $\theta = 270°$ (b).

For the same time series on which the spectral analysis was performed, Probability Density Functions (PDF) were calculated as well. At 180°, the PDF obtained by phase randomisation results to be very different from the others (see Figure 9a), which have a similar shape to each other. Randomisation of the phase gives rise to a left tail indicating the presence of fluctuations of predominant negative amplitude. Phase randomisation, in the statistical sense, introduces fluid expansions that play a key role in mitigating interaction noise. In contrast, it can be seen that no statistical variation due to phase randomisation is introduced in the wake (see Figure 9b). The phenomenon of noise mitigation is therefore local and does not introduce significant effects in the slipstream.

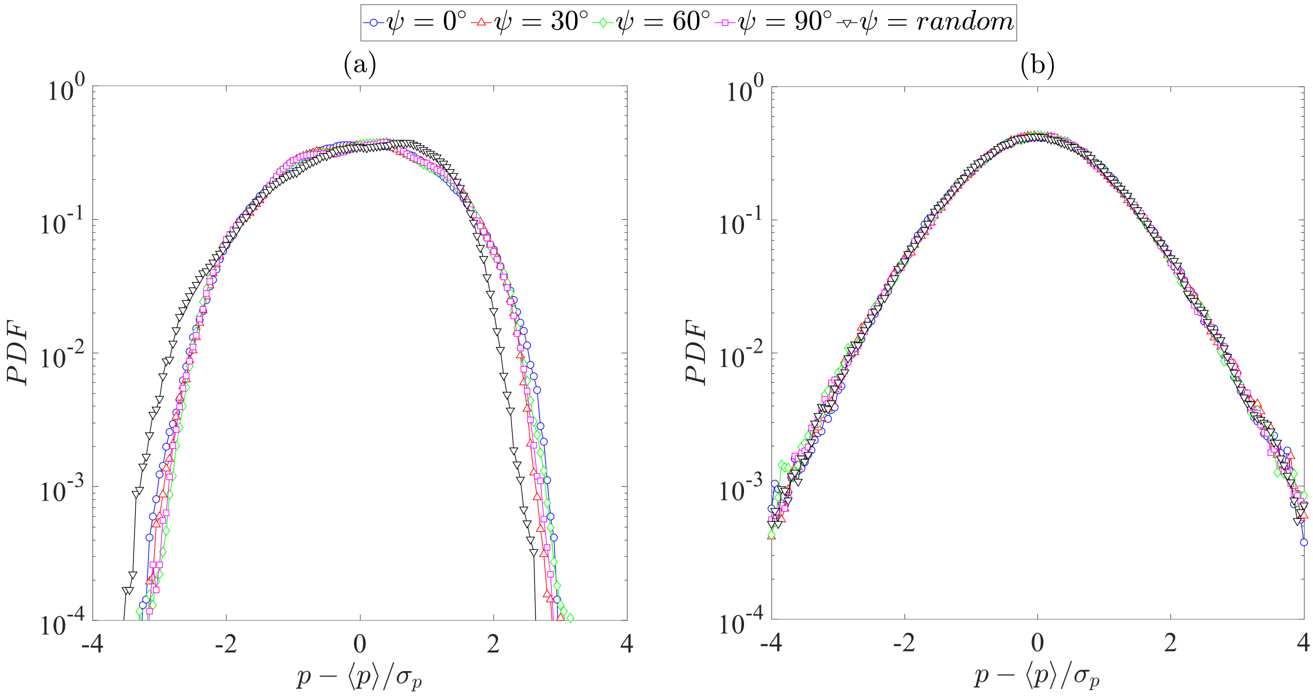


Figure 9: Probability density function of the pressure fluctuations time series, for the test case at 5200 RMP and d=409, acquired at two different polar angle: $\theta = 180°$ (a) and $\theta = 270°$ (b).

## 4. Conclusions

In this work, the noise generated by twin rotors for mini drone propulsion was investigated. The experimental study conducted by varying the speed, distance and phase of the propellers showed that the noise is influenced by all these parameters. An advanced phase control system allowed both to keep constant the rotor-rotor phase and to apply an active noise control technique using a phase randomisation strategy. The control technique developed is very effective when rotors are in close proximity giving a maximum noise mitigation of 8 dB. In addition, the control technique seems to work on both the tonal and the broad band component of the noise. It is also interesting to note that the statistical analysis reveals the presence of an important left tail in the PDF, which indicates the generation of pressure waves of negative amplitude, i.e. expansions, more likely than compression waves.

**References**


1. M Cherney. Delivery drones cheer shoppers, annoy neighbours, scare dogs. Wall Street Journal, 578, 2018.
2. Hakjin Lee and Duck-Joo Lee. Rotor interactional effects on aerodynamic and noise characteristics of a small multirotor unmanned aerial vehicle. Physics of Fluids, 32(4):047107, 2020.
3. Giorgia Sinibaldi and Luca Marino. Experimental analysis on the noise of propellers for small uav. AppliedAcoustics, 74(1):79–88, 2013.
4. Wenwu Zhou, Zhe Ning, Haixing Li, and Hui Hu. An experimental investigation on rotor-to-rotor interactions of small uav propellers. 35th AIAA applied aerodynamics conference, page 3744, 2017.
5. Charles E Tinney and Jayant Sirohi. Multirotor drone noise at static thrust. AIAA Journal, 56(7):2816–2826, 2018.
6. Zhongqi Jia and Seongkyu Lee. Acoustic analysis of urban air mobility quadrotor aircraft. In Vertical Flight Society (VFS) Aeromechanics for Advanced Vertical Flight Technical Meeting, 2020.
7. Zhongqi Jia and Seongkyu Lee. Impulsive loading noise of a lift-offset coaxial rotor in high-speed forward flight. AIAA Journal, 58(2):687–701, 2020.
8. Jeongwoo Ko, Jonghui Kim, and Soogab Lee. Computational study of wake interaction and aeroacoustic characteristics in multirotor configurations. In INTER-NOISE and NOISE-CON Congress and Conference Proceedings, volume 259, pages 5145–5156. Institute of Noise Control Engineering, 2019.